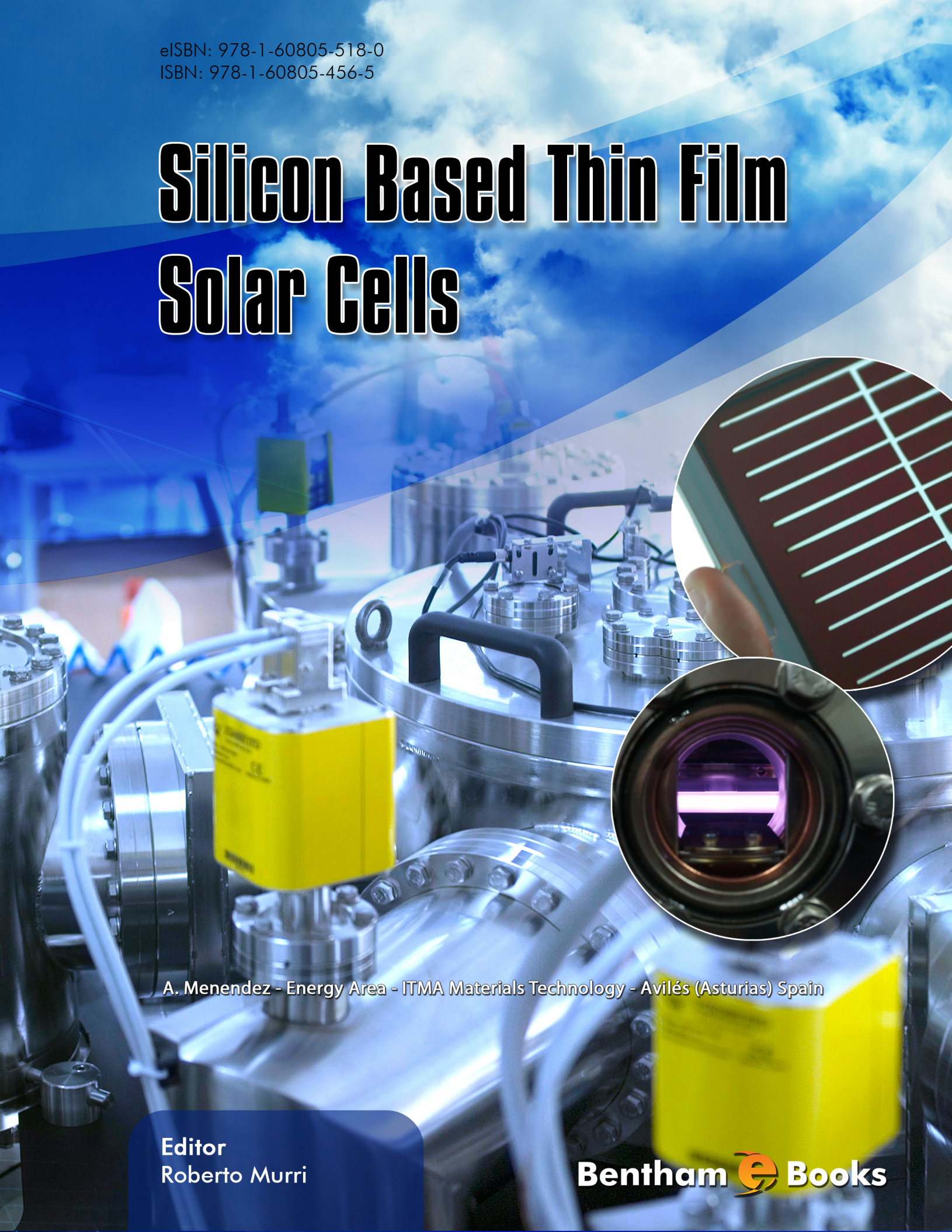
eISBN: 978-1-60805-518-0
ISBN: 978-1-60805-456-5

Silicon Based Thin Film Solar Cells



A. Menendez - Energy Area - ITMA Materials Technology - Avilés (Asturias) Spain

Editor
Roberto Murri

Bentham Books

Silicon Based Thin Film Solar Cells

Edited By

Roberto Murri

University of Camerino

School of Science and Technology

Physics Division

Italy

Bentham Science Publishers
Executive Suite Y - 2
PO Box 7917, Saif Zone
Sharjah, U.A.E.
subscriptions@benthamscience.org

Bentham Science Publishers
P.O. Box 446
Oak Park, IL 60301-0446
USA
subscriptions@benthamscience.org

Bentham Science Publishers
P.O. Box 294
1400 AG Bussum
THE NETHERLANDS
subscriptions@benthamscience.org

Please read this license agreement carefully before using this eBook. Your use of this eBook/chapter constitutes your agreement to the terms and conditions set forth in this License Agreement. This work is protected under copyright by Bentham Science Publishers to grant the user of this eBook/chapter, a non-exclusive, nontransferable license to download and use this eBook/chapter under the following terms and conditions:

1. This eBook/chapter may be downloaded and used by one user on one computer. The user may make one back-up copy of this publication to avoid losing it. The user may not give copies of this publication to others, or make it available for others to copy or download. For a multi-user license contact permission@benthamscience.org

2. All rights reserved: All content in this publication is copyrighted and Bentham Science Publishers own the copyright. You may not copy, reproduce, modify, remove, delete, augment, add to, publish, transmit, sell, resell, create derivative works from, or in any way exploit any of this publication's content, in any form by any means, in whole or in part, without the prior written permission from Bentham Science Publishers.

3. The user may print one or more copies/pages of this eBook/chapter for their personal use. The user may not print pages from this eBook/chapter or the entire printed eBook/chapter for general distribution, for promotion, for creating new works, or for resale. Specific permission must be obtained from the publisher for such requirements. Requests must be sent to the permissions department at E-mail: permission@benthamscience.org

4. The unauthorized use or distribution of copyrighted or other proprietary content is illegal and could subject the purchaser to substantial money damages. The purchaser will be liable for any damage resulting from misuse of this publication or any violation of this License Agreement, including any infringement of copyrights or proprietary rights.

Warranty Disclaimer: The publisher does not guarantee that the information in this publication is error-free, or warrants that it will meet the users' requirements or that the operation of the publication will be uninterrupted or error-free. This publication is provided "as is" without warranty of any kind, either express or implied or statutory, including, without limitation, implied warranties of merchantability and fitness for a particular purpose. The entire risk as to the results and performance of this publication is assumed by the user. In no event will the publisher be liable for any damages, including, without limitation, incidental and consequential damages and damages for lost data or profits arising out of the use or inability to use the publication. The entire liability of the publisher shall be limited to the amount actually paid by the user for the eBook or eBook license agreement.

Limitation of Liability: Under no circumstances shall Bentham Science Publishers, its staff, editors and authors, be liable for any special or consequential damages that result from the use of, or the inability to use, the materials in this site.

eBook Product Disclaimer: No responsibility is assumed by Bentham Science Publishers, its staff or members of the editorial board for any injury and/or damage to persons or property as a matter of products liability, negligence or otherwise, or from any use or operation of any methods, products instruction, advertisements or ideas contained in the publication purchased or read by the user(s). Any dispute will be governed exclusively by the laws of the U.A.E. and will be settled exclusively by the competent Court at the city of Dubai, U.A.E.

You (the user) acknowledge that you have read this Agreement, and agree to be bound by its terms and conditions.

Permission for Use of Material and Reproduction

Photocopying Information for Users Outside the USA: Bentham Science Publishers grants authorization for individuals to photocopy copyright material for private research use, on the sole basis that requests for such use are referred directly to the requestor's local Reproduction Rights Organization (RRO). The copyright fee is US $25.00 per copy per article exclusive of any charge or fee levied. In order to contact your local RRO, please contact the International Federation of Reproduction Rights Organisations (IFRRO), Rue du Prince Royal 87, B-I050 Brussels, Belgium; Tel: +32 2 551 08 99; Fax: +32 2 551 08 95; E-mail: secretariat@ifrro.org; url: www.ifrro.org This authorization does not extend to any other kind of copying by any means, in any form, and for any purpose other than private research use.

Photocopying Information for Users in the USA: Authorization to photocopy items for internal or personal use, or the internal or personal use of specific clients, is granted by Bentham Science Publishers for libraries and other users registered with the Copyright Clearance Center (CCC) Transactional Reporting Services, provided that the appropriate fee of US $25.00 per copy per chapter is paid directly to Copyright Clearance Center, 222 Rosewood Drive, Danvers MA 01923, USA. Refer also to www.copyright.com

CONTENTS

Foreword *i*

Preface *iii*

List of Contributors *v*

Introduction *vii*

CHAPTERS

SECTION I - THIN FILM SOLAR CELLS: GENERAL ASPECTS AND DEPOSITION TECHNIQUES

1. Basics of Thin Film Solar Cells **3**
Marco Ficcadenti and Roberto Murri

2. Deposition of Thin Films: PECVD Process **29**
Armando Menéndez, Pascal Sánchez and David Gómez

3. Sputtering of Thin Films **58**
Paolo Rava

4. Molecular Beam Epitaxy (MBE) **81**
Lorenzo Morresi

SECTION II - EXPERIMENTAL TECHNIQUES TO MEASURE FILM AND DEVICE PARAMETERS

5. Infrared and Raman Spectroscopies **108**
Ubaldo Coscia, Deepak K. Basa and Giuseppina Ambrosone

6. Morphological and Structural Properties **146**
Angelica M. Chiodoni and Elena Tresso

7. Optical Properties of Semiconductors **177**
Marian Nowak

8. Electrical Properties of Semicoductors **243**
Nicola Pinto, Marco Ficcadenti and Lorenzo Morresi

SECTION III - PHOTOVOLTAIC DEVICES

9. Heterojunction for Silicon Photovoltaics **277**
Mario Tucci, Luca Serenelli, Massimo Izzi, Enrico Salza, Simona de Iuliis, Pietro Mangiapane, Giampiero de Cesare and Domenico Caputo

10. Micromorph Cells **359**
Maurizio Acciarri

11. Light Trapping in Thin Silicon Solar Cells **395**
Mario Tucci, Luca Serenelli, Simona de Iuliis, Domenico Caputo and Giampiero de Cesare

Index **474**

FOREWORD

For eons, Earth's water was allowed to fall naturally from mountains to seas, converting vast stores of potential energy primarily and wastefully into heat. The discovery of methods to put water power to use in mills of various sorts led eventually to its industrial exploitation on a grand scale in the eighteenth and nineteenth centuries. With the discovery of electricity, the power of falling water led to hydroelectric generation in the nineteenth and twentieth centuries, culminating in today's huge enterprises at Itaipu in Brasil (14 GW) and Three Gorges in China (22.5 GW).

Similarly, today we allow much of the Sun's solar insolation (800 watts per square meter, peak), mostly in the form of infrared radiation, to fall unproductively onto Earth as heat, adding to the already worrisome heat burden of the Planet. Thus, analogous to earlier experience with falling water, it behooves one to utilize at least part of this infrared radiation productively, to create the useful artifacts of civilization, before depositing a lesser amount of it on the Planet as heat.

Solar photovoltaic energy conversion addresses precisely this goal, in the form of photovoltaic cells made of various semiconductor materials, of which silicon is predominant. Thin films of silicon used for the construction of solar photovoltaic cells comprise the focus of the present volume.

One might do well to take a "top-down" view of one of the semiconductor materials challenges of solar photovoltaic energy conversion on a massive scale, to gather an overall sense of the magnitude of the endeavor. For this purpose, we may posit a few simple estimates, which leads to the scope of the issue at hand. To wit, there are 7 billion human inhabitants on Earth. Insofar as there is a general and historical movement toward improved standards of living, including electrical energy usage at a fully loaded, annual average level of about one kilowatt per person, and about 1% per year of the population experiences this relative advancement, there is an estimated need for 60 GW of additional electrical energy generating capacity worldwide each year.

It would be a pleasant environmental happenstance to have a significant fraction of this 60 GW arise from solar photovoltaic energy conversion, say 10 GW. However, due to diurnal effects, cloud cover, solar cell conversion efficiency, and so on, a useful estimate is that one square meter of solar cells (unconcentrated) provides an average of 25W of electrical power as an annual average. Therefore, 10 GW implies 400 million square meters annual production of solar cell materials. Due to the relatively small infrared absorption coefficient of silicon, the thickness of the silicon thin film must be at least about 40 microns.

Combining the above numbers, 4×10^{8} m^2 and 4×10^{-5} m, one finds that the annual production rate of photovoltaic silicon must be around 37,000 tonnes. While this may seem a daunting figure for a nascent enterprise, it does not greatly exceed current world-wide production of single-crystal silicon for electronics applications, generally.

Thus, one is led to conclude that impressive levels of production of thin-film photovoltaic silicon will be necessary if the enterprise is to succeed, giving cause to pay special attention to such large-area deposition methods as chemical vapor deposition (CVD) and its plasma variants, as well as

the proven large-area method of choice, physical vapor deposition (PVD, or sputtering), which among others are well treated in the present volume.

Stepping back from the above grand overview, and observing a related technology, one cannot help but be impressed by the magnificent improvements wrought by the use of compositional heterostructure technology for photovoltaic cells in the case of the rather expensive compound semiconductors, which is their drawback. Alternatively, structural (as opposed to *compositional*) heterostructure technology is well-established in high-frequency low-noise compound semiconductor transistor technology. Unfortunately, Mother Nature's periodic table of the elements leaves silicon with a relatively paltry offering consisting primarily of carbon and germanium for compositional heterostructure technology. However, as is discussed in this volume, silicon does allow a myriad of possibilities for *structural* heterostructure technology, with silicon in its microcrystalline and amorphous states.

The microcrystalline forms of silicon exhibit increased energy gaps so that band-gap engineering may be usefully possible, *i.e.* heterostructure technology. Solid-state theorists are rather far behind the front lines of this initiative and their assistance might be helpful. Perhaps a hint could be offered? Pauling showed long ago ("The Nature of the Chemical Bond") that dangling bonds, such as are widespread in microcrystalline silicon, cause strengthening of back-bonds and contraction of interatomic bond lengths. This type of behavior has also been observed for the near-surface atomic layers of semiconductors. However, reduced interatomic bond length in semiconductor structures causes increased energy band gap. Therefore, there may be an essential interplay between the grain size of microcrystalline silicon (for grain sizes comparable to the de Broglie wavelength) and energy band gaps, notwithstanding Tamm states and deep-trap recombination.

There is ample opportunity here to do good for humanity and the environment, as well as to advance the solid-state and materials sciences. Further great work needs to be accomplished on a grand scale, comprising the microscopic nature of thin-film silicon and its myriad device possibilities, its commercial production on an impressive scale, and its insertion into the marketplace.

One can clearly see that there is an ongoing need for educational materials to advance the state of the art, and editor Professor Murri and his colleagues who have written this volume provide us with an important and generous contribution in this regard, for which we are grateful.

Daniel L. Rode

Shangri-La, Paraná-Brazil &
Washington University in St. Louis
USA

PREFACE

Thin film silicon solar cells present all the basic physical pre-conditions for a successful development of the next generation of low cost, high efficiency photovoltaic devices, capable to fulfill the needs of a future Green Energy Society.

Their industrial development still presents, however, a number of problems associated to the diverse nature of these devices, with respect to the today generation of solar cells based on the use of crystalline silicon. In fact, here a multidisciplinary micro- and nano-technological approach is requested, applied to thin film modellization, large scale deposition, material characterization and solar cells fabrication, paying attention, as well, to quanto-mechanical issues, whose full application will only allow to go above the classical Shockley and Queissser limit of photovoltaic efficiency.

While the physics and engineering of crystalline silicon solar cells is covered by the content of a relevant number of Handbooks and Textbooks, the same does not apply to thin film solar cells, and this is the main reason why the publication of this eBook seems appropriate to supply, on time, to the absence. It is intended for non-specialists, i.e. for graduate and PhD students with a sufficient background in solid-state physics as well as for professional physicist and engineers who are not fully familiar with all the aspects of thin film technology, but who might be potential contributors to the development and industrialization of this opportunity. This eBook critically covers, in fact, in its three Sections all the main aspects of thin film solar cells physics and engineering and is co-authored by recognized experts in the field, whose view is not at all a personal view, but reflects the state of the art of the field and the opinion of the international thin film community.

Section I contains four Chapters describing, respectively, the basic elements of thin film solar cells (Ch.1) and deposition of thin films by: Ch.2, plasma enhanced chemical vapor deposition (PECVD), sputtering (Ch.3) and, finally, Ch.4, molecular beam epitaxy (MBE).

Experimental techniques to measure film and device parameters are discussed in the four Chapters of Section II. In details, Infrared and Raman spectroscopies (Ch. 5), Morphological and structural properties (Ch.6), while Ch.7 and Ch. 8 present how to measure optical and electrical parameters, respectively.

The last three Chapters of Section III discuss the physics of two classes of devices, Heterojunctions for silicon photovoltaics (Ch. 9) and Micromorph cells (Ch.10), widely studied as structures able to improve the conversion efficiency of a solar cell. Finally, Ch.11 underlines the role of light trapping increasing the capture of solar radiation and then, again, the conversion efficiency.

I would like to thank all Authors, Prof. Daniel Rode for writing the Foreword, Prof. Sergio Pizzini for his Introduction discussing the general aspects of the subject of the eBook, Mrs. Lisa Kramer Taruschio for language revision of Chapters 1,4,7 and 8 and Bentham Science Publishers, in particular Mrs. Salma Sarfaraz for her support, efforts and patience. The University of Camerino - School of Science and Technology, togheter with Elena Tresso -DISAT, Department of Applied

Science and Technology, Politecnico di Torino, and Maurizio Acciarri - Department of Materials Science and Solar Energy Research Center (MIBSOLAR) Università degli Studi Milano Bicocca, partially supported the publication costs of the eBook for its open access.

Roberto Murri

University of Camerino
School of Science and Technology
Physics Division
Italy

List of Contributors

Angelica M. Chiodoni Center for Space Human Robotics (CSHR@POLITO), Italian Institute of Technology, Corso Trento 21, Torino, IT-10129, Italy.

Armando M. Estrada Energy Area, ITMA Materials Technology, Parque Empresarial P.E.P.A., c/Calafates 11, Parcela L.3.4, 33417, Avilés (Asturias) Spain.

David Gómez Energy Area, ITMA Materials Technology, Parque Empresarial P.E.P.A., c/Calafates 11, Parcela L.3.4, 33417, Avilés (Asturias) Spain.

Dipak K. Basa Department of Physics, Utkal University, Bhubaneswar-751004, India.

Domenico Caputo DIET Department of Information, Electronics and Telecommunication Engineering, University of Rome "Sapienza, Via Eudossiana 18, 00184 Rome, Italy.

Elena Tresso DISAT, Dipartimento di Scienza Applicata e Tecnologia, Politecnico di Torino, Corso Duca degli Abruzzi 24, 10129 Torino, and Center for Space Human Robotics (CSHR@POLITO), Italian Institute of Technology, Torino Italy.

Enrico Salza ENEA, Research Center Casaccia, Via Anguillarese 301, 00123 Roma Italy.

Giampiero de Cesare DIET Department of Information, Electronics and Telecommunication Engineering, University of Rome "Sapienza, Via Eudossiana 18, 00184 Rome, Italy.

Giuseppina Ambrosone Department of Physical Sciences, University of Naples "Federico II", Complesso Universitario MSA, Via Cintia, 80126 Napoli, Italy and CNR-SPIN, Complesso Universitario MSA, Via Cintia, 80126 Napoli, Italy.

Lorenzo Morresi School of Science and Technology, Physics Division, University of Camerino, Via Madonna delle Carceri, 9-62032 CAMERINO (MC) Italy.

Luca Serenelli ENEA, Research Center Casaccia, Via Anguillarese 301, 00123 Roma Italy.

Marco Ficcadenti School of Science and Technology, Physics Division, University of Camerino, Via Madonna delle Carceri, 9-62032 Camerino (MC) Italy, now at CESI Spa,Via Rubattino 54, 20134 Milan, Italy.

Marian Nowak Institute of Physics, Silesian University of Technology, 8 Krasińskiego, Katowice, PL-40019, Poland.

Mario Tucci ENEA, Research Center Casaccia, Via Anguillarese 301, 00123 Roma Italy.

Massimo Izzi ENEA, Research Center Casaccia, Via Anguillarese 301, 00123 Roma Italy.

Maurizio Acciarri Department of Materials Science and Solar Energy Research Center (MIB-SOLAR,)Università degli Studi Milano Bicocca, Via Cozzi, 53-20125 Milan, Italy.

Nicola Pinto School of Science and Technology, Physics Division, University of Camerino, Via Madonna delle Carceri,9-62032 Camerino (MC) Italy.

Pascal Sánchez Energy Area, ITMA Materials Technology, Parque Empresarial P.E.P.A., c/Calafates 11, Parcela L.3.4, 33417, Avilés (Asturias) Spain.

Pietro Mangiapane ENEA, Research Center Casaccia, Via Anguillarese 301, 00123 Roma Italy.

Roberto Murri University of Camerino, School of Science and Technology, Physics Division, Via Madonna delle Carceri 9, 62032 Camerino (MC) Italy.

Paolo Rava Elettrorava SpA, Via Don Sapino 176, 10078 Venaria, Torino, Italy.

Sergio Pizzini Department of Materials Science, Università degli Studi Milano Bicocca, Via Cozzi, 53-20125 Milan, Italy.

Simona de Iuliis ENEA, Research Center Casaccia, Via Anguillarese 301, 00123 Roma Italy.

Ubaldo Coscia CNISM Naples Unit, Complesso Universitario MSA, Via Cintia, 80126, Napoli, Italy and Department of Physical Sciences, University of Naples "Federico II", Complesso Universitario MSA, Via Cintia, 80126 Napoli, Italy.

INTRODUCTION

Sergio Pizzini*

University of Milano-Bicocca, Department of Materials Science, Via Cozzi, 53-20125, Milano, Italy

Abstract: This short introduction presents the general situation of photovoltaic conversion, with emphasis on possible use of thin film solar cells.

This work is intended as a textbook which deals with thin films technologies and device structures for silicon based photovoltaic applications. Therefore, the focus of the eBook is to present an overview of the deposition and characterization methods of thin film silicon solar cells. These kinds of cells can make photovoltaic power production more economically viable than to crystalline silicon cells, contributing to a major expansion of the related market. In fact, nowadays about 90% of solar cells are manufactured from crystalline Si substrates with a typical thickness of about 0.2 mm but which are still expensive to produce, although extremely efficient. To reduce these costs, a transition from bulk crystalline Si solar cells to thin-film technologies, with both reduced usage of active material in the device and the introduction of new technological concepts such as nanotechnologies, might be the ultimate solution. Despite their importance, the scientific development and understanding of new solar cell concepts are not very advanced, and the education of specialized engineers and scientists has not even started. The primary reason for this is the multidisciplinary nature of thin film growth technology. Other reasons for the lack of development and recognition are the complexity of the multi-parameter growth processes, the complex phase transformation from the precursor's liquid or gaseous phase toward a solid one, and the scaling problem with the required growth-interface control on the nanomicrometer scale within growth systems of micrometer scale.

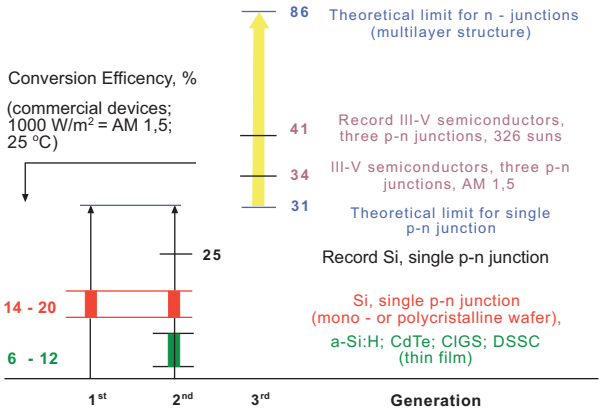


Figure 1: Summary of the efficiency values for different types of solar cells classed by generation. Data are taken from: Solar cell efficiency Tables (Version 38), M. A. Green, K. Emery, Y. Hishikawa, W. Warta and E. D. Dunlop, Prog. Photovolt: Res. Appl. 2011; 19:565–572. Published online in Wiley Online Library (wileyonlinelibrary.com). DOI: 10.1002/pip.1150

***Address correspondence to Sergio Pizzini:** Department of Materials Science, Università degli Studi Milano Bicocca, Via Cozzi, 53-20125 Milan, Italy; Email: sergio.pizzini@mpvresearch.eu

Therefore, the text is designed to provide much needed information on the fundamental scientific aspects of thin films growth technologies, as well as a clear understanding of the properties of the material and how it is employed in new generation photovoltaic solar cells.

The following Table **1** (M.Tao, The Electrochemical Society Interface, vol. 17, no. 4, pp. 30-5 (2008)) summarizes all the main properties and requirements of materials suitable for terrestrial photovoltaic conversion.

Table 1: Material requirements for terrestrial solar cells (reproduced by permission of ECS-The Electrochemical Society)

Material Requirement		Material Meeting Requirement
1.	Abundant material	Si
2.	Low-cost material	CdTe, CIGS
3.	Low-cost synthesis	CdTe, CIGS
4.	Non-toxic material	Si, CIGS
5.	Stable material	Si, III-V, CdTe, CIGS
6.	High mobility	Si, III-V, CdTe, CIGS
7.	High carrier lifetime	Si, III-V
8.	Suitable band gap	III-V, CdTe, CIGS
9.	Control of conduction type	Si, III-V, CdTe, CIGS
10.	Control of resistivity	Si, III-V, CdTe, CIGS

As one can see in the Table, there is not one “winning” material, but a plurality of materials, all suitable for photovoltaic (PV) devices, even if with differing fields of applicability.

While early in the PV age solar cells built on silicon wafer controlled the market, its today's market sharing is presented in Fig. **2**, where it is shown that thin film materials already play a significant role into the market, which is forecast to overcome that of silicon in the next decade.

Among materials suitable for thin film applications, the III-V compound semiconductors (GaAs, InP, and their alloys or compounds), even if nearly ideal due to their direct bandgap, remain too expensive for large scale terrestrial applications and are mainly used for concentration applications. Their high costs are determined by the chemical precursors required for deposition and by the sophisticated deposition techniques (Molecular Beam Epitaxy, MBE or Metalorganic Chemical Vapour Deposition, MOCVD).

II-VI compound semiconductors (Cadmium Telluride, CdTe or Copper Indium Diselenide, $CuInSe_2$ or similar), which share a consistent fraction of the thin film market, allow for tailoring the bandgap, the optimization of the optical absorption and the design of multijunction solar cells. Thin films of these materials can be easily deposited with passivated grain boundaries and then with low recombination rates for excess carriers.

The content of this eBook is limited to solar cells based on silicon thin film, the main reason for this choice being the environmental friendship of silicon and the almost unlimited source of silicon

precursors in the earth crust. It should be noted that thin films of crystalline silicon need to improve their optical absorption properties by using nanotechnologies to insert into the structure of the PV device optical active layers with modified physical properties. This point will be a prominent part of the future research in the field of thin film crystalline Si.

The general intent of the eBook is to provide the basic elements and the reasons for this choice, discussing the fundamental aspects of silicon thin films suitable for solar radiation conversion.

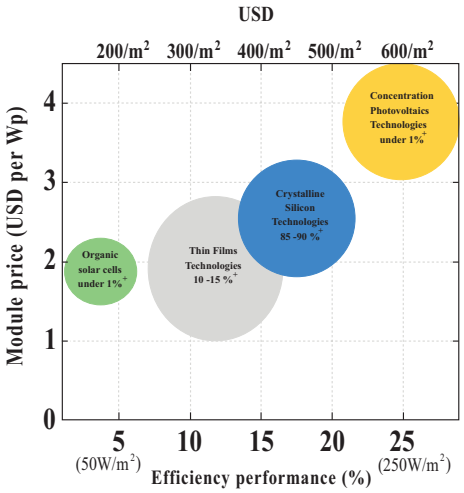


Figure 2: Sharing of the PV market among different technologies of PV cells. All values refer to 2008. * percentage share of 2008 market. Reproduced from IEA International Energy Agency-Technology Roadmap-Solar photovoltaic energy (2010), www.iea-pvps.org

All this to give the core subjects to deposit and to characterize thin films suitable to design and to produce structures able to improve the conversion efficiency of the solar radiation.

This last is the main objective, to be achieved by the study and selection of a multiplicity of possible solutions based on inorganic and/or organic materials. While it is likely that many of these solutions could lead to efficient devices, the differences among them will be generated by the technologies employed and by how these can be transferred to an industrial production process, if we like to use extensively photovoltaic conversion for mass energy production.

In this context, the “third generation” photovoltaics will utilise new concepts to design and new technologies to produce high efficiency devices. It is reasonable to expect that within the next 10-15 years, photovoltaics will move to third generation devices with a significant cost reduction. It is difficult to define values for competitive solar energy, which depends on the scenario proposed for the future of fossil fuels. However, if we correctly assume that this cannot be the only parameter for the evaluation and decision-making regarding the use of the PV energy, the PV costs must be considered together with the efficiency in a larger technical, environmental and political picture.

Very good reviews discussing the physics and the problems of photovoltaics cells can be found in:

Nelson, J. The physics of solar cells. London: Imperial College Press 2003; Aberle AG. Thin-film solar cells. Thin Solid Films 2009; 517: 4706–10; Markvart T. Castañer L. (Eds). Practical Handbook of Photovoltaics: Fundamentals and Applications. Oxford: Elsevier 2006; Boreland MB, Bagnall DM. Current and future photovoltaics. Foresight 2006; 1-21. Available at: http://eprints.ecs.soton.ac.uk/14403/; Shah A. (Ed). Thin-Film Silicon Solar Cells. Lausanne: EPFL Press 2010; and Poortmans J. Arkhipov V. (Eds). Thin Film Solar Cells: Fabrication, Characterization and Applications. Chichester, UK. John Wiley and Sons, Ltd 2006.

SECTION I - THIN FILM SOLAR CELLS: GENERAL ASPECTS AND DEPOSITION TECHNIQUES

Send Orders of Reprints at reprints@benthamscience.net
Silicon Based Thin Film Solar Cells, 2013, 3-28 3

CHAPTER 1

Basics of Thin Film Solar Cells

Marco Ficcadenti[*,+] **and Roberto Murri**

University of Camerino, School of Science and Technology, Physics Division, Via Madonna delle Carceri 9, Camerino, 62032, Italy

Abstract: The chapter presents a short review of the general principles of photovoltaic conversion and different types of thin films solar cells. The aim is to present how a device can evolve from the classical Si *p-n* junction, with its physical constraints limiting the conversion efficiency, to devices where higher absorption of the light and improved structural design result in higher conversion efficiency. It is now well recognized that these devices have to be based on thin film structures. As a consequence, we have to be able to design the whole stacked thin film structure, and within this, each film must be deposited with well-defined properties. Several deposition techniques can be used, and we will shortly discuss the so-called Plasma Enhanced Chemical Vapour Deposition (PECVD), considering the evolution of the film structure.

Keywords: Solar cells, thin films, silicon, microcrystalline, protocrystalline, amorphous, cadmium telluride, copper indium diselenide, PECVD, CVD, sputtering, p-n junction solar cells, solar energy conversion, conversion efficiency, electron-hole pair, antireflection coating, light absorption, energy gap, photon energy, parasitic resistance, stacked cell, graduated band gap, thin film structure, protocrystalline film, density of states (DOS), deposition parameters, dilution ratio, crystal nucleation, growth mechanisms, thin film hydrogenation, light soaking.

1. INTRODUCTION

The production of solar cells was and is still based mainly on crystalline silicon wafers holding about 81% of the photovoltaic world market [1]. Despite that, the wafer based technology is seen as a limiting factor for the growth of the market.

The development and the time duration of a diffused photovoltaic market requires that solar cells have higher conversion efficiencies and lower costs than actual devices (cells and modules). Much research and many technological efforts have been carried out to attempt to reduce the thickness of the silicon wafers. Sanyo has been able to produce HIT (heterojunction with intrinsic thin layer) cells on about 70 μm thick wafer, compared with about 180 μm of normal production p-n junction cells [2].

Other attempts have been made using the so-called transfer [3] and silicon ribbon technologies [4]. In the former instance, the complexity of the technology can be a deterrent for the mass production of solar cells, even if relatively high conversion efficiencies are present [5]. In principle, silicon ribbon can be used to develop on-line production, with a strong reduction of costs [3, 4, 6].

In this chapter and in the eBook as well, we will focus mainly on a discussion of thin film silicon (Si) technology. However, other materials are now being used for low cost photovoltaic. In particular, Cadmium Telluride, CdTe) [7] and Copper Indium (Gallium) Selenide, $CuIn(Ga)Se_2$ (CI(G)S), seem to

[*]**Address correspondence to Marco Ficcadenti:** CESI SpA,Via Rubattino 54, 20134 Milan, Italy; Tel: +39 221255183; E-mail: marco.ficcadenti@cesi.it
[+]Now at CESI SpA, Via Rubattino 54, 20134 Milan, Italy

Roberto Murri (Ed)
All rights reserved-© 2013 Bentham Science Publishers

be very promising, thanks in part to the considerable research carried out and technology investments made over many years. For the most part, First Solar is pushing for CdTe realm [8]. Different structures are involved in CI(G)S solar cell research and technology development [9, 10].

Starting from the broad experience of research on amorphous silicon, many ideas are being tested, the common goal being high conversion efficiency and low cost per W_p. The base material is nano-crystallized silicon (nc-Si), while the cell device combines nc-Si with amorphous silicon (*a*-Si) in different junction structures (tandem, micro-morph, and multiple junctions).The focal point is the ability to control the physical properties of the deposited silicon thin films. In fact their features must be suitable for the role that each functional layer carries out in the whole solar structure. This means that we have to modulate deposition parameters in order to obtain given structural and physical properties of each layer. In particular, the "crystallinity" of the film must span a wide range reaching from amorphous to micro-crystalline material. Ample work has been done on the evolution of crystallinity [11-15]. Werner and Bergman operatively defined three possible categories of thin silicon solar cells [16]:

1) Thin film solar cells built with nano-or micro-crystalline silicon films. Deposition is made on glass with different techniques, but mainly with Plasma Enhanced Chemical Vapour Deposition (PECVD) to form p-i-n structures, heterojunction or tandem cells. This technique can be implemented in an on-line process.

2) Thick silicon layers deposited on different substrates, suitable for the re-crystallization process. Cells are formed with classical p-n design or by epitaxial growth of stacked layers.

3) Growth of an epitaxial layer on mono crystalline silicon substrate and bonding of the film on glass substrate, after it is separated from silicon wafer.

In this chapter we will discuss some physical properties of silicon thin films deposited by PECVD, with the film structure as the leading parameter [17].

We begin with a consideration of amorphous structures and progress by increasing the crystallinity of the film, to end with polycrystalline films. We will try to demonstrate how to obtain the desired properties of the material through precise control.

2. *p-n* JUNCTION SOLAR CELLS

We will shortly review the basic concepts of solar energy conversion using a silicon *p-n* junction solar cell [18-20].

A solar cell is an electronic device which directly converts sunlight into electricity. Light shining on the solar cell produces both a current and a voltage to generate electric power. This process requires first, a material in which the absorption of light raises an electron to a higher energy state, and second, the movement of this higher energy electron from the solar cell into an external circuit. The electron then dissipates its energy in the external circuit and returns to the solar cell.

In principle, a variety of technologies using different materials and processes can satisfy the requirements for photovoltaic conversion. In practice nearly all photovoltaic devices need an internal electric field leading to the separation of the photogenerated charge carriers (electrons and holes).

At the present time, the conversion devices use, for the most part, semiconductor materials in the form of a p-n junction.

The general design pattern scheme of a crystalline silicon solar cell based on a p-n junction is shown in Fig. **1**. To date, this structure has been commonly built using mono or poly crystalline silicon wafers, 200-300 micron thick [20, 21].

The electrical contact layer on the front of the cell where light enters is a metallic grid pattern designed to minimize the covering of the surface of the cell but to maximize the photogenerated carrier collection.

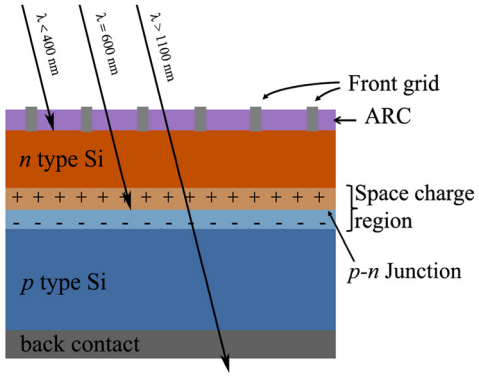


Figure 1: Structure of a standard p-n junction solar cell.

Specialized simulation software allows for striking a balance between two opposite needs. The grid pattern must be widely spaced to allow light to enter the solar cell, but not to the extent that fingers have difficulties collecting the current produced by the cell. These restrictions do not apply to the rear metallic contact layer, which need function only as an electrical contact and thus cover the entire back surface of the cell. To improve the conversion efficiency of a solar cell, the amount of reflected light (about 30 %), must be minimized [19, 20]. To increase the amount of light absorbed by the cell, an antireflection coating (ARC) is typically applied on the front surface [22].

Today silicon nitride is commonly used as ARC due to its functional optical properties and, in addition, to its excellent surface passivation properties which prevent carrier recombination at the surface of the solar cell [23-25]. Silicon nitride is typically deposited in the shape of a thin layer (about 70 nanometres) using PECVD [22, 25-27].

The photons of the radiation incident on the surface of a semiconductor can be either reflected from the top surface or absorbed into the material. Failing these two processes, they are

transmitted through the material. If the photon is absorbed, it will raise an electron from the valence band to the conduction band. For photovoltaic devices, reflection and transmission are typically considered loss mechanisms because photons that are not absorbed do not generate free carriers.

The key factor in determining if a photon is absorbed or transmitted is its energy, E_{ph}, and its relationship with the energy gap, E_g, of the semiconductor material.

The three possibilities are shown in Fig. **2**:

1) $E_{ph} < E_g$: photon interacts only weakly with the semiconductor, passing through it;

2) $E_{ph} = E_g$: photon has the right energy to create an electron-hole pair and is then efficiently absorbed;

3) $E_{ph} > E_g$: photon moves the electron to the conduction band, leaving a hole in the valence band. The electron-hole pair releases energy greater than Eg as heat, and releases the electron-hole energy, $E_{e\text{-}h}=E_g$ to the band edges.

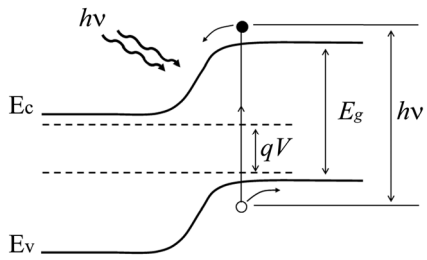


Figure 2: Energy diagram of a *p-n* junction under illumination.

The electrical equivalent circuit of a solar cell is a current generator in parallel with an asymmetric, nonlinear resistive element, *i.e.* a diode (see Fig. **3**).

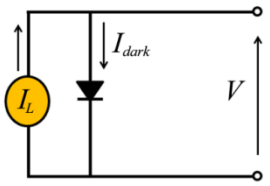


Figure 3: Equivalent circuit of an ideal solar cell.

The current voltage relationship of a p-n junction diode in the dark is given by [18-20]:

$$I_{dark} = I_o(e^{qV/nkT} - 1), \quad \textbf{(1)}$$

while under illumination the ideal current-voltage characteristic is given by:

$$I = I_o(e^{qV/nkT} - 1) - I_L \quad \textbf{(2)}$$

where I_L is the light generated current, I_0 is the dark saturation current of the diode, n is the ideality factor (typically in the range 1 to 2), q is the electronic charge, k the Boltzmann's constant and T is the temperature in degrees Kelvin.

Fig. **4** plots the current-voltage (I-V) characteristic for a solar cell in dark conditions (see the curve a).

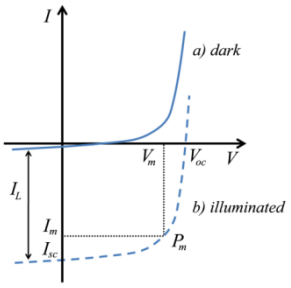


Figure 4: Current-voltage characteristic of ideal solar cell in the light and the dark.

Curve b) in Fig. **4** shows the I-V characteristic of the illuminated device, shifted in the fourth quadrant, where the device can generate electrical power.

Usually this curve is presented reflected around the voltage axis as shown in Fig. **5**. Ideally the short circuit current I_{sc} is equal to the light generated current I_L.

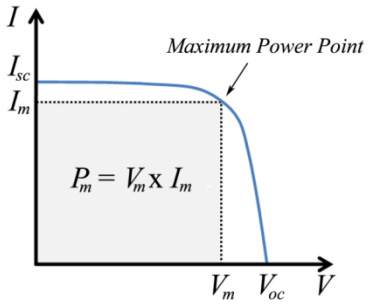


Figure 5: Output characteristic of a solar cell as normally plotted.

Setting I to zero in Eq. **2**, gives the open circuit voltage V_{oc}:

$$V_{oc} = \frac{nkT}{q} \ln\left(\frac{I_L}{I_0} + 1\right) \quad \textbf{(3)}$$

The voltage operating regime of the solar cell is the range from 0 to V_{oc}, in which the cell can supply power to an external load. The output power is given by:

$$P = V \times I \quad \textbf{(4)}$$

P reaches a maximum at the cell's operating point or maximum power point. This occurs at a well-defined point with coordinates V_m-I_m (Figs. **4** and **5**), defining the optimum resistive load as V_m/I_m.

A working parameter for solar cells is the Fill Factor, *FF*, defined as:

$$FF = \frac{I_m V_m}{I_{sc} V_{oc}} \quad \textbf{(5)}$$

It measures how P_m covers the ideal power given by $I_{sc}V_{oc}$. In practice, it is a measure of how "square" the output characteristics are. The conversion efficiency η of a solar cell is the power delivered to the operating point as a fraction of the incident light power P_{in},:

$$\eta = \frac{I_m V_m}{P_{in}} \quad \textbf{(6)}$$

Conversion efficiency relates to I_{sc} and V_{oc} using FF,

$$\eta = \frac{I_{sc} V_{oc} FF}{P_{in}} \quad . \quad \textbf{(7)}$$

The four quantities I_{sc}, V_{oc}, *FF*, and η are the key parameters for defining energy conversion performances of a solar cell, and should be given for well-defined illumination conditions. The Standard Test Condition (STC) for solar cells is the Air Mass 1.5 spectrum, an incident power density of 1000 W/m^2 and temperature of 25 °C [28, 29].

2.1. Effect of Parasitic Resistances

Resistive effects in real solar cells reduce efficiency by dissipating power in the resistances. The most common parasitic resistances are series resistance (R_s) and shunt resistance (R_{sh}).

The inclusion of the series and shunt resistance on the solar cell equivalent circuit is shown in Fig. **6**.

Series resistance derives from three causes: i) the movement of carriers through the emitter (*n* type zone) and base (*p* type zone) of the solar cell; ii) the interface between metallic contact and silicon; and iii) the resistance of the metallic films used for both top grid and rear contacts.

The main impact of series resistance is to reduce the fill factor; excessively high values may also reduce the short-circuit current. Significant power losses caused by the presence of shunt resistance are typically due to manufacturing defects, rather than poor solar cell design. Low shunt

resistance causes power losses in solar cells because it provides an alternative current path for the light-generated current. Such a diversion reduces the amount of current flowing through the solar cell junction and reduces the voltage of the solar cell. The looping effect of shunt resistance is particularly severe at low light levels. The light-generated current diminishes and the loss of this current to the shunt therefore has greater impact. In addition, at lower voltages where the effective resistance of the solar cell is high, the impact of parallel resistance is relatively larger.

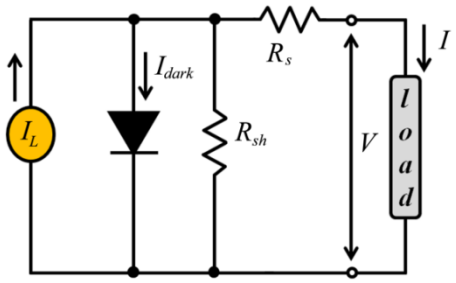


Figure 6: Equivalent circuit including series and shunt resistance.

Including the parasitic resistances the current voltage equation is given by [19, 20]:

$$I = I_L - I_0 \left\{ e^{\left[\frac{q(V+R_s I)}{nkT}\right]} - 1 \right\} - \frac{V + R_s I}{R_{sh}}. \quad \textbf{(8)}$$

3. FROM VOLUME TO THIN FILM SOLAR CELL

Recent research and technological developments tend to broaden the realm of photovoltaic devices, adding to the classical silicon wafer technology and to other amorphous silicon *p-i-n* devices, perhaps more complex but of higher conversion efficiency and at lower cost. Polycrystalline silicon thin film converters on glass and tandem solar cells built by stacking microcrystalline and amorphous silicon films in a due sequence are about to enter the market. However, studies continue to improve the properties of amorphous silicon devices that can stabilize the physical properties of the basic material.

The high growth rate of the photovoltaic market all over the world requires production levels of hundreds of GW/year to contribute significantly to the generation of electricity worldwide. This mass production must be based on reliable and safe technologies and reasonable cost, even when the internal and external costs of the price per Wp are included [30].

The reliable crystalline silicon wafers technology dominates the market [1], but the high cost of silicon wafers and the demands energy makes on silicon ingots production preclude cost reduction. The wafer accounts for more than 50 % of the cost at the module level. This problem forced production of Si substrates of so called solar grade Si [31] which have more lax specifications in terms of impurities as compared with electronic grade material.

Thinner wafers, an increased efficiency in Si production and an increase of the module efficiency to about 18-20 % will have to contribute to cost reduction in the next ten years.

In any case, if we think of other ways involving i) reduced semiconductor material consumption, ii) lowered energy needs, iii) technologies to fabricate solar cells on inexpensive large area substrates and (iv) integration technologies to electrically connect the fabricated solar cells, we find that thin-film PV has the potential of achieving module costs less than €1 per W_p [32].

A critical point when comparing different PV technologies is the energy pay-back time (EPBT), *i.e.* the time in which the energy input during the PV system life-cycle is compensated by electricity generated by the PV system [33].

The thin film technologies have an EPBT of about 1 year, (depending on the technology) compared with multicrystalline Si modules EPBT of about 1.5-2 years in southern regions as reported by M. de Wild Scholten in [33]. An accurate comparison of the payback times must take into account all the components of the photovoltaic system.

A well accepted working definition of thin film was given by Chopra *et al.* [34] as a material created *ab initio* by the random nucleation and growth processes of individually condensing/reacting atomic/ionic/molecular species on a substrate. The structural, chemical, metallurgical and physical properties of such a material are strongly dependent on a large number of deposition parameters and may also be thickness dependent. Thin films may encompass a considerable thickness range, varying from a few nanometers to tens of micrometers and thus are best defined in terms of the production processes rather than by thickness".

Plasma deposition, sputtering, evaporation, deposition from the liquid phase, *etc.* all meet the previous definition of thin film and in addition allow for tailoring of its electrical and morphological properties (crystalline, amorphous and intermediary forms).

We will discuss in some detail inorganic non-crystalline Si deposition which allows for the formation of charge-carrier separating junctions: homojunction (*p*-*n* in Si) or heterojunction with other materials to collect the excess carriers created by the light exposition. Ideally, the absorber material of an efficient terrestrial solar cell should be a semiconductor with a band gap of 1–1.5 eV, with a high solar optical absorption ($10^4 \div 10^5$ cm^{-1}) in the wavelength region of 350 nm ÷ 1000 nm, a high quantum yield for the excited carriers, a long diffusion length and low recombination velocity.

For historical reasons (development of electronic devices), Si and its wafers dominate the market, even if its 1.1 eV band gap, with indirect character for photons with energy lower than 3.4 eV, make it less than ideal for thin-film solar cells. Nevertheless, many efforts have gone into developing thin-film solar cells based on amorphous-microcrystalline-crystalline Si. The prospect of borrowing technologies from microelectronic production supports these research efforts.

Due to its low absorption coefficient, Si layers have to be at least 30 μm thick to absorb enough light, but optical light trapping or confinement improve the effective absorption.

Si can also be deposited in its amorphous form. Amorphous hydrogenated silicon (*a*-Si:H) has a number of properties which make it attractive as an absorber layer for thin-film solar cells. The

band gap, the density of states distribution and the ratio between crystalline and amorphous phases (crystallinity) of the deposited material can be modulated by the method and conditions of deposition, achieving efficient doping and suitable high optical absorption coefficient. Recent results [11, 13] show how to reduce instability problems. Furthermore, developments around multijunction structures and micro/nanocrystalline Si extensions provide space for solar cells using "amorphous" silicon.

To summarize, we can have different kinds of silicon thin film solar cells.

a) Crystalline Silicon Thin Film Solar Cells

The *p-n* homojunction structure is built by depositing, by epitaxial growth, a thin crystalline Si film on a low cost Si substrate or non-Si substrate which is, however, prepared to accept the Si films.

b) Amorphous and Microcrystalline Silicon Thin Film Solar Cells

Typically, amorphous silicon thin-film cells use *p-i-n* structure, see Fig. **7**.

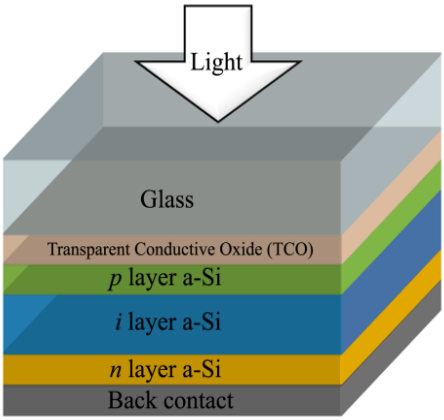


Figure 7: Schematic of a *p-i-n* solar cell on a glass substrate.

The top layer is *p*-type *a*-Si, the middle layer is intrinsic silicon, and the bottom layer is *n*-type *a*-Si. The *p-i-n* structure is sandwiched between a transparent conductor (*i.e.* tin oxide or zinc oxide) and the back metallization. The transparent conductive oxide (TCO) layer is made thin enough and relatively transparent to allow light to pass right through it, generating free electrons in the intrinsic layer. The structure can be deposited on glass or other substrate. This geometry sets up an electric field, between the *p*-type and *n*-type regions, that stretches across the middle intrinsic resistive region and separates the photogenerated free carriers.

It is possible to absorb the solar spectrum more efficiently and to improve cell stability by using stacked *p-i-n* structures and different band gaps to produce 'double junction' or 'triple junction', see Fig. **8**.

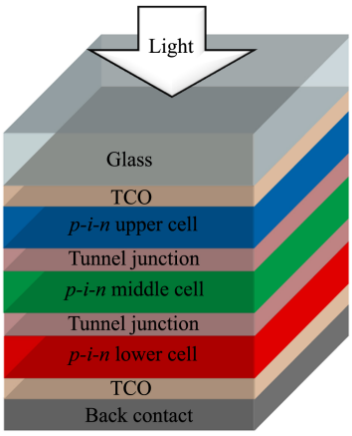


Figure 8: Schematic of a triple junction amorphous Si solar cell.

Another possible structure is the micromorph cell (see chapter 5). In addition to the *a*-Si cell, the micromorph cell has a tandem structure with an additional microcrystalline absorber, see Fig. **9**. This layer allows for conversion of the energy of the red and near infrared spectrum, providing increased efficiency.

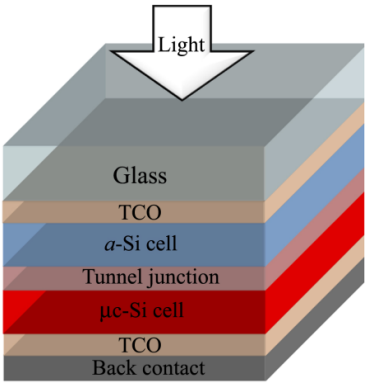


Figure 9: Schematic structure of micromorph tandem cell.

We will focus our work on b) class of solar cells.

Good reviews of problems linked to various kinds of Si solar cells are given in [5, 35, 36] with different approaches.

4. THIN FILMS DEPOSITION

A thin film is a structure with low dimensionality (2D) grown step-by-step according to a well-defined deposition sequence [37].

The energetic atomic, molecular or ionic species impact the substrate and, losing part of their energy, are adsorbed on the substrate surface (physi-adsorption), see Fig. **10**.

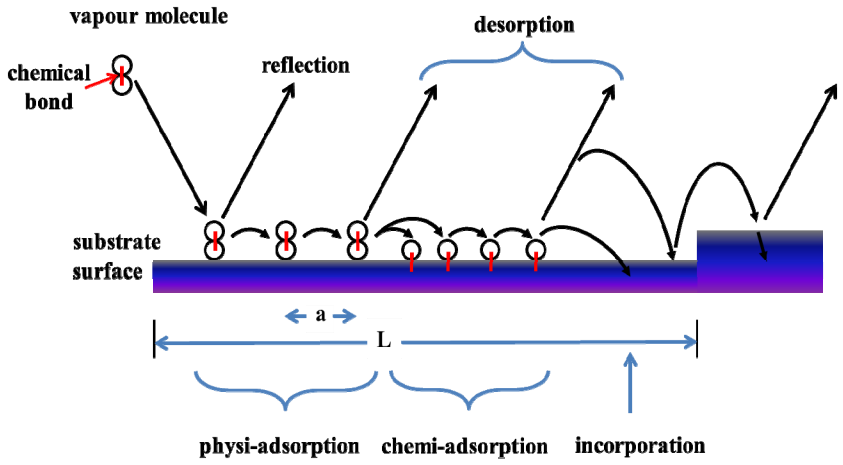


Figure 10: Adsorption processes. A red vertical connecting bar denotes a chemical bond.

The temperature differences among impinging particles and substrates stimulate lateral movements of the particles on the surface.

The interaction of moving particles allows clusters to form. These structures, thermodynamically unstable, tend to be desorbed from the substrate unless other interactions create appropriate energy conditions to start a so-called nucleation stage of minimal critical size. This nucleation process takes place in many substrate points, randomly distributed.

Going through complicated chemical-physical processes (species and energies of the impinging particles, impinging rates, adsorption-desorption rates, thermal diffusion, substrate and its surface properties, *etc.*), the rate of lateral growth is higher than the perpendicular growth, originating the so-called islands.

A continuous film originates from a coalescence process, where islands agglomerate, favoured by high surface mobility. The film assumes a continuous structure when the coalescence of the islands fills all the open channels. As a result, the outer surface presents a coarse, textured structure.

The very complex processes leading to the growth of a thin film are statistical processes of particle-particle and particle-substrate interaction.

Depending on the thermodynamics of the process and on the substrate surface, the initial stages of thin film growth on a solid substrate correspond to three possible situations: i) fragmented island structure (Volmer-Weber model); ii) uniform film (Frank-van der Merwe model), and iii) a mixed, fragmented island structure on uniform film (Stranski-Krastanov type).

The thickness of a thin film ranges from several nanometres to several tens of micrometres; over this generic limit, the film behaves like a thick structure, low dimensional too, but with a "volume" (3D) response.

The properties of the thin film material are determined by the deposition conditions not only at macroscopic level (substrate temperature and chemistry, pressure, power, *etc.*), but also at nucleation stage; however, this must not be interpreted negatively but rather as a powerful key for achieving fine tuning of the material properties.

Thin film deposition allows for the construction of artificial nano-materials, structures with one or more dimensions of nanometre size (1 nm = 10^{-7} cm = 10Å).

Examples of nanostructure are a quantum dot (0 D); a quantum wire (1 D) and a superlattice or, in general, a thin film (2 D).

The ratio among the nanodimensions and the value of other physical parameters sets the size depending upon the behaviour of the physical properties of the artificial structure. Physical parameters to be considered are, for example: conditions of quantum confinement (≤ 100 atoms); mean free path of conduction carriers (< 10 nm); mean free path of hot electron (< 1nm); de Broglie wavelength (< 1 nm) and Bohr excitation diameter (Si = 8,5 nm; GaAs = 196 nm; CdS = 6 nm) [38].

In general it can be said that the deposition method controls the properties of each thin film, see Fig. **11**.

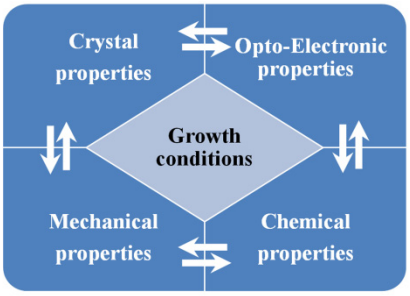


Figure 11: Correlations between growth conditions and the properties of the resultant thin films.

Among these methods, Chemical Vapour Deposition, CVD, implies a decomposition of source material, while Sputtering (SP) uses energetic species (1-10 eV) irradiated from a solid source. In CVD deposition, and in thermal evaporation as well, material grows in thermodynamic equilibrium; films deposited by SP are far from equilibrium because species impinging on the substrate lose their energy very rapidly. As a general result, the density of lattice defects is greater than in the same bulk material.

A variety of experimental techniques are employed to characterize thin films (see Table **2.9** and Table **2.10** in [38]).

5. SILICON THIN FILMS

We begin with a consideration of today's most common procedure for depositing silicon thin films: PECVD of silicon based gas compound and mixture of other gases such as methane, ammonia, *etc*.

Work on thin films deposition using PECVD started in the sixties with a strong emphasis on amorphous silicon, its hydrogenation (*a*-Si:H) and doping. The studies were focused on the properties of *a*-Si alloys materials and their applications [39-41].

The properties of films deposited by PECVD are defined and controlled by many parameters, all more or less critical. This strong dependence is negative in some aspects, requiring a fine control of the deposition process, but on the other hand it allows for wide variability of the material properties. PECVD allows controlled changes in structure and chemical composition of the films through very fine tuning of the values of the parameters during growth.

Another interesting and powerful aspect of PECVD is that the deposition process can take place at low temperatures, thus enabling large area deposition and uniformly high thickness on a great variety of substrates.

As one can see in Fig. **12**, the structure of the deposited films changes according to the deposition parameters, in this case hydrogen dilution, allowing for modulation of the properties of each film in a multilayered structure. In particular both microstructure evolution and network reconstruction, during the growth process, are strongly dependent on hydrogen dilution.

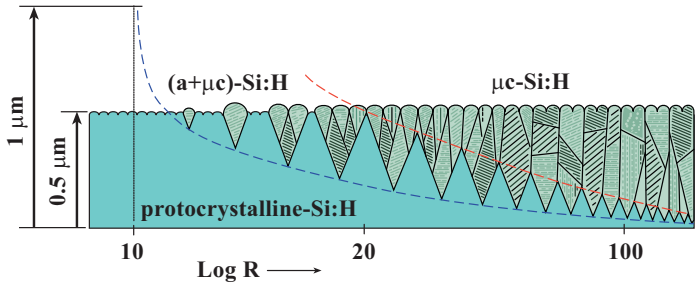


Figure 12: Scheme of the phase evolution in the protocrystalline growth regime as a function of the hydrogen dilution ratio, [12].

The presence of hydrogen plays a specific and crucial role in the nucleation and the coalescence of film (Fig. **12**) as well as in the grown bulk and the growing surface [42-45]. Phase diagrams of growing structure can be obtained by using *in situ* real time spectroscopic ellipsometry [46]. Measuring the increasing thickness of the film, one follows the transition from initial amorphous film (*a*-Si:H) to microcrystalline film (*μc*-Si:H) passing through a mixed amorphous-microcrystalline phase. It is interesting to note that the evolutionary structure of thin film influences the way in which hydrogen links to the structure and *vice versa,* looping a feedback circuit. This feedback controls the transition from an amorphous to a microcrystalline network, and then the band gap, E_g.

Wronsky and Collins [11, 40, 42] introduced the concept of protocrystalline state, for *a*-Si:H growth regime, as an evolutionary state but able, under specific growth conditions, to produce well defined physical properties (band gap, doping, *etc.*) and, most importantly, reproducible.

A strong argument for using amorphous silicon is its very high absorption coefficient. This originates from the continuous distribution of electronic localised states in the material band gap, E_g. Optical transitions can be done without preserving momentum: as a consequence *a*-Si behaves like a direct band gap semiconductor. In the visible range, the optical absorption coefficient α, of *a*-Si, is much higher than that of crystalline phase, see Fig. **13**.

The two properties (strong optical absorption and band gap, modulated varying deposition parameters) are key in preparing amorphous silicon suitable for use in efficient solar cells.

Thin film also means less material than in crystalline wafer cell. Incorporating hydrogen, germanium and carbon in the *a*-Si network, to form *a*-Si:H, *a*-SiGe:H and *a*-SiC:H, respectively, removes defects, thus lowering the density of their states in the gap, and affects the band gap E_g, increasing its value. Diluting silane with hydrogen (H), the band gap can move from about 1.4 eV of unhydrogenated material to about 2.0 eV when H ≈ 10 at. % is included in the film. High content of H in the film network tends to cause the electronic properties of the material to deteriorate and to coerce the film structure to evolve from proto to microcrystalline in a very thin layer [48-51].

Use of PECVD allows for the deposit of *a*-Si-H material with a density of dangling bond defects lower than 10^{16} cm^{-3} hydrogen content is about 10 at. %.

The creation of free carriers needed for an efficient solar converter requires an absorption coefficient higher than $\approx 10^3$ cm^{-1}. In this situation, energy of photons is greater than the band gap of the material. The different alloying of amorphous silicon means that E_g can be spanned in the range from ≈ 1.9 eV (*a*-Si:H) to ≈ 1.3 eV (*a*-SiGe:H), which is useful for building efficient solar cells in different junction configurations.

A fundamental point in the design of a solar cell based on silicon films is the knowledge of the density of states (DOS) and their energy distribution into the band gap of the material. The DOS general structure is now well recognized as represented by two tails entering the band gap from the valence and conduction band and a complicated in gap structure, strongly dependent on the deposition conditions (temperature, silane dilution, radio frequency power, *etc.*). The design of efficient solar cells requires a deep knowledge of the DOS.

Experimental measurements of the DOS distribution can be taken by different methods, given that it is a very complicated measurement subject to a high degree of uncertainty. Suitable techniques are: Deep level transient spectroscopy (DLTS), Photoconductivity (PC) and photoconductivity decay (PCD), Capacitance-Voltage curves (CV), Field Effect (FE), *etc.* [52-54].

The structure of the defects distribution in the centre of the gap (deep states) presents a multipeaked profile. In general, the profile presents three dangling-bonds (***D***) peaks: $\boldsymbol{D^0}$, (neutral

states) in the centre of the band gap, $\boldsymbol{D}^{-}$, (negatively charged states) below the centre of the gap and $\boldsymbol{D}^{+,}$ (positively charged states) above the centre of the gap.

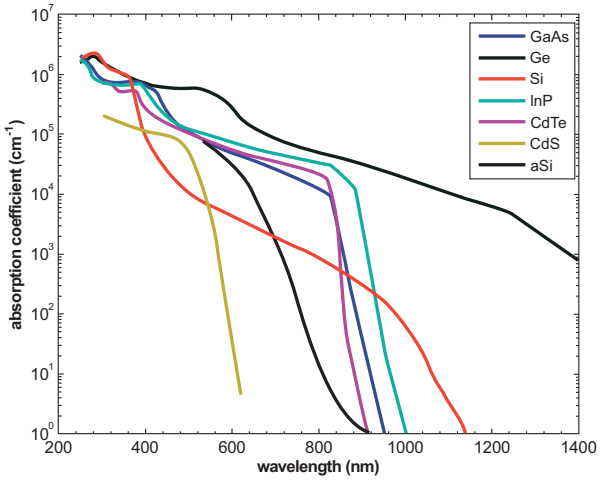


Figure 13: The absorption coefficient, α, in a variety of semiconductor materials at 300K as a function of the vacuum wavelength of light (http://pvcdrom.pveducation.org/index.html).

Intrinsic materials (*i.e.* nominally undoped) have Fermi level E_F near the centre of the band gap. The conduction process is *via* extended states for free carriers, even if with very low mobility μ. In *a*-Si:H, μ is about $10 \div 15$ cm^2 V^{-1} s^{-1} for electrons and about 1 cm^2 V^{-1} s^{-1} for holes.

Deep lying states with their distribution inside the mobility gap control the collection of photogenerated carriers, acting as traps or recombination centres, and values of the order $10^{15} \div 10^{16}$ cm^{-3}, typical for good deposited *a*-Si:H, are focal points for an efficient solar cell conversion. With those values, lifetimes are in the range $10^{-8} \div 10^{-6}$ s and the depletion region extends over the entire thickness of the solar cell.

Doping of amorphous materials can be made when the density of states at midgap is low, *i.e.* when the Fermi level is at or near the middle of the gap. Typically, *a*-Si:H based materials meet this condition and, as a consequence, they can be doped: the Fermi level moves towards the conduction or valence band, according to the donor or acceptor doping type. Doping can be done using the same elements as in the case of crystalline silicon: phosphorous for *n*-type and boron for *p*-type, respectively. The consequent increase of defect states near midgap limits both doping efficiency and free carrier lifetimes [55], thus precluding the use of amorphous doped silicon as an active absorbing layer in solar cells. However, doped materials can be used as contact layers. For example, by incorporating *n*-type *a*-Si:H (Fermi level about 0.2 eV from conduction band edge) or *n*-type *μc*-Si:H (E_F about 0.05 eV from E_C) into a *p*-*i*-*n* or a *n*-*i*-*p* structure, the ohmic behaviour of the contacts allows for built-in voltages of higher than one volt [56].

In a specular sense, *p*-type *a*-SiC:H (E_F about 0.4 eV from E_V) and *p*-type protocrystalline-Si:H (E_F about 0.05 eV from E_V) layers act efficiently as window contacts [56].

The possibility of graduating band gap and density of deep lying gap states of the intrinsic layer in a wide range, in combination with doped *p*-type and *n*-type layers of well controlled characteristics, is the main argument for use of this kind of material.

A weakness in the case for the use of amorphous materials is the need for hydrogenation to reduce the density of states, passivating dangling bonds. It is well known that hydrogen plays an important role in the so-called Stabler-Wronski effect [57].

In essence, the effect concerns the creation of defects under illumination, lowering both photoconductivity and dark conductivity. These quantities evidence reversible behaviours, returning to as-deposited values with an annealing at a relatively high temperature (~ 150 °C) [57].

The mechanism of the Stabler-Wronski effect is not yet completely understood, although there is clear relationship with the microstructure of the deposited film. For example, solar cells made with protocrystalline *a*-Si:H material show an improvement in fill factor under prolonged sun illumination [58, 59], see Fig. **14**.

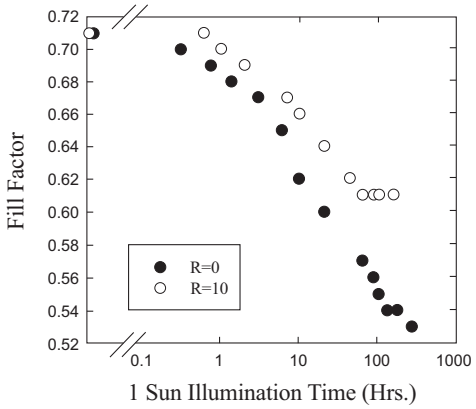


Figure 14: Degradation of the fill factor of a *a*-Si:H *p-i-n* cells with undiluted (R=0= and protocrystalline (R=10) intrinsic layers under 1 sun illumination at 25 °C [59].

To attain a broader use of silicon thin films deposited by PECVD technique, a greater understanding of the microscopic mechanisms of the effect of hydrogen incorporation is needed. The main objective is to achieve a thorough description of the growth process. Thus the interaction of the incipient film with the substrate and its evolution during growth must be described. Considerable work has been done on these points [11, 14, 60].

In particular, van Elzakker [60] recently presented his PhD thesis stating an improvement of the conversion efficiency of amorphous solar cells from 7 to 9% [61].

The hydrogen-silane dilution ratio, $R = H_2/SiH_4$, can be used as an efficient parameter to represent the structural evolution of Si films deposited by PECVD. We can focus on *R* because the other parameters (pressure, power, *etc.*) must be set to obtain, at least in principle, the highest decomposition ratio of the reactor filing mixture.

As show in Fig. **12**, we can picture the evolution of the film structure evolution as a function of R. Wronsky *et al.* [11] proved that the growth of the film evolves through three phases. In the range where the dilution ratio is lower than 10, the film structure is truly amorphous. Structure changes can be induced, and more importantly, controlled, moving *R* towards higher values than 10: in a wide range of *R*, the structure is mixed (amorphous + microcrystalline), attaining microcrystallinity at very high *R* values.

The great advantage of the protocrystalline silicon is its high insensitivity to light action, avoiding light soaking. This fundamental property must be compared to the situation of *a*-Si:H films deposited with low hydrogen content. These last typically show Staebler-Wronsky effects, attributed to structural instabilities.

In the last decade, extensive work has been done toward greater understanding of how deposition conditions influence the growth of the thin films and their physical properties.

Collins and Ferlauto obtained a detailed deposition phase diagram [47].

Using this phase diagram, the deposition region suitable for the application of the PECVD deposited films can be chosen. A device structure can be built with each layer deposited according to well-defined conditions. In particular, protocrystalline films have been incorporated in solar cells structures [47].

In-depth knowledge of the amorphous-microcrystalline transition is also essential to the design of the micromorph solar cell. This last structure is recognized as a possible solution to increase the conversion efficiency.

Van Elzakker *et al.* [60] performed a series of experiments to trace the transition from amorphous to microcrystalline structure of PECVD silane films. The evolution of structural properties was followed using cross sectional TEM micrographies.

Van Elzakker's results are presented in Fig. **15**. The varying deposition parameter is the dilution ratio *R*.

Results of the van Elzakker study show that crystal grains start to nucleate when *R* is greater than 25 and thickness is around 100 nm from the substrate: nuclei are dispersed in the top layer of the film. This first result shows the influence of both *R* and film thickness on nucleation.

By increasing *R*, nucleation of crystals starts almost immediately and the transition between mixed and microcrystalline phases appears at a thickness of about 500 nm, even if an amorphous layer is still present in contact with the substrate. At R=40, nucleation starts immediately with a dense population of nuclei.

The mixed nucleation layer is very thin: about 50 nm. The evolution of the crystalline phase inside the deposited layer is also shown by the diffraction pattern. These results allow for control of the structural properties of Si:H, going from a fully amorphous layer for thicknesses lower than about 1 μm and $R \leq 20$ to an evolutionary situation when $R \geq 25$. In this case, the mixed phase tends to

be diffused and slowly evolving for films with lower dilution. Van Elzakker *et al.* found a clear correspondence between these results and optical measurements taken on the same samples.

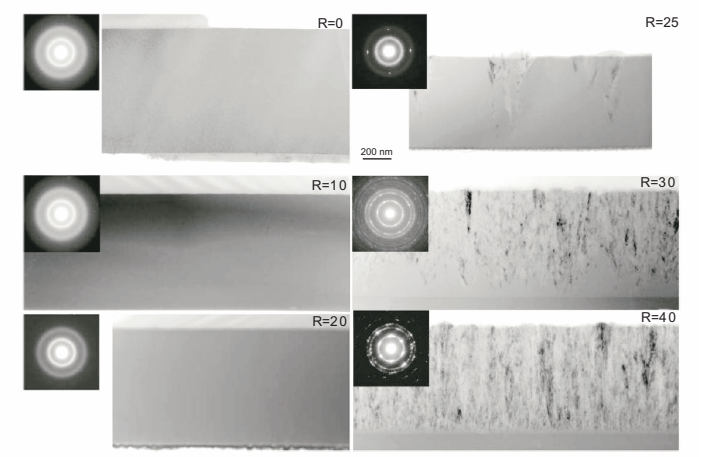


Figure 15: Bright field electron micrographs of Si:H layers deposited on glass with dilution ratios R as indicated. The inserted diffraction patterns were taken from each layer with a selective aperture of 1 μm diameter. The scale bar applies to all images [61].

Absorption spectra can estimate the density of defect states at low photon energy, using suitable calibration factors [62]. The density of defects evolves from about 9 x 10^{15} cm^{-3} (R = 0) to about 1.7 x 10^{17} cm^{-3} for R = 40.

Increasing hydrogen dilution creates material with both increasing real defect density and Urbach characteristic energy.

The density of states and their energy distribution in the layer, used as light absorber, is one of the most important parameters both in solar cell simulation and hence in real cells.

Techniques to measure density of states are for example Photothermal Deflection Spectroscopy (PDS) and Dual Beam Photoconductivity (DBP) [63, 64].

a-Si:H light conversion devices made by using specific dilutions of silane with hydrogen are promising for solar conversion because they show better performance after light exposure. In particular, the enhancement of performance could be related to three possible different phases of thin film growth: i) amorphous, ii) protocrystalline, (*i.e.* amorphous with various crystalline content) and iii) microcrystalline.

Values and ranges of deposition parameters define the protocrystalline regime. Given that proto-crystallinity requires hydrogen dilution, silicon deposited under these conditions presents improved stability against light soaking. However, even if hydrogen dilution is beneficial, it tends to speed up the structural transition of the film to microcrystallinity. Unfortunately, the best absorption coefficient is presented by amorphous silicon and the problem now becomes how to

obtain high quality amorphous layers at high dilutions. Possible approaches are: a) dilution profile: *R* is decreased during growth to avoid transition to microcrystallinity; and b) layer-by-layer technique, to avoid phase transition.

An amorphous silicon layer is deposited by diluted silane, followed by a very thin layer of pure silane (interlayer). The role of this last layer should be to create an amorphous interface to support the growth of another silicon film deposited with increased dilution [65, 66].

Van Elzakker *et al.* used Raman spectroscopy to evaluate the crystalline fraction according to standard methods [13].

Depending on the thickness of the inter-layers, the crystallinity of the whole stacked structure is changing. It looks like a mixed phase when interlayers are 5 nm thick, with a decreasing crystalline fraction for increasing interlayer thickness.

As clearly presented in the following Fig. **16**, the optical absorption, α, is close to values and behavior of *a*-Si, in samples with an interlayer 15 nm thick.

The α difference between amorphous reference and 15 nm thick layer can be partially attributed to the absorption of microcrystalline phase.

Detailed studies of the growth mechanisms, done using real time spectroscopic ellipsometry [11, 34, 38], provided an understanding of the properties of undoped and doped thin films and their behaviour when used in solar cell structures. For example, one can define the optimal *R* range to deposit *p*-layers for V_{oc} maximization, according to the required crystalline structure of the layers. The general problem is to obtain the lowest recombination at *p/i* interface. Studies by Wronky *et al.* clearly show that the deposited material must be in its protocrystalline *a*-Si:H phase [67]. The low recombination at *p/i* interface is attributed to the modification of the sub-interface volume inside the intrinsic layer during the growth of the *p* doped contact film. High hydrogen content and protocrystalline phase during *p*-Si:H film growth seem to be the keys for the beneficial effect on lowering of carrier recombination.

An interesting point concerns the relationship between PECVD frequency and hydrogen dilution. Wronsky *et al.* [68] found that a frequency (f) of 60 MHz improves the properties of silicon films at high deposition rates when compared to f = 13.56 Mhz. However, if the deposition is made with parameter values near the phase border between amorphous and mixed (amorphous + microcrystalline material), high deposition rates lead to good material regardless of the choice of frequency.

6. OTHER KINDS OF Si THIN FILM

Till now we have discussed deposition of Si thin films by radio frequency (RF) PECVD, considering crystalline structure evolution with its phase diagram, suitable for obtaining thin layers with defined and controlled properties.

However, many different techniques and deposition methods have been presented, and many of these are possible candidates for photovoltaic devices with high conversion efficiency.

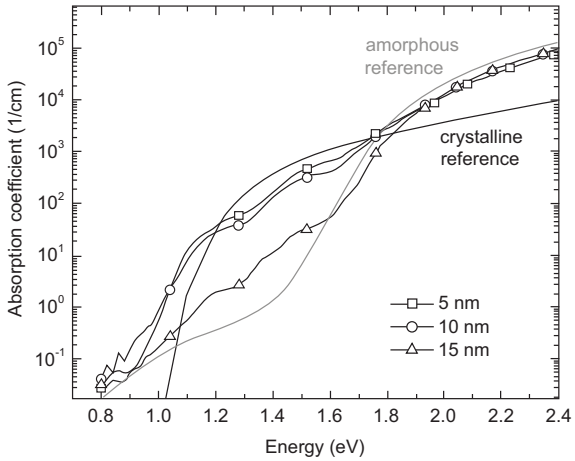


Figure 16: Absorption coefficient spectra of samples with different interlayer thicknesses in the as-deposited state compared to crystalline and amorphous reference curves [61].

Extensive reviews can be found in Bergmann [5, 15].

Moreover, updated numerical values of photovoltaic parameters in experimental devices can be found with references in the Solar Cells Efficiency Tables presented by M.A Green *et al.* [69]. The references quoted in [69] allow the reader to go as far as the description of the device details.

We will try to give a short non-exhaustive survey of the possible methods.

The development of silicon thin film solar cells rather than wafer cells means lower costs. The actual wafer thickness is about 180 ÷ 200 μm. Further reduction is possible but it seems unlikely that a value of 50 μm, well recognized as effective thickness (= ratio of cell volume to cell area) with wafer structures, can be attained.

It is difficult to give a short and overall breakdown of the technologies due to the large quantity of variables to be controlled: designs of the cell and sequence of layer deposition, substrates, and different deposition techniques, each with its own parameters. All these variables must be defined according to cell or module production, cost savings, and large scale production.

We decided to follow the working scheme presented by Brendel [5], using substrate as the guide to classify photovoltaic structures. The substrate is necessary to mechanically support the structure, but the physico-chemical properties of the substrate surface and of the growing interface define the properties of the Si layers. Following Brendel's scheme, we have:

1) High temperature substrates suitable for high temperature deposition (T_d > 800 °C);

2) Low temperature substrates when the deposition temperature is lower than T_d < 800 °C);

3) Substrates suitable for layer transfer process after a high temperature deposition.

In detail, we have:

1) High temperature deposition (1000-1200 °C) is made using CVD or PECVD and silane or chlorosilane. The high deposition rate (several μm min^{-1}) limits the Si grain dimensions in the range 1-5 μm as an acceptable compromise to shortening deposition time. An annealing process performed with light or laser allows a recrystallization of the Si layer, increasing grain dimensions up to several millimetres. The reduction of the density of grain boundaries is required to control the recombination effects, which limit the conversion efficiency.

It is important to note that the deposition and annealing steps are energy intensive, thus increasing the costs of the cell, even if the cell is a high efficiency structure.

Mullite, a mixture of Al_2O_3 : SiO_2 seems to be the most promising substrate given its high reflectance of light, which generates a light trapping mechanism.

However, graphite, glass, mono-and polycrystalline silicon or silicon charged with other materials, metals and ceramics of different kinds have can be used to deposit the silicon film [70, 71].

Published results for cells built using high temperature deposition of silicon lead to conversion values in the range of 8-11 % [72, 73].

2) The low temperature deposition range essentially fits the PECVD technique, where deposition is made in the temperature range of 150-500 °C. All these points have been already discussed, having used PECVD widely to deposit thin silicon films.

In addition to the parameters previously quoted, we can choose an excitation frequency of 13,56 MHz (High Frequency, HF) or higher than 50 MHz (Very High Frequency, VHF), for the plasma process.

According to the film growth mechanism, using VHF leads to a less damaged structure due to the reduced energy of the ions impinging on the growing surface [67, 68]. This fact adds another degree of freedom in the growing parameters-material properties matrix, so that in principle the characteristics of the material can be tailored to the application.

Updated conversion efficiencies of devices made using PECVD films under different conditions can found in “Solar cell efficiency tables” by Green *et al.* [69]

3) The third point to consider is the layer transfer process method. In this case, silicon layer(s) are deposited, according to a given structure on an expressly prepared substrate permitting transfer of the device layered structure from the high cost reusable substrate to a low cost one. The substrate growing surface can be prepared in different ways. Today several layer transfer processes are being studied. Presently, the best efficiency for devices built with this technique attains 16,7% on an area of about 4 cm^2 [69].

7. BASIC PRINCIPLE OF LIGHT TRAPPING

The problem of the relatively weak absorption of near-band gap energy photons in thin silicon solar cells can be overcome by attempting to augment the optical path of the light inside the solar

cell. One solution might be to implement mechanisms of light trapping, *i.e.* multiple reflections of light between the two outer surfaces of cell structure. The back side of the cell can be roughened (by blazing, texturing, grooving, *etc.*) but must be back-reflective, coated with a metal or by achieving a discontinuity in refractive index. The inner wafer surface acts as a reflective mirror when the thin cell structure is deposited on this substrate.

The multiple reflections of light increase the length of the optical path several times. In this way, the effective thickness of the cell is several times its actual thickness, greatly increasing the light absorption and carrier generation. Several constraints should be met to improve the light absorption. For example, the two outer surfaces of the cell must be non-parallel, and the antireflective optical coating on the front surface of the cell must be accounted for to maximise transmission. The symmetry of light transmission reduces the internal reflection upon the front surface. Moreover, if the incidence angle of the rays coming from inside on the top surface is greater than about 16 degrees, the light is completely reflected internally.

Barnett *et al.* [74] studied the behaviour of cell parameters open circuit voltage, V_{OC}, and short circuit current, I_{sc} from Z, ratio of effective optical thickness to actual thickness under weakly light absorption conditions.

A detailed discussion of light trapping principles will be given in Chapter 11.

ACKNOWLEDGEMENT

Declared none.

CONFLICT OF INTEREST

The author(s) confirm that this chapter content has no conflict of interest.

REFERENCES

[1] Razykov TM, Ferekides CS, Morel D,. Stefanakos E, Ullal HS. Solar photovoltaic electricity: Current status and future prospects. Sol. Energy 2011. doi:10.1016/j.solener.2010.12.002. (accessed 29 December 2010).

[2] Tsunomura Y, Yoshimine Y, Taguchi M, *et al.* Twenty-two percent efficiency HIT solar cell. Sol. Energ. Mat Sol C 2009; 93: 670–3.

[3] Reuter M, Brendle W, Tobail O, Werner JH. 50 μm thin solar cells with 17.0% efficiency. Sol. Energ. Mat Sol C 2009; 93: 704-6.

[4] Hahn G and Schonecker A. New crystalline silicon ribbon materials for photovoltaics. J Phys Condens Matter 2004; 16: R1615–48.

[5] Brendel R. Thin-Film Crystalline Silicon Solar Cells: Physics and Technology. 1st ed. Weinheim: Wiley-VCH Verlag GmbH & Co. KGaA 2003.

[6] Yoo J. Solar cell fabrication using edge-defined film-fed growth (EFG) silicon wafers. Appl Surf Sci 2010; 257: 1612-15.

[7] Romeo N, Bosio A, Romeo A. An innovative process suitable to produce high-efficiency CdTe/CdS thin-film modules. Sol Energ Mat Sol C 2010; 94: 2–7.

[8] First Solar Inc, http://www.firstsolar.com (accessed 10 December 2011).

[9] Matsunaga K, Komaru T, Nakayama Y, Kume T, Suzuki Y. Mass-production technology for CIGS modules. Sol Energ Mat Sol C 2009; 93: 1134-38.

[10] Seike S, Shiosaki K, Kuramoto M, *et al.* Development of high-efficiency CIGS integrated sub modules using in-line deposition technology. Sol. Energ. Mat Sol C 2011; 95: 254-6.

[11] Wronski CR, Collins RW. Phase engineering of a- Si:H solar cells for optimized performance Sol Energy 2004; 77: 877-85.

[12] Wronski CR, Von Roedern B, Kolodziej A. Thin- film Si:H-based solar cells. Vacuum 2008; 82: 1145–50.

[13] Van Elzakker G, Tichelaar FD, Zeman M. Suppression of crystalline growth in silicon films deposited from hydrogen diluted silane using a layer-by-layer approach. Thin Solid Films 2007; 515: 7460–64.

[14] Rath JK, Verkerk AD, Liu Y, Brinza M, Goedheer WJ, Schropp REI. Gas phase considerations for the growth of device quality nanocrystalline silicon at high rate. Mater Sci Eng B 2009; 159– 160: 38–43.

[15] Bergmann RB. Crystalline Si thin-film solar cells: a review. Appl Phys A 1999; 69: 187–94.

[16] Bergmann RB and Werner JH. The future of crystalline silicon films on foreign substrates. Thin Solid Films 2002; 403-404: 162-69.

[17] Rath JK. Nanocystalline silicon solar cells. Appl Phys A 2009; 96: 145-52.

[18] Chapin DM, Fuller CS, and Pearson GL. A new silicon p-n junction photocell for converting solar radiation into electrical power. J Appl Phys 1954; 25: 676.

[19] Green MA. Solar Cells: Operating Principles, Technology and System Applications. Englewood Cliffs, NJ: Prentice-Hall, Inc 1982.

[20] Archer MD, Hill R. Clean Electricity from Photovoltaics (Series on Photoconversion of Solar Energy, Vol.1. London: Imperial College Press 2001.

[21] Lee J, Lakshminarayan N, Dhungel SK, Kim K, Yi J. Optimization of fabrication process of high-efficiency and low-cost crystalline silicon solar cell for industrial applications. Sol Energ Mat Sol C 2009; 93: 256–61.

[22] Aberle AG. Overview on SiN surface passivation of crystalline silicon solar cells. Sol Energ Mat Sol C 2001; 65: 239-248.

[23] Kerr MJ, Schmidt J, Cuevas A, Bultman JH. Surface recombination velocity of phosphorus- diffused silicon solar cell emitters passivated with plasma enhanced chemical vapor deposited silicon nitride and thermal silicon oxide. J Appl Phys 2001; 89: 3821-26.

[24] Kerr MJ and Cuevas A. Recombination at the interface between silicon and stoichiometric plasma silicon nitride. Semi Sci and Tech 2002; 17: 166-72.

[25] Moschner J, Henze J, Schmidt J and Hezel R. High-quality surface passivation of silicon solar cells in an industrial-type inline plasma silicon nitride deposition system. Progress in Photovoltaics: Research and Applications 2004; 12: 21-31.

[26] Soppe W, Rieffe H and Weeber A. Bulk and Surface Passivation of Silicon Solar Cells Accomplished by Silicon Nitride Deposited on Industrial Scale by Microwave PECVD. Progress in Photovoltaics: Research and Applications 2005; 13: 551–69.

[27] Schwab C, Hofman M, Rentsch J, Preu R. Front Surface passivation for industrial-type solar cells by silicon oxynitride silicon nitride stacks. In 25th European PV solar Energy Conference and Exhibition; 2010, Valencia, Spain: WIP- Renewable Energies 2010; 2307-10.

[28] International Electrotechnical Commission. IEC 60904-3:2008. Photovoltaic devices-Part 3: Measurement principles for terrestrial photovoltaic (PV) solar devices with reference spectral irradiance data. Geneva: IEC; 2008.

[29] American Society for Testing and Materials. ASTM G173–03:2008. Standard Tables for Reference Solar Spectral Irradiances. West Conshohocken, PA: ASTM; 2008.

[30] European Commission: ExternE-Externalities of Energy. A research project of the European Commission. http://www.externe.info/externpr.pdf (accessed 13 April 2011).

[31] Pizzini S Towards solar grade silicon: Challenges and benefits for low cost photovoltaics. Sol. Energ. Mat Sol C 2010; 94: 1528-33.

[32] Buechel G. Based on Oerlikon Solar's Product KAI. In 2nd EPIA Thin-Film Conference; 2009: Munich.
[33] De Wild Scholten M. LCA of the whole life cycle of PV: "From cradle to cradle". In 1st International Conference on PV module recycling; 2010: Berlin, Germany.
[34] Chopra KL, Paulson PD, DuttaV. Thin-Film Solar Cells: An Overview. Prog Photovolt: Res Appl 2004; 12:69–92.
[35] Mauk M, Sims P, Rand J, Barnett A. In Markvart T, Castaner Eds. Practical Handbook of Photovoltaics: Fundamentals and Applications. Oxford, UK: Elsevier Science. 2003; pp 185-225.
[36] Poortmans J, Arkhipov V. Thin film solar cells: fabrication, characterization and applications. West Sussex, England: John Wiley & Sons Ltd. 2003.
[37] Ohring M. Materials Science of Thin Films. 1st ed. Singapore: Elsevier 2006.
[38] Wasa K, Kitabatake M, Adachi H. Thin film materials technology. Heidelberg: Springer-Verlag GmbH 2004.
[39] Carlson DE, Rajan K, Arja RR, Wiling F, Yang L. Advances in amorphous silicon photovoltaic technology. J Materials Research 1998; 13(10): pp 2754-62.
[40] Wronski CR, Pearce JM, Koval RJ, *et al.* Light induced defect creation kinetics in thin film protocrystalline silicon materials and their solar cells. Mat Res Soc Symp Proc 2002; 715: A13.4.
[41] Street RA, Hydrogenated amorphous silicon. 14th ed. New York: Cambridge University Press 2001.
[42] Collins RW, Ferlauto AS, Ferreira GM, *et al.* Application of deposition phase diagrams for the optimization of a- Si:H-based materials and solar cells. Mater Res Soc Symp Proc 2003; 762: A10.1.
[43] Collins RW, Koh J, Ferlauto AS, *et al.* Real time analysis of amorphous and microcrystalline silicon film growth by multichannel ellipsometry. Thin Solid Films 2000; 364: 129–37.
[44] Tsu DV, Chao BS, Ovshinsky SR, Guha S, Yang J. Effect of hydrogen dilution on the structure of amorphous silicon alloys. Appl Phys Lett 1997; 71: 1317–19.
[45] Yang J, Lord K, Guha S. Amorphous silicon alloy solar cells near the threshold of amorphous-to-microcrystalline transition. Mater Res Soc Proc 2000; 609: A1541–46.
[46] Collins RW, An I, Nguyen HV, Li Y, Lu Y. In: Vedam K, Ed. Physics of Thin Films, New York: Academic Press. 1994; pp 49-125.
[47] Collins RW, Ferlauto AS. Advances in plasma- enhanced chemical vapor deposition of silicon films at low temperatures. Curr Opin Sol State Mater Sci 2002; 6: 425–37.
[48] Ganguly G, Matsuda A. Role of hydrogen dilution in improvement of a-SiGe:H alloys. J Non-Cryst Solids 1996; 198-200: 559-62.
[49] F erlauto AS, Koval RJ, Wronski CR, and Collins RW. Extended phase diagrams for guiding plasma-enhanced chemical vapor deposition of silicon thin films for photovoltaics applications. Appl Phys Lett 2002; 80(15): 2666.
[50] Koval RJ, Ferlauto AS, Pearce JM, Collins RW and Wronski CR. Mobility gap profiles in Si:H intrinsic layers prepared by H2-dilution of SiH4: effects on the performance of p–i–n solar cells. J Non-Cryst Solids 2002; 299-302: 1136- 41.
[51] Dawson RM, Li YM, Güneş M, *et al.* Optical properties of component materials in multi- junction hydrogenated amorphous silicon based solar cells. In Guimaraes L Ed. Proceedings of 11th European PV Solar Energy Conference; 1992: Montreux, Switzerland: Harwood Academic Publisher 1992; pp 680-3.
[52] Czichos H, Saito T, Smith L. Springer Handbook of Materials Measurement Methods. Heidelberg: Springer-Verlag GmbH 2006.
[53] Nadazdy V and Zeman M. Origin of charged gap states in a-Si:H and their evolution during light soaking. Phys Rev B 2004; 69: 165213.
[54] Redfield D, Bube RH. Photo-induced Defects in Semiconductors. Stanford: Cambridge Studies in Semiconductor Physics and Microelectronic Engineering (No. 4): 1996.
[55] Wronski CR, Abeles B, Tiedje T and Cody GD. Recombination centres in phosphorous doped hydrogenated amorphous silicon. Solid State Commun 1982; 44: 1423-26.

[56] Lee Y, Ferlauto AS. Wronski CR. Contributions of bulk, interface and built-in potential to the open circuit voltage of a-Si:H solar cells. In Photovoltaic Specialists Conference, Conference Record of the Twenty-Sixth IEEE; 1997: Anaheim: IEEExplore digital library 2002; pp 683- 86.

[57] Staebler DL and Wronski CR. Reversible conductivity changes in discharge produced amorphous Si. Appl Phys Lett 1977; 31: 292.

[58] Lee Y, Jiao L, Liu H, Lu Z, Collins RW, Wronski CR. Stability of a s-Si solar cells and corresponding intrinsic materials fabricated using hydrogen diluted silane. In Proc. 25th IEEE Photovoltaic Specialist Conference; 1996: Washington, DC; pp 1165-68.

[59] Wronski CR, Pearce JM, Koval RJ, Ferlauto AS, Collins RW, Progress in amorphous silicon based solar cell technology. In Krauter SCW Ed. Proceedings of RIO 02-World Climate & Energy Event;2002: Rio de Janeiro, Brazil; pp 67-72.

[60] Van Elzakker G, Nadady V, Tichelaar FD, Metselaar JW, Zeman M. Analysis of structure and defects in thin silicon films deposited from hydrogen diluted silane. Thin Solid Films 2006; 511-512: 252-57.

[61] Van Elzakker G. Hydrogenated Amorphous Silicon Solar Cells Deposited from Silane Diluted with Hydrogen. PhD thesis. Delft University of Technology; 2010.

[62] Wyrsch N, Finger T, McMahon TJ, Vanecek M. How to reach more precise interpretation of subgap absorption spectra in terms of deep defect density in a-Si:H. J Non-Cryst Solids 1991; 137-138: 347-50.

[63] Jackson WB, Amer NM, Boccara AC, Fournier D. Photothermal deflection spectroscopy and detection. Applied Optics 1981; 28 (8): 1333–44.

[64] Güneş M, Akdaş D, Göktaş O, Carius R, Klomfass J and Finger F. Photoconductivity spectroscopy in hydrogenated microcrystalline silicon thin films. Journal of Materials Science: Materials in Electronics 2003; 14: 729-30.

[65] Roca i Cabarrocas P, Layadi N, Drévillon B and Solomon I. Microcrystalline silicon growth by the layer-by-layer technique: long term evolution and nucleation mechanisms. J Non-Cryst Solids 1996; 198–200: 871.

[66] Roca i Cabarrocas P, Hamma S, Hadjadj A, Bertomeu J, Andreu J. New features of the layer by layer deposition of microcrystalline silicon films revealed by spectroscopic ellipsometry and high resolution transmission electron microscopy Appl Phys Lett 1996; 69: 529.

[67] Wronski CR, Collins RW, Pearce JM *et al.* Optimization of Phase-Engineered a-Si:H-Based Multijunction Solar Cells. NCPV and Solar Program Review Meeting 2003; NREL/CD-520- 33586: 789.

[68] Wronski CR, Collins RW**,** Vlahos V *et al.* Optimization of Phase-Engineered a-Si:H-based Multi-junction Solar Cells. Second Annual Technical Status Report January 2003-January 2004; Centre for Thin Film Devices. The Pennsylvania State University, University Park, PA.

[69] Green MA, Emery K, Hishikawa Y, Warta W. and Dunlop D. Solar cell efficiency Tables (Version 38), M. A. Green, K. Emery, Y. Hishikawa, W. Warta and E. D. Dunlop, Prog. Photovolt: Res. Appl. 2011; 19:565–572. Published online in Wiley Online Library (wileyonlinelibrary.com). DOI: 10.1002/pip.1150

[70] Bourdais S, Beaucarne G, Mazel F, Slaoui A, Poortmans J, Fantozzi F. Poly crystalline silicon thin films deposited onto mullite substrates: from material preparation to photovoltaic devices. In Scheer H, McNelis B, Palz W, Ossenbrink HA, Helm P, Eds. Proceedings of 16th European Photovoltaic Solar Energy Conference; 2000: London: James & James 2000; pp. 1496.

[71] Van Zutphen AJ, Zeman M, Metselaar JW. Film silicon on ceramic substrates for solar cells. In Scheer H, McNelis B, Palz W, Ossenbrink HA, Helm P, Eds. Proceedings of 16th European Photovoltaic Solar Energy Conference; 2000: London: James & James 2000; pp. 1412.

[72] Bourdais S, Reber S, Lautenschlager H, Slaoui A, Fanozzi G, Hurrle A. Recrystallized silicon thin-film solar cells on mullite ceramic substrates. In Scheer H, McNelis B, Palz W, Ossenbrink HA, Helm P, Eds. Proceedings of 16th European Photovoltaic Solar Energy Conference; 2000: London: James & James 2000; pp. 1493.

[73] Heidler K (Red). Fraunhofer Institut Solare Energiesysteme, Leistungen und Ergebnisse Jahresbericht 1997; (FhG-ISE, Freiburg, 1997): p. 80.

[74] Barnett AM, Rand JA, Domian FA, Ford DH, Kendall CL, Rock ML, Hall RB. Efficient Thin Silicon-Film Solar Cells on Low-Cost Substrate. In Proc. 8th European Photovoltaic Energy Conference 1988; Florence: pp 149-55.

Send Orders of Reprints at reprints@benthamscience.net
Silicon Based Thin Film Solar Cells, 2013, 29-57

CHAPTER 2

Deposition of Thin Films: PECVD Process

Armando Menéndez*, Pascal Sánchez and David Gómez

Energy Area, ITMA Materials Technology, Parque Empresarial P.E.P.A., c/Calafates 11, Parcela L.3.4, 33417, Avilés (Asturias) Spain

Abstract: Plasma enhanced chemical vapor deposition technique plays a key role in the development of solar cells based on amorphous and microcrystalline silicon thin films. The deposition process depends strongly on physical and chemical interactions in the plasma. Subsequently, the film properties are dependent on different parameters such as power and frequency, the substrate temperature, the gas pressure and composition, the magnitude and the pattern of the gas flow, the electrode geometry, *etc.* The aim of this chapter is to discuss all effects of these parameters in detail.

Keywords: Plasma deposition, deposition rate, solar cell, PECVD system, flow rate, high frequency, amorphous silicon, microcrystalline silicon, large area, electrode, production system, roll-to-roll, photovoltaic, thin film, vapor deposition, substrate, microstructure, cluster configuration, in-line configuration, bandgap.

1. FUNDAMENTALS OF CVD PROCESS

1.1. Definition

Over the last years, Chemical Vapor Deposition (CVD) has emerged as one of the most interesting deposition techniques in industry. In spite of being a mature and well-known technology, recent developments (for example, new plasma sources or novel activation methods for low temperature deposition) have allowed CVD to be used successfully in different fields, such as microelectronics, optics, manufacturing or photovoltaics.

Chemical Vapor Deposition may be defined as a deposition technique in which a solid is obtained on a heated surface from a chemical reaction where the precursor or precursors are introduced in the vapor phase. The reaction mechanisms are usually considered as atomistic, that is, the deposition takes place atom by atom or molecule by molecule. As an example, Fig. **1** represents a CVD reaction where A and B are precursor gases and C is a solid product of this reaction acting as a coating on a given substrate.

CVD has many advantages when compared to other deposition techniques as (i) the process allows a high quality conformal deposition, even in complex three dimensional structures, with aspect ratios above 10:1 [1], (ii) the deposition rates are usually high, which leads to competitive industrial implementation and (iii) the CVD equipment is simple and flexible. In addition,

*Address correspondence to Armando Menéndez: Energy Area, ITMA Materials Technology, Parque Empresarial P.E.P.A., c/Calafates 11, Parcela L.3.4, 33417, Avilés (Asturias) Spain; Tel: +34 985129120 (ext. 351); Fax: +34 985129008; E-mail: a.menendez@itma.es.

Roberto Murri (Ed)
All rights reserved-© 2013 Bentham Science Publishers

although CVD is only considered as a deposition technique, its availability for the synthesis of nanomaterials in different shapes (nanotubes, foams, whiskers, fibers, *etc.*) has attracted a great deal of attention in the last years and CVD represents a commercial way of fabricating nanoparticles, carbon nanotubes [2], graphene [3], *etc.*

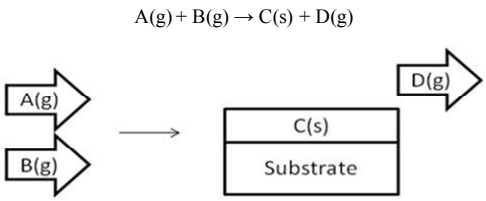


Figure 1: Typical CVD reaction process.

On the other hand, one of the main disadvantages of CVD is the need of heating the substrate to be coated up to very high temperatures, which disables the use of this technology for some applications. As will be explained later, the development of CVD techniques as new plasma activated methods or metal organic strategies have allowed the extention of the range of process application. Nowadays, some industrial CVD processes are carried out at temperatures below 200ºC. It is also important to remark in this section that some CVD processes still require inexpensive and toxic gas precursors. In other cases, this problem involves the gas by-products and special exhaust devices and cleaning procedures are required. A great effort has been made in the last decade for new processes to overcome these issues.

A thorough understanding of the CVD process specifies the analysis of different scientific and technological areas, such as thermodynamics, kinetic theory or fluid dynamics. From a chemical point of view, the proper selection of precursor gases leads to pyrolysis, oxidation, reduction, nitride and carbide formation, *etc.*, that allows the synthesis of a wide range of coatings. The way these reactions are activated (thermally, by plasma, by laser, *etc.*) split the CVD concepts into different CVD specific techniques such as Plasma Enhanced CVD, Hot Wire CVD, Metal-Organic CVD, as described in detail below.

1.2. The Physics of CVD

Besides chemistry, CVD processes involve many other scientific and technological disciplines such as thermodynamics, plasma physics, fluid dynamics or growth mechanisms to be considered. In this section, a general overview of these aspects is given.

a) Thermodynamics of CVD

The satisfaction of thermodynamic laws is a necessary condition for any irreversible process. In this sense, thermodynamics is a general criterion that makes the hypothetical process be possible or impossible even though it does not state how long it will take for the possibility to be fulfilled. According to these laws, a desired CVD reaction will take place if the free energy changes the reaction, ΔG_r, is negative. This analysis can be carried out starting from free energy values corresponding to the products and reactants, ΔG_f (products) and ΔG_f (reactants), respectively:

$$\Delta G_r = \Delta G_f \text{ (products)} - \Delta G_f \text{ (reactants)} < 0$$

ΔG_r depends on the product's and reactant's nature, composition and dilution. The selection of initial products (gas precursors) on the basis of this analysis constitutes an important issue in order to achieve the optimal and favorable growth mechanism. It is also important to point out that some external factors such as pressure and temperature are also involved in estimating ΔG_r. This determines the way that different CVD processes are activated.

The calculation of ΔG_r is usually made by minimizing the Gibbs free energy, which delimits the thermodynamical equilibrium condition. When temperature, volume and pressure are considered as additional parameters this calculation becomes complicated and numerical methods are commonly used for this purpose (see, for example, [4]). These theoretical results are then compared with initial experimental processes.

(i) Fluid Dynamics and Deposition Kinetics

The knowledge of fluid dynamics and deposition kinetics represent a key issue in order to:

- Control the composition, structure and homogeneity of desired coating materials to be developed (see, for example, [5]).

- Design and build new reactor geometries for novel CVD processes and deposition strategies (see, for example, [6]).

The analysis of a CVD process from a fluid-dynamical point of view clearly represents a complex problem as gas precursors are conducted through pipes and valves to a deposition chamber where a heterogeneous reaction takes place and gaseous by-products exhaust. This sequence is summarized in Fig. **2**.

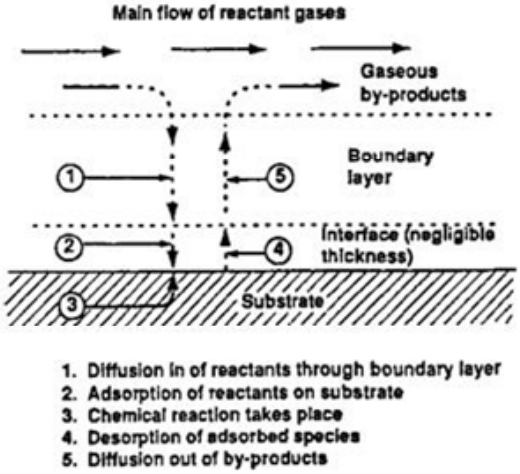


Figure 2: Chemical Vapor Deposition sequence from a fluid dynamic perspective [1].

In general, processes and reactor design are considered in order to obtain the laminar flow, that leads to null velocity in the substrate surface and creates a boundary layer where the reaction takes place. The thickness of this layer is proportional to $R^{-0.5}$, where R represents the Reynolds number. In a similar way, a boundary layer is also created in the upper wall of the reactor and a velocity profile created (Fig. **3a**). Following a similar procedure for temperature, a temperature profile is generated (Fig. **3b**).

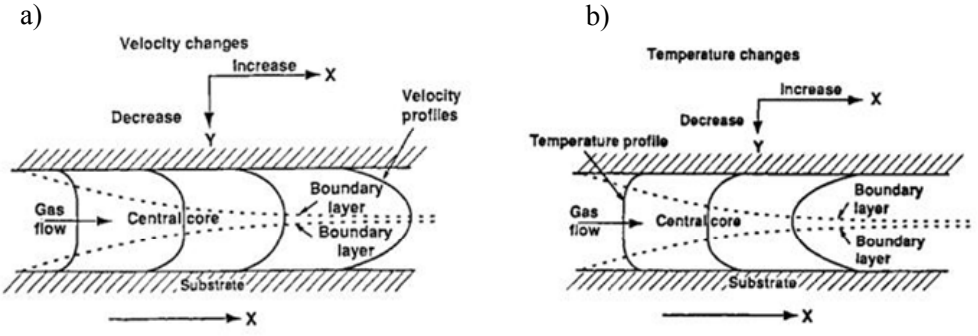


Figure 3: Velocity (a) and temperature (b) profiles along a tubular reactor geometry [1].

(ii) Growth Mechanism

The deposition mechanisms governing CVD are still a focus of controversy and nowadays complex thermodynamic and atomistic nucleation theories coexist [1]. From a practical point of view, three important concepts have to be considered so as to understand the nature and properties of CVD coatings:

Epitaxy: Consists of the growth of a crystalline layer on a crystalline substrate of the same material (homoepitaxy) or different (heteroepitaxy). The growth of epitaxial layers leads to high quality materials and it is commonly desired in the semiconductor industry. In the case of heteroepitaxy, this is only possible when the lattice constants of the coating and substrate are similar. For lattice mismatches above 10%, the use of buffer (intermediate) layers has to be considered.

Gas Phase Precipitation: Under some experimental conditions, the CVD reaction can be carried out in the gas phase instead of the substrate, which leads to the subsequent precipitation of particles in the surface. Although this has been seen as a source of defects primarily affecting coating homogeneity, this is currently being applied to the manufacturing of powder and nanoparticles.

CVD processes are always related to thermal stresses, as the sample is heated and cooled in a predetermined sequence. Once the CVD coating is formed, this stress can lead to crack generation. In order to solve this difficulty, buffer layers are considered when low temperature processes such as plasma assisted or metal-organic CVD processes are not possible.

Basically, the structure of CVD materials is classified according to three different morphologies: columnar, faceted-columnar and equiaxed grains, as shown in Fig. **4**.

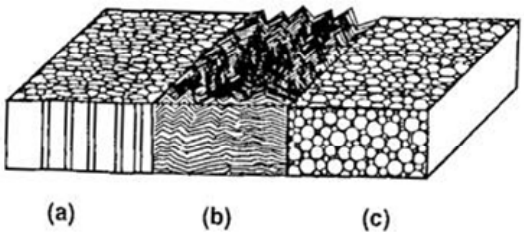


Figure 4: Different morphologies of CVD grown materials. (a) columnar, (b) faceted-columnar and (c) equiaxed grains [1].

i. The morphology of CVD coatings is mainly dominated by:

ii. The nature of the material: For example, oxides and nitrides are deposited in amorphous phase with small grain microstructure. On the other hand, metal is more crystalline, with pronounced columnar structure.

The deposition parameters, such as temperature, pressure, saturation and selected reaction sequence.

2. CLASSIFICATION OF CVD TECHNIQUES

As previously commented, CVD is a coating technique where gas precursors are introduced in a deposition chamber and react, giving as results a solid product (coating) and gaseous by-products. This definition represents a broad concept and comprises different specific CVD techniques grouped according to different criteria.

Depending on the **experimental conditions**, CVD can be classified as Atmospheric Pressure CVD, Low Pressure CVD and Ultrahigh Vacuum CVD. In a similar way, CVD processes have emerged considering the **activation mechanism** of the CVD reaction. This leads to thermally (Thermal CVD, Hot Wire CVD), optically (Photo CVD, Laser CVD) or plasma (Plasma Enhanced CVD, Microwave CVD, Remote Plasma Enhanced CVD) activated processes. Finally, it is important to remark on the CVD techniques based on the **nature of precursors**. Aerosol assisted CVD, Direct Liquid Injection CVD and Metal Organic CVD are some examples of these processes.

Although the description of all these techniques is not approached in this work, some of the most representative are briefly depicted. Those that are usually implemented in solar cell production have been selected.

Low Pressure Chemical Vapor Deposition (LPCVD): In the case of LPCVD, the coating is deposited at a low pressure in a heated CVD reaction chamber. Basically, the LPCVD configuration is similar to a conventional CVD chamber (heaters, temperature control, gas inlet and exhaust, *etc.*), adding a vacuum system (pumps, valves and sensors).

LPCVD processes lead to highly reproducible, uniform and throughput coatings and are commonly used in the semiconductor industry for the development of thin film dielectrics (SiO_2, Si_3N_4, Al_2O_3), thin film conductors and semiconductors (polysilicon, molybdenum, TiSi) and hard coatings (TiN, SiC, WC).

LPCVD is used in the photovoltaic sector for the development of transparent conductive oxides. In particular aluminum and boron doped zinc oxide materials are commonly obtained by means of this technique [7]. The process allows a precise control of the roughness surface. This fact represents an important issue for this application, since texturing favors light trapping mechanisms and subsequent increase in solar cell efficiency [8].

Plasma Enhanced Chemical Vapor Deposition (PECVD). The PECVD process uses electrical energy to create a glow discharge, plasma, and the energy is transferred into a gas mixture. Plasma is achieved by having a radio frequency in between two electrodes and energy is used to ionize and transform the precursor gases into reactive radicals, ions, neutral atoms, and molecules. Since the formation of the reactive and energetic species occurs in the gas phase by collision, thermal activation is minimized and the substrate can be maintained at low temperatures. This constitutes one of the most interesting advantages of PECVD, decreasing operating temperatures to below 200ºC in many cases. This permits the use of polymeric materials such as substrate. In a similar way, PECVD allows the fabrication of thin film coatings with excellent mechanical properties, as stress can easily be controlled and deformation and cracking are avoided.

The PECVD process has been widely used in microelectronic and optoelectronic applications for the deposition of semiconductor and dielectric materials. In photovoltaic, this technique has allowed the development of silicon based thin film solar cells as an interesting alternative to conventional crystalline and polycrystalline technologies.

Hot Wire Chemical Vapor Deposition (HWCVD). Hot Wire CVD (also called Catalytic CVD) is a low pressure CVD process based on the decomposition of precursor sources on a hot filament (1200ºC–2000ºC) [9]. The solid product is then deposited on the substrate, heated by an external source or by the filament itself. A schematic view of a typical HWCVD reactor is presented in Fig. **5**.

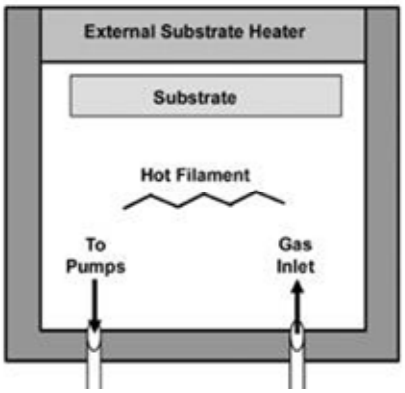


Figure 5: Schematic view of a HWCVD reactor [10].

The main advantages of HWCVD when compared to other CVD techniques are:

- Substrates don't have an active role in the reaction which assures no surface damage or modification. In a conventional HWCVD, ions reach energies in the substrate of below 0.2eV.
- The process is easily scalable by increasing the catalytic area (for example, a higher number of filaments) [11].
- Deposition rates are higher than 5nm/s.
- High quality coatings (high step coverage and uniformity) with properties differing to those obtained by other methods.
- HWCVD has been successfully used as an interesting alternative to PECVD in the development of microcrystalline silicon materials for thin film solar cells (see for example, [12]). For a more thorough discussion, Klein *et al.* [13] have compared both techniques and results obtained in the fabrication of silicon based thin film solar cells.

Metal-Organic Chemical Vapor Deposition (MOCVD). MOCVD is a technique that was initially developed in the 60s for the deposition of high quality semiconductors, in particular indium phosphide and indium antimonide. Metallo-organic compounds are usually referred to as molecules formed by a metallic (or semiconductor) atom bound to one or more atoms of an organic hydrocarbon group. Under appropriate experimental conditions, a pirolytic CVD reaction occurs and metallic (or semiconductor) coatings can be obtained with good quality, thickness control and epitaxy. In addition, this technology represents the only way to obtain some materials such as coatings in the nanometric range.

Although MOCVD has been widely used for microelectronic and optoelectronic applications due to the high requirements in these sectors, the process has also been extensively used as a deposition technique for the fabrication of solar cells. Initial studies were made in the use of MOCVD for the development of gallium based materials (GaAs, GaInP, AlGaAs, GaInAs) [14, 15]. In a similar way, MOCVD is currently used in the development of buffer layers for CIGS cells [16] and CdTe compounds [17] and novel transparent conductive oxides with enhanced properties [18].

3. PLASMA ENHANCED CHEMICAL PLASMA DEPOSITION

Today, silicon-based thin-film solar cell is a well-established technology and must be taken into account in the race to achieve the important goal of cost reduction of photovoltaic devices. First hydrogenated amorphous silicon (a-Si (-H)) devices were carried out by Sterling and Swann [19] and by Spear and Lecomber [20] using a reactor with a silane (SiH_4) glow discharge induced by radio frequency (RF) voltages. This was the base of the nowadays plasma enhanced chemical vapor deposition (PECVD). An important advantage of PECVD deposition is that the deposition temperature of a-Si (-H) is usually quite low, between 150ºC and 350ºC which allows the use of a variety of low cost materials such as a substrate, glass, stainless steel and flexible plastic foils. Since the pioneer experiments, a wide range of different deposition techniques have been

investigated with the intention of achieving higher material quality and increasing the deposition rates. RF-PECVD [21, 22], "high power high pressure" regime RF-PECVD [23, 24], very high frequency (VHF) PECVD [25, 26] and microwave (MW) assisted CVD [27, 28] are some of the main techniques being extensively explored. However, although its main drawback is its low deposition rate (1Å/s–2Å/s), the RF-PECVD using an excitation frequency of 13.56MHz is still the most widely used technique today both in laboratory and industrial scales to manufacture silicon-based thin film solar cells.

In this chapter, an overview is proposed of the deposition of a-Si (-H) and microcrystalline silicon (μc-Si) based thin films by using these different techniques. Deposition conditions, mechanisms of layers growing, advantages and drawbacks of the different methods are extensively described.

3.1. Amorphous Silicon Deposition by PECVD

3.1.1. RF-PECVD Technique

Although different ways of depositing amorphous silicon have been investigated, the RF-PECVD, considering an excitation frequency of 13.56MHz, is still the most widely used deposition technique. RF-PECVD systems may be designed with different geometries, generally with substrate and electrodes placed horizontally for research devices and vertically for industrial processes.

PECVD System

Basically, a PECVD deposition system is composed of the following parts:

1) A reactor made of stainless steel. Inside the chamber, electrodes, a heating system, a substrate holder and a gas entrance nozzle are located. Outside the reactor, a RF power and the gas inlet are found.

2) A turbomolecular pump coupled with a mechanical rotary pump is fixed at the exit of the reactor so as to a reach high vacuum in the chamber before the gas mixture entrance.

3) A gas system, located before the reactor, allows the obtention of the gas flow mixture necessary for the different layers. Generally, the gas is introduced through the lateral part of the reactor in a laminar flow parallel to the electrodes. The entrance of the gas can also be located through the electrode (showerhead configuration). In this case, a better layer of uniformity is reached, especially when μc-Si is deposited.

4) An electronic and control part.

5) An exhaust system for the process gases with a scrubber or a burn box. In order to decrease the gas concentration, a dilution with nitrogen is carried out typically after the turbomolecular pump, inside the rotary pump and at the entrance of the scrubber.

In cluster configuration systems, (Fig. **6**), a transfer system is employed to move the sample inside the vacuum system between various deposition chambers. Gate valves are used to separate the different chambers.

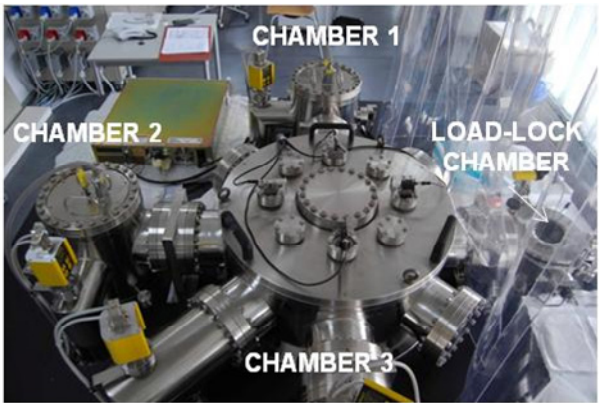


Figure 6: RF-PECVD multi-chamber (Elettrorava-ITALY) for silicon based thin film depositions installed at ITMA Materials Technology, Energy Area (Avilés, Spain).

Film Growth: Basic Chemical Approach

When a process is working, SiH_4 molecules will be dissociated inside the plasma by collisions with electrons, creating active particles called radicals. The growth of a-Si (-H) film is accomplished by attaching these reactive particles to the surface of the growing film. a-Si (-H) film growth from SiH_4 plasma in a PECVD system is a complex phenomenon and several spectroscopic techniques, such as optical emission spectroscopy, optical absorption spectroscopy and residual gas mass analyzer, have often been used to study the plasma and to determine the concentration of different species inside the reactor. From the results obtained, it seems that the SiH_3 radical is the main responsible molecule for the growth of high-quality a-Si (-H) films [29]. SiH_3 radical does not readily bond to the growing film but diffuses over the surface until it finds a dangling bond due to the fact that most of the growing substrate is ended by H_2 [30]. Bonding of the SiH_3 to the growing surface requires available dangling bonds, which are created when H_2 is removed from the surface by thermal excitation or by abstraction by a SiH_3 radical (in that case a dangling bond and a SiH_4 molecule are formed).

Other possible radical forms involved in the plasma during the process, such as SiH_2 and higher SiH_4 radicals contribute much less to the growth but they play an important role in determining the properties of the film. The SiH_2 and higher SiH_4 radicals have higher sticking coefficients than SiH_3 and can be incorporated directly in the H_2 terminated surface [31]. The presence of these radicals in the plasma should be avoided because their contribution to the growth results in poor quality films.

Process Conditions

Typical deposition parameters to obtain uniform films of device quality a-Si (-H) in a laboratory RF-PECVD deposition system are the pressure, the substrate temperature, the electrode spacing, gas flows and RF power density.

Pressure: the pressure range is usually set between 500mTorr and 800mTorr. Low pressure generally allows uniform deposition whereas high pressure is used for microcrystalline silicon films preparations.

Substrate temperature: is usually fixed between 150ºC and 350ºC. Low substrate temperature allows the incorporation of more H_2 in the layer and a slight increase of the bandgap of a-Si (-H) is reached. However, it is important to notify that a lower substrate temperature than 150ºC would induce the formation of silicon polyhydride powder.

RF power density: one of the main parameters leading the deposition rate is the power absorbed by the plasma. In fact, by applying a high power, a high electron density and electron temperature in the plasma is achieved. As a consequence, more SiH_4 molecules are dissociated in SiH_3 and other radicals which contribute to a higher deposition rate. The RF power density should be set between 20mW/cm^2 and 50mW/cm^2 for a capacitively coupled reactor. Below 10mW/cm^2 it is difficult to maintain the plasma. Higher power is desirable but, above 100mW/cm^2, silicon polyhydride powder can appear due to rapid reactions in the gas.

Electrode spacing: in an RF a glow discharge reactor is usually set between 1cm and 5cm for a-Si (-H) deposition. Narrow spacing is more desirable for a uniform deposition, whereas a large one offers an easier condition to maintain the plasma.

Flow rates: the flow rate required depends on the area of the reactor plates and the deposition rate. Some of the silicon atoms in the gases directed into the chamber are deposited onto the substrates or the chamber walls; the remainder gets pumped to the exhaust. For a research system with a 200cm^2 electrode area and for the deposition of a-Si (-H) at the rate of 1Å/s-2Å/s, only around 20sccm of SiH_4 flow is necessary. For the deposition of high-quality, stable a-Si (-H) material, a H_2 dilution at an appropriate level is also used. Depositing a 350nm thick a-Si (-H) intrinsic layer (i-layer) takes from 30 to 60 minutes which is an important drawback for industrial production. Therefore there is a lot of investigation focused on increasing the deposition rate with the aim of reaching 10Å/s–20Å/s.

Another important aspect of the growth of high-quality a-Si (-H) films is the presence of contaminants, such as oxygen, carbon, nitrogen, or metal elements. Concentration levels of O, C, and N higher than 1.3×10^{19}, 2.2×10^{18}, and 1.7×10^{17}at/cm^3, respectively, in the i-layer show poorer solar cell performance mainly due to the difficulty of photogenerated carriers diffusion. To avoid the presence of contaminants, a high vacuum level ($<1x10^{-7}$mTorr) is desirable prior to the introduction of the bearing gas. On the other hand, H_2 dilution of the SiH_4 gas mixture during a-Si (-H) deposition (both for intrinsic and doped layers) has been found to reduce the density of defect states, to improve the stability of the material against light-soaking effects and to show better solar cells performance. However, as the H_2 increases, the deposition rate declines.

3.1.2. VHF-PECVD Technique

The main drawback of the a-Si (-H) achieved by RF-PECVD is its low deposition rate (1Å/s–2Å/s). As mentioned in the previous section, high RF power allows the increase of the growth rate but silicon polyhydride powder may also appear. The VHF-PECVD, with an excitation frequency between 30MHz and 300MHz, is a solution as it presents the advantage of high plasma densities and low ion bombardment. Therefore, it has been widely used to deposit silicon thin films.

The Institute of Microtechnology of the University of Neuchâtel (IMT) was pioneered as a very high frequency glow discharge (VHF-GD) deposition technique and showed how it was possible

to considerably increase a-Si (-H) deposition rates. Since then, it has been demonstrated [32] that, at constant power, the increase of the frequency shows a linear increase of the deposition film. Several research groups have found higher deposition rates, up to ten times, maintaining good quality a-Si (-H) films. Applying higher excitation frequencies allows the modification of the electron energy distribution function in plasma. As a consequence, faster dissociation rates of source gases and higher deposition rates can be observed. Moreover, the VHF deposition technique allows the application of higher power densities in plasma at the same time as a powder free operational regime is established [33] due to fundamental physical changes in the capacitively coupled glow discharge plasma. As a consequence of these physical modifications (in the plasma impedance and with a reduction of the sheath thickness), a much better coupling of the RF power into the bulk plasma rather than into the sheath can be obtained at higher excitation frequencies. Thus, higher electron densities and better SiH_4 dissociation in the bulk plasma, as well as increased radical and ion flux onto the growing surface, can be achieved resulting in an increase in the deposition rate.

Although the advantages of using VHF deposition for high-rate growth have been clearly demonstrated, the main challenges to apply VHF-PECVD on an industrial scale are:

- Non uniformity of the deposited layers on a large, production scale substrate. RF standing waves may be formed on the electrode at high frequencies (>60MHz) when the electrode size is comparable to half the wavelength of the RF wave.
- An effective VHF power coupling from the generator to large electrodes is difficult to reach.

3.1.3. Alternatives Deposition Techniques

High pressure RF-PECVD mode: in this mode, higher gas pressures between 4 to 10Torr instead of about 500mTorr (conventional deposition mode) are employed. The main objective of this high pressure mode is to increase the ions collisions in the plasma in order to reduce their energy and offer a softer impact of the substrate surface. As a consequence, it is possible to highly increase the power fed to the plasma and also the deposition rate. Thin film solar cells based on amorphous silicon have been produced with a deposition rate of 12Å/s with a stabilized efficiency of 6.5% [23]. The depositions were carried out under high pressure (4Torr-7.5Torr) and high RF-power density ($270mWcm^{-2}$–$530mWcm^{-2}$) at 190ºC using a gas mixture of SiH_4 and H_2. It is shown that the increase of SiH_4 flow rate in the gas mixture as well as of the RF power can lead to higher concentration of reactive species and, therefore, can stimulate secondary reactions in the gas phase which lead to the growth of microcrystalline silicon. An increase has been observed in the bandgap and the open circuit voltage (V_{oc}) for high rate a-Si (-H) cells compared to standard a-Si (-H) prepared at a low H_2 dilution and at a low rate (1.5Å/s). Therefore, the results obtained make a-Si (-H) into interesting candidate for top cells in a-Si (-H)/a-Si (-H) stacked solar cells.

Microwave frequency (MW): glow discharge deposition at a microwave frequency of 2.45GHz also allows very high deposition rates to be reached. Two chamber configurations have been studied; direct contact and remote mode between the MW plasma and the substrate. The first case has the advantage of high deposition rates (>100Å/s) but the deposited layers show poor optoelectronic properties. In contrast, the remote MW-PECVD method shows high-quality films.

In this case, the plasma is generated, by MW excitation in a remote chamber, in a carrier gas such as He, H_2 or Ar that passes through the MW zone toward the substrate which is located outside the plasma region. The excited carrier gas then excites SiH_4 which is introduced into the chamber close to the substrate. The plasma is characterized by a high density of high energy electrons, which leads to a high dissociation rate. Another advantage is that the plasma can be maintained at low pressures (1mTorr). Furthermore, the concentration of SiH_3 radicals can be sustained, while the concentrations of other radicals (SiH_2, SiH, *etc.*) are minimized. Generally, the structural and optoelectronic properties of a-Si (-H) layers carried out by MW technique are worse than RF-deposited films. However, if only the very high deposition rate (for example 50Å/s) is considered, the MW-deposited films quality will be better than layers carried out by using RF and VHF techniques.

3.1.4. Amorphous Silicon Doped Layers

The main aim of doping is to modify the electrical conductivity and its magnitude of layers that encompass the photosensitive one in order to establish an electrical field necessary for a correct extraction of the electrons generated in the intrinsic film. It is important to point out that a-Si (-H) solar cell cannot work successfully as a p-n junction because the diffusion length of charge carriers in doped a-Si (-H) is very small compared to single crystal silicon. For this reason, a relatively defect free intrinsic layer has to be inserted between the p type and n type layers for the generation of the charge carriers and the role of the doped films is to set up the electrical field.

The doping process is carried out by adding a controlled amount of special impurity so as to get defect density two or three orders of magnitude larger than intrinsic a-Si (-H). Pioneer works carried out by Spear and LeComber in 1975 [20] showed that a-Si (-H) could be doped by addition of boron and phosphorus.

The performance of solar cells strongly depends on the properties of the p-layer, generally called the "window layer" that should meet the requirements of high conductivity and low absorption. Unfortunately, boron tends to alloy with a-Si (-H) instead of doping it which leads to a strong reduction in the bandgap. This drawback can be solved by adding carbon (CH_4) to the lattice. Moreover, boron originated from B_2H_6 tends to cluster within the network which also degrades the transmission of the layer. Other dopant gases can be used such as $B(CH_3)_3$, BF_3, and $B(C_2H_5)_3$, having claimed to lead superior p properties. On the other hand, boron from the p type layer may diffuse into the intrinsic one and lead to a back diffusion of the photogenerated electrons from the intrinsic into the p type layer. A possible solution is to incorporate a thin buffer layer at the p/i interface made of a-SiC (-H) with a low defect density.

Physical Properties

Typical criteria for intrinsic and doped a-Si (-H) layers for application in p-i-n or n-i-p type solar cells are listed in Table **1**.

3.2. Microcrystalline Silicon Deposition by PECVD

The term microcrystalline silicon (μc-Si) designates a material containing amorphous tissues and crystalline grains (typically 20nm–30nm). The depositions are carried out at low temperatures

(<400ºC) by PECVD technique, commonly from a mixture of SiH_4 and H_2. Low temperature process allows the reduction of contaminations as well as to offer a better incorporation of H_2 in order to passivate the electronic defects and grain boundaries. Fig. **7** shows an electronic microscope image obtained from n-type μc-Si layer.

Table 1: Physical properties of intrinsic and doped a-Si (-H). σ_d, dark conductivity; σ_{ph}, photoconductivity; Eg, energy gap; Ea, activation energy; α, absorption coefficient; [H], hydrogen concentration.

Property	Intrinsic a-Si (-H)	p-type a-Si (-H)	n-type a-Si (-H)
σ_d $(\Omega.cm)^{-1}$	$<1x10^{-10}$	$>10^{-5}$	$>10^{-3}$
σ_{ph} $(\Omega.cm)^{-1}$	$>1x10^{-5}$		
Eg (eV)	<1.8	>2.0	>1.75
Ea (eV)	0.8	<0.5	<0.3
α (600nm)	$>3.5x10^4$	$<1x10^4$	$<3x10^4$
α (400nm)	$>5x10^5$	$<10^5$	
[H] (%)	9-11		

Pioneer works were reported by Veprek and Marecek [34] in 1968 by using a chemical vapor transport technique with deposition precursors based on SiH_4 related radicals and atomic H_2 which plays a crucial role in layer growth. In 1979, Usui and Kikuchi [35] observed that it was easy to dope μc-Si comparing with a-Si (-H). But the first μc-Si layers, mainly due to their high defect density, own a poor quality level and it was concluded that it would be very difficult to manufacture solar cells based on μc-Si intrinsic layer.

The use of μc-Si as the active layer within a thin-film solar cell was not easy, for the following reasons:

a) μc-Si is a material with an indirect bandgap and its absorption coefficient in the visible part of the solar spectrum is much lower than that of a-Si (-H). As a consequence slightly thick μc-Si intrinsic films are necessary to get sufficient absorption and photogeneration;

b) The many grain boundaries present in the μc-Si layers can block the electronic transport in the case that a passivation by H_2 is not carried out correctly.

Such as in a-Si (-H), one still always uses the p-i-n type configuration for manufacturing μc-Si cells (instead of p-n junction) because the diffusion lengths are far too low, even though doping is far easier in μc-Si than in a-Si (-H), and even though doped μc-Si layers do not have additional defects introduced by the doping process. Consequently, in a first step, only p-type μc-Si layers were used for incorporation within p-i-n type thin-film silicon solar cells, where the active intrinsic layer consists of a-Si (-H) [36], due to its high conductivity and low absorption coefficient in the visible range.

Another useful application is also for the tunnel/recombination junctions that form the connection between individual cells, in a double-junction (tandem) or triple-junction a-Si (-H) solar cell. In 1996, J. Meier and *et al.* [37] reported on a p-i-n type fully microcrystalline thin film silicon solar

cells with an efficiency value of 7.7%. The intrinsic microcrystalline layer was carried out by using a gas purifier with low oxygen content and consequently it was observed that this μc-Si solar cell was not suffering from a pronounced Staebler–Wronski effect.

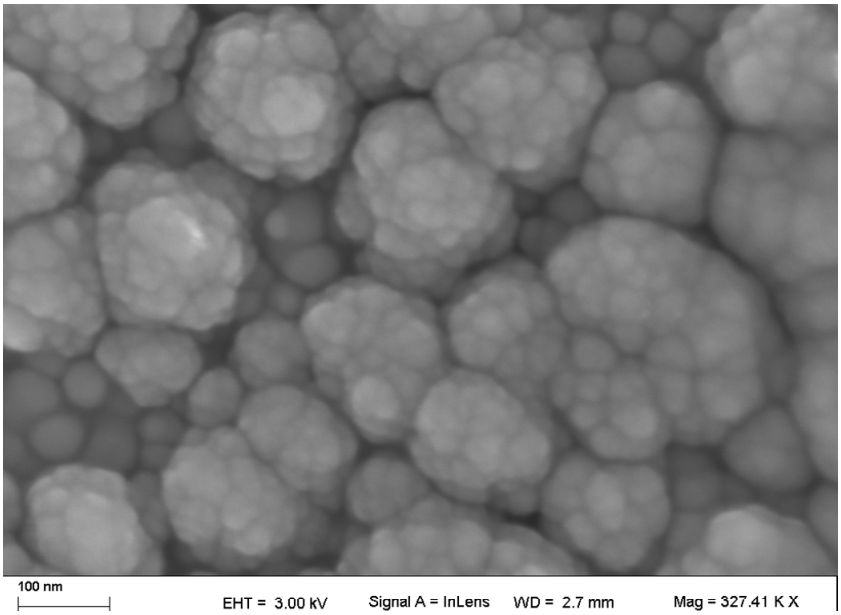


Figure 7: Emission field secondary electron microscope image corresponding to n-type μc-Si layer.

Nowadays the best way to advantageously employ a fully μc-Si solar cell is to combine it with an a-Si (-H) solar cell in a tandem system called the ‘‘micromorph’’ or ‘‘hybrid’’ concept and up till now, efficiencies up to 14.7% have been reached on laboratory scale.

High density of atomic hydrogen is a crucial condition for μc-Si [38] and it can be reached in different ways. The easiest one consists of increasing the hydrogen flow to the plasma. Higher plasma excitation frequency or plasma power are also valid solutions. One of the main drawbacks of μc-Si is its low absorption coefficient compared with a-Si (-H). Therefore, intrinsic layer with thickness of between 1μm-2μm is necessary. Consequently, important research lines are focused on high rate deposition regime (>5Å/s).

3.2.1. Effect of H_2 Dilution on Layer Crystallinity and Microstructure

In the usual type of PECVD reactor where the resulting layers are amorphous, pure SiH_4 plasma is used for the deposition. If H_2 is now added to the plasma, the layer quality is slowly altered and if the concentration of H_2 is further increased, crystallites begin to deposit. Then the crystalline volume fraction rapidly increases until layers will be essentially microcrystalline. By increasing the H_2 dilution of the plasma even more, the microstructure of the layers is varied and at high values of H_2 dilution, high columns separated by cracks appear. The three following points can explain the effects of H_2 dilution during the μc-Si growth:

1) Firstly, atomic H_2 acts as an etching agent, removing strained weaker bonds that are in energetically unfavorable locations;

2) Secondly, the surface diffusivity of atoms is promoted by a high flux of atomic H_2 in order to reach more energetically stable positions and form stronger bonds;

3) Finally, a more stable structure is promoted by the diffusion of atomic H_2 into the network.

For the same reasons, sufficiently large H_2 dilution induces the formation of microcrystalline Si and the best microcrystalline solar cells quality is deposited near the threshold concentration. For very high values of H_2 dilution, cracks that can provoke shunts in the solar cells and also act as channels by which contamination (*e.g.* oxygen) can enter into the layer appear and are responsible for a non usability of this material for solar cells. The amorphous phase is the first phase deposited. A minimum thickness called the incubation phase is generally needed before a localized phase transformation takes place, which is called nucleation. Finally from the nucleation centers the crystals start their growth. Other deposition conditions than the H_2 dilution level influence in the transition from amorphous to microcrystalline. High substrate temperatures (above 300ºC) and low substrate temperatures (below 250ºC) require higher H_2 dilution in order to reach the amorphous/microcrystalline transition. This is respectively due to the low sticking coefficient of H_2 and to the low surface diffusivity of H_2 during growth.

Physical Properties

Typical criteria for intrinsic and doped μc-Si layers for application in p-i-n or n-i-p type solar cells are listed in Table **2**.

Table 2: Intrinsic and doped μc-Si physical properties. σ_d, dark conductivity; σ_{ph}, photoconductivity; Eg, energy gap; Ea, activation energy.

Property	**i-type μc-Si**	**p-type μc-Si (300nm)**	**n-type μc-Si (70nm)**
σ_d $(\Omega.cm)^{-1}$	$<1.5\ 10^{-7}$	1.5	20
σ_{ph} $(\Omega.cm)^{-1}$	$>1.5\ 10^{-5}$		
Indirect bandgap (eV)	1.0-1.1		
Eg (eV)		1.4	1.9
Ea (eV)	0.53–0.57	0.025	0.01
Crystalline volume fraction (%)	>90	67	
Orientation of the grains	predominantly (220)		

3.2.2. High Pressure Depletion (HDP) RF-PECVD

The use of HPD allows that a great amount of atomic H_2 generated in the plasma, owing to the depletion of SiH_4, promotes crystallization without increasing ion bombardment under a high deposition pressure condition [39]. The HPD method has the advantage that good crystalline μc-Si film can easily be obtained in a large area by optimizing the deposition condition without

modifying the deposition system. However, it is also necessary to have plasma conditions where SiH_4 is depleted and relatively more H_2 is present in the plasma in order to obtain μc-Si rather than a-Si (-H) growth. Non uniform layers, high H_2 consumption and powder formation are some of the problems that have to be faced when optimizing HPD deposition. Moreover, film quality parameters such as defect density and crystallinity deteriorates gradually with an increasing growth rate of over 50Å/s.

Researchers from Juelich Institute (Germany) reported μc-Si solar cells with deposition rates of 5Å/s by using 13.56MHz [40]. Higher values (11Å/s) were achieved at a frequency of 95MHz [41] and an excellent efficiency of 9.8% was obtained. On the other hand, Suzuki [42] has improved the film qualities such as crystallinity and defect density of μc-Si films ($2.6x10^{16}cm^{-3}$) at a growth rate of 58Å/s by using a triode technique and a shower-head cathode combined with the HPD deposition conditions. High input powers are also an effective method for increasing the growth rate by keeping the low defect density because the high electron density and the low electron temperature can be simultaneously obtained [43]. It was reported [44] that, employing high pressures of up to 24Torr, very high growth rates of μc-Si photovoltaic layers can be reached. Future investigation is now focused on designing a production type large area reactor based on a combination of HPD and VHF principles [45].

3.2.3. Deposition of μc-Si by VHF-PECVD

A high deposition rate with uniform layer properties is necessary due to the requirement of a relatively large thickness of the microcrystalline absorber (1μm–2μm) in order to be competitive for industrial production. Up to now, VHF-PECVD [46] and RF-PECVD [47] in the high power, high pressure depletion regime allow the best solar cell results to be reached. VHF plasmas allow high deposition rates due to changes in the plasma leading to an enhanced dissociation of the SiH_4 in the plasma. Moreover, due to a reduction of the energies of the ions impinging on the growing surface observed at higher frequencies, a "softer" plasma is led that induces a reduction of the defect creation in crystallites. These results might explain why VHF plasmas allow a better growth of μc-Si as compared to conventional plasma deposition at 13.56MHz. These phenomenon, prevalent in VHF plasmas, are also propitious to the growth of high-quality μc-Si layers at high rates. Some authors [48] have investigated that crystallite size increases, as excitation frequency (f_{exc}) is increased. Because the deposition rate is one of the main existing bottlenecks when one wants to reduce the production cost of μc-Si solar cells and modules, this increase is a significant advantage for an industrial plant. Finally, one also has to take into account the powder limit factor which can be defined as the maximum power level or maximum deposition rate above which a significant amount of powder is formed in the reactor.

High deposition rates from 4.5Å/s to 45Å/s at 60MHz were achieved by Gordjin *et al.* [49] and microcrystalline single junction solar cells efficiencies of 10% and 6.4% were reached, respectively. This increase by a factor of ten of the deposition rate involved a higher defect density (growing in the same proportion) was also found.

It is important to notify that the curves of the deposition rate *vs.* excitation frequency possess, in general, a maximum at a certain "optimal" frequency and show, thereafter, a decrease of the deposition rate for yet higher frequencies. This decrease can be attributed to engineering aspects

such as reactor design. On the other hand, fundamental physical changes in the capacitively-coupled glow discharge plasma can explain the general trend of an increase in deposition rate with increasing excitation frequency. As the excitation frequency is increased, the sheath thickness decreases and the plasma impedance significantly changes.

Using the VHF-PECVD technique, researchers at the University of Neuchâtel in the 1990s succeeded in manufacturing the first hydrogenated microcrystalline silicon (μc-Si) cells at 200°C with reasonable efficiencies [50]. Importantly, the efficiencies of up to 4.6% of these cells were stable under light soaking conditions, giving hope to significantly elevate the stable module efficiency more for a-Si (-H) modules. Y. Nakano *et al.* [51] found that the distance between the substrate and the electrode has a substantial influence in order to satisfy both high rate and high-quality deposition of μc-Si. Gap length of 10mm or less allows a cell efficiency of 8.5% at a deposition rate of 3.1nm/s in μc-Si single junction p-i-n solar cells to be obtained. Finally, new research shows that the microstructure evolution in μc-Si films can be controlled by VHF power profiling [52]. The profiling parameters such as the amount and the rate of change in VHF power allows a control of the microstructure evolution and a reduction of ion bombardments on the growth surface. Using this method, a significant improvement in the solar cell performance is achieved. A high conversion efficiency of 9.36% was obtained for a single-junction μc-Si p-i-n solar cell at a deposition rate of 12Å/s.

3.2.4. Microwave (MW) CVD

In MW plasmas, high deposition rates are achieved for μc-Si due to the reduction of the ion bombardment compared with the standard 13.56MHz plasma deposition process. The use of MW allows high SiH_4 decomposition rates and a large amount of H_2 etching of the film growth surface, as required for microcrystalline film formation. Research on the application of MW technique for the deposition of μc-Si has started recently, demonstrating the potential of high deposition rates [53, 54].

The effect of Ar dilution on the deposition process of μc-Si by MW-PECVD has also been investigated [28]. Ar helps to stabilize the MW plasma, in particular at high H_2/SiH_4 ratios and at low power conditions, but it has a detrimental effect on the density of the layers. No significant effect of Ar on the growth rate of the layers was observed. The structure of the layers becomes more amorphous and the layers contain more defects when H_2 is partially replaced by Ar as a process gas. The main effect of Ar dilution to the growth of silicon layers in MW-PECVD is probably due to a change in plasma chemistry, where Ar metastable forms favor the formation of (unwanted) SiH_2 species at the expense of SiH_3 formation.

On the other hand, research has demonstrated the fast deposition of hydrogenated chlorinated microcrystalline Si (μc-Si:Cl) films (27Å/s) with less volume fraction of void using a high-density MW plasma source of a SiH_2Cl_2–H_2 mixture rather than those from SiH_4 [55]. The role of chlorine in the growth of μc-Si:Cl films is the effective termination of dangling bonds and the suppression of the excess film crystallization on the growing surface. Other authors report high-density MW plasma [56] obtained using a spokewise antenna in order to produce microcrystalline films from SiH_4 (without H_2 dilution and applying SiH_4 depletion and low pressure) at a growth rate of 4.7nm/s and a low substrate temperature of 250ºC.

3.2.5. Light-Induced Degradation

The Staebler–Wronski effect or light-induced degradation effect is a generalized defect of all kinds of a-Si (-H) layers and solar cells produced up till now. Not having, in general, any light-induced degradation seems quite surprising for μc-Si solar cells [57]. But it is important to notify that, by the term μc-Si, several different materials, showing appreciable differences such as crystallite orientation and form, microstructure and crystalline/amorphous volume fraction, can be considered. Therefore, it must be pointed out that certain types of μc-Si layers may suffer from light-induced degradation [58].

3.2.6. Post-Oxidation

Oxygen contained in the air will contaminate microcrystalline silicon layers when exposed to air over a period of weeks or longer. This phenomenon called "post-oxidation" induces a change in the Fermi level which is pushed towards the conduction band edge. Due to this, characterization measurement such as electrical conductivity and long-term electrical transport on μc-Si layers are delicate. Microcrystalline silicon layers produced by high plasma power and strong H_2 dilution, due to the possible cracks induced, are more susceptible to present post-oxidation than the more compact μc-Si layers produced near the amorphous/microcrystalline transition [59]. Although post-oxidation is a severe problem for μc-Si layer measurements, μc-Si solar cells have shown to be unaffected by this problem. This may be mainly due to the sealing effects provided by the relatively thick TCO (transparent conductive oxide) and metallic contact layers, on both sides of the cell.

4. LARGE AREA DEPOSITION

The solar cell production scale is very important for economic reasons. In order to accelerate the spread of solar cells and further expansion of the photovoltaic (PV) market, it is crucial to develop application systems that utilize building integration (*i.e.* walls of industrial factories, public buildings or architectural structures) as the final objective. These systems must be made up of large area photovoltaic devices. a-Si (-H) thin film has been the most promising material in the PV application, especially for low cost and large area solar cells. Therefore, a-Si (-H) thin film solar cells technology is suitable to achieve this purpose. Moreover, in the last few years, the development of tandem solar cells consisting of a-Si (-H) top cells and microcrystalline silicon (μc-Si) bottom cells are promising for the achievement of high conversion efficiency.

For the cost-effective mass production of thin film silicon solar cells, the industry requires higher deposition rates and uniform film thickness over large areas, while maintaining a high quality. Consequently, it is necessary to have suitable deposition techniques capable to satisfy these requirements, especially in the case of μc-Si solar cell, where intrinsic layer thickness of around 1.5μm is used due to the low absorption coefficient. PECVD deposition technique is particularly suitable for producing thin films for large areas, although some design modifications are necessary when going from small to large areas in order to maintain the material quality and the film's uniformity.

The ultra high vacuum (UHV) used in laboratory scale deposition equipment is required to reduce contaminant incorporation. However, the UHV is very difficult to maintain in sufficiently large

size reactors and cannot be applied to large area equipment due to excessive costs. An approach used to simulate UHV conditions in large area reactors is the double shell geometry or plasma box configuration [60], and it is widely used in production systems. In this configuration, the plasma box forms an enclosed, separately pumped volume within the deposition chamber as a double shell, in which plasma is confined between the electrodes and the substrate, the temperature is uniform and the deposition volume is protected from impurities. The outer shell is pumped to a low pressure while the plasma box, containing the substrate, is pumped *via* a throttle valve to the process pressure. In systems without a plasma box configuration, similar low contamination levels can be obtained by using a continuous flow arrangement using high purity gases.

VHF-PECVD is a particularly suitable technique for large scale thin films deposition, because it provides high deposition rate plasma reactors and a good uniformity of the film thickness at high power. The field of VHF-PECVD in terms of high rate and high quality deposition has been active since the late 1980s, when various researchers reported deposition rates improvements on a-Si (-H) thin films [61, 62]. Subsequently, a study on a-Si (-H)/μc-Si tandem solar cells using the same deposition technique was reported from Neuchatel University (Switzerland) in the mid-1990s [37, 50]. However, the high frequencies studies were performed in small reactors and they needed to be upscaled in order to meet the large area requirements for industrial applications.

Results have been reported by using 13.56MHz PECVD in order to avoid the non-uniform voltage distribution across the electrode and, therefore, to facilitate a-Si (-H) and μc-Si thin films depositions on larger substrates. It was found that a high deposition pressure ("high pressure deposition regime") is one of the key factors necessary to obtain high deposition rates and still maintain a good thin film quality [26, 63].

As was mentioned before, VHF plasma is more suitable for high rate and high quality deposition thin films than conventional RF (13.56MHz) plasma by using the most common electrode design of two conventional plane parallel plates. However, in the field of large areas, a lot of electrical problems were reported when the frequency of the RF power source was increased [64-66]. These electrical problems occur when the electrode's dimension become comparable to a quarter of the free-space wavelength associated with the excitation frequency (5.53m at 13.56MHz but only 0.75m at 100MHz), and generates non-uniform voltage distribution across the electrode area. For example, at 80MHz power frequency, the limit in the size of parallel plate type electrodes to obtain uniform deposition is reported to be 40cmx40cm [67]. Consequently, results in inhomogeneous thin film RF plasma deposition in large-area reactors were obtained. The problem of voltage distribution across the electrode surface becomes important if the RF frequency is increased for a fixed reactor size, or at the standard 13.56MHz frequency for larger reactors.

Many attempts have been made by researchers to overcome the problem mentioned above to realize low cost and large area uniform VHF-PECVD systems for the deposition of a-Si (-H) thin films on square substrates higher than $1m^2$. The aim of these attempts was to take special care in the power feeding system in order to introduce VHF power efficiently and uniformly to the plasma source. Three different electrode concepts are promising to overcome the non-uniform voltage distribution: ladder-shaped electrode, linear source and U-shapped array antenna. These designs are detailed below.

Murata *et al.* and Takeuchi *et al.* developed a novel CVD technique using an electrode of a ladder-shaped antenna, first at the conventional frequency of 13.56MHz [68-70] and later at VHF [26, 45, 71, 72]. A schematic diagram of the ladder-shaped electrode is shown in Fig. **8**. As can be seen, the RF power goes through a power divider and is applied to eight loading points on the ladder-shaped antenna.

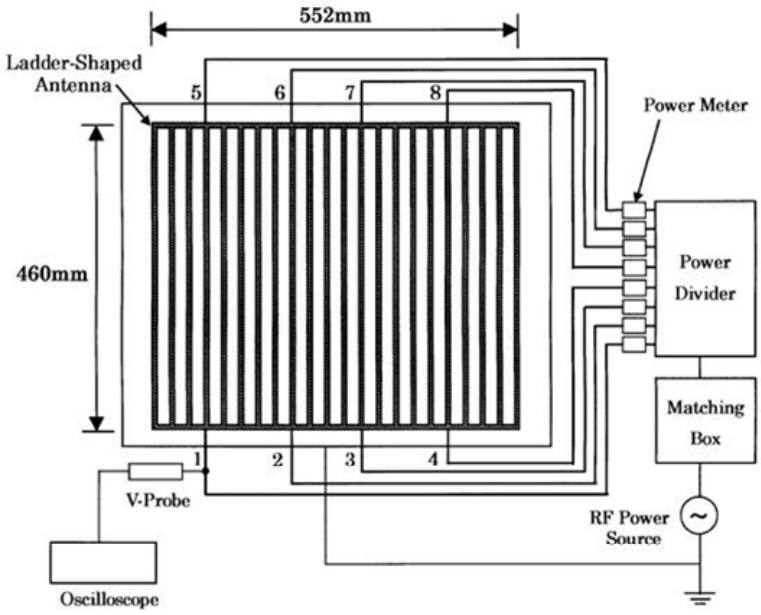


Figure 8: A schematic of the ladder shaped antenna [71].

These studies resulted in a high quality and high deposition rate (15Å/s) thin films a-Si (-H) over large area glass substrates, up to 1.1mx1.4m [73], with distribution ±10% in both of them, and therefore, the subsequent development of a VHF-PECVD technique based on a ladder-shaped electrode suitable for the production of a large area and high quality a-Si (-H) thin film deposition.

On the other hand, Applied Films (Germany) developed the linear plasma source designed to decrease the active electrode area in one spatial dimension [74-76]. Through this configuration, uniform plasma with high density is obtained in the longitudinal direction by feeding power by multiple points. In this way, deposition of a-Si (-H) and μc-Si thin films on large area substrates (30cmx30cm) is achieved by moving the substrate in the direction perpendicular to the longitudinal dimension of the electrode (continuous deposition process). Using this continuous deposition method, which is also well suited for roll-to-roll processes, a high productivity can be achieved. Deposition rates up to 11Å/s and film homogeneity better than ±5% were obtained. Fig. **9** shows a sketch of the source module developed (LQ500 or LQ type plasma source) which is implemented as complete electrical units on rectangle flanges. The excitation frequency used was 81.36MHz, which represents a compromise between a high deposition rate and minimum rate film homogeneity over the source width. The number of power feed-ins is generally determined by the source width and the excitation frequency.

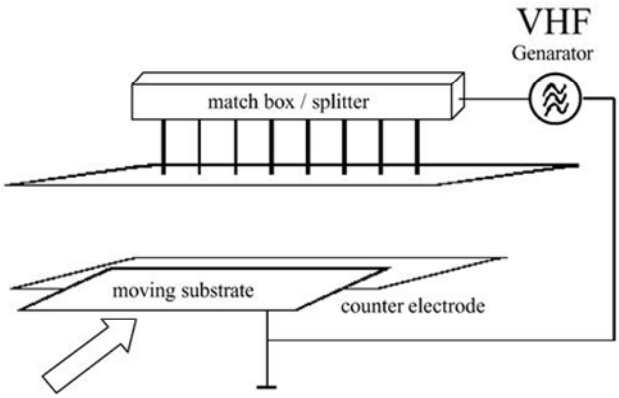


Figure 9: A schematic of the linear source (one dimensional electrode) [75].

The U-shaped array antenna consists of plural U-shaped loop antenna type electrodes where uniform deposition is realized by controling the power and the phase VHF power introduced to the electrodes [77-79]. This electrode was designed to generate and maintain plasma at a specific power frequency. Fig. **10** shows a schematic diagram of U-shaped electrode, where one end is connected to the chamber wall (grounded point) and the other end to the power-feeding point.

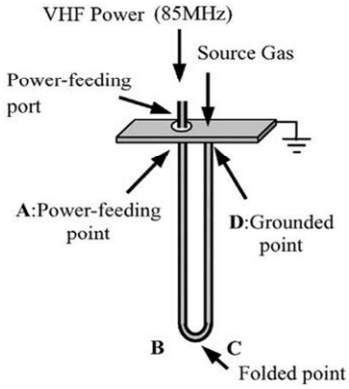


Figure 10: Schematic diagram of a U-shaped electrode [77].

In a VHF-PECVD system, a group of U-shaped electrodes are arranged to form one array of antenna, as can be seen in Fig. **11**. A pair of glass substrates is placed on both sides of array antenna, facing each other. Homogeneous deposition a-Si (-H) and μc-Si thin films on square glass substrates higher than $1m^2$ at 85MHz were obtained by using this configuration.

Since high plasma densities and low ion energies are key issues for efficient PECVD processes, microwave energy appears to be the best choice for high rates. However, the main problem is again how to sustain a uniform and steady plasma discharge over areas much larger than the wavelength of the applied wavelength power. To overcome this problem, the coaxial line plasma source appears to be the only industrially viable way of microwave PECVD (MWCVD) for large area depositions, in the area range higher than $1m^2$ [80].

5. PRODUCTION SYSTEMS

Taking into account the configurations of the thin film solar cells, there are several possibilities for processing the different layers on large areas (m^2-size). In general, it is possible to distinguish different production schemes, such as single panel, batch (where several substrates are processed at the same time) and roll-to-roll processes. The final design of the PECVD equipment is determined by these possibilities.

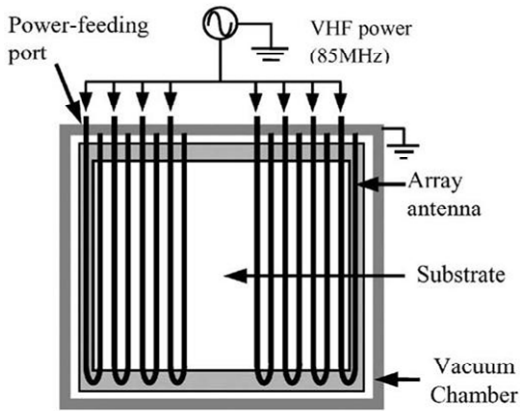


Figure 11: Schematic side view of VHF-PECVD system with an array antenna [77].

In single panel and in batch processing, the deposition of all layers can be carried out either in a single chamber system or each individual layer is deposited in an independent chamber. Next, both possibilities will be compared.

5.1. Single Chamber System

This system has the advantage that p-i-n layer deposition takes place in a static deposition mode without movement of the substrates during the deposition process under vacuum conditions. Therefore, the capital investment is low compared to other configurations. However, precautions need to be taken in order to avoid cross contamination between the doped and the intrinsic layers depositions, particularly boron tailing from the p layer into the intrinsic layer. Consequently, several purge and pump-down steps are required to obtain a good quality and uniform layer.

As an example, a successful and proven single chamber PECVD system has been developed by Oerlikon Solar and is so-called "KAI" (concept of UNAXIS) [81]. This system is based on the plasma box concept and large area deposition up to $5m^2$ has already been demonstrated. In KAI 1200 system, 20 reactors operate in parallel and, therefore, 20 sheets of glass, with a size of $1.4m^2$, can be processed simultaneously.

5.2. Multichamber System

The multichamber system configuration has the advantage that the deposition parameters such as temperature, internal geometry or even the discharge frequency can be optimized for each

individual layer. However, the investment cost is quite large compared with the single chamber configuration. Besides, the size of the panels may be limited. Two types of multichamber configurations can be distinguished, depending on the movement of the substrate during the deposition process.

5.2.1. In-line Configuration

An important challenge for the cost effective mass production of silicon thin film solar cells is the development of highly productive dynamic in-line deposition systems, although it must be noted that the equipment cost is very high, because special isolation chambers and vacuum valves are needed between the deposition chambers.

Some industrial lines for the dymanic in-line deposition of a-Si (-H) and μc-Si have been developed to demonstrate the feasibility of this configuration, based on MWCVD [27, 28], U-shaped electrode [79] or linear plasma source [76], all of them in combination with moving substrates. In Fig. **12** a schematic view of an example of in-line deposition system consisted of three deposition chambers (p-i-n layers) and a load lock to charge the carrier is shown. Note that the substrate is located on the grounded carrier and moves horizontally inside the tunnel.

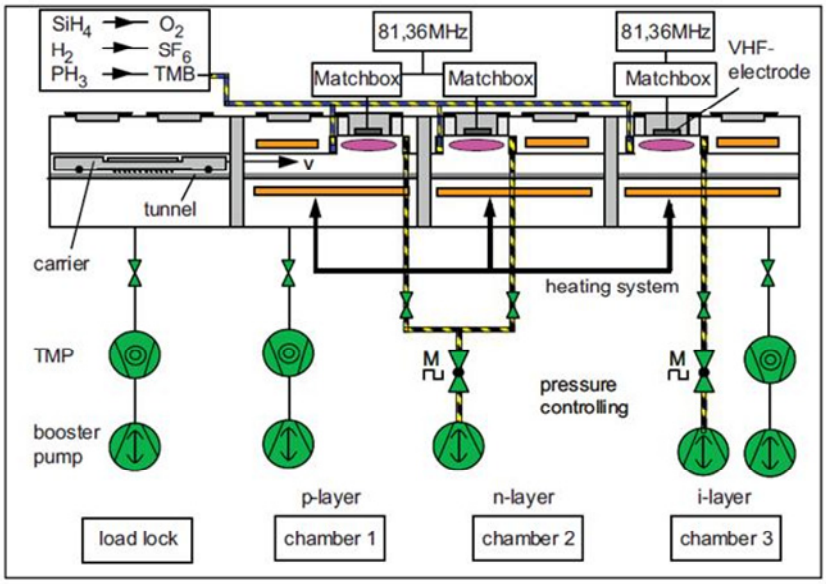


Figure 12: Schematic view of an entire in-line deposition system [76].

5.2.2. Cluster Configuration

This configuration has all the advantages of the multichamber system, *i.e.* control of the deposition parameters in each individual layer, complete control of the level of dopants and other contaminants, lower investment than in-line configuration due to the fact that transport and isolation chambers can be shared by many deposition chambers, *etc.* In addition, this configuration

makes it possible that the transfer from the laboratory to the production scale represents only a small step. Applied Materials has developed a standard PECVD production equipment based on cluster configuration (model AKT) to deposit silicon thin films on large areas [82]. This equipment is basically the same design as in a small area laboratory multichamber system [83]. In Fig. **13** a scheme of a cluster PECVD configuration is represented.

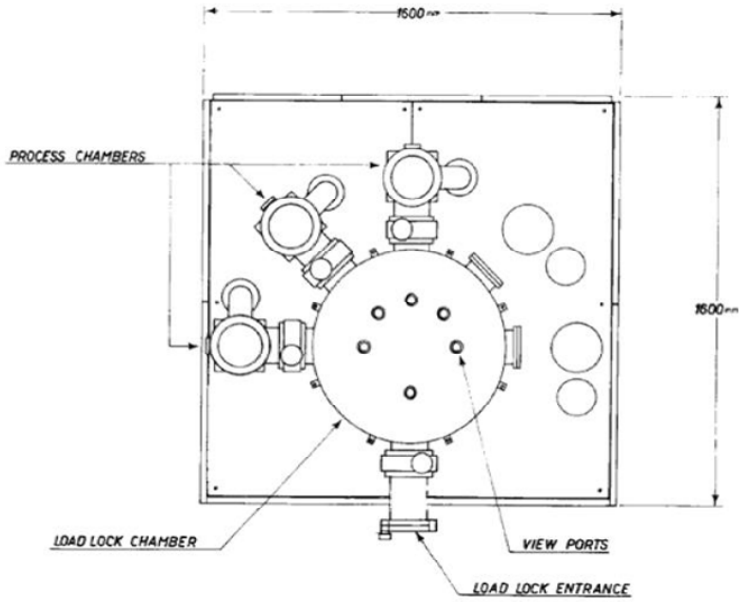


Figure 13: Schematic of the cluster PECVD configuration [83].

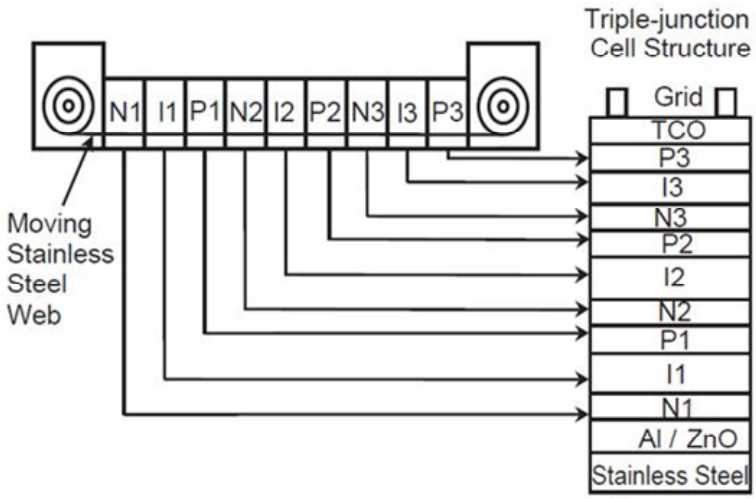


Figure 14: Schematic diagram of a roll-to-roll a-Si (-H) alloy triple-junction solar cell processor [85, 86].

5.2.3. Roll-to-Roll Configuration

Another important PECVD configuration for the development of low-cost photovoltaic modules based on a-Si (-H) solar cells on flexible substrates in a large scale production is a dynamic roll-to-roll method. Various research and industrial groups have developed their own device structures and processes, such as United Solar [84-87], Helianthos project [88], VHF-Technologies [89] and Fuji Electric [90], which uses the "stepping" roll-to-roll (non continuous motion). In all of these processes, the transport mechanism can be cheaper than in most in line systems described before. As an example, Fig. **14** illustrates the roll-to-roll triple-junction deposition scheme followed by United Solar, where a roll of 127μm thick stainless steel (SS) substrate goes through four consecutive roll-to-roll machines first to wash, and then to deposit the back reflector, triple-junction structure, and top conductive layer. The width of the SS rolls used is 356mm, and the length is 2.59km.

One of the most important problems is to prevent cross contamination due to the fact that all deposition zones are connected to each other. This problem was solved by Energy Conversion Devices by using a laminar gas flow through a constant geometrical cross section opposite to the diffusion gradient of the dopant gasses.

ACKNOWLEDGEMENT

Declared none.

CONFLICT OF INTEREST

The author(s) confirm that this chapter content has no conflict of interest.

REFERENCES

[1] Pierson HO. Handbook of Chemical Vapour Deposition: Principles, Technology and Applications. New Jersey: Noyes Publications 1999.

[2] Gohier A, Minea TM, Point S, *et al.* Early stages of the carbon nanotube growth by low pressure CVD and PE-CVD. Diamond and Related Materials 2009; 18 (1): 61-5.

[3] Park HJ, Meyer J, Roth S, Skakalova V. Growth and properties of few-layer graphene prepared by chemical vapor deposition**.** Carbon 2010; 48 (4): 1088-94.

[4] Gueroudji L, Hwang LM. Thermodynamic limits for the substrate temperature in the CVD diamond process. Diamond and Related Materials 2000; 9: 205-11.

[5] Xia B, Smith RC, Moersch TL, Gladfelter WL. Balancing reactor fluid dynamics and deposition kinetics to achieve compositional variation in combinatorial chemical vapor depositions. Appl Surf Sci 2004; 223: 14-9.

[6] Luo G, Vanka SP, Glumac N. Fluid flow and transport processes in a large area atmospheric pressure stagnation flow CVD reactor for deposition of thin films. International Journal of Heat and Mass Transfer 2004; 47: 4979-949.

[7] Fay S, Steinhauser J, Nicolay S, Ballif C. Polycrystalline ZnO: B grown by LPCVD as TCO for thin film silicon solar cells. Thin Solid Films 2010; 518: 2961-6.

[8] Müller J, Rech B, Springer J, Vanecek M. TCO and light trapping in silicon thin film solar cells. Solar Energy 2004; 77: 917-30.

[9] Matsumura HJ. Study on catalytic chemical vapor deposition method to prepare hydrogenated amorphous silicon. Appl Phys 1989; 65: 4396-402.
[10] Christine Esber Richardson, PhD Thesis, California Institute of Technology (2006)
[11] Ledermann A, Weber U, Mukherjee C, Schröeder B. Influence of gas supply and filament geometry on the large-area deposition of amorphous silicon by hot-wire CVD. Thin Solid Films 2001; 395: 61-5.
[12] Klein S, Finger F, Carius R *et al.* Intrinsic microcrystalline silicon prepared by hot-wire chemical vapour deposition for thin film solar cells. Thin Solid Films 2003; 430: 202-7.
[13] Klein S, Repmann T, Brammer T. Microcrystalline silicon films and solar cells deposited by PECVD and HWCVD. Solar Energy 2004; 77: 893-908.
[14] Moto A, Tanaka S, Tanabe T, Takagishi S. GaInP/GaAs and mechanically stacked GaInAs solar cells grown by MOCVD using TBAs and TBP as V-precursors. Solar Energy Materials & Solar Cells 2001; 66: 585-92.
[15] Soga T, Baskar K, Kato T, Jimbo T, Umeno M. MOCVD growth of high efficiency current-matched AlGaAs/Si tandem solar cell. Journal of Crystal Growth 1997; 174: 579-84.
[16] Spiering S, Bückert L, Hariskos D, *et al.* MOCVD indium sulphide for application as a buffer layer in CIGS solar cells. Thin Solid Films 2009; 517: 2328-31.
[17] Goren D, Amir N, Khanin E, Asa G, Nemirovsky Y. Single crystalline CdTe solar cells grown by MOCVD. Solar Energy Materials & Solar Cells 1996; 44: 341-56.
[18] Addonizio ML, Antonaia A. Surface morphology and light scattering properties of plasma etched ZnO:B films grown by LP-MOCVD for silicon thin film solar cells. Thin Solid Films 2009; 518 (4): 1026-31.
[19] Sterling HF, Swann RCG. Chemical vapour deposition promoted by r.f. discharge. Sol State Elec 1965; 8: 653-4.
[20] Spear W, LeComber P. Substitutional doping of amorphous silicon. Sol State Comm 1975; 17: 1193-6.
[21] Yamamoto K, Nakajima A, Yoshimi M, *et al.* A high efficiency thin film silicon solar cell and module. Solar Energy 2004; 77: 939-49.
[22] Rech B, Kluth O, Repmann T, *et al.* New materials and deposition techniques for highly efficient silicon thin film solar cells. Solar Energy Materials & Solar Cells 2002; 74: 439-47.
[23] Rech B, Roschek T, Müller J, Wieder S, Wagner H. Amorphous and microcrystalline silicon solar cells prepared at high deposition rates using RF (13.56 MHz) plasma excitation frequencies. Solar Energy Materials & Solar Cells 2001; 66: 267-73.
[24] Roschek T, Repmann T, Müller J, Rech B, Wagner H. Comprehensive study of microcrystalline silicon solar cells deposited at high rate using 13.56 MHz plasma-enhanced chemical vapor deposition. J Vac Sci Technol 2002, 2, 492-9.
[25] Meier J, Vallat-Sauvain E, Dubail S, *et al.* Microcrystalline/micromorph silicon thin-film solar cells prepared by VHF-GD technique. Solar Energy Materials & Solar Cells 2001; 66: 73-84.
[26] Takeuchi Y, Nawata Y, Ogawa K, Serizawa A, Yamauchi Y, Murata M. Preparation of large uniform amorphous silicon films by VHF-PECVD using a ladder-shaped antenna. Thin Solid Films 2001, 386, 133-6.
[27] Soppe WJ, Biebericher ACW, Devilee C, Donker H, Schlemm H, High rate growth of micro-crystalline silicon by microwave-PECVD. In: Proceedings of the Third World Conference and Exhibition on Photovoltaic Solar Energy Conversion; 2003: Osaka, Japan; pp. 1655–60.
[28] Soppe WJ, Devilee C, Geusebroek M, Löffler J, Muffler HJ. The effect of argon dilution on deposition of microcrystalline silicon by microwave plasma enhanced chemical vapor deposition. Thin Solid Films 2007; 515: 7490-4.
[29] Matsuda A, Nomoto K, Takeuchi Y, Suzuki A, Yuuki A, Perrin J. Temperature dependence of the sticking and loss probabilities of silyl radicals on hydrogenated amorphous silicon. Surf Sci 1990; 227: 50-6.
[30] Toyoshima Y, Arai K, Matsuda A, Tanaka KJ. *In situ* characterization of the growing a-Si:H surface by IR spectroscopy. Non-Cryst Solids 1991; 137: 765-70.
[31] Street R. Hydrogenated Amorphous Silicon. Cambridge University Press: Cambridge 1991.

[32] Shah A, Dutta J, Wyrsch N, *et al.* VHF plasma deposition: A comparative overview, in Amorphous silicon thechnology. Mater. Res. Soc. Proc. 1992; 258: 15-26.

[33] Dorier JL, Hollenstein C, Howling AA, Kroll U. Powder dynamics in very high frequency silane plasmas. J Vac Sci Technol A 1992; 10: 1048-53.

[34] Veprek S, Marecek V. The preparation of thin layers of Ge and Si by chemical hydrogen plasma transport. Sol State Elec 1968; 11: 683-4.

[35] Usui S, Kikuchi M. Properties of heavily doped GD-Si with low re sistivity. Journal of Non-Crystalline Solid 1979; 34: 1-11.

[36] Hattori Y, Kruangam T, Toyama T, Okamoto H, Hamakawa Y, High efficiency amorphous heterojunction solar cell employing ECR-CVD produced p-type microcrystalline SiC film. Technical Digest of the International PVSEC-3; 1987: Tokyo, Japan; pp. 171.

[37] Meier J, Torres P, Platz R, *et al.* On the way towards high efficiency thin film silicon solar cells by the "micromorph" concept in Amorphous Silicon Technology. In: Hack M, Schiff EA, Wagner S, Schropp R, Matsuda A, Eds. Proceedings of the Materials Research Society Symposium; 1996: Pittsburgh: Materials Research Society 1996; pp. 3-14.

[38] Matsuda A. Growth mechanism of microcrystalline silicon obtained from reactive plasmas. Thin Solid Films 1999; 337: 1-6.

[39] Fukawa M, Suzuki S, Guo L, Kondo M, Matsuda A. High rate growth of microcrystalline silicon using a high-pressure depletion method with VHF plasma. Solar Energy Materials & Solar Cells 2001; 66: 217-23.

[40] Repmann T, Appenzeller W, Sehrbrock B, Zahren C, Rech B. Advanced PECVD processes for thin film silicon solar cells on glass. Proceedings of the 19th European Photovoltaic Specialist Conference; 2004: Paris, France; pp. 1334–1351.

[41] Mai Y, Klein S, Wolff J, Lambertz A, Geng X, Finger F. Microcrystalline silicon solar cells deposited at high rates by combination of VHF-PECVD and highworking pressure. Proceedings of the 19th European Photovoltaic Solar Energy Conference; 2004: Paris, France; pp. 1399–1402.

[42] Suzuki S, Kondo M, Matsuda A. Growth of device grade μc-Si film at over 50Å/s using PECVD. Solar Energy Materials & Solar Cells 2002; 74: 489-95.

[43] Matsuda A. Microcrystalline silicon: Growth and device application. J. Non-Cryst. Solids 2004; 338–340: 1-12.

[44] Sobajima Y, Nakano S, Toyama T, Okamoto H. High-Rate Deposition of Microcrystalline Silicon Photovoltaic Active Layers by Plasma-Enhanced Chemical Vapor Deposition at Kilo-Pascal Pressures. Jpn J Appl Phys 2007; 46: 199-201.

[45] Takatsuda H, Noda M, Yonekura Y, Takeuchi Y, Yamauchi Y. Development of high efficiency large area silicon thin film modules using VHF-PECVD. Solar Energy 2004; 77: 951-60.

[46] Mai Y, Klein S, Carius R, *et al.* Microcrystalline silicon solar cells deposited at high rates. J Appl Phys 2005; 97: 114913-25.

[47] Rech B, Roschek T, Repmann T, Müller J, Schmitz R, Appenzeller W. Microcrystalline silicon for large area thin film solar cells. Thin Solid Films 2003; 427: 157-65.

[48] Kroll U, Shah A, Keppner H, Meier J, Torres P, Fisher D. Potential of VHF-plasmas for low cost production of a-Si:H solar cells. Solar Energy Materials & Solar Cells 1997; 48: 343-50.

[49] Gordjin A, Hodakova L, Rath JK, Schropp REI. Influence on cell performance of bulk defect density in microcrystalline silicon grown by VHF PECVD. J Non-Crystalline Solids 2006; 352: 1868-71.

[50] Meier J, Flückiger R, Keppner H, Shah A. Complete microcrystalline pin solar cell crystalline or amorphous cell behavior. Appl Phys Lett 1994; 65: 860-2.

[51] Nakano Y, Goya S, Wanatabe T, Yamashita N, Yonekura Y. High-deposition-rate of microcrystalline silicon solar cell by using VHF PECVD. Thin Solid Films 2006; 506: 33-7.

[52] Han X, Hou G, Zhang X, *et al.* Improvement of hydrogenated microcrystalline silicon solar cell performance by VHF power profiling. Solar Energy Materials & Solar Cells 2010; 94: 254-7.

[53] Soppe WJ, Muffler HJ, Biebericher AC, *et al.* Optical and Structural Properties of Microcrystalline Silicon Grown by Microwave PECVD. Proceedings of the 20th European Photovoltaic Solar Energy Conference; 2005: Barcelona, Spain; pp. 3DV.3.21.

[54] Guha S, Yang J. Subcontract Report NREL/SR-520-38355. 2005.

[55] Saha JK, Ohse N, Hamada K, *et al.* Fast deposition of microcrystalline Si films from SiH_2Cl_2 using a high density microwave plasma source for Si thin film solar cells. Solar Energy Materials & Solar cells 2010; 94: 524-30.

[56] Sakuma Y, Haiping L, Ueyama H, Shirai H. High density microwave plasma for high rate and low temperature deposition of silicon thin film. Vacuum 2000; 59: 266-76.

[57] Kleider JP, Longeaud C, Bruggemann R, Houze F. Electronic and topographic properties of amorphous and microcrystalline silicon thin films. Thin Solid Films 2001; 383: 57-60.

[58] Ray S, Mukhopadhyay S, Jana T, Carius R. Transition from amorphous to microcrystalline Si:H: effects of substrate temperature and hydrogen dilution. J Non-Cryst Solid 2002; 299: 761-6.

[59] Goerlitzer M, Torres P, Beck N, *et al.* Structural properties and electronic transport in intrinsic microcrystalline silicon deposited by the VHF-GD technique. J Non-Cryst Solids 1998; 227: 996-1000.

[60] Schmitt JPM, Meot J, Roubeau P, Parrens P. New reactor design for low contamination amorphous silicon deposition. In: Solomon I, Equer B, Helm P, Eds. Proceedings of the 8th European Community Photovoltaic Solar Energy Conference; 1988: Florence; pp. 964-8.

[61] Curtins HC, Wyrsch N, Favre M, Shah AV. Influence of plasma excitation frequency for a-Si:H thin film deposition. Plasma Chem. Plasma Processing 1987; 7: 267-74.

[62] Oda S, Noda J, Matsumura M. Diagnostic Study of VHF Plasma and Deposition of Hydrogenated Amorphous Silicon Films. Jpn J Appl Phys 1990; 29: 1889-95.

[63] Guo L, Kondo M, Fukawa M, Saitoh K, Matsuda A. High Rate Deposition of Microcrystalline Silicon Using Conventional Plasma-Enhanced Chemical Vapor Deposition. Jpn J Appl Phys 1998; 37: L1116-8.

[64] Schmitt JPM. Amorphous silicon deposition: Industrial and technical challenges. Thin Solid Films 1989; 174: 193-202.

[65] Kuske J, Stephan U, Steinke O, Rohlecke S. Power feeding in large area PECVD of amorphous silicon. Mat. Res. Soc. Symp. Proc. 1995; 377: 27-32.

[66] Sansonnens L, Pletzer A, Magni D, Howling AA, Hollenstein Ch, Schmitt JPM. A voltage uniformity study in large-area reactors for RF plasma deposition. Plasma Sources Sci Technol 1997; 6: 170-8.

[67] Kroll U, Fisher D, Meier J, Sansonnens L, Howling A, Shah A. Fast deposition of a-Si:H layers and solar cells in a large-area (40×40 cm^2) VHF-GD reactor. Mater. Res. Soc. Symp. Proc. 1999; 557: 121-6.

[68] Murata M, Takeuchi Y, Sasagawa E, Hamamoto K. Inductively coupled radio frequency plasma chemical vapor deposition using a ladder-shaped antenna. Rev Sci Instrum 1996; 67: 1542-6.

[69] Murata M, Takeuchi Y, Nishida S. Magnetically enhanced inductively coupled plasma CVD for a-Si:H fabrication. Vacuum 1997; 48: 1-6.

[70] Mashima H, Murata M, Takeuchi Y, *et al.* Characteristics of Very High Frequency Plasma Produced Using a Ladder-Shaped Electrode. Jpn J Appl Phy 1999; 38: 4305-8.

[71] Kawai Y, Yoshioka M, Yamane T, Takeuchi Y, Murata M. Radio-frequency plasma production using a ladder-shaped antenna. Surf Coat Technol 1999; 116: 662-5.

[72] Mashima H, Takeuchi Y, Murata M, *et al.* Characteristics of the electron temperature in VHF-excited SiH_4/H_2 plasma produced using a ladder-shaped electrode. Vacuum 2004; 74: 503-7.

[73] Takatsuka H, Noda M, Yonekura Y, Takeuchi Y, Yamauchi Y. Development of high efficiency large area silicon thin film modules using VHF-PECVD. Solar Energy 2004; 77: 951-60.

[74] Kuske J, Stephan U, Stahr F, *et al.* In: McNelis B, Palz W, Ossenbrink HA, Helm P, Eds. Proceedings of the 17th European Photovoltaic Solar Energy Conference; 2001: Munich: WIP-Munich and ETA-Florence 2001; pp. 2884.

[75] Rüdiger J, Brechtel H, Kottwitz A, Kuske J, Stephan U. VHF plasma processing for in-line deposition systems. Thin Solid Films 2003; 427: 16-20.

[76] Strobel C, Zimmermann T, Albert M, Bartha JW, Kuske J. Productivity potential of an inline deposition system for amorphous and microcrystalline silicon solar cells. Solar Energy Materials & Solar Cells 2009; 93: 1598-1607.

[77] Takagi T, Ueda M, Ito N, Watabe Y, Sato H, Sawaya K. Microcrystalline silicon solar cells fabricated by array antenna type VHF-PECVD system. In: Proceedings of the 20th European Photovoltaic Solar Energy Conference; 2005: Barcelona; pp. 1541-1543.

[78] Takagi T, Ueda M, Ito N, Watabe Y, Sato H, Sawaya K. Large area VHF plasma sources. Thin Solid Films 2006; 502: 50-4.

[79] Takagi T, Ueda M, Ito N, Watabe Y, Kondo M. Microcrystalline Silicon Solar Cells Fabricated using Array-Antenna-Type Very High Frequency Plasma-Enhanced Chemical Vapor Deposition System. Jpn J Appl Phys 2006; 45: 4003-5.

[80] Liehr M, Wieder S, Dieguez-Campo M. Large area microwave coating technology. Thin Solid Films 2006; 502: 9-14.

[81] Shah A, Meier J, Bueche A, *et al.* Towards very low-cost mass production of thin-film silicon photovoltaic (PV) solar modules on glass. Thin Solid Films 2006; 502: 292-9.

[82] Chae Y, Won TK, Li L, *et al.* Deposition of amorphous silicon/microcrystalline silicon for tandem solar cells using cluster PECVD tool on jumbo size subtrates. In: Proceedings of the 22nd European Photovoltaic Solar Energy Conference; 2007: Milan; pp. 1807-1809.

[83] Madan A, Rava P, Schropp REI, Roedern B. A new modular multichamber plasma enhanced chemical vapor deposition system. Appl Surf Sci 1993; 70: 716-21.

[84] Guha S. Amorphous silicon alloy photovoltaic technology and applications. Renew Energy 1998; 15: 189-94.

[85] Yang J, Yan B, Guha S. Amorphous and nanocrystalline silicon-based multi-junction solar cells. Thin Solid Films 2005; 487: 162-9.

[86] Izu M, Ellison T. Roll-to-roll manufacturing of amorphous silicon alloy solar cells with *in situ* cell performance diagnostics. Solar Energy Materials & Solar Cells 2003; 78: 613-26.

[87] Yue G, Yan B, Ganguly G, Yang J, Guha S, Teplin CW. Material structure and metastability of hydrogenated nanocrystalline silicon solar cells. Appl Phys Lett 2006; 88: 263507-9.

[88] Donker MN, Gordijn A, Stiebig H, *et al.* Flexible amorphous and microcrystalline silicon tandem solar modules in the temporary superstrate concept. Solar Energy Materials & Solar Cells 2007; 91, 572-80.

[89] Fisher D, Closset A, Ziegler Y. Electric energy generating modules with a two-dimensional profile and method of fabricating the same. US 11/521874. 2007 Jan.

[90] Ichikawa Y, Toshida T, Hama T, Sakai H, Harashima K. Production technology for amorphous silicon-based flexible solar cells. Solar Energy Materials & Solar Cells 2001; 66: 107-15.

Send Orders of Reprints at reprints@benthamscience.net

CHAPTER 3

Sputtering of Thin Films

Paolo Rava*

Elettrorava SpA, Via Don Sapino 176, 10078 Venaria, Torino, Italy

Abstract: Sputtering is one of the most widely used techniques for deposition of thin films. This chapter reviews the physical foundations of sputtering in a plasma and its application to the deposition of thin films. Different sputtering techniques are described and their advantages and disadvantages are highlighted.

Keywords: Sputtering, plasma, glow discharge, thin films, magnetron cathode, ion beam, deposition, targets, ionization, gases.

1. INTRODUCTION

Sputtering is a process whereby atoms are ejected from a solid target material due to the bombardment of the target by energetic particles [1]. It is commonly used for thin-film deposition, etching and analytical techniques.

2. PHYSICS OF SPUTTERING

Physical sputtering is driven by momentum exchange between the ions in an ionized gas (plasma) and the atoms in the solid material, as a result of collisions [1-3]. The primary particles for the sputtering process are supplied in general by either a plasma generated by a cathode or by an ion source (Fig. **1**).

The figure illustrates the effect of an incident gas atom from the initial impact collision onto a target surface. This generates primary, secondary, tertiary and quaternary recoils of the target atoms. Two of the atoms are shown being ejected from the sample, *i.e.* sputtered.

The incident ions set off collision cascades in the target. When such cascades recoil and reach the target surface with an energy above the surface binding energy, an atom can be ejected. The average number of atoms ejected from the target per incident ion is called the sputter yield and depends on the ion incident angle, the energy of the ion, the masses of the ion and target atoms, and the surface binding energy of atoms in the target. For a crystalline target, the orientation of the crystal axes with respect to the target surface is also relevant.

Physical sputtering has a well-defined minimum energy threshold which is equal to or larger than the ion energy at which the maximum energy transfer of the ion to a sample atom equals the binding energy of a surface atom. This threshold is typically in the range 10–100 eV.

***Address correspondence to Paolo Rava:** Elettrorava SpA, Via Don Sapino 176, 10078 Venaria, Torino, Italy; Tel: 0039-011-4240237; E-mail: paolo.rava@elettrorava.com

Roberto Murri (Ed)
All rights reserved-© 2013 Bentham Science Publishers

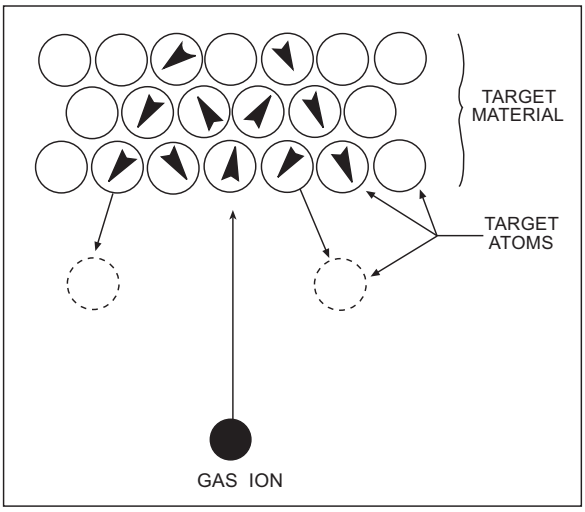


Figure 1: Sputtering from a linear collision cascade (courtesy of Materials Research Corporation Inc.).

3. FILM SPUTTERING DEPOSITION

Sputter deposition is a physical vapor deposition (PVD) method of depositing thin films which involves the ejection of material from a target, that is then deposited onto a substrate.

In this thin film deposition technique, the source material (target) is placed in the form of a plate as the cathode in a vacuum chamber and ionization of a gas is generated by a high voltage discharge (Fig. **2**). Positive ions are accelerated against the cathode causing removal of atoms from the target as a direct result of mechanical collisions. Sputtered atoms ejected from the target have a wide energy distribution, typically up to tens of eV (100000°K). A small fraction of the ejected particles are ionized (typically around 1%). These ions travel from the target in straight lines and impact energetically on the substrates or vacuum chamber walls causing resputtering (re-emission of the deposited material during the deposition process by ion or atom bombardment).

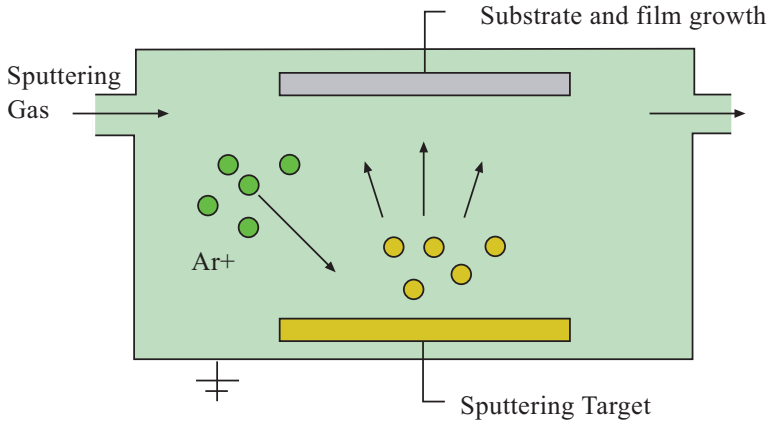


Figure 2: Schematics of sputtering [4].

Alternatively, at higher gas pressures, the ions collide with the gas atoms that act as a moderator and move diffusively, reaching the substrates or vacuum chamber walls and condensing there after undergoing a random walk. A wide range of different energy collisions from high-energy ballistic impact to low-energy thermalized motion can be obtained by varying the background gas pressure. Sputtered atoms ejected into the gas phase are not in their thermodynamic equilibrium state, and tend to deposit on all surfaces in the vacuum chamber: in particular they deposit on the substrates to be coated which act as an anode, where they condense to form the desired film.

The sputtering process begins when a negative voltage is applied to the target: the positive gas ions move towards the target, and, on impact, some atoms from the surface are displaced.

For efficient momentum transfer, the atomic weight of the sputtering gas should be close to the atomic weight of the target, so for sputtering light elements neon is preferable, whilst for heavy elements krypton or xenon can be used. In practice a gas with an intermediate weight such as Ar is commonly used as it is easily available. Reactive gases can also be used to sputter compounds. The compound can be formed on the target surface, in-flight or on the substrate depending on the process parameters.

Sputtering deposition can overcome problems related to weak binding forces between atoms during the deposition of a thin film.

The process of sputtering uses as a source of ions a glow discharge generated by the application of a potential between two electrodes immersed in a gas. A series of ionization processes occur (formation of electrons and positive ions) leading to the creation of plasma.

The availability of many parameters that control sputter deposition makes it a complex process, but also allow experts a large degree of control over the growth and microstructure of the film that is deposited.

The figure illustrates the effect of an incident gas atom from the initial impact collision onto a target surface. This generates primary, secondary, tertiary and quaternary recoils of the target atoms. Two of the atoms are shown being ejected from the sample, *i.e.* sputtered.

The incident ions set off collision cascades in the target. When such cascades recoil and reach the target surface with an energy above the surface binding energy, an atom can be ejected. The average number of atoms ejected from the target per incident ion is called the sputter yield and depends on the ion incident angle, the energy of the ion, the masses of the ion and target atoms, and the surface binding energy of atoms in the target. For a crystalline target, the orientation of the crystal axes with respect to the target surface is also relevant.

Physical sputtering has a well-defined minimum energy threshold which is equal to or larger than the ion energy at which the maximum energy transfer of the ion to a sample atom equals the binding energy of a surface atom. This threshold is typically in the range 10–100 eV.

4. PLASMA

Plasma can be defined as a gas containing electrically charged species and electrically neutral species [5]. Therefore it contains electrons, positive ions, negative ions, atoms and molecules. In

overall terms a plasma is electrically neutral and any charge imbalance is compensated for by the existing electric field moving the charged particles in order to maintain neutrality. The first important consideration that emerges is that in a plasma the sum of the density of electrons and of negative ions present is equal to the density of positively charged ions.

Usually, plasma characteristics vary greatly depending on the type of atoms or molecules that constitute the gas, and on their density and energy levels. However, there is a common factor in all types of plasma: free charges present in the gas respond to the effects of an electric field in the same way, *i.e.* trying to minimize the effects of this field. In particular, electrons are lighter and more mobile so that they respond more quickly to the effect of an electric field whereas ions are strongly influenced by their mass and show a large inertia to field variations.

As stated previously, plasma is characterized by a balance between ionic and electronic density, in which the various recombination processes are immediately offset by ionization processes. The existence of this dynamic balance condition is subject to a constant energy input from outside, which can create, through the formation of an electric field, the appropriate environment for the plasma regime.

Although plasma is a neutral gas in terms of total charge, it is characterized by a strong interaction between atoms and electrons with collisions and local energy transfer. Atoms are effectively stationary with respect to electrons because of their mass and can be considered to represent the "targets" of electrons. The main phenomena deriving from inelastic collisions of electrons and atoms are:

- Ionization when a primary electron removes an electron from a gas atom.

- Excitation when an incident electron transfers energy to an electron of the gas atom exciting it to a higher energy level.

- Relaxation when an electron returns to its ground state releasing energy as a photon.

- Recombination when an electron and a positive ion recombine to form a neutral atom. Recombination cannot occur directly between the two species, but must take place through a third body, either through a negatively charged ion, or through the emission of a photon.

In a normal plasma regime the temperature of the gas ions is close to room temperature; however the electron gas dramatically raises the plasma temperature to thousands of degrees Kelvin. To produce the ions necessary to sustain the plasma, in the case of sputtering, DC (direct current) or RF (radio frequency) glow discharges are used.

5. COLLISION PROCESSES IN PLASMA

As previously noted, plasma is characterized by interaction between atoms and electrons which collide and create local energy transfers.

The target particles may be considered spherical, with a cross section for electron impact equal to the area of their midsection. A sphere of radius r has a section $\sigma = \pi r^2$, where σ is the cross-section, which is proportional to the probability that a given collision can occur.

Considering n molecules enclosed in a volume of section A and thickness Δx, the probability that an electron collides into one of these molecules is:

$$P = (n A \sigma)\Delta x/A = n \sigma \Delta x \quad \textbf{(1)}$$

The average distance that an electron can travel within the volume between collisions is the mean free path (MFP) and is denoted by λ:

$$\lambda = 1/n \sigma \quad \textbf{(2)}$$

Collision processes require a preliminary distinction: they can be:

- Elastic, if the collision does not lead to a variation of the potential energy of the particles and if their total kinetic energy remains constant.

- Inelastic, if the potential energy after the collision of two bodies varies.

If during an elastic collision a particle of mass m_i and speed v_i hits a stationary particle of mass $m_{t,}$, the transfer function of kinetic energy;

$$E_t/E_i = 4m_i m_t \cos^2\theta/(m_i + m_t)^2 \quad \textbf{(3)}$$

indicates that an efficient energy transfer occurs between atoms of the same gas and from atoms to electrons whereas if an electron strikes an atom or molecule a very small amount of energy is transferred.

When the collision between a particle of mass m_i and speed v_i against a stationary particle of mass m_t is inelastic, the particle of mass m_t increases its potential energy by a value of ΔU and the transfer function;

$$\Delta U/E_i = m_t\cos^2\theta/(m_i + m_t) \quad \textbf{(4)}$$

indicates that the electron kinetic energy is efficiently transferred into potential energy of the atom. The pure transfer of kinetic energy from an electron to an atom in the case of an inelastic collision is negligible. Inelastic collisions are of great importance when analyzing the phenomena that occur within a plasma.

6. BREAKDOWN

The phenomenon of breakdown is the process immediately preceding the formation of a glow discharge. The simplest system capable of creating and sustaining a glow discharge consists of two electrodes connected to an external generator (DC or RF) which are placed at a distance d, and enclosed in a volume V into which an inert gas (Ar) is introduced.

If a DC generator is used to create a potential difference V_p between the electrodes, the electric field accelerates the few electrons present in the gas from the cathode to the anode, providing them with the necessary energy to ionize neutral particles along their path. This will lead to a rapid

increase in the number of electrons in the gas. The electric field accelerates the ions in the opposite direction. When the ions strike the cathode, they cause the emission of secondary electrons. The process repeats again and again, thus generating more and more ions and electrons. The "avalanche" generation of electrons and ions leads to a marked increase in the value of the anode current and to a potential drop across the electrodes: the system is now in the state of dc breakdown.

If the electric field created is oscillating as in the case of radio frequency (RF), the phenomenon shows some differences with respect to DC excitation. In fact, the electrons gain energy by simply following the oscillations induced by the electric field. The alternating electric field can then provide enough energy to electrons so that they can sustain ionization processes. In this case the contribution of secondary electrons is not required.

Before breakdown, a constant electric field and therefore a voltage drop across the electrodes is applied. Following breakdown, a glow discharge is formed with an intensity that increases with the applied voltage to the electrodes. The increase in current leads to the avalanche formation of ions and electrons so that the discharge enters the full state of breakdown.

7. DC GLOW DISCHARGE

The glow discharge formed as a result of breakdown, is composed of several regions with different characteristics, arranged so as to balance the energy input from the outside with processes involving particles in the gas (Fig. **3**).

Although the DC glow discharge is composed of several regions that merge into each other, for an effective description it is convenient to separate and analyze these regions separately.

The most extended zone is the negative glow which forms the plasma discharge in most deposition systems. It is a luminous plasma region, in which electronic and ionic densities are nearly equal.

Because of the lighter and faster electrons, the random ionic current density (*i.e.* without applied electric field);

$$J_i = n_e c_i/4 \quad \textbf{(5)}$$

is much smaller than the random electronic current density;

$$J_e = n_e c_e/4 \quad \textbf{(6)}$$

Therefore, in order to maintain the same current densities in the negative glow region, a certain number of electrons must move away from it. The lack of electrons in that region brings it to a positive potential higher than all the other regions that make up the glow discharge; the equality of electronic and ionic density make this region equipotential and therefore this region has a very low electric field.

The sources for energy input to the negative glow include secondary electrons emitted from the cathode and accelerated through the sheaths, and electrons accelerated into the glow region. Their

acceleration is given by the presence of a strong electric field adjacent to the glow region. The electric field automatically changes its intensity so that the discharge glow in this region can be sustained.

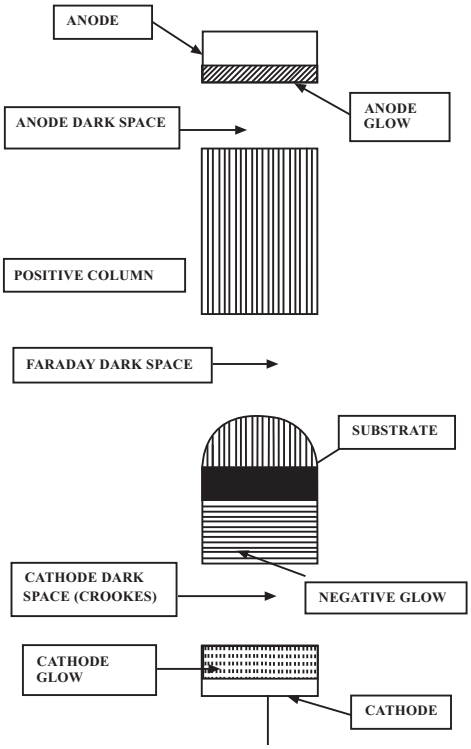


Figure 3: Glow discharge zones [5].

The ions generated in the negative glow are instead accelerated toward the cathode, contributing to the generation of secondary electrons.

The negative glow region is surrounded by sheaths: the cathode sheath separates it from the cathode, on the opposite side are the Faraday dark space sheaths.

Sheaths are regions with varying potential, where electric fields are formed and can influence the motion of electrons and ions.

The sheaths have a strong influence on the electrons, whereas ions are not strongly influenced due to their relatively high mass.

Variations in potential due to the sheaths are observed near the electrodes, and they balance the current supplied to the system from outside with the current flowing to the electrodes. The electric field formed near the cathode (cathode dark space sheath) has sign and value such as to attract the ions and repel the electrons and has a positive space charge.

The cathode sheath plays an important role in accelerating and transferring charged particles to the plasma. The ions accelerated by the sheath collide with electrically neutral species, and exchange charge (Fig.**4**).

The cathode sheath plays a fundamental role also with regard to the ionization of particles: ionization occurs not only in the cathode sheath but also at its interface with the negative glow region. In addition, plasma is sustained partly from the generation of secondary electrons as previously described.

Sheaths are also present on an insulating substrate immersed in a plasma. In fact, by placing an insulating substrate in the plasma, it is negatively charged due to the higher electron current than ionic current. In order to restore the balance between the densities on the surface of the substrate, the incident electron current decreases down to the value of ion current. This creates a positive space charge sheath on the substrate, at a potential lower than the plasma potential, which can repel the electrons.

On the anode there is another positive dark space charge sheath (anode sheath) with an electric field that is of value and sign to decrease the density of electron current to the electrode. The most common systems on the market use different elements as the anode. Dependent on the geometric characteristics of the plasma, the walls of the deposition reactor, the substrate or both can function as an anode. In order for the electrical circuit formed between the anode and cathode through the discharge to have continuity, the ionic current at the cathode must be equal to the electron current present on the anode. If the geometric dimensions of the anode are not sufficient to carry the required electron current, an electric field is generated of value and sign such as to increase the electronic current to the required value.

Far away from the negative glow region, towards the anode, are located the Faraday dark space sheath and the positive column. The Faraday dark space sheath is located adjacent to the negative glow. The border between the two regions is the point up to which the electrons of the negative glow can travel (Fig. **4**).

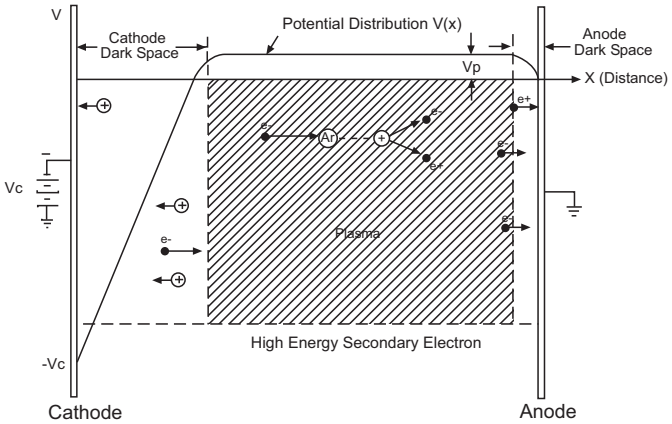


Figure 4: Processes and zones in a DC Diode Discharge (courtesy of Materials Research Corporation Inc.).

The positive column consists of a relatively large bright area, with characteristics that approach those of an ideal plasma. In this region the electrons are in equilibrium with the electric field present: they gain energy as a result of their acceleration which is induced by the field, and they lose energy through recombination, emission and diffusion towards the walls of the chamber. The regions between the negative glow and the anode are not significant in plasma applications for sputter deposition.

8. RF GLOW DISCHARGE

DC glow discharges have limitations that confine their use only to special cases: the vast majority of the input power is used for the transport of ions to the cathode across the sheaths. This means that only a small fraction of the energy supplied from outside is available to accelerate the secondary electrons, which are the main source of the plasma, generated by ionic impact on the cathode. In addition, DC glow discharges require flow of electrical current to sustain the discharge. The presence of insulating parts in the system can make it difficult to control or even to establish the plasma process. AC discharges provide a solution to these problems (Fig. **5**). If the system under consideration involves the use of fields (and current) at low frequency and the presence of only conducting elements, the discharge shows a behavior very similar to a DC glow discharge. If an insulating electrode is placed in the system, the following phenomena occurs: its surface becomes electrically charged within a certain period of time, quenching the discharge in the first half of the cycle, and then igniting it again in the opposite direction, during the second half of the cycle. The system is fully comparable to a capacitor, being charged by plasma in alternating directions during each cycle. By increasing the frequency of the field up to 100 kHz, the ratio between the insulating substrate charging and discharging time and the cycle time can be increased. The effect is a continuous flow of current inside the plasma, despite the presence of the insulating substrate. If radio frequency excitation is used, ions show a large inertia in responding to changes in the field, whereas the lighter electrons do not present any difficulty in oscillating with the field.

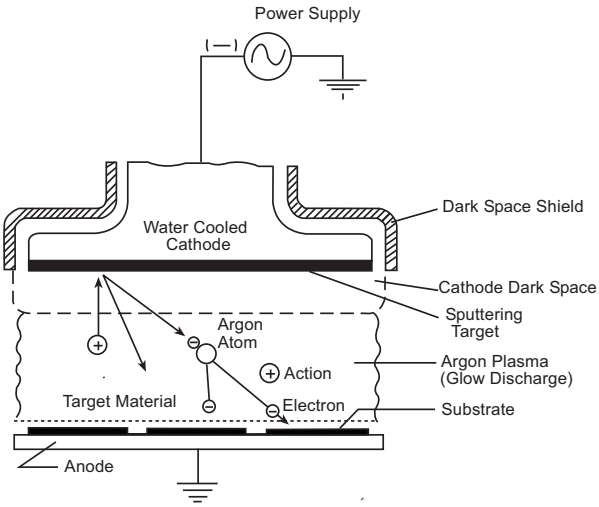


Figure 5: Schematic of a Conventional Diode Sputtering System (courtesy of Materials Research Corporation Inc.).

In properly configured systems, the phenomenon described above causes deviations in the curve of the applied potential. The characteristic current response of a plasma with respect to an applied voltage is in fact asymmetric, and qualitatively similar to that of a diode (Fig. **5**). There is in fact a large electron discharge current at a positive potential and a small ion current at a negative potential. To satisfy the condition of the balance at the electrodes between the ionic and the electronic current, the potential curve for the discharge generated is shifted so as to increase the ionic component and to decrease the electronic component. The points of the maxima and minima on the graph progressively move to lower values to achieve that balance. This is possible only by means of an appropriate configuration: capacitive coupling between the RF power generator and the plasma and proper sizing of the electrodes. The capacitor accumulates and redistributes the current generated in the plasma at a rate dependent on the resistance encountered by the charges: the electron current will be discharged faster than the ionic current because of the higher electron mobility. The electrode connected to the capacitor must be smaller than the other (grounded) electrode. The asymmetry of the system and the presence of the capacitor make the plasma potential on average greater than zero. The self-bias, which is the phenomenon of deviation of the potential in the plasma, appears on the smaller electrode. As a result, the plasma potential, even though it is subject to an oscillating field, remains constant at a value greater than zero.

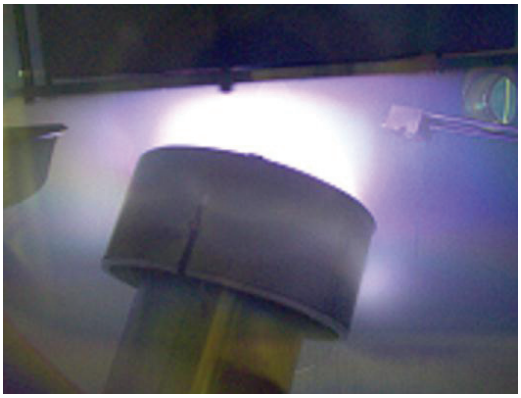


Figure 6: Sputtering cathode with plasma.

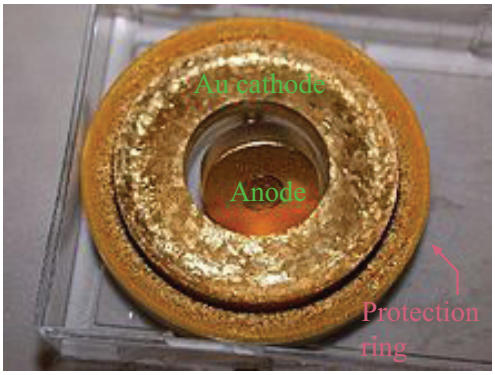


Figure 7: Typical ring-geometry sputter target (gold) showing the cathode made of the material to be deposited, the anode counter-electrode and an outer ring designed to prevent sputtering of the hearth that holds the target [4].

9. USES OF SPUTTERING

Sputtering (Figs. **6-8**) is used extensively in the semiconductor industry to deposit thin films of various materials in integrated circuit processing and in the optical industry to deposit thin antireflection coatings or multilayer filters on glass for optical applications. Because of the low substrate temperatures used, sputtering is an ideal method to deposit contact metals for thin-film transistors. Perhaps the most familiar products of sputtering are low-emissivity coatings on glass, used in double-pane window assemblies. The coating is a multilayer containing silver and metal oxides such as zinc oxide, tin oxide, or titanium dioxide. Sputtering is also used to metalize flexible plastics. A large industry has developed around tool bit coating using sputtered nitrides, such as titanium nitride, creating the familiar gold colored hard coat. Sputtering is also used as the process to deposit the metal (*e.g.* aluminum) layer during the fabrication of CD and DVD discs. Hard disk surfaces use sputtered CrO_x and other sputtered materials. Sputtering is one of the main processes of manufacturing optical waveguides and is another way for making efficient photovoltaic solar cells.



Figure 8: A commercial sputtering system for thin film deposition.

10. COMPARISON WITH OTHER DEPOSITION METHODS

An important advantage of sputter deposition is that even materials with very high melting points are easily sputtered while evaporation of these materials in a resistance evaporator or Knudsen cell is problematic or sometimes impossible. Sputter deposited films have a composition close to that of the source material. The variance is due to different elements spreading differently as a consequence of their different mass (light elements are deflected more easily by the gas) but this difference is constant. Sputtered films typically have a better adhesion on the substrate than evaporated films. A target contains a large amount of material and is maintenance free which means that the technique is well suited for ultrahigh vacuum applications. Sputtering sources contain no hot parts (to avoid heating they are typically water cooled) and they are also compatible with reactive gases such as oxygen. Sputtering can be performed either bottom-up or top-down whilst evaporation must be performed bottom-up. Advanced processes such as epitaxial growth

are possible. One disadvantage of the sputtering process is that the process is more difficult to combine with a lift-off process for structuring the film. This is a consequence of the diffuse transport characteristic of sputtering, which makes a perfect shadow impossible. Thus, one cannot fully restrict where the atoms go, which can lead to contamination problems. Also, active control for layer-by-layer growth is difficult in the sputtering process compared to pulsed laser deposition and inert sputtering gases can become incorporated into the growing film as impurities.

11. SPUTTERING PROCESSES

Sputtering processes can be divided into 4 subcategories:

- DC sputtering
- RF sputtering
- Sputtering with magnetic enhancement
- Reactive Sputtering

Different combinations or variants can be deposited using these four main types of sputtering.

11.1. DC Sputtering

This system uses a direct current to generate the discharge. The deposition rate of thin films depends on the sputtering pressure as well as on the applied current and voltage. The pressure in particular is a variable that should be treated with some care to achieve an efficient process. At low pressures (about 20 mTorr) the cathode sheath is extended, so the ions have difficulty in reaching the target, which implies a low ionization efficiency. If the pressure is increased, whilst maintaining a constant voltage to the electrodes, the mean free path of electrons decreases: this leads to an increase of the ionization efficiency and hence to an increased current flow. If the pressure increases further, then the electronic scattering also increases, with resulting decrease in sputtering rate.

11.2. RF Sputtering

Charge build-up on insulating targets can be avoided by the use of RF sputtering (Fig. **9**), where the sign of the anode-cathode bias is varied at a high rate. RF sputtering works well to produce highly insulating oxide films but this is only possible with the addition of RF power supplies and impedance matching networks. The principle of the discharge by applying a radio frequency voltage was already discussed above. Now the system as a whole is analyzed. Forward and Reflected power are shown separately on the generator; a matching network is placed between the generator and the load with the function to increase the power dissipation in the discharge. A matching network is composed of an inductor connected in series with a variable capacitor and in parallel with another variable capacitor.

RF sputtering works thanks to the ability of the target to charge to a negative potential and then behave like a classic target in a DC sputtering configuration. Due to the different mobility of ions

and electrons and to the positioning of a series capacitor close to the target, the net current is still zero but the large flow of electrons keeps the target at a negative voltage.

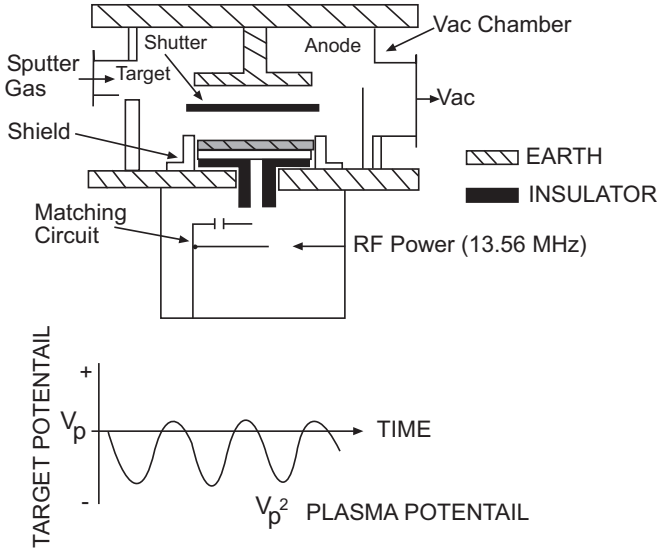


Figure 9: RF Diode schematics (courtesy of Materials Research Corporation Inc.).

The target surface area must be less than that of any other electrode in the sputtering chamber. In practice the area of the target placed on the cathode must be less than the area of the anode. The anode typically consists of the chamber walls, the substrate support, and the system ground connection.

RF sputtering is used in almost all cases, except in systems that use another method for plasma enhancement.(*e.g.* magnetrons).

11.3. Sputtering Systems with Magnetic Intensification

Sputtering sources are usually magnetrons that utilize strong electric and magnetic fields to trap electrons close to the surface of the magnetron, where the material target is placed. The electrons follow helical paths around the magnetic field lines and undergo more ionizing collisions with gaseous neutrals near the target surface than they would otherwise encounter (Fig. **10**). The extra argon ions created as a result of these collisions result in a higher deposition rate being achieved. It also means that the plasma can be sustained at a lower pressure. The sputtered atoms are neutrally charged and so are unaffected by the magnetic trap. In these systems a magnetic field B is applied in order to increase the plasma ionization by electrons. The magnetic field can be applied parallel or perpendicular to the electric field ξ. In the former case the magnetic fields, in opposition to applied electric fields, are called axial. The law that relates the electric field ξ with the magnetic field B is given by:

$$F = [m\, dv]/dt = -e(\xi + vB) \quad \textbf{(7)}$$

When electrons are emitted normal to the target, the term vB disappears and they are only influenced by the electric field that accelerates them linearly towards the anode. If the electric field is negligible, the magnetic field moves the electrons towards the anode in a spiral motion. If both fields are applied, the motion of electrons will be spiral but the pitch will increase with time. The magnetic fields extend the residence time of the electrons in the plasma, so increasing the probability of ionic collisions and therefore the discharge current and the deposition rate. The increase in the percentage of ionization is caused by the corresponding increase in the mean free path of electrons that enhances the number of collisions. This effectively reduces their speed to zero on the walls and so reduces the possibility for them to recombine to form neutral atoms. Similar DC discharges require the application of larger currents and pressures.

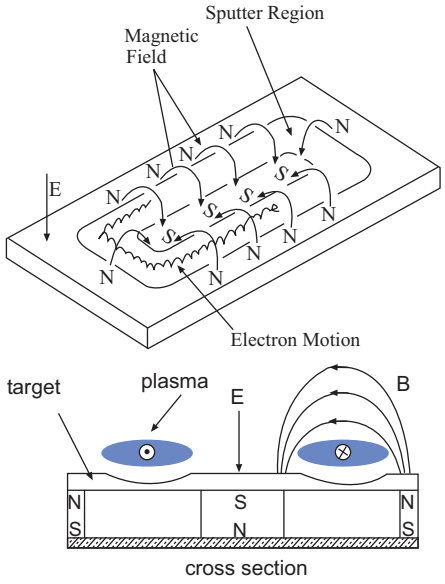


Figure 10: Magnetron source schematics (courtesy of Materials Research Corporation Inc.).

A second type of magnetic sputtering system uses intensification transverse magnetic fields (magnetron).

Historically magnetrons originated as thermoelectric power microwave tubes capable of amplifying signals at high frequency up to 5 MW power with an efficiency range of between 40% and 70%. By using a magnetic field parallel to the target and perpendicular to the electric field, the electrons cannot reach the anode and remain in the vicinity of the target, so increasing the ionization efficiency. The electrons initially emitted from the cathode are accelerated towards the anode, moving in a spiral motion, (Fig. **11**) the parallel magnetic field then sends them back towards the target. This path results in a reduction of the recombination losses both at the anode and at the chamber walls.

In this system the electron follows cycloid orbits with electron cyclotron frequency;

$$\omega^2 = e\,\xi_0/m_eL + (eB/m_e)^2 \qquad \textbf{(8)}$$

where ξ_0 is the electric field at the target, L is the width of the dark space, B is the applied magnetic field, m_e is the electron mass, e is the elementary charge.

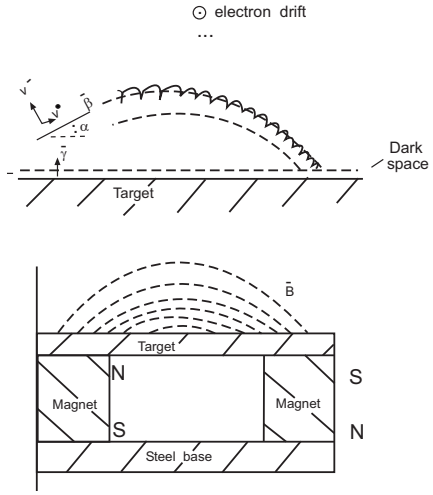


Figure 11: Electronic paths in a magnetron (courtesy of Materials Research Corporation Inc.).

Currently this technique is widely used for most sputtering systems due to its ability to deliver deposition rates up to ten times higher than the other techniques. On the other hand, its main limitation is the difficulty this sputtering technique can have in achieving uniform deposition thickness: this derives from the impossibility of creating uniform magnetic fields. The magnetron sputtering configurations that are commonly used include the use of planar, toroidal and conical-toroidal targets (Figs. **12** and **13**).

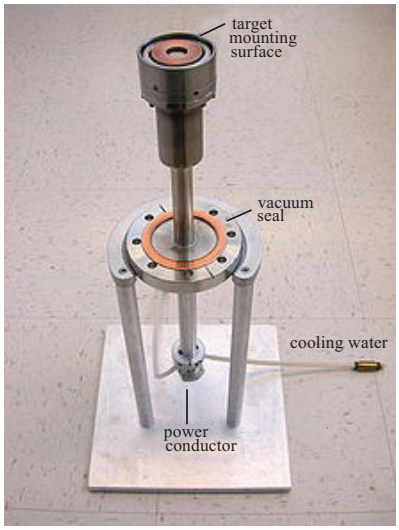


Figure 12: A magnetron sputter source showing the target-mounting surface, the vacuum feedthrough, the power connector and the water lines. This design uses a disc target as opposed to the ring geometry illustrated above [4].

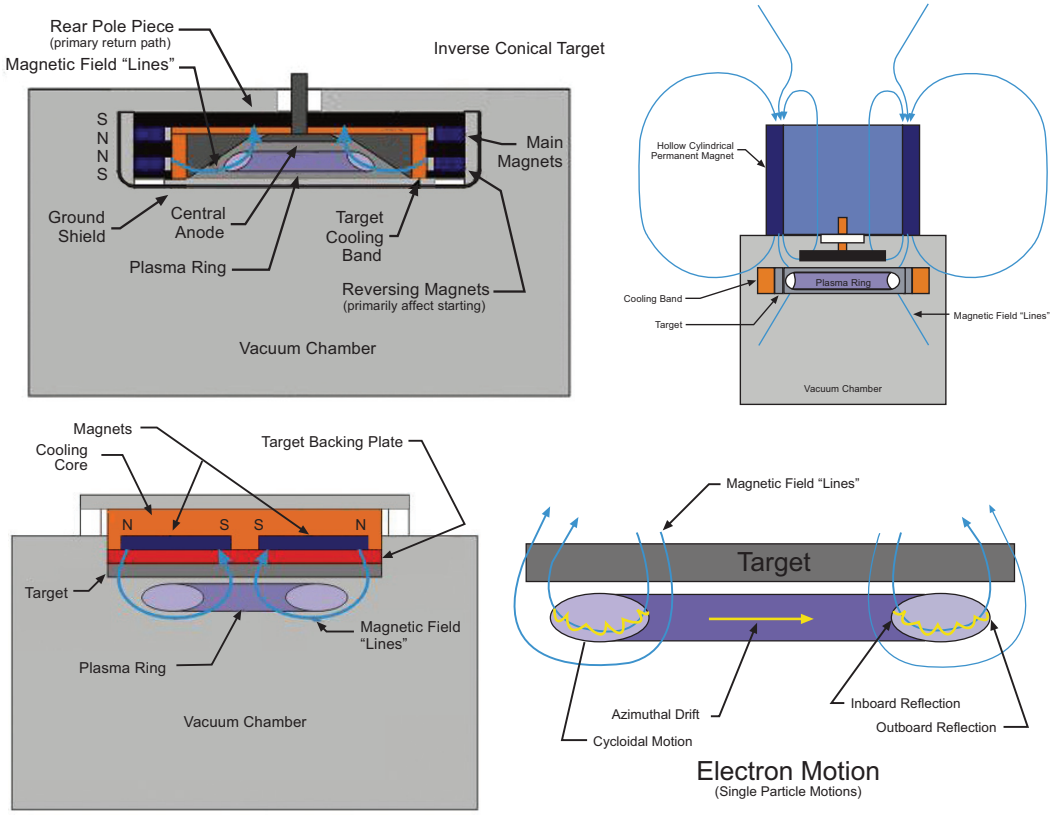


Figure 13: Magnetron sputter sources configurations [4].

The common point between the three devices shown is the formation of an intense ring-shaped plasma. Free electrons in the plasma perform cycloid motion along the magnetic field lines and the electron cloud moves around the ring, generating a strong current. It is to be noted that the impedance of the system varies whilst the target is subject to erosion.

In contrast to other sputtering systems, the current density within a magnetron discharge is highly uneven, but of very high value. This leads to a high but non uniform deposition rate and also to non-uniform heating of the target surface. Fortunately, sputtering yields are rather insensitive to slight variations in temperature. Whilst the target is being eroded by the sputtering process, the geometry and position of the discharge changes, moving to regions with higher magnetic field. A variation of the field affects the motion of electrons and even the voltage, current and power curves can change drastically. Too low a pressure may also increase the volume of the discharge until it becomes too large compared to the target, thus extinguishing the discharge.

Stray magnetic fields leaking from ferromagnetic targets can disturb the sputtering process. Specially designed sputter sources with unusually strong permanent magnets must often be used to compensate for this (Fig. **14**).

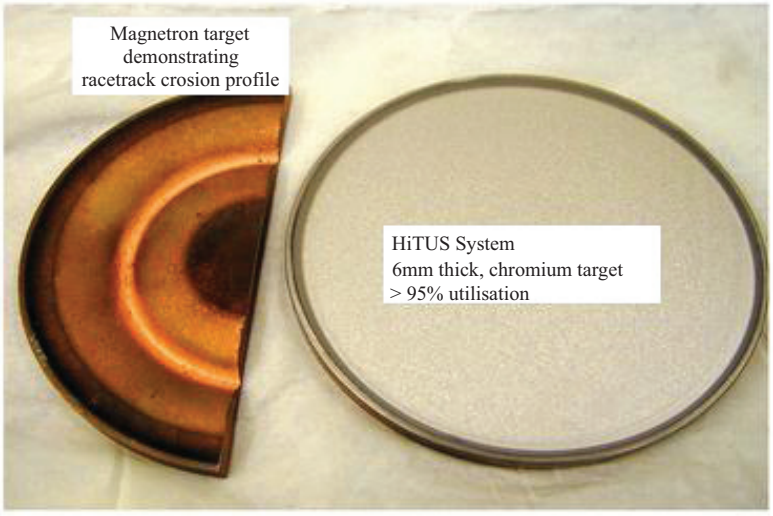


Figure 14: Two used targets: on the left is a target used on a normal magnetron, on the right is one used on a special magnetron with magnetic field developed for high target utilization [4].

11.4. Reactive Sputtering

In this technique, thin film layers are deposited by sputtering from metal targets in the presence of a reactive gas (*e.g.* O_2, N_2), usually mixed with the usual inert gas (Ar). Sputtering is mostly accomplished by the inert gas, whereas the reactive gas combines with the sputtered atoms to form the compound. The most common compounds that can be deposited by this technique include oxides (Al_2O_3, SiO_2), nitrides (TiN), sulfides (CdS, ZnS, CuS), carbides (TiC, WC).

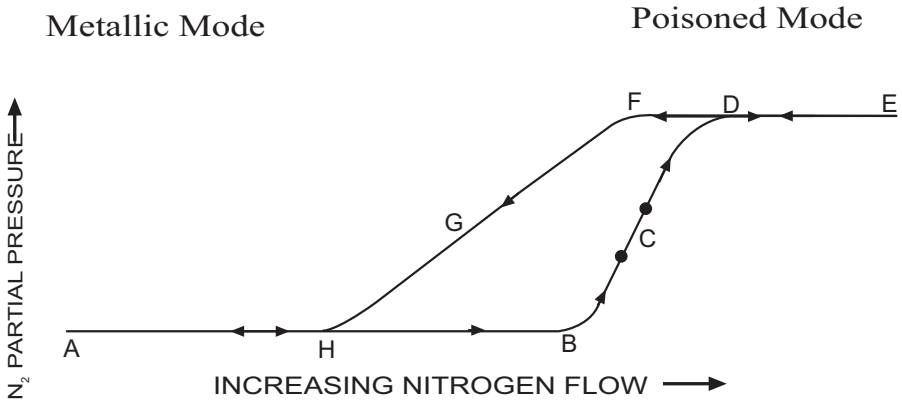


Figure 15: Hysteresis Curve for Reactive Sputtering (courtesy of Materials Research Corporation Inc.).

During reactive sputtering the exact composition of the resulting film, formed by one of the target components mixed with the reactive gas, can be largely controlled by varying the relative pressures of the inert and reactive gases; however the exact composition will depend also on several other process parameters, such as the total pressure and the sputtering power. The

sputtering of a compound can be managed by controling the total pressure of the system as a function of flow rate of reactive gas. The total pressure of the system should increase when a partial pressure of reactive gas is injected into the chamber. However, as the reactive gas combines with an element of the target to form a solid compound, the amount of reactive gas used is no longer seen in the gas phase and therefore it cannot make a contribution to the increase in system pressure. When reactive sputtering from a metal target, changes in target composition can occur as a direct consequence of varying the reactive gas flow and over time the target surface can become "poisoned" with the reactive gas changing some sputtering parameters and causing a hysteresis effect (Figs. **15** and **16**).

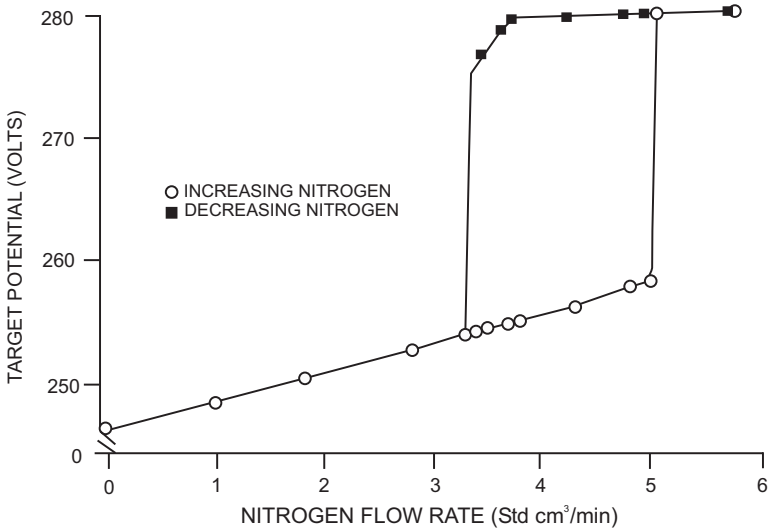


Figure 16: Voltage Hysteresis Curve (courtesy of Materials Research Corporation Inc.).

Film stoichiometry is an important parameter for optimizing functional properties like the stress in SiN_x and the index of refraction of SiO_x. The transparent indium tin oxide and zinc oxide conductors that are used in optoelectronics and solar cells are deposited by reactive sputtering.

12. COMPARISON OF DIFFERENT SPUTTERING TECHNIQUES

Figs. **17** and **18** show the working regions for the different sputtering systems previously presented. In summary:

- DC Diode is characterized by: high voltage & low current, high pressure, low deposition rate, substrate heating from electrons.

- RF Diode is characterized by: possibility of sputtering of insulators, target self-biased, more efficient than DC diode, lower pressure than DC diode.

- DC & RF Magnetron is characterized by: electrons magnetically confined, increased plasma density, higher deposition rates, lower pressure operation.

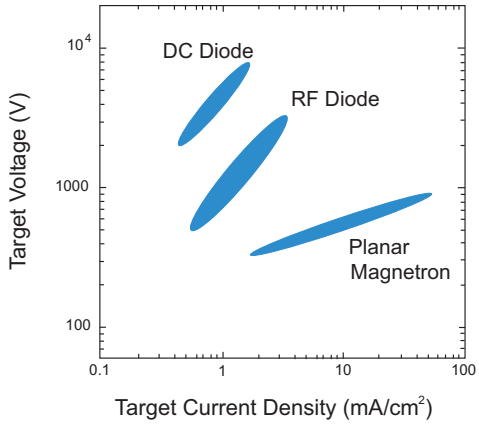


Figure 17: Comparison of 3 sputtering techniques (courtesy of Materials Research Corporation Inc.).

	DC Diode	RF Diode	Magnetron
Voltage	2-8kV	1-3kV	300-800 V
Current	~0.5 A	~0.5 A	~15 A
Pressure	~75 mT orr	~10 mT orr	~1 mT orr
Deposition Rate	~5 Å/s	~10 Å/s	~150 Å/s
Plasma Density	~10^9 cm^{-3}	10^9- 10^{10} cm^{-3}	10^{11}- 10^{12} cm^{-3}

Figure 18: Typical Operating Parameters (courtesy of Materials Research Corporation Inc.).

13. BIAS SPUTTERING

This technique resorts to the modification of electric fields by the application of a separate and additional externally generated voltage onto the substrate to vary the flow and energy of the incident charged species to the substrate. It has been applied in the industrial field in all its possible configurations (DC, RF, magnetron, reactive). The main characteristic of bias sputtering is to achieve significant changes in the properties of deposited films. The most reliable theories claim that the bias voltage can control parameters such as gas content and stress in the deposited thin film. Also the effect of resputtering from the substrate can be controlled by the application of bias to help control the deposited thickness on non-conformal surfaces: the so called step coverage.

In conclusion, bias voltage applied to the substrate determines the conditions of film growth on the substrate; the amount of weak and strong bonds during the film growth can be controlled with ensuing effects on the resistivity, hardness, dielectric properties, optical properties, density and adhesion.

14. SPUTTERING OF ALLOYS

Preferential sputtering can occur at the start of the sputtering process when a multicomponent solid target is bombarded and there is no solid state diffusion. If the energy transfer is more efficient

with one of the target components compared to another, and/or it is less strongly bound to the solid, it will sputter more efficiently and its sputtering yield S will be higher. If in an AB alloy the component A is sputtered preferentially, during the first stages of the process the surface layer of the target is depleted of the target compound of higher sputtering yield S. Then the surface of the solid will, during prolonged bombardment, become depleted in the A component and enriched in the B component thereby increasing the probability that B is sputtered such that the composition of the sputtered material will be AB.

Only after the stoichiometry of the target surface has reached a dynamic equilibrium, should the deposition process be started by opening a shutter that allows the sputtered material to reach the substrate. To be able to deposit a film of a given composition it is necessary to know that the surface composition of the target is different from the composition of the inner areas not affected by the sputtering process.

15. ION BEAM SPUTTERING

Ion-beam sputtering (IBS) is a method in which the target is external to the ion source. A source can work without any magnetic field, as in a hot filament ionization gauge. In a Kaufman source, ions are generated by collisions with electrons that are confined by a magnetic field as in a magnetron. They are then accelerated by the electric field emanating from a grid towards a target. As the ions leave the source they are neutralized by electrons from a second external filament. IBS has an advantage in that the energy and flux of ions can be controlled independently. Since the flux that strikes the target is composed of neutral atoms, either insulating or conducting targets can be sputtered. IBS has found application in the manufacture of thin-film heads for disk drives. A pressure gradient between the ion source and the sample chamber is generated by placing the gas inlet at the source and shooting through a tube into the sample chamber. This minimizes gas usage and reduces contamination in UHV applications.

15.1 Ion-Assisted Deposition

In ion-assisted deposition (IAD), the film growing on the substrate originating from a primary deposition source (thermal or electron beam evaporation, sputtering) is exposed to a secondary ion beam operating at a lower power than the sputter gun. Usually a Kaufman source similar to that used in IBS supplies the secondary beam. IAD can be used to deposit carbon in diamond-like form onto a substrate. Any carbon atoms landing on the substrate which fail to bond properly in the diamond crystal lattice will be knocked off by the secondary beam. NASA used this technique to experiment with depositing diamond films on turbine blades in the 1980's. IAD is used in other important industrial applications such as those for creating tetrahedral amorphous carbon surface coatings on hard disk platters, hard transition metal nitride coatings on medical implants and hard coatings for optical devices.

A Dual Ion Beam Source Sputter Deposition (DIBSD) System uses an Ion Beam Source to sputter materials from a multiple target carousel and a second Ion Beam Source to bombard the film growing on the substrate (Fig. **19**). The primary sputtering IBS typically operates at voltages around 1000 V to provide the ions with the energy required for effective sputtering. The second (so called assist) IBS operates at voltages around 100-250 V to provide the ions with the energy

required for film densification by removing weak bonds. A DIBSD system with appropriate layout of components can be used to deposit films with extremely high uniformity and excellent materials properties and represents the state of the art in sputtering technology.

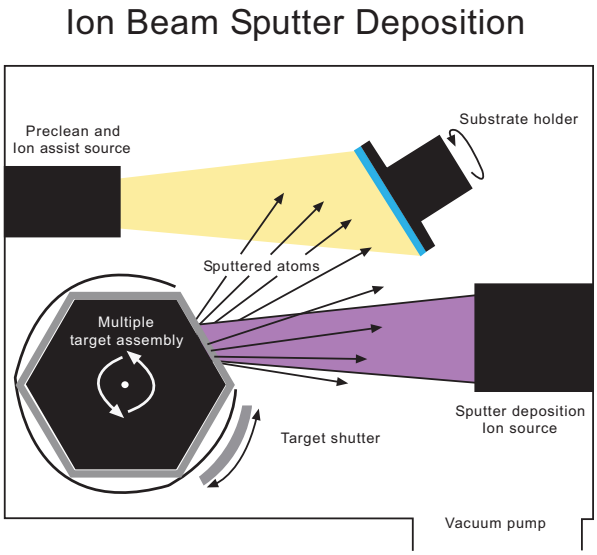


Figure 19: Dual Ion Beam Sputtering System (courtesy of Kaufman & Robinson Inc.).

16. GAS FLOW SPUTTERING

Gas flow sputtering makes use of the hollow cathode effect, the same effect by which hollow cathode lamps operate. In gas flow sputtering a working gas like argon is led through an opening in a metal subjected to a negative electrical potential [6, 7]. Enhanced plasma densities occur in the hollow cathode, if the pressure in the chamber p and a characteristic dimension L of the hollow cathode obey the Paschen relation 0.5 Pa·m < p·L < 5 Pa·m.This causes a high flux of ions on the surrounding surfaces and a large sputter effect. The hollow-cathode based gas flow sputtering may thus be associated with large deposition rates up to values of a few µm/min [8]. Hollow cathode devices are also used as electron sources to neutralize an ion beam emitted from a Kaufman source.

17. STRUCTURE AND MORPHOLOGY

In 1974 J. A. Thornton applied the structure zone model for the description of thin film morphologies to sputter deposition. In a study on metallic layers prepared by DC sputtering [9], he extended the structure zone concept initially introduced by Movchan and Demchishin for evaporated films [10]. Thornton introduced a further structure zone, which was observed at low argon pressures and characterized by densely packed fibrous grains. The most important point of this extension was to emphasize the pressure p as a decisive process parameter. In particular, if hyper thermal techniques like sputtering *etc.* are used for the sublimation of source atoms, the pressure governs (*via* the mean free path), the energy distribution with which they impinge on the

surface of the growing film. Next to the deposition temperature T_d the chamber pressure or mean free path should thus always be specified when considering a deposition process.

Since sputter deposition belongs to the group of plasma-assisted processes, both neutral atoms and charged species (like argon ions) can also strike the surface of the growing film, and this component may exert a large effect. Denoting the fluxes of the arriving ions and atoms by F_i and F_a, it turned out that the magnitude of the F_i/F_a ratio plays a decisive role on the microstructure and morphology obtained in the film [9]. The effect of ion bombardment may quantitatively be derived from looking at structural parameters like the preferred orientation of crystallites or texture and from the state of residual film stress.

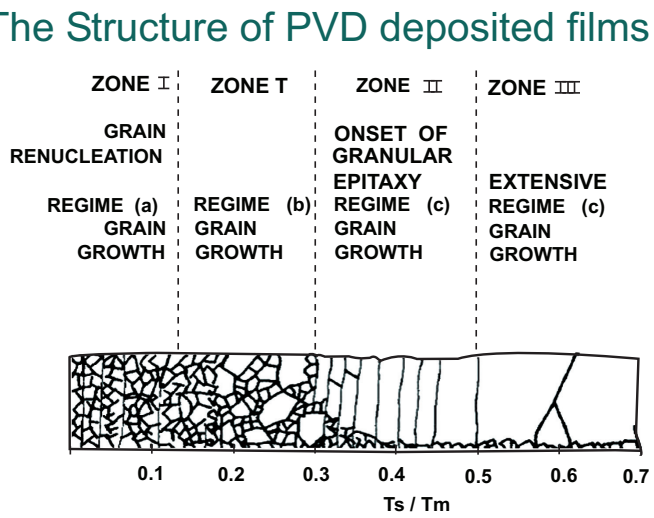


Figure 20: The structure of PVD deposited films (courtesy of Materials Research Corporation Inc.).

18. SPUTTER ETCHING AND CHEMICAL SPUTTERING

The sputtering technique can also be applied by configuring the elements so that they reverse their function: the substrate is placed on the cathode and its surface layers are removed by ionic bombardment: this layer removal technique is called sputter etching. It is the reverse process compared to sputter deposition and is often used for substrate surface cleaning before sputter deposition is started. Removing atoms by sputtering with an inert gas is called `ion miling' or 'ion etching'. The main parameter of interest is the "etching rate", *i.e.* the rate at which the surface of the substrate is etched.

Sputtering can also play a role in reactive ion etching (RIE), a plasma process carried out with chemically active ions and radicals, for which the sputtering yield may be enhanced significantly compared to pure physical sputtering. Reactive ions are frequently used in Secondary Ion Mass Spectrometry (SIMS) equipment to enhance the sputter rates. The mechanisms causing the sputtering enhancement are not always well understood, but for instance the case of fluorine etching of Si has been modeled well theoretically.

ACKNOWLEDGEMENTS

The author wishes to acknowledge Thin Film Equipment srl and Kaufman & Robinson Inc. for providing some of the figures used in the article.

CONFLICT OF INTEREST

The author(s) confirm that this chapter content has no conflict of interest.

REFERENCES

[1] Mattox DM. The Foundations of Vacuum Coating Technology. Norwich (NY): Noyes Publications 2003.
[2] Westwood WD. Sputter Deposition AVS Education Committee Book Series Vol. 2. New York (NY): American Vacuum Society Education Committee AVS 2003.
[3] Wolf B. Handbook of ion sources. Boca Raton (FL): CRC Press 1995.
[4] https://en.wikipedia.org/wiki/Sputter_deposition#Uses_of_sputtering (September 2011).
[5] Chapman B. Glow Discharge Processes. Hoboken (NJ): John Wiley & Sons 1980.
[6] Ishii K. High-rate low kinetic energy gas-flow-sputtering system. J Vac Sci Technol A 1989; 7: 256–258.
[7] Jung T, Westphal A. Zirconia thin film deposition on silicon by reactive gas flow sputtering: the influence of low energy particle bombardment. Mat Sc Eng A 1991; 140: 528–533.
[8] Ortner K, Birkholz M, Jung T. Neue Entwicklungen beim Hohlkatoden-Gasflusssputtern. Vac Praxis 2003; 15: 236–239.
[9] Thornton JA. Influence of apparatus geometry and deposition conditions on the structure and topography of thick sputtered coatings. J Vac Sci Tech 1974; 11: 666–670.
[10] Movchan BA, Demchishin AV. Study of the structure and properties of thick vacuum condensates of nickel, titanium, tungsten, aluminum oxide and zirconium dioxide. Phys Met Metallogr 1969; 28: 83–90.

Send Orders of Reprints at reprints@benthamscience.net
Silicon Based Thin Film Solar Cells, 2013, 81-107

CHAPTER 4

Molecular Beam Epitaxy (MBE)

Lorenzo Morresi*

University of Camerino-School of Science and Technology-Physics Division, Via Madonna delle Carceri, 9-62032 CAMERINO (MC), Italy

Abstract: Molecular Beam Epitaxy (MBE) represents a widely used growth technique to approach the basic research applied to the growth of semiconductor films and multilayer structures. The main features that distinguish the MBE from other growth techniques are the precise reproducibility of all parameters involved during the epitaxial process, the growth conditions far from thermodynamic equilibrium, and the possibility of controling the kinetic evolution of the outermost layers of the epitaxial film. Nowadays, MBE is also used to grow and investigate nanosized semiconducting materials, which are profoundly interesting for photovoltaic future applications as well.

Keywords: Molecular beam epitaxy, semiconductor thin films, nucleation in film growth, nanocrystalline materials, electron beam deposition, doping thin films, impurities in crystals, quantum dots, RHEED, surface reconstruction, dislocations.

1. INTRODUCTION

Molecular Beam Epitaxy (MBE) is a technology used for the deposition of thin film compound semiconductors, metals or insulators that allows a precise control of compositional profiles by using a process far from the thermodynamic equilibrium. The term epitaxy originates from the Greek roots “epi” and “taxis” which mean to arrange upon. In other words, the epitaxy is the arrangement of one or more thermal particles atop a heated and ordered crystalline substrate to form a thin layer whose crystallinity matches that of the substrate even though the composition of the materials may differ (*e.g.* SiGe/Si, GaAlAs/GaAs, CdTe/GaAs,…). Again, the term beam means that evaporated elements (atoms and/or molecules) do not interact with each other or with vacuum chamber gases until they impinge the substrate because of their long mean free paths which are involved in the deposition process.

This unique growth technique is widely used to produce superlattice structures consisting of many alternate thin layers with single thickness as low as ~10 Å. Furthermore, impurities are evaporated onto the growing film through separate sources. In this way the doping profile, orthogonal to the surface, may be varied and controlled with a spatial resolution not easily achieved by more conventional techniques.

MBE was developed by Alfred Cho and John Arthur at Bell Telephone Labs in the early 1970s, in

***Address correspondence to Lorenzo Morresi:** University of Camerino, School of Science and Technology, Physics Division, Via Madonna delle Carceri 9, Camerino, 62032, Italy; Tel: +39 333 9961198/+39 737 402528; Fax: +39 737402853; E-mail: lorenzo.morresi@unicam.it

Roberto Murri (Ed)
All rights reserved-© 2013 Bentham Science Publishers

an attempt to develop a new variety of high-frequency and high-temperature devices such as injection lasers, electro-optic phase modulators, photocathodes and oscillators [1], as well as IMPATT diodes [2], mixer diodes [3] and optical waveguides [4] all based on the same requirement: the development of thin layer structures. Their pioneering work was focused mainly on preparing $A_{III}B_V$ compound films (like GaAs) overlapping compliance due to the large difference in vapor pressures between the group III and group V elements. Their efforts bring to the formation of stoichiometric III-V films by the molecular beam epitaxy method, and demonstrated by optical and electron diffraction measurements [5, 6].

Adding the Auger spectroscopy for the surface chemical analysis to the vacuum system, and the reflection electron diffraction for *in situ* structural analysis, they were able to resolve the original uncertainties over film stoichiometry and substrate cleanliness. Improving the characterization of both the epitaxial layer and the substrate by incorporating these surface diagnostic techniques into the chamber process, the progress in MBE was very rapid.

The strength of this particular growth process is due to the very low deposition rates (generally few Å per second) generated by the sublimation of extremely pure solid elements heated in separate effusion cells (mostly based on Knudsen concept). In fact, the source material is transformed into its gaseous state by raising its vapor pressure through an increase in temperature. The gaseous particles expand into the evacuated space between the orifice's source and the substrate, where the condensation process takes place. The condensate reacts with the surface until the epitaxial arrangement takes place and the crystalline structure grows with a comparable growth rate. To reduce the impurity levels in the growing layers to an as low as possible value, the epitaxial growth occurs in Ultra-High-Vacuum (UHV) conditions, with a total pressure within the deposition chamber lower than 10^{-10} Torr.

Intricate structures of few monolayers (MLs) composed by different materials may be fabricated by controling the movements of shutters placed in front of each evaporator source. Such control has allowed the development of structures with abrupt and sharp interfaces where the charge carriers can be bi-dimensionally confined in space, due to quantum wells [7-10], or even one-dimensionally confined, due to quantum dots [11-13]. Such layers are nowadays a critical part of many modern semiconductor devices (Fig. **1**), including semiconductor lasers [14-16], light-emitting diodes [17], photodetectors [18, 19] and solar cells [20-23].

The UHV conditions in the environment and control of the quality of the source materials allow much higher film purity, compared to other growth techniques.

Moreover, the vacuum condition allows for the use of electron diffraction probes, which provide fundamental information on the growth mechanisms. On the other hand, MBE suffers of lower yield compared to other techniques such as Liquid Phase Epitaxy (LPE), Metal-Organic Vapor Phase Deposition (MOCVD), Sputtering and Plasma Enhanced Chemical Vapor Deposition (PECVD) due to a lower speed process and dimension wafer capability.

2. MBE SYSTEM

A molecular beam epitaxy system is basically a vacuum evaporation apparatus. What may be considered a standard MBE system is shown schematically in Fig. **2**.

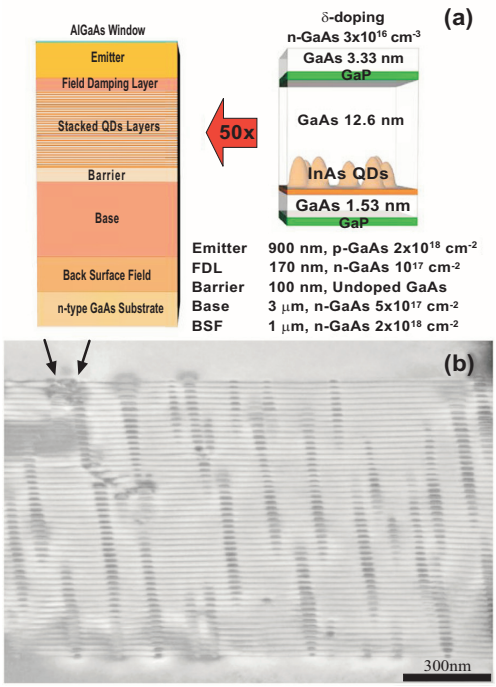


Figure 1: (a) Structure of the 50 stacked quantum dot solar cell grown by MBE. Each GaP layer has a nominal thickness of 1 ML = 0.273 nm. (b) Cross-sectional TEM image of the 50 stacked quantum dot layers. The arrows indicate the defects observable in the image (AIP license n. 2546451267415).

The system consists of a stainless-steel growth chamber connected to other chambers by gate valves. These latter are needed to avoid contamination of components and materials sources by both external and process gases, and to maintain pressure into the growth chamber as low as possible. Modern systems are provided with a proper treatment chamber, and a load lock module represents the only way to transfer the sample to and from the air.

The pumping system, a combination of ion pump, titanium sublimation pump and liquid N_2 cryopanels, can reduce the residual impurity density to a minimum. The two parameters that characterize the vacuum into the growth chamber are: the mean free path, L, (average distance traversed by reactant gas molecules between successive collisions), and the partial pressure of the residual gas molecules, p_r. The highest admissible p_r value depends on L being larger than the distance from the outlet orifice of the beam source to the substrate surface ($L > 0.2$ m).

Using the ordinary assumptions of the kinetic theory of an ideal gas and, for example, the typical numerical data for conventional MBE growth of Si, the maximum value of the residual gas pressure is $\approx 10^{-5}$ Torr [24], well behind the UHV conditions present in the chamber. Again, one can assume that the time required for the deposition of 1 mono- layer (ML) of residual contaminants is 10^5 times those necessary for the deposition of 1 ML of film from the molecular beams. Consequently, it can be demonstrated that very low deposition rates (*i.e.* 1 ML s^{-1}) should be employed in an UHV environment [24]. However, it should be noted that p_r increases during

deposition due to the increased heat load from the effusion cells and the substrate. In the event that this occurs, a titanium filament sublimation pumping can reduce the residual gas pressure down to the minimum values. The entire vacuum system is bake able up to 250 °C for extended periods of time, to minimize outgassing from the internal walls during the deposition process. After a complete bake out cycle, the system with all the components installed reaches ~ 2×10^{-10} Torr, using only the main ion pump. Moreover, both CO_2 and H_2O gas pressure is drastically reduced by cooling the cryopanels with liquid nitrogen. Cryogenic temperatures act as an entangled for impurities, so vacuum levels of the orders of 10^{-11} Torr can be obtained. The substrate older is located a few centimeters away from the openings of the effusion cells, along the centerline of the system. The temperature of the substrate can be set during the deposition (from room temperature up to about 1400 °C), at a suitable temperature depending on the epitaxial process. It can also be heated before deposition primarily for cleaning and\or surface reconstruction, and afterwards for various heat treatments. As shown in Fig. **2**, the chamber is provided with a spectral mass analyzer to detect the residual atoms or molecules and thus to monitor the environment under which the film is grown.

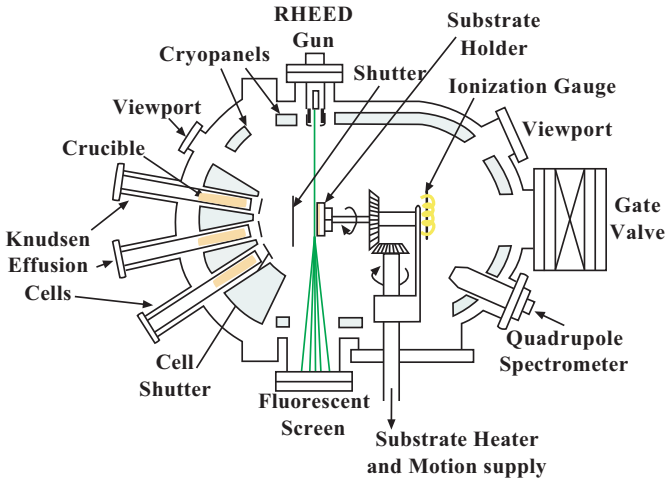


Figure 2: Schematic representation of a molecular beam epitaxy growth chamber. The main experimental features component the system are shown.

2.1. Effusion Cells

Fig. **2** shows three effusion cells, although as many as ten can be found in modern apparatus. A schematic illustration of a standard effusion cell is shown in Fig. **3 (a)**. In the growth of compound semiconductors the materials contained in the crucible could be the compounds themselves, their components, or different elements to be used as doping impurities. The crucible is usually made of pirolytic boron nitride (PBN), which can stand temperatures up to ~ 1400 °C without harmful material dissociation on the grown layers. Standard effusion cells are limited to operate at a temperature lower than 1200 °C, which is only just within the range of that required for Si, Ge, Al, Ga evaporation. The shape can be either cylindrical or conical, with different tapering angles, depending on the material to be evaporated as well as its diameter.

The total effusion rate can be approximately described by the Knudsen effusion equation [24]:

$$R = 8.33 \times 10^{22} \frac{p \cdot A_e}{\sqrt{M \cdot T}} \left[molecules\ s^{-1} \right] \quad \textbf{(1)}$$

where p is the pressure in the effusion cell, A_e is the surface area from which molecules evaporate, M is the molecular weight of the evaporating species and T is the temperature of the melt. Combining the Knudsen equation with the cosine law (given that the ideal Knudsen cell exhibits an angular distribution of the evaporated particles) [24], the impingement rate (also called flux) at the central point of the substrate axially aligned with the orifice can be written in the form:

$$I = 2.653 \times 10^{22} \frac{p \cdot A_e}{r^2 \sqrt{M \cdot T}} \left[mol\ m^{-2}\ s^{-1} \right] \quad \textbf{(2)}$$

where r is the distance between the orifice and impingement point. The rate at the edge point of the substrate, forming an angle θ with respect to central point can be easily calculated by multiplying the previous relation by $\cos 4\theta$. A standard effusive cell can assure flux stability greater than 1% during the deposition process, with a daily variation lower than 5% [25]. A Ta filament (or foils in other models) provides heating, while multiple Ta foils provide heat shielding to improve both the temperature stability and the thermal efficiency. Generally, a W-Re (5% and 26% Re) thermocouple is properly attached to both measure the material temperature and assure chemical stability. These refractory materials are thermally inert and suitable for operating at elevated temperatures.

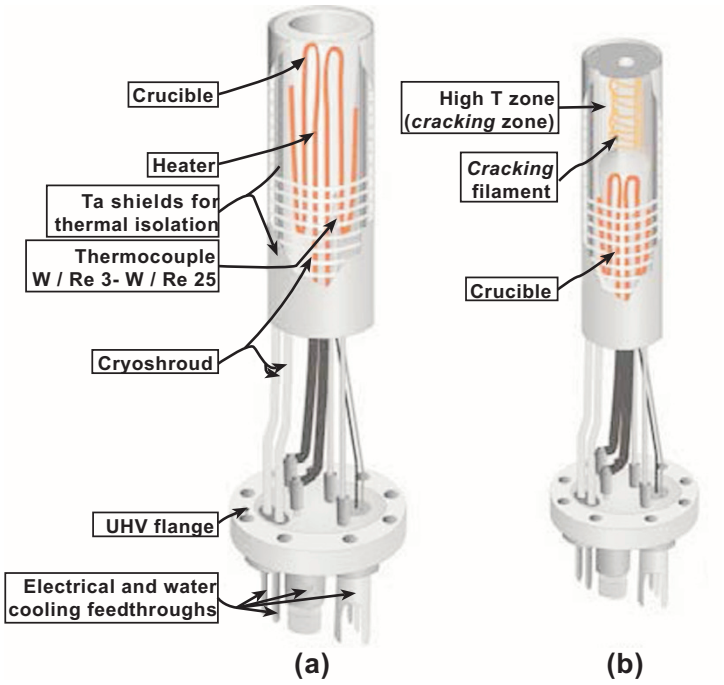


Figure 3: Schematic illustration of two present-day effusion cells used in MBE systems: (a) Standard Knudsen cell; (b) Two stage Cracking effusion cell (Courtesy of Prof. Klaus H. Ploog).

PID regulators provide high precision temperature regulation of ± 1 °C up to the maximum operating temperatures. Mechanical or pneumatic shutters, usually made of Ta or Mo, are placed in front of the orifices to trigger the fluxes (see Fig. **2**). The shutters operate faster than the growth rate (typically 0.1 s), and should be computer controlled to provide reproducible growth structures.

An important variation to the standard designs is provided by the so-called cracking cells. They are mainly employed for evaporation of group-V and VI elements (see Fig. **3 (b)**). In this cell, the material is first thermally evaporated (in form of tetramers) from the crucible; subsequently it passes through a hotter cracking zone where molecules are dimerized.

2.2. Electron Beam Evaporator

Molecular beams for MBE may also be generated by electron bombardment of suitable sources, by concentrating the heating energy onto just the evaporating load. The main property of this evaporation technique is the fast response process time, which permits high growth rates for low vapor pressure materials, especially when high purity of the evaporant is desired [26].

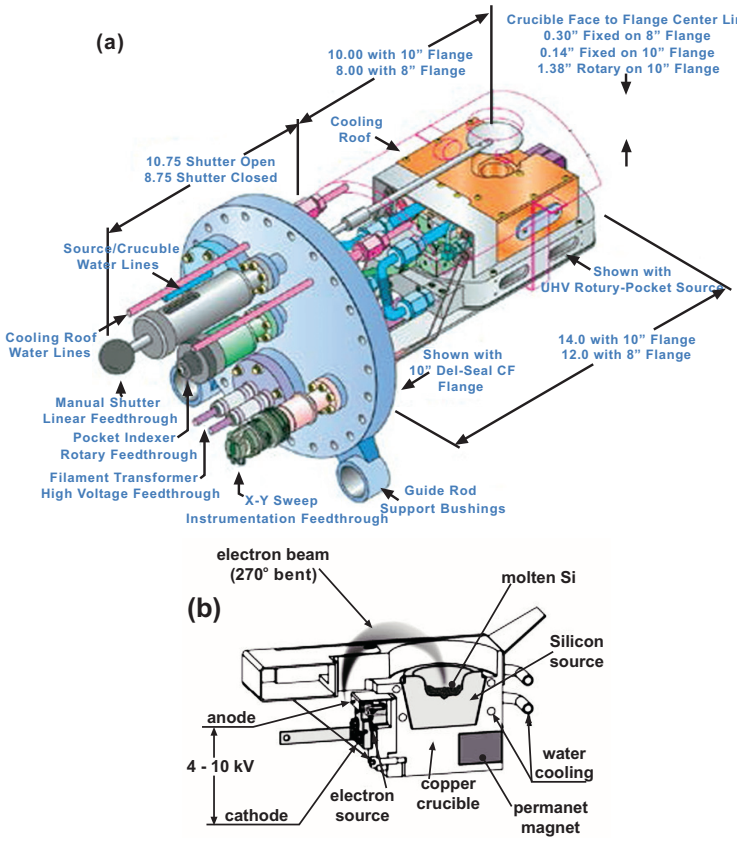


Figure 4: (a) Schematic overview of an electron-beam gun, with a horizontal source assembly (Courtesy of MDC Vacuum Limited). (b) Silicon electron bent-beam heated MBE source; electrons are forced into a curved path through a transverse magnetic field that permits focusing of the electron beam.

A proper filament emits electrons, and the stream is accelerated through a field of typically 4-10 kV. The electron gun is designed to eliminate nearly all ion bombardment effects on the filament thanks to the 270° electron beam deflection and the very sharply bent electron beam path near the exit of the aperture. Fig. **4 (a)** shows the inside of an electron gun mounted in a MBE chamber through 10" CF Flange. The figure shows the main assembly features including rotary, linear and electrical feedthroughs, clamps, linkages, water flow switch and water connections. In principle, due to the electrons impinging on the source, almost all the kinetic energy is converted into heat, and temperature exceeding 1500 °C may be obtained. During the film growth, the electron beam impinges on the center of the truncated cone of shaped source (Fig. **4 (b)**) [24]. For an electron beam current of 150 mA, the molten area can be lower than 10 mm in diameter. Electron beam evaporators are frequently used for evaporation of refractory metals, *e.g.* Mo, Nb, Ta, W, Zr, and are well suited for high-rate evaporation of Al, and of course for semiconductors like Si and Ge. Finally, a typical application is SiGe MBE for the generation of the main lattice element.

2.3. RHEED

For *in situ* monitoring of the thin films epitaxial growth, the system further incorporates a scanning high-energy electron diffraction apparatus, employing the small glancing angle reflection mode of operation (RHEED in Fig. **2**).

The feature of glancing incidence makes RHEED sensitive to the very uppermost layers, rather than the bulk structure. This tool reveals in real time changes either in the growing surface or in the surface structure (crystallographic orientation and morphology) of a thin film, without any interference with the growth process [27]. In RHEED, an incident electron beam strikes the sample's surface at near-grazing incidence (typically making an angle of incidence of lower than 3°) and is reflected onto a phosphorescent screen, as shown in Fig. **5**.

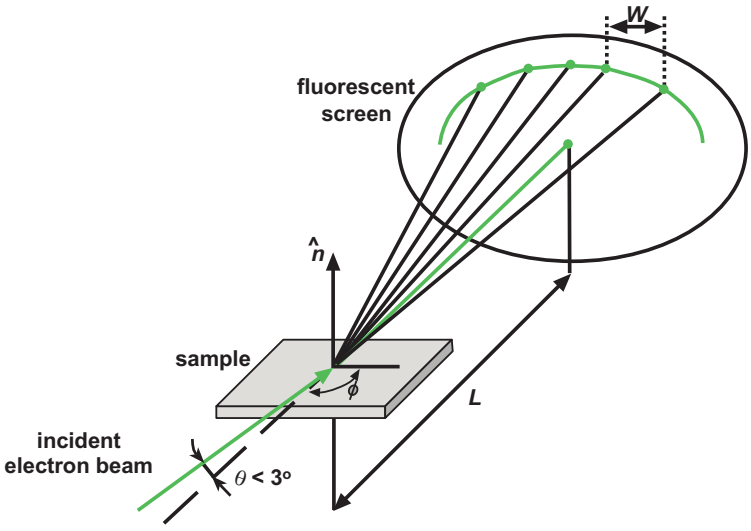


Figure 5: Schematic diagram of RHEED geometry showing the incident beam at an angle θ to the surface plane; ϕ is the azimuthal angle. W indicates the spacing among spot features; L is the distance between the point of incidence and the screen.

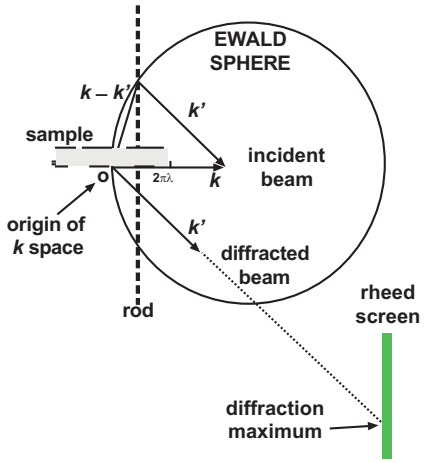


Figure 6: Intersection between the Ewald sphere and a particular reciprocal lattice rod. The corresponding electrons (having *k'* wave vectors) that satisfy this particular Laue condition form a diffraction spot on the screen.

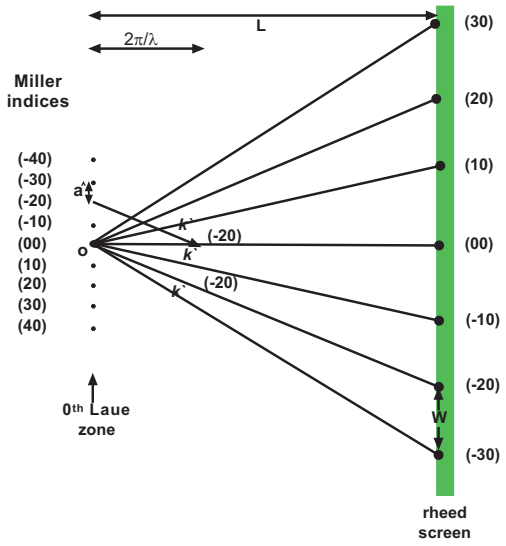


Figure 7: Schematic representation of the relation between the intrarow spacing a^* of the reciprocal lattice rods and the spacing W of the observed streaks.

In the framework of the Laue diffraction, the maximum intensity of the diffracted beams originates when the difference between the wave vectors of the incident and diffracted beams (*k* and *k'* respectively) intercept the reciprocal lattice rods. In this way it can be defined an Ewald sphere of radius *k* (Fig. **6**). The intersection of the Ewald sphere with the reciprocal lattice rods selects the electrons with wave vectors *k'*, forming some spots on the screen. If the surface is not flat, many electrons will be transmitted through surface asperities and scattered in different directions, resulting in a RHEED pattern constituted by many spotty features. However, thermal vibrations and lattice imperfections can cause the reciprocal lattice rods to have a finite thickness, while the

Ewald sphere itself has some finite thickness, due to divergence and dispersion of the electron beam [28].

Therefore, diffraction from a perfectly flat surface results in a diffraction pattern consisting of a series of streaks with modulated intensity (rather than points) superimposed on a fairly uniform background, due to inelastically scattered electrons. Therefore, RHEED analysis provides important information concerning the flatness of the growing film surface. Furthermore, it is evident that diffraction from an amorphous surface (such as an oxide on top of the substrate) gives no diffraction pattern at all. In this case only a diffuse background will result. The distance between the streaks of static RHEED pattern is an indication of the surface lattice unit cell size.

Fig. **7** shows a single row of rods that has a lateral spacing of a^* and indicate the Miller (hk) indices of several points of the reciprocal net; these same indices are given to their rods, and to the spots or streaks they create in the RHEED pattern. The observed streak spacing is W; the distance to the screen from the point of incidence is L. We may utilize the principle of similar triangles to show that $W/L \sim a^*/(2\pi/\lambda)$. Thus, the observed streak spacing indicates a rod spacing of:

$$a^* = \frac{2\pi \cdot W}{\lambda \cdot L} \tag{3}$$

where the wavelength $\lambda = 12.3/[V\,(1+1.95 \times 10^{-6}\,V)]^{1/2}$ Å, is expressed as function of the accelerating potential, V [28]. Potentialities of this method are expanded to oscillations of the electron beam reflected from a growing film surface in the process of MBE (RHEED oscillations) [29].

For a 2D growth, one oscillation period of a specular electron beam corresponds exactly to a monolayer of the film grown during this period. The oscillation period depends on the material flux to the surface, the substrate temperature and the growth mechanisms.

As an example, Fig. **8** compares different evolution of either RHEED intensity oscillation (left side) and RHEED patterns (right side) taken during and after, respectively, the growth of 5.5 ML (monolayers) of strained Ge on Si (100) at 400 °C, followed by heteroepitaxial Si growth at deposition rates with **(a)** and without **(b)** H supplies. The pattern **(c)** corresponds to case **(a)** followed, however, by a quick (1 min) after growth desorption annealing at 600 °C.

The top figures show the oscillation vanishing after 5 ML relative to the Ge cluster installation and the corresponding RHEED pattern signature. One oscillation period corresponds to the growth of one atomic ML [30].

3. SURFACE RECONSTRUCTION

A clean substrate is an important prerequisite for epitaxial growth, since its oxidation due to atmospheric exposure causes crystal defects that degrade both the optical and electrical features of the epitaxial layer. Nowadays, vendors supply ‘epi-ready’ wafers pre-cleaned and oxidized in a controlled environment, in order to form an oxide protective layer that can be removed inside the growth chamber.

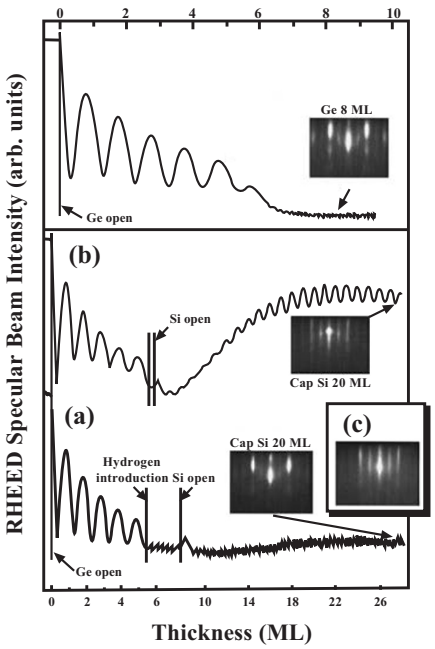


Figure 8: The top figure provides the corresponding signatures of an uninterrupted Ge growth. Si capping growth modes with (a) or without (b) hydrogen onto strained Ge. (c) Surface restoration and growth reorganization of the rough homogeneous Si covering into a smooth one (Elsevier license n. 2558160456690).

The use of such 'epi-ready' wafers has led to consistent results without the need for elaborate wafer cleaning procedures, such as Shiraki for the Si (100) and Si (111) [31], or Hakane for the Ge (100) [32]. However, even using 'epi-ready' substrates, proper thermal treatments must be used to obtain well-ordered surfaces after the oxide removal. In fact, in order to minimize the under coordinated surface, which presents one or more highly energetic dangling bonds, the system tries to arrange the surface atoms in different configurations, which differ from the bulk-like positions.

These new arrangements, involving the elimination of some atoms or their movement to non-epitaxial sites as well, are called surface reconstructions and deeply affect the further epitaxial processes.

The (001) is one of the most popular and widely studied surfaces for silicon and germanium.

It presents a very simple structure characterized, for the as-cut configuration, by square symmetry (see Fig. **9 (a)**, where the 1×1 surface unit cell is indicated). The surface lattice parameter is $a_s = a\sqrt{2}/2 = 3.84$ Å for Si and $a_s = 4.0$ Å for Ge, where a is the equilibrium bulk lattice constant. In the as cut geometry, each surface atom has two dangling bonds, making this a highly unstable configuration.

To reduce the dangling bonds density, neighboring Si atoms pair to form parallel dimmers, which represent the fundamental unit characteristic of the Si (001) (Fig. **9 (b)**). The dimerization has the

direct effect of modifying the surface periodicity along the direction of the dimer bond, leaving the perpendicular direction unchanged. Therefore, the reconstruction is defined as (2×1) Si (001). The dimerization process allows the system to reduce the number of unsatured bonds through the formation of a covalent directional σ bond connecting the two surface atoms. Moreover, the system can reduce its total energy by some hybridization processes, and reconstruction like $p(2\times1)$ and $c(4\times2)$ can be obtained (see Fig. **9 (c)** and **(d)** respectively).

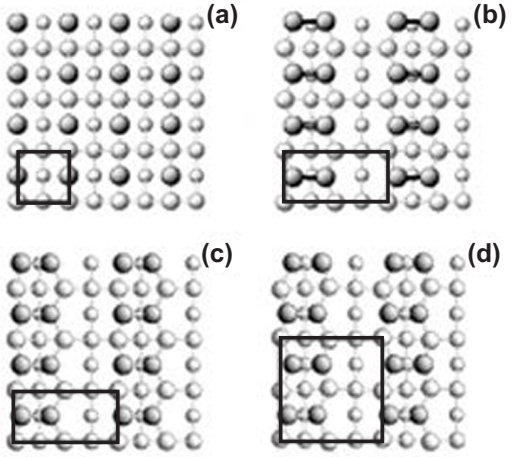


Figure 9: The topmost layer is painted in dark gray. (a) Top view of Si (001) in the as cut geometry, showing a surface unitary (1×1) cell. (b) (2×1) dimerized Si (001). (c) Dimerized Si (001) with all the dimers tilted along the same direction, forming a (2×1) periodicity. (d) Si (001) whose (2×2) dimers are tilted alternately along the dimmers row.

In the case of Si (111), the system presents the lowest dangling bond density over the surface area (d_H = 0.07 Å). Fig. **10 (a)** shows the top view of non-reconstructed Si (111).

Having such a low dangling bond density, the Si (111) is the cleavage surface obtained when an external strain is applied to split a Si crystal, but it is also one of the most frequently exposed surfaces when microcrystalline structures nucleate into amorphous matrix. The (111) surface assumes different reconstructions, like the π chain geometry (Fig. **10** (**b**)).

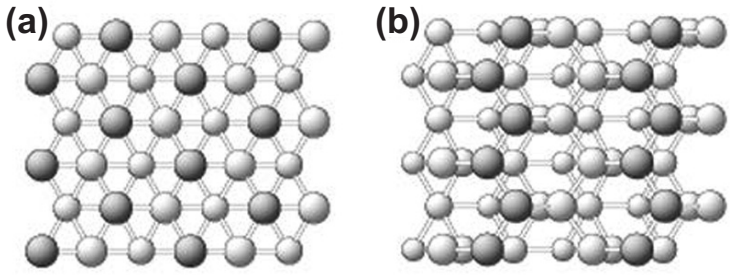


Figure 10: The topmost layer is painted in dark gray. (a) Top view of Si (111) in the as-cut geometry. (b) Top view of Si (111) π-chain.

4. DEPOSITION PROCESSES

The main substrate surface processes are schematically illustrated in Fig. **11**.

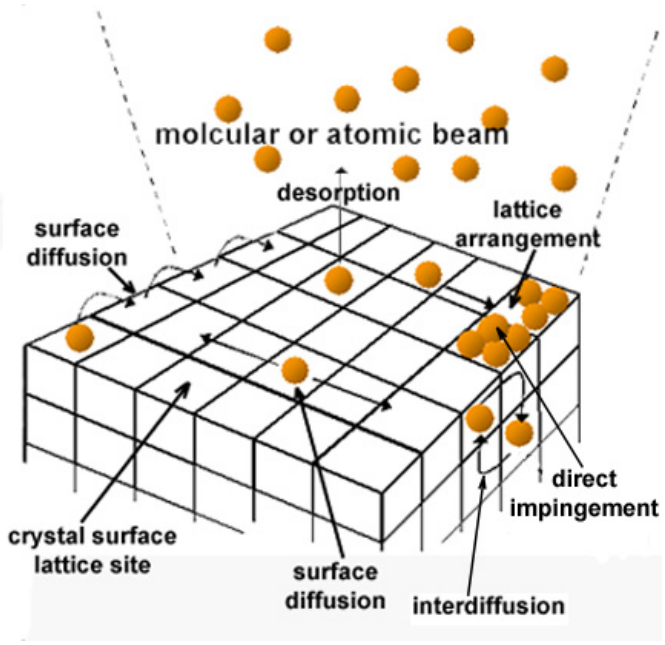


Figure 11: Schematic illustration of the surface processes occurring during MBE growth.

These processes involved during the epitaxial growth can be summarized as: a) adsorption of the evaporated atoms or molecules impinging on the surface; b) surface diffusion and dissociation of the absorbed atoms; c) atoms arrangement into the crystal lattice; d) thermal desorption of the species not arranged into the lattice [24]. The adsorbed molecules (or atoms) first combine to reach a critical size, **i**, and then become stable nuclei (or clusters) on the substrate. The main factors affecting **i** are the substrate temperature, the arrival rates and the affinity with the substrate. Subsequent molecules (or atoms) may condense directly onto these nuclei, decreasing the rate of formation of new nuclei and increasing the size of existing ones to form islands that may coalesce upon surface contact.

However, a distinction must be made in the initial growth process between the heteroepitaxial and homoepitaxial. Fig. **12** shows the behavior of the deposition rate as a function of arrival rate (the flux described by eq. 2), at a given substrate temperature. For the MBE growth of compound semiconductors, the required fluxes are typically between 10^{18}-10^{20} *atoms* m^{-2} s^{-1}.

Fig. **12 (a)** represents the case of a single component A. The dashed line indicates the asymptotic deposition rate applicable to both homoepitaxial growth at all stages and heteroepitaxial growth after nucleation. In order to initiate the nucleation process for heteroepitaxial growth at the given substrate temperature, the super saturation rate must be greater than the reevaporation rate: $R^S_A >$

R^E_A. The solid line indicates the case where other low-energy sites (*i.e.* surface impurities) are available to initiate the nucleation.

For a process involving an *AB* compound (see Fig. **12 (b)**) with a fixed evaporation rate of B, R_B, nucleation initiate when the evaporation rate of A exceeds the super saturation rate of the compound: $R_A > R^S_{AB}$. After nucleation, the deposition rate is proportional to R_A and becomes a constant, and R_B limits it. In the case of $R_A > R^S_A$ the deposition rate increases, and the growing film becomes A-rich [33].

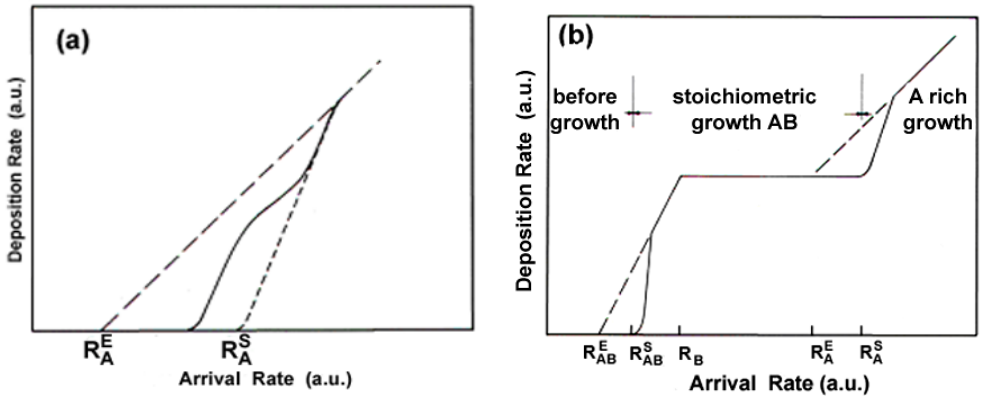


Figure 12: Schematic illustration of deposition rate *vs.* arrival rate of component A for (a) one component system; (b) two component system A and B, with a fixed arrival rate of component B. Superscripts E and S indicate reevaporation and super saturation, respectively.

The whole growth process can generally be described by few parameters, such as the sticking coefficient, s, the thermal accommodation coefficient, a_c, the condensation coefficient, c, the diffusion coefficient, D, and the mean stay time, τ_a:

$$s = \frac{N_{adh}}{N_{tot}} \tag{4}$$

the sticking coefficient is the ratio of the number of atoms (or molecules) adhering to the surface to the number of atoms (or molecules) arriving there. Depending on the growth regime, s could be less than unity when the adsorption energy of atoms is low, or the surface temperature is high;

$$a_c = \frac{T_i - T_e}{T_i - T_s} \tag{5}$$

the thermal accommodation coefficient defines the atoms (or molecules) fraction that is in thermodynamic equilibrium with the substrate. T_i is the effusion cell temperature; T_e is the energy corresponding temperature of atoms that immediately re-evaporate; T_s is the substrate temperature;

$$c = \frac{N'_{adh}}{N_{tot}} \tag{6}$$

the condensation coefficient, differently by *s*, describes the fraction of atoms (or molecules) that immediately adhere to the surface. In this case atoms (or molecules) are desorbed before their chemical-physical reaction to the surface;

$$D = \left(\frac{\alpha \cdot \upsilon}{N_0}\right) \exp\left(-\beta E_d\right)\left[cm^2\ s^{-1}\right] \tag{7}$$

the diffusion coefficient is defined as the product of the atom surface diffusion length before lattice incorporation and its surface mean speed. In this case α depends on the lattice parameter, υ is the atomic vibration frequency, N_0 (cm^{-2}) is the substrate sites number of equal adsorption energy E_a of isolated adatoms on the substrate, β is written for $(kT_s)^{-1}$, k is the Boltzmann's constant and T_s is the surface temperature;

$$\tau_a^{-1} = \upsilon \cdot \exp\left(-\beta E_a\right)\left[s^{-1}\right] \tag{8}$$

finally, τ_a is the atomic mean stay time on the substrate surface before their reevaporation [33, 24].

4.1. Processes of Nucleation and Growth

The formation of a large cluster is an example of a chain reaction that starts with the formation of a small stable nucleus. In fact, above the critical size (n > **i**), growth is more probable than decay, and all large clusters may be considered stable, even if some atoms leave them during the growth process. The single atoms can diffuse across the substrate to join a stable cluster, or they can impinge directly on the growing clusters and be incorporated by them, as illustrated in Fig. **11**. The binding energy E_j of a *j*-cluster (with size $j \geq$ **i**) can be related to the energy E_2 of a pair of atoms on the substrate, by considering nearest-neighbor bonds [34].

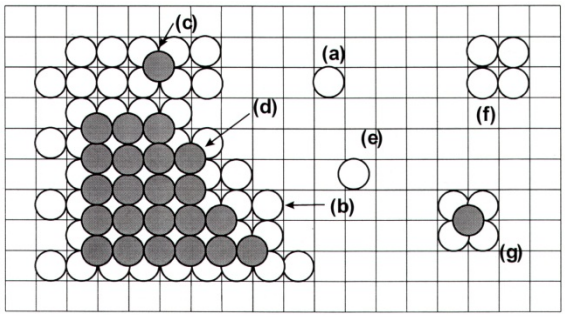


Figure 13: Binding energies of atoms and clusters that nucleate and growth on a square lattice. Single atoms: (a) E_a; (b) $E_a + 2E_2$; (c) $E'_a=4E_2$; (d) $E'_a+2E_2=6E_2$; (e) E_a-E_d; clusters; (f) $4E_a+4E_2$; (g) $4E_a+8E_2$. E_d is the diffusion energy; E'_a is the adsorption energy of an atom on a monolayer of the condensate; E'_d is the diffusion energy of an isolated atom on top of a monolayer; (f) and (g) refer to the 2D and 3D surface nucleation of clusters respectively.

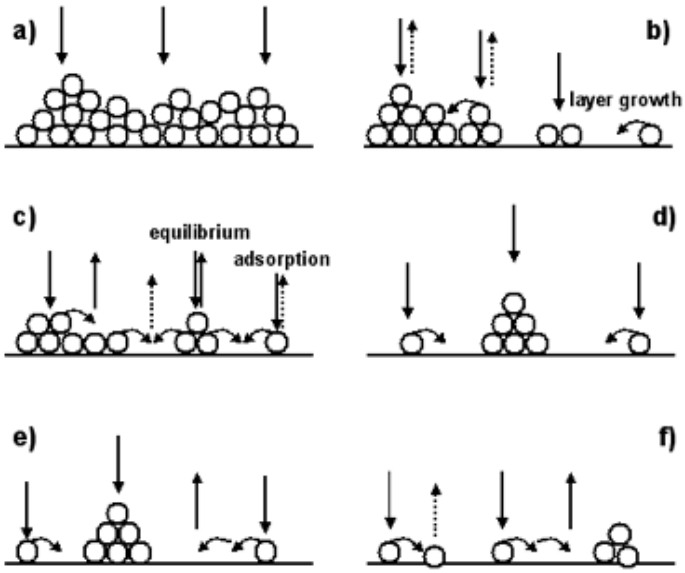


Figure 14: Regimes of nucleation and growth of clusters.

The processes are illustrated schematically in Fig. **13**, for an epitaxial growth in an orientation with four-fold symmetry. The three most important activation energies E_a, E_2 and E_d, with the experimental variables R and T_s, determine the nucleation regime observed (see Fig. **14**), which can be described using the parameter $R/N_0^2 D$. The growth process at the lowest temperature T_s and higher arrival rate R is described in Fig. **14 a)**. In this case $R/N_0^2 D \geq 1$ and the atoms stay exactly where they have arrived. An irregular layer is built up, and if atoms have directional bonds the layer will tend to be amorphous. The second regime, illustrated in Fig. **14 b)**, is the case of "layer-by-layer" growth. It is characterized by $R/N_0^2 D << 1$, $E_a \geq E'_a$, and T_s must be low enough so that 2D crystal layers can grow, even though single atoms may reevaporate. The regime illustrated in Fig. **14 c)** corresponds to the equilibrium adsorption, where the same conditions as case **b)** apply, but the surface temperature is higher or the arrival rate lower. Furthermore, atoms, at least from the highest layers, are quickly desorbed parallel to the surface, and the film growth only proceeds to a certain thickness whilst bulk crystals do not grow. In this case, there is no stable microstructure of the film in the long term, and adsorption is usually described only in thermodynamic terms.

In the regimes illustrated in Fig. **14 d)** and **e)** the film initially forms a three dimensional cluster on the substrate, the condition $4E_2 \geq E_a$ applies and the surface temperature is lower for case **d)** and higher for the case **e)**. If $E_2 > E_a$, the cluster will have a 3D shape from the beginning of growth. For the regime illustrated by case **d)**, all atoms condense, since the rate of formation of new clusters is faster compared to the rate of reevaporation, whilst for case **e)** the condensation is incomplete. Finally, in the regime illustrated in Fig. **14 f)**, if either E_2/kT or E_a/kT is small, the nucleation will be impossible on a perfect substrate, due to the effect of defects sites on the surface. An intermediate regime occurs when E'_a is lower than the value for an infinite crystal after some finite layers have been deposited. In this case growth starts in the "layer-by-layer" mode and then 3D crystals nucleate on the top. The term to describe this regime is the "Stranski-Krastanov"

growth mode [34]. The three growth modes previously described are schematically illustrated in Fig. **15**.

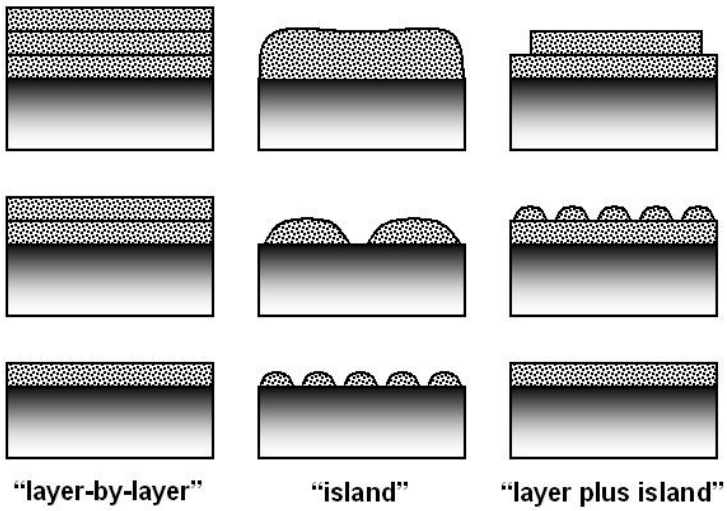


Figure 15: Schematic illustration of the three main growth modes: "layer-by-layer"-Frank-Van der Merwe; "island"-Volmer-Weber; "layer plus island"-Stranski-Krastanov.

These modes can also be classified by the behavior of the surface free energy during the epitaxial process, since it strongly determines the equilibrium morphology. In fact, considering a lattice-matched growth mode, in Frank-Van der Merwe, the sum of the free energy associated with the free surface of the epitaxial film, $\gamma_{e/v}$, and with the interface between the substrate and the epitaxial surface, $\gamma_{s/e}$, is less than or equal to that associated with the original substrate surface, $\gamma_{s/v}$. Then, the overall free energy decreases faster over the first layer (or two), before settling down to a steady state slope for thicker films. Therefore, the system is thermodynamically stabilized against breakup into inhomogeneous regions, some thicker and some thinner. In Volmer-Weber, the sum $\gamma_{e/v}$ and $\gamma_{s/e}$ is greater than $\gamma_{s/v}$. The overall free energy then increases over the first layer (or two), before reversing and decreasing as next layers are deposited. Therefore, the system of uniform thickness is thermodynamically unstable for breakup into inhomogeneous regions, some very thick and some completely uncovered. In Stranski-Krastanov, the sum $\gamma_{e/v}$ and $\gamma_{s/e}$ is less than $\gamma_{s/v}$. Therefore, the surface free energy decreases rapidly as the first layer (or two) is deposited, before decreasing, less steeply than the "layer-by-layer" growth mode, for thicker films. Therefore, films thicker than a few monolayers are unstable and can breakup into inhomogeneous regions, some very thick and some having only one layer (or two) [35]. For a strained epilayer there is the additional possibility that island formation may allow the system to introduce misfit dislocations underneath the islands to relax strain energy. For a system with small interface free energy but large lattice mismatch, initial growth is "layer-by-layer", but a thicker layer has greater strain energy and can lower its total energy by forming isolated thick islands in which the strain is relaxed by interfacial misfit dislocations [36].

5. MISFIT DISLOCATIONS AND DEFECTS

Generally, a heteroepitaxy process is related to lattice mismatch since a layer with atomic spacing or lattice symmetry different from those of the substrate is epitaxial grown. This disregistry can accommodate by strain connected to a relevant interfacial energy or by structural defects in the layer. In fact, when both the epilayer thickness and the mismatch between the stress-free lattice parameters of the two crystals are small, the separation of the dislocation becomes infinite and all mismatch is accommodated by elastic strain [37]. In order to introduce an easy explanation of the misfit concept, some important parameters will be considered, and the simplest situation where both layers have rectangular symmetry (i = x, y) at the interface plane is used. If the thickness of the epitaxial layer is thinner than that of the substrate, the mismatch parameter can be defined by:

$$f_i = \frac{a_{si} - a_{ei}}{a_{ei}} \tag{9}$$

where a is the lattice parameter and s and e indicate the substrate and the epitaxial layer, respectively. A positive value of f implies that the strain is tensile. Moreover, the misfit strain is defined as:

$$e_i = \frac{a^s_{ei} - a_{ei}}{a_{ei}} \tag{10}$$

where a^s_e indicates the lateral atomic spacing in the strained epilayer. However, when the coherence between the strained layer and the substrate is lost, the misfit strain is shared between a plastic strain component, d, due to the misfit dislocations and a residual elastic strain component:

$$f_i = e_i + d_i \tag{11}$$

The value of d can be estimated from the misfit dislocation spacing, S: $d = b_n/S$, where b_n is the interface-plane component of the Burgers vector in the direction of the misfit dislocation spacing. It is well known that under adequate conditions, overgrow layers can be deposited epitaxially on the substrate with different lattice parameters up to a critical thickness h_{crit} [38, 34]. Epilayers thinner than h_{crit} adapt the lattice parameter of the substrate, a condition known as "pseudomorphic" growth [39, 40].

The misfit between the substrate and the overgrown layer is sufficiently small, and the first deposited layers are strained to match the substrate and a coherent (perfect matched) epilayer is formed. The situation is depicted in Fig. **16**. If the lattice parameter of the epilayer is greater than that of the substrate, the film grown undergoes a compressive strain on the interface plane. *Vice versa*, the strain will be tensile. Moreover, since the total volume of the unit cell must remain unchanged, the cell is also distorted perpendicularly to the plane interface. As the epilayer thickness increases, overlapping h_{crit}, the homogeneous strain energy becomes favorable for the introduction of misfit dislocations (see Fig. **16**) [40]. Fig. **17** reports an example of the result of the Matthews-Blakeslee theory for 60° a/2 <101> misfit dislocation in the $Si_{1-x}Ge_x$/Si (100) system and experimental measurement of critical thickness h_{crit} for different growth\annealing temperatures [40]. It is also possible to change the value of h_{crit} by growing one or more

subsequent epilayers. In fact, if an epilayer B is deposited on a substrate A, and the layer thickness exceeds the critical value, it might be possible to restore coherency by the deposition of a layer of the same material of A.

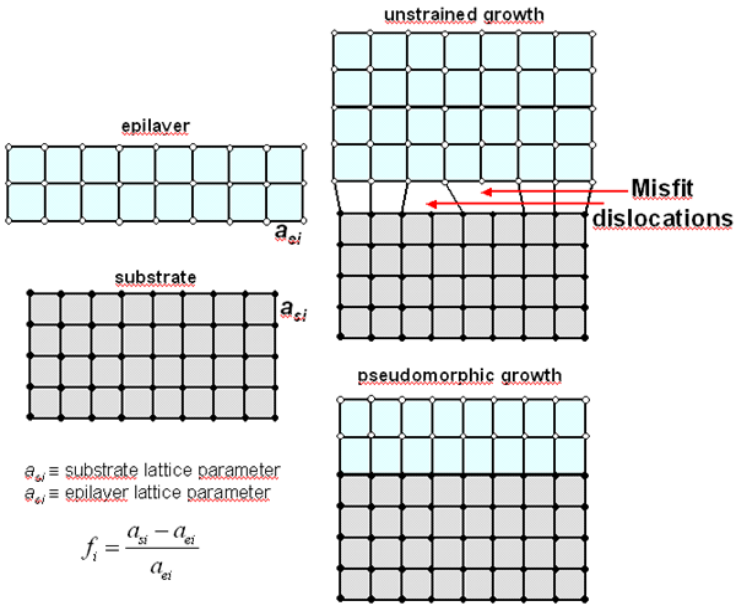


Figure 16: Growth of a layer on a substrate with different lattice parameters; the pseudomorphic (coherent mode) and the unstrained growth cases are illustrated. The red arrows indicate the presence of misfit dislocations at the interface, due to a non-coherent growth.

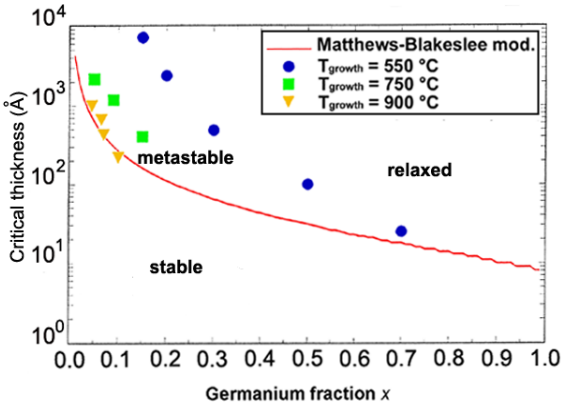


Figure 17: Measurement of critical thickness in the $Si_{1-x}Ge_x/Si$ (001) system for different growth temperatures *vs.* the prediction of the Matthews–Blakeslee model [40].

However, there is a second critical thickness of the epilayer B, above which it is not possible to restore coherency. Depending on the crystalline structure of the growing material and on the

quality of both the epitaxial process and the surface of deposition, a wide variety of dislocations and effects can originate in the epilayers. Even though the presence of most of these crystalline defects is undesirable, certain types are essential in semiconductor manufacturing. In the following sections the most common will be described briefly.

5.1. Dislocations

Considering a single epilayer in which the perfect coherent registry with the substrate is broken, the simplest consequence might consist of a half plane missing from the epitaxial film. In this case, the most useful definition to introduce is that related to the Burgers circuit. It is the atom-to-atom path that forms a closed loop in a crystal with dislocations. If the same atom-to-atom sequence is formed in a dislocation free crystal, and the circuit does not close, then the original loop must enclose one or more dislocations. The vector required to fill the gap in the circuit is called the Burgers vector (the red arrows illustrated in Fig. **18**).

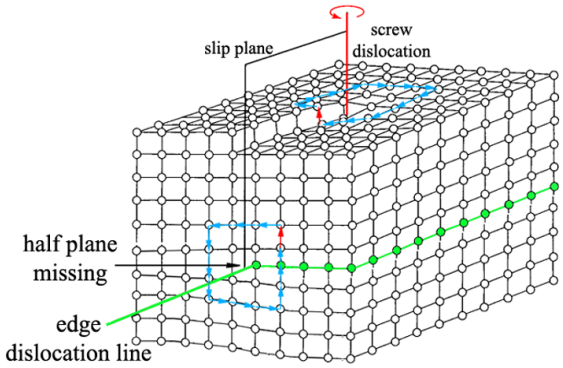


Figure 18: Pure edge and pure screw dislocations arising from the missing half of the epitaxial plane. The blue arrows indicate the Burgers vectors circuit. The red arrows indicate the Burgers vector $\vec{b}$.

In particular an edge dislocation has $\vec{b}$ perpendicular to the dislocation line. It marks the edge of a missing (or extra) half-plane of atoms. On the other hand, in a screw dislocation atoms are connected in a spiral around the screw dislocation. It has $\vec{b}$ parallel to the dislocation line. Generally, in most cases, the dislocation line lies at an arbitrary angle to its Burgers vector and the dislocation line has a mixed edge and screw character [41].

5.2. Stacking Faults

A stacking fault is a planar defect due to the interruption of the regular sequence layers within the crystal in a local region. This type of defect destroys the perfection of the host crystal, and the associated energy per unit area of fault is known as the “stacking fault energy”. Two types of stacking faults referred as to intrinsic and extrinsic are expected in a face centered cubic lattice. These are best described by considering the change in sequence resulting from the removal or introduction of an extra layer (see Fig. **19**).

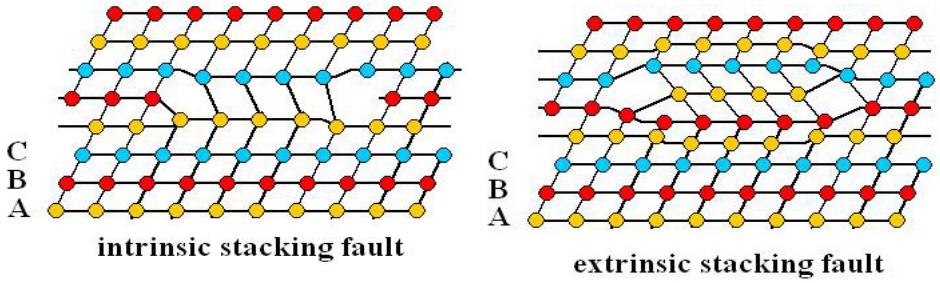


Figure 19: Stacking faults in the face-centered cubic structure.

In the intrinsic stacking fault, part of a layer has been removed which results in a break in the stacking sequence. Clearly, the stacking sequence above and below the fault plane are continuous right up to the fault itself. In the extrinsic stacking fault, an extra layer has been introduced. There are two breaks in the stacking sequence, and the extra layer does not belong to the continuing patterns of the lattice either below and or above the fault.

5.3. Grain Boundaries

A crystalline solid can also consist of a large number of randomly oriented grains (single crystals) separated by grains boundaries (defects). When the misorientation between the grains is too great, the atomic arrangements at the boundaries are very complex and vary significantly with the angles of misorientation (see Fig. **20**).

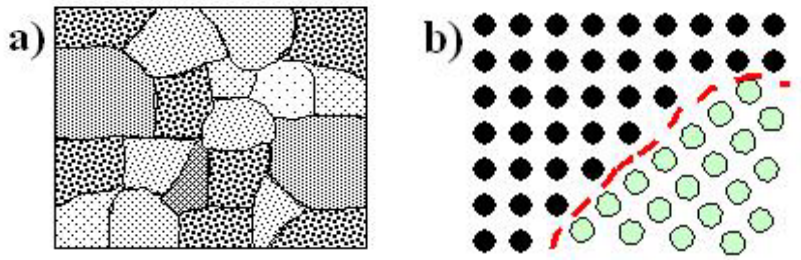


Figure 20: (a) Schematic illustration of differently oriented crystal grains in a polycrystalline material. (b) Representation of a grain boundary separating two crystallites.

A notable feature of the boundary structure is that the region of disorder is very narrow, limited to one or two atoms on each side of the boundary.

5.4. Twinning

Formation of twin boundaries is a process in which a region of a crystal undergoes a homogeneous shear that produces the original crystal structure in a new orientation. Deformation twinning can be induced by plastic deformation and is particularly important in body-centered and close packed hexagonal crystals. For example, in a face-centered cubic crystal the “ABC” notation adopted in

section **5.2** can be used to represent the relative atom positions in matrix and twin. Fig. **21** shows the stacking sequence of a (111) twin. The planes I-II and III-IV indicate the "coherent" twin planes; nearest-neighbor atom distances are unchanged across these planes. The plane II-III is called an "incoherent" twin plane; the two lattices do not fit exactly on them, and consequently there is considerable atomic misfit.

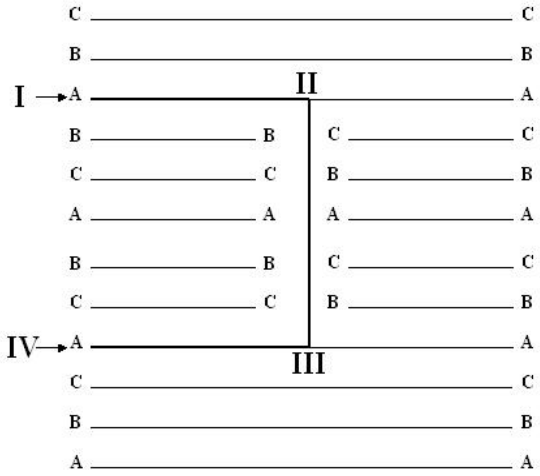


Figure 21: Stacking of (111) planes in a face-centred cubic crystal showing an embedded twin.

5.5. Point Defects

The 1D defect is called a point defect, since it involves only one atom surrounded by a perfect lattice. However, the presence of a point defect may affect the properties of its nearest neighbors, and by elastic interactions, a sizable spherical region of the lattice surround itself. Fig. **22** shows some forms of crystal point defects. A defect where an atom is missing from a lattice site is known as a vacancy defect. Vacancies are expected at high growth temperatures because the surface atoms mobility (*i.e.* the diffusion coefficient in eq. 7) in these cases must be quite high for them to change their positions leaving behind empty lattice sites.

If an atom is located in a non-lattice site within the crystal, it is said to be an interstitial defect. When the interstitial defect involves an extra atom, it is referred to as a self-interstitial defect. Vacancies and self-interstitial defects are classified as intrinsic point defects. A substitutional defect refers to an atom of a different type than the lattice composition, which has replaced one of the bulk atoms in the lattice. Substitutional and interstitial defects are classified as extrinsic point defects because foreign atoms are involved. If an atom leaves its site in the lattice, creating a vacancy, and then moves toward the surface of the crystal, it becomes a Schottky defect. On the other hand, an atom that vacates its position and transfers to an interstitial position in the crystal is known as a Frenkel defect. However, the management of defects during the epitaxial growth is an indispensable factor for obtaining materials with engineered performances (both electrical and optoelectronic). In fact, defects can be classified as undesired or desired impurities: the former generally refer to the contaminants into the lattice, the latter to the dopants.

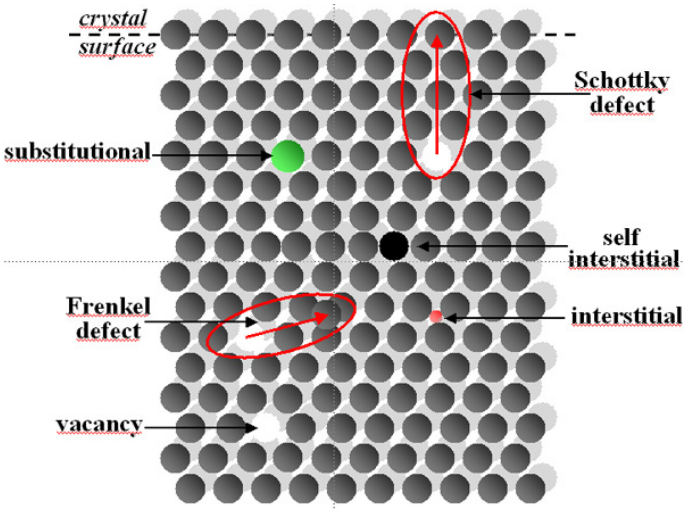


Figure 22: Schematic representation of the most common point defects in crystals.

6. DOPING

The main problem with the application of MBE for the fabrication of semiconductor devices is dopant incorporation. From a grower point of view, this topic should be divided into two parts: unintentional (and generally undesired) doping, which is caused by the presence of residual gases in the deposition chamber, and intentional (desired) doping, achieved for example by a thermal beam co-deposition process. As to the contribution of residual gas species, it should be noted that the value of the residual gas pressure achieved during the epitaxial deposition is lower than 5×10^{-11} Torr. At this low pressure the residual gas contains mainly H_2, H_2O, N_2 and CO_x molecules. In order to reduce to a minimum the incorporation of these contaminants it is a good practice turn off all hot filaments (such as the ionization gauges in Fig. **2**) not necessary during the epitaxial process. Moreover, it is important to restrict temporal and spatial variations in the temperature of LN_2 cryopanel surfaces during growth, as these spatial and temporal variations can result in variations in desorption and adsorption of trapped gas molecules. During the intentional doping of a semiconducting compound A^iB^j (A and B are the elements, while i and j are the numbers denoting columns in the Mendeleeev's table), different chemical reactions can take place [24]. If a cation element (A) is replaced by an element atom (C) of the group (i-1), a p-type doping is achieved:

$$C_g^{(i-1)} + V_{Ai} \leftrightarrow C_{Ai}^{(i-1)(-)} + h \qquad \textbf{(12)}$$

where V_{Ai} is a vacant A site in the A^iB^j compound, $C_{Ai}^{(i-1)(-)}$ is the ionized C acceptor, h is a free hole in the valence band of A^iB^j, and (g) denotes the gas phase of the element. If an anion atom (B) is replaced by an element atom (D) of the group (j + 1), an n-type doping is achieved:

$$\frac{1}{2} D_{2(g)}^{(j+1)} + V_{Bj} \leftrightarrow D_{Bj}^{(j-1)(+)} + e \qquad \textbf{(13)}$$

where e is a free electron in the conduction band of A^iB^j, $D_{Bj}^{(j-1)(+)}$ is an ionised donor. Replacement of a cation atom by doping atom (D) of the group $(i+j)/2$ of the periodic table gives n-type doping:

$$D_{(g)}^{(i+j)/2} + V_{Ai} \leftrightarrow D_{Ai}^{(i+j)/2(+)} + \left(j - i/2\right)e \tag{14}$$

Replacement of the anion atoms by doping elements (C) of the group $(i+j)/2$ gives p-type doping:

$$C_{(g)}^{(i+j)/2} + V_{Bj} \leftrightarrow C_{Bj}^{(i+j)/2(-)} + \left(j - i/2\right)h \tag{15}$$

However, the analysis of the previously illustrated reactions requires knowledge of quantities such as the enthalpy and entropy of the system of defects involved in the doping. A good approach to understanding the principles of this problem is that proposed by Heckingbottom [42], where thermodynamic considerations can determine whether a doping process is possible or not during the epitaxial deposition. This model is useful in the selection of dopants that are more suitable. In a more detailed study of a particular reaction, the comparison of the thermodynamic framework with experimental data provides identification of any kinetic barriers and hence leads to a clearer understanding of the reaction mechanism [43].

7. IV-GROUP MBE

The "Stranski-Krastanov" growth mode illustrated in sec. **4.1** is a powerful technique applied for fabrication of a large number of high-quality nanosized atomic clusters (quantum dots-QDs). These dots have unique properties which can be tuned by the grower by varying the epitaxial growth parameters. Due to the importance of Si in opto-electronic device applications and energetic device productions, nano-sized materials based on silicides are under continuous investigation to optimize their performance and to scale down dimensions. Arrays of Ge, Si and SiGe nano-islands, so called "pyramid" and "dome" clusters, grown on Si(001) are typical examples of such systems (see Fig. **23**). However, as previously illustrated, different growth conditions play crucial roles for the appearance of these islands grown on Si (001).

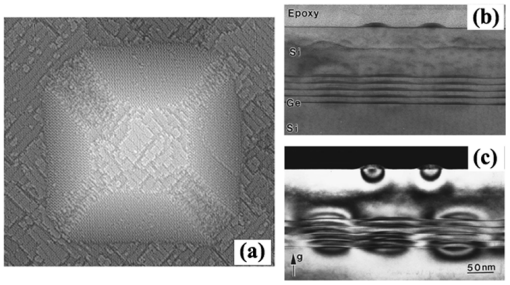


Figure 23: (a) Scanning Tunneling Microscopy (STM) image (108 × 108 nm^2) of a faceted island obtained by depositioning $Si_{0.6}Ge_{0.4}$ on Si (001) [44]. (b) Cross-sectional TEM image of a Ge/Si multilayer structure consisting of five individual Ge layers. (c) Dark field image exhibiting Ge islands buried in the Si layers (AIP license n. 2571411082174) [45].

Table **1** shows the results obtained by A. Malachias *et al.* [46], demonstrating how strong changes in interdiffusion and resulting atomic ordering arise from the different growth parameters used during the MBE deposition of Ge domes on Si(001). Another intriguing possibility is related to the formation of a patterned substrate, above which nanocrystals are subsequently self-assembled by solid phase epitaxy [47-49].

Table 1: Growth parameters used during MBE deposition of Ge:Si(001) films. Domes with different width/height ratio can be obtained.

Growth Temperature (°C)	Coverage	Dome width/height (nm)
620	6.7 ML Ge	87/19
700	11 ML Ge	143/36
750	11 ML Ge	170/34
840	6 ML Ge	338/37

Legend. The monolayer (ML) thickness is considered as 0.1413 nm for Ge, and 0.1385 nm for $Si_{0.5}Ge_{0.5}$.

In this model highly dense two-dimensional periodic arrays of ordered QDs can be nucleated, with lateral dimensions depending on the holes' properties. The 2D array of holes with different size, depth and pitches can be fabricated by a focused ion beam (FIB), both on SiO_2/Si(001) and Si(001) substrates. After the MBE evaporation of few monolayers of Ge (at room temperature), the system is annealed at about 500-550 °C, in order to raise the surface mobility of the Ge atoms, and then fill the holes by Ge QDs (see Fig. **24**). However, several theoretical models include the utilization of intermediate band solar cells [50], up-conversion for the absorption of sub-band gap light [51], and control of the strain, shape, and local Ge fraction in multicrystalline SiGe for the absorption of the near-infrared light [52]. Furthermore, experiments were also performed to improve the performance of the solar cells by 1) absorbing the low-energy photons, 2) by using SiGe multicrystalline with microscopic compositional distribution to enhance the absorption performance [53, 54], and 3) by exploiting the advantage of quantum well solar cells to independently optimise the absorption edge and spectral characteristics [55]. Another way to absorb the low-energy photon might be the incorporation of doped Ge dots in the intrinsic region of Si-based solar cells [23, 56-61].

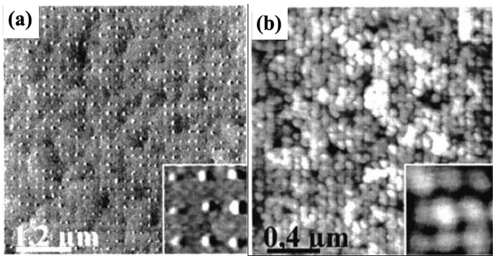


Figure 24: Atomic force microscopy (AFM) image of the organization of Ge dots on patterned areas by Ga^+ source (FIB), at a growth temperature of 550 °C and Ge thickness of 14. The initial holes diameter was 40 nm with a pitch of (a) 200 nm, and (b) 75 nm (AIP license n. 2573690146603).

Even though the MBE cannot represent a valuable growth technology for large production of semiconducting devices, it does represent an excellent way to investigate the basic properties of the materials and solutions previously mentioned, in order to employ them in either opto-electronic or energetic device applications produced by other industrial growth technologies widely used in the field of device fabrication.

ACKNOWLEDGEMENT

Declared none.

CONFLICT OF INTEREST

The author(s) confirm that this chapter content has no conflict of interest.

REFERENCES

[1] Cho AY. Film Deposition by Molecular-Beam Techniques. J Vac Sci Technol 1971; 8: S31-S38.
[2] Cho AY, Dunn CN, Kuvas RL, Schroeder WE. GaAs IMPATT diodes prepared by molecular beam epitaxy. Appl Phys Lett 1974; 25: 224-226.
[3] Cho AY, Ballamy WC. GaAs planar technology by molecular beam epitaxy (MBE). J Appl Phys 1975; 46: 783-785.
[4] Cho AY, Reinhart FK. Growth of three-dimensional dielectric waveguides for integrated optics by molecular-beam-epitaxy method. Appl Phys Lett 1972; 21: 355-356.
[5] Cho AY, Chen YS. Epitaxial growth and optical evaluation of gallium phosphide and gallium arsenide thin films on calcium fluoride substrate. Solid State Commun 1970; 8: 377-379.
[6] Cho AY. Epitaxial Growth of Gallium Phosphide on Cleaved and Polished (111) Calcium Fluoride. J Appl Phys 1970; 41: 782-786.
[7] Cho AY. Growth of periodic structures by the molecular beam method. Appl Phys Lett 1971; 19: 467-468.
[8] Dingle R, Wiegmann W, Henry CH. Quantum states of confined carriers in very thin $Al_xGa_{1-x}As/GaAs/Al_xGa_{1-x}As$ heterostructures. Phys Rev Lett 1974; 33: 827-830.
[9] Wachter M, Thonke K, Sauer R, SchaftIer F, Herzog HJ, Kasper E. Photoluminescence of confined excitons in MBE-grown $Si_{1-x}Ge_x/Si(100)$ single quantum wells. Thin Solid Films 1992; 222: 10-14.
[10] For a good collection of papers, see Proceedings on the Second International Conference on Modulated Semiconductor Structures, Kyoto: Japan 1985.
[11] Petroff PM, DenBaars SP. MBE and MOCVD growth and properties of self-assembling quantum dot arrays in III-V semiconductor structures. Superlattices Microstruct 1994; 15: 15-30.
[12] Leonard D, Krishnamurthy M, Reaves CM, Denbars SP, Petroff PM. Direct formation of quantum-sized dots from uniform coherent islands of InGaAs on GaAs surfaces. Appl Phys Lett 1993; 63: 3203-3205.
[13] Shen XQ, Tanaka S, Iwai S, Aoyagi Y. The formation of GaN dots on $Al_xGa_{1-x}N$ surfaces using Si in gas-source molecular beam epitaxy. Appl Phys Lett 1998; 72: 344-346.
[14] Waters RG, Wagner DK, Hill DS, Tihanyi PL, Vollmer BJ. High-power conversion efficiency quantum well diode lasers. Appl Phys Lett 1987; 51: 1318-1319.
[15] Wang J, Smith B, Xie X, Wang X, Burnham GT. High-efficiency diode lasers at high output power. Appl Phys Lett 1999; 74: 1525-1527.
[16] Fafard S, Hinzer K, Raymond S, *et al.* Red-Emitting Semiconductor Quantum Dot Lasers. Science 1996; 274: 1350-1353.

[17] Jo M, Ishida K, Yasuhara N, Sugawara Y, Kawamoto K, Fukatsu S. A Si-based quantum-dot light-emitting diode. Appl Phys Lett 2005; 86: 103509-3.
[18] Choi KK. The Physics of Quantum Well Infrared Photodetectors. River Edge, NJ; World Scientific 1997.
[19] Pan D, Towe E, Kennerly S. Normal-incidence intersubband (In, Ga)As/GaAs quantum dot infrared photodetectors. Appl Phys Lett 1998; 73: 1937-1939.
[20] Luque A, Martí A, López N, *et al.* Experimental analysis of the quasi-Fermi level split in quantum dot intermediate-band solar cells. Appl Phys Lett 2005; 87: 083505-3.
[21] Bimberg D, Grundmann M, Ledenstov NN. Quantum Dot Heterostructures. London: Wiley 1999.
[22] Alonso-Álvarez D, Taboada AG, Risalda JM, *et al.* Carrier recombination effects in strain compensated quantum dot stacks embedded in solar cells. Appl Phys Lett 2008; 93: 123114-3.
[23] Konle J, Presting H, Kibbel H, Banhart F. Growth studies of Ge-islands for enhanced performance of thin film solar cells. Mater Sci Eng B 2002; 89: 160-165.
[24] Herman MA, Sitter H. Molecular Beam Epitaxy. Berlin: Springer-Verlag 1989.
[25] Foxon CT, Joice BA. Growth and Characterisation of Semiconductors. Hilger: RA Stradling and PC Klipstein 1990.
[26] Malik RJ. Electron beam source molecular beam epitaxy of III–V compounds. J Vac Sci Technol B 1987; 5: 722-724.
[27] Somorjai GA. Treatise on Solid State Chemistry. New York: Hannay NB-Plenum 1976.
[28] Mahan JE, Geib KM, Robinson GY, Long RG. A review of the geometrical fundamentals of reflection high-energy electron diffraction with application to silicon surfaces. J Vac Sci Technol A 1990; 8: 3692-3700.
[29] Neave JH, Joyce BA, Dobson PJ, Norton N. Dynamics of film growth of GaAs by MBE from Rheed observations. Appl Phys A 1983; 31: 1-8.
[30] Dentel D, Bischoff JL, Kubler L, Bolmont D. Role of hydrogen during Si capping of strained Ge or $Si_{1-x}Ge_x$ hut clusters. Thin Solid Films 1998; 336: 49-52.
[31] Ishizaka A, Shiraki Y. Low temperature surface cleaning of Silicon and its application to Silicon MBE. J Electrochem Soc 1986; 133: 666-671.
[32] Hakane T, Okumura H, Tanaka J, Matsumoto S. New Ge substrate cleaning method for $Si_{1-x-y}Ge_xC_y$ MOMBE growth. Thin Solid Films 1997; 294: 153-156.
[33] Matthews JW, Ludeke R. Epitaxial Growth part A. New York: Academic Press Inc 1975.
[34] Matthews JW. Epitaxial Growth part B. New York: Academic Press Inc 1975.
[35] Tsao JY. Materials Fundamentals of Molecular Beam epitaxy. San Diego: Academic Press Inc 1993.
[36] Shaw DW, Bean JC, Keramidas VG, Peercy PS. Epitaxial Heterostructures. Pennsylvania: MRS 1990
[37] Matthews JW. Defects associated with the accommodation of misfit between crystals. J Vac Sci Technol 1975; 12: 126-133.
[38] Frank FC, van der Merwe JH. One-Dimensional Dislocations. I. Static Theory; II. Misfitting Monolayers and Oriented Overgrowth. Proc R Soc 1949; 198: 205-225.
[39] Finch AI, Quarrel AG. Crystal structure and orientation in zinc-oxide films. Proc Phys Soc 1934; 46: 148-162.
[40] Kasper E. Properties of strained and relaxed Silicon Germanium. London: INSPEC 1995.
[41] Hull D, Bacon DJ. Introduction to dislocations. Oxford: Butterworth-Heinemann 2001.
[42] Chang LL, Ploog K. Molecular Beam Epitaxy and Heterostructures. NATO ASI Ser, Ser E 87, Dordrecht: Martinus Nijhoff 1985.
[43] Heckingbottom R, Todd CJ, Davies GJ. The Interplay of Thermodynamics and Kinetics in Molecular Beam Epitaxy (MBE) of Doped Gallium Arsenide. J Electrochem Soc 1980; 127: 444-450.
[44] Tersoff J, Spencer BJ, Rastelli A, von Kanel H. Barrierless Formation and Faceting of SiGe Islands on Si(001). Phys Rev Lett 2002; 89: 196104-4.
[45] Kienzle O, Ernst F, Ruhle M, Schmidt OG, Eberl K. Germanium "quantum dots" embedded in silicon: Quantitavive study of self-alignment and coarsening. Appl Phys Lett 1999; 74: 269-271.

[46] Malachias A, Stoffel M, Schmidbauer M, *et al.* Atomic ordering dependence on growth method in Ge:Si(001) islands: Influence of surface kinetic and thermodynamic interdiffusion mechanisms. Phys Rev B 2010; 82: 035307-9.

[47] Karmous A, Cuenat A, Ronda A, Berbezier I. Ge dot organization on Si substrates patterned by focused ion beam. Appl Phys Lett 2004; 85: 6401-6403.

[48] Berbezier I, Karmous A, Ronda A, *et al.* Two-dimensional arrays of ordered, highly dense and ultra small Ge nanocrystals on thin SiO_2 Layers. J Phys Conf Ser 2005; 10: 73-76.

[49] Szkutnik PD, Sgarlata A, Motta N, Placidi E, Berbezier I, Balzarotti A. Influence of patterning on the nucleation of Ge islands on Si and SiO_2 surfaces. Surf Sci 2007; 601: 2778-2782.

[50] Cuadra L, Marti A, Luque A. Type II broken band heterostructure quantum dot to obtain a material for the intermediate band solar cell. Physica E 2002; 14: 162-165.

[51] Trupke T, Green MA, Wurfel P. Improving solar cell efficiencies by up-conversion of sub-band-gap light. J Appl Phys 2002; 92: 4117-4122.

[52] Usami N, Ichitsubo T, Ujihara T, *et al.* Influence of the elastic strain on the band structure of ellipsoidal SiGe coherently embedded in the Si matrix. J Appl Phys 2003; 94: 916-920.

[53] Nakajima K, Usami N, Fujiwara K, *et al.* Growth and properties of SiGe multicrystals with microscopic compositional distribution for high-efficiency solar cells. Sol Energy Mater Sol Cells 2002; 73: 305-320.

[54] Nakajima K, Usami N, Fujiwara K, *et al.* Melt growth of multicrystalline SiGe with large compositional distribution for new solar cell applications. Sol Energy Mater Sol Cells 2002; 72: 93-100.

[55] Barnham KWJ, Duggan G. A new approach to high-efficiency multi-band-gap solar cells. J Appl Phys 1990; 67: 3490-3493.

[56] Alguno A, Usami N, Ujihara T, *et al.* Effects of spacer thickness on quantum efficiency of the solar cells with embedded Ge islands in the intrinsic layer. Appl Phys Lett 2004; 84: 2802-2804.

[57] Yakimov AI, Markov VA, Dvurechenskii AV, Pchelyakov OP. Coulomb staircase in a Si/Ge structure. Philos Mag B 1992; 65: 701-705.

[58] Morresi L, Ayoub JP, Pinto N, *et al.* Structural, magnetic and electronic transport properties of MnxGe1-x/Ge(001) films grown by MBE at 350°C. Surf Sci 2007; 601: 2632-2635.

[59] Morresi L, Ayoub JP, Pinto N, *et al.* Formation of Mn5Ge3 nanoclusters in highly diluted MnxGe1-x alloys. Mat Sci Semic Proc 2006; 9: 836-840.

[60] Pinto N, Morresi L, Ficcadenti M, *et al.* Magnetic and electronic transport percolation in epitaxial GeMn films. Phys Rev B 2005; 72: 165203-7.

[61] Morresi L, Pinto N, Ficcadenti M, *et al.* Magnetic and transport polaron percolation in diluted GeMn films. Mat Sci Eng B 2006; 126: 197-201.

SECTION II - EXPERIMENTAL TECHNIQUES TO MEASURE FILM AND DEVICE PARAMETERS

Send Orders of Reprints at reprints@benthamscience.net

CHAPTER 5

Infrared and Raman Spectroscopies

Ubaldo Coscia[1,2,*], Deepak K. Basa[3] and Giuseppina Ambrosone[2,4]

[1]CNISM Naples Unit, Complesso Universitario MSA, via Cintia, 80126, Naples, Italy; [2]Department of Physical Sciences, University of Naples "Federico II", Complesso Universitario MSA, Via Cintia, 80126 Naples, Italy; [3]Department of Physics, Utkal University, Bhubaneswar-751004, India and [4]CNR-SPIN, Complesso Universitario MSA, via Cintia, 80126 Napoli, Italy

Abstract: The chapter is devoted to the Fourier transform infrared (FTIR) and Raman spectroscopy. The theory of both techniques has been briefly treated and the most widely used experimental apparatus have been described. The use of the FTIR and Raman spectroscopy for the characterization of silicon based films and the optimization of microcrystalline solar cell parameters, as examples of applications, have been reported. In particular, it has been shown that by means of FTIR it is possible to detect oxygen impurity in microcrystalline silicon, to individuate the device grade microcrystalline silicon for solar cells fabrication and to study the phase transition due to the thermal annealing of amorphous silicon carbon alloys (a-$Si_{1-x}C_x$:H) and a-$Si_{1-x}C_x$:H/SiC multilayers. Furthermore, it has been demonstrated that the Raman spectroscopy can be used for the optimization of J-V parameters of microcrystalline silicon solar cells, for the study of boron doping effect on the crystalline volume fraction in microcrystalline silicon carbon, for the investigation of crystallization process induced by thermal annealing in a-$Si_{1-x}C_x$:H/SiC multilayers, for determining the influence of the carbon alloying as well as the substrate on the crystalline volume fraction in nanostructured silicon carbon films and, finally, for the study on the medium range order in nanocrystalline silicon.

Keywords: Fourier transform infrared spectroscopy, raman scattering, vibrational modes, structural properties, silicon (hydrogenated) thin films, silicon carbon (hydrogenated) thin films, silicon nanocrystallites, solar cells parameters, thermal annealing, plasma enhanced chemical vapour deposition, average grain dimension, crystalline volume fraction, microstructure factor, oxygen impurities.

1. INTRODUCTION

Silicon based thin films are widely used in photovoltaic (PV) applications. Hydrogenated amorphous silicon (a-Si:H) and related alloys have been employed in the production of single and multijunction solar cells [1-4]. However, a-Si:H solar cells undergo a loss of efficiency under light soaking conditions due to the Staebler-Wronski effect [5]. Hydrogenated micro/nano crystalline silicon films, because of their better transport properties, resistance to light-induced degradation and superior long wavelength response as compared to amorphous counterpart, have been used to replace or supplement amorphous Si in solar cells in order to improve their stability and efficiency [6-8]. Indeed, these materials have been incorporated in p-i-n and n-i-p structures [9-16] or in

***Address correspondence to Ubaldo Coscia:** Department of Physical Sciences, University of Naples "Federico II", Complesso Universitario MSA, Via Cintia, 80126 Naples, Italy; Tel: +39 081 67 6102; Fax: +39 081 67 6346; E-mail: coscia@na.infn.it

Roberto Murri (Ed)
All rights reserved-© 2013 Bentham Science Publishers

stacked tandem cells in micro morph configuration [17-20] as well as in triple junction solar cells [3, 21].

Recently, nanostructured films composed of silicon nanocrystals (SiNCs) embedded in amorphous dielectric matrix of different kinds (SiO_2, Si_3N_4, SiC) have opened up alluring possibilities for the third generation "all Si" tandem solar cells [22-25]. Nanocrystals having size less than 7 nm dispersed in such matrices behave as quantum dots exhibiting quantum confinement effects of carriers [26, 27] which results in an enlargement of the band gap and efficient light emission in the visible range at room temperature [28-34]. It has been reported that SiNCs embedded in a near stoichiometric amorphous silicon carbide matrix can exhibit larger quantum confinement effects as compared to SiNC in SiO_2 or Si_3N_4 matrix because of a significantly lower barrier height of SiC matrix [35-39]. In order to obtain highly efficient solar cells an optimization process of the optical, electrical and structural properties of the above-mentioned materials has become indispensable.

The structural characterizations are performed by using several techniques such as transmission electron microscopy (TEM), X-ray diffraction (XRD), Fourier transform infrared (FTIR) spectroscopy, Raman spectroscopy. In this chapter, we focus on FTIR and Raman spectroscopy that have the capacity to analyse samples in different phases such as crystalline, micro crystalline, nanocrystalline and amorphous both in bulk and thin film. These techniques are popular as structural probes because of their speed, accuracy, sensitivity and, above all, their being non-destructive.

Infrared and Raman techniques have common attributes. They are optical probes and are spectroscopic in nature implying that the intensity of signal is measured *versus* wavenumber (inverse of wavelength). Both Infrared and Raman spectroscopy require a light source, a means to set and/or measure the wavelength, a detector and a spectra recorder. However, the techniques are distinctly different because of the different processes they are based on (absorption for infrared and scattering for Raman) and the different intensity levels they handle. In Infrared spectroscopy, infrared energy covering a wide range of frequencies is directed onto the sample. Absorption occurs at certain resonant frequencies resulting in a series of vibrational peaks in the spectrum, which are used for the identification and quantification of the vibrational modes. In the Raman spectroscopy, on the other hand, a radiation of single frequency impinges on the sample and the scattered radiation, which is one vibrational unit of energy different from that of the incident beam, is detected. The study of the intensity distribution of inelastically scattered light provides valuable dynamical and structural information on the sample.

The FTIR spectroscopy is a very powerful tool to determine the bonding configurations as well as the hydrogen and oxygen contents, in hydrogenated amorphous, microcrystalline and nanocrystalline silicon based films. This technique is therefore extensively used in investigating the properties of these materials affected by hydrogen, oxygen and other impurities. Indeed, hydrogen plays an important role by passivating the dangling bonds in a-Si:H and its alloys as well as the grain boundaries in the micro/nano crystalline materials, thus improving their electrical and optical properties [40, 41]. Further, it is well-known that hydrogenated microcrystalline silicon (μc-Si:H) layers show a pronounced n-type behaviour [19, 42] due to the unwanted oxygen impurities. Since p-i-n solar cells require intrinsic μc-Si:H as absorber layers a reduction of the inherent oxygen impurities is necessary.

Raman spectroscopy, on the other hand, is sensitive to the structural changes and, in the case of Si based materials, gives information on the degree of disorder and provides a means for quantitative measurements of Si crystalline size and volume fraction useful for solar cell optimization.

In this chapter we will first treat briefly the background and the theory of FTIR and Raman spectroscopy, then we will describe their experimental apparatus. Furthermore, we will discuss the quantities and the properties obtained by means of these techniques taking a few examples from the literature concerning a-Si:H, hydrogenated amorphous silicon carbon alloys (a-$Si_{1-x}C_x$:H), micro/nano crystalline Si films and nanostructured materials composed of Si nanocrystals embedded in a-$Si_{1-x}C_x$:H matrices. Structural properties of micro crystalline and polycrystalline SiC as well as self-organized nanostructured films obtained by post thermal annealing of amorphous precursors were also dealt with.

2. FOURIER TRANSFORM INFRARED SPECTROSCOPY

In the conventional dispersive method, which is a standard technique for the visible light spectroscopy, a dispersive grating (prism) spectrometer is used as the wavelength selector and the wavelength (energy) of the incident radiation on the sample is varied over the desired range to obtain the spectrum. IR spectroscopy in earlier time was based on this conventional technique. However, because the power available for the infrared sources is low (particularly at longer wavelength useful to study impurities, lattice modes and free carriers) and the grating technique does not make the most effective use of the limited infrared power, the Fourier transform infrared spectroscopy has been developed. FTIR spectroscopy allows the simultaneous analysis of many frequency components in a single operation as well as the efficient use of the low power IR sources.

In Fourier transform infrared spectroscopy, the dispersive grating is replaced by the Michelson interferometer and the sample is exposed to a single pulse of radiation consisting of many frequencies to obtain the interferogram, *i.e.* the Fourier transform of the desired spectrum. The spectrum (intensity *versus* wavenumber) is constructed from the interferograms using extensive computer manipulation.

2.1. Background

Although the theory of Fourier transform, developed by J. B. Fourier in 1807, is at the heart of FTIR technique, the science and the technology of Fourier transform spectroscopy was initiated in 1880 with the invention of Michelson interferometer by Albert A Michelson. Michelson was also the first to demonstrate that the inverse Fourier transform of the interferogram coincides with the spectrum, but, even though he was well aware of the potential of the interferometer, he could not take advantage of his technique in the absence of computer and other associated algorithm [43, 44]. During the 1950s, Strong and his group [45] made a serious attempt to study the fundamental aspect of the technique and develop the applications of FTIR which generated interest in the interferometric spectroscopy.

Important developments were made possible by the work of Cooley and Tukey [46] in 1965 on the fast Fourier transform (FFT) algorithm, which allowed one to calculate easily the Fourier

transforms using electronic computers. Interestingly, by 1970 commercial Fourier transform spectro-meters were made available and were also widely accessible. There is a number of excellent books on FTIR spectroscopy. For an in-depth examination see the refs. [44, 47-50].

2.2. FTIR Spectroscopy Advantages

The distinctive advantages of FTIR spectroscopy over the conventional dispersive spectroscopy stem from higher signal-to-noise ratio as well as from the higher accuracy in the frequency measurement of the spectra. Further merit is the high stray light rejection efficiency, because the sample is placed between the interferometer and the detector. Multiplex or Fellgett advantage [51] and throughput or Jacquinot advantage [52] make possible the increased signal-to-noise ratio of the FTIR technique, while Connes advantage [53] offers improvement in frequency accuracy. In the following, we will describe them briefly.

2.2.1. Multiplex or Fellgett Advantage

Fellgett advantage states clearly that the signal-to-noise ratio of FTIR spectrometer is higher than that of a dispersive instrument for the same resolution and spectral range [51]. This is due to the different ways in which the various frequencies of radiation are handled. In Fourier spectroscopy many wavelengths are measured simultaneously while in a dispersive instrument a narrow band of frequencies is measured for unit time. This advantage emphasizes that Fourier spectroscopy takes less time than dispersive spectroscopy to measure the entire spectrum.

If a broad spectrum between wavenumber f_1 and f_2 is scanned in time T with a resolution of Δf, the number of spectral elements in the band, M, is given by:

$$M = \frac{f_2 - f_1}{\Delta f} \tag{1}$$

In the dispersive spectroscopy using grating (or prism), each small band Δf can be observed for a time (T/M), therefore, the signal in Δf is proportional to (T/M). The noise is proportional to $(T/M)^{1/2}$ because it is random and independent of signal level. Hence, signal-to-noise ratio for the dispersive spectroscopy $(S/N)_G$ should be:

$$\left(\frac{S}{N}\right)_G \propto \left(\frac{T}{M}\right)^{\frac{1}{2}} \tag{2}$$

In the Fourier spectroscopy, all the small bands of resolution Δf in the broad band $(f_2\text{-}f_1)$ are detected simultaneously. Therefore, the signal in Δf is proportional to T. The noise is proportional to $(T)^{1/2}$ for being random and independent of signal level. Therefore, the signal to noise ratio for the Fourier spectroscopy $(S/N)_F$ should be:

$$\left(\frac{S}{N}\right)_F \propto T^{\frac{1}{2}} \tag{3}$$

Assuming the proportionality constant to be the same, the following ratio can be obtained:

$$\left(\frac{S}{N}\right)_F : \left(\frac{S}{N}\right)_G = M^{\frac{1}{2}} \quad \textbf{(4)}$$

Because M is normally very large (typically around 10^4 or more), the $(S/N)_F$ is at least 10^2 times more than $(S/N)_G$. However, this improvement in $(S/N)_F$ is possible only if the noise of the spectrum is due to the detector noise which, in turn, is not proportional to the detector signal.

2.2.2. Jacquinot or Throughput Advantage

Jacquinot was the first to demonstrate [52] the increase in throughput of FTIR spectroscopy (Jacquinot advantage). This advantage essentially means that high resolution can be obtained in FTIR spectroscopy without using narrow slits, while in the dispersive spectroscopy there is always a trade-off between the resolution and the amount of light reaching the sample.

In the dispersive spectroscopy, the gratings (or prisms) allow the observation of the desired nearly monochromatic frequency domain and the spectra are recorded by scanning them at successive resolution intervals. Better resolution requires the presence of narrower entrance and exit slits which, in turn, decrease the energy entering the monochromators. Accordingly, only a small portion of the energy emitted by the source can be utilized by the detector, requiring the increase in the time of measurement thus decreasing the scanning rate. Clearly, the requirement for good resolution results in throwing away most of the valuable energy. In the Fourier transform spectroscopy, the wide circular apertures as well as the use of the collimator (to focalize the radiation) ensure that more energy reaches the sample and detector thus increasing the signal-to-noise ratio.

The throughput U is defined as the product of the cross-sectional area A and solid angle Ω of the beam at any focus of the optical beam. The product also determines the total radiant power accepted by the optical system for a source of given brightness. Therefore, it is essential to maximize the throughput and, accordingly, the energy reaching the detector, in order to maximize the signal-to-noise ratio [44].

In the Fourier transform spectroscopy, the resolving power of the Michelson interferometer R_F is given by [49]:

$$R_F = \frac{8F^2}{d^2} \quad \textbf{(5)}$$

where d is the diameter of the circular infrared source and F is the focal length of the collimating mirror. The solid angle subtended by the source at the collimating mirror, taking into account the eq. (5), results as:

$$\Omega_F = \frac{\pi d^2}{4F^2} = \frac{2\pi}{R_F} \quad \textbf{(6)}$$

Assuming the area of the collimating mirror to be A_F, the throughput of the Fourier transform spectroscopy U_F is given as:

$$U_F = A_F \Omega_F = \frac{2\pi A_F}{R_F} \quad \textbf{(7)}$$

In the dispersive (grating) spectroscopy, the area of the slit is essentially the effective area of the source. If A_G is the area of the grating, d is the dimension of the slit, F is the focal length of the collimating mirror and R_G is the resolving power of the grating, the energy throughput of the grating spectrometer U_G is given by [44]:

$$U_G = \frac{d A_G}{F R_G} \quad \textbf{(8)}$$

Assuming the resolving power, the area and the focal length of the collimating mirror to be the same for Fourier transform and dispersive spectrometer, the ratio of the throughputs of the Fourier transform and dispersive spectrometer is given by:

$$\frac{U_F}{U_G} = 2\pi\left(\frac{F}{d}\right) \quad \textbf{(9)}$$

For the good quality spectrometers (F/d) values are typically around 30, indicating that U_F is about 200 times more than U_G. Clearly, about 200 times more power can be put through the Fourier transform spectrometer as compared to the dispersive spectrometer. This throughput advantage is of considerable importance since IR sources are inherently weak.

2.2.3. Laser Reference or Connes Advantage

In the dispersive spectroscopy, the ability of the electro-mechanical mechanism to move the gratings and slits uniformly as well as the precise calibration with an external standard determine the accuracy and precision in the frequency measurements. In the FTIR spectrometer, the frequency is measured by direct comparison with a visible laser output (usually He-Ne laser), thus making redundant the calibration using an external standard. Furthermore, since the laser wavelength is known very accurately and is also very stable, the FTIR spectroscopy allows a considerable improvement in frequency accuracy as determined by Connes [53] for the first time (Connes advantage). This advantage offers the accurate alignment of the spectra thus facilitating measurements of difference spectra.

2.3. Theory

The cardinal principle of Fourier transform spectroscopy is the light wave interference. Although different FTIR apparatus use different interferometers such as Michelson, lamellar grating, and Fabry-Perot, Michelson interferometer is the most preferred one because of its easy construction and operation as well as high resolving power.

The schematic diagram of the Michelson interferometer is shown in Fig. (**1**). The radiation from the source reaches the beam splitter (BS). Part of the beam passes through the beam splitter and is reflected back from the fixed mirror while the part reflected from the BS is reflected back again from the moving mirror. The movement of mirror introduces path difference Δ between the two light beams. The beams recombine producing an intensity variation which depends on Δ, known as interferogram I(Δ) and is given by:

$$I(\Delta) = \int_{-\infty}^{\infty} S(f)\left[1+\cos\left(2\pi f\Delta\right)\right]df = \frac{1}{2}I(0) + \int_{-\infty}^{\infty} S(f)\cos(2\pi f\Delta)df \qquad \textbf{(10)}$$

where S(f) is the intensity spectrum of the source as a function of wavenumber and I(0) is the intensity at zero path difference.

Clearly, the interferogram is the Fourier transform of the spectrum emitted by the source. Accordingly, one can express S(f) as the inverse Fourier transform of the interferogram I(Δ) by calculating the integral for every wavenumber f:

$$S(f) = \int_{-\infty}^{\infty}\left[I(\Delta) - \frac{1}{2}I(0)\right]\cos(2\pi f\Delta)d\Delta \equiv F^{-1}(I(\Delta)) \qquad \textbf{(11)}$$

The equation (11) is of considerable importance since it enables the determination of the spectrum of the source for every wavenumber from the interferogram I(Δ). To measure the sample transmission, rather than the source spectrum, the sample is to be placed between BS and detector. The eq. (11) then yields the measure of $T_R(f)S(f)$ where $T_R(f)$ is the wavenumber dependent transmission coefficient. If $T_R(f)S(f)$ is measured when the sample is present and the source spectrum S(f) is measured when the sample is removed, the ratio of the two quantities gives $T_R(f)$.

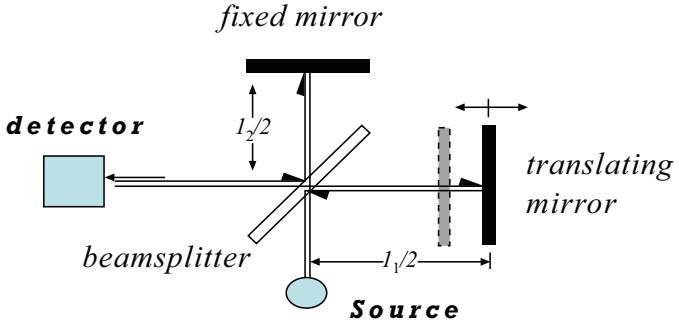


Figure 1: Schematic diagram of Michelson interferometer.

In order to compute the spectrum of the source from the interferogram, important mathematical procedures have to be used in FTIR spectroscopy. First, it is to be noted that the equations (10) and (11), which relate the source spectrum to the interferogram, have been derived on the assumption that the optical path difference between the two beams is known from-∞ to + ∞. On the other hand, the movable mirror of the interferometer has limited displacement from-L to +L which limits the acquired values of interferogram to the same interval. As a result, the interferogram has

not only the central peak with finite width but also negative side lobes. These lobes introduce artefacts causing distortions, making the calculated spectrum different from the actual one. In order to match the calculated and actual spectra, these negative side lobes have to be eliminated by means of a procedure called apodization (from Greek word "apodos" meaning "without feet"), which consists of multiplying the interferogram by suitable mathematical functions (apodization functions) prior to Fourier transformation. Codding and Horlick [54] may be referred for details on various apodization functions.

Secondly, an interferogram ideally should be symmetric about the point of zero path difference, while in reality the interferogram is never symmetric since all the frequency components of the wave do not reach their maxima at exactly the same time thus requiring a phase correction. By using a linear function that relates the phase shift with frequency, a correction for this asymmetry is obtained [54, 55]. Finally, when the spectrum of the source consists of various absorption lines close to each other, it is quite likely that they will overlap due to the instrumental enlargement caused by the finite optical path displacement. Therefore, it is necessary to determine the criterion which ensures that two adjacent spectral lines are resolved. Rayleigh criterion of resolution is also used for the interferograms. In FTIR spectroscopy the resolution is found to depend only on the maximum displacement of the movable mirror. Fourier self deconvolution is currently becoming popular as a method for band sharpening as well as a means for peak finding in systems of overlapping infrared bands whose widths are considerably larger than the instrumental resolution [56, 57].

2.4. Experimental Apparatus

The infrared radiation covers a wide range spanning from 10 to 5.5×10^4 cm^{-1} corresponding to far infrared (10-400 cm^{-1}), mid infrared (400-4400 cm^{-1}) and near infrared (4400-5.5×10^4 cm^{-1}) regions. The Fourier transform infrared spectroscopy apparatus essentially consists of interferometer (involving light sources, beam splitter, mirrors), detectors and a dedicated computer. The computer controls the optical components, collects and stores data, carries out mathematical operations (apodization, phase correction and Fourier self deconvolution) before computing the spectrum from the interferogram.

Fig. (**2**) displays the schematic diagram of commercial Fourier transform infrared set up using the Michelson spectrometer. The infrared source corresponding to the desired spectral range is selected and a mirror collimates the source radiation. The resulting parallel beam is sent to the beam splitter of the Michelson interferometer. The thickness and the coating of the beam splitter have to be proper and right in order to ensure that short wavelengths are not retarded or advanced with respect to the long wavelengths, avoiding the frequency-dependent delay in phase. The beam is divided by the beam splitter and one part of the beam goes to the fixed mirror while the other part to the moving mirror. A frictionless bearing with an electromagnetic drive is used to ensure smooth travel of the moving mirror. The returned beams from the mirrors recombine again at the beam splitter and pass through the sample and are focused onto the detector. The motion of the mirror introduces path difference between two interfering beams and the detected signal as a function of the optical path difference, *i.e.* the interferogram, is recorded. Each wavelength will produce its own characteristic intensity pattern of particular magnitude. Clearly, for a source of many frequencies, the interferogram will be the sum of variation of intensity of each wavelength pattern at the detector.

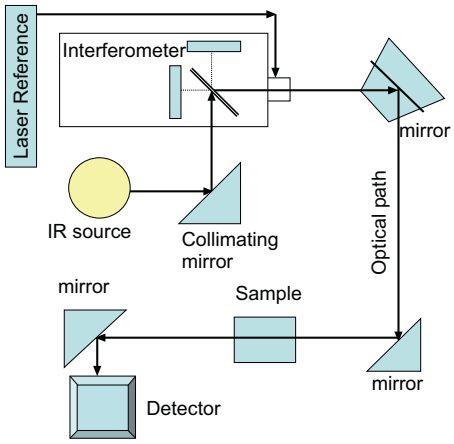


Figure 2: Schematic diagram of typical FTIR set up using the Michelson interferometer.

The sample is always put between the interferometer and the detector to have high stray light rejection since this arrangement allows the modulation of infrared light by the interferometer, while the emission from the sample would not be modulated and accordingly will not contribute to the spectrum. The position of the moving mirror and hence the path difference is measured by the He-Ne laser (reference laser in Fig. **2**). Because the wavelength of the laser is known very precisely the mirror position can be determined very accurately by counting the number of fringes in a highly defined laser pattern. The point of zero path length difference is obtained by using white light in place of He-Ne laser and finding the position of the highest amplitude intensity.

Since the IR radiation covers a wide range, different kinds of sources and beam splitters are used. Fast response time detectors (pyroelectric or semiconductors detectors) are necessary because of the fast movement of the mirror. The standard configuration corresponding to the mid infrared range (400-4400 cm^{-1}) uses globar source, a potassium bromide (KBr) beam splitter and a pyroelectric detector, comprising single crystal wafer of triglycerine sulphate (TGS). Germanium, mylar or quartz as beam splitters and mercury-cadmium-telluride (MCT) or indium antimonide (InSb) units operating at 77 K as semiconductor detectors are also used in the mid infrared region. In the near infrared region (4400 cm^{-1} to 5.5 $\times 10^4$ cm^{-1}), quartz halogen lamp source, calcium fluoride (CaF_2) or quartz beam splitters and cooled InSb or lead selenide (PbSe) detectors are employed while the far infrared (10 to 400 cm^{-1}) requires a mercury vapour arc lamp, mylar or metal mesh beam splitters and pyroelectric detectors.

2.5. IR Spectra

In the interaction of the IR radiation with matter some of the radiation is absorbed by the atoms of the sample and some is transmitted. The absorption peaks of the resulting spectrum correspond to the frequencies of vibrations between the bond of atoms forming the material. IR spectroscopy accordingly enables one to identify different atoms (qualitative analysis) and also to perform a quantitative analysis because the intensity of the peaks allows an evaluation of bond concentrations. The frequency of the fundamental modes depends on the masses of the oscillating atoms and the strength of the bond between the atoms.

The vibrational spectra of hydrogenated amorphous silicon and hydrogenated amorphous silicon carbon films with different carbon content x (x =[C]/([C]+[Si]) covering the mid infrared region (2.5-50 μm/400-4000 cm^{-1}) are shown in Fig. (**3**) as an example [58]. The spectrum of hydrogenated amorphous silicon film (x = 0) exhibits peaks near 2000 cm^{-1} and 640 cm^{-1} and feeble peaks near 800-900 cm^{-1} corresponding to Si-H stretching, Si-H rocking/wagging and SiH_2 bending modes respectively [59-61]. It is noteworthy that vibrational modes due to the a-Si structures, *i.e.* Si-Si bonding are absent for being IR inactive.

The spectra of hydrogenated amorphous silicon carbon films, in addition to the above said peaks, display others in the 2800-3000 cm^{-1}, near 1000 cm^{-1} and near 780 cm^{-1} regions, ascribed to C-H stretching, CH_n wagging and Si-C stretching modes, respectively [62-64]. In a-$Si_{1-x}C_x$:H spectra, the peak of Si-H stretching modes moves toward the higher wavenumber due to the presence of the carbon back bonded to Si-H bond [64].

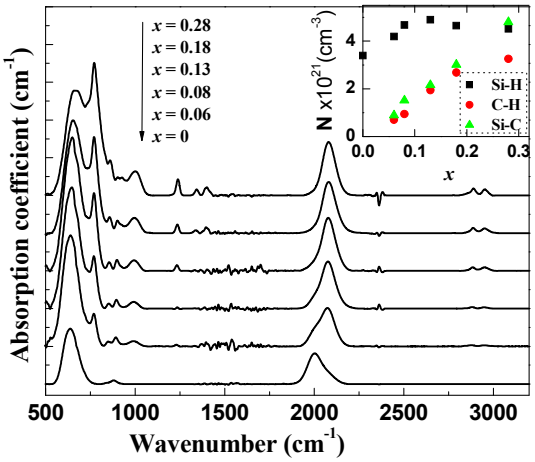


Figure 3: IR spectra of amorphous silicon and amorphous silicon carbon alloys with different carbon content x. In the inset the bond concentration N of Si-H, C-H, Si-C *vs.* x. (Reprinted with permission from Ambrosone *et al.* Ref [58], Copyright (2008), American Institute of Physics).

The IR spectra of hydrogenated microcrystalline silicon films exhibit similar modes to that of hydrogenated amorphous silicon. Interesting differences, observed in the Si-H stretching region, have been utilized to identify the device quality microcrystalline silicon films which will be discussed in the paragraph 4.

The FTIR spectroscopy is a powerful technique for the detection and for the quantitative evaluation of impurities. For example, the oxygen, if incorporated in amorphous or microcrystalline silicon and related alloys, can give rise to Si-O stretching mode in the 950-1200 cm^{-1} range and also can cause the shift of Si-H stretching mode to higher wavenumber.

The bond concentrations of Si-C, (N_{Si-C}), Si-H (N_{Si-H}), C-H (N_{C-H}), Si-O (N_{Si-O}) are given by:

$$N_{XY} = A_{XY} \cdot \int \frac{\alpha(f)}{f} df \quad \text{XY = Si-C, Si-H, C-H, Si-O} \tag{12}$$

where $\alpha(f)$ is the absorption coefficient. The integration is performed on the respective IR deconvoluted peaks after the subtraction of the baseline. In eq. (12) A_{XY} is the appropriate inverse cross-section which assumes the following values:

$$A_{Si-C} = 2.13 \times 10^{19} \text{ cm}^{-2} \text{ [63]}$$

$$A_{Si-H} = 1.4 \times 10^{20} \text{ cm}^{-2} \text{ [65]}$$

$$A_{C-H} = 1.35 \times 10^{21} \text{ cm}^{-2} \text{ [63]}$$

$$A_{Si-O} = 1.5 \times 10^{19} \text{ cm}^{-2} \text{ [63]}$$

The characteristics of the spectra such as the position, the full width at half maximum (FWHM), the intensity and the line shape of the peaks are related to the physical properties of the materials, as discussed in paragraph 4.

3. RAMAN SCATTERING

Raman scattering is the inelastic scattering of light by the matter. Since the energy of the incoming and scattered photons are different, the difference in energy must have to be provided or absorbed by the excitations of the material. The nature of these excitations can be vibrational (phonons), electronic, magnetic *etc.* and, accordingly, Raman scattering can yield structural and dynamical information on molecular levels. In the crystalline solids, the scattering by optical phonons is known as Raman scattering while the scattering by acoustic phonons is termed Brillouin scattering. The Raman scattering process involves a change in photon frequency. The scattered photons can lose energy by emitting a phonon (Stokes shift) or gain energy by absorbing a phonon (anti-Stokes shift) according to the energy and momentum conservation rules. It has been shown [66] that the conservation rules allow only the phonons with wave vector $q \approx 0$ (the phonons near the centre of the Brillouin zone) to be effective in one-phonon process resulting in the narrow peaks in the Raman spectrum of the crystalline materials. In the amorphous materials there is no well-defined crystal momentum. As a result of which the $q \approx 0$ selection rule does not exist. In principle, all vibrational states can take part in the scattering process and, therefore, the Raman spectrum is observed to have broad peaks.

The Raman scattering is always accompanied by the dominant elastic scattering of light (Rayleigh scattering). The Rayleigh scattering process tends to be very intense since most photons are scattered elastically, while in Raman scattering approximately one photon in 10^6-10^9 is scattered inelastically. Furthermore, Raman peak is not only very weak but also very near in energy to the exciting signal because the energy of the scattered photon differs by one vibrational unit from that of the incident photon. In consequence, the feeble Raman peak must be measured against the background of a very close and intense Rayleigh peak.

The technological advancement in the fabrication of lasers, multi-channel detection systems, Rayleigh filters and detectors have made the non-destructive Raman scattering an indispensable technique for material characterization. There are a number of excellent books on Raman spectroscopy [50, 67-75] to refer just a few. In this paragraph, we will discuss briefly about the history and theory of Raman scattering, which will be followed by the details of experimental techniques.

3.1. Background

The inelastic scattering of light postulated by A. Smekal in 1923 [76] was observed experimentally for the first time in 1928 by C.V. Raman [77, 78], who was awarded Noble prize in 1930. In the original experiment conducted in India by C.V. Raman, sun-light was focused onto purified liquid as well as onto dust-free vapour by a telescope and a second lens was placed near the sample to collect the scattered light. A system of optical filters was used to demonstrate the existence of the scattered light with different frequencies as compared with incident light which is the essence and characteristic of Raman effect. Because Raman scattering is inherently weak, the wide application of Raman spectroscopy had to wait until the development of lasers. The pulsed Ruby laser operating in near IR (694 nm) was used as the light source to obtain the first laser Raman measurements. Pulsed laser sources usually have significant pulse-to-pulse energy fluctuation which, in turn, results in low spectral signal-to-noise ratio implying the need for continuous wave (CW) lasers. Accordingly, the red 632.8 nm CW He-Ne laser was the first to be incorporated in the commercial Raman instruments and subsequently higher power lasers like CW Ar+ and Kr+ lasers have been employed [79, 80]. Many others, such as IR diode or diode pumped lasers [81], have been developed since then for the purpose.

3.2. Theory

In the Raman effect, the inelastic scattering of light manifests itself by a frequency shift from the incident light. The vibrations (or other excitations) modulate the polarizability tensor and cause the induced dipole moments to radiate at frequencies different from that of the electric field vector of the incident light wave.

The precise treatment of Raman scattering requires the quantum mechanical theory. However, a simple classical theory is adequate to understand the basic process. The frequency shifted Raman bands can be described as the side bands at the phonon frequency due to the non-linear interaction between the incident light and the lattice. In classical theory [73] this nonlinear interaction depends on the change in polarizability of the lattice. If u is the co-ordinate describing the phonon normal modes, the dependence of the dielectric function ε(ω) on u, where ω is the radiation frequency, can be expanded as Taylor series.

$$\varepsilon(\omega,u) = \varepsilon(\omega) + \left(\frac{d\varepsilon}{du}\right)u + \frac{1}{2}\left(\frac{d^2\varepsilon}{du^2}\right)u^2 + \ldots \qquad \textbf{(13)}$$

Since $\vec{P} = \varepsilon\vec{E}$, where $\vec{P}$ is the dipole moment induced by the electric field $\vec{E}$ of the incident light, this implies:

$$\vec{P} = \varepsilon(\omega)\vec{E} + \left(\frac{d\varepsilon}{du}\right)u\vec{E} + \frac{1}{2}\left(\frac{d^2\varepsilon}{du^2}\right)u^2\vec{E} + \ldots \quad \textbf{(14)}$$

Since $\vec{E} = \vec{E}_0 \cos\omega t$ and u = $u_0$cos ω_St, where ω_S is the phonon frequency, neglecting the higher order terms in (14) one obtains

$$\vec{P} = \varepsilon(\omega)\,\vec{E}_0 \cos\omega t + \left(\frac{d\varepsilon}{du}\right)u_0\,\vec{E}_0 \cos\omega t \cos\omega_S t$$

or

$$\vec{P} = \varepsilon(\omega)\vec{E}_0 \cos\omega t + \frac{1}{2}\left(\frac{d\varepsilon}{du}\right)u_0\vec{E}_0 \cos(\omega+\omega_S)t + \frac{1}{2}\left(\frac{d\varepsilon}{du}\right)u_0\vec{E}_0 \cos(\omega-\omega_S)t \quad \textbf{(15)}$$

Clearly, the first term of equation (15) describes Rayleigh scattering. The second and third terms represent the frequency-shifted inelastically scattered light, known as anti-Stokes and Stokes Raman scattering respectively.

A Hertzian dipole emits electromagnetic radiation whose intensity Y is proportional to the square of the absolute value of the second time derivative of the induced dipole moment.

$$Y \propto \left|\ddot{\vec{P}}\right|^2 \quad \textbf{(16)}$$

The intensity of the Stokes and anti-Stokes lines for the single phonon term in equation (14) and (15), as reported by Cardona [73], is:

$$Y \propto \omega^4 \left(\frac{d\varepsilon}{du}\right)^2 \left\langle u^2 \right\rangle \quad \textbf{(17)}$$

where the term in the angle bracket is the thermal average of the phonon displacement. The ω^4 dependence is the characteristic of the scattering process (for example, Rayleigh scattering). The square dependence of small polarization term (dε/du) demonstrates the low intensity of Raman scattering even for single phonon and the higher order terms of equation (14) are still weaker making Raman scattering inherently a weak process.

The intensity ratio of the anti-Stoke to Stokes line is given by the Boltzmann factor exp(-$\hbar\omega_S$/$k_B T_0$) where $\hbar$ is the Plank's constant divided by 2π, k_B is the Boltzmann constant and T_0 is the absolute temperature. Accordingly, the Stokes lines are stronger and generally dominate in the measurements. Further, for the crystalline material it must be emphasized that since the scattering process involves the interaction of electric field vector and the polarization vector, the direction of electric field relative to the crystal geometry defines the strength of the Raman signal and the Raman intensity is further proportional to the square of the Raman tensor as given by the equation

$$Y \propto \left|\hat{e}_i \cdot R \cdot \hat{e}_S\right|^2 \quad \textbf{(18)}$$

where $\hat{e}_i$ and $\hat{e}_S$ are unit vectors in the direction of the incident and scattered electric field respectively, while R is the Raman tensor which embraces the geometric information about the crystal. The above equation determines which phonon modes are allowed and forbidden for different orientations.

3.3. Experimental Apparatus and Techniques

The Raman scattering signal is inherently weak and very close to the intense Rayleigh signal (the relative intensity ratio is around 10^9 [79]) implying that a feeble Raman peak must be measured against an intense background. Accordingly, powerful laser as the exciting source is required, while the large disparity between the Rayleigh and Raman intensities makes the optical methods for Rayleigh rejection mandatory.

It is known [70, 82] that the fluorescence bands, which can be intrinsic or due to trace impurities, are excited by resonance with electronic states. These bands are broader and much stronger than the Raman peaks, which lead to significant reduction in the signal-to-noise ratio. Furthermore, the contribution of fluorescence to signal-to-noise degradation is maximum for the excitation wavelengths covering the range 300-600 nm. Clearly, a minimization of sample fluorescence is necessary.

High spectral signal-to-noise ratio is the most prominent requirement of Raman spectroscopy and it has been well established that Fourier transform technique can enhance the signal-to-noise ratio. All these considerations have to be taken into account in the design of the Raman spectroscopy apparatus.

At present, most laboratories of the world use either a dispersive or FT-Raman spectroscopy. The dispersive Raman spectroscopy apparatus uses a ultra-violet (UV) or visible laser for excitation, a dispersive spectrometer and detectors (photomultiplier tubes, PMT, or charged coupled device, CCD) and a single monochromator with Rayleigh rejection filter or double/triple monochromator (gratings) as the dispersive element. The FT Raman spectroscopy apparatus, on the other hand, employs a near IR laser for excitation, an interferometer as spectrometer and IR detectors such as CCD or photodiode.

A schematic setup for Raman spectroscopy using a single monochromator and filter for Rayleigh rejection is shown in Fig. (**4**). Raman scattering is excited either by Ar+ or Ti:Sapphire laser. The scattered light is collected through the notch filter for Rayleigh rejection and focused onto the monochromator which separates out the different energies of the Raman scattering and finally focused onto the CCD detector.

These Raman instruments are dominating the market because of their small size and efficiency. However, the filter based dispersive Raman systems have the disadvantage that the Raman signal, very close to the exciting laser line cannot be detected. Moreover, the change of laser wavelength is a costly affair because it requires also the change of filter of the corresponding wavelength.

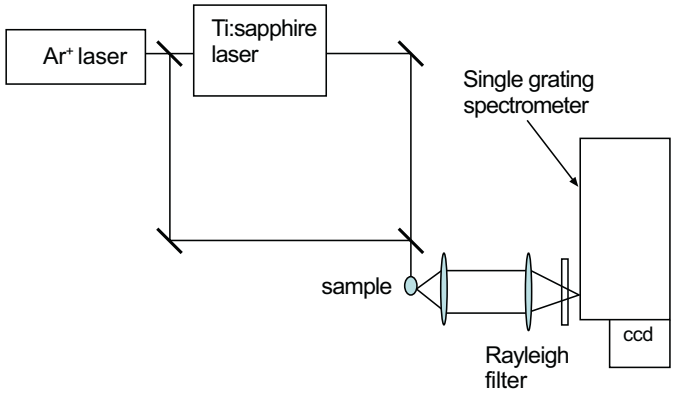


Figure 4: Schematic diagram of Raman spectroscopy apparatus using a single grating spectrometer and filter for Rayleigh rejection.

Instead of single monochromator with rejection filter, a double or triple monochromator can be used to discriminate the weak Raman signal from the strong Rayleigh light and reduce considerably the intensity of stray back ground light. A typical schematic diagram of dispersive Raman spectroscopy using double monochromator is shown in Fig. (**5**). The exciting laser light is focused on the sample and the scattered light is reflected by the mirror and collected by the lens for transmission to the double monochromator that essentially consists of two ganged gratings which turn together and sequentially select the desired Raman signal. Triple monochromators are used for still better performance. In spite of the limitations such as loss in light throughput and their relatively large size, the Raman spectroscopy utilizing double or triple monochromators is still used extensively for its high resolution and because it can operate on a wide range of wavelengths. This kind of spectroscopy is also the preferred choice if the change of exciting wavelength or the use of techniques such as resonance Raman scattering or flexible sampling are required during the measurements.

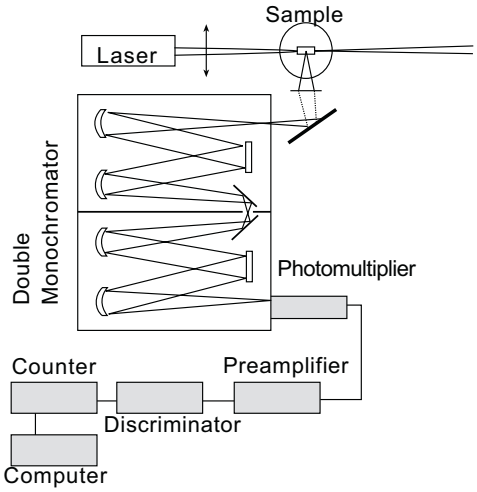


Figure 5: A typical schematic diagram of dispersive Raman spectroscopy apparatus using double monochromator.

The near infrared lasers as the exciting sources are used to avoid the fluorescence prevalent in the visible region. However, the smaller Raman cross-section in the near IR gives poorer performance requiring the FT-Raman instruments based on the interferometric method.

The schematic diagram of a FT Raman set up using the Nd:YAG (Neodymium:Yttrium Aluminium Garnet) laser as the exciting source is shown in Fig. (**6**). The scattered radiation is focused on the entrance part of the conventional FTIR spectrometer which essentially replaces the internal IR light source. FT-Raman spectroscopy not only offers multiplex and throughput advantages, resulting in significant increase in signal-to-noise ratio but also provides the higher wavelength accuracy of the interferometric method.

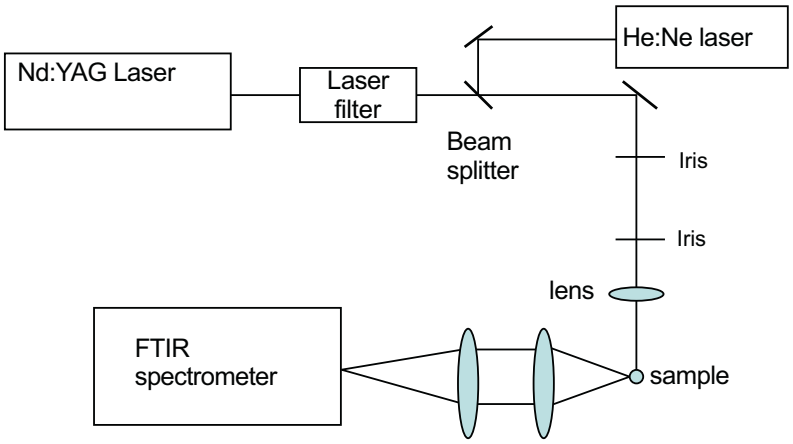


Figure 6: The schematic diagram of a FT Raman set up using the Nd:YAG laser.

3.3.1. Laser Sources

Being a high intensity and single frequency light source, laser is ideally suited as an excitation source for the Raman spectroscopy. However, incident laser power must be kept low so as to ensure that focused laser power density is below the value that causes thermal and/or photochemical degradation as well as nonlinear optical processes. In Raman spectroscopy the continuous wave lasers are used instead of the pulsed lasers because the latter have low signal-to-noise ratio and increased peak power, facilitating nonlinear processes and degradation of the samples. Furthermore, equation (17) reveals that intensity of Raman scattering depends on the fourth power of the frequency implying that lasers of higher frequencies, like UV and visible used as excitation sources, improve Raman sensitivity. UV lasers, accordingly, are the most preferred choice for Raman spectroscopy and have also higher signal-to-noise ratio because there is no or less fluorescence as compared with visible lasers. However, UV laser sources suffer from the following limitations [83]: they are more complex, quite expensive, have inherent problems with safety, require specialized optics and finally, the UV high power can lead to sample degradation.

The visible lasers as exciting sources for Raman spectroscopy are largely used because they provide reasonably high intensity of Raman peaks and require less expensive optical components. CW Ar^+ and Kr^+ lasers are the most popular in the visible region because of their reasonable power, flexibility and limited ability to excite resonance. Moreover, these lasers can be used to

pump dye lasers for obtaining tunable lasers, necessary for resonant Raman scattering experiments. The only limitation of visible lasers is the presence of fluorescence in the visible region, which reduces the signal-to-noise ratio.

The near infrared laser as exciting source is also used in spite of the reduction in the Raman scattering intensity, and hence in the sensitivity, due to the low frequency (see equation 17). In order to compensate for the loss in sensitivity, the Fourier transform technique is incorporated in Raman apparatus. The advantage of this source is that fluorescence is less likely.

In recent years, near IR diode lasers operating ~780 nm [81] as well as diode pumped YAG lasers operating ~1064 nm have become popular as the exciting source for the new generation of inexpensive, small commercial Raman spectrometers because of their low cost, small size, low power consumption and reliability.

3.3.2. Rayleigh Rejection Filters and Detectors

The most used Rayleigh rejection filters are holographic notch filters [84], crystalline colloidal array Bragg diffraction filters [85] and dielectric edge filters [86, 87]. These filters, particularly the notch filters, being small and efficient, have reduced the size of the Raman spectrometers and improved their efficiency.

The most widely used detectors are PMT or CCD. PMT are almost ideal detectors because of their broad spectral range. The cooled PMTs typically have higher sensitivity and linear dynamic range greater than 10^6. CCD detectors have the following characteristics: a high dynamic range (about 10^5), high quantum efficiency (about 90%), wide spectral range, low readout noise (2-5 e/pixel) and relatively small size.

The PMT detectors are indispensable for very high resolution Raman measurements because of their limit of a few micron much less than ≈25 μm limit associated with CCD detectors. However, multichannel CCD detectors [88] are far superior for relatively lower resolution studies (> 1 cm^{-1}) because of their multiplex advantage resulting in the improved spectral signal-to-noise ratio.

3.3.3. Raman Microprobe

Raman microprobe, which is essentially Raman spectroscopy with microscope, is becoming widespread for Raman characterization of the samples, because the use of high quality microscope in a 180° back scattering geometry eliminates the need to continuously adjust the laser and the sample and to focus the scattered light on the spectrometer.

The high numerical aperture of microscope objectives greatly increases the spatial resolution and the optical collection power of the Raman microprobe. In addition, the exciting visible light is coupled with the sample by means of a microscope whose objective lens focuses the laser beam to a small spot size (approximately 1 μm) of the sample and the scattered light is transmitted through the beam splitter to the double monochromator (see Fig. **7**). Surely, the use of visible laser and associated visible optics is an inherent advantage of Raman microprobe.

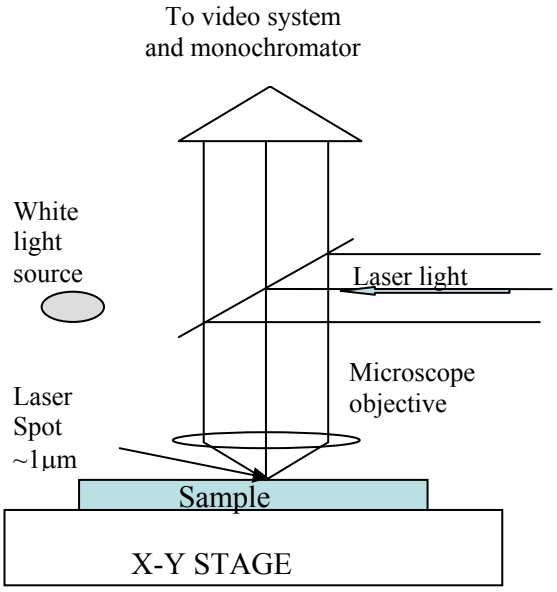


Figure 7: Schematic diagram of a Raman microprobe apparatus.

The Raman microprobe has made possible the study of extremely small samples by means of a video camera that allows one to obtain the real time image of the sample surface area as small as beam size. Finally, this technique can also discriminate the weak signal against fluorescence because an extremely small region of the sample is irradiated with high power laser.

3.4. Raman Spectra

Raman spectroscopy allows one to characterize layers as well as bulk materials because a wide range of penetration depth is possible by changing the wavelength (from UV to NIR) of laser exciting source. A depth profile of samples can also be obtained from different kinds of laser radiation. All the Raman spectra parameters such as peak position, intensity, line shape and line width are useful for characterization of the materials. The line widths increase when a material is damaged or disordered. The broadening arises from increased phonon damping due to the decrease in the life time of phonons or relaxation of momentum conservation in the Raman scattering process.

The typical Raman spectra of amorphous and nanocrystalline silicon films [89] in the range 100-600 cm^{-1} are shown as examples in Fig. **8(a)** and Fig. **8(b)** respectively. In the spectrum of a-Si:H film four peaks can be identified: the transverse acoustic (TA) located at ~150 cm^{-1}, the longitudinal acoustic (LA) located at ~310 cm^{-1}, the longitudinal optical (LO) located at ~380 cm^{-1} and the transverse optical (TO) located at ~475 cm^{-1}. In the spectra of the nano/micro crystalline silicon films two additional peaks at 520 and ~510 cm^{-1} are observed due to crystalline and crystallinelike (nanocrystals and/or grain boundary) phases.

The width of the TO peak is a good measure of the local order [64] and is well correlated with disorder related parameters (for example, the Urbach energy). Moreover, the TA mode provides a description of the medium-range order and the TA/TO intensity ratio depends on bond angle distribution [89].

The determination of the crystalline volume fraction and the size of the crystallites for microcrystalline and nanostructured silicon films is commonly obtained by the analysis of TO mode of the Raman spectra. The crystalline volume fraction I_c^{RS} of the films is determined using the empirical expression [90].

$$I_c^{RS} = (I_c + I_m)/(I_c + I_m + yI_a) \quad \textbf{(19)}$$

where I_c, I_m and I_a are the integrated intensity of peaks at ~520 cm^{-1}, at ~510 cm^{-1} and ~475 cm^{-1} corresponding to the crystalline, crystalline like and amorphous Si phase respectively. The y represents the Raman emission cross-section ratio which depends upon the size of crystallites and also on the excitation wavelength used for the Raman experiment. Usually, the value of y is chosen to be 1 [91].

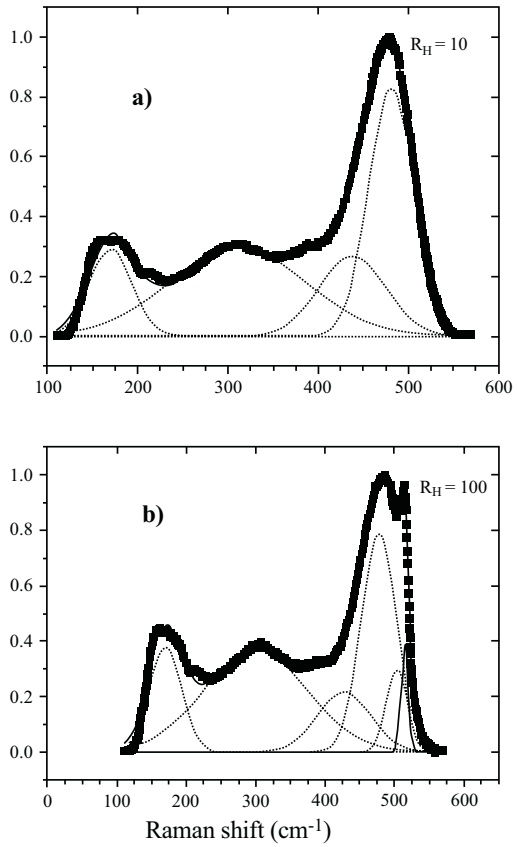


Figure 8: a) Raman spectra of amorphous and b) nanocrystalline silicon films. R_H is the hydrogen dilution $H_2/(H_2+SiH_4)$. (Reprinted with permission from Zhang S *et al.* [89]. Copyright (2006) Elsevier Science B.V.).

The size of the crystallites G is obtained from the empirical formula [92]:

$$G = 2\pi(B/\Delta\omega)^{1/2} \quad \textbf{(20)}$$

where B is a constant with the value of 2 cm^{-1} nm^2 and $\Delta\omega$ is the difference between the TO peak frequency of monocrystalline Si and TO peak frequency of Si crystallites.

4. APPLICATIONS

In this paragraph we will illustrate the applications of FTIR and Raman spectroscopy taking the examples concerning the microcrystalline and nanocrystalline silicon films used in solar cells as well as the nanostructured silicon carbon films that have emerged as the potential material for the new third generation solar cells [22-24]. However, the examples presented are not exhaustive but limited and fragmentary.

4.1. Applications of FTIR Spectroscopy

We will discuss the use of FTIR spectroscopy as applied to following topics:

- Detection of oxygen in microcrystalline silicon.
- Individuation of device grade microcrystalline silicon for solar cells.
- The study of phase transitions due to thermal annealing of a-$Si_{1-x}C_x$:H thin films and a-$Si_{1-x}C_x$/SiC multilayers.

4.1.1. Detection of Oxygen Impurities

The detection and quantification of oxygen is a major concern in the semiconductor industry. The unintentional oxygen incorporation during the growth leads to a pronounced n-type behaviour of the microcrystalline silicon layer in solar cells thus causing deterioration of their electrical properties. Torres *et al.* [93] have demonstrated that there is considerable increase in the spectral response of μc-Si:H solar cells with decreasing oxygen impurity, obtained by means of a feed gas purifier during the growth (see Fig. **9**).

Furthermore, amorphous and microcrystalline silicon as well as related alloy films can easily incorporate oxygen from the atmosphere with time or when subjected to annealing [63].

The incorporation of oxygen with time results in the formation of Si-O bonds. Indeed, the out-diffusion of the loosely bonded hydrogen present in low-density region causes dangling bonds which are satisfied by the oxygen from the atmosphere. In the case of thermal annealing at high temperature, more dangling bonds are formed because of the breaking of the bonds by thermal agitation, and their satisfaction with oxygen also results in increased number of Si-O bonds [63].

The oxygen incorporated in the films is easily detected by the presence of the relatively strong absorbing Si-O stretching mode in the 950-1200 cm^{-1} region. The bond density of Si-O mode is determined from the integrated area of the peak using the inverse cross section value of 1.5×10^{19}

cm^{-2} [63]. The incorporation of oxygen also results in the upshift of the Si-H stretching mode. Smets *et al.* [11] have reported that in μc-Si:H films oxidation of crystalline grain boundaries results in O_ySiH_x mode near 2250 cm^{-1}.

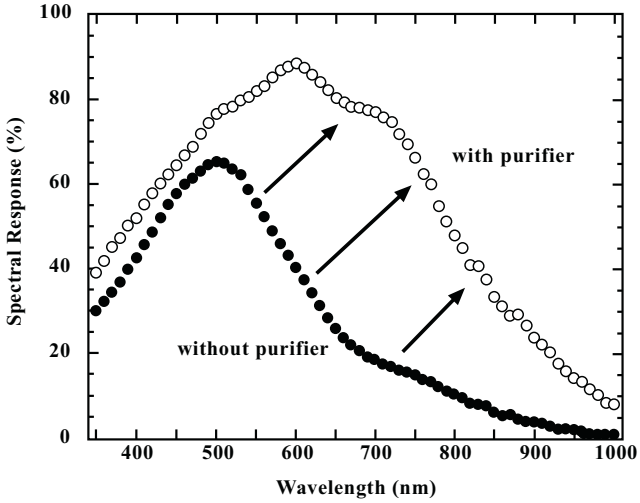


Figure 9: Comparison of the spectral response of two entirely μ*c*-Si:H solar cells. One produced with and one without a feed gas purifier. (Reprinted with permission from Torres *et al.* Ref [93]. Copyright (1996), American Institute of Physics).

4.1.2. Optimization of μc-Si:H Films for Solar Cells

Device quality a-Si:H films are optimized by the microstructure factor defined as $A_{2100}/(A_{2000}+A_{2100})$, where A_{2000} and A_{2100} are the area under the deconvoluted Si-H stretching peaks at 2000 and 2100 cm^{-1} respectively [94]. However, it is difficult to quantify the device grade microcrystalline silicon films using the microstructure factor because of the presence of the grain boundaries in these films. The only reliable way to quantify the "device grade" material involves the time-consuming process of the integration of every intrinsic film in a solar cell. Smet *et al.* [11, 95] have demonstrated that the properties of microcrystalline silicon bulk for solar cells can be optimized by monitoring the presence of crystalline grain boundaries, that can easily be detected *via* the crystalline surface hydrides contribution to narrow high stretching mode (SM) using FTIR spectroscopy. Therefore, this technique can be used as a simple, fast and reliable optimization tool for assessing the "device grade" microcrystalline silicon material for solar cells.

Fig. (**10**) displays the FTIR spectrum of undoped microcrystalline silicon film representing all the silicon hydride (Si-H) stretching modes, identified by Smet *et al.* [11, 95]. In the following we will summarize their results. The low stretching mode (LSM) covering the range 1980-2010 cm^{-1} and the high stretching mode (HSM) spanning the range 2070-2100 cm^{-1} have their origin from the a-Si:H tissue in the bulk [96]. However, for the μc-Si:H phase, the range of HSM is further extended due to the presence of two other additional modes located near 2120 and 2150 cm^{-1}. In the FTIR spectrum of the μc-Si:H, the presence of the crystalline surfaces (grain boundaries) in the bulk is revealed by the NHSMs at 2083, 2102 and 2137 cm^{-1} corresponding to mono, di and tri hydrides of crystalline grain boundaries [97]. In the region below LSM, three modes located near 1895,

1929 and 1950 cm^{-1} termed as extreme LSM (ELSM) are also present in the μc-Si:H. ELSMs are unique to μc-Si:H and have the maximum intensity only when NHSMs are absent.

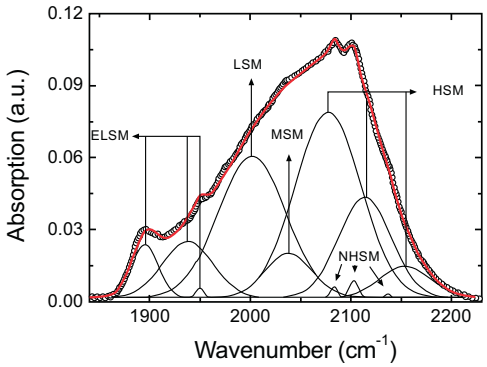


Figure 10: A close-up of the hydride stretching modes (open circles) in the IR spectrum of a μ*c*-Si:H film. This example of a spectrum shows all possible modes observed for the μ*c*-Si:H phase. The lines correspond to the total fit and the 11 Gaussian shaped stretching modes. (Reprinted with permission from Smets *et al.* Ref [11], Copyright (2008), American Institute of Physics).

The NHSMs are dominantly present in less dense μc-Si:H with a high crystallinity. Furthermore, these modes exhibit post-deposition oxidation when exposed to the ambient atmosphere reflected through the presence of Si-O-Si modes in the range 950-1200 cm^{-1} as well as the O_3-Si-H modes (near 2250 cm^{-1}), whose intensity increases while the intensity of NHSMs decreases with longer exposure to atmosphere as shown in Fig. **11(a-d)**. The presence of crystalline grain boundaries, reflected through NHSMs and the associated post-deposition oxidation, is a clear signature of inferior material quality and inferior efficiency of 4.5% of the fabricated solar cells.

The FTIR spectra of the intrinsic μc-Si:H film, shown in Fig. **11 (e)** and **(f)**, do not have NHSMs, while the ELSMs absorption is at its maximum and no post deposition oxidation is observed, reflecting device grade material. The p-i-n device, incorporating this material as intrinsic layer, reaches a conversion efficiency of 9.1 %.

4.1.3. Characterization of Phase-Transition

It has been demonstrated [36-39] that Si nanocrystals embedded in the SiC matrix can be formed by the high temperature post deposition thermal annealing of the single Si-rich a-$Si_{1-x}C_x$ precursor layer as well as a-$Si_{1-x}C_x$/SiC multilayers which are subsequently used for the fabrication of Si nanocrystals/c-Si heterojunction photovoltaic devices. It is needless to state that these devices are an important step towards the realization of "all Si" tandem solar cell based on Si nanocrystal materials [22, 23]. Clearly, an understanding of the structural changes brought about by thermal annealing of hydrogenated amorphous silicon carbon films has become necessary.

Basa *et al.* [63, 98] have demonstrated that the evolution of structural changes from amorphous to microcrystalline and to polycrystalline phase, for amorphous silicon carbon film thermal annealed from 250 to 1200 °C, has been concluded using only FTIR spectroscopy by analysing line shape along with the peak position and peak width (FWHM) of IR modes. Basa *et al.* [63, 98] have reported that the intensity of hydrogen related mode, Si-H rocking/wagging (r/w) at ≈630 cm^{-1},

decreases while the intensities of non-hydrogenated modes, Si-C stretching (s) and Si-O(s) at ≈780 and ≈1100 cm^{-1}, respectively, increase with the increase in the annealing temperature T_a (see Fig. **12**). The line shape of Si-C(s) as well as Si-O(s) are Gaussian up to 650 °C while for T_a in the range 800-1000 °C the line shape changes to Lorentzian. The sample annealed at 1200 °C exhibits only an asymmetric Si-C stretch peak without any Si-O stretch peak. The peak position and the FWHM as a function of T_a are shown in Fig. **13(a)** for Si-C(s) and in Fig. **13(b)** for Si-O(s).

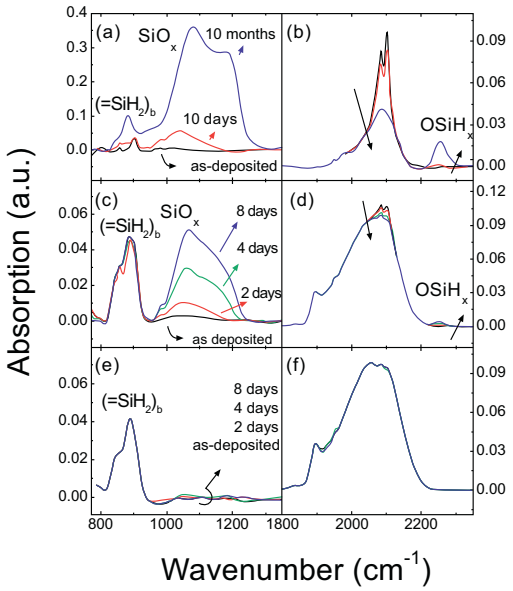


Figure 11: (a) and (b) depict the measured Si–O–Si SMs and the hydride SMs for porous highly crystalline μ*c*-Si:H as deposited, 10 days and 10 months after deposition. (c) and (d) depict the Si–O–Si modes and the hydride SMs for μ*c*-Si:H films, when integrated into a *p-i-n* device, resulting in a conversion efficiency of 4.5%. (e) and (f) depict the Si–O–Si modes and the hydride SMs for μc-Si:H films, when integrated into a *p-i-n* device, resulting in an conversion efficiency of 9.1%.(Reprinted with permission from Smets *et al.* Ref [11], Copyright (2008), American Institute of Physics).

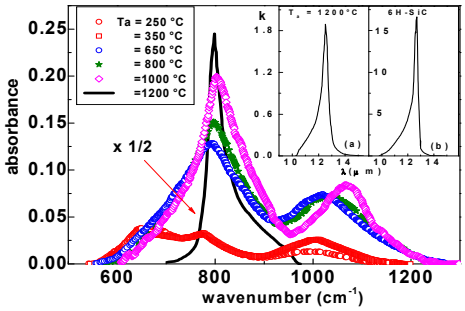


Figure 12: Absorbance of Si–C(s), Si–O(s) and Si–H(r, w) modes *vs.* wavenumber for a-$Si_{1-x}C_x$:H sample after thermal annealing at the indicated temperatures T_a. In the inset: (a) extinction coefficient k *vs.* wavelength λ of a-$Si_{1-x}C_x$:H film annealed at 1200 °C and (b) extinction coefficient k *vs.* wavelength λ of crystalline SiC. (Reproduced with permission from Basa *et al.* Ref [98]. Copyright (2009) Elsevier Science B.V.).

The interesting features associated with Si-C(s) and Si-O(s) modes are as under. The blue shifts of peak position of Si-C and Si-O stretch occur up to 1000 °C while above that temperature Si-O(s) bonds disappear and Si-C(s) mode shifts to a lower wavenumber. The peak widths (FWHM) of both Si-C (s) and Si-O(s) increase up to T_a = 650 °C then suddenly drop to lower value for T_a = 800 °C and keep decreasing with further increase in T_a. The normalized area under Si-C(s) increases in all T_a range indicating that the increase in annealing temperature favours the formation of additional Si-C bonds.

The Gaussian line shape indicates a Gaussian distribution of bond lengths and bond angles typical of the amorphous phase. The Lorentzian line shape, on the other hand, reflects smaller bond angle distortion and narrow bond angle distribution, indicating a more uniform and ordered environment which is characteristic of crystalline phase [63]. The change in the line shape of Si-C(s) and Si-O(s) modes from Gaussian to Lorentzian together with the decrease in the FWHM for T_a = 800 °C, demonstrates clearly the transition from the amorphous to microcrystalline phase. With increase in T_a from 800-1000 °C the peak shifts to higher wavenumber along with the decrease of FWHM because of the increase in the crystallinity degree [99]. The extinction coefficient k of the film annealed at 1200 °C, inset (a) of Fig. (**12**), being very close to k of the hexagonal polycrystalline SiC, inset (b) of Fig. (**12**), demonstrates the further transition from microcrystalline to poly crystalline phase [100] with increasing T_a.

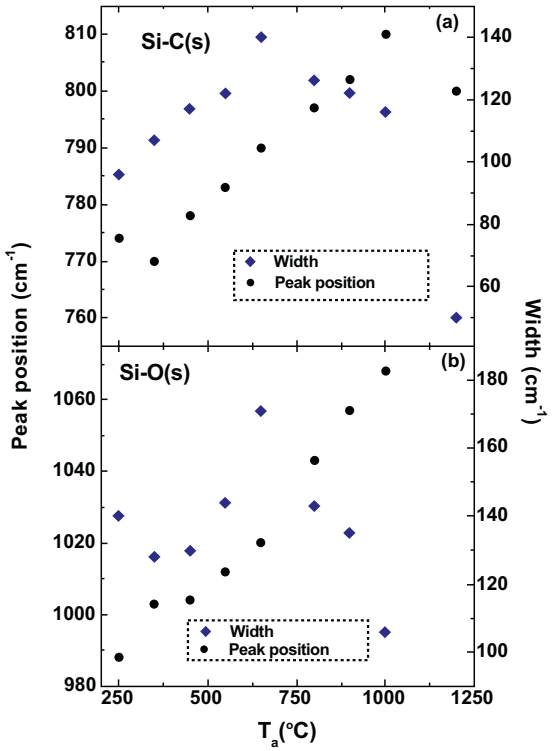


Figure 13: (a) Peak position and width of Si–C(s) *vs.* annealing temperature T_a and (b) peak position and width of Si–O(s) *vs.* annealing temperature T_a. (Reproduced with permission from Basa *et al.* Ref [98]. Copyright (2009) Elsevier Science B.V.).

The increase of Si-O bonds during the annealing from 250 to 1000 °C, as shown by the increased normalized area under Si-O(s) (see Fig. **12**), is due to the substitution of the effused hydrogen from the low-density regions of the film with the oxygen from atmosphere and the disappearance of Si-O bond at T_a = 1200 °C is attributed to the formation of Si-O (*via* the reaction Si + SiO_2 = 2SiO) which being volatile at 1200 °C leaves the film [101].

Recently, Song *et al.* [36-39], in order to obtain self-organized Si nanocrystals embedded in dielectric SiC matrix, have annealed at high temperature multilayers of Si-rich a-$Si_{1-x}C_x$ and near-stoichiometric a-SiC deposited by magnetron co-sputtering [36-37]. The FTIR spectra of these multilayers as a function of the annealing temperature T_a are displayed in Fig. (**14**) [39].

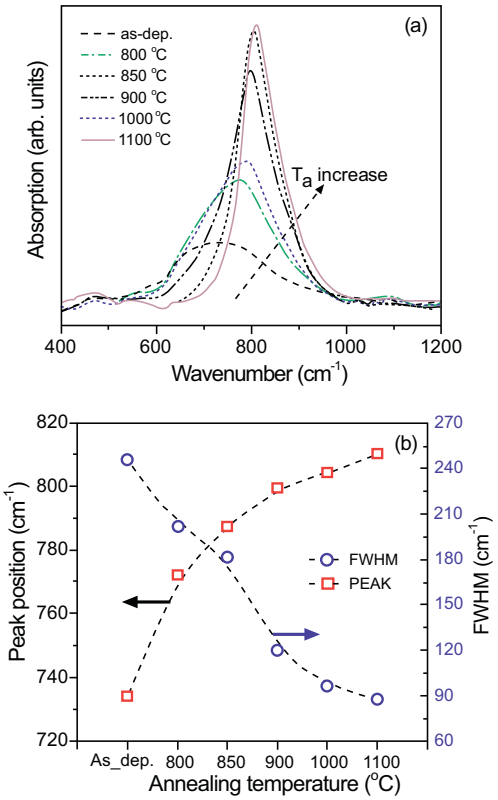


Figure 14: (a) FTIR absorption spectra obtained from $Si_{0.96}C_{0.04}$/SiC multilayer films with annealing temperature as a parameter; (b) The peak position and FWHM of the Si–C absorption peak *vs.* annealing temperature. The dashed lines are guides for the eye. (Reprinted with permission from Song *et al.* Ref [39], Copyright (2008), American Institute of Physics).

The evolution of the Si-C stretching peak with T_a reveals that: i) the absorption band becomes more pronounced and the peak position is shifted to a higher wavenumber, ii) the FWHM decreases, and iii) the lineshape changes from Gaussian distribution to a mixture of Gaussian and Lorentzian distribution, implying the formation of nanocrystallites. These results along with other measurements (XRD and Raman) have demonstrated the transition from amorphous to nanocrystalline phase.

Finally, the Si-C bond concentration increases, confirming that the thermal annealing leads to the formation of additional Si-C bonds. The line shape analysis of IR modes supported by other measurements have also demonstrated [31] a transition from micro crystalline to nanocrystalline phase. Thus, establishing that FTIR spectroscopy can be a effective probe similar to XRD and Raman to investigate phase transitions. However, it turns out to be ineffective when the crystallization is confined to the thin top layer, as is the case with the excimer laser annealed silicon based films [98].

4.2. Applications of Raman Spectroscopy

We will discuss the use of Raman spectroscopy as applied to the following topics:

- Optimization of J-V parameters of μc-Si solar cells and control of the structure depth profile by means of the crystalline volume fraction.
- Study of boron doping effect on crystallinity degree in microcrystalline $Si_{1-x}C_x$:H films.
- Investigation of the thermal annealing effect in a-$Si_{1-x}C_x$:H/SiC multilayers.
- Carbon alloying effect on crystallinity degree in nanostructured silicon carbon films.
- Role of substrate on the growth of the crystalline phase in nanostructured silicon carbon films.
- Study of medium range order (MRO) in nanocrystalline silicon films.

4.2.1. Crystalline Volume Fraction and μc-Si Solar Cell Performances

Crystallinity affects many parameters of Si thin films such as optical band gap, defect density, dark and photo conductivity [5-10, 102-104] as well as J-V parameters of solar cells such as efficiency η, fill factor FF, open circuit voltage V_{OC}, and short circuit current density J_{SC} [17-20, 91, 105].

Many authors [91, 105-107] have characterized the μc-Si solar cells by Raman scattering and related the crystalline volume fraction I_C^{RS} with the J-V parameters in order to optimize cell performances. In the following we report the data of Mai *et al.* [106, 107] concerning different μc-Si solar cells. Three different μc-Si solar cells series were prepared with plasma enhanced chemical vapour deposition (PECVD) i layers, hot wire (HW) CVD i layers and PECVD i layers with HWCVD p/i buffer layers on similar substrates with identical doped layers and similar total i layer thickness. Fig. **15** [106] shows the J-V parameters of μc-Si solar cells as a function of the i-layer crystalline volume fraction.

An efficiency of 8% is obtained at intermediate I_C^{RS} for solar cells of HWCVD and PECVD series, demonstrating that both deposition techniques are able to provide high quality materials. V_{OC} increases with decreasing i-layer crystallinity and the V_{OC} values of HWCVD series are about 20 mV greater than V_{OC} of PECVD series corresponding to I_C^{RS} in the range 10-60%. In particular,

the efficiency of the PECVD series reaches the maximum at 540 mV, in agreement with others [12, 108], while the HWCVD solar cells series have V_{OC} about 588 mV at maximum η. In the region 10-60% of I_c^{RS} the FF of the HWCVD series is also higher than those of the PECVD ones. Finally, the I_{SC} of both series are similar and decrease with decreasing crystallinity in the range 60-10% because with an increase in the amorphous phase the absorption coefficient of long wavelength light reaches low values.

4.2.2. Raman Scattering as a Probe of Structural Depth Profiles

The structural development of μc-Si:H solar cells was also investigated [107] by Raman scattering experiments with different excitation wavelengths (488 and 647 nm). The solar cells were prepared on texture-etched ZnO-coated glass substrates. μc-Si:H p and i layers were prepared in VHF-PECVD system while a-Si:H n layers were deposited in rf-PECVD. Different series were deposited by varying the discharge power and total flux in high pressure-high power (hphP) conditions. In order to obtain i-layers with different crystallinity for each series the silane concentration was varied. A series deposited in low power and low pressure conditions (lplP) was also presented for comparison.

Crystalline volume fractions I_c^{RS} obtained for different laser wavelength are compared in Fig. (**16**) [107] and it has been shown that the samples deposited at low pressure and low power have a very homogeneous structure along the growth direction while a structure composition difference between the top and bottom is present for cells deposited at high pressure and high power.

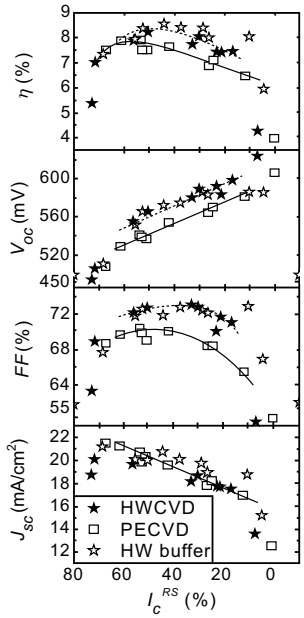


Figure 15: *J-V* characteristics, η, V_{OC}, FF, and J_{SC}, of μc-Si:H solar cells with *i* layers deposited by PECVD (open squares) or HWCVD (solid stars), plotted as a function of crystalline volume fraction I_C^{RS}. A 100 nm thick HW *p*/*i* buffer layer in PECVD solar cells (open stars) nearly eliminates the differences between the PECVD and HWCVD solar cells. Lines are guides for the eye. (Reprinted with permission from Mai *et al.* Ref [106], Copyright (2005), American Institute of Physics).

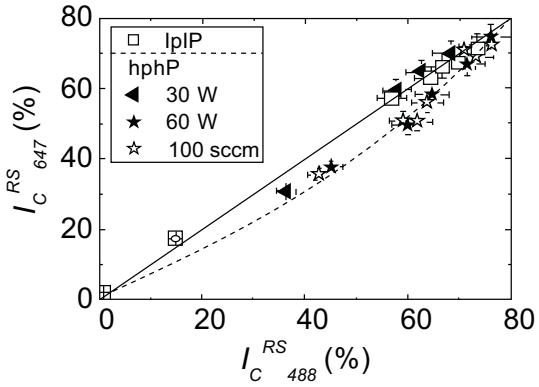


Figure 16: $I_C{}^{RS}{}_{647}$ of the lplP and hphP solar cells plotted as a function of $I_C{}^{RS}{}_{488}$. (Reprinted with permission from Mai *et al.* Ref [107], Copyright (2005), American Institute of Physics).

A better evaluation of the crystallinity at different stages of the i-layer growth is obtained by means of Raman measurements with 488 nm excitation carried out on craters with different depth, etched into solar cells by KOH. In Fig. (**17**), I_c^{RS} is plotted as a function of the crater depth where 0 and 1000 along the growth direction correspond to the position of n and p layers, respectively. Clearly, the lplP solar cells have no structure evolution, while the hphP cells have differences of up to 20% between the top and the bottom of the i-layer.

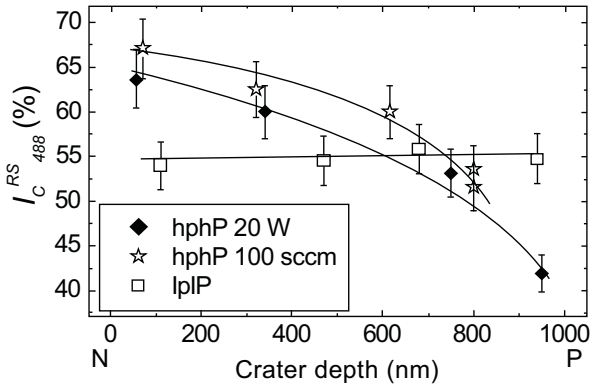


Figure 17: The $I_C{}^{RS}{}_{488}$ at different depths in the *i* layer show the structure development along the growth axis. Solar cells are optimum cells of three SC series deposited by lplP and hphP. For the 1 μm thick solar cells, crater depth of 0 and 1000 nm correspond to the *n* and *p* layers position, respectively. (Reprinted with permission from Mai *et al.* Ref [107], Copyright (2005), American Institute of Physics).

4.2.3. Crystallinity Evolution in p-Type Microcrystalline $Si_{1-x}C_x$:H Films

In order to understand the effect of boron doping on crystalline volume fraction the Raman spectroscopy was used by Miyajima *et al.* [109]. Fig. (**18**) [109] exhibits the Raman spectra of p-type microcrystalline $Si_{1-x}C_x$:H films prepared from silane and acetylene diluted in hydrogen with different doping ratio r = $B_2H_2/(SiH_4 + C_2H_2)$ using capacitively coupled PECVD system. The carbon content of the films is approximately 8 at%. It is reported that as doping ratio increases from 0 to 0.0714, the crystalline volume fraction decreases from 44.4% to 27.4%.

4.2.4. Crystallinity Evolution in Nanostructured Silicon Carbon Films

The nanostructured films composed of silicon nanocrystallites embedded in the amorphous silicon carbon matrix have generated considerable interest in recent years [30, 31, 35, 39, 110] as materials for new generation solar cells. Indeed, the relatively lower bandgap (~2.5 eV) of SiC matrix as compared to ~9 eV for SiO_2 and ~5.3 eV for Si_3N_4 is more favourable for the carrier transport.

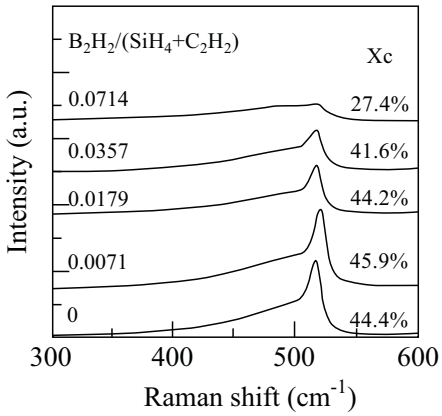


Figure 18: Raman spectra of p-type μc-$Si_{1-x}C_x$:H films deposited at different doping ratios. (Reproduced with permission from Miyajima *et al.* Ref. [109]). Copyright (2003) Elsevier Science B.V.).

In the following we will discuss the use of Raman spectroscopy to study the dependence of the crystalline degree of the nanostructured silicon carbon films on annealing temperature, carbon alloying and the kind of substrate.

In order to obtain self organized silicon nanocrystals embedded in dielectric SiC matrix, Song *et al.* [37-39] have performed the thermal annealing of multilayers of Si-rich a-$Si_{1-x}C_x$ and near stoichiometric SiC, deposited by magnetron co-sputtering. The Raman spectra of two multilayers $Si_{0.9}C_{0.1}$/SiC and $Si_{0.96}C_{0.04}$/SiC are displayed for different annealing temperatures T_a in Fig. **19(a)** and **19(b)** [39] respectively. The spectra of the two as deposited multilayers are very similar showing only an asymmetric bump centred at 470 cm^{-1}, due to TO mode of a-Si. After annealing at 800 °C the spectrum of $Si_{0.9}C_{0.1}$/SiC multilayer reveals the still amorphous structure while the spectrum of the $Si_{0.96}C_{0.04}$/SiC sample exhibits a small peak at 511 cm^{-1}, which can be attributed to Si nanocrystals. For $T_a \geq 900$ °C Si nanocrystals were formed in both samples as revealed by pronounced Raman peak at 511 cm^{-1}. In addition, a feeble band at 940 cm^{-1}, attributed mainly to SiC, is identified [111] implying the formation of SiC nanocrystals.

It is known that the increase in carbon content in silicon carbon hinders the formation of silicon crystallites [30, 112]. The evolution of crystallinity with carbon content in a-$Si_{1-x}C_x$:H can be monitored by Raman spectroscopy as reported by Cheng *et al.* [110]. Fig. **20(a)** displays the Raman spectra of Si nanocrystals embedded in an a-$Si_{1-x}C_x$:H matrix of different carbon content prepared by a low frequency (460 kHz), low pressure, thermally non equilibrium, high density inductively coupled plasma reactor using silane and methane without hydrogen dilution [110].

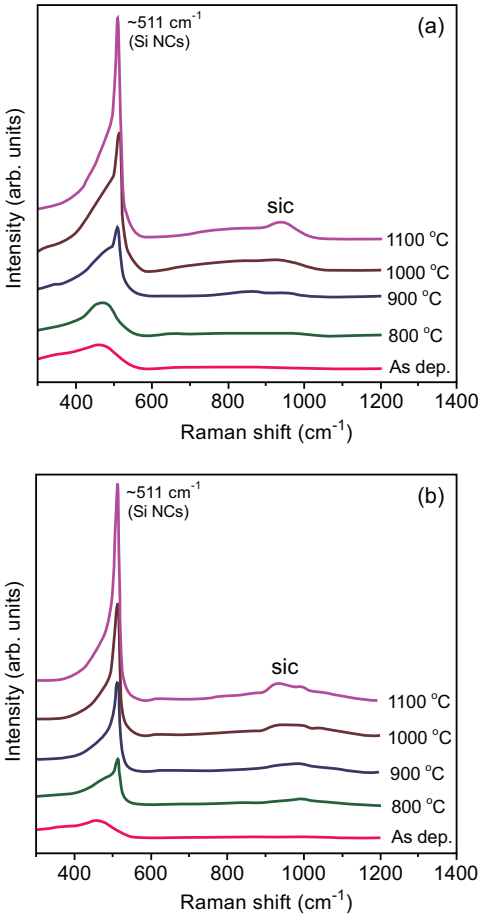


Figure 19: Raman spectra of (a) $Si_{0.9}C_{0.1}$/SiC and (b) $Si_{0.96}C_{0.04}$/SiC multilayer films with annealing temperature as a parameter. The films were deposited on quartz substrates. (Reprinted with permission from Song *et al.* Ref [39]. Copyright (2008), American Institute of Physics).

The Fig. **20(a)** reveals that only a broad peak near 480 cm^{-1} is present in the spectrum of sample with carbon content of 18.3 at%. When the carbon content decreases to 10.7 at% two peaks near 480 and 510 cm^{-1} appear in the spectrum. With further reduction of carbon content to 6.1at%, the crystalline silicon peak located near 515 cm^{-1} dominates the spectrum. Typical deconvolution of Raman spectrum using three Gaussian curves centred at ~480, ~510 and ~520 cm^{-1}, shown in Fig. **20(b)**, allows one to calculate the crystalline volume fraction using the formula (19). The crystalline volume fraction displayed as a function of carbon content in Fig. **20(c)** is found to decrease with increase in carbon content.

The undoped nanocrystalline silicon carbon films are potentially suitable as active layer for multijunction solar cells, UV photodetectors and LEDs. To fabricate these devices, the active layer is usually grown after the deposition of p-layer on transparent conductive oxide like tin oxide (SnO_2) substrate.

Accordingly, Coscia *et al.* [113] using Raman spectroscopy have compared the evolution of the growth of the silicon nanocrystals embedded in a-$Si_{1-x}C_x$:H matrix on p-layer/SnO_2 and Corning glass by varying rf power in PECVD system using silane and methane mixture highly diluted in hydrogen.

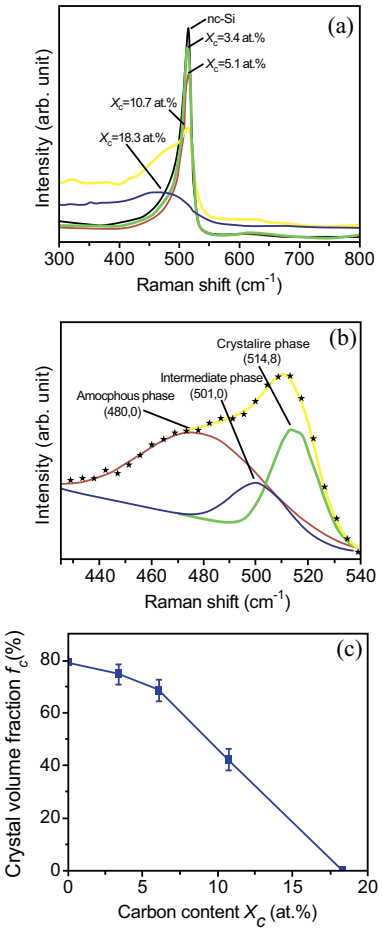


Figure 20: (a) Raman spectra of the samples with different carbon contents X_C (b) A typical deconvoluted Raman spectrum of the sample with the carbon content X_C = 10.7 at.%. (c) Variation of the crystalline volume fraction as a function of X_c. (Reproduced with permission from Cheng *et al.* Ref. [110]. Copyright (2010) Elsevier Science B.V.).

From the Raman spectra of Figs. (**21**) and (**22**) [113] it can be seen that the samples deposited on p-layer/tin oxide have a more pronounced crystalline phase even at higher rf power implying that this kind of substrate favours the nucleation process.

The Si crystallite size and crystalline volume fraction, determined as described in 3.4, are plotted as a function of rf power in Fig. (**23**) for the films deposited on both substrates. These quantities decrease with increase in rf power for the films deposited on both substrates and are observed to

be higher for the films deposited on p-layer/tin oxide. The decrease in crystalline fraction and Si crystallite size results because an increase in rf power leads to an increase in carbon content [114] which, in turn, hinders the formation of crystallites.

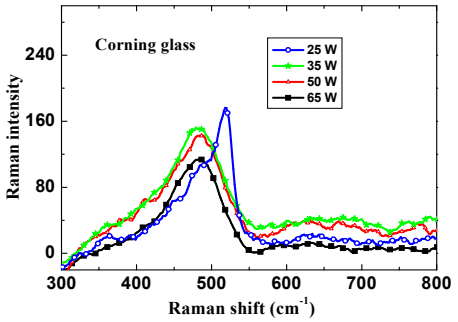


Figure 21: The Raman spectra of samples deposited on Corning glass at different rf powers. (After Coscia *et al.* Ref [113]. Copyright Wiley-VCH Verlag GmbH & Co. KGaA. Reproduced with permission).

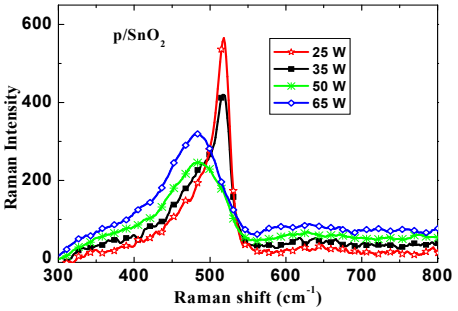


Figure 22: The Raman spectra of samples deposited on p/SnO_2 at different rf powers. (After Coscia *et al.* Ref [113]. Copyright Wiley-VCH Verlag GmbH & Co. KGaA. Reproduced with permission).

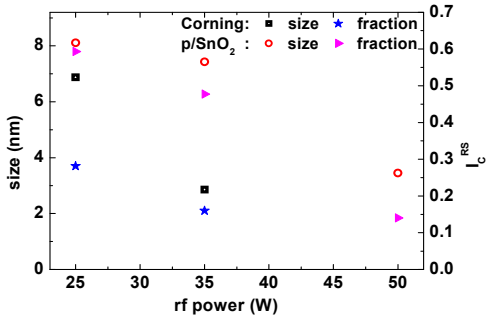


Figure 23: The Si crystallite size and crystalline volume fraction I_C^{RS} of samples deposited on Corning glass and p/SnO_2 *vs.* the rf powers. (After Coscia *et al.* Ref [113] Copyright Wiley-VCH Verlag GmbH & Co. KGaA. Reproduced with permission).

4.2.5. Raman Spectroscopy as a Probe of Medium Range Order in Nanocrystalline Silicon

It is well known that crystalline/microcrystalline materials are characterized by long range order (LRO) while the amorphous materials are identified by short range order (SRO). The medium range order, the next higher level of order with respect to SRO, is the characteristic of nanocrystalline materials. A signature of MRO has been reported by Williamson [115] using XRD analysis, by Voyles *et al.* [116] using the fluctuation electron microscopy and by Basa *et al.* [31] using FTIR and other measurements. On the other hand, Raman spectroscopy allows one to obtain information easily on MRO by evaluating the behaviour of TA and TO modes, centred at ~150 and ~475 cm^{-1}, respectively. With this objective Zhang *et al.* [89] have compared the Raman spectra, displayed in Figs. **8(a)** and **8(b)**, of amorphous and nanocrystalline silicon films deposited with the hydrogen dilution $R_H = H_2/(H_2+SiH_4)$ of 10 and 100 respectively, in PECVD system. From the observed decrease of the width of TA mode and TA/TO intensity ratio with increasing the hydrogen dilution, the authors have demonstrated the improvement of medium range order in nanocrystalline films.

ACKNOWLEDGEMENT

Declared none.

CONFLICT OF INTEREST

The author(s) confirm that this chapter content has no conflict of interest.

REFERENCES

[1] Carlson DE, Rajan K, Arya RR, Wiling F, Yang L. Advances in amorphous silicon photovoltaic technology. Journal of Materials Research 1998. 13: 2754-2762.

[2] Guha S, Yang J. Progress in amorphous and nanocrystalline silicon solar cells. J Non Cryst Solid 2006; 352: 1917-21.

[3] Shah A. Thin-film silicon solar cells. Lausanna: EPFL Press 2011.

[4] Schropp REI, Zeman M. Amorphous and microcrystalline silicon solar cells: modeling, materials, and device technology. Norwell, Ma: Kluwer Academic Publishers 1998.

[5] Staebler DL, Wronski CR. Reversible conductivity changes in discharge-produced amorphous Si. Appl Phys Lett 1977; 31: 292-294.

[6] Shah A, Meier J, Vallat-Sauvain E, *et al.* Material and solar cell research in micro-crystalline silicon. Solar Energy Mater & Solar Cells (2003); 78: 469-471.

[7] Ali AM. Optical properties of nano-crystalline silicon films deposited by plasma-enhanced chemical vapor deposition. Optical Materials 2007; 30: 238-243.

[8] Hazra S, Ray S. Nanocrystalline silicon as intrinsic layer in thin film solar cells. Solid State Commun 1999;109: 125-128.

[9] Meier J, Fluckiger R, Keppner H, Shah A. Complete microcrystalline p-i-n solar-cell-crystalline or amorphous cell behavior. Appl Phys Lett 1994; 65: 860.

[10] Sancho-Parramon J, Gracin D, Modreanu M, Gajovic A. Optical spectroscopy study of nc-Si-based p-i-n solar cells. Solar Energy Mater & Solar Cells 2009;93: 1768-1772.

[11] Smets AHM, Matsui T, Kondo M. High-rate deposition of microcrystalline silicon p-i-n solar cells in the high pressure depletion regime. J Appl Phys 2008; 104: 034508.

[12] Vetterl O, Finger F, Carius R, *et al.* Intrinsic microcrystalline silicon: A new material for photovoltaics. Solar Energy Mater & Solar Cells 2000; 62: 97-108.

[13] Shah A, Torres P, Tscharner R, *et al.* Photovoltaic technology: The case for thin-film solar cells. Science 1999; 285: 692-698.

[14] Cao XM, Stoke JA, Li J, *et al.* Fabrication and optimization of single junction nc-Si:H n-i-p solar cells using Si:H phase diagram concepts developed by real time spectroscopic ellipsometry. J Non Cryst Solids 2008; 354: 19-25.

[15] Pearce JM, Podraza N, Collins RW, *et al.* Optimization of open circuit voltage in amorphous silicon solar cells with mixed-phase (amorphous plus nanocrystalline) p-type contacts of low nanocrystalline content. J Appl Phys 2007; 101: 114301.

[16] Hamma S, Cabarrocas PRI. Low-temperature growth of thick intrinsic and ultrathin phosphorous or boron-doped microcrystalline silicon films: Optimum crystalline fractions for solar cell applications. Solar Energy Mater & Solar Cells 2001; 69: 217-239.

[17] Shah A, Meier J, Vallat-Sauvain E, *et al.* Microcrystalline silicon and 'micromorph' tandem solar cells. Thin Solid Films 2002; 403:179-187.

[18] Meier J, Dubail S, Cuperus J, *et al.*Recent progress in micromorph solar cells. J. Non-Cryst. Solid 1998; 227-230: 1250-1256.

[19] Meier J, Dubail S, Platz R *et al.* Towards high-efficiency thin-film silicon solar cells with the "micromorph" concept. Solar Energy Mater & Solar Cells 1997; 49:35-44.

[20] Keppner H, Meier J, Torres P, Shah A. Microcrystalline silicon and micromorph tandem solar cells. Appl Phys A 1999; 69: 169-177.

[21] Schropp REI, Li H, Franken RH *et al.* Nanostructured thin films for multiband-gap silicon triple junction solar cells. Thin Solid Films 2008; 516: 6818-6823.

[22] Green MA. Third generation photovoltaics, advanced solar energy conversion. Berlin: Springer 2003.

[23] Conibeer G. Third-generation photovoltaics. Materials Today 2007; 10: 42-50.

[24] Tsakalakos L. Nanostructures for photovoltaics. Mater Sci & Eng R 2008; 62: 175-189.

[25] Conibeer G, Green M, Corkish R, *et al.* Silicon nanostructures for third generation photovoltaic solar cells. Thin Solid Films 2006; 511: 654-662.

[26] Park NM, Choi CJ, Seong TY, Park SJ. Quantum confinement in amorphous silicon quantum dots embedded in silicon nitride. Phys Rev Lett 2001; 86: 1355-1357.

[27] Allan G, Delerue C, Lannoo M. Electronic structure of amorphous silicon nanoclusters Phys Rev Lett 1997; 78: 3161-3164.

[28] Liu XN, Wu XW, Bao XM, He Y. Photoluminescence from nanocrystallites embedded in hydrogenated amorphous-silicon films prepared by plasma-enhanced chemical-vapor-deposition. Appl. Phys. Lett. 1994; 64: 220-222.

[29] Ali AM. Origin of photoluminescence in nanocrystalline Si:H films. J. Lumin. 2007;126: 614-622.

[30] Coscia U, Ambrosone G, Basa DK. Room temperature visibile photolumine-scence of silicon nanocrystallites embedded in amorphous silicon carbide matrix. J. Appl. Phys.2008; 103: 063507.

[31] Basa DK, Ambrosone G, Coscia U. Microcrystalline to nanocrystalline silicon phase transition in hydrogenated silicon carbon alloy films. Nanotechnology 2008; 19: 415706.

[32] Pavesi L, Dal Negro L, Mazzoleni C, Franzo G, Priolo F. Optical gain in silicon nanocrystals. Nature 2000; 408: 440-444.

[33] Zacharias M, Heitmann J, Scholz R, Kahler U, Schmidt M, Blasing J, Size-controlled highly luminescent silicon nano-crystals: a SiO/SiO_2 superlattice approach. Appl Phys Lett 2002; 80: 661-663.

[34] Torrison L, Tolle J, Smith DJ *et al.* Morphological and optical properties of Si nanostructures imbedded in SiO_2 and Si_3N_4 films grown by single source chemical vapor deposition. J Appl Phys 2002; 92: 7475-7480.

[35] Chang G, Ma F, Ma D, Xu K. Multi-band silicon quantum dots embedded in a amorphous matrix of silicon carbide. Nanotchnology 2010; 21: 455605.

[36] Song D, Cho EC, Cho YH, *et al.* Evolution of Si (and SiC) nanocrystal precipitation in SiC matrix. Thin Solid Films 2008; 516: 3824-3830.

[37] Song D, Cho EC, Conibeer G, *et al.* Fabrication and characterization of Si nanocrystals in SiC matrix produced by magnetron co-sputtering. J. Vac. Sci. Technol. B 2007; 25: 1327-1335.

[38] Song D, Cho EC, Conibeer G, Flynn C, Huang Y, Green MA. Structural, electrical and photovoltaic characterization of Si nanocrystals embedded in SiC matrix and Si nanocrystals/c-Si heterojunction devices. Solar Energy Mater& Solar Cells 2008;92: 474-481.

[39] Song D, Cho EC, Conibeer G, Huang Y, Flynn C, Green MA. Structural characterization of annealed $Si_{1-x}C_x$/SiC multilayers targeting formation of Si nanocrystals in a SiC matrix. J Appl Phys 2008; 103: 083544.

[40] Madan A, Le Comber PG, Spear WE. Investigation of the density of localized states in a-Si using the field effect technique. J Non Cryst Solid 1976; 20: 239-257.

[41] Freeman EC, Paul W. Optical constants of rf sputtered hydrogenated amorphous Si. Phys Rev B 1979; 20: 716–728.

[42] Veprek S, Iqbal Z, Kuhne RO, Capezzuto P, Sarott FA, Gimzewski JK. Properties of microcrystalline silicon. IV. Electrical conductivity, electron spin reso-nance and the effect of gas adsorption. J. Phys c, Solid State Physics, 1983; 16: 6241-6262.

[43] Grasselli J. On the Relative Motion of the Earth and the Luminiferous Ether. Appl. Spectrosc. 1987; 41: 933-935.

[44] Bell RJ. Introduction to Fourier Transform Spectroscopy. New York: Academic Press 1972.

[45] Strong J. Interferometry for the Far Infrared. J. Opt. Soc. Am. 1957; 47: 354-357.

[46] Cooley JW, Tukey JW. An algorithm for the machine calculation of complex Fourier series. Math Comput 1965; 19: 297-301.

[47] Tolstoy P, Chernyshova IV, Skryshevsky VA. Handbook of Infrared Spectroscopy of Ultrathin Films. Hoboken, New Jersey: Wiley Interscience 2003.

[48] Griffiths PR, de Haseth JA. Fourier Transform Infrared Spectroscopy. New York: John Wiley and Sons 1986.

[49] Jaggi N, Vij DR. In: Vij DR, Ed. Hand Book of Solid State Spectroscopy. New York: Springer 2006; pp 411-450.

[50] Perkowitz S. Optical Characterization of Semiconductors: Infrared, Raman and Photolumi-nescence. London, San Diego, New York: Academic Press 1993.

[51] Fellgett PI. Les principes généraux des méthodes nouvelles en spectroscopie inter-férentielle-A propos de la théorie du spectromètre interférentiel multiplex. J. Phys. Radium 1958; 19: 187-191.

[52] Jacquinot P. Characteristics common to the new methods of inteferometric spectroscopy; the factor of merit. J Phys Radium 1958; 19: 223-229.

[53] Connes J, Connes P. Near-Infrared Planetary Spectra by Fourier Spectroscopy. I. Instruments and Results, J. Opt. Soc. Am 1966;56: 896-910.

[54] Codding EG, Horlick G. Apodization and Phase Information in Fourier Transform Spectroscopy. Appl Spectrosc 1973; 27: 85-92.

[55] Green DW, Reddy GT. In: Ferraro JR, Baaile LJ Ed. Fourier Transform Infrared Spectroscopy Applications to Chemical Systems. NewYork: Academic Press 1978; pp 18-38.

[56] Kauppinen JK, Moffatt DJ, Mantsch HH, Cameron DG. Fourier Self-Deconvolution: A Method for Resolving Intrinsically Overlapped Bands. Appl Spectrosc 1981; 35: 271-276.

[57] Ramhelow K, Hubner W. Fourier Self-Deconvolution: Parameter Determination and Analytical Band Shapes. Appl Spectrosc 1996; 50: 795-804.

[58] Ambrosone G, Basa DK, Coscia U, Fathallah M. Study on the microstructural and overall disorder in hydrogenated amorphous silicon carbon films. J Appl Phys 2008; 104: 123520/1-4.

[59] Zanzuchi PJ. In: Pankove JJ Ed. Semiconductors and Semimetals vol 21, Orlando: Academic Press 1984; pp 113-140.

[60] Cardona M. Vibrational-spectra of hydrogen in silicon and germanium. Phys Status Solidi B 1983; 118; 463-481.

[61] Lucovsky G, Nemanich RJ, Knights JC. Structural interpretation of the vibrational spectra of *a*-Si: H alloys. Phys Rev B 1979; 19: 2064-2073.

[62] Wieder H, Cardona M, Guarnieri CR. Vibrational-spectrum of hydrogenated amorphous Si-C films. Phys Status Solidi B 1979; 92: 99-113.
[63] Basa DK, Smith FW. Annealing and crystallization processes in a hydrogenated amorphous Si-C alloy film. Thin Solid Films 1990; 192: 121-133.
[64] Bullot J, Schmidt MP. Physics of amorphous-silicon carbon alloys. Phys Status Solidi B 1987;143: 345-418.
[65] Langford AA, Fleet ML, Nelson BP, Landford WA, Maley N. Infrared-absorption strength and hydrogen content of hydrogenated amorphous-silicon. Phys Rev B 1992; 45: 13367-13377.
[66] Lannin JS. In: Pankove JJ, Ed. Semiconductors and semimetals vol 21, Orlando: Academic Press 1984; pp 159-195.
[67] McCreery RL. Raman Spectroscopy For Chemical Analysis. NewYork, Wiley 2000.
[68] Weber WH, Merlin R, Eds. Raman Scattering in Material Science. New York: Springer 2000.
[69] Lewis IR, Edwards HGM, Eds. HandBook of Raman Spectroscopy. NewYork: Dekker 2001.
[70] Chase DB, Rabolt JF, Eds. Fourier Transform Raman Spectroscopy. San Diego: Academic Press 1994.
[71] Smith E, Dent G. Modern Raman Spectroscopy A Practical Approach. Chichester, UK: Wiley 2005.
[72] Hayes W, Loudon R. Scattering of Light by crystals. New York: John Wiley & Sons 1978.
[73] Cardona M. In: Cardona M, Ed. Light Scattering in Solids I: Topics in Applied Physics vol 8. Berlin: Springer-Verlag 1975; pp. 1-20.
[74] Cardona M, Guntherodt G. Light Scattering in Solids II, Basic Concepts and Instrumentation: Topics in Applied Physics vol 50. Berlin: Springer-Verlag 1982.
[75] Cardona M, Guntherodt G. Light Scattering in Solids V, Superlattices and Other Microstructures: Topics in Applied Physics vol 66. Berlin: Springer-Verlag 1989.
[76] Smekal A. Zur Quantentheorie der Dispersion. Naturwissenschaften 1923; 43: 873-875.
[77] Raman CV. A new radiation. Indian J. Phys 1928; 2: 387.
[78] Raman CV, Krishnan KS. A new type of secondary radiation. Nature 1928; 121: 501-502.
[79] Long DA. Raman Spectroscopy. New York: McGraw-Hill 1977.
[80] Strommen DP, Nakamoto K. Laboratory Raman Spectroscopy. NewYork: Wiley 1984.
[81] Cooney TF, Skinner HT, Angel SM. Evaluation of external-cavity diode lasers for Raman spectroscopy. Appl Spectrosc 1995; 49: 1846-1851.
[82] Asher SA, Johnson CR. Raman-spectroscopy of a coal liquid shows that fluorescence interference is minimized with ultraviolet excitation. Science 1984; 225: 311.
[83] Asher SA, Munro CH, Chi ZH. UV lasers revolutionize Raman spectroscopy. Laser Focus World 1997; 33:99-109.
[84] Schoen CL, Sharma SK, Helsley CE, Owen Hl. Performance of a holographic supernotch filter. Appl Spectrosc 1993; 47: 305-308.
[85] Flaugh PL, O'Donnell SE, Asher SA. Development of a New Optical Wavelength Rejection Filter: Demonstration of Its Utility in Raman Spectroscopy. Appl Spectrosc 1984; 38: 847-850.
[86] Futamata M. Dielectric filter for highly sensitive Raman spectroscopy. Appl Spectrosc 1996; 50: 199-204.
[87] Munro CH, Pajcini V, Asher SA. Dielectric Stack Filters for *Ex Situ* and *In Situ* UV Optical-Fiber Probe Raman Spectroscopic Measurements Appl Spectrosc 1997; 51: 1722-1728.
[88] Lyon LA, Keating CD, Fox AP *et al.* Raman Spectroscopy. Anal Chem 1998;70: 341R-361R.
[89] Zhang S, Liao X, Raniero L, *et al.* Silicon thin films prepared in the transition region and their use in solar cells. Solar Energy Mater & Solar Cells 2006; 90: 3001-3008.
[90] Kaneko T, Wakagi M, Onisawa K, Minemura T. Change in crystalline morphologies of polycrystalline silicon films prepared by radiofrequency plasma-enhanced chemical-vapor-deposition using SiF_4+H_2 gas-mixture at 350-delta-c. Appl Phys Lett 1994; 64: 1865-1867.
[91] Droz C, Vallat-Sauvain E, Bailat J, Feitknecht L, Meier J, Shah A. Relationship between Raman crystallinity and open-circuit voltage in microcrystalline silicon solar cells. Solar Energy Materials & Solar Cells 2004; 81:61-71.

[92] He Y, Yin C, Cheng G, Wang L, Liu X, Hu GY. The structure and properties of nanosize crystalline silicon films. J Appl Phys 1994; 75: 797-803.

[93] Torres P, Meier J, Fluckiger R, *et al.* Device grade microcrystalline silicon owing to reduced oxygen contamination. Appl Phys Lett 1996; 69: 1373-1375.

[94] Mahan AH, Menna P, Tsu R. Influence of microstructure on the Urbach edge of amorphous SiC-H and amorphous SiGe-H alloys. App Phys Lett 1987; 51: 1167-1169.

[95] Smets AHM, Matsui T, Kondo M. Infrared analysis of the bulk silicon-hydrogen bonds as an optimization tool for high-rate deposition of microcrystalline silicon solar cells. Appl Phys Lett 2008; 92: 033506.

[96] Smets AHM, Kessels WMM, van de Sanden MCM. Vacancies and voids in hydrogenated amorphous silicon. Appl Phys Lett 2003; 82: 1547-1549.

[97] Burrows VA, Chabal YJ, Higashi GS, Raghavachari K, Christman SB. Infrared spectroscopy of Si(111) surfaces after HF treatment: Hydrogen termination and surface morphology. Appl Phys Lett 1998; 53: 998-1000.

[98] Basa DK, Ambrosone G, Coscia U, Setaro A. Crystallization of hydrogenated amorphous silicon carbon films with laser and thermal annealing. Appl Surf Sci 2009; 255: 5528-5531.

[99] Kerdiles S, Berthelot A, Gourbilleau F, Rizk R. Low temperature deposition of nanocrystalline silicon carbide thin films. Appl Phys Lett 2000; 76: 2373-2375.

[100] Spitzer WG, Kleinman D,Walsh D. Infrared Properties of Hexagonal Silicon Carbide. Phys Rev 1959; 113: 127-132.

[101] Smith FW, Ghidini G. Reaction of Oxygen with Si(111) and (100): Critical Conditions for the Growth of SiO_2. J. Electrochem Soc 1982;129: 1300-1306.

[102] Houben L, Luysberg M, Hapke P, Carius R, Finger F, Wagner H. Structural properties of microcrystalline silicon in the transition from highly crystalline to amorphous growth. Philos Mag B 1998; 77: 1447-1460.

[103] Mishima Y, Miyazaki S, Hirose M, Osaka Y. Characterization of plasma-deposited microcrystalline silicon. Philos Mag B 1982; 46: 1-12.

[104] Alpuim P, Chu V, Conde JP. Amorphous and microcrystalline silicon films grown at low temperatures by radio-frequency and hot-wire chemical vapor deposition. J Appl Phys 1999, 86: 3812-3821.

[105] Nath M, Cabarrocas PRI, Johnson EV, Abramov A, Chatterjee P. The open-circuit voltage in microcrystalline silicon solar cells of different degrees of crystallinity. Thin Solid Films 2008; 516: 6974-6978.

[106] Mai Y, Klein S, Carius R, Stiebig H, Geng X, Finger F. Open circuit voltage improvement of high-deposition-rate micro-crystalline silicon solar cells by hot wire interface layers. Appl Phys Lett 2005; 87: 073503.

[107] Mai Y, Klein S, Carius R, *et al.* Microcrystalline silicon solar cells deposited at high rates. J Appl Phys 2005; 97: 114913.

[108] Klein S, Finger F, Carius R, Stutzmann M. Deposition of microcrystalline silicon prepared by hot-wire chemical-vapor deposition: The influence of the deposition parameters on the material properties and solar cell performance. J Appl Phys 2005; 98: 024905.

[109] Miyajima S, Yamada A, Konagai M. Highly conductive microcrystalline silicon carbide films deposited by the hot wire cell method and its application to amorphous silicon solar cells. Thin Solid Films 2003; 430: 274-277.

[110] Cheng Q, Xu S, Ostrikov KK. Single-step, rapid low-temperature synthesis of Si quantum dots embedded in an amorphous SiC matrix in high-density reactive plasmas. Acta Materialia 2010; 58: 560-569.

[111] Lattemann M, Nold E, Ulrich S, Leiste H, Holleck H. Investigation and characterisation of silicon nitride and silicon carbide thin films. Surface & Coatings Technology 2003; 174: 365-369.

[112] Goldstein B, Dickson CR, Fauchet PM. Properties of p+ microcrystalline films of SiC-H deposited by conventional rf-glow discharge. Appl Phys Lett 1988; 53: 2672-2674.

[113] Coscia U, Ambrosone G, Basa DK, *et al.* Characterizations of nanostructured silicon-carbon films deposited on p-layer by PECVD. Phys. Status Solidi (c) 2010;7: 766-769**.**

[114] Coscia U, Ambrosone G, Lettieri S, *et al.* Preparation of microcrystalline silicon-carbon films. Solar Energy Mater & Solar Cells 2004; 87: 433-444.

[115] Williamson DL. Microstructure of amorphous and microcrystalline Si and SiGe alloys using X-rays and neutrons. Solar Energy Mater.& Solar Cells 2003;78: 41-84.

[116] Voyles PM, Gerbi JE, Treacy MMJ, Gibson JM, Abelson JR. Absence of an abrupt phase change from polycrystalline to amorphous in silicon with deposition temperature. Phys. Rev. Lett. 2001; 86: 5514-5517.

Send Orders of Reprints at reprints@benthamscience.net

CHAPTER 6

Morphological and Structural Properties

Angelica M. Chiodoni[1,*] and Elena Tresso[1,2]

[1]Center for Space Human Robotics (CSHR@POLITO), Italian Institute of Technology, Corso Trento 21, Torino 10129, Italy and [2]DISAT, Politecnico di Torino, Corso Duca degli Abruzzi 24, Torino, IT-10129, Italy

Abstract: The chapter is devoted to the surface and structural characterisations of the materials used in photovoltaic applications for the determination of the topographic/morphological and structural properties.

In the first part of the chapter Scanning Electron Microscopy (SEM), Transmission Electron Microscopy (TEM), Atomic Force Microscopy (AFM) and X-ray Diffraction (XRD) are illustrated, with particular emphasis on the working principles. In the second part, some examples of application of these techniques to the silicon-based thin films solar cells are described. Recent and important experimental results obtained in these fields are examined and discussed, showing what kind of information they have provided.

Keywords: Atomic force microscopy (AFM), X-ray diffraction (XRD), transmission electron microscopy (TEM), scanning electron microscopy (SEM), surfaces, interfaces, morphology, structural properties, amorphous thin films, amorphous metals, microcrystalline thin films, crystalline fraction, growth processes, crystallization processes, nanostructures, semiconductors, defects, roughness, texture, crystal size.

1. INTRODUCTION

In the recent past, silicon-based solar cells have witnessed a rapid commercial development, mainly due to both reduced costs through large-scale production, and quite good cell efficiency values, in comparison with other solar cells.

There is not doubt that surface and structural characterisations play an essential role in determining the topographic/morphological and structural properties of the materials used in solar cell applications. In fact, the control of the interfaces and of the roughness of the materials, of the eventual doping, of the quality of the material and the presence of macro-micro or nano-defects has to be considered one of the most important topic to be optimized while a solar cell is configured and produced. Since the first generation of solar cells, based on mono-crystalline, poly-crystalline, micro-crystalline and amorphous Si, or a combination of some of them, it has always been necessary to control the structural and the morphological properties of these materials. This means that some techniques such as scanning and transmission electron microscopies (SEM,

[*]**Address correspondence to Angelica M. Chiodoni:** Italian Institute of Technology, Corso Trento 21, 10129, Torino, Italy; Tel: +39 110903402 (ext.7385); Fax: +39 110903401; Italy; E-mail: angelica.chiodoni@iit.it

Roberto Murri (Ed)
All rights reserved-© 2013 Bentham Science Publishers

Scanning Electron Microscopy; TEM, Transmission Electron Microscopy), atomic force microscopy (AFM) and X-ray diffraction become strategically important. This chapter is devoted to illustrate how these techniques work and what kind of information they can provide. In Section 2 we will describe the working principles of SEM, TEM, AFM and XRD instrumentations, while in Section 3 we will focus on some applications of these techniques to the study of morphological and structural properties of silicon based thin films solar cells.

2. INSTRUMENTATION

All of the described techniques are characterized by a probe and a detection system that is able to collect the signals coming from the specimen after the interaction with the probe itself. Each technique investigates, from a different point of view, the structural and/or morphological characteristic of the material constituting the specimen. In the following, a brief description of the instruments and the physical principles behind the techniques are reported.

2.1. Scanning Electron Microscopy (SEM)

The first generation of scanning electron microscopes was introduced in the 1930's. In academic and industrial research institutes, it is one of the most diffused non-destructive large-area surface imaging techniques, because it provides relatively fast and high depth-of-field images of the surface of samples with a simple preparatory procedure. An SEM is an important and versatile tool to investigated large area (some centimetres) samples, powders, nanostructures, bulk materials, thin films, multilayers, and small devices. It can be used to characterise metals, ceramics, oxides, nitrides, semiconductors, soft materials, and with some dedicated instruments, also biological materials. Depending on the configuration of the microscope, it is possible to have an overview of centimetre-sized samples and at the same time to get information at the nanometer-scale. A simplified scheme of an SEM is depicted in Fig. **1**.

The working principle of the system can be described in a number of quite simple steps [1]. A high-energy electron beam (up to 30 KeV), produced by an electron source, is accelerated across the column and focalized with electromagnetic lenses along the optical axis. The electron beam strikes the sample by a raster scanning of the surface, producing a number of signals, mainly electrons but also photons, which provide information about topography (secondary electrons), compositional contrast (backscattered electrons) and composition (characteristic X-rays), as in Fig. **2**.

The sources of the electron beam are of two different types: the thermoionic sources and the field effect sources. The field effect sources exhibit superior performances with respect to the thermoionic ones. In the thermoionic sources, which are usually made up of a W filament or a LaB_6 single crystal, the materials are heated to a certain temperature (some hundreds of Kelvin degrees) to overcome the work function and let the electrons escape from the material, thus producing the electron beam.

In the field effect sources, usually a cold cathode or a Schottky cathode, a high electric field is applied between a W nanowire ending with a sharp tip and an extractor electrode. In this case, it is mainly the electric field that lowers the work function and promotes the emission of the electrons.

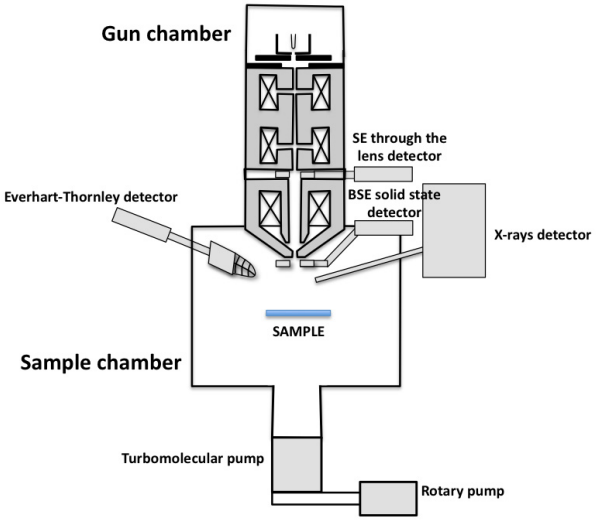


Figure 1: Scheme of a scanning electron microscope.

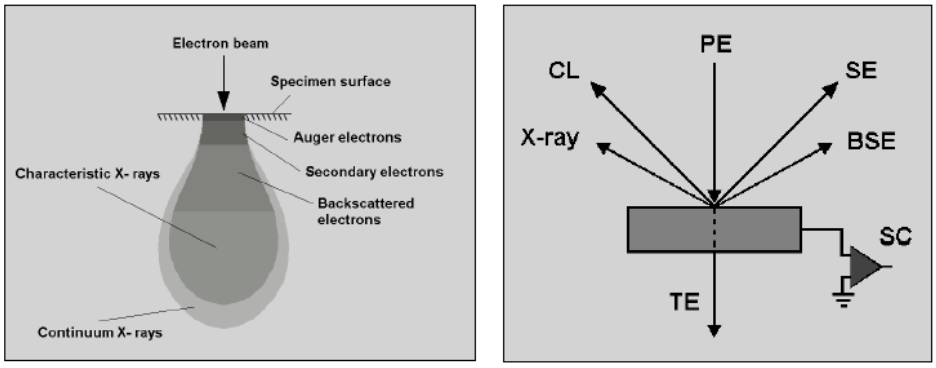


Figure 2: Signals produced by the electron-matter interaction. Reprinted with permission of Carl Zeiss NTS GmbH [2].

The electromagnetic lenses control the electron path along the column down to the end of the objective lens, as the glass lenses do in the optical microscope. At the end of the column the scanning coils can be found, which provide the rastering of the beam on the sample. In Fig. **3** a scheme of the lenses in an SEM is reported.

The signal produced by the rastering of the electron beam on the surface of the sample is collected by dedicated detectors, which reproduce a grey-scale image on a screen. The collection of secondary electrons (SE) is provided by the standard Everhart-Thornley (ET) detector or by the more efficient through-the-lens detector. In both, the electrons strike a scintillator that converts electrons into photons. Subsequently, the photons are collected by a light-pipe and sent into a

photomultiplier tube for amplification, at the end of which an electrical signal is provided. The collection of backscattered electrons (SE) is provided by the standard Everhart-Thornley (ET) detector or by the more efficient dedicated solid-state detectors, one placed at the end of the objective lens (AsB) and the other in the column (EsB). The dedicated BSE detector is usually a p-n junction that, when hit by electrons, produces electron-hole pairs in a number proportional to the atomic number.

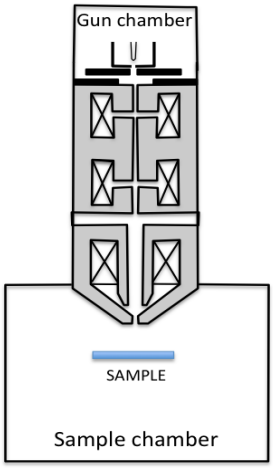


Figure 3: Scheme of the lenses in scanning electron microscope.

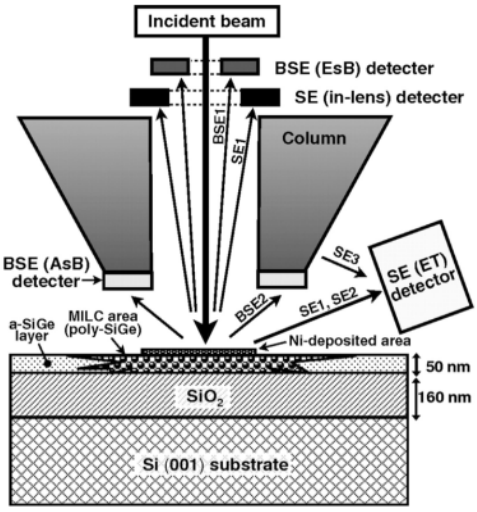


Figure 4: Schematic drawings related to the position of the main SEM detectors in the columns or in the chamber: upper SE (in-lens) detector, lateral ET detector, upper EsB detector and AsB detectors. Reprinted with permission of Itakura *et al*. [3], Copyright (2010), Oxford Journals.

The characteristic X-rays are collected by a dedicated detector (Energy Dispersive X-rays-EDX detector), usually cooled by liquid nitrogen. This is composed of a thin silicon crystal doped with lithium, so that the central intrinsic region is sandwiched between a thin p-type layer and a thin n-type layer. When an X-ray photon hits the detector, it produces electron-hole pairs in the Si(Li) region. The electrons are accelerated towards the positive side, and the holes towards the negative side. Thus, a pulse of current, which is proportional to the X-ray energy, is generated.

As an example, in Fig. **4** a scheme showing the position of the detectors in a microscope used to characterize SiGe whiskers and in an amorphous matrix is reported [3].

2.2. Transmission Electron Microscopy (TEM)

Transmission Electron Microscopy (TEM) is an important characterization technique to get local (few microns) and extremely detailed structural information about mainly crystalline but also amorphous materials. It is a powerful but destructive technique, because a small piece (1-2 mm) of specimen has to be cut from the sample of interest and thinned down to about 100-200 nm in order to be electron transparent and produce a transmitted electron beam to analyse. The TEM is the only technique able to provide at the same time information about structure, composition and defects at the atomic scale.

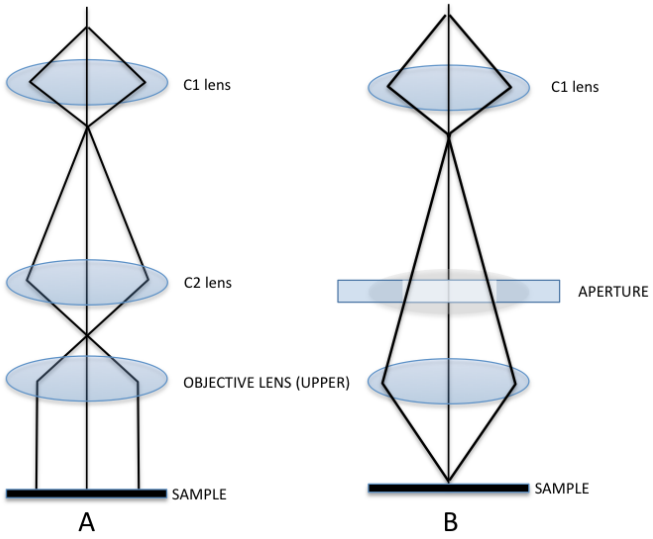


Figure 5: The two illumination systems in a TEM: (A) Parallel-beam mode; (B) Convergent-beam/probe mode.

The first Transmission Electron Microscope has been built by Ruska and Knoll, in Berlin in the early 1930s. In a transmission electron microscope [4], the illumination system is constituted by a high-energy electron beam that is focused on a very thin sample by means of electromagnetic lenses, and is transmitted to image and analyze the microstructure of materials with atomic scale resolution. The image is observed on a fluorescent screen, or recorded on film or digital camera. The electrons, produced by guns similar to those described in §2.1, are accelerated at several

hundreds of kV, corresponding to wavelengths much smaller than that of light. For example, electrons accelerated at 200kV have a wavelength of 0.0025 nm. Even if the wavelength is so small, the final resolution of the microscope is limited by the aberrations related to the electromagnetic lenses. As it is shown in Figs. **5** and **6**, several lenses have important roles in determining the illumination and the collection modes.

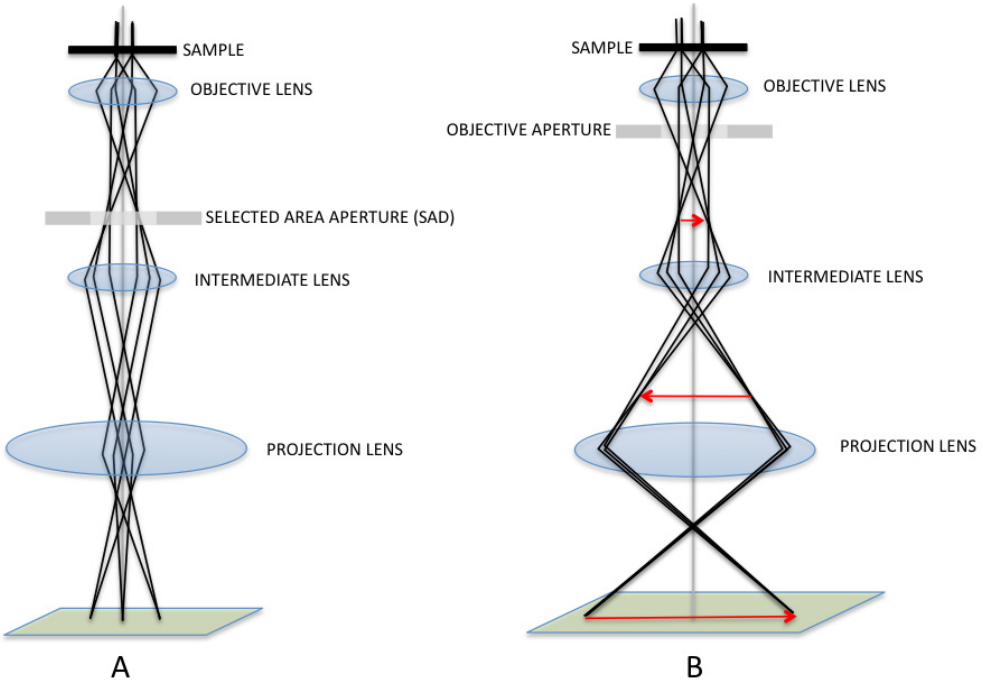


Figure 6: The two basic operations of the TEM imaging system: (A) diffraction mode, projecting the diffraction pattern onto the viewing screen; (B) image mode, projecting the image onto the screen.

The C1 and C2 lenses determine the illumination mode. Two main illumination modes are possible: the parallel beam and the convergent beam. The first is used for TEM imaging and for selected-area diffraction (SAD), while the second is used for scanning TEM (STEM) imaging, for convergent beam electron diffraction (CBED) and for spectroscopy (X-ray and electron energy loss spectroscopies).

The objective lens and the specimen holder/stage system is the heart of the TEM. Here the beam-specimen interactions take place and the creation of images and diffraction patterns occur. These images and patterns are subsequently magnified for viewing and recording. Several lenses (intermediate and diffraction lenses) are used to magnify the image or the diffraction pattern produced by the objective lens and to focus these on the viewing screen or computer display *via* a detector, CCD, or TV camera (projector lens).

Parallel-illumination TEM mode is chosen for diffraction-contrast imaging and SAD pattern formation. To see the diffraction pattern, the back focal plane of the objective lens has to be set as

the object plane for the intermediate lens. Then the diffraction pattern is projected onto the viewing screen/CCD as shown in Fig. **6A**. Otherwise, to look at an image, the object plane of the intermediate lens has to be set as the image plane of the objective lens. The image is then projected onto the viewing screen/CCD, as shown in Fig. **6B**. When the SAD pattern is projected onto the viewing screen/CCD, it is possible to use the pattern to perform the two most basic imaging operations in the TEM. No matter what kind of specimen is, the SAD pattern will include a bright central spot that contains the direct-beam electrons and some scattered electrons. By selecting the direct beam, a Bright Field (BF) image is formed. By selecting only electrons that are not in the direct beam, a Dark Field (DF) image is formed.

The TEM images the crystal lattice of a material as an interference pattern between the transmitted and diffracted beams. Thus, TEM provide information about planar and line defects, grain boundaries, interfaces, *etc.* with an atomic scale resolution. The bright-field and dark-field imaging modes of the microscope, which provide morphological (bright-field) and Z-contrast (dark-filed) information, combined with electron diffraction, which provide crystallographic information, are invaluable tools to have a complete knowledge of the examined materials.

TEM microscope could also be optionally equipped with a STEM module, which provides the scanning of the electron beam on the sample and is essential for the Energy Dispersive X-ray Spectroscopy (EDS) and the Electron Energy Loss Spectroscopy (EELS). EDX and EELS are complementary techniques and are essential to get information about composition of the samples with a resolution close to the probe size. In Fig. **6**, the ray diagram for the different operating modes is reported.

2.3. Scanning Probe Microscopy (SPM)

Scanning Probe Microscopy (SPM) refers to a group of techniques that use the interaction of a microscopic probe, usually a sharp tip, with the surface of a sample to measure characteristics of the sample at localized points. This technique is not destructive and extremely surface-sensitive. The interaction between the probe and the sample provides topographical information. As the scanning range is reduced (hundreds of microns down to tenths of nanometres), it is not possible to map “big” surfaces in one single step. The basis of the scanning probe microscopy is depicted in Fig. **7**. The resolution obtainable with this technique can reach the atomic scale and with some cases it is also possible to map the position of single atoms.

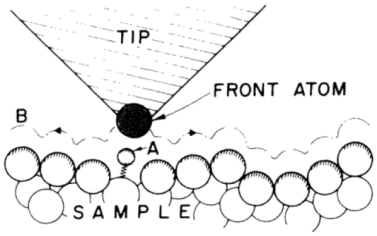


Figure 7: Basis of the scanning probe microscopy. Reprinted with permission of Binning and Quate [5], Copyright (1986), American Physical Society.

2.4. Atomic Force Microscopy (AFM)

Among the SPM techniques, there is the Atomic Force Microscopy (AFM), invented by Binning, Quate and Gerber in 1985 [5]. It is related to the repulsive force between the probe and the surface of the sample. In AFM, imaging is produced by measuring the deflection of a cantilever hosting the tip (in an ideal case, a single atom), while raster scanning the sample surface (Fig. **8**). The deflection is due to the interaction force between the tip and the surface.

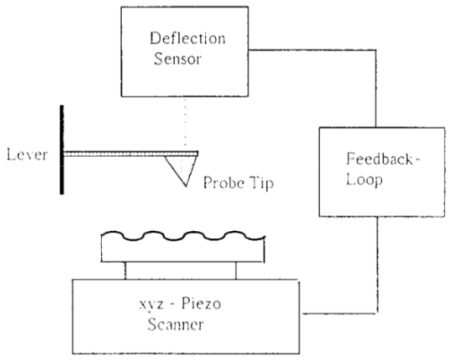


Figure 8: Sketch of the basis of the AFM technique. Reprinted with permission of Meyer [6], Copyright (1992), Elsevier.

AFM is essentially based on the collection of short-range repulsive interatomic forces, which are low repulsive forces (in the scale of nano-Newton or less). In addition to these short-range forces, also long-range forces such as Coulomb forces, dipole-dipole interaction, van der Waals dispersion forces, polarisation and capillary forces, which are attractive or repulsive, could also be encountered, but they can be minimized in order to improve the resolution and to reduce possible damage to the sample [6].

In Fig **9**, an example of a force-distance curve is reported [7], showing how the force changes when the tip approaches the sample.

The AFM can operate at a constant force or at a constant height. In the latter there is a risk that the tip may collide with the surface, thus causing damage. There are also two main operation modes: the static mode and the dynamic mode. In static mode, the cantilever is swept along the surface of the sample and therefore measures the surface topography directly by using the deflection of the cantilever. In the dynamic mode (also commonly referred to as tapping mode or non-contact mode), the cantilever is externally oscillated at or close to its fundamental resonance frequency or a harmonic. These changes in oscillation with respect to the external reference oscillation provide information about the sample's characteristics.

2.5. Conductive Atomic force Microscopy (C-AFM)

Conductive atomic force microscopy (C-AFM) is a variation of atomic force microscopy. It uses an electrical current to construct the surface profile of the studied conducting specimen. This

current flows through the metal-coated tip of the microscope and the sample. It is acquired simultaneously with the usual topographical mapping of the standard AFM. This enables to correlate a spatial feature on the sample with its conductivity. The C-AFM can be operated in the imaging mode and spectroscopic mode. The imaging mode is the same as described in § 2.4. In the spectroscopic mode, the tip is stationary, while the voltage is being swept. This allows recording conventional current–voltage characteristic from tiny areas of the sample. Thereby information on the local electronic properties, such as local density of states, can be extracted.

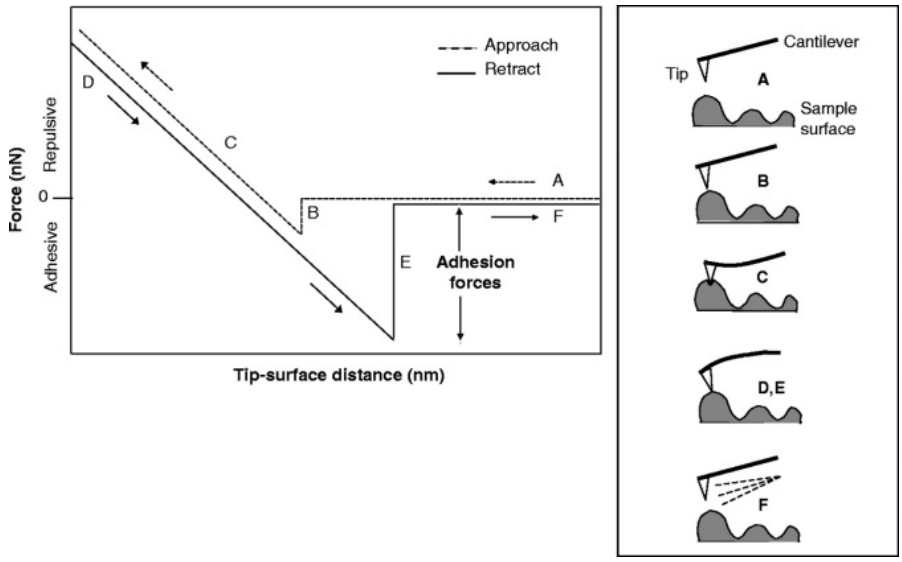


Figure 9: Force-distance curve, showing how the force changes when the tip approaches the sample. Reprinted with permission of Shahin *et al.* [7], Copyright (2005), The Company of Biologists Ltd.

2.6. X-ray Diffraction (XRD)

X-ray diffraction is one of the most powerful tools for investigating the crystalline structure of materials. In fact, the discovery in the early 1900s made by Laue of the ordered atomic arrangement of crystalline materials, opened new possibilities to go deeper into the structure of the matter. This technique is based on the elastic scattering of X-rays from the electron clouds of individual regularly arranged atoms that constitute the crystalline structure of materials.

X-ray diffraction is a versatile technique that is useful not only for obtaining information about the crystalline orientation but also on the texture and on the quality of the materials. Nowadays, new instrument technology development has provided modular systems, which in few minutes are able to vary measurement configuration. In addition, new detection systems are now able to collect spectra with a very good signal-to-noise ratio within a couple of hours. New tools also allow the warming or cooling of the samples to follow the phase transitions.

The basis of the technique is depicted in Fig. **10**. The X-ray plane waves incident on a crystal lattice at angle θ, are partially reflected by successive parallel crystal planes of spacing d. The

superimposed reflected waves interfere constructively if the Bragg condition $2d\sin\theta = n\lambda$ is satisfied [8].

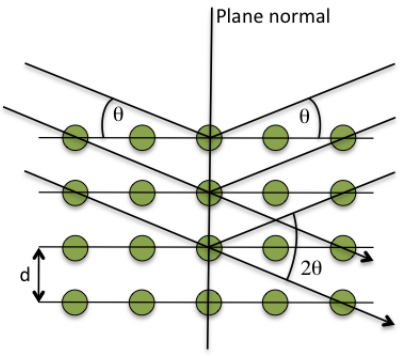


Figure 10: Scheme showing plane waves interacting with a crystal lattice.

The source of the X-rays is a tube where an accelerated electron beam hits a specific target, usually Cu, but also Co and other transition metals. As described in § 2.1, the electron matter interaction produces a number of signals, and among them there are characteristic X-rays. For the Cu target, the X-ray wavelength is 0,154 nm. Different geometries can be selected for this technique, depending on the information needed. In order to check the phase identification, the crystalline quality and the orientation, the most widely employed geometry is the Bragg-Brentano geometry (Fig. **11**), usually chosen for randomly oriented powders, bulk materials and thin films. In this configuration, the X-rays are focused on the sample at an angle θ and the diffracted beam is collected at the same angle θ. The angle is scanned in a defined angular range selected on the basis of the material to be measured. The incidence angle is the same as the collecting angle. Several detection systems exist, such as proportional counters, scintillation counters, semiconductor counter, CCDs. One of the most widely used is the proportional counter, where the ionization of an inert gas contained in a small chamber by an X-ray photon in an electrical field produces an avalanche of electrons. Since the number of electrons collected is proportional to the number of X-rays collected at a certain angle θ, the detector is able to give a spectrum providing the X-ray intensity as a function of the scanned angle. For thin film analysis, the thin film geometry (Fig. **12**) is preferred in order to suppress the substrate signal and improve the surface sensitivity by increasing the length of X-ray's path through the film. In this configuration, the incident angle ω is fixed. The detector scans over an angular range, and collects the diffraction peaks. The penetration depth can be varied by changing the incidence angle ω of the X-ray beam to the sample surface. The drawback of this technique is that usually the resolution is worse when compared to Bragg-Brentano geometry. The analysis of the diffraction pattern can be very complex, especially when the material presents some preferred orientation of when it does not have a fixed stoichiometry. To assign an "identity" for each peak in the diffraction pattern, scientists usually refer to the JCPDS (Joint Committee on Powder Diffraction Standards) database, which contains thousands of diffraction patterns of inorganic materials.

By analyzing a diffraction pattern, it is also possible to evaluate the size of the coherent diffraction domains, which may be smaller or equal to the grain size. This analysis works if the crystallites are

less than approximately 100 nm in size. In this case, an appreciable broadening in the X-ray diffraction lines occurs. A very simple way to evaluate the average crystallites size is to apply the Scherrer formula [9]:

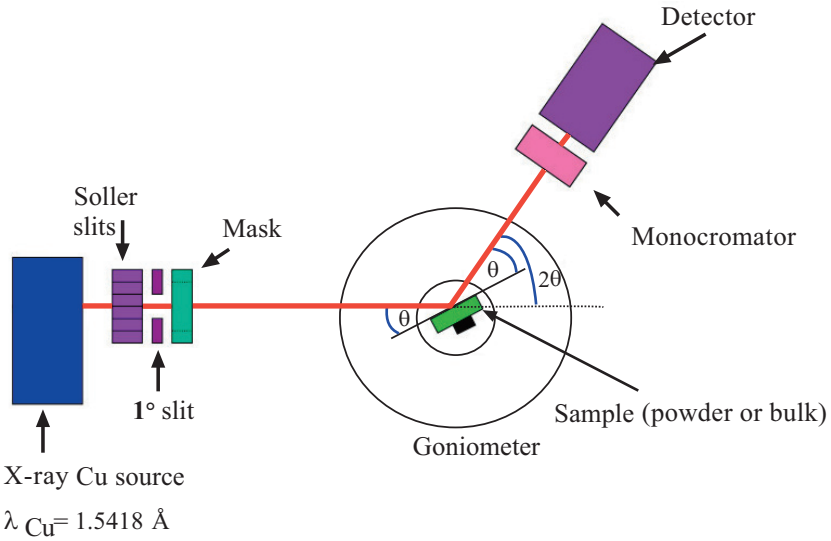


Figure 11: Scheme of the Bragg-Brentano geometry.

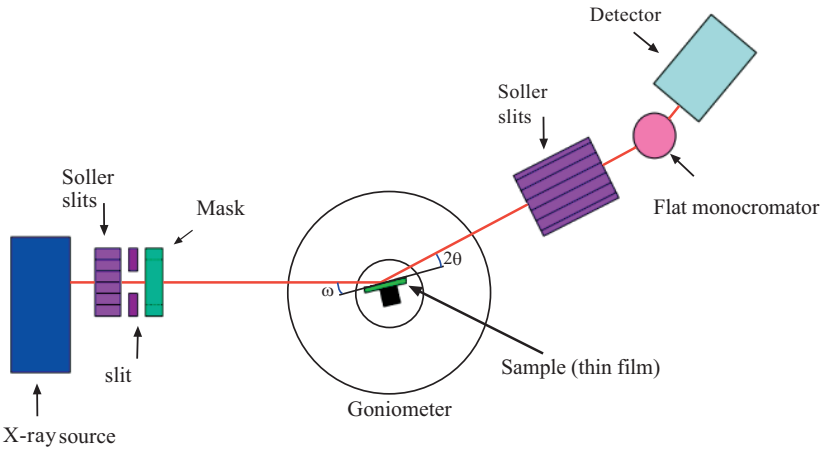


Figure 12: Scheme of the thin film geometry.

$$D = \frac{K\,\lambda}{\beta\cos\theta}$$

where K is a dimensionless shape factor, usually fixed at 0.9, λ is the X-ray wavelength, β is the line broadening at half the maximum intensity (FWHM) in radians, θ is the Bragg angle and D is the mean size of the ordered (crystalline) domains. This method is based on the assumption that

the material is stress-free and the shape of the crystalline domains is spherical and can be considered reliable when the contribution of the instrument to the broadening of the peaks is properly taken into account. By using this method, the size can be estimated from a single diffraction peak.

When both the stress and the particle size are influencing the broadening of the diffraction peaks, a more comprehensive method must be used to separate the different contributions. The most common method of strain/size analysis is based on the assumption that the broadenings from the two different sources have different angular relationships. For instance, the size broadening, as described in the Scherrer method, has a $1/\cos(\theta)$ relationship, while the strain follows a $\tan(\theta)$ function. The Williamson-Hall plot [10] can be used to compute the average particle size D and the strain ε simultaneously, by using the following equation:

$$\beta = \frac{\lambda}{D\cos\theta} + 4\,\varepsilon\, tg\theta$$

Also in this case the instrument contribution to the peaks broadening must be taken into account and must "subtracted" to the total line broadening β at FWHM.

3. APPLICATIONS TO THE ANALYSIS OF THIN FILMS AND DEVICES

In Fig. **13**, the basic structure of an amorphous silicon solar cell is reported: starting from the top, it consists of a sequence of different layers (a "multilayer") on a glass substrate which is coated with a transparent conductive oxide which allows both the light to enter and the electrical current to be collected; the back contact is generally made in stainless steel. Since the first cells appeared, a lot of research efforts have been devoted to modifying this basic structure in order to enhance the performance, and different multilayer configurations have been proposed and produced, by introducing various modifications: wide-bandgap alloy, micro and nano-crystalline semiconducting layers, texturized front contact layers, highly reflective back contacts, tandem cells incorporating amorphous silicon based alloys, buffer layers, nanostructures such as quantum-dots and nanocrystals.

The morphological and structural properties of each layer that constitute the multilayer, do affect the performance of the final device and for this reason they have to be carefully measured and correlated to electrical, optical and photovoltaic properties.

Up to now the previously described techniques (AFM, SEM, TEM and XRD) have been used to study and investigate the following:

a. the structure of the semiconducting films,

b. the surface of the front contact,

c. the interface properties,

d. the growth processes,

e. the crystallization processes of amorphous layers,

f. the introduction of advanced nanostructures for a new generation of solar cells.

In the following section the recent and most important experimental results obtained in these fields will be examined and discussed.

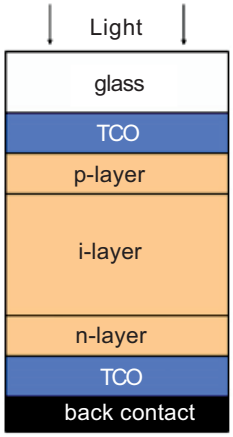


Figure 13: Structure of a typical amorphous silicon solar cell.

3.1. Semiconducting Films Structure

The material quality of the semiconducting films and the efficiency of the solar cells continue to improve, and a big research effort has focused on the structure of the semiconducting films. Recently, the use of hydrogenated nanocrystalline silicon (nc-Si:H) in the middle and/or bottom cells in hydrogenated amorphous silicon (a-Si:H)-based multi-junction solar cells has been studied in depth. These new complex film structures are generally obtained under deposition conditions close to the amorphous/nanocrystalline transition and include nanocrystallines, grain boundaries, and amorphous regions. Microscopy measurements provide valuable information for characterizing material properties. In particular the morphological study of the silicon-based films used in solar cell fabrication is often performed by means of SEM, which enables the identification of crystal grains and of the amorphous phase. In general, due to the small examined area and to the difficulty of evaluating crystal fractions, only a qualitative information is obtained from SEM or TEM images, but these images are invaluable for supporting the results obtained from structural analysis such as Raman or XRD. As an example in Fig. **14** the SEM images of hydrogenated silicon films deposited by Plasma Enhanced Chemical Vapor Deposition with crystalline phases ranging from 0 to 75% are reported: in (a) the typical amorphous morphology, corresponding to a low-roughness, homogeneous surface is shown; in (b) and (c) a uniform distribution of silicon grain aggregates separated by an amorphous phase is evidenced. In (b) smaller crystallites of silicon in the agglomerated form are distributed over the scanned area, and also a bigger cluster can be seen at the centre of the image; in (c) uniformly distributed dense crystalline structures confirm the presence of 75% of the crystalline phase, with an average crystallite size of 12 nm, obtained from Raman measurements [11].

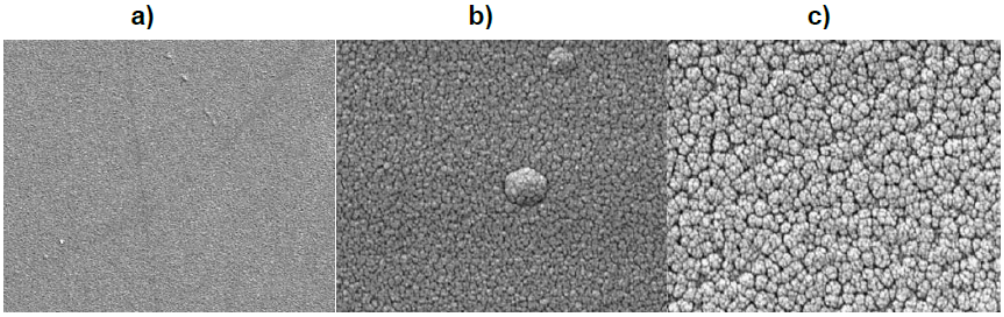


Figure 14: SEM images obtained for PECVD films of amorphous (a) and nano-crystalline silicon films with crystalline fractions of 45% (b) and 75% (c). Reprinted with permission from Parashar *et al.* [11], Copyright (2010), Elsevier.

Another example is given in Fig. **15** where TEM images, taken from [12] are reported and related to amorphous hydrogenated silicon carbide thin films deposited from argon diluted silane, ethylene, and hydrogen mixture by PECVD. In (a), a typical low-magnification cross section is reported showing the contrast between the thin film and the crystalline silicon substrate; in (b), a typical cross section high resolution (HR) TEM image of an a-Si_{1-x} C_x:H/c-Si (001) specimen is reported. The micrograph reveals an abrupt interface, with a maximum asperity of three atomic planes, attributed to the substrate pre-treatment (HF dip) or etching in the early stages of the film growth. In (c) a typical plane view HR-TEM image of an a-Si_{1-x} C_x:H thin film is reported. HR-TEM observation reveals a homogeneous micro-structure without any nanocrystalline clusters in all the samples. This result is also confirmed by the Selected Area electron Diffraction (SAD) patterns, which show diffused rings that are characteristic of an amorphous material.

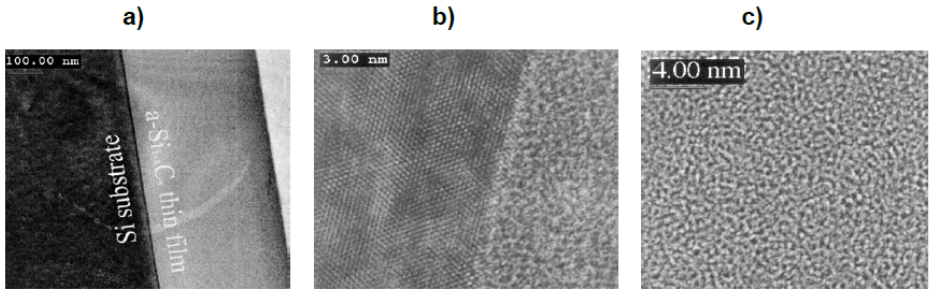


Figure 15: TEM images as described in text. Reprinted with permission from Wang *et al.* [12], Copyright (2002), Elsevier.

The SAD is indeed frequently used in TEM investigations of amorphous, micro or nano-crystalline silicon films in order to obtain important information such as the orientation of crystallites or the presence of defects. As an example [13] in Fig. **16** diffraction patterns are reported, taken on films of hydrogenated microcrystalline silicon–carbon deposited on c-Si substrate by PECVD at different power densities and with different crystalline microstructures (varying from columnar silicon crystals to crystallites uniformly dispersed in an amorphous matrix). In both images the diffraction spots coming from the silicon substrate in <110> orientation can be seen and the

corresponding cell is highlighted by the continuous lines. Only silicon crystals are present. The three main diffraction rings, shown in the Fig. **16(a)** and **16(b)**, are due to <111>, <220> and <311> planes of c-Si. The diffraction rings visible in Fig. **16(b)** indicate that the crystals are randomly oriented in this film and the diffused intensity among the rings is attributed to the presence of an amorphous phase. The sample of Fig. **16 (a)**, deposited at lower power, shows diffraction rings that are discontinuous in intensity because of a non-homogeneous distribution in the orientation of the crystallites. Moreover, the superposition of several diffraction patterns does not reveal a preferred crystal orientation.

The micro-structure of the micro-and nano-crystalline silicon-based films can be determined from the X-ray diffaction (XRD) patterns. As can be seen in Fig. **17,** the typical Si(111) peak is located at 2θ=28.5°, the Si(220) peak at 2θ=47,4° and the Si(311) peak at 2θ=56,2°. Moreover the average crystallite size can be estimated as a first approximation according to the Scherrer formula. In Ref.4 the evolution of the layer crystallinity of p-doped microcrystalline hydrogenated silicon thin films deposited under different substrate temperature is demonstrated with an XRD spectrum.

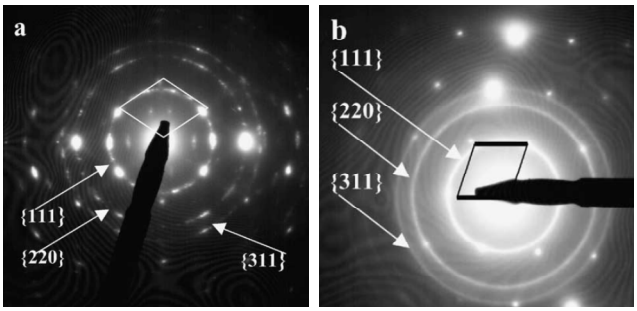


Figure 16: Selected Area Electron Diffraction patterns for micro-crystalline hydrogenated silicon carbide films at different power densities: (a) 5W, completely crystallized film, with generally columnar crystal shape; (b) 25 W, silicon crystallites uniformly dispersed in an amorphous matrix. Reprinted with permission from Ambrosone *et al.* [13], Copyright (2004), Elsevier.

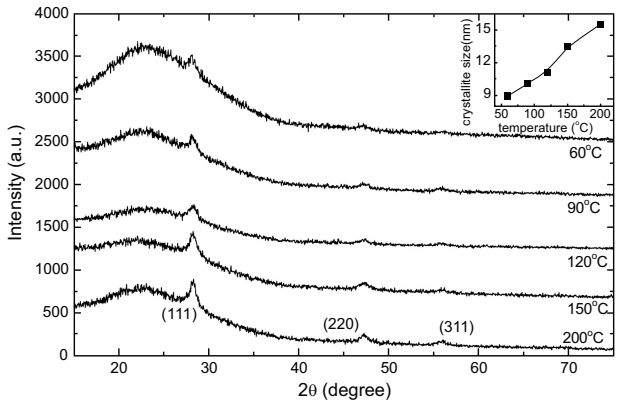


Figure 17: XRD measurement of p-doped microcrystalline hydrogenated silicon films thin films (about 30–40 nm thickness) deposited on glass under different substrate temperature. The inset shows the change of the average crystallite size deduced using the Scherrer formula. Reprinted with permission from Tao *et al.* [14], Copyright (2010), Elsevier.

From the XRD pattern reported in Fig. **17**, it can be seen that the X-ray diffraction signal becomes weaker as the substrate temperature decreases, and the diffraction peak Si (311) disappears to temperatures below 150°C. In fact, the amorphous films do not show peaks in diffraction analysis, but only a typical broad band at around 2θ=20°-30°. The decrease of the crystallite size with decreasing temperature was calculated from (111) peak and is reported in the inset.

Scanning probe microscopies such as AFM are used in studies of hydrogenated amorphous silicon-based films, even if the complex structure of the films, which has a markedly statistical character, can give an ambiguous interpretation of the results. The film surface is generally very smooth, with the root-mean-square (rms) surface roughness in the range 1-2 nm, and hence suitable for the integration of the film in a device structure. As an example, in Fig. **18** a typical three-dimensional AFM image of an as-deposited amorphous silicon carbide thin film is shown, taken from ref. [12].

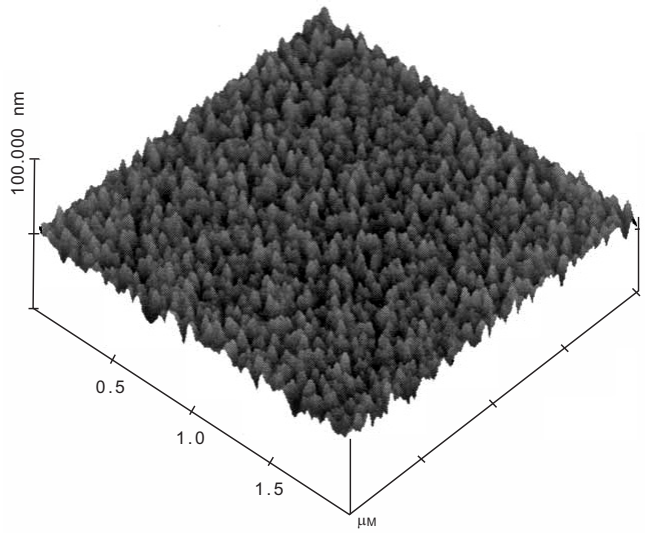


Figure 18: Typical three-dimensional AFM image of PECVD as deposited amorphous silicon carbide thin film. Reprinted with permission from Wang *et al.* [12], Copyright (2002), Elsevier.

A number of structural elements of the amorphous film surfaces have been identified: densely-packed convex structures ("hills") covering the total surface area [15], with dimensions ranging from few to several tenths of nm [16]; atomically smooth areas of approximately 0.03 nm rms local roughness occurring predominantly at the top of the hills and extended regions covered by sub-nanometric structures [17]. Finally, it is interesting to note that particular techniques such as conductance AFM (C-AFM) are useful for studying the transport mechanism in the material and for correlating electrical conduction to morphological properties. C-AFM has been used for measuring the local current flow distribution in mixed-phase (amorphous and nanocrystalline) solar cells, in the area of no ITO coverage. The results have been interpreted with the assumption that the nanocrystallines embedded in the amorphous phase behave as microscopic diodes [18]. Moreover cone formation and tree-like nanocrystalline structures, correlated to the hydrogen dilution used during the deposition, have been demonstrated to have a strong effect on the light induced open circuit voltage value [19].

3.2. Front Contact Layer Surface

As reported in Fig. **19**, the front contact layer, which is generally made of transparent conductive oxides (TCO) such as tin oxide (SnO_2) or indium tin oxide (ITO), has the role of permitting the electrical current collection. The structure and the morphology of the first layer, which is exposed to the solar radiation, are of fundamental importance.

Any roughening of the surface of the front TCO contributes to enhance the light absorption, since it reduces reflection by increasing the possibility that the reflected light bounces back to the surface rather than out to the surrounding air. TCO morphology depends on a wide variety of growth factors, such as deposition temperature, flow rate of the gases, gas precursor used and substrate material. The demand for these TCO films is rapidly increasing due to the extensive market growth in photovoltaic areas. A lot of different solutions are continuously being studied and proposed, in order to fulfil the requirements on low resistivity, high transmittance, large area deposition, low cost manufacturing.

Furthermore the ability for fine patterning, light scattering and precise alignment of the electronic structure to the surrounding semiconductors are frequently requested.

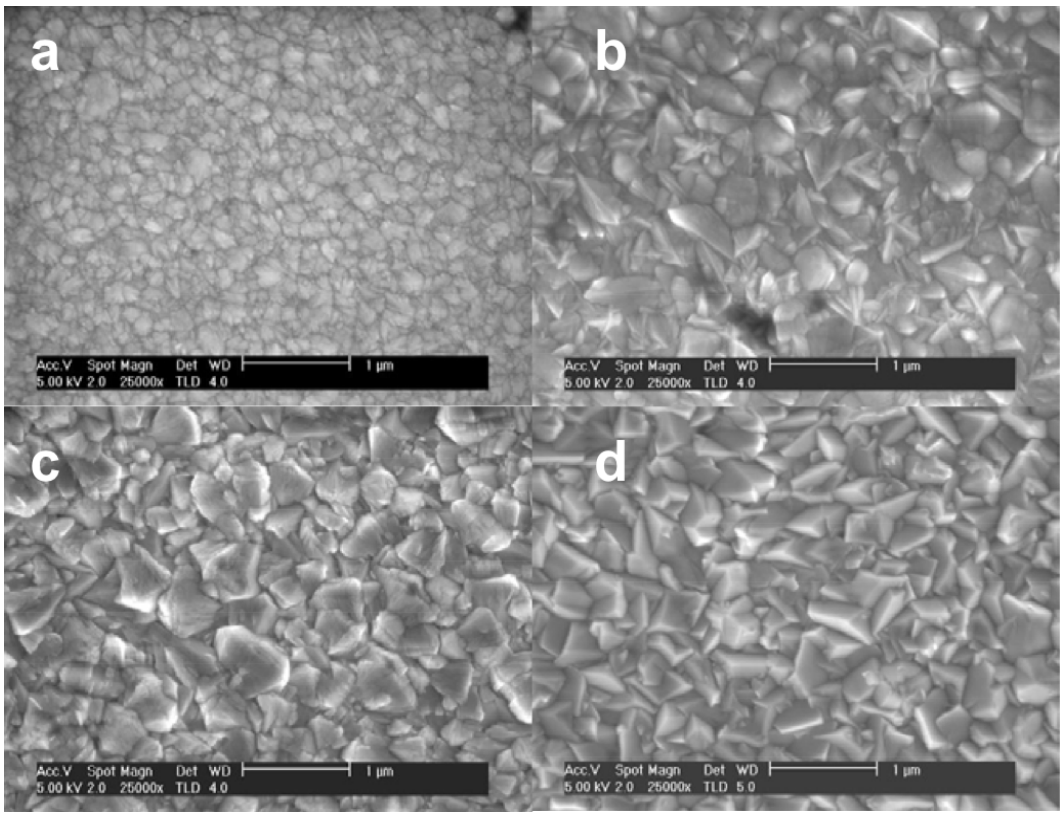


Figure 19: SEM images of SnO_2:F deposited with different precursors: (a). TMT, (b). MBTC, (c). TTC, (d). Asahi U-type. Reprinted with permission from De Graaf *et al*, [21], Copyright (2010), Elsevier.

Fig. **19** shows SEM images of SnO_2 layers produced with different tin precursors [20, 21]. From these images it becomes clear that the highest surface roughness is obtained by using tin tetrachloride (TTC). The morphology resembles that of the commercially available and largely used Asahi U-type, which is also deposited with TTC. In contrast, tetramethyltin (TMT) yields much smoother layers. The RMS surface roughness measured on an area of 5 × 5 μm^2 is as follows: a. 7 nm, b. 22 nm, c. 39 nm, d. 40 nm.

In [22] the optimization procedures followed for enhancing the photovoltaic efficiency by an appropriate design of the indium–tin oxide (ITO) thin films are reported. In particular the deposition conditions of ITO film by electron-gun evaporation were optimized for hetero-junction microcrystalline silicon solar cells. Microstructure, surface morphology, electrical and optical properties of these films were characterized and analyzed. The substrate temperature and the ITO thickness were optimized, arriving at a solar cell conversion efficiency of 16.4%. In Fig. **20** the SEM and AFM images of the ITO film surfaces are reported.

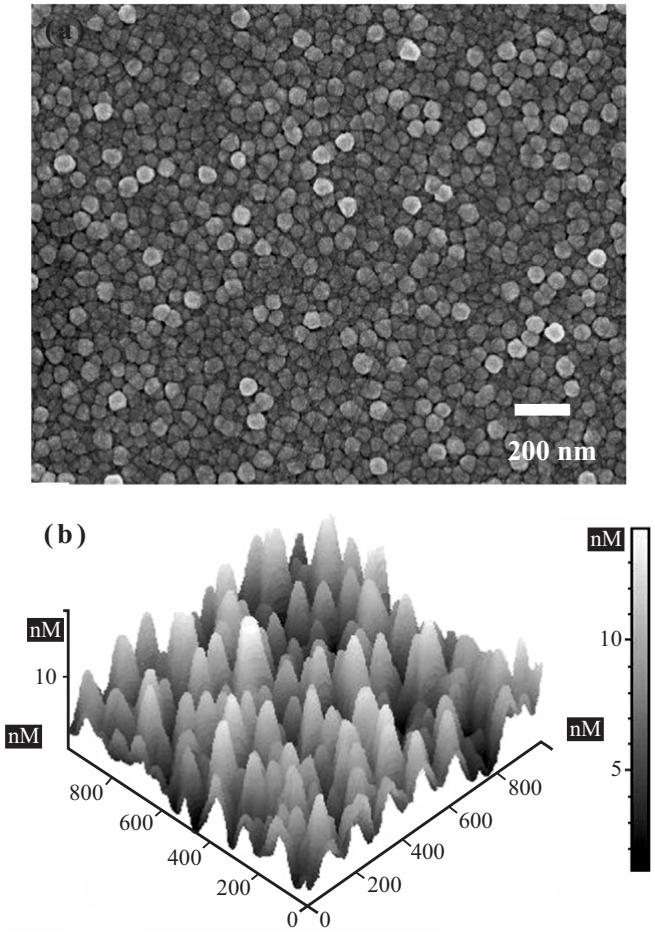


Figure 20: (a) SEM and (b) AFM images of ITO films prepared by electron gun evaporation at a substrate temperature of 230 °C. Reprinted with permission from Lien SY, [22], Copyright (2010), Elsevier.

The fundamental solar cell parameters (the fill factor, FF, open circuit voltage, V_{OC}, and also the short circuit current, J_{sc}) exhibit a strong dependence on the surface properties of the front contact layer [23, 24]. In ref [23], the plasma-induced chemical and morphological modifications of the boron doped zinc oxide front layer are shown to produce appreciable PV performance improvements for solar cells produced on these plasma treated substrates. By varying the etching time, different surface roughnesses were obtained and the evolution of the surface morphology was correlated with its scattering properties. The best device parameters have been reached through a compromise between an effective sharp edge rounding off (improved ZnO:B/p-layer interface) and a sufficiently high roughness (high J_{sc} value).

3.3. Interface Properties

Since the last century, major improvements in the performance of amorphous silicon solar cells have been obtained by changing the initial p-i-n configuration, using wide-bandgap alloys and microcrystalline p-layers, enhanced reflective back contacts, tandem cells incorporating a-Si/Ge:H alloys, and buffer layers [25]. For an appropriate design of the solar cell it is necessary to characterise and control the morphology of the interfaces, in particular the interface between the back contact and the bottom semiconducting film. As an example, in hetero-junction solar cells, the hetero-interfaces have been particularly studied, since they can affect the device performances.

The use of textured metal oxide back contacts instead of plain stainless steel ones can provide a significant current enhancement. The textured interface acts as a diffuse scattering mirror, which results in the lengthening of the optical path in the cell. Optimized back reflectors can lead to an enhancement of the photocurrent by as much as 50%. However, as reported in [26], the morphology of the surfaces needs to be controlled to avoid cavities and shunting paths. A further drawback of such rough metallic surfaces is the parasitic absorption due to surface particle plasmons. The surface properties of gallium doped zinc oxide (GZO) films, used as back contacts in amorphous silicon thin film solar cells, have significant influence in the final conversion efficiency. In Fig. **21**, taken from [27], a comparison of the GZO films with and without texturing obtained by plasma etching is shown: (a) as-grown GZO film (3.2 wt% Ga^2O^3) on a-Si cell and (b) the same GZO film after 30 min roughening. The treatment increases the optical scattering reflectance and reflection haze, and consequently, the relative increase in the solar cell efficiency is 4.6%.

Also in the fabrication of flexible solar cells, with flexible substrates such as metal or plastic foils (in polyethylene-naphtalate, PEN), a substrate texture has been proposed to scatter the light at each interface and to increase the light trapping in the active layer, together with the use of a buffer layer at the n/i interface [28]. TEM measurements have been used for investigating the relation between voids or nanocrack formations in the intrinsic layer and the textured substrate. An example of an obtained TEM micrograph of the interface is given in Fig. **22**.

Finally, interface characterization is essential in the fabrication of amorphous–crystalline silicon (a-Si:H/c-Si) heterojunctions [29, 30]. These cells present unique technological advantages with respect to homo-junction silicon cells such as low processing temperatures (below 230 °C) and the ability to rapidly deposit the thin amorphous emitter on large areas using PECVD. The a-Si:H passivates the silicon surface excellently, and cell efficiencies up to 22.3% have been recently

demonstrated by Sanyo, with a-Si:H/c-Si cells based on high-quality CZ-c-Si [31]. AFM and SEM [30] have been used together with surface photovoltage and photoluminescence measurements. As a consequence, the relation between structural imperfections at the structured silicon surfaces, energetic distribution of interface state densities, recombination loss at a-Si:H/c-Si interfaces and solar cell characteristics have also been investigated. It has been shown that the morphological and electronic properties of the substrate surface are strongly related to the preparation method.

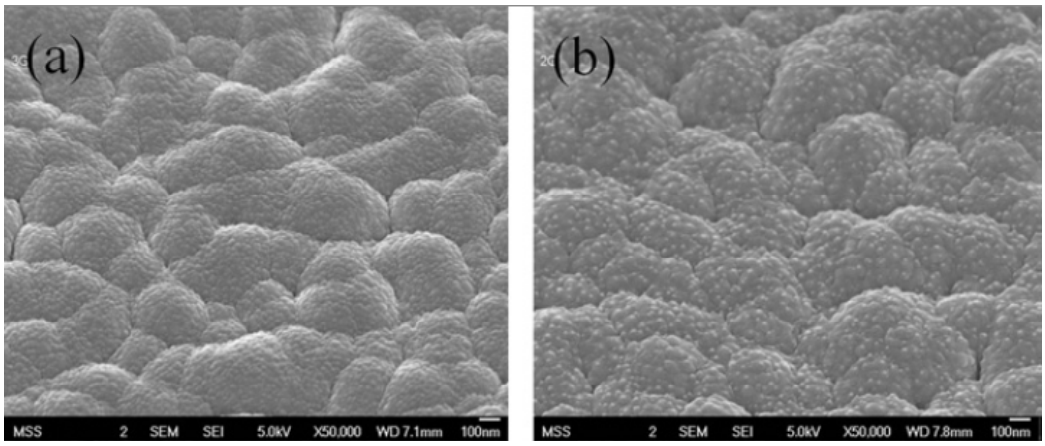


Figure 21: SEM micrographs of surface morphology of gallium doped zinc oxide films on a-Si solar cell before (a) and after (b) 30 min roughening treatment by plasma etching. Reprinted with permission from La *et al.* [27], Copyright (2011), Elsevier.

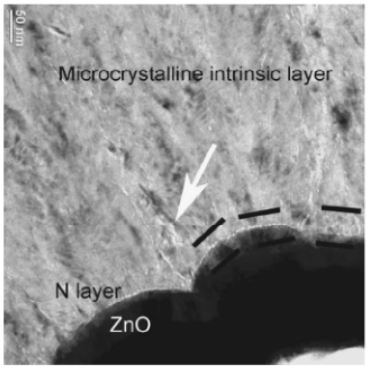


Figure 22: Cross-sectional TEM micrograph of a microcrystalline silicon cell on textured substrate coated with 80 nm of sputtered ZnO. Reprinted with permission from Soderstrom *et al.* [28], Copyright (2004), American Institute of Physics.

Wet-chemical oxidation and etching steps have been carefully optimized to obtain textured silicon substrates, with randomly distributed Si (111) pyramids Fig. **23**. The preparation-induced surface micro-roughness and the density of electronically active defects have been reduced and significantly lower micro-roughness, densities of surface states and recombination loss at a-Si:H/c-Si interfaces have been achieved when compared to conventional pre-treatments.

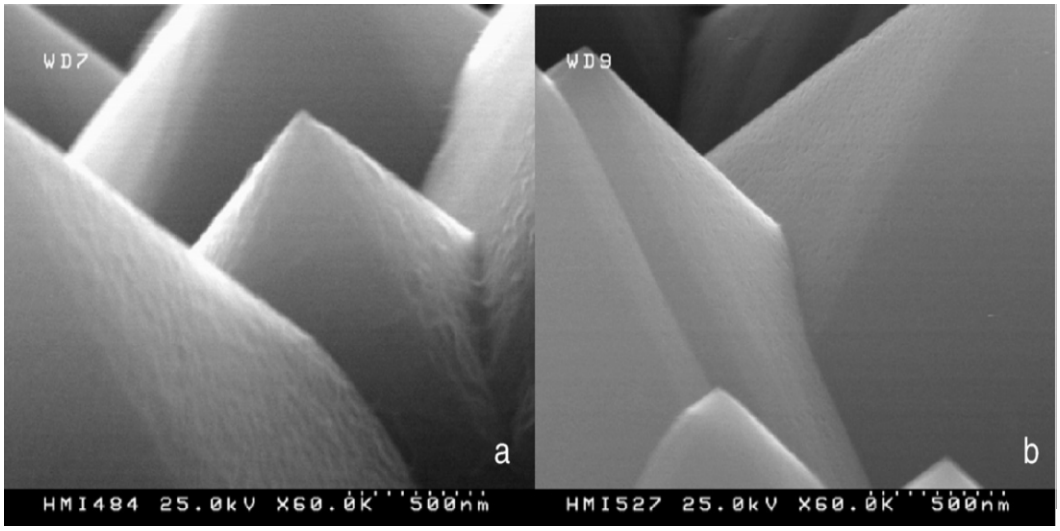


Figure 23: SEM micrographs (tilted by 30°) of silicon substrates with randomly distributed pyramids, (a) after H-termination by NH4F (48%), and (b) after subsequent wet-chemical oxidation in H2SO4/H2O2+HF dip (120 s). Reprinted with permission from Angermann *et al.* [30], Copyright (2008), Elsevier.

3.4. Growth Processes

The growth of device-grade thin film silicon remains an active research topic, and different thin film structures have been proposed for solar cell fabrication. On one side, there is microcrystalline silicon (μc-Si:H), at the other amorphous silicon (a-Si:H), and in between a complex mixture of crystalline grains and/or columns, disordered material, cracks and voids, whose detailed structure strongly depends on preparation conditions. Much progress has been made in the past few years regarding the material performance and preparation, using plasma enhanced chemical vapour deposition (PECVD) processes. Nevertheless, a better understanding of the growth mechanisms and of the influence of deposition parameters on the performance of the final device is necessary. For this, the study of morphological and structural properties can be useful.

Hydrogenated microcrystalline silicon thin films are produced mainly by chemical vapour decomposition of SiH_4+H_2gas mixtures, by means of different processes such as PECVD, Very High Frequency PECVD, Electron Cyclotron PECVD and Hot-wire PECVD. Structural studies using electron microscopies (SEM and TEM) and X-ray diffraction [32, 33 and references therein] have been used for the interpretation of the growth mechanisms. The characteristic features of the growth of this material are the pronounced columnar structure and an initial amorphous layer. It has been demonstrated that such films grow in complicated heterogeneous and anisotropic structures, which depend on the film thickness and on the substrate type. By using a proper choice of the deposition parameters (a high substrate temperature, a low deposition rate) it is possible to influence the columns growth strongly and to avoid the amorphous layer formation. In Fig. **24** the columnar growth is evidenced by SEM and TEM micrographs of microcrystalline silicon film by ECR-CVD on glass and on Si(111) from [32]: the images show for both the substrates a fibre-like arrangement of crystalline columns, separated by incoherent boundaries with little variation in the typical column size from bottom to top.

In [34] large area microcrystalline silicon films grown by ECR-CVD have been measured with XRD characterization in thin film configuration, using an incident angle of 0.5°.

Each peak of the diffraction pattern was fitted with a pseudo-Voigt function and the full weight half maximum, FWHM, was used to calculate the grain dimension through the Scherrer equation. The percentage of the amorphous phase was calculated as the fraction of the areas of the two overlapped peaks of the amorphous and crystalline phases at above 27.4° and 28.4°, respectively. In Fig. **25** the XRD spectra of two samples deposited at a substrate temperature of 218°C and at different microwave power (800 W and 360 W respectively) are shown. It is possible to observe for the sample deposited at a microwave power of 800 W, the typical diffraction pattern of (111), (220) and (311) crystalline silicon. In contrast, the sample deposited at 360 W exhibits a broad band, which is typical of an amorphous silicon structure. It has been observed that both substrate temperature and microwave power strongly influence the crystallinity fraction and the crystal dimensions. TEM images have been performed by an electron microscope operating at 200 kV: the data of crystal dimensions for several orientations extracted from XRD have been compared to the average ones obtained by TEM micrographs and the results showed a good consistency.

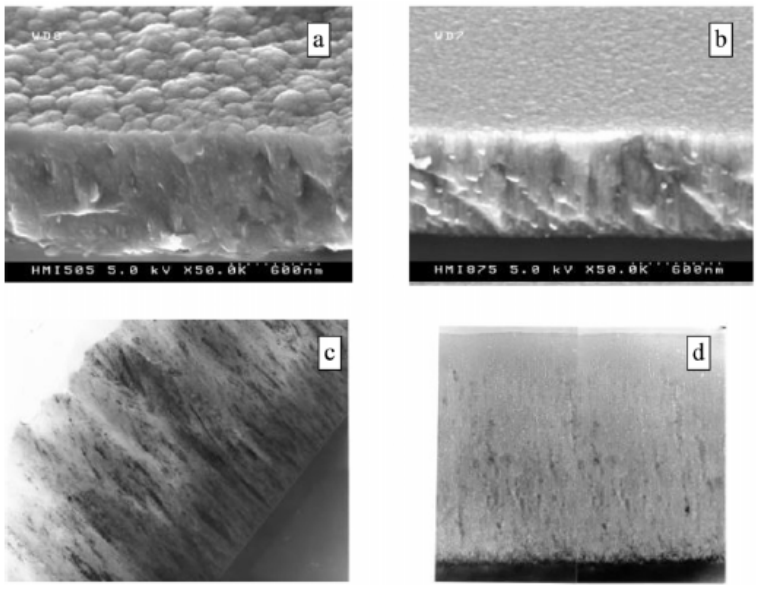


Figure 24: SEM pictures of fractional area of microcrystalline silicon film (a) on glass and (b) on Si(111) and cross-sectional TEM micrographs (c) on glass and (d) on Si(111). Reprinted with permission from Sieber *et al.* [32], Copyright (2002), Elsevier.

Finally, morphological characterization is very useful for the experimental observation of the grain shape evolution during growth (the term ‘grain’ denotes that, in microcrystalline silicon films, the aggregates are composed of nanometer sized subgrains). The shape of the grains is often studied by cross section TEM [35] but it has also been deduced from the AFM topography of different series of samples with varying thickness [36].

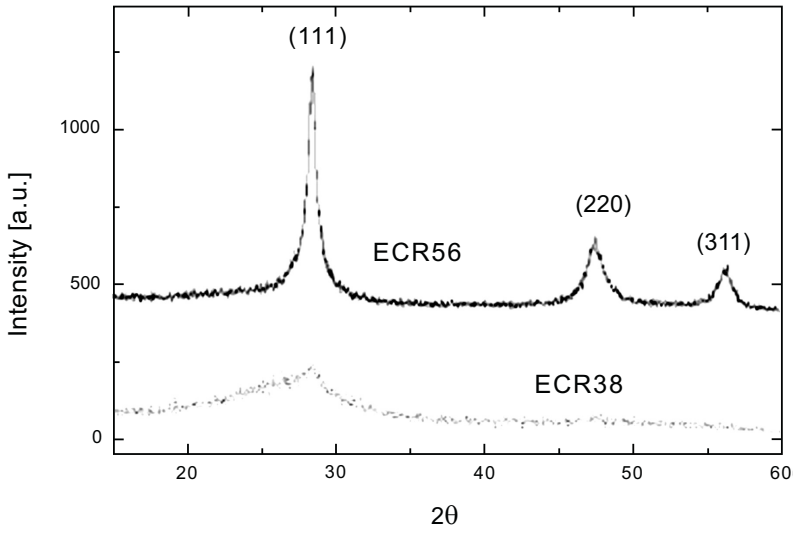


Figure 25: Typical X-ray diffraction patters of amorphous and microcrystalline silicon films grown by ECR-CVD at different power (800 W for ECR56 and 360 W for ECR38). Reprinted with permission from Ferrero *et al.* [34], Copyright (2001), Elsevier.

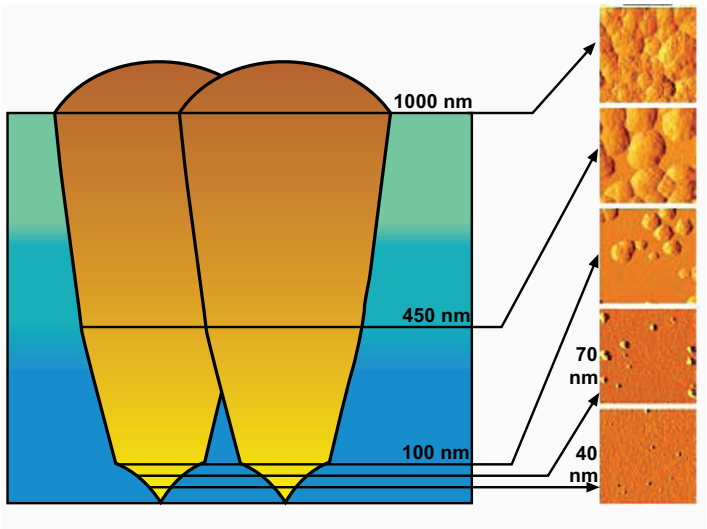


Figure 26: Schematic picture of the specific shape of crystal grains based on AFM topography of microcrystalline silicon films with varying thicknesses. Reprinted with permission from Fejfar *et al.* [36], Copyright (2004), Elsevier.

In Fig. **26**, an interesting example of a model for the grain evolution with the film thickness is shown, taken from [36]. It was observed that the grains evolve in two distinct stages: an expansion stage and later an elongation stage. The shape of the grain cap is spherical. At the largest thickness the grains already collide and fill the whole surface, and the remaining surface of the grain is spherical.

It was observed that the grains evolve in two distinct stages: an expansion stage and later an elongation stage. The shape of the grain cap is spherical. At the largest thickness the grains already collide and fill the whole surface, and the remaining surface of the grain is spherical.

3.5. Crystallization Processes of Amorphous Thin Films

The crystallization of silicon amorphous layers is a promising way for obtaining polycrystalline silicon thin films. Such films are of great interest for thin film transistors which are used in active matrix liquid crystal displays and active matrix organic light emission displays. They have also been employed for the fabrication of low-cost stable solar cells. By controling the parameters of the crystallization process as well as the structure, the composition and the thickness of the single layer, it is possible to control the resulting crystal and electronic quality of the polycrystalline film and thus the cell performance.

Different methods are used to develop thin poly-silicon films from amorphous silicon. These include annealing in the furnace, laser crystallization and rapid thermal annealing. Metal-induced crystallization has also been proposed to crystallize amorphous films at relatively low temperature: metals such as aluminium, nickel or palladium can lead to crystalline silicon grain formation of micrometric dimensions with considerable grain growth. In these grains the internal structure changes from the amorphous to crystalline structure resulting in a metal-induced phase transition.

The crystallization kinetics and the crystal quality of the films are studied by the combination of different techniques. These include Raman spectroscopy, Infrared absorption measurements, X-ray diffraction, optical, electronic and atomic force microscopies. In the following, some examples of morphological characterizations developed in order to understanding the crystal formation mechanisms will be examined. In Fig. **27** FESEM top-view images of amorphous silicon carbide (a-SiC:H) films with different C content are shown before and after laser annealing treatment [37, 38]. Although prior to laser treatment a weak increase in the roughness was noted with increasing carbon content, no substantial morphological differences were observed in the sample surfaces that appear quite smooth and homogeneous, as would be expected for amorphous films. By contrast, important morphological differences are observable in the images of the samples after the treatment, revealing the formation of structures on a sub-micrometric scale, which were attributed both to the presence of crystallites and of molten and re-solidified material. This is greatly influenced by the laser energy and the cooling velocity. Furthermore, the morphology of such structures appears to be strongly related to the carbon content, since the agglomerate dimensions appear to increase with x.

FESEM cross-sectional images of samples deposited on c-Si substrates, Fig. **28**, revealed that the crystallization process took place close to the top surface, and depended on the film composition. The depth of the annealed region increased with carbon content, and the topography changed from a compact, quite uniform crystalline zone to a structured region with agglomerates of increasing dimensions.

Atomic force microscopy (AFM) is often used to observe the surface morphology of the crystallized samples after annealing. In [39] a detailed investigation of laser crystallization of amorphous silicon thin films is presented which compares Raman spectroscopy and AFM results.

P-doping of the films strongly decreased the threshold of crystallization and a great deal of tensile stress remains as can be observed from the red-shift of the Raman peak intensity. Laser annealing at appropriate energy densities induces a considerable stress release and increases the crystalline fraction till to 82%. The disordered structure with defects induced by laser annealing were observed in AFM images and were found to be responsible for the degeneration of electron mobility in the film.

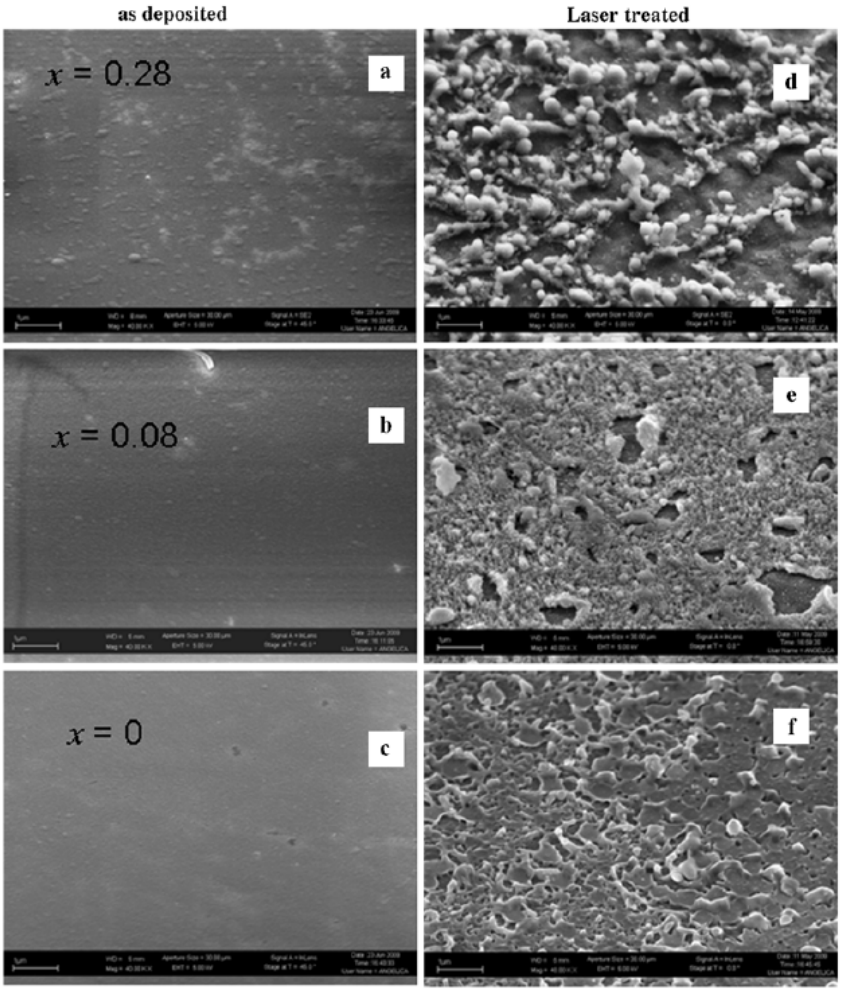


Figure 27: FESEM top-view images of a-SiC:H films with different C content, before and after laser treatment of the surface. Reprinted with permission from Coscia *et al.* [38], Copyright (2010), Elsevier.

In [40] annealed hydrogenated amorphous silicon films were analyzed using atomic force microscopy, Raman and FTIR spectroscopy. The crystalline formations and the shape of the film surfaces were found to be dependent on the annealing time as well as on the substrate employed during the deposition process.

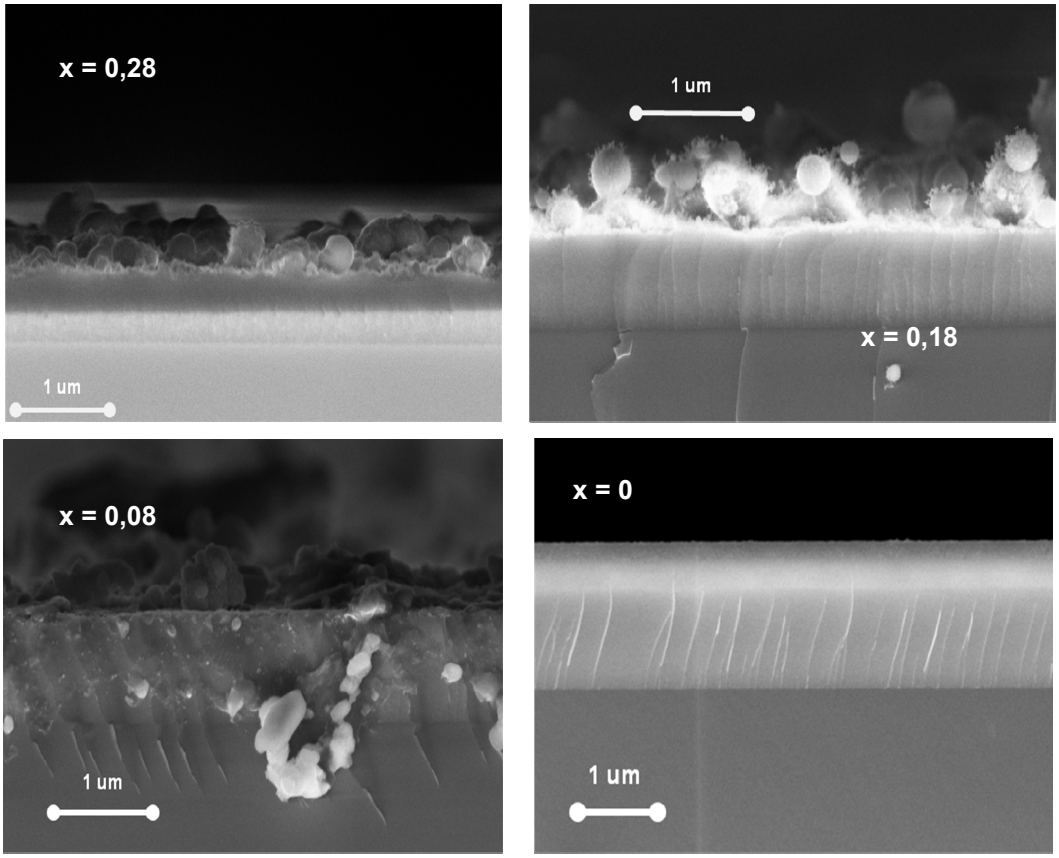


Figure 28: FESEM cross-section images of a-SiC:H films deposited on Si substrates with different C content, after laser treatment of the surface.

3.6. Advanced Nanostructures for New Concepts in Silicon Thin Film Solar Cells

In the design and fabrication of modern solar cells, different efforts are now being devoted to enhance the light absorption and to increase the efficiency. The different means currently in use are summarized under the term of "photon management". In particular, in amorphous silicon-based solar cells, the intrinsic low diffusion length of the holes limits the thickness of the light absorbing layers to a few hundred nanometers. As a consequence, these thicknesses are not sufficient for absorbing all incoming photons. Therefore, various modifications to the solar cell structure have been implemented. The main purpose is to elongate the path of the photons in the light absorbing layer and thus increase the absorption probability. Micro-and/or nanostructures are used, such as randomly textured surfaces, dielectric gratings, photonic crystals and suitably engineered metal nanostructures integrated to the cell designs [41].

All of the previously examined morphological characterization techniques have been proposed in order to study the nanostructured samples. Up to the present, the most compeling physical information about the existence of nanometric crystalline structures has been given by high

resolution transmission electron microscopy. The spacing of atomic lattice planes often apparent in such images also give clues to the associated chemical properties.

One example of how structures with nanoscale properties are used to increase the performance of thin film silicon solar cells is reported in [42]. Ultrathin film amorphous silicon solar cells were designed and constructed with nanostructured plasmonic back contacts. They demonstrated an enhanced short circuit current density compared to cells that had flat or randomly textured back contacts. The plasmonic light trapping patterns on the rear glass substrate have been made into a sol-gel silica layer by using substrate conformal imprint lithography. This layer was then overcoated with Ag and ZnO:Al to form the back contact. In Fig. **29** the SEM image of Ag overcoated patterns showing 290 nm diameter particles with 500 nm pitch is reported, while in Fig. **30** the comparison between the surface topography of nanopatterned and randomly textured solar cells is shown. Tapping-mode AFM images were obtained on the top ITO contacts for two cells.

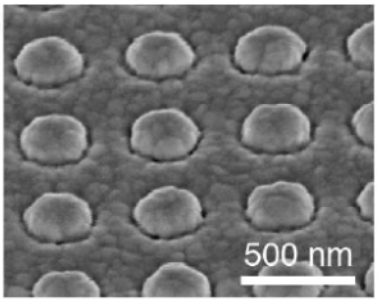


Figure 29: SEM image of plasmonic patterns employed in ultrathin amorohous silicon solar cells: 290 nm diameter particles with 500 nm pitch. Reprinted with permission from Ferry *et al.* [42], Copyright (2010), Optical Society of America.

The AFM scan on the plasmonic cell revealed the underlying nanopatterns that were imprinted into the sol-gel glass layer, and transferred to the back contact of the cell at a pitch of 500 nm. By contrast, the randomly textured Asahi glass showed an uncorrelated distribution of height variations.

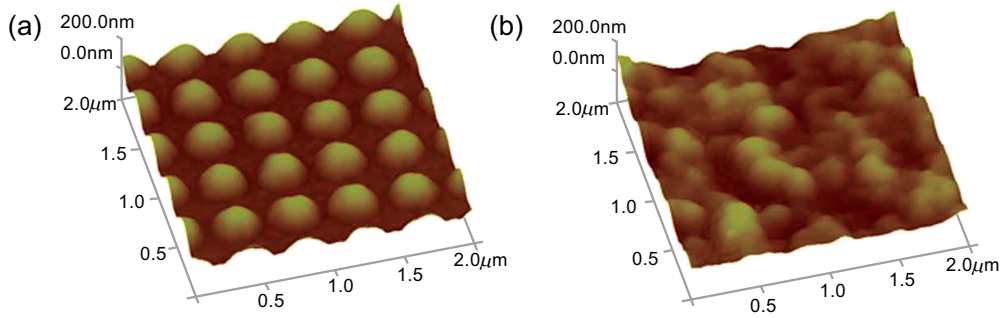


Figure 30: Surface topography of nanopatterned and randomly textured solar cells: (a) Patterned cell with 500 nm pitch, (b) Cell on randomly textured Asahi U-type glass substrate. Reprinted with permission from Ferry *et al.* [42], Copyright (2010), Optical Society of America.

In [43] a series of thin silicon films with different degrees of crystallinity were prepared by glow discharge. The crystallite size, shape, and the crystallinity fraction were investigated by high-resolution transmission electron microscopy (HRTEM), selected area electron diffraction (SAED), Raman spectroscopy (RS), and X-ray powder diffraction (XRD). The crystallite fraction and the average crystallite size calculated from both XRD and HRTEM images, reported in Fig. **31**, were in accordance with the results estimated from Raman spectra. The mutual agreement of the results obtained by completely different physical phenomena shows that the vibrational properties of the investigated material are directly influenced by nanometric crystallite sizes due to quantum confinement.

Finally nanoparticles which are confined in all three spatial dimensions, referred to as the quantum dots, have been implemented in various photovoltaic applications. Novel materials consisting of silicon nanocrystals embedded in a dielectric matrix have attracted considerable interest in the field of third generation photovoltaics. When Si nanocrystals are made very small (<7 nm in diameter), they behave as quantum dots due to the three-dimensional quantum confinement of carriers. In [44] Si quantum dots were formed by the alternate deposition of silicon oxide (SiO_2) and silicon-rich SiO_x with magnetron co-sputtering, followed by high-temperature annealing. The corresponding TEM images in both low and high magnification are reported in Fig. **32**.

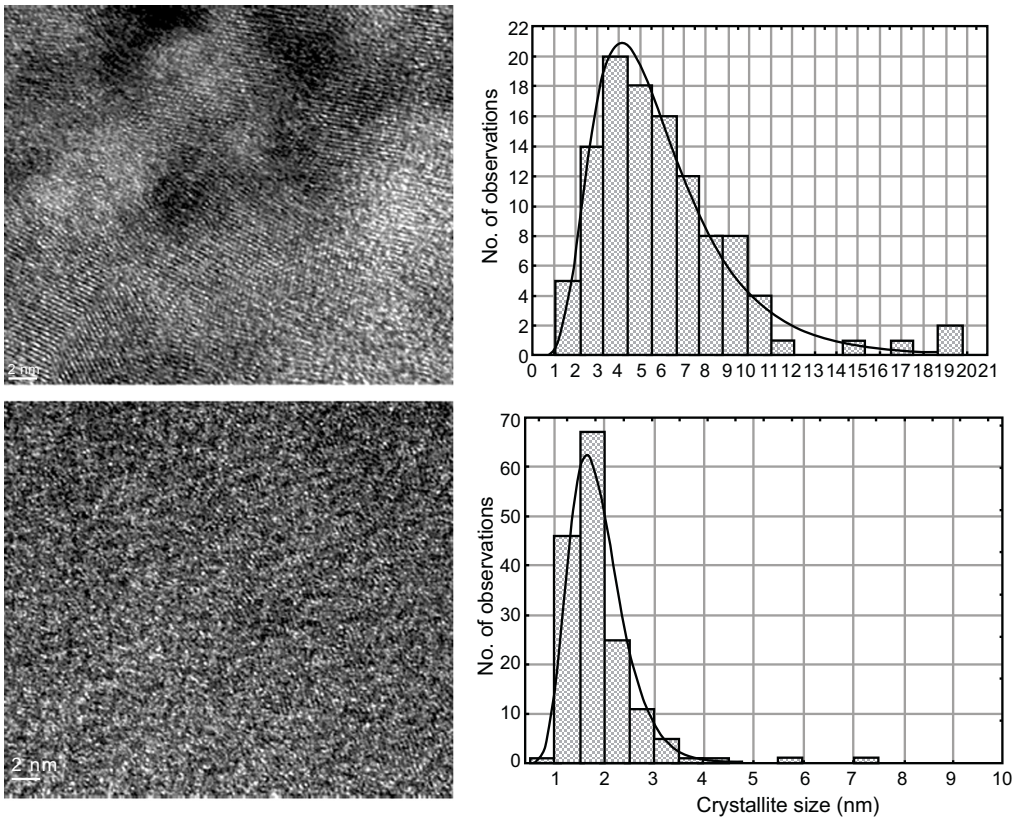


Figure 31: HRTEM images and distribution of the measured crystallite sizes fitted to log-normal distribution. Reprinted with permission from Gajovic *et al.* [43], Copyright (2008), Elsevier.

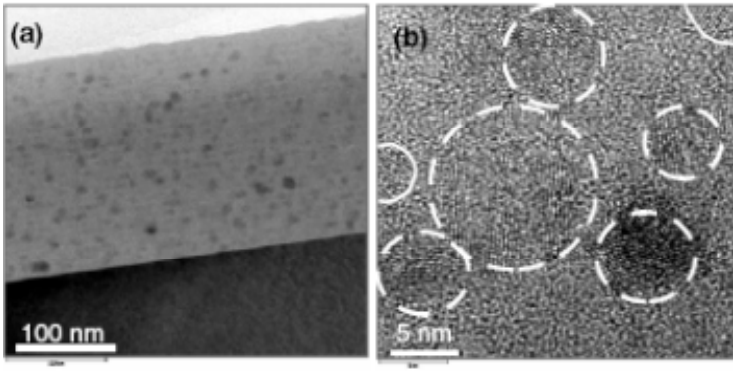


Figure 32: TEM images of Si QDs in a SiO2 matrix: (a) low-magnification image and (b) high-resolution image. Reprinted with permission from Cho *et al.* [44], Copyright (2008), IOP publishing.

ACKNOWLEDGEMENT

Declared none.

CONFLICT OF INTEREST

The author(s) confirm that this chapter content has no conflict of interest.

REFERENCES

[1] Goldstein J, Newbury D, Joy D, *et al.* Scanning Electron Microscopy and X-ray Microasnalysis. 3rd Ed. NY (USA): Springer 2003.
[2] Carl Zeiss NTS GmbH, Manual of Field Emission Scanning Electron Microscope, model Supra 40.
[3] Itakura M, Kuwano N, Sato K, *et al.* Variations in contrast of scanning electron microscope images for microstructure analysis of Si-based semiconductor materials. Journal of Electron Microscopy 2010; 59: S165-73.
[4] Williams DB, Barry Carter C. Transmission Electron Microscopy. A textbook for Material Science. 2nd Ed. NY (USA): Springer 2009.
[5] Binning G, Quate CF, Atomic Force Microscope. Physical Review Letter 1986; 56: 930-3
[6] Meyer E, Atomic Force Microscopy. Progress in Surface Science, 1992; 41: 3-49.
[7] Shahin V, Ludwig Y, Schafer C, *et al.* Glucocorticoids remodel nuclear envelope structure and permeability Journal of Cell Science 2005; 118: 2881-9.
[8] Cullity BD, Elements of X-Ray Diffraction. 2nd Ed., USA: Addison-Wesley Publishing Company Inc. 1978.
[9] Scherrer P. Bestimmung der Größe und der inneren Struktur von Kolloidteilchen mittels Röntgenstrahlen. Nachrichten von der Gesellschaft der Wissenschaften zu Göttingen. Mathematisch-Physikalische Klasse 1918; 2: 98-100.
[10] Williamson GK, Hall WH. X-ray line broadening from filed aluminium and wolfram. Acta Metallurgica 1953; 1: 22-31.
[11] Parashar A, Kumar S, Gope J, *et al.* Influence of argon dilution on growth and properties of hydrogenated nanocrystalline silicon films. Solar Energy Materials & Solar Cells 2010; 94: 892–9.
[12] Wang YH, Lin J, Huan CHA. Multiphase structure of hydrogenated amorphous silicon carbide thin films. Materials Science and Engineering 2002; B95: 43-50.

[13] Ambrosone G, Barucca G, Coscia U *et al.* Deposition of microcrystalline silicon–carbon alloys in low power regime. Journal of Non-Crystalline Solids 2004; 338–340: 163–7.

[14] Tao K, Zhang D, Zhao J *et al.* Low temperature deposition of boron-doped microcrystalline Si:H thin film and its application in silicon based thin film solar cells. Journal of Non-Crystalline Solids 2010; 356: 299–303.

[15] Herion J, Szot K, Ross C, *et al.* Towards a better understanding of surfaces of hydrogenated amorphous silicon: investigation by STM and AFM. Journal of Non-Crystalline Solids 1998; 227–230: 78-82.

[16] Stutzin GC, Ostrom RM, Gallagher AC *et al.* Nanoscale study of the as-grown hydrogenated amorphous silicon surface. J. Appl. Phys. 1993; 74: 91-100.

[17] Herion J, Szot K, Barzen S *et al.* AFM and STM investigations of hydrogenated amorphous silicon: topography and barrier heights. J. Anal. Chem. 1997; 358: 338-42.

[18] Yan B, Jiang C, Teplin CW *et al.* Local current flow in amorphous and microcrystalline mixed-phase silicon solar cells. Journal of Applied Physics 2007; 101: 033712 8.

[19] Yan B, Jiang CS, Yan Y *et al.* Effect of hydrogen dilution profiling on the microscopic structure of amorphous and nanocrystalline mixed-phase solar cells. Physica Status Solidi C 2010; 7: 513-6.

[20] Sundqvist J, Lu J, Ottosson M, Harsta A. Growth of SnO2 thin films by atomic layer deposition and chemical vapour deposition: A comparative study. Thin Solid Films 2006; 514: 63-8.

[21] De Graaf A, Van Deelen J, Poodt P *et al.* Development of atmospheric pressure CVD processes for high quality transparent conductive oxides. Energy Procedia 2010; 2: 41–8.

[22] Lien SY. Characterization and optimization of ITO thin films for application in heterojunction silicon solar cells. Thin Solid Films 2010; 518: S10–13.

[23] Addonizio ML, Antonaia A. Surface morphology and light scattering properties of plasma etched ZnO:B films grown by LP-MOCVD for silicon thin film solar cells. Thin Solid Films 2009; 518: 1026–31.

[24] Meier J, Spitznagel J, Kroll U *et al.* Potential of amorphous and microcrystalline silicon solar cells. Thin Solid Films 2004; 451-452: 518-24.

[25] Guha S, Yang J. Science and technology of amorphous silicon alloy photovoltaics. IEEE Trans. Electron. Dev. 1999; 46: 2080-4.

[26] Schropp REI, Li H, Rath JK, Van Der Werf CHM. Thin film nanocrystalline silicon and nanostructured interfaces for multibandgap triple junction solar cells. Surface and Interface Analysis 2008; 40: 970-3.

[27] La KC, Wang JH, Lu C *et al.* Plasma-induced TCO texture of ZnO:Ga back contacts on silicon thin film solar cells. Solar Energy Materials & Solar Cells 2011; 95: 415–8.

[28] Söderström T, Haug FJ, Terrazzoni-Daudrix V, Ballif C. Optimization of amorphous silicon thin film solar cells for flexible photovoltaics. Journal of Applied Physics 2008; 103: 114509.

[29] Korte L, Conrad E, Angermann H *et al.* Advances in a-Si:H/c-Si heterojunction solar cell fabrication and characterization. Solar Energy Materials & Solar Cells 2009; 93: 905–10.

[30] Angermann H, Korte L, Rappich J *et al.* Optimisation of electronic interface properties of a-Si:H/c-Si hetero-junction solar cells by wet-chemical surface pre-treatment. Thin Solid Films 2008; 516: 6775–81.

[31] Taira S, Yoshimine Y, Baba T *et al.* Our approaches for achieving HIT solar cells with more than 23% efficiency. Proceedings of the 22nd European Photovoltaic Solar Energy Conference, Milano (Italy), WIP-Renewable Energies; 2007; 932–5.

[32] Sieber I, Wanderka N, Kaiser I, Fuhs W. Electron microscopic characterization of microcrystalline silicon thin films deposited by ECR-CVD. Thin Solid Films 2002; 403-404: 543–8.

[33] Klein S, Finger F, Carius R *et al.* Intrinsic microcrystalline silicon prepared by hot-wire chemical vapour deposition for thin film solar cells. Thin Solid Films 2003; 430: 202–7.

[34] Ferrero S, Mandracci P, Cicero G *et al.* Large area microcrystalline silicon films by ECR-CVD. Thin Solid Films 2001; 383: 181-4.

[35] Fujiwara H, Kondo M, Matsuda A. Real-time spectroscopic ellipsometry studies of the nucleation and grain growth processes in microcrystalline silicon thin films. Physical Review B 2001; 63: 115306.
[36] Fejfar A, Mates T, Certik O *et al.* Model of electronic transport in microcrystalline silicon and its use for prediction of device performance. Journal of Non-Crystalline Solids 2004; 338–340: 303–9.
[37] Ambrosone G, Basa DK, Coscia U *et al.* Study on the excimer laser annealed amorphous hydrogenated silicon carbon films deposited by PECVD. Physica Status Solidi C 2010; 7: 770–3.
[38] Coscia U, Ambrosone G, Basa DK *et al.* Morphological and structural modifications induced in a-SiC:H films by excimer laser annealing. Applied Physics A 2010; 100: 1163–8.
[39] Jin J, Yuan Z, Huang L *et al.* Laser crystallization of amorphous silicon films investigated by Raman spectroscopy and atomic force microscopy. Applied Surface Science 2010; 256: 3453–8.
[40] Rojas-López M, Orduna-Díaz A, Delgado-Macuil R *et al.* a-Si:H crystallization from isothermal annealing and its dependence on the substrate used. Materials Science and Engineering B 2010; 174: 137–40.
[41] Derkacs D, Lim SH, Matheu P *et al.* Improved performance of amorphous silicon solar cells *via* scattering from surface plasmon polaritons in nearby metallic nanoparticles. Applied Physics Letters 2006; 89: 093103.
[42] Ferry VE, Verschuuren MA, Li HBT *et al.* Light trapping in ultrathin plasmonic solar cells. Optics Express 2010; 18: A237-45.
[43] Gajovic A, Gracin D, Djerdj I *et al.* Nanostructure of thin silicon films by combining HRTEM, XRD and Raman spectroscopy measurements and the implication to the optical properties. Applied Surface Science 2008; 254: 2748–54.
[44] Cho E, Park S, Hao X *et al.* Silicon quantum dot/crystalline silicon solar cells. Nanotechnology 2008; 19: 245201.

Send Orders of Reprints at reprints@benthamscience.net
Silicon Based Thin Film Solar Cells, 2013, 177-242

CHAPTER 7

Optical Properties of Semiconductors

Marian Nowak*

Institute of Physics, Silesian University of Technology, 8 Krasińskiego, Katowice, PL-40019, Poland

Abstract: Optical properties of semiconductors, dielectrics and metals play a key role in the development of thin film solar cells. While these devices belong to photon photodetectors both the photon and wave nature of light affects their performance. Some of these problems are discussed in this chapter. The efficiency of photogeneration of free carriers by light as well as its spatial distribution is taken into consideration. This distribution is strongly affected by light interfering in a structure of many thin films. The possible geometrical and optical inhomogeneities of the solar cell structure are discussed. A few methods of determining surface and averaged overall film thickness refractive indices of semiconductor materials are presented. Techniques for determining different components of absorption of light in semiconductors are also reported. Examples of optical methods useful for determining essential parameters of semiconductors (*e.g.*, optical energy gap, carrier diffusion length, and parameters of electron states) are presented as well.

Keywords: Semiconductors, transmittance, reflectance, quantum efficiency of photogeneration, linear distribution of intensity of reflected and transmitted radiation, graded energy gap semiconductor, optical properties of multilayer structure, amorphous silicon, refractive index, absorption coefficient, spatial distribution of radiation intensity, photogeneration of free carriers, recombination, electronic states parameters, steady state photocarrier grating, photoconductivity, photoelectromagnetic effect, optical inhomogeneity.

1. INTRODUCTION

While solar cells belong to photon detectors, both the photon and wave nature of light affects their performance. Therefore when optimizing the features of these devices different optical phenomena-for example, the penetration of light into a semiconductor, the spatial distribution of radiation in it (sometimes the cell can be equivalent to the so-called resonant cavity), and the efficiency of photogeneration of free carriers - must be taken into account. Construction of solar cells usually requires structure of many films. The radiation is divided into reflected and transmitted parts each time the beam strikes an interface (Fig. **1**).

To describe the optical phenomena mentioned above the following parameters are involved: coefficient of reflectivity of light; real part of refractive index of the investigated material, and absorption and scattering coefficients of light as well as quantum efficiency coefficients (QECs) for photogeneration of free electrons and holes. These parameters are discussed in many textbooks on optics (*e.g.* [1,2]) and semiconductors (*e.g.* [3,4]), as well as in monographs on photoelectric effects (*e.g.* [5,6]) and experimental methods of semiconductor investigations (*e.g.* [7-10]).

***Address correspondence to Marian Nowak:** Institute of Physics, Silesian University of Technology, 8 Krasińskiego, Katowice, PL-40019, Poland; Tel: 48-326034167; E-mail: marian.nowak@polsl.pl

Roberto Murri (Ed)
All rights reserved-© 2013 Bentham Science Publishers

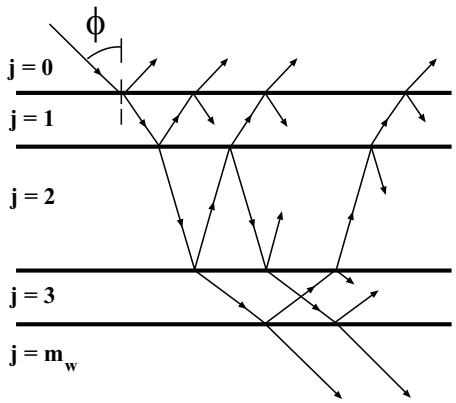


Figure 1: Scheme of radiation propagation in a multilayer structure of a semiconductor and dielectric films.

The aim of this paper is to describe special aspects of the influence of optical and geometrical inhomogeneities on spatial distribution of light in a multilayer structure of semiconductor and dielectric films. Several techniques useful for determining surface and bulk values of optical parameters are reviewed. Methods applied to distinguish between different components of absorption of light in semiconductors are reported as well. To enhance efficiency of solar cells one should control, among others aspects, the carrier diffusion length and parameters of electron states in energy gap of the used semiconductor. Therefore, some optical methods suitable for determining these parameters are presented.

Owing to the limited length of this paper, the optical properties of the quantum nanostructures (*e.g.* [11,12]) as well as the Raman scattering (*e.g.* [13]), IR absorbance (*e.g.* [14]), luminescence (*e.g.* [15]), electroreflectance and electroabsorption (*e.g.* [16]) are not presented. Nor are the properties of anisotropic films (*e.g.* [17,18]) and radiative recombination of electrons and holes (*e.g.* [19,20]) reviewed in this chapter.

2. OPTICAL PARAMETERS OF SEMICONDUCTORS

Complex refractive index $N_j = n_j - i\kappa_j$ (where i=$\sqrt{-1}$) is the main optical parameter of a semiconductor. The real part of this index represents the ratio of electromagnetic wave velocities in a vacuum and in the investigated material [1]. The extinction coefficient κ_j describes the attenuation of the electric field of the wave in the material and determines the absorption coefficient of light

$$\alpha_j = \frac{4\pi\kappa_j}{\lambda} \quad \textbf{(1)}$$

where λ is the wavelength of radiation. The value of the last parameter is an inverse of the material thickness that makes an intensity of light *e*-times smaller.

It should be noted that sometimes absorption of light is described by optical density of a sample (also called absorbance)

$$A_{10} = log\left(\frac{I_0}{I}\right) = log\left(\frac{1}{T_o}\right) = -logT_o \quad \textbf{(2)}$$

where I is the transmitted light intensity, I_0 is the incident light intensity, and T_o represents the transmittance coefficient. The logarithm to the base of 10 applied here is commonly used in chemistry, while physicists usually adopt the natural logarithm.

According to the Bouguer-Lambert law

$$I = I_0 e^{-\alpha_j w_j} \quad \textbf{(3)}$$

the absorbance is proportional to the sample thickness w_j and the absorption coefficient α_j. Therefore, one can find

$$\alpha_j = \frac{2.303}{w_j} A_{10} \quad \textbf{(4)}$$

It should be noted that absorptance (not absorbance) is defined as the ratio of absorbed to incident radiation.

In some cases the complex refractive index is represented by the real (ε_j') and imaginary (ε_j'') parts of the complex electric permittivity

$$N_j = \sqrt{\varepsilon_j^{'} - i\varepsilon_j^{''}} \quad \textbf{(5)}$$

The Kramers–Kronig formulae are often used to relate the real and imaginary parts of refractive index. Therefore, one can find [3]

$$n_j(\mathrm{h\nu}) = 1 + \frac{ch}{2\pi^2} \mathrm{P} \int_0^{+\infty} \frac{\alpha_j(E^{'})}{(E^{'})^2 - (h\nu)^2} dE^{'} \quad \textbf{(6)}$$

where Ƥ denotes the Cauchy principal value, hν is photon energy, c is the light velocity in vacuum, and h is the Planck constant. One can estimate spectrum of n_j in the range of strongly absorbed radiation from the known, full spectrum of light absorption.

Sometimes, values of optical parameters are described by the effective medium theory (EMT) as functions of the volume fractions V_j of j components in a matrix [21, 22]

$$\sum_j V_j \frac{\varepsilon_j^{'} - \varepsilon_x^{'}}{\varepsilon_j^{'} + 2\varepsilon_x^{'}} = 0 \quad \textbf{(7a)}$$

$$\alpha_x = \sum_j V_j \alpha_j \quad \textbf{(7b)}$$

where ε_x' and α_x are so-called effective values of parameters for composite material. In the case of a rough surface one of the components is the surrounding ambient and the other one is consistent with the film material.

2.1. Absorption Coefficient

The measured absorption coefficient (α_{exp}) usually is a sum of the (true) optical absorption coefficient (α_{aj}) and the scattering coefficient (α_{sc}) [22]

$$\alpha_{exp} = \alpha_{aj} + \alpha_{sc} \quad \textbf{(8)}$$

where α_{sc} has units of inverse length (m^{-1}). Despite the method presented in [22], the values of α_{aj} and α_{sc} can be determined using the diffuse reflectance (DRS) and the diffuse transmittance (DTS) spectroscopy [23]. When a material, consisting of many particles, or nanoparticles, is illuminated, some of the impinging radiation penetrates the sample and some is reflected from its surface. The portion that penetrates the sample is scattered at a large number of points in its path as well as transmitted through the particles a number of times. Only the part of this radiation that is returned to the surface of the sample and comes back out is considered to be diffuse reflection [24]. DRS is a suitable, non-destructive, and simple method of investigation, especially important in examinations of porous, nanocrystalline materials and gels [25]. It is impossible to examine such materials applying specular reflection and it is also extremely difficult to determine their path length in an optical transmittance. The following factors are related to high spectral quality of diffuse reflectance: dilution of the sample with a nonabsorbing matrix ensures a deeper penetration of the incident beam into the sample, which increases the contribution of the scattered component in the spectrum and minimizes the specular reflection component; and smaller particles improve the quality of DRS spectra.

The diffuse reflectance $R_d = I_{dif}/I_{stand}$ (the ratio of intensities of radiation reflected in a diffuse manner from the sample and from the known standard) can be converted to the Kubelka-Munk function [24]

$$F_{KM} = \frac{(1-R_d)^2}{2R_d} = \frac{\alpha_{aj}}{\alpha_{sc}} \quad \textbf{(9)}$$

In some cases, α_{sc} is constant (*e.g.* when thickness of the sample is much bigger than the individual particle [9]). The advantage of the Kubelka-Munk model is that the scattering and absorption coefficients may be directly expressed in terms of the measured R_d and a diffuse transmittance (T_d, *i.e.* the ratio of intensity of radiation transmitted in a diffuse manner through a sample, and I_0) [23]

$$\alpha_{sc} = \frac{1}{w_j A_y} ln\left[\frac{1-R_d(A_x-A_y)}{T_d}\right] \quad \textbf{(10a)}$$

$$\alpha_{aj} = (A_x - 1)\alpha_{sc} \quad \textbf{(10b)}$$

where $A_x = \frac{1+R_d^2-T_d^2}{2R_d}$ and $A_y = \sqrt{A_x^2 - 1}$.

Various mechanisms of absorption of electromagnetic radiation can be observed in semiconductors, *e.g.* direct allowed (α_{Da}) or direct forbidden (α_{Df}) absorption, indirect allowed absorption with absorption and/or emission of phonons (α_{Ia}), indirect forbidden absorption (α_{If}), Tauc

absorption (α_T), Urbach ruled absorption (α_U), free carrier absorption (α_F), exciton absorption, intraband absorption, impurity absorption, lattice absorption, *etc.* (*e.g.* [3,4,26,27])

$$\alpha_{Da} = A_{Da}\sqrt{\mathrm{h}\nu - E_{gDa}} \text{ for } \mathrm{h}\nu \geq E_{gDa} \quad \textbf{(11a)}$$

$$\alpha_{Df} = \frac{A_{Df}}{\mathrm{h}\nu}\left(\mathrm{h}\nu - E_g\right)^{3/2} \text{ for } \mathrm{h}\nu \geq E_{gDf} \quad \textbf{(11b)}$$

$$\alpha_{Ia} = A_{Ia}\frac{\left(\mathrm{h}\nu - E_{gIa} + E_{ph}\right)^2}{exp\left(\frac{E_{ph}}{k_B T}\right) - 1} \text{ for } \mathrm{h}\nu \leq E_{gIa} \quad \textbf{(11c)}$$

$$\alpha_{Ia} = A_{Ia}\left[\frac{\left(\mathrm{h}\nu - E_{gIa} + E_{ph}\right)^2}{exp\left(\frac{E_{ph}}{k_B T}\right) - 1} + \frac{\left(\mathrm{h}\nu - E_{gIa} - E_{ph}\right)^2}{1 - exp\left(-\frac{E_{ph}}{k_B T}\right)}\right] \text{ for } \mathrm{h}\nu > E_{gIa} \quad \textbf{(11d)}$$

$$\alpha_{If} = A_{If}\left(\mathrm{h}\nu - E_{gIf}\right)^3 \text{ for } \mathrm{h}\nu \geq E_{gIf} \quad \textbf{(11e)}$$

$$\alpha_T = \frac{A_T}{\mathrm{h}\nu}\left(\mathrm{h}\nu - E_g\right)^2 \text{ for } \mathrm{h}\nu \geq E_g \quad \textbf{(11f)}$$

$$\alpha_U = A_U exp\left(\frac{\mathrm{h}\nu}{E_U}\right) \quad \textbf{(11g)}$$

$$\alpha_F = A_F \lambda^2 \quad \textbf{(11h)}$$

where E_{gDa} and E_{gIa} are direct and indirect allowed energy gaps (*e.g.* [3,4]), E_{gDf} and E_{gIf} are direct and indirect forbidden energy gaps (*e.g.* [3,4]), E_g is the Tauc energy gap in an amorphous semiconductor [26], E_{ph} is phonon energy (in general, the absorption can simultaneously involve phonons of different energies [28]), E_U is so-called Urbach energy (that represents the widths of the exponential tail in the Urbach spectral dependence of absorption coefficient [27]), A_{Da}, A_{Df}, A_{Ia}, A_T, A_U, and A_F are constants.

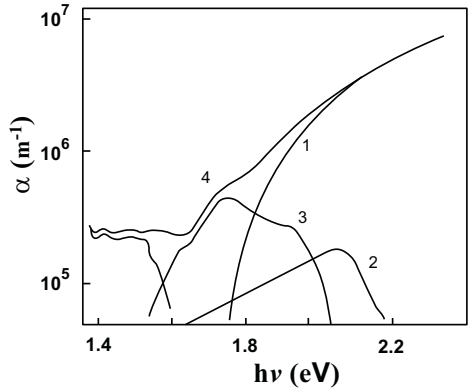


Figure 2: Spectral dependence of absorption coefficient of radiation of a-Si:H,F thin film [29] (1, $\boldsymbol{\alpha_T}$; 2, $\boldsymbol{\alpha_U}$; 3, coefficient estimated for extrinsic photogeneration of carriers; 4, total absorption coefficient estimated from the optical transmittance of the film).

Various mechanisms of absorption of light can be observed in semiconductors; some of these can coexist in the same spectral range (Fig. **2**). The optical properties of amorphous semiconductors are dominated by the presence of a tail on the optical absorption which falls into the spectral region which is normally transparent in crystals. This tail is attributed to the presence of localized electronic states near the band edges in the amorphous semiconductors. Above the tail the absorption remains high due to the presence of interband electronic transitions identical to those which occur in crystals. Absent, however, are the singularities which are the result of the band structure in crystalline semiconductors. Rather, the amorphous materials exhibit much smoother absorption spectra in the interband region (Fig. **2**).

Therefore, the total absorption coefficient should be described as follows:

$$\alpha_{aj} = \sum_l \alpha_l \tag{12}$$

where α_l describes various mechanisms of light absorption. A very important question is the mechanism of light absorption in a semiconductor. One of the best methods to determine it and the energy gap of the semiconductor is to perform the multiabsorption fitting of the spectrum of absorption coefficient (*e.g.* [25,30]). In this procedure one minimizes the following least square function

$$\chi^2 = \sum_i \left[\alpha_{aj}(h\nu_i) - A_\alpha \sum_l \alpha_l(h\nu_i)\right]^2 \tag{13}$$

where i represents photons of different energy, α_l describes various mechanisms of light absorption (*e.g.* Eq. (11)), and A_α is the proportionality factor.

The different components in the total absorption coefficient as well as in refractive index are distinguishable due to their different spectral dependences (*e.g.* Eq. (11)), and due to their different influences on various optical and photoelectromagnetic (PEM) effects. Review [6] describes the first-order PEM phenomenon which causes electromotive force parallel to the illuminated surface of a semiconductor owing to the charge separation by the magnetic field, of photogenerated carriers diffusing because of their different concentrations in various parts of a sample. This effect depends strongly on wavelength, intensity and polarization of radiation and magnetic field induction, as well as on the individual properties of the material investigated, and the configuration of the sample relative to the direction of applied magnetic field and optical illumination [6].

Contrary to photoconductivity (PC), the PEM effect occurs essentially in the case of interband (intrinsic) photoexcitation of electrons and holes. Therefore, PC and the PEM effect have attracted considerable interest as potential tools in investigations of many problems related to the fundamental properties of semiconductors [6]. They have been studied not only in many crystalline semiconductor materials but also in amorphous silicon. The first observation of PEM effect in a-Si:H, and the use of it for estimation of carrier mobility and lifetime, was reported by Moore [31].

2.2. Determination of Optical Parameters Using QECs of Carrier Photogeneration

In general, the PC and PEM responses are proportional to the following effective QECs for photogeneration of free carriers [6,29]

$$\beta_{PC} = \frac{\mu_e\tau_e\beta_e+\mu_h\tau_h\beta_h}{\mu_e\tau_e+\mu_h\tau_h} \quad \textbf{(14a)}$$

$$\beta_{PEM} = \frac{n_h\tau_e\beta_e+n_e\tau_h\beta_h}{n_h\tau_e+n_e\tau_h} \quad \textbf{(14b)}$$

where μ_e and μ_h are drift mobilities of electrons and holes, τ_e and τ_h represent lifetimes of photogenerated electrons and holes, n_e and n_h are electron and hole concentrations, and β_e and β_h are QECs for photogeneration of electrons and holes. In the case of an extrinsic semiconductor, measurements of PC has yielded information about the majority carriers because of trapping of the minority carriers (semi-insulating GaAs may be a rare exception). PEM effect is connected with a diffusion process, so it is controlled by the transport and recombination parameters of the minority carriers. Therefore, in the case of a strongly doped p-type semiconductor, the QEC for photogeneration of holes can be determined using the PC data

$$\beta_h = \frac{\alpha_h}{\alpha_{aj}}\eta \quad \textbf{(15a)}$$

where α_h describes absorption processes in that free holes are photogenerated, and η is the number of carriers generated by one photon (η can be greater than one in the case of photon energies greater than the energy gap of the investigated semiconductor). In the case of PEM investigations in the same p-type semiconductor, the QEC for photogeneration of electrons can be determined

$$\beta_e = \frac{\alpha_e}{\alpha_{aj}}\eta \quad \textbf{(15b)}$$

where α_e represents the absorption processes in that free electrons are photogenerated.

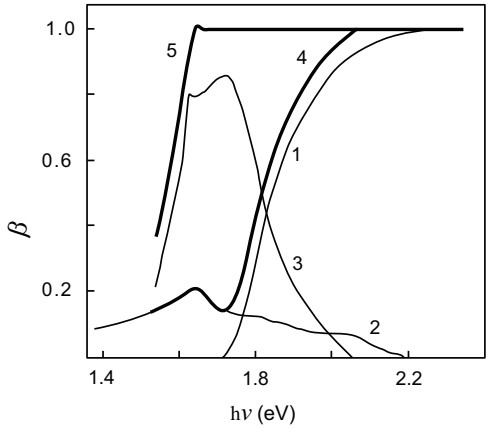


Figure 3: Spectral dependence of quantum efficiency coefficients of radiation of a-Si:H,F thin film [29] (1, coefficient calculated with the assumption that free carriers are photogenerated due to Tauc absorption; 2, coefficient calculated with the assumption that free carriers are photogenerated due to Urbach ruled absorption; 3, coefficient calculated for extrinsic photogeneration of carriers; 4, $\boldsymbol{\beta_{PEM}}$; 5, $\boldsymbol{\beta_{PC}}$).

The values of β_{PC} and β_{PEM} (Fig. **3**) can be evaluated by applying normalized ratios of the measured responses to the theoretically evaluated values

$$\beta_{PC}(h\nu) = \frac{\sigma_{PCexp}(h\nu)}{\sigma_{PC}(h\nu)} \quad \textbf{(16a)}$$

$$\beta_{PEM}(h\nu) = \frac{i_{PEMexp}(h\nu)}{i_{PEM}(h\nu)} \quad \textbf{(16b)}$$

where $\sigma_{PCexp}(h\nu)$ and $i_{PEMexp}(h\nu)$ are the measured photoconductivity and short-circuited current evoked by the PEM effect. The $\sigma_{PC}(h\nu)$ and $i_{PEM}(h\nu)$ are calculated for the values of sample parameters obtained by fitting the experimental results with appropriate theoretical formulae in the range of a known or very probable value of the QEC (usually, it is assumed that β_{PC}=1 and β_{PEM}=1 for photon energies slightly higher than that for which $\sigma_{PCexp}(h\nu)$ and $i_{PEMexp}(h\nu)$ attain maxima, see [29,32,33]).

Using Eq. (14b), the determined values of $\beta_{PEM}(h\nu)$, and the values of total absorption coefficients (derived from optical transmittance), one can calculate the absorption coefficients describing intrinsic photogeneration of carriers [29]. Fig. **3** presents the differences in the intrinsic and extrinsic spectra of QECs of radiation of a-Si:H,F thin film. If the values of $\beta_{PEM}(h\nu)$ are subtracted from $\beta_{PC}(h\nu)$, one obtains the values of QECs for the extrinsic photogeneration of free carriers [29]. Using these values, one calculates absorption coefficients related to extrinsic photogeneration of carriers (Fig. **2**).

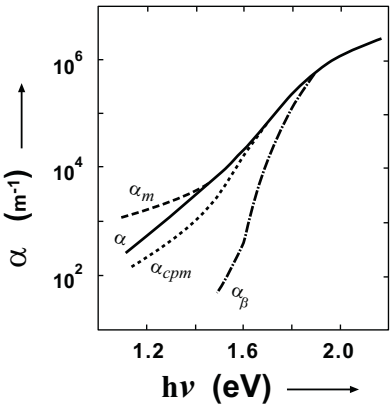


Figure 4: Comparison of the spectra of absorption coefficients derived using optical transmittance ($\boldsymbol{\alpha}$), the CPM method ($\boldsymbol{\alpha_{cpm}}$), the method of Moddel *et al.* [37] ($\boldsymbol{\alpha_m}$) and the quantum efficiency coefficient ($\boldsymbol{\alpha_\beta}$) [32].

Contrary to traditional methods that are reliable only for larger values of α_{aj}, the PC and PEM methods are especially convenient to determine the low sub-band-gap absorption related to the density of state (DOS) distribution in the mobility gap of an amorphous semiconductor [34]. Fig. **4** shows the values of absorption coefficients derived using the optical transmittance method, the constant photocurrent method (CPM) [35,36], the method proposed by Moddel *et al.* [37], and the quantum efficiency coefficient. The absorption coefficients for weakly absorbed radiation can be determined applying classical CPM method

$$\alpha_{cpm} = \frac{A_{cpm}}{I_f} \quad \textbf{(17)}$$

where A_{cpm} represents a constant normalized for a known value of absorption coefficient (obtained from optical transmittance measurements, see Fig. **4**), and I_f is illumination intensity (in photons) that assures a constant photocurrent flowing through a sample for different values of photon energies.

The method of Moddel *et al.* [37] allows one to determine another absorption coefficient for weakly absorbed radiation

$$\alpha_m = \alpha_{0m} \frac{I_{0m}}{I_0} \left(\frac{\sigma_{PCexp}}{\sigma_{mPCexp}} \right)^{1/\zeta} \quad \textbf{(18)}$$

where σ_{PCexp} represents photoconductivity measured for light intensity I_0 (in photons). Subscript $0m$ refers to reference photon energy at which the α_{0m} is directly measured (in optical transmittance measurements, see Fig. **4**). The ζ is a power coefficient in the semi-empirical power-law formula

$$\sigma_{PCexp} = \mathrm{a}_{PC} I_0^{\zeta} \quad \textbf{(19)}$$

where a_{PC} is the proportionality factor.

The evaluated values of α_{cpm} and α_m are different from the values of α_β. However, it should be emphasized that they were evaluated without taking into account the possible influence of excess carrier concentration on recombination processes in the semiconductor. It must be noted that the optical energy gap increases with the electron concentration in the material (Burnstein-Moss shift). Hence, the energy-gap gradient can be caused by strong illumination of the sample [38]. Such illumination of a semiconductor can influence its optical parameters, too.

It should be emphasized that the PC and PEM methods can be used not only for measurements of absorption coefficients but also for investigations of real parts of refractive indices and thicknesses of dielectric films that cover the semiconductors (*e.g.* [6,39,40]). For example, the ratio of PEM responses, in the cases of oblique sample illumination with plane polarized radiation that has electric vector in and normal to the plane of incidence, is equal to the ratio of the intensities of variously polarized radiation which enters a sample. If the radiation intensity is low, this ratio of PEM responses is independent of the parameters of carriers in a semiconductor (*e.g.*, mobilities, lifetimes, and surface recombination velocities of carriers), and provides information on optical parameters of the investigated material. The ratio of PME responses for variously polarized radiation is independent of the distribution of light intensity over a sample surface. Hence, the spot-light method of PME investigation can be used for determining local properties of the sample [6].

Measurements of the ratio of PEM responses for plane polarized radiation were used [40] to determine values of refractive indices of SiO_2 surface layers obtained by thermal oxidation of (100) oriented silicon in different gases (Fig. **5**). Such measurements are complementary to ellipsometry [7] but they should be more effective in investigations of samples with surface texturing (see Chapter 9 in this volume) because the intensity of radiation that enters a semiconductor through the investigated surface layer can be immediately determined.

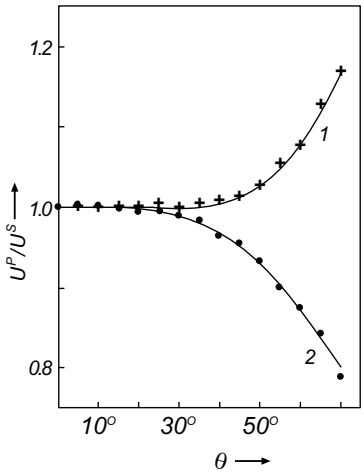


Figure 5: Ratio of PEM responses for plane polarized radiation with electric vector in and normal to the plane of incidence *versus* angle of radiation incidence for different thicknesses of the surface film of SiO_2 on n-type, (100) oriented Si, obtained by thermal oxidation in O_2 with *2%* HCl [40] (●, $\boldsymbol{w_1}$=*121.5 nm*; +, $\boldsymbol{w_1}$=94 nm. Solid curves represent the theoretical dependences for different values of thickness and refractive index of the film: (1) $\boldsymbol{w_1}$=94 nm, $\boldsymbol{n_1}$=1.49; (2) $\boldsymbol{w_1}$=127.5 nm, $\boldsymbol{n}$=1.43, $\boldsymbol{\lambda}$=632.8 nm, $\boldsymbol{n_2}$(Si)= 3.9, $\boldsymbol{\kappa_2}$(Si)=0.02).

The need for electrical contacts is the main disadvantage of the known PC and PEM methods of measurements of the optical parameters (see, *e.g.* [39,40]). However, it is interesting to explore the application of contactless methods of PEM investigations (*e.g.* [41,42]) to determine the refractive indices of more sophisticated coating layers of solar cells.

2.3. Interfaces and Optical Inhomogeneity

The technology of the deposition process as well as the physical and chemical properties of the substrate can strongly influence values of optical parameters of thin films. Values of a real part of the refractive index and absorption coefficient can change substantially with the depth in a thin semiconductor film, *e.g.*, in the amorphous silicon (a-Si) films [43,44]. The changes are particularly great near the interfaces' air-semiconductor film and semiconductor-substrate. In so-called graded-gap semiconductors, for example in $Si_{1-x}Ge_x$ structures with a position dependent energy band-gap [45,46], the values of optical parameters are also strongly dependent on the position in a sample.

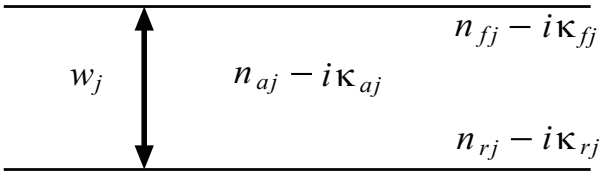


Figure 6: Scheme of a semiconductor film with optical inhomogeneity (description in the text).

The optical inhomogeneity of the j film with thickness w_j (Fig. **6**) can be characterized by different refractive indices N_{fj}=$n_{fj} - i\kappa_{fj}$ and N_{rj}=$n_{rj} - i\kappa_{rj}$ at front and rear surface [47], as well as by refractive index N_{aj}=$n_{aj} - i\kappa_{aj}$ averaged through the film thickness

$$n_{aj} = \frac{1}{w_j}\int_0^{w_j} n_j(y)dy \quad \textbf{(20a)}$$

$$\kappa_{aj} = \frac{1}{w_j}\int_0^{w_j} \kappa_j(y)dy \quad \textbf{(20b)}$$

where y represents depth in the j film, $n_j(y)$ and $\kappa_j(y)$ are the local values of a real part of refractive index and extinction coefficient. The values of n_{aj} and κ_{aj} determine the change in phase and intensity of the radiation transmitted through the film.

Values of $n_{fj} - i\kappa_{fj}$ and $n_{bj} - i\kappa_{bj}$ affect the Fresnel reflection and transmission coefficients (*i.e.*, ratios of electric fields of reflected/incident and transmitted/incident radiation) at an interface. Thus they determine intensity and phase of the radiation reflected and transmitted through the appropriate interface. For front illumination [from (j-1) to j medium] these coefficients are given by

$$r_{sj} = \frac{\left(a_{r(j-1)} - ib_{r(j-1)}\right) - \left(a_{fj} - ib_{fj}\right)}{\left(a_{r(j-1)} - ib_{r(j-1)}\right) - \left(a_{fj} - ib_{fj}\right)} = \left|r_{sj}\right| e^{-i\varphi_{sj}} \quad \textbf{(21a)}$$

$$r_{pj} = \frac{N_{r(j-1)}^2\left(a_{fj} - ib_{fj}\right) - N_{fj}^2\left(a_{r(j-1)} - ib_{r(j-1)}\right)}{N_{r(j-1)}^2\left(a_{fj} - ib_{fj}\right) + N_{fj}^2\left(a_{r(j-1)} - ib_{r(j-1)}\right)} = \left|r_{pj}\right| e^{-i\varphi_{pj}} \quad \textbf{(21b)}$$

$$t_{sj} = \frac{2\left(a_{r(j-1)} - ib_{r(j-1)}\right)}{\left(a_{r(j-1)} - ib_{r(j-1)}\right) - \left(a_{fj} - ib_{fj}\right)} = \left|t_{sj}\right| e^{-i\beta_{sj}} \quad \textbf{(21c)}$$

$$t_{pj} = \frac{2N_{r(j-1)}N_{fj}\left(a_{r(j-1)} - ib_{r(j-1)}\right)}{N_{r(j-1)}^2\left(a_{fj} - ib_{fj}\right) + N_{fj}^2\left(a_{r(j-1)} - ib_{r(j-1)}\right)} = \left|t_{pj}\right| e^{-i\beta_{pj}} \quad \textbf{(21d)}$$

where

$$a_{xj}^2 = \frac{1}{2}\left(n_{xj}^2 - \kappa_{xj}^2 - n_0^2\sin^2\phi\right) + \sqrt{\frac{1}{4}\left(n_{xj}^2 - \kappa_{xj}^2 - n_0^2\sin^2\phi\right) + n_{xj}^2\kappa_{xj}^2} \quad \textbf{(21e)}$$

$$b_{xj} = \frac{n_{xj}\kappa_{xj}}{a_{xj}} \quad \textbf{(21f)}$$

indices p and s represent plane polarized radiation with the electric vector in and normal to the plane of incidence; index $j=0$ is used to describe the parameters of the surrounding ambient, and ϕ represents the angle of incidence of radiation upon the sample. Index x must be replaced by indices f and r for front and rear interfaces of the film, respectively. If index x equals a in Eqs. (21e) and (21f), the a_{aj} and b_{aj} represent the effective refractive index and extinction coefficient of radiation in the bulk of a film.

In the case of a semi-infinite solid, ellipsometry is a direct technique which measures the complex reflectance ratio

$$\frac{r_{p1}}{r_{s1}} = \tan\psi\, e^{i\Delta} \quad \textbf{(22)}$$

where ψ and Δ are so-called ellipsometric angles (easily represented by formulae (21a) and (21b)). See [7] for an overview of this technique.

For back illumination [from (j+1) to j medium] the Fresnel reflection coefficients are $\tilde{r}_{sj} = -r_{sj}$ and $\tilde{r}_{pj} = -r_{pj}$, while the Fresnel transmission coefficients are given by

$$\tilde{t}_{sj} = \frac{2(a_{fj}-ib_{fj})}{\left(a_{r(j-1)}-ib_{r(j-1)}\right)-(a_{fj}-ib_{fj})} = \left|\tilde{t}_{sj}\right|e^{-i\tilde{\beta}_{sj}} \tag{23a}$$

$$\tilde{t}_{pj} = \frac{2\left(n_{r(j-1)}-i\kappa_{r(j-1)}\right)(n_{fj}-i\kappa_{fj})(a_{fj}-ib_{fj})}{N^2_{r(j-1)}(a_{fj}-ib_{fj})+N^2_{fj}\left(a_{r(j-1)}-ib_{r(j-1)}\right)} = \left|\tilde{t}_{pj}\right|e^{-i\tilde{\beta}_{pj}} \tag{23b}$$

The losses from the specular light beam by scattering at the rough interface between media *j-1* and *j* can be described by the scattering factors. Thus, in comparison with a smooth interface, the reflection and transmission Fresnel coefficients should be reduced by the following factors [22]

$$s_j^r = exp\left[-\frac{\left(4\pi n_{b(j-1)}\sigma_{RMS}\sin\phi\right)^2}{2\lambda^2}\right] \tag{24a}$$

$$s_j^t = exp\left\{-\frac{\left[2\pi\left(n_{b(j-1)}-n_{fj}\right)\sigma_{RMS}\sin\phi\right]^2}{2\lambda^2}\right\} \tag{24b}$$

where σ_{RMS} is the rms surface roughness of the boundary interface. Formulae (24) assume σ_{RMS} smaller than λ and small correlation length of the surface roughness.

3. OPTICAL TRANSMITTANCE AND REFLECTANCE

After a summary of the electric fields of waves reflected from a single film (taking into account the waves internal reflected in it and transmitted back), one obtains the effective Fresnel reflection coefficient of the film

$$\varrho_{\mathrm{vj}} = \frac{r_{\mathrm{vj}}+r_{\mathrm{v}(j+1)}exp(-\mathrm{K}_j)exp(-i\Gamma_{j0})}{1+r_{\mathrm{vj}}r_{\mathrm{v}(j+1)}exp(-\mathrm{K}_j)exp(-i\Gamma_{j0})} = \left|\varrho_{\mathrm{vj}}\right|e^{-i\theta_{\mathrm{vj}}} \tag{25a}$$

where index v must be replaced by indices p and s for plane polarized radiation with the electric vector in and normal to the plane of incidence, respectively, $\Gamma_{j0} = 4\pi w_j a_{aj}/\lambda$ is the change in phase of the beam on traversing twice a film, and $\mathrm{K}_j = 4\pi w_j a_{aj}\kappa_{aj}/\left(\lambda n_{aj}\right)$ is the effective, dimensionless absorption coefficient that describes the attenuation of radiation intensity in the direction normal to the front surface of the film.

The effective reflection for reversed illumination (from *j* to *(j-1)* film) is given by

$$\tilde{\rho}_{\mathrm{vj}} = \frac{-r_{\mathrm{v}(j+1)}-r_{\mathrm{vj}}exp(-\mathrm{K}_j)exp(-i\Gamma_{j0})}{1+r_{\mathrm{vj}}r_{\mathrm{v}(j+1)}exp(-\mathrm{K}_j)exp(-i\Gamma_{j0})} = \left|\tilde{\varrho}_{\mathrm{vj}}\right|e^{-i\tilde{\theta}_{\mathrm{vj}}} \tag{25b}$$

The effective Fresnel transmission coefficients of the film (for front and back illumination) are described by

$$\tau_{\mathrm{v}j} = \frac{t_{\mathrm{v}j}t_{\mathrm{v}(j+1)}exp(-0.5\mathrm{K}_j)exp(-i\Gamma_{j0})}{1+r_{\mathrm{v}j}r_{\mathrm{v}(j+1)}exp(-\mathrm{K}_j)exp(-i\Gamma_{j0})} = \left|\tau_{\mathrm{v}j}\right|e^{-i\vartheta_{\mathrm{v}j}} \quad \textbf{(26a)}$$

$$\tilde{\tau}_{\mathrm{v}j} = \frac{\tilde{t}_{\mathrm{v}j}\tilde{t}_{\mathrm{v}(j+1)}exp(-0.5\mathrm{K}_j)exp(-i\Gamma_{j0})}{1+r_{\mathrm{v}j}r_{\mathrm{v}(j+1)}exp(-\mathrm{K}_j)exp(-i\Gamma_{j0})} = \left|\tilde{\tau}_{\mathrm{v}j}\right|e^{-i\tilde{\vartheta}_{\mathrm{v}j}} \quad \textbf{(26b)}$$

Formulae (25) and (26) can be used recurrently to reduce a system of multilayers to a single surface with appropriate effective reflection and transmission coefficient

$$\varrho_{\mathrm{v}m_w} = \sum_{j=2}^{m_w} \frac{\varrho_{\mathrm{v}(j-1)}+r_{\mathrm{v}(j+1)}exp(-\mathrm{K}_j)exp(-i\Gamma_{j0})}{1+\tilde{\rho}_{\mathrm{v}(j-1)}r_{\mathrm{v}(j+1)}exp(-\mathrm{K}_j)exp(-i\Gamma_{j0})} = \left|\varrho_{\mathrm{v}m_w}\right|exp\left(-i\theta_{\mathrm{v}m_w}\right) \quad \textbf{(27a)}$$

$$\tau_{\mathrm{v}m_w} = \sum_{j=2}^{m_w} \frac{\tau_{\mathrm{v}(j-1)}t_{\mathrm{v}(j+1)}exp(-0.5\mathrm{K}_j)exp(-i\Gamma_{j0})}{1+\tilde{\rho}_{\mathrm{v}(j-1)}r_{\mathrm{v}(j+1)}exp(-\mathrm{K}_j)exp(-i\Gamma_{j0})} = \left|\tau_{\mathrm{v}m_w}\right|exp\left(-i\vartheta_{\mathrm{v}m_w}\right) \quad \textbf{(27b)}$$

where m_w is the number of media in the multilayer structure. Index v must be replaced by indices p and s for plane polarized radiation with the electric vector in and normal to the plane of incidence.

The changes of amplitudes $\left|\varrho_{\mathrm{p}m_w}\right|$, $\left|\varrho_{sm_w}\right|$, $\left|\tau_{\mathrm{p}m_w}\right|$, and $\left|\tau_{sm_w}\right|$ as well as the changes of phases $\theta_{\mathrm{p}m_w}$, θ_{sm_w}, $\vartheta_{\mathrm{p}m_w}$, and ϑ_{sm_w} of the electric fields of radiation reflected and transmitted through the m_w film structure are dependent on wavelength and angle of light incidence. They can be determined applying, for example, the variable angle spectroscopic ellipsometry (VASE) [7]. However, an appropriate model must always be constructed on the assumed values of indices of refraction, layer thicknesses, alloy fractions, void fractions, roughness parameters, *etc.*

The energetic transmittance and reflectance of multilayer structure (*i.e.*, ratios of intensities of transmitted/incident and reflected/incident radiation) are squares of the appropriate Fresnel coefficients

$$T_{z\mathrm{v}} = \left|\tau_{\mathrm{v}m_w}\right|^2 \quad \textbf{(28a)}$$

$$R_{z\mathrm{v}} = \left|\varrho_{\mathrm{v}m_w}\right|^2 \quad \textbf{(28b)}$$

where index v must be replaced by indices p and s for plane polarized radiation with the electric vector in and normal to the plane of incidence, respectively.

Interference of radiation internally reflected in parallel-sided samples affects characteristic extrema in spectral distributions of optical transmittance $T_o(\lambda)$ and reflectance $R_o(\lambda)$. The main feature, distinguishing these from absorbance extrema, is the correlation between maxima and minima in $T_o(\lambda)$ and $R_o(\lambda)$ (Fig. **7**). This is well described by the Eq. (28). The other feature consists in the relation between positions λ_m and λ_{m+1} of the extrema in optical characteristics and the changes in phases of the beam on traversing twice the film of thickness w_j:

$$\frac{4\pi w_j a_{aj}(\lambda_m)}{\lambda_m} - \frac{4\pi w_j a_{aj}(\lambda_{m+1})}{\lambda_{m+1}} = 2\pi \quad \textbf{(29)}$$

where m and $m+1$ represent orders of extrema. Sometimes Eq. (29) is used to estimate sample thickness or refractive index of materials. However, the exact description of these parameters requires a more cumbersome approach. In the case of negligible absorption of radiation, the positions (λ_m) of interference extrema are described by

$$m\lambda_m = 2n_{aj}w_j\sqrt{1 - \frac{sin^2\phi}{n_{aj}^2}} \quad \textbf{(30)}$$

The wavelengths λ_m of interference extrema decrease as the angle of light incidence and the order of interference fringes increase (*e.g.* [49]). In the case of an anisotropic medium the values of λ_m depend on polarity of the used light and crystallographic orientation of the sample. Recently, the interference spectrogoniometric method [49] of investigations of anisotropic materials was based on Eq. (30). This method is very convenient in cases of relatively thick films.

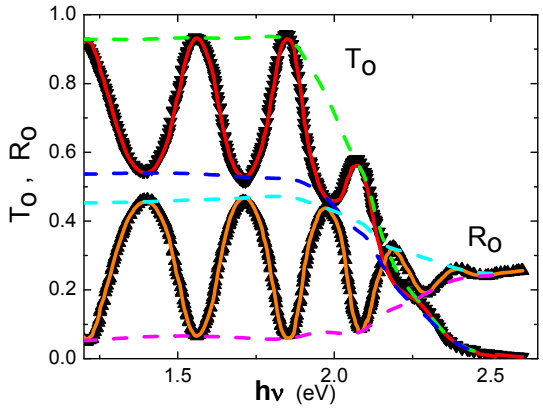


Figure 7: Spectral distribution of transmittance (▼) and reflectance (▲) of a-Si:H film [48]. Solid curves show theoretical dependencies calculated for fitted $\boldsymbol{w_1}$=571.1 nm, $\boldsymbol{\sigma_{w1}}$=3.3 nm, and the parameters presented in Figs. **15** and **16**. Broken curves are envelopes of the experimental characteristics.

The additional layers of different materials which cover the semiconductor surfaces can be simply described as the interference filters [2]. Their effective reflectivities and changes in phase of radiation reflected by them depend on refractive indices of the film and the surrounding media as well as film thickness, angle of incidence and polarization of radiation. This problem is well-known in thin film optics [2] and will not be discussed in detail in the present paper. The question of a surface texturing is discussed in Chapter 9 by M. Tucci *et al.* in this volume.

3.1. Influence of Uncertainty of a Change in Phase of the Beam on Transmittance and Reflectance

Formulae (28) were derived for the case of perfect coherence of radiation interfering in the films, *i.e.*, for the strict values of Γ_{j0}. This is an idealization of the experimental situation. In fact the radiation used in every experiment (even in experiments with laser illumination) has some

bandwidth $\Delta\lambda$ of the wavelengths. It is also probable that the real film is inhomogeneous or has non-parallel or rough surfaces. For example, Swanepoel [50] has analyzed the influence of linear, triangular, and rectangular surface roughness on a semiconductor film transmittance. A similar surface roughness of coating layers can be analyzed. In general, it creates some uncertainties σ_{naj} and σ_{wj} of the real part of refractive index and thickness of the film over the illuminated sample area. All these factors can cause some uncertainty $\sigma_{\Gamma j}$ of the change in phase of the beam upon traversing the film:

$$\sigma_{\Gamma j} = \left(\frac{\sigma_{wj}}{w_j} + \frac{\sigma_{naj}}{n_{aj}} + \frac{\Delta\lambda}{\lambda}\right)\Gamma_j \tag{31}$$

It is very probable [51] that the changes of semiconductor film and coating layers thicknesses as well as their refractive indices are random over the illuminated sample area. Also the distribution of radiation intensity over the wavelength range can be Gaussian. Thus the change in phase Γ_j of the beam on traversing a semiconductor or coating layer should be described by the Gaussian distribution with the average value Γ_{j0} and standard deviation $\sigma_{\Gamma j}$. Therefore, in the case of three films in a multilayer structure (Fig. **1**), the energetic transmission and reflection coefficients should be calculated using the triple integral

$$T_{zvG}(\Gamma_2,\Gamma_1,\Gamma_3) = \int_{\Gamma_2=0}^{+\infty}\int_{\Gamma_1=0}^{+\infty}\int_{\Gamma_3=0}^{+\infty} \frac{1}{\sigma_{\Gamma 2}\sqrt{2\pi}} exp\left[-\frac{(\Gamma_{20}-\Gamma_2)^2}{2\sigma_{\Gamma 2}^2}\right]\cdot \frac{1}{\sigma_{\Gamma 1}\sqrt{2\pi}} exp\left[-\frac{(\Gamma_{10}-\Gamma_1)^2}{2\sigma_{\Gamma 1}^2}\right]\cdot \frac{T_{zv}}{\sigma_{\Gamma 3}\sqrt{2\pi}} exp\left[-\frac{(\Gamma_{30}-\Gamma_3)^2}{2\sigma_{\Gamma 3}^2}\right] d\Gamma_3 d\Gamma_1 d\Gamma_2 \tag{32a}$$

$$R_{zvG}(\Gamma_2,\Gamma_1,\Gamma_3) = \int_{\Gamma_2=0}^{+\infty}\int_{\Gamma_1=0}^{+\infty}\int_{\Gamma_3=0}^{+\infty} \frac{1}{\sigma_{\Gamma 2}\sqrt{2\pi}} exp\left[-\frac{(\Gamma_{20}-\Gamma_2)^2}{2\sigma_{\Gamma 2}^2}\right]\cdot \frac{1}{\sigma_{\Gamma 1}\sqrt{2\pi}} exp\left[-\frac{(\Gamma_{10}-\Gamma_1)^2}{2\sigma_{\Gamma 1}^2}\right]\cdot \frac{R_{zv}}{\sigma_{\Gamma 3}\sqrt{2\pi}} exp\left[-\frac{(\Gamma_{30}-\Gamma_3)^2}{2\sigma_{\Gamma 3}^2}\right] d\Gamma_3 d\Gamma_1 d\Gamma_2 \tag{32b}$$

where T_{zv} and R_{zv} are given by Eq. (28), index v must be replaced by indices p and s for plane polarized radiation with the electric vector in and normal to the plane of incidence, respectively. For $\sigma_{\Gamma 1}$=$\sigma_{\Gamma 2}$=$\sigma_{\Gamma 3}$=0 the density of Gaussian distribution is represented by the δ −Dirac and Eq. (32) reduce into the forms (28) for an ideal instance of perfect coherence of radiation interfering in the multilayer structure of thin films (see [2]).

The formulae (32) involve a few integrals and are rather time consuming for numerical calculations in cases of thick layers. The last situation occurs very often in investigations of amorphous thin films performed on a specific double layer structure: a thin semiconductor film of thickness w_1 covers a relatively thick, transparent, parallel-sided substrate of thickness $w_2 \gg w_1$. The sample is uniformly illuminated with radiation that has components in wavelength range $\Delta\lambda$, and

$$\frac{\lambda^2}{2n_{a2}w_2} \ll \Delta\lambda \ll \frac{\lambda^2}{2n_{a1}w_1} \tag{33}$$

where n_{a1} and n_{a2} are real parts of refractive indices of the semiconductor film and the substrate, respectively. According to Eq. (33); the interference of internally reflected radiation occurs in a semiconductor film and is negligible in the substrate (*e.g.* [1]). In this case a simpler description of optical phenomena can be used because the phases of electric fields of beams internally reflected in the thick substrate are random. Therefore, the energetic transmission and reflection coefficients should be calculated by summing up intensities (no electric fields) of radiation of the multiple reflected beams

$$T_{f\mathrm{v}} = \frac{|\tau_{\mathrm{v}1}|^2|t_{\mathrm{v}3}|^2}{1-|\tilde{\varrho}_{\mathrm{v}1}|^2|r_{\mathrm{v}3}|^2} \tag{34a}$$

$$R_{f\mathrm{v}} = |\varrho_{\mathrm{v}1}|^2 + \frac{|\tau_{\mathrm{v}1}|^2|\tilde{\tau}_{\mathrm{v}1}|^2}{1-|\tilde{\varrho}_{\mathrm{v}1}|^2|r_{\mathrm{v}3}|^2} \tag{34b}$$

where $|r_{\mathrm{v}3}|$, $|t_{\mathrm{v}3}|$, $|\varrho_{\mathrm{v}1}|$, $|\tilde{\varrho}_{\mathrm{v}1}|$, $|\tau_{\mathrm{v}1}|$ and $|\tilde{\tau}_{pj}|$ are given by Eqs. (21), (25) and (26); index v must be replaced by indices p and s for plane polarized radiation with the electric vector in and normal to the plane of incidence, respectively; index *f* indicates that the sample is illuminated from the semiconductor side; for a sample immersed in air N_{r0}=N_{f3}=1.

To determine values of optical parameters at both interfaces of a thin semiconductor film, a double layer structure should be investigated under illumination from the free surface side as well as from the substrate side (*e.g.* [52]). In the case of incidence of radiation upon the back sample surface, the energetic transmission and reflection coefficients are given by

$$T_{b\mathrm{v}} = \frac{|\tilde{\tau}_{\mathrm{v}1}|^2|t_{\mathrm{v}3}|^2}{1-|\tilde{\varrho}_{\mathrm{v}1}|^2|r_{\mathrm{v}3}|^2} \tag{35a}$$

$$R_{b\mathrm{v}} = |r_{\mathrm{v}3}|^2 + \frac{|t_{\mathrm{v}3}|^2|\tilde{t}_{\mathrm{v}3}|^2}{1-|\tilde{\varrho}_{\mathrm{v}1}|^2|r_{\mathrm{v}3}|^2} \tag{35b}$$

where symbols have their usual meanings.

Taking into account the possible Gaussian distribution of the change in phase of the beam upon traversing the semiconductor film in the double layer structure, one obtains

$$T_{d\mathrm{vG}} = \int_0^{+\infty} \frac{T_{d\mathrm{v}}}{\sigma_{\Gamma 1}\sqrt{2\pi}} exp\left[-\frac{(\Gamma_{10}-\Gamma_1)^2}{2\sigma_{\Gamma_1}^2}\right] d\Gamma_1 \tag{36}$$

$$R_{d\mathrm{vG}} = \int_0^{+\infty} \frac{R_{d\mathrm{v}}}{\sigma_{\Gamma 1}\sqrt{2\pi}} exp\left[-\frac{(\Gamma_{10}-\Gamma_1)^2}{2\sigma_{\Gamma_1}^2}\right] d\Gamma_1 \tag{37}$$

where index d must be replaced by indices f and b for the front and back illumination of the sample (the other symbols have the same meanings as in Eqs. (32), (34) and (35)).

Numerical calculations were done to analyze the influence of Gaussian distributions of Γ_j on the spectral characteristics of $T_{d\mathrm{vG}}$. Fig. **8** presents the strong influence of σ_{w1} on the $T_{d\mathrm{vG}}$ of a thin

semiconductor film. The calculations show that serious consideration must also be given to the wavelength bandwidth of radiation which illuminates the sample. When $\Delta\lambda$ increases with decreasing λ [53], the influence of wavelength bandwidth on $T_{d\mathrm{vG}}$ is stronger for higher $h\nu$.

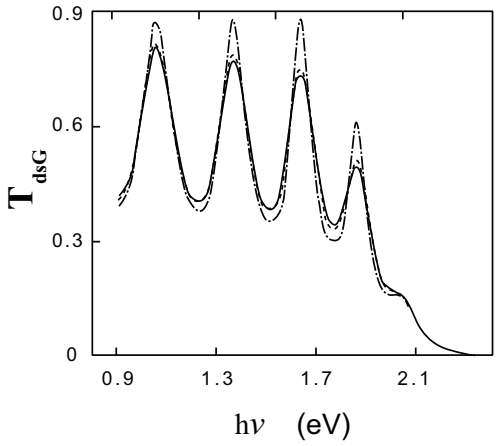


Figure 8: Spectral dependence of optical transmittance of a thin film calculated for different $\boldsymbol{\sigma_{w1}}$ and $\boldsymbol{\Delta\lambda}$ (chain curve, for $\boldsymbol{\sigma_{w1}}$=0 and $\boldsymbol{\Delta\lambda}$=0; broken curve, for $\boldsymbol{\sigma_{w1}}$=12.3 nm and $\boldsymbol{\Delta\lambda}$=0; solid curve, for $\boldsymbol{\sigma_{w1}}$=12.3 nm and $\boldsymbol{\Delta\lambda(\lambda)}$ taken from [53] for 2 mm output slot of the monochromator; $\boldsymbol{w_1}$=0.473 μm, $\boldsymbol{n_{a1}(\lambda)}$ and $\boldsymbol{\alpha_{a1}(\lambda)}$ from [51], $\boldsymbol{n_{f1}}$=$\boldsymbol{n_{r1}}$=$\boldsymbol{n_{a1}}$, $\boldsymbol{\alpha_{f1}}$=$\boldsymbol{\alpha_{r1}}$=$\boldsymbol{\alpha_{a1}}$, $\boldsymbol{\phi = 0°}$).

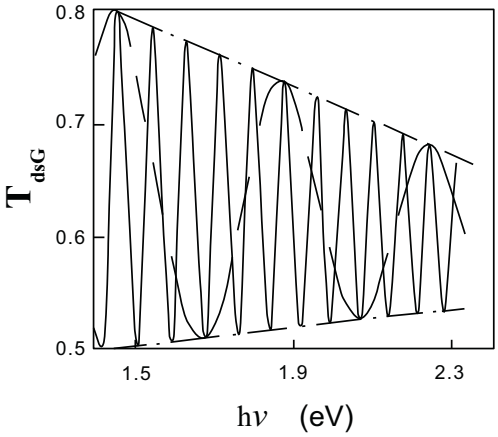


Figure 9: Influence of thin-film thickness on spectral characteristics of optical transmittance (broken curve, $\boldsymbol{w_1}$=0.4 μm, $\boldsymbol{\sigma_{w1}}$=20 nm; solid curve, $\boldsymbol{w_1}$=2 μm; $\boldsymbol{\sigma_{w1}}$= 20 nm; $\boldsymbol{n_{f1}}$=$\boldsymbol{n_{r1}}$=$\boldsymbol{n_{a1}(\lambda)}$ taken from [29]; $\boldsymbol{\alpha_{f1}}$=$\boldsymbol{\alpha_{r1}}$=$\boldsymbol{\alpha_1(\lambda)}$=0, $\boldsymbol{\sigma_{na1}}$= $\boldsymbol{\Delta\lambda}$=0, $\boldsymbol{\phi = 0°}$; $\boldsymbol{\phi = 0°}$; chain curves are envelopes of the characteristics).

It is obvious (Fig. **9**) that thin-film thickness and n_{a1} influence the positions of interference fringes in the spectral characteristics of $T_{d\mathrm{vG}}$. However, it does not influence the envelopes of the spectral characteristics (Fig. **9**). The shape of the envelope depends strongly on the standard deviation σ_{w1} of the distribution of film thickness over the illuminated area of the sample (Fig. **10**). It is an advantage that in the case of Gaussian distribution of Γ_1 values of maxima in the spectral characteristics of $T_{d\mathrm{vG}}$ decrease with decreasing λ, while values of minima increase, attain a

maximum value and then decrease with decreasing λ (all in the range of negligible absorption of light in a sample), see Fig. **10**. This behavior of the spectral characteristics of T_o is the main evidence for influence of the radiation wavelength bandwidth $\Delta\lambda$ and/or changes of thin film thickness σ_{w1} and changes of refractive index σ_{naj} on optical transmittance. This stated tendency of changing magnitudes of interference fringes with changing radiation wavelength is very often observed experimentally [50].

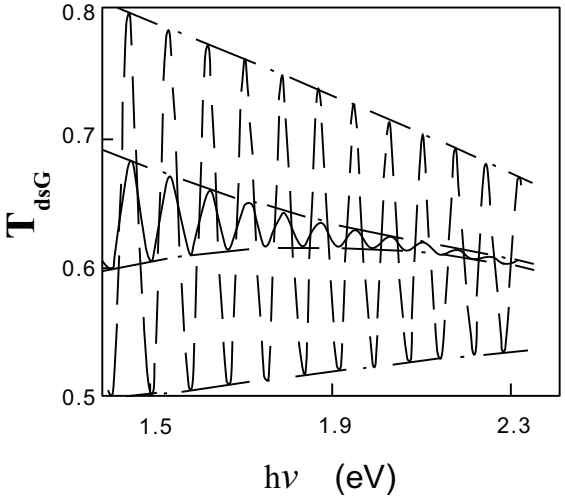


Figure 10: Influence of thickness changes in an illuminated area of thin film on spectral characteristics of optical transmittance (broken curve, $\boldsymbol{\sigma_{w1}}$= 20 nm; solid curve, $\boldsymbol{\sigma_{w1}}$= 40 nm; $\boldsymbol{w_1}$=2 μm; other parameters are the same as in Fig. **9**; chain curves are envelopes of the characteristics).

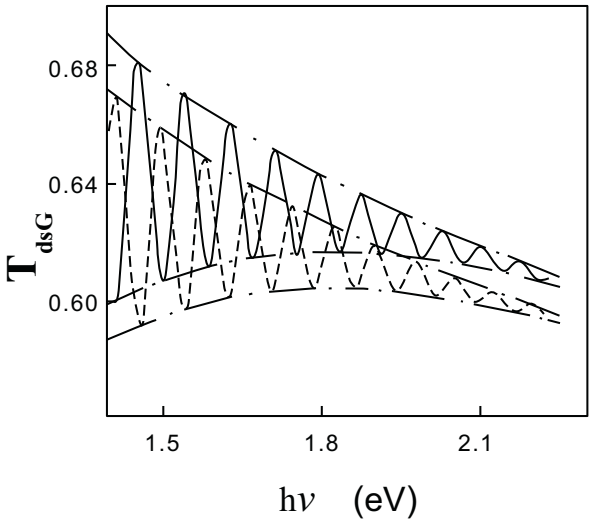


Figure 11: Influence of real part of refractive index of thin film on spectral characteristics of optical transmittance (solid curve, $\boldsymbol{n_{f1}(\lambda)}$ taken from [29]; broken curve, $\boldsymbol{n_{f1}(\lambda)}$ from [29] increased by 0.1; $\boldsymbol{\sigma_{w1}}$= 40 nm, other parameters are the same as in Fig. **9**; chain curves, envelopes of the characteristics).

It is evident in the transmittance calculated for Gaussian distribution of Γ_1 that the increase of standard deviation σ_{w1} decreases the interference fringes in the spectral characteristics of transmittance (Fig. **10**). It does not influence the so-called averaged magnitude of optical transmittance. This magnitude strongly depends on the value of real parts of refractive indices n_{f1} and n_{r1} (Fig. **11**), and obviously it depends on the absorption coefficient α_{aj}. Increase of n_{f1} affects the decrease of optical transmittance due to the increase of reflection coefficient. The same conclusions are true for reflectance (*e.g.* [48]).

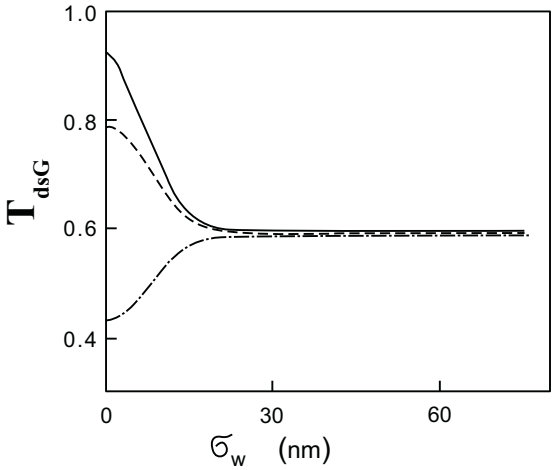


Figure 12: Influence of the parameter $\boldsymbol{\sigma_{w1}}$ of Gaussian distribution of $\boldsymbol{\Gamma_1}$ on optical transmittance of a thin film (solid curve, $\boldsymbol{w_1 n_{a1}/\lambda}$=10.0; broken curve, $\boldsymbol{w_1 n_{a1}/\lambda}$=10.11; chain curve, $\boldsymbol{w_1 n_{a1}/\lambda}$=10.23; the other parameters are the same as in Fig. **10**).

Nevertheless, it is a great difference between the spectral characteristics of optical transmittance and reflectance calculated for linear and Gaussian distributions of the change in phase of radiation traversing a thin film (*e.g.* [48,51]). It is important to note that transmittance and reflectance are monotonic functions of σ_{w1} (*e.g.* Fig. **12**) only in the latter case.

3.2. Negligible Interference of Light in a Semiconductor

In some cases the interference fringes are not observed in spectral characteristics of optical reflectance and/or transmittance. It can be evoked by strong absorption of light in a semiconductor (*e.g.* the $T_o(\lambda)$ and $R_o(\lambda)$ characteristics presented in Fig. **7** for larger photon energies). In this case one can pass over the components of light that are hypothetically internally reflected several times in a semiconductor. The second component of light (internally reflected) that contributes to the beam transmitted through a film is more diminished than the second component of light that contributes to the beam reflected from the film. The former traverses the film three times while the latter traverses the film only twice (Fig. **13**). Therefore, the interference fringes are evident in a reflectance spectrum in the photon energy range in which the spectrum of optical transmittance is relatively smooth (compare the $R_o(\lambda)$ and $T_o(\lambda)$ spectra presented in Fig. **7** for $h\nu > 2.25\ eV$).

In the case of relatively strong absorption of light, the transmittance and reflectance of a single semiconductor film are given by

$$T_{fv} = \frac{|t_{v1}|^2|t_{v2}|^2 exp(K_1)}{1-|\tilde{r}_{v1}|^2|r_{v2}|^2 exp(-2K_1)} \quad \textbf{(38a)}$$

$$R_{fv} = |r_{v1}|^2 + \frac{|t_{v1}|^2|\tilde{t}_{v1}|^2|r_{v2}|^2 exp(-2K_1)}{1-|\tilde{r}_{v1}|^2|r_{v2}|^2 exp(-2K_1)} \quad \textbf{(38b)}$$

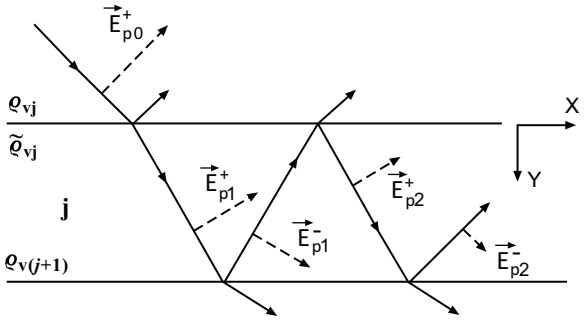


Figure 13: Scheme of radiation propagation and its electric field in a single film (XY is the coordinate system; description of the symbols in the text).

In the case of the double layer structure of a semiconductor film on a thick, transparent, parallel-sided substrate as analyzed above, one should replace in Eqs (38) the values of $|t_{v2}|^2$ and $|r_{v2}|^2$ with

$$\bar{\bar{T}}_{fv} = \frac{|t_{v2}|^2|t_{v3}|^2}{1-|\tilde{r}_{v2}|^2|r_{v3}|^2} \quad \textbf{(39a)}$$

$$\bar{\bar{R}}_{fv} = |r_{v2}|^2 + \frac{|t_{v2}|^2|\tilde{t}_{v2}|^2|r_{v3}|^2}{1-|\tilde{r}_{v2}|^2|r_{v3}|^2} \quad \textbf{(39b)}$$

The other reason for the lack of interference fringes in spectral characteristics of optical transmittance and reflectance of a film is the incoherence of the beams internally reflected and superimposed on each other. This can occur in the case of relatively large uncertainty of the change in phase of the beam upon traversing the film ($\sigma_{\Gamma j} > 2\pi$), and consequently in the case of a relatively thick film, when $\Delta\lambda \gg \lambda^2/(2n_{aj}w_j)$ (see Eq. (31)). In such a situation the Eqs. (32) or (36) and (37) should be used.

3.3. Method of Transmittance and Reflectance Data Treatment

The treatment of transmittances and reflectances of a-Si:H film on a thick BK-7 substrate (presented in Fig. **7)** is presented step by step. Details of the experiment were given in [48]. Similar to the method of Swanepoel [50], the envelopes of the spectral dependences of optical transmittance and reflectance were determined. Then a few wavelengths λ_j, were chosen from the range of negligible absorption of radiation in the sample (Fig. **14**). The value σ_{w1}=3.3 nm and the set of values $n_1(\lambda_j)$ (see Fig. **15**) were found by minimization of the following function

$$\chi^2 = \sum_j \left\{ \left[T_{max}(\lambda_j) - t_{max}(\lambda_j)\right]^2 + \left[T_{min}(\lambda_j) - t_{min}(\lambda_j)\right]^2 + \left[R_{max}(\lambda_j) - r_{max}(\lambda_j)\right]^2 + \left[R_{min}(\lambda_j) - r_{min}(\lambda_j)\right]^2 \right\} \quad \textbf{(40)}$$

where $T_{max}(\lambda_j)$, $T_{min}(\lambda_j)$, $R_{max}(\lambda_j)$ and $R_{min}(\lambda_j)$ are maximum and minimum values from the envelopes of optical transmittance and reflectance determined for wavelength λ_j. The $t_{max}(\lambda_j)$, $t_{min}(\lambda_j)$, $r_{max}(\lambda_j)$ and $r_{min}(\lambda_j)$ are the maximum and minimum values of $T_\vartheta[\lambda_j, n_{a1}(\lambda_j), \sigma_{w1}, w_{10}, \vartheta]$ and $R_\vartheta[\lambda_j, n_{a1}(\lambda_j), \sigma_{w1}, w_{10}, \vartheta]$ calculated for $\vartheta \in (0,2\pi)$, where T_ϑ and R_ϑ are given for $\phi = 0°$ by Eqs. (36) and (37) in which T_{dv} and R_{dv} are substituted by T_{fs} and R_{fs} after replacing Γ_{10} with $\Gamma_\vartheta = \Gamma_{10} + \vartheta$. In this approach the σ_{n1}/n_{a1} was assumed to be negligible in comparison with the other components in Eq. (31). The spectral dependence of the wavelength bandwidth $\Delta\lambda(\lambda)$ was taken from [54] for the 2 mm output slot of the monochromator. The spectral characteristics of the refractive index n_{f2}=n_{r2}=n_{a2} of the BK-7 substrate plate were assumed after [55]. It was assumed that α_{a1}=0, due to the treatment of the optical data for the spectral range of negligible absorption, *i.e.*, the spectral range in which the slopes of the envelopes of T_o and R_o are very small. In addition, in all the above calculations an optional value of w_{10} was assumed. This is congruent with the statement made in the previous section: for negligible absorption the envelopes of T_{dsG} and R_{dsG} are independent of w_1 (Fig. **9**).

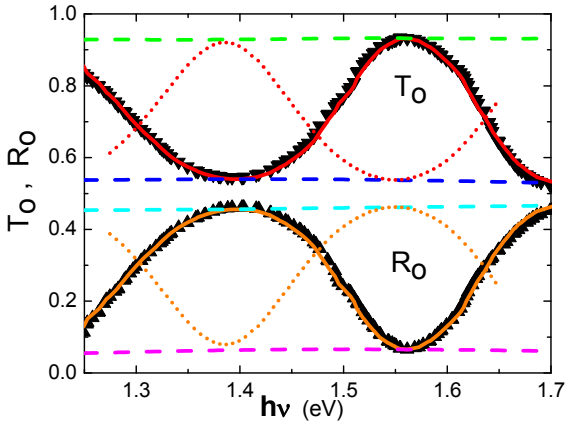


Figure 14: Parts of the spectral dependences of optical transmittance (▼) and reflectance (▲) from Fig. **7** (broken lines, parts of the envelopes of the data; dot and solid curves, first and secondary fitted spectral dependence of $\boldsymbol{T_{fsG}}$ and $\boldsymbol{R_{fsG}}$; description in text).

Taking wavelengths λ_1 and λ_2 of two close maxima and minima and choosing the appropriate $n_1(\lambda_1)$ and $n_1(\lambda_2)$, the film thickness was calculated using the classical formula

$$\bar{w}_1 = \frac{\lambda_1\lambda_2}{4[\lambda_2 n_1(\lambda_1) - \lambda_1 n_1(\lambda_2)]} \tag{41}$$

The theoretical transmittance calculated for the found value $\bar{w}_1$=651 nm and the previously determined $n_1(\lambda_1)$, σ_{w1}, and α_{a1}=0 is shown as the dot curve in Fig. **15**. In comparison with the experimental data the shift of the curve thus obtained is observed (as for every sample examined [51]). Hence, $\bar{w}_1$ is taken only as the initial value of the thickness w_1 calculated numerically by minimization of the function

$$\chi^2 = \sum_j \left\{ [T_o(\lambda_j) - T_{fsG}(\lambda_j, w_1)]^2 + [R_o(\lambda_j) - R_{fsG}(\lambda_j, w_1)]^2 \right\} \tag{42}$$

where $T_o(\lambda_j)$ and $R_o(\lambda_j)$ are the optical transmittance and reflectance measured for wavelength λ_j (from the spectral range of negligible absorption), $T_{fsG}(\lambda_j, w_1)$ and $R_{fsG}(\lambda_j, w_1)$ are theoretical transmittance and reflectance calculated using Eqs. (37) and (38), and the previously determined σ_{w1} and $n_1(\lambda_j)$. The value of w_1=571.1 nm was obtained from the last minimization. The optical transmittance and reflectance calculated using this w_1, σ_{w1}, and $n_1(\lambda_j)$ are shown in Fig. **14** as the solid curves. The experimental points with these characteristics fit rather well (It appears that the value of the standard deviation of a film thickness determined using the method of investigations presented herein is comparable to the value of the mean surface roughness evaluated from the AFM studies [56]).

Using the known values of w_1 and σ_{w1}, the values of n_{f1}, n_{a1}, n_{r1}, and α_{f1}=α_{a1}=α_{r1} were found numerically by minimization of the following function (the α_{f1} and α_{r1} different from α_{a1} have rather small influence on T_o and R_o)

$$\chi^2 = \sum_j \left\{ \left[T_o(\lambda_j) - T_{fsG}(\lambda_j)\right]^2 + \frac{1}{2}\left[T_{max}(\lambda_j) - t_{max}(\lambda_j)\right]^2 + \frac{1}{2}\left[T_{min}(\lambda_j) - t_{min}(\lambda_j)\right]^2 + \left[R_o(\lambda_j) - R_{fsG}(\lambda_j)\right]^2 + \frac{1}{2}\left[R_{max}(\lambda_j) - r_{max}(\lambda_j)\right]^2 + \frac{1}{2}\left[R_{min}(\lambda_j) - r_{min}(\lambda_j)\right]^2 + \left[\frac{1-R_o(\lambda_j)}{T_o(\lambda_j)} - \frac{1-R_{fsG}(\lambda_j)}{T_{fsG}(\lambda_j)}\right]^2 \right\} \quad \textbf{(43)}$$

where $T_{fsG}(\lambda_j)$ and $R_{fsG}(\lambda_j)$ are the theoretical transmittance and reflectance calculated using Eqs. (36) and (37) or (38) and (39) for λ_j, w_1, σ_{w1}, $n_{f1}(\lambda_j)$, $n_{a1}(\lambda_j)$, $n_{r1}(\lambda_j)$, and α_{f1}=α_{r1}=$\alpha_{a1}(\lambda_j)$. The $T_{max}(\lambda_j)$, $T_{min}(\lambda_j)$, $R_{max}(\lambda_j)$, and $R_{min}(\lambda_j)$ are the appropriate magnitudes from the envelopes of $T_o(\lambda_j)$ and $R_o(\lambda_j)$. The $t_{max}(\lambda_j)$, $t_{min}(\lambda_j)$, $r_{max}(\lambda_j)$, and $r_{min}(\lambda_j)$ represent values of the envelopes $T_{fsG}(\lambda_j)$ and $R_{fsG}(\lambda_j)$. Because the interference fringes are almost completely absent in $[1 - R_o(\lambda)]/T_o(\lambda)$ function [57], it was also used to facilitate the numerical analysis. The values of the fitted refractive indices and absorption coefficients are presented in Figs. **15** and **16**, respectively. The theoretical transmittance and reflectance calculated for the fitted parameters are shown in Fig. **7**. The experiment data fit rather well with the theoretical transmittance and reflectance.

One can see (Fig. **15**) that the refractive index n_{a1} averaged through the investigated a-Si:H film has values higher than the refractive index n_{f1} near the free surface of the film. This can be explained by the possible penetration of oxygen into the imperfect layer of silicon, causing the decrease of the real part of refractive index from the value appropriate for the bulk a-Si:H to the value similar to the parameter of SiO_2. Simultaneously, for almost all investigated wavelengths the values of n_{a1} are lower than the refractive indices near the film-substrate interface. Such inhomogeneities and the no monotonic spectral dependences of $n_{f1}(\lambda_j)$ and $n_{r1}(\lambda_j)$ should be carefully investigated in the future. More reliable results should be obtained under illumination from the free surface side as well as from the substrate side of a sample (*e.g.* [52]).

The multiabsorption fitting (Eq. (13)) of $\alpha_{a1}(\lambda_j)$ was performed. Fig. **16** presents the best theoretical dependence fit for the sum of Tauc absorption (Eq. (11f)), Urbach absorption (Eq. (11g)), and a constant absorption term that is considered as the sum of the scattering and absorption independent of hν near the absorption edge. Thus the optical gap E_g=1.838(7) eV and the Urbach energy E_U=128(2) meV of the investigated material have been determined.

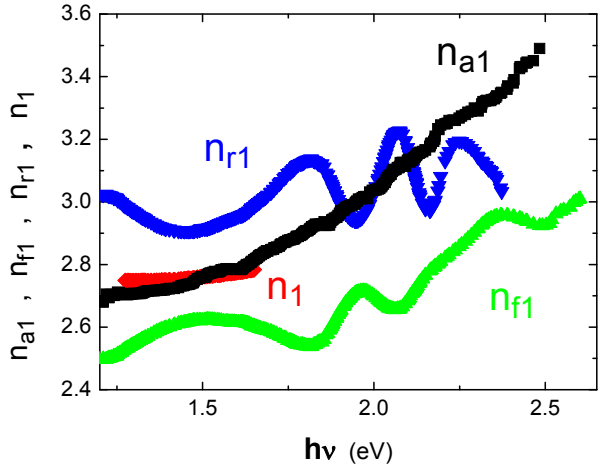


Figure 15: Spectral dependences of refractive indices near the free surface ($\boldsymbol{n_{f1}}$), near the film-substrate interface ($\boldsymbol{n_{r1}}$), and averaged ($\boldsymbol{n_{a1}}$) over the thickness of a-Si:H thin film on a thick BK-7 substrate; $\boldsymbol{n_1}$, values determined with the assumption of negligible absorption; other details in the text.

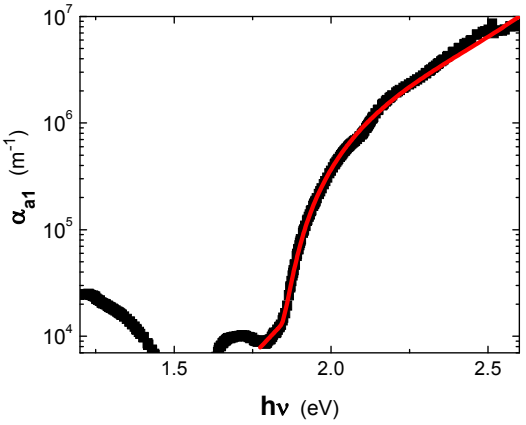


Figure 16: Spectral dependence of absorption coefficient (■) of radiation in a-Si:H thin film on a thick BK-7 substrate (solid curve, the least square theoretical dependence fit for the sum of Tauc absorption, Urbach absorption, and a constant absorption term; description in the text).

3.4. Linear Distribution of Intensity of Reflected and Transmitted Radiation

Very often the parallel-sided substrates of thin films are transparent for radiation used in optical measurements and usually they are much thicker than the films. If the incident beam has a finite diameter, owing to multiple internal reflection for oblique illumination, there are series of parallel but displaced beams in both the transparent and reflected directions (Fig. **17**). This can evoke a specific linear distribution of intensity of reflected and transmitted radiation. This effect can be observed when the sample is illuminated with a laser beam (*e.g.* [58]). This effect is stronger in the case of reflectance than in transmittance (*e.g.* [59]). To simplify, one may assume the same double layer structure previously analyzed. Additionally it is assumed that the spatial distribution of

incident radiation intensity is Gaussian ($I(r) = I_0 exp[-2(r/b)^2]$ where r is the distance from the beam axis, I_0 is maximum intensity of radiation, and b represents the beam radius at $I = I_0 exp(-2)$).

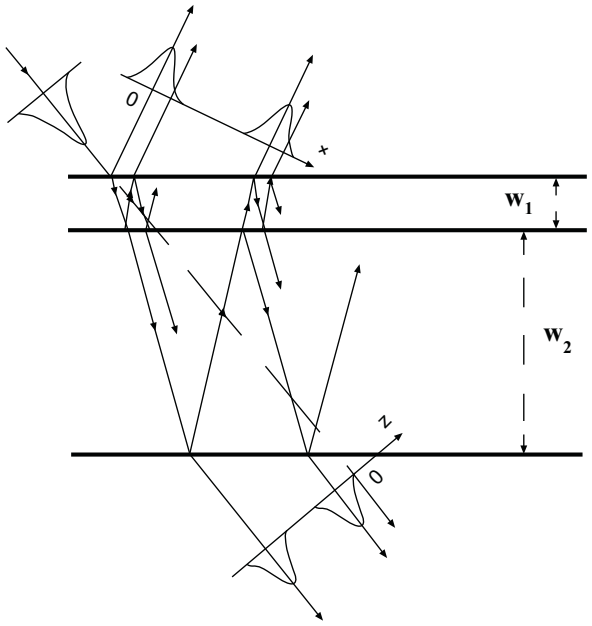


Figure 17: Scheme of radiation propagation and distribution of intensity in laser beams reflected from and transmitted through a thin film on a thick parallel-sided plate (*x,* distance from axis of the beam reflected in the point of radiation incidence upon a sample; *z.* distance from axis of the beam incident upon a sample; the other parameters are described in the text).

Because no interference occurs between radiation of beams affected by internal reflection in the thick substrate (Eq. (33)), the total radiation intensity reflected from the sample is given by a simple sum of the radiation intensities of several components (Fig. **17**). Therefore the total intensity of reflected radiation is given by the following function of the distance x from the axis of the beam reflected in the point of radiation incidence upon a sample

$$I_{d\mathrm{vG}} = \int_0^{+\infty} \frac{I_{d\mathrm{v}}}{\sigma_{\Gamma 1}\sqrt{2\pi}} exp\left[-\frac{(\Gamma_{10}-\Gamma_1)^2}{2\sigma_{\Gamma_1}^2}\right] d\Gamma_1 \quad \textbf{(44)}$$

where

$$I_{\mathrm{dv}} = I_{d1} exp\left[-2\frac{(x-x_1)^2}{b^2}\right] + I_{d2} exp\left[-2\frac{(x-x_2)^2}{b^2}\right] + \sum_{l=3} I_{dl} exp\left[-2\frac{(x-x_l)^2}{b^2}\right] \quad \textbf{(45a)}$$

$$I_{dl} = |\tilde{\varrho}_{\mathrm{v}1}|^2 |r_{\mathrm{v}3}|^2 |\tilde{\tau}_{\mathrm{v}1}|^2 I_{l-1} \quad \textbf{(45b)}$$

$$x_1 = 0, \text{and } x_l = x_{l-1} + \frac{w_2 n_0 sin\phi}{\sqrt{n_{a2}^2 - n_0^2 sin^2\phi}} \quad \textbf{(45c)}$$

represent positions of maximum intensities in the successive beams (l=2,3,4,⋯). For front illumination of the sample

$$I_{d1} = |\varrho_{v1}|^2 I_o \quad \textbf{(45d)}$$

$$I_{d2} = |\tau_{v1}|^2 |r_{v3}|^2 |\tilde{\tau}_{v1}|^2 I_o \quad \textbf{(45e)}$$

while for the back-illuminated sample

$$I_{d1} = |r_{v3}|^2 I_o \quad \textbf{(45f)}$$

$$I_{d2} = |t_{v3}|^2 |\tilde{\varrho}_{v1}|^2 |\tilde{t}_{v3}|^2 I_o \quad \textbf{(45g)}$$

Formula (44) does not describe the influence of multiple internal reflection of radiation in the thin film on the spatial distribution of reflected radiation. This effect can be neglected owing to the very small thickness of this film in comparison with the thick substrate thickness. The Goos-Hanchen effect [60] is not taken into account because it is much smaller than the beam shift evoked by internal reflection in a thick substrate.

The spatial distributions of the reflected radiation can be examined using not only a linear photodetector but also a goniometer [58,61,62]. The angular distributions of the reflected radiation (ADIRR) can be described using the following relation

$$\frac{\Delta x}{a} = sin\Delta\theta_d \cong \Delta\theta_d \quad \textbf{(46)}$$

where Δx is the linear shift of the reflected beam, a is the length of a goniometer arm on which a detector is placed to measure the radiation intensity, θ_d represents the angle between the goniometer arm and the direction of the beam incident on a sample, and $\Delta\theta_d$ is the angular shift of the reflected beam. The last relation is correct for $\Delta x \ll a$.

Numerical calculations were performed to analyze the influence of optical parameters of a sample on ADIRR. Some results are shown in Fig. **18**. The typical parameters of a-Si thin films were used to perform the calculations (Table **1**) and a=0.25 m was assumed. To simplify the analysis, the standard deviation $\sigma_{\Gamma 1}$=0 of the change in phase of radiation traversing a thin film was also assumed.

Different values of the real part of refractive index at the surfaces and in the bulk of a thin film strongly influence the ratio of successive maxima in the ADIRR (Fig. **18**). Also, the inhomogeneous absorption influences the ADIRR (Fig. **18**). The changes in the values of surface and bulk optical parameters affect the ADIRR calculated for front and back illumination of the sample in different ways. The value of ϕ determines the intensities of the first and second component of reflected radiation differently (Fig. **18**). The influence of sample parameters on the ADIRR varies with the polarization of light incident upon a sample. All this suggests using the measured ADIRR to estimate the optical parameters of thin films on thick substrates.

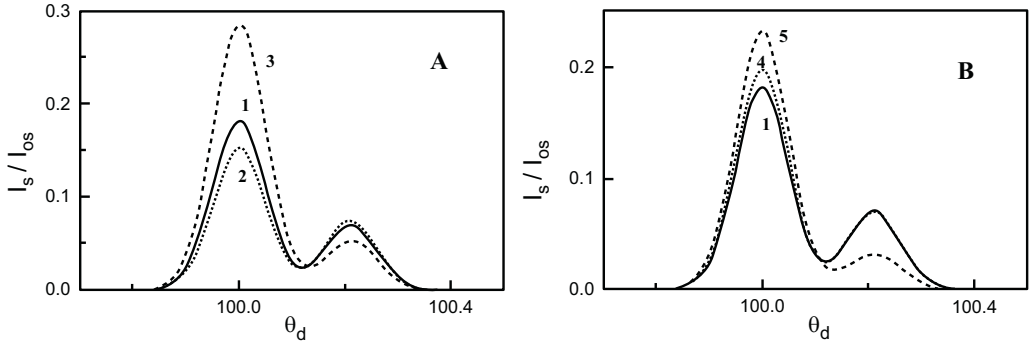


Figure 18: Influence of the surface and bulk values of real part of refractive index and absorption coefficient on ADIRR calculated for an inhomogeneous thin film on a thick substrate [63] (curve values are shown in Table 1; $\boldsymbol{w_1}$=0.2 μm, n_{a2}=1.5, w_2=1 mm, λ=632.8 nm, $\boldsymbol{\phi}$=50°, plane polarised radiation with the electric vector normal to the plane of incidence, b=1.3 mm).

Table 1: Values for the curves in Fig. **18**.

Parameter	Curve No.				
	1	**2**	**3**	**4**	**5**
n_{f1}	3.5	3.5	3.3	3.5	3.5
α_{f1} (10^5 m^{-1})	1	1	1	1	5
n_{a1}	3.5	3.5	3.5	3.5	3.5
α_{a1} (10^5 m^{-1})	1	1	1	1	1
n_{r1}	3.5	3.3	3.5	3.5	3.5
α_{r1} (10^5 m^{-1})	1	1	1	5	1

Table 2: Optical and geometrical parameters obtained by fitting ADIRR presented in Fig. **19**.

Parameter	Figure			
	A	**B**	**C**	**D**
$\boldsymbol{n_{f1}}$	3.07(1)	3.06(1)	3.17(3)	3.11(2)
$\boldsymbol{\alpha_{f1}}$, $\mathbf{10^5}$ **m^{-1}**	6.9(2)	6.1(1)	6.1(3)	8.9(1)
$\boldsymbol{n_{a1}}$	3.37(1)	3.37(1)	3.43(2)	3.43(4)
$\boldsymbol{\alpha_{a1}}$, $\mathbf{10^5}$ **m^{-1}**	11.0(3)	10.5(3)	10.9(2)	10.1(1)
$\boldsymbol{n_{r1}}$	2.86(3)	2.82(2)	2.91(2)	2.95(5)
$\boldsymbol{\alpha_{r1}}$, $\mathbf{10^5}$ **m^{-1}**	11.5(7)	12.5(4)	11.3(6)	10.9(1)
$\boldsymbol{w_1}$, **nm**	198(13)	198(4)	201(3)	199(2)

Fig. **19** presents the ADIRR reported in [63] for front-and back-illuminated sample of a-Si film on a 0.98 mm thick BK-7 substrate. The measurements were performed at room temperature for the p-and s-polarized radiation. The ADIRR was determined using the experimental set-up described in [58]. The samples were illuminated with a plane-polarized He-Ne TEM_{00} laser beam of

wavelength λ=632.8 nm and beam radius b=1.5 mm. The ADIRR was measured with 0.01° steps. To make Fig. **19** clearer, only some of the results are shown (data scattering was almost negligible). The two separated reflected beams are well recognized. The first beam is reflected at a point of radiation incidence on the sample. The second beam leaves the sample due to internal reflection in the thick parallel-sided substrate (see Fig. **17**).

The experimental ADIRR data presented in Figs. **19** are at least in qualitative agreement with the results of theoretical calculations presented above. Therefore, the data have been least-squared fitted with formula (44). The determined parameters of the investigated sample are presented in Table **2**. One can recognize that the results obtained in different experiments correspond. The value of n_{f1} is smaller than n_{a1} but greater than n_{r1}. The value of α_{a1} is similar to α_{r1} but greater than α_{f1}. It is possible that the low values of n_{f1} and α_{f1} are affected by the oxidation of a-Si.

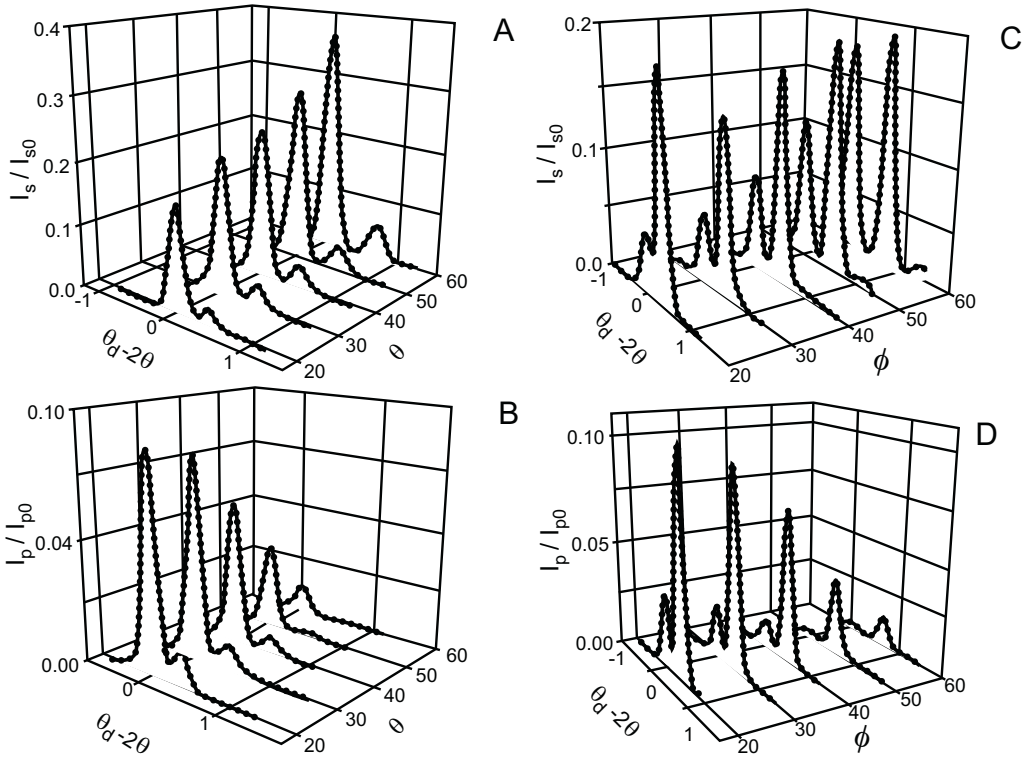


Figure 19: ADIRR of front-illuminated (A, B) and back-illuminated (C, D)) film of a-Si (w_l=198 nm) on a 0.98 mm thick BK-7 substrate plotted against angle of incidence $\boldsymbol{\phi}$ and the angle $\boldsymbol{\theta_d}$ between the incident beam and goniometer arm with the photodetector [63]. (A, C) s and (B, D) p polarized radiation; $\boldsymbol{\lambda}$=632.8 nm; $\boldsymbol{n_{a2}}$=1.51(2); points, the experimental results; solid curves, the fitted theoretical dependencies. The fitted semiconductor parameters are presented in Table 2.

Fig. **20** shows the dependences of maximum intensities of the components in ADIRR on angle of illumination incidence upon a sample composed of a-Si thin film on a thick BK-7 substrate. These dependences were [62] least-squared fitted with Eq. (44). The fitted parameters of the investigated

sample are presented in Table **3**. Parameters presented in columns A and B were obtained from simultaneous fitting of first and second maximum ADIRR components for s and p polarized radiation, respectively. The parameters obtained from simultaneous fitting of the angular dependencies of the first and second maximum ADIRR components as well as the s and p polarization are given in column A+B. It is recognized that the results obtained in different experiments and in different fittings correspond. Due to the greater number of fitted data, the values of parameters determined from simultaneous fitting of data obtained in experiments with s and p polarized radiation seem to be the more reliable. The fitted value of n_{f1} is smaller than n_{a1} but greater than n_{r1}. The fitted value of α_{a1} is 22% greater than α_{r1} but only 18% greater than α_{f1}. It is possible that the low values of n_{f1} and α_{f1} are affected by the oxidation of a-Si.

The same experimental data (Fig. **20**) were also fitted assuming optical homogeneity of the investigated sample (*i.e.* n_{f1}=n_{a1}=n_{r1}, α_{f1}=α_{r1}=α_{a1}). However, the residual squares of the differences between the theoretical and experimental data are much greater in this case than those obtained for the model of optically inhomogeneous film (compare the solid and broken curves in Fig. **20**). Therefore, the investigated sample of a-Si seems to be optically inhomogeneous over its thickness. The investigations of optical inhomogeneity of thin films of a-Si should be taken into account in optimization of technological conditions.

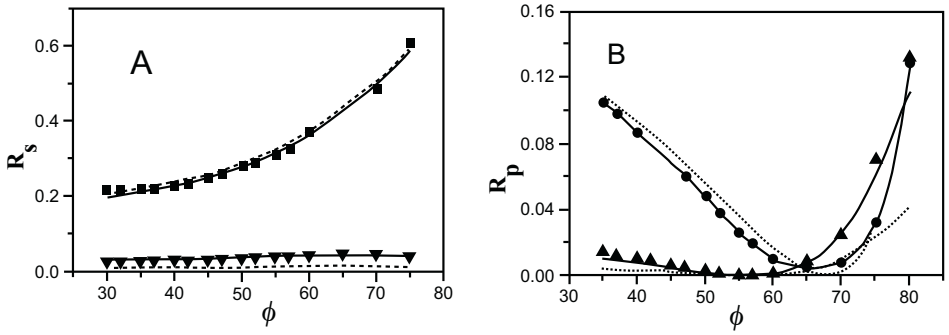


Figure 20: Reflectivity measured for the first (■,●) and second (▼,▲) maximum intensities in ADIRR of a 198 nm thick a-Si film on a thick BK-7 substrate against angle of radiation incidence on a sample [62] ($\boldsymbol{\lambda}$=632.8 nm, $\boldsymbol{n_{a2}}$=1.51(2), $\boldsymbol{w_2}$= 0.98 mm): (A) s and (B) p polarized radiation; points, the experimental results; solid and broken curves, the fitted theoretical dependencies for inhomogeneous and homogeneous films, respectively. The fitted parameters are presented in Table 3.

Simultaneous investigations of the angular dependence of radiation intensities of the two separated beams, reflected from a thin film on a thick, parallel-sided, transparent substrate, give more data and seem to be more accurate as well as more reliable than the standard variable angle reflectometry (VAR) method that takes into account the summarized intensity of the radiation reflected from a sample [62]. The presented method of investigations shares with the multiple angle ellipsometry and the VAR technique a common advantage over interference spectroscopy: measurements using these techniques are made at a single wavelength. Therefore, these techniques are free from the complications caused by refractive index dispersion.

Comparing the technique of angular investigations of radiation intensities of the two separated beams, reflected from a thin film on a thick substrate with the standard ADIRR method, the

simpler interpretation and theoretical description of the experimental results should be evident. In fact, the intensity of the first component of the reflected beam can be described without taking into account the multiple reflections of radiation in the thin-film substrate. The spatial distribution of the incident light is not so crucial for the fitting of the maximum intensities of the reflected radiation.

Table 3: Values of optical and geometrical parameters obtained by fitting different components of reflected radiation (Fig. **20**).

Parameter	Figure		
	A	B	A+B
n_{f1}	3.11(2)	3.12(2)	3.08(3)
α_{f1}, 10^5 m^{-1}	11.1(2)	10.7(2)	10.9(5)
n_{a1}	3.53(3)	3.48(1)	3.50(2)
α_{a1}, 10^5 m^{-1}	12.6(5)	14.1(3)	13.3(3)
n_{r1}	2.84(6)	2.93(1)	2.89(4)
α_{r1}, 10^5 m^{-1}	11.4(6)	10.2(2)	10.4(7)
w_1, nm	190(13)	189(9)	190(5)

4. SPATIAL DISTRIBUTION OF RADIATION INTENSITY IN A SEMICONDUCTOR FILM IN A MULTILAYER STRUCTURE

Very often the intensity of radiation in parallel-sided semiconductor film that is part of a multilayer structure should be determined. To simplify the consideration we assume the following: An isotropic, parallel-sided semiconductor film (Fig. **6**) is part of a multilayer structure (Fig. **1**). It is infinite in the XZ plane and is bounded by two non-absorbing coating layers of thicknesses w_1 and w_3 for the front and back sides, respectively. The layer structure is bounded in Y direction by two semi-infinite layers of refractive indices n_0 and n_4-iκ_4 for the front and back sides (Fig. **1**) (n_0=1 and n_4-iκ_4=1 for a sample immersed in air). Radiation of wavelength λ, which propagates in the XY plane, hits the structure with the angle of incidence ϕ. The radiation intensity is uniformly distributed over the sample surface.

The total electric vector $\vec{E}$ of radiation in a semiconductor film can be obtained from summing up the multiple reflected elements

$$\vec{E}_{vj} = \sum_{l=1}^{+\infty}(E_{vl}^{+} + E_{vl}^{-}) \quad \textbf{(47)}$$

where E_{vl}^{+}-electric field of the *l*-th beam (see Fig. **13**) which propagates from the front to back side, and E_{vl}^{-}-electric field of the *l*-th beam which propagates from the back to front side. Index v must be replaced by indices p and s for plane-polarized radiation with electric vector in and normal to the plane of incidence. After elementary summing up one obtains:

$$\vec{E}_{sj} = \frac{E_0\tau_{sj}exp\left[\frac{2\pi i}{\lambda}(ct - xn_0\sin\phi)\right]}{1-\varrho_{sj}\varrho_{s(j+1)}exp(-K_j)exp(-i\Gamma_{j0})}\left\{\begin{matrix} exp\left(-\frac{k_j+i\gamma_j}{2}y\right) + \\ \varrho_{s(j+1)}exp\left[\frac{k_j+i\gamma_j}{2}(y-2w_j)\right]\end{matrix}\right\}\vec{e}_z \quad \textbf{(48a)}$$

$$\vec{E}_{pj} = \frac{E_0\tau_{pj}exp\left[\frac{2\pi i}{\lambda}(ct-xn_0\sin\phi)\right]}{1-\tilde{\varrho}_{pj}\varrho_{p(j+1)}exp(-K_j)exp(-i\Gamma_{j0})}\left[\left\{\begin{matrix} exp\left(-\frac{k_j+i\gamma_j}{2}y\right)+ \\ \varrho_{p(j+1)}exp\left[\frac{k_j+i\gamma_j}{2}(y-2w_j)\right]\end{matrix}\right\}\vec{e}_x\cos\psi_j + \left\{exp\left(-\frac{k_j+i\gamma_j}{2}y\right)+ \varrho_{p(j+1)}exp\left[\frac{k_j+i\gamma_j}{2}(y-2w_j)\right]\right\}\langle\vec{e}_y\sin\psi_j\rangle\right] \quad \textbf{(48b)}$$

where E_0 is the amplitude of the electric vector of the wave incident upon the structure, $\vec{e}_x$, $\vec{e}_y$, $\vec{e}_z$ are the versors of the axis (Fig. **13**), $\psi = arcsin\left[n_0\left(n_0^2\sin^2\phi + a_{aj}^2\right)^{-1/2}\sin\phi\right]$ is the angle of radiation refraction in the j film, $\gamma_j = 4\pi a_{aj}/\lambda$, $k_j = a_{aj}\alpha_{aj}/n_{aj}$, t is the time, y is the distance from the front surface of the semiconductor j film. Other parameters retain their previous meanings.

Using Eqs. (48a) and (49b), the intensity of radiation (in photons) in the semiconductor film can be found from the Poynting vector

$$I_{\rm v} = \frac{1}{T_{em}}\frac{\lambda n_{aj}}{hc}\sqrt{\frac{\varepsilon_0}{\mu_0}}\int_0^{T_{em}}\left|\vec{E}_{\rm vj}\right|^2 dt \quad \textbf{(49)}$$

where the index v must be replaced by indices p and s for plane-polarized radiation with the electric vector in and normal to the plane of incidence; T_{em} is the period of the electromagnetic wave; and ε_0 and μ_0 are the electric permittivity and magnetic permeability of free space, respectively.

For the plane-polarized radiation with electric vector in the plane of incidence, $I_p(y)$ can be calculated numerically using Eqs. (48b) and (49). However, in the case of plane-polarized radiation with the electric vector normal to the plane of incidence it is relatively easy to find the following analytical formula

$$I_s(y) = I_{s0}\left[\begin{matrix} exp(-k_j y) + \left|\varrho_{s(j+1)}\right|^2 exp(k_j y - 2K_j) + \\ 2\left|\varrho_{s(j+1)}\right|exp(-K_j)\cos(\gamma_j y + \theta_{s(j+1)} - \Gamma_{j0})\end{matrix}\right] \quad \textbf{(50)}$$

where

$$I_{s0} = \frac{\left(1-\left|\varrho_{\rm sj}\right|^2\right)I_0}{1+\left|\tilde{\varrho}_{\rm sj}\right|^2\left|\varrho_{s(j+1)}\right|^2 exp(-2K_j)-2\left|\tilde{\varrho}_{\rm sj}\right|\left|\varrho_{s(j+1)}\right|exp(-K_j)\cos\left(\tilde{\theta}_{\rm sj}+\theta_{s(j+1)}-\Gamma_{j0}\right)} \quad \textbf{(51)}$$

is the so-called effective intensity of radiation (in photons) that enters the semiconductor, and I_0 is the intensity (in photons) of radiation incident upon the sample.

The spatial distribution of radiation intensity in a semiconductor film is a function of the sample geometrical and optical parameters, polarization and angle of incidence of radiation. However, it should be noted that by taking into account additional assumptions, the general formula (50) can be

reduced into some much simpler formulae, which apply to special experimental conditions (*e.g.* [64,65]). For normal radiation incidence upon a single semiconductor film surrounded by air, Eq. (50) is reduced to the expression presented in [66]. With the additional assumption, that the internal reflection of radiation is negligible, Eq. (50) is reduced to the Bouguer-Lambert law (see Eq. (3)).

Fig. **21** shows the effective intensity of radiation which enters a semiconductor film perpendicularly as a function of the reflection coefficient of a non-absorbing layer which covers the front surface of the semiconductor. The calculations were performed using Eq. (50). The curves in Fig. **21** represent different values of radiation reflectivity from the back semiconductor surface, different absorption of radiation in the semiconductor, and different changes in phase of the beam traversing the semiconductor film and reflected from its surfaces. It can be seen that the intensity of radiation in a semiconductor is very sensitive to all these parameters. Only in the case of negligible internal reflection does the radiation intensity in a semiconductor decrease linearly with the increasing reflection coefficient of the front surface film. The value of $|\varrho_{v3}|$ should be as high as possible. The highest intensity of radiation can be achieved in a semiconductor when the interference effect occurs and the sum of changes in phase of the beam traversing the semiconductor film and reflected from its surfaces is given by

$$\tilde{\theta}_{sj} + \theta_{s(j+1)} - \Gamma_{j0} = 2m\pi \quad \textbf{(52)}$$

where m=0,1,2,.

Table 4: Values for the curves in Fig. **21**.

Parameter	Curve No.				
	1	2	3	4	5
$\alpha_{2a}w_2$	0.1	0.1	0.1	0.1	10
$\|\varrho_{v3}\|^2$	1	1	0.75	0.5	1
$\tilde{\theta}_{sj} + \theta_{s(j+1)} - \Gamma_{j0}$	0	π	0	0	0

The value of front surface reflection coefficient, for which the radiation intensity in a semiconductor can achieve the greatest value, depends on the back surface reflection coefficient and absorption of radiation in the investigated semiconductor

$$|\tilde{\varrho}_{v1}|^2 = |\varrho_{v3}|^2 exp(-2K_j) \quad \textbf{(53)}$$

The value of front surface reflection coefficient selected in this way makes the internal reflection, and consequently the interference of internally reflected radiation, very effective. Simultaneously, an effectively large part of radiation which hits the multilayer structure can enter the semiconductor film. Authors of Chapter 9 of this eBook have presented special aspects of light trapping in thin silicon solar cells.

Radiative recombination of photogenerated carriers can influence the spatial distribution of radiation intensity in a semiconductor. One can say that part of the incident light is transformed

into bandgap radiation, emitted in this process, for which the absorption coefficient is smaller. This effect is not discussed in this paper.

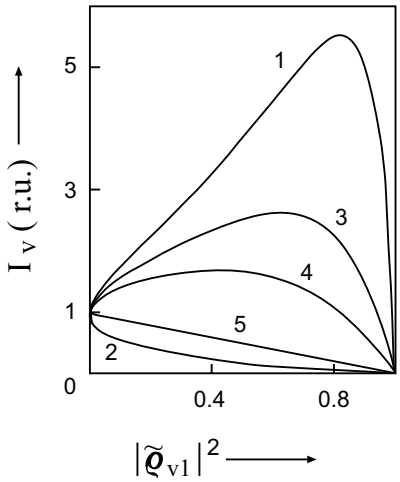


Figure 21: Effective intensity of radiation that enters a semiconductor film in a multilayer structure (Fig. **1**) *versus* the value of the reflection coefficient for back illumination of the front surface of the film, for different optical parameters of the sample (curve values are shown in Table 4).

4.1. Influence of Sample Parameters and Experimental Conditions on Radiation Intensity in a Semiconductor Film

Formula (50) is an idealization of the experimental situation: it was derived for the study of the perfect coherence of radiation interfering in a semiconductor film. It was pointed out in cases of transmittance and reflectance changes in phase Γ_j of the beam on traversing a semiconductor and the coating layers can be described by Gaussian distribution with the average values Γ_{10}, Γ_{20}, and Γ_{30}, and with standard deviations $\sigma_{\Gamma 1}$, $\sigma_{\Gamma 2}$, and $\sigma_{\Gamma 3}$, respectively. Hence, the total intensity of radiation in a semiconductor film should be calculated using integral

$$I_{Gv}(\Gamma_2,\Gamma_1,\Gamma_3) = \int_{\Gamma_2=0}^{+\infty}\int_{\Gamma_1=0}^{+\infty}\int_{\Gamma_3=0}^{+\infty} \frac{1}{\sigma_{\Gamma 2}\sqrt{2\pi}} exp\left[-\frac{(\Gamma_{20}-\Gamma_2)^2}{2\sigma_{\Gamma 2}^2}\right]\cdot \frac{1}{\sigma_{\Gamma 1}\sqrt{2\pi}} exp\left[-\frac{(\Gamma_{10}-\Gamma_1)^2}{2\sigma_{\Gamma 1}^2}\right]\cdot \frac{I_v}{\sigma_{\Gamma 3}\sqrt{2\pi}} exp\left[-\frac{(\Gamma_{30}-\Gamma_3)^2}{2\sigma_{\Gamma 3}^2}\right] d\Gamma_3 d\Gamma_1 d\Gamma_2 \quad \textbf{(54)}$$

where I_v is given by Eqs. (49) or (50). For $\sigma_{\Gamma 1}$=$\sigma_{\Gamma 2}$=$\sigma_{\Gamma 3}$=0 the density of Gaussian distribution is represented by the δ −Dirac and $I_{Gv}(\Gamma_2,\Gamma_1,\Gamma_3) = I_{Gv}(\Gamma_{20},\Gamma_{01},\Gamma_{30})$. In this case formula (54) reduces into the forms (49) or (50) for the ideal instance of perfect coherence of radiation interfering in a semiconductor film.

To simplify, one might limit the analysis of $I_{Gv}(y)$ to a double layer structure of a thin semiconductor film of thickness w_1, which covers a relatively thick, transparent, parallel-sided substrate of thickness w_2. As in the cases of transmittance and reflectance, it is assumed that the

interference of internally reflected radiation occurs in a semiconductor film and is negligible in the substrate (Eq. (33)). Obviously, some part of radiation incident on the front surface of the double layer structure is transmitted through the semiconductor thin-film, and then internally reflected from the back side of the substrate entering into the semiconductor from its rear. One can call this part of radiation secondary illumination in contrast to primary (front) illumination. According to Eq. (33); the phases of waves incident upon the semiconductor from the back side are random in comparison to the phases of radiation which illuminates the semiconductor film from the front side. Due to multiple internal reflection of radiation in the substrate, the secondary illumination consists of a set of beams. By totaling the radiation of these beams, the total intensity of the secondary illumination of the film is obtained [67]

$$I_{v0}^{-} = \frac{|\tau_{v1}|^2 |r_{v3}|^2}{1-|\tilde{\varrho}_{v1}|^2 |r_{v3}|^2} I_0 \tag{55}$$

where index v must be replaced by indices p and s for plane polarized radiation with the electric vector in and normal to the plane of incidence, respectively; all the other symbols retain their previous meanings. To calculate intensity of the p and s plane polarized radiation, the orientation of its electric field must be taken into account. For the primary illumination of the investigated thin semiconductor film on a thick substrate, the electric fields $\vec{E}_{s1}^{+}$ and $\vec{E}_{p1}^{+}$ are given by Eq. (48). In the case of secondary illumination of the investigated film, one obtains

$$\vec{E}_{s1}^{-} = \frac{E_0^{-} \tilde{t}_{s2} exp\left[\frac{2\pi i}{\lambda}(ct - x n_0 \sin\phi)\right]}{1 + r_{s1} r_{s2} exp(-K_1) exp(-i\Gamma_{10})} \begin{Bmatrix} exp\left[\frac{k_1 + i\gamma_1}{2}(y - w_1)\right] - \\ r_{p1} exp\left[-\frac{k_1 + i\gamma_1}{2}(w_1 + y)\right] \end{Bmatrix} \vec{e}_z \tag{56a}$$

$$\vec{E}_{p1}^{-} = \frac{E_0^{-} \tilde{t}_{p2} exp\left[\frac{2\pi i}{\lambda}(ct - x n_0 \sin\phi)\right]}{1 + r_{p1} r_{p2} exp(-K_1) exp(-i\Gamma_{10})} \left[\begin{Bmatrix} exp\left[\frac{k_1 + i\gamma_1}{2}(y - w_1)\right] - \\ r_{p1} exp\left[-\frac{k_1 + i\gamma_1}{2}(w_1 + y)\right] \end{Bmatrix} \vec{e}_x \cos\psi_1 + \left\{ exp\left[\frac{k_1 + i\gamma_1}{2}(y - w_1)\right] + r_{p1} exp\left[-\frac{k_1 + i\gamma_1}{2}(w_1 + y)\right] \right\} \vec{e}_y \sin\psi_1 \right] \tag{56b}$$

where the amplitude of the secondary illumination electric field is given by

$$\left|\vec{E}_0^{-}\right|^2 = \frac{|\tau_{v1}|^2 |r_{v3}|^2}{1-|\tilde{\varrho}_{v1}|^2 |r_{v3}|^2} \left|\vec{E}_0\right|^2 \tag{57}$$

One can find the intensity of p plane polarized radiation (in photons) in an ideal semiconductor film from the Poynting vector

$$I_p(y) = \frac{1}{T_{em}} \frac{\lambda n_{a1}}{hc} \sqrt{\frac{\varepsilon_0}{\mu_0}} \int_0^{T_{em}} \left[\left|\vec{E}_{p1}^{+}\right|^2 + \left|\vec{E}_{p1}^{-}(\phi)\right|^2 \right] dt \tag{58}$$

For the s polarized radiation, it is relatively easy to find the analytical formula describing distribution of radiation intensity in a thin film for the sum of primary and secondary illumination [67].

$$I_s(y) = I_{s0}\begin{bmatrix} g_1 e^{-k_j y} + g_2 e^{-(k_j y + K_j)} + \\ 2g_3 e^{-K_j}\cos(\gamma_j y + \psi) \end{bmatrix} \quad \textbf{(59)}$$

where $g_1 = 1 + D|r_{s1}|^2 e^{-K_j}$ **(60a)**

$$D = \frac{|\tau_{s1}|^2 |r_{s3}|^2 (1-|r_{s2}|^2)^2}{(1-|r_{s1}|^2)^2 (1-|\tilde{\varrho}_{v1}|^2 |r_{v3}|^2)} \quad \textbf{(60b)}$$

$$g_2 = |r_{s1}|^2 e^{-K_j} + D \quad \textbf{(60c)}$$

$$\sin\psi = \frac{|r_{s2}|\sin(\varphi_{s2} - \Gamma_{10}) - D|r_{s1}|\sin\varphi_{s1}}{g_3} \quad \textbf{(60d)}$$

$$\cos\psi = \frac{|r_{s2}|\cos(\varphi_{s2} - \Gamma_{10}) - D|r_{s1}|\cos\varphi_{s1}}{g_3} \quad \textbf{(60e)}$$

$$g_3 = |r_{s2}|^2 + D^2|r_{s1}|^2 - 2D|r_{s1}||r_{s2}|\sqrt{cos(\varphi_{s1} + \varphi_{s2} - \Gamma_{10})} \quad \textbf{(60f)}$$

$$I_{s0} = \frac{(1-|r_{s1}|^2) I_0}{1 + |r_{s1}|^2 |r_{s2}|^2 e^{-2K_j} + 2|r_{s1}||r_{s2}| e^{-K_j}\cos(\varphi_{s1} + \varphi_{s2} - \Gamma_{10})} \quad \textbf{(60g)}$$

I_{s0} is the so-called effective intensity of radiation (in photons) which enters the semiconductor, and I_0 is the intensity (in photons) of radiation incident upon the sample.

Taking into account the possible Gaussian distribution of the change in phase of the beam upon traversing the semiconductor film in the double layer structure, one should calculate

$$I_{vG}(y) = \int_0^{+\infty} \frac{I_v(y)}{\sigma_{\Gamma 1}\sqrt{2\pi}} exp\left[-\frac{(\Gamma_{10} - \Gamma_1)^2}{2\sigma_{\Gamma 1}^2}\right] d\Gamma_1 \quad \textbf{(61)}$$

where index v must be replaced by indices p and s for plane polarized radiation with the electric vector in and normal to the plane of incidence; other symbols retain their previous meanings.

Fig. **22** shows $I_v(y)$ calculated for a typical a-Si film in a double layer structure illuminated perpendicularly with radiation of different wavelengths. In the case of short wavelength and relatively strong radiation absorption (K_1>>1), the radiation intensity decreases exponentially with increasing distance from the illuminated semiconductor surface (chain curve in Fig. **22**). However, in the case of radiation weakly absorbed in optically thin films (K_1<1), a steady light wave occurs in the film (solid and broken curves in Fig. **21**) due to the interference of radiation internally reflected from its surfaces. This was first observed more than one hundred years ago by O. Wiener [68] in photographic emulsion that covered a mirror surface.

The period of interference changes of the radiation intensity in a sample equals

$$w_{in} = \frac{\lambda}{2a_{a1}} \quad \textbf{(62)}$$

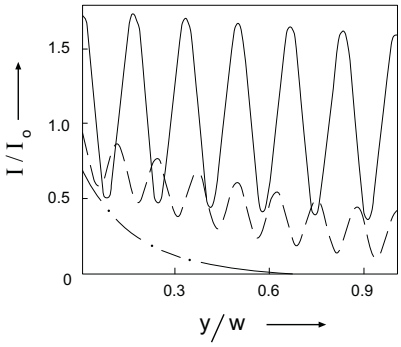


Figure 22: Spatial distribution of radiation intensity in a thin film on a thick, transparent substrate for different wavelengths of the radiation [67] (solid curve, λ=0.8 μm, n_{a1}=3.18, α_{a1}=2.48·10^5 m^{-1}; broken curve, λ=0.6328 μm, n_{a1}=3.29, α_{a1}=1.7·10^6 m^{-1}; chain curve, λ=0.528 μm, n_{a1}=3.45, α_{a1}=7.7·10^6 m^{-1}; ϕ=0°, w_1=0.76 μm; n_{f1}=n_{r1}=n_{a1}; α_{f1}=α_{r1}=α_{a1}; $\sigma_{\Gamma 1}$=0; N_{r2}=N_{f2}=N_{a2}=1.51; N_{r0}=N_{f3}=1).

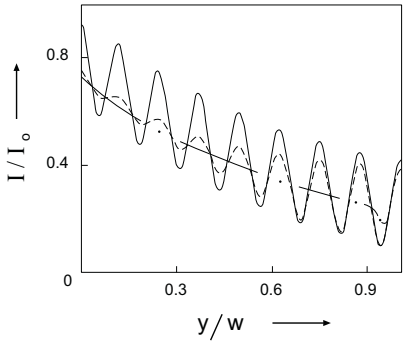


Figure 23: Influence of standard deviation $\sigma_{\Gamma 1}$ in the Gaussian distribution of the change in phase of a beam traversing a thin film on a thick, transparent substrate on the spatial distribution of radiation intensity [67] (solid curve, $\sigma_{\Gamma 1}/\Gamma_{10}$=0; broken curve, $\sigma_{\Gamma 1}/\Gamma_{10}$=0.05 ($\sigma_{\Gamma 1}$=1.49); chain curve, $\sigma_{\Gamma 1}/\Gamma_{10}$=0.5 ($\sigma_{\Gamma 1}$=24.8); other parameters are the same as in Fig. **22**).

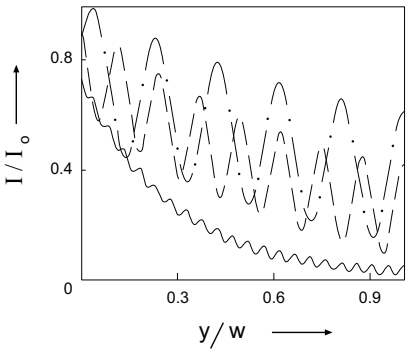


Figure 24: Spatial distribution of radiation intensity in a thin film on a thick transparent substrate for different thicknesses of the film [67] (solid curve, w_1=2 μm; broken curve, w_1=0.76 μm; chain curve, w_1=0.5 μm; λ=632.8 nm, n_{a1}=3.29, α_{a1}=1.7·10^6 m^{-1}, other parameters are the same as in Fig. **22**).

and decreases with the decreasing wavelength and angle of incidence of radiation. Thus, the λ is important for the spatial distribution of radiation intensity in a semiconductor film not only because of its influence on values of optical parameters of a semiconductor but also because of its direct influence on the spatial distribution of the steady light wave in a sample (Fig. **22**).

When $0<\sigma_{\Gamma 1}<2\pi$, the characteristic fringes in $I_v(y)$ decrease with increasing $\sigma_{\Gamma 1}$. The decrease is stronger near the front surface of a semiconductor (Fig. **23**). The periodicity of the spatial oscillations remains practically the same as for ideal interference. However, for $\sigma_{\Gamma 1}>2\pi$ the amplitudes decrease as the distance from both film surfaces increases. In this case spatial distribution $I_v(y)$ becomes relatively smooth in the middle of the film. Yet, even for great $\sigma_{\Gamma 1}$ there are relatively large changes of $I_v(y)$ with increasing distance from semiconductor surfaces, especially near the rear surface (Fig. **23**). It is a consequence of the total of the electric fields of incident and reflected waves close to the surface. It is not disturbed by the wave front deformation in the bulk of a semiconductor film. This effect cannot be described by the formulae derived in [66,69] for negligible interference of radiation.

The number of interference fringes of radiation intensity in the film is proportional to its thickness (Fig. **24**) and is inversely proportional to the radiation wavelength. The depth of interference oscillations vanishes with increasing film thickness (Fig. **24**) and with absorption coefficient of the radiation.

It should be emphasized that when a semiconductor is bounded by a rear medium which has smaller optical density ($n_{f2}<<n_{r1}$), the radiation intensity is relatively high near the rear semiconductor sample surface (Figs. **22-24**).

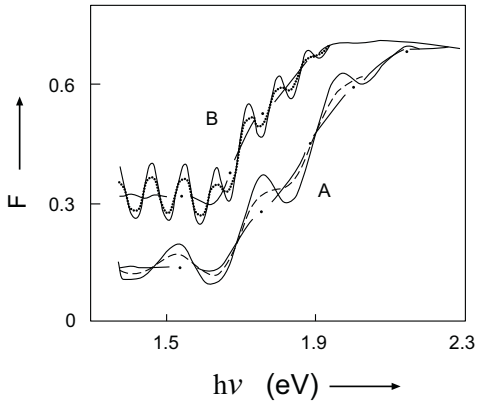


Figure 25: Influence of $\boldsymbol{\sigma_{\Gamma 1}}$ in the Gaussian distribution of the change $\boldsymbol{\Gamma_1}$ in phase of a beam traversing a semiconductor film on a thick transparent substrate on the spectral dependencies of the ratio of absorbed to incident photons for semiconductor films of different thicknesses [67] (A: $\boldsymbol{w_1}$=0.76 $\boldsymbol{\mu}$m; solid curve, $\sigma_{\Gamma 1}/\Gamma_{10}$=0; broken curve, $\sigma_{\Gamma 1}/\Gamma_{10}$=0.03; chain curve, $\sigma_{\Gamma 1}/\Gamma_{10}$=0.1; B: $\boldsymbol{w_1}$=2 $\boldsymbol{\mu}$m, solid curve, $\sigma_{\Gamma 1}/\Gamma_{10}$=0; broken curve, $\sigma_{\Gamma 1}/\Gamma_{10}$=0.01; chain curve, $\sigma_{\Gamma 1}/\Gamma_{10}$=0.03; $\boldsymbol{n_{a1}(\lambda)}$ and $\boldsymbol{\alpha_{a1}(\lambda)}$ taken from [29], other parameters are the same as in Fig. 22).

The ratio F of the number of photons absorbed in the whole semiconductor to the number of photons incident upon it equals:

$$F = \frac{1}{I_0}\int_0^{w_j} \alpha_j \, I_{\mathrm{v}}(y)dy. \quad \textbf{(63)}$$

It must be emphasized that the thickness of a semiconductor film strongly influences not only the spatial distribution (Fig. **24**) but also the total energy of radiation in it (Fig. **25).** In general, the spectral characteristics of F are very complicated due to simultaneous contributions of interference effects in semiconductor film and in the coating layers. Typical for these are oscillations that vanish with the increasing semiconductor thickness and absorption coefficient of radiation (thus increasing hν). The period of these oscillations depends on λ and n_{a1}, and decreases with increasing w_1. Due to different thicknesses of a semiconductor film and the coating layers, the appropriate periods of oscillations in spectral characteristics may differ. For some values of sample thickness, F can be comparable to its value where absorption of radiation in a very thick sample is strong (*e.g.* [70]).

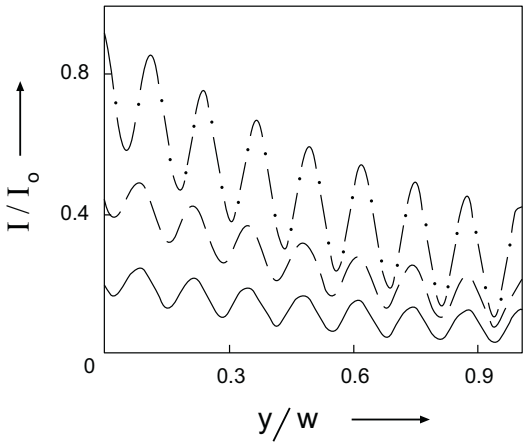


Figure 26: Spatial distribution of radiation intensity in a thin film on a thick, transparent substrate for different polarization and angle of incidence of radiation [67] (chain curve, $\phi = 0°$; broken curve, $\phi = 60°$, p plane polarized radiation with the electric vector in the plane of incidence; solid curve, $\phi = 60°$, s plane polarized radiation with the electric vector normal to the plane of incidence; w_1=0.76 μm, other parameters are the same as in Fig. **22**).

Increase of the standard deviation $\sigma_{\Gamma 1}$ does not influence the positions of the interference fringes in spectral characterisics of F (Fig. **25**). However, it does decrease the magnitude of the fringes. For a fixed λ the ratio F increases or decreases with increasing $\sigma_{\Gamma 1}$ (Fig. **25**) depending on the fact that λ can be appropriate for destructive or constructive interference of light in the sample.

The dependence of the spatial distribution of radiation intensity on polarization and the angle of incidence of radiation (Fig. **26**) is caused by two agents. First, by changing the angle of incidence and polarization of radiation, the intensity of radiation that enters the semiconductor structure is changed due to the change of $r_{\mathrm{v}1}$. Second, the value of the effective absorption coefficient α_{a1} increases with increasing angle ϕ. The angular dependence of α_{aj} can be relatively strong in semiconductors with small n_{aj} or bounded by an optically dense medium ($n_{a(j-1)}<n_{aj}<n_{a(j+1)}$) in which radiation propagates in high degree to the semiconductor surface.

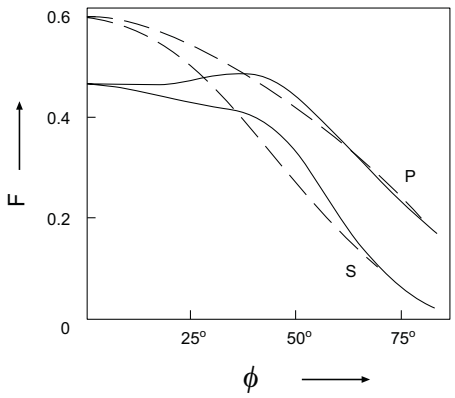


Figure 27: Ratio of absorbed to incident photons *vs.* angle of incidence for different film thicknesses and different polarization and wavelengths of radiation [67] (broken curve, w_1=0.76 μm, λ=0.6328 μm (n_{a1}=3.29, α_{a1}=1.7·10^6 m^{-1}); solid curve. w_1=2 μm, λ=0.7 μm (n_{a1}=3.23, α_{a1}=5.78·10^5 m^{-1}); p, s: values for plane polarized radiation with the electric vector in and normal to the plane of incidence; other parameters are the same as in Fig. **22**).

Due to the increase of the period w_i of changing radiation intensity in a film with increasing ϕ (Fig. **26**), the radiation intensity near the front semiconductor surface can attain the maxima and minima with an increase in the angle of incidence. If the period w_{in} is much smaller than the film thickness, the angular dependencies of F can be non-monotonous (Fig. **27**) or even oscillatory as observed experimentally, for example, in [71]. These oscillations are more evident for plane polarized radiation with the electric vector normal to the plane of incidence. If the radiation is strongly absorbed in a sample, the interference effect does not occur and the angular dependence of F becomes monotonous.

The interference peaks in spectral characteristics of F are shifted to shorter wavelengths with an increase in the angle of radiation incidence (Fig. **28**). In the case of non-normal illumination of a single semiconductor film, which strongly absorbs radiation, the intensity I_p (for plane-polarized radiation with the electric vector in the plane of incidence) is always greater than intensity I_s for radiation with electric vector normal to the plane of incidence. It is because of the smaller reflectivity of such polarized radiation from the front surface of the semiconductor. However, in the case of interference of weakly absorbed radiation this is not always true (see Fig. **28**). It occurs because s-polarized radiation is more strongly internally reflected from the sample surfaces. This dependence may be strongly influenced by the optical and geometrical parameters of surface coating layers [70]. For a relatively thick coating layer the oscillatory angular dependence of I_v should be also observed but such experimental conditions are less probable.

Assuming the same parameters as those presented in descriptions of Figs. **22**-**28**, the appropriate calculations of I_v and F were done [67] using the general theory represented by Eq. (54). These calculations were performed taking into account substrate thickness w_2=1 mm and the standard deviation $\sigma_{\Gamma 2}$=10 of the change in phase of a beam traversing the thick substrate. This value of standard deviation represents relatively small $\sigma_{\Gamma 2}/\Gamma_{20}$=10^{-4} variation of the change in phase of the beam traversing the substrate. However, $\sigma_{\Gamma 2}$=10 is greater than 2π and it is sufficient for discounting the interference effect in the substrate (see [70]). The results obtained in this case were

[67] exactly the same as those presented in Figs. **22-28**. Therefore, Eq. (61) can be applied as a good approximation of the general theory for a thin semiconductor film on a thick, transparent, parallel-sided substrate. Using this approximation makes the calculation about fifty times faster, so it is very important, for example, for the least square fitting of spectral PC or PEM characteristics with theoretical dependences.

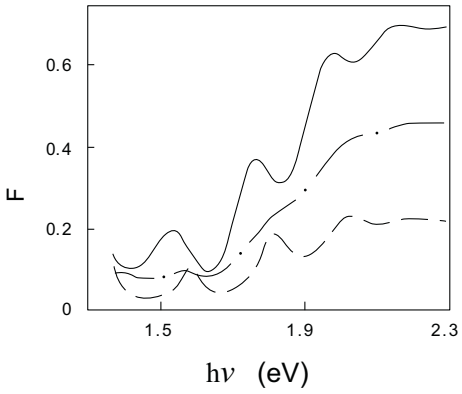


Figure 28: Spectral dependencies of the ratio of absorbed to incident photons for different polarizations and angles of incidence of radiation [67] (solid curve, $\phi = 0°$; chain curve, $\phi = 60°$ and p plane polarized radiation with the electric vector in the plane of incidence; broken curve, $\phi = 60°$ and s plane polarized radiation with the electric vector normal to the plane of incidence; w_1=0.76 μm; $\sigma_{\Gamma 1}/\Gamma_{10}$=0; other parameters are the same as in Fig. **25**).

Due to the interference effect, the change of the real part of the semiconductor refractive index with some of the experimental parameters (*e.g.*, electric field, magnetic field, temperature or illumination intensity) can cause an oscillatory dependence of F (*e.g.* [72]). This mechanism is similar to those that cause the oscillatory dependencies of F on λ, ϕ, and w_1.

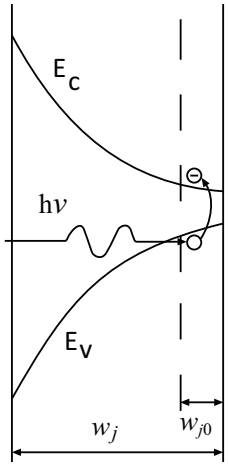


Figure 29: Energetic model of carrier photogeneration in a graded-gap semiconductor ($\boldsymbol{w_{j0}}$ is the width of the effective absorption region where the energy gap is smaller than the photon energy, $\boldsymbol{E}_{\mathrm{V}}$ and $\boldsymbol{E}_{\mathrm{C}}$ are the top of the valence band and bottom of the conduction band, respectively).

4.2. Spatial Distribution of Radiation Intensity in Graded Energy Gap Semiconductors

To simplify the analysis we assume that the energy gap gradient is parallel to the y-direction, and it is also parallel to illumination (ϕ=0°). In this case the absorption of radiation and photogeneration of excess carriers take place only in this part of a semiconductor film, where the semiconductor energy gap is smaller than photon energy (see Fig. **29**). Of course, the thickness w_{j0} of this part of a semiconductor can be much less than the thickness w_j of the whole semiconductor film (Fig. **29**). Thus, due to the weak absorption of radiation in a relatively thick, parallel-sided semiconductor film, the interference of radiation internally reflected from the sample surfaces can extremely influence the spatial distribution of radiation intensity in this part of the sample where carrier photogeneration occurs. Using the presented above approach, the intensity of radiation in a graded energy gap semiconductor can be described with Eq. (54), but the spatial distribution of radiation intensity I_v in that equation must be replaced by

$$I_s(y) = I_{s0}\left[\begin{array}{c} exp\left(-\int_0^y \alpha\, d\xi\right) + \left|\varrho_{s(j+1)}\right|^2 exp(-2K_j) exp\left(-\int_0^y \alpha\, d\xi\right) + \\ 2\left|\varrho_{s(j+1)}\right| exp(-K_j)\cos\left(\int_0^y \frac{4\pi}{\lambda} n\, d\xi + \theta_{s(j+1)} - \Gamma_{j0}\right) \end{array}\right] \quad \textbf{(64)}$$

where I_{s0} is given by Eq. (51) with $\left|\varrho_{sj}\right|$, $\left|\tilde{\varrho}_{sj}\right|$, and $\theta_{s(j+1)}$ described by Eq. (25). The other symbols retain their previous definitions.

For a single film bounded by semi-infinite, non-absorbing layers and for $\sigma_{\Gamma 2}$=0, Eq. (54) with (64) is reduced into formula presented in [73]. In general, equation (54) with (64) has no analytical solution. However it is possible to calculate $I_{Gv}(\Gamma_2, \Gamma_1, \Gamma_3)$ numerically using the appropriate spatial dependences of $n_j(y)$ and $\alpha_j(y)$. It was done, for example, in [73] for a single graded-gap $Cd_xHg_{1-x}Te$ film.

4.3. Spatial Distribution of Radiation Intensity in a Semiconductor Illuminated with Two Beams

One of the most promising methods of determining values of diffusion length of carriers in amorphous semiconductors is based on the steady state photocarrier grating (SSPG) model [75,76]. This technique uses an interference pattern obtained over the illuminated sample surface when two coherent radiation beams hit the sample at different angles of incidence (Fig. **30**). Due to this interference effect, the sample area between two electrodes consists of many regions of varying concentrations of free carriers. In places of constructive interference, if the incident photons have energy exceeding the energy gap of investigated semiconductors, they are likely to generate excess carriers in contrast to sites of destructive interference, where such excess carriers are not generated. Therefore, in a rough approximation the electrical conductivity (σ_{coh}) of the sample in the direction normal to the interference fringes is represented by a sum of several components, characterizing areas of photoconductivity (σ_{PCi}) and so-called dark conductivity (σ_{Dj})

$$\sigma_{coh}^{-1} = \sum_i \frac{l_i}{l}\sigma_{PCi}^{-1} + \sum_j \frac{l_j}{l}\sigma_{Dj}^{-1} \quad \textbf{(65)}$$

where l_i and l_j are lengths of the areas of constructive and destructive interference, and $l = \sum_i l_i + \sum_j l_j$ is the distance between electrodes.

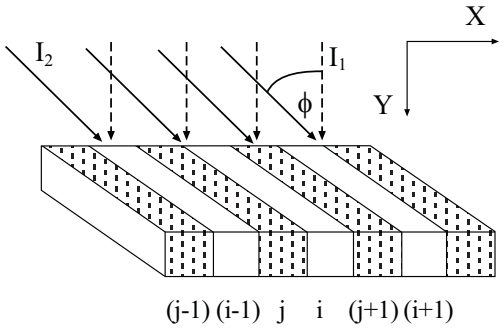


Figure 30: Graph illustration of the two beams showing an interference pattern in the case of steady state photocarrier grating technique of carrier diffusion length investigations [74].

After the changing polarization of radiation in one of the beams incident upon the sample under constant illumination, the interference effect vanishes and the concentration of free carriers is homogeneous. In this case, the electric conductivity (σ_{incoh}) of the sample is simply represented by its photoconductivity evoked by the sum $(I_{10} + I_{20})$ of the intensities of light in the beams incident upon the sample. In the SSPG method of investigations, the ratio $\sigma_{coh}/\sigma_{incoh}$ of the conductivities of the sample with and without the interference of radiation incident upon the sample depends on the carrier diffusion length L [75]

$$\frac{\sigma_{coh}}{\sigma_{incoh}} = \sqrt{1 - \frac{C_0}{\left[1+\left(\frac{2\pi L}{\Lambda}\right)^2\right]^2}} \quad \textbf{(66)}$$

$$\text{where } C_0 = 4\zeta^2\eta_0^2 \frac{I_{10}I_{20}}{(I_{10}+I_{20})^2} \quad \textbf{(67)}$$

$\Lambda = \lambda/\sin\phi$ represents the grating period, ϕ is the angle between the beams, ζ is a power coefficient in the semi-empirical power-law formula (19), and η_0 is a quantity representing an empirical factor [75] between zero and unity that describes the fringe visibility reduced due to partial coherence between the beams, light scattering and mechanical vibration. The other symbols retain their previous definitions.

The sample used in SSPG measurements usually consists of the double layer structure: a thin, isotropic, semiconductor film on a thick, parallel-sided, uniform, isotropic, transparent substrate (Fig. **31**). It is located in the *XZ* plane and is bound in the *Y* direction by two semi-infinite layers. The sample is illuminated with two beams of plane-polarized radiation of wavelength λ that has components in the wavelength range Δλ. The planes of light polarization of the two beams can be parallel or perpendicular, respectively. One of the beams illuminates the sample normally and the second beam impinges upon the sample with an angle of incidence ϕ (Fig. **30**). The radiation intensity of each of the beams is uniformly distributed over the sample surface. The reflections from the air-semiconductor, semiconductor-substrate and substrate-air interfaces are specular.

Owing to the variation in thin film thickness w_1, surface roughness, variation in the real part of refractive index n_{a1} over the illuminated sample area, and the distribution of radiation intensity over the wavelength range, the change Γ_1 in the phase of radiation traversing a semiconductor film has the Gaussian distribution (*e.g.* [70,76]) around the most probable value of Γ_{10} with a standard deviation $\sigma_{\Gamma 1}$ over the illuminated sample area. Interference of internally reflected radiation occurs in the thin semiconductor film and is negligible in the substrate.

Some part of the radiation incident on the front surface is obviously transmitted through the semiconductor thin-film and then internally reflected from the rear side of the substrate (Fig. **31**). We call this part of the radiation a 'secondary illumination' in contrast to the 'primary (front) illumination'. Assuming that no interference of radiation takes place in the semiconductor substrate, the phases of the waves incident on the semiconductor from the rear are random in comparison to the phases of radiation which illuminate the semiconductor from the front. The sum of the radiation of the multiple reflected beams gives the total intensity $I_{\mathrm{v}0}^{-}$ of the secondary illumination (Eq. (55)).

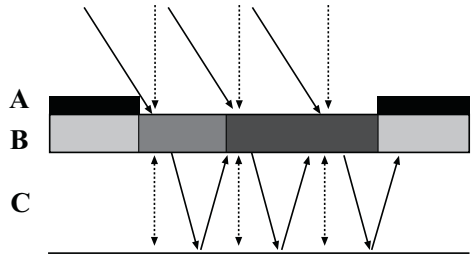


Figure 31: Schematic representation of radiation propagation in a sample used in a SSPG technique of carrier diffusion length investigations [76] (A, electrode; B, thin film of the investigated material; C, thick, parallel-sided, transparent substrate; solid and dashed arrows represent the two beams of light incident on and passing through the sample; the different shadows in the semiconductor film (B) show the relative intensity of the radiation).

To calculate the intensity of the *p* and *s* plane polarized radiation (*i.e.*, with the electric vector in and normal to the plane of incidence) the orientation of its electric field must be taken into account. For the primary illumination of the investigated thin semiconductor film on a thick substrate, the electric fields $\vec{E}_{s1}^{+}$ and $\vec{E}_{p1}^{+}$ are given by the Eqs. (48). The adequate electric fields $\vec{E}_{s1}^{-}$ and $\vec{E}_{p1}^{-}$ are described by Eq. (56). The intensity of radiation (in photons) in an ideal semiconductor film illuminated with two beams (incident upon the sample with angles of incidence ϕ and 0°) can be found from the Poynting vector:

$$I_{\mathrm{v}}(x,y) = \frac{1}{T_{em}} \frac{\lambda n_{a1}}{hc} \sqrt{\frac{\varepsilon_0}{\mu_0}} \int_0^{T_{em}} \left[\left| \vec{E}_{\mathrm{v}1}^{+}(\phi) + \vec{E}_{\mathrm{v}1}^{+}(0°) \right|^2 + \left| \vec{E}_{\mathrm{v}'1}^{-}(\phi) + \vec{E}_{\mathrm{v}'1}^{-}(0°) \right|^2 \right] dt \qquad \textbf{(68)}$$

where indices v and v′ describe the polarization direction of the two incident beams. These indices should be replaced with *p* or *s* for the appropriate polarization direction.

Taking into account the Gaussian distribution of the phase of radiation traversing a semiconductor film, the total intensity of radiation in a semiconductor film illuminated with two beams must be calculated using (68) in the following integral:

$$I_G(x,y) = \int_0^{+\infty} \frac{I_V(x,y)}{\sigma_{\Gamma_1}\sqrt{2\pi}} exp\left[-\frac{(\Gamma_{10}-\Gamma_1)^2}{2\sigma_{\Gamma_1}^2}\right] d\Gamma_1 \quad \textbf{(69)}$$

Numerical calculations were done [76] to analyze the influence of the optical and geometrical parameters of the sample as well as the experimental conditions on the spatial distribution of radiation intensity in a sample examined with the SSPG method of determining carrier diffusion length. Some of results are shown in Figs. **32** and **33** (values of parameters essential for different sections of the figures are given in Tables **5** and **6**). The values of the optical parameters of amorphous silicon [51] were used to describe the semiconductor film. The value of N_{r2}=N_{f2}=N_{a2}=1.51 was assumed as the refractive index of the substrate.

To simplify the analysis, one can distinguish two important results of the SSPG tests: (A) The two beams that hit a sample have the same polarization. (B) The two radiation beams are plane polarized in normal directions. In the former instance, there is interference of the electromagnetic fields of the two beams, affecting the interference pattern in the illuminated surface of the sample (Fig. **32**). In the latter, no interference occurs between the two beams and the sample is uniformly illuminated at its surface with radiation intensity equaling the sum of the two components (Fig. **33B**).

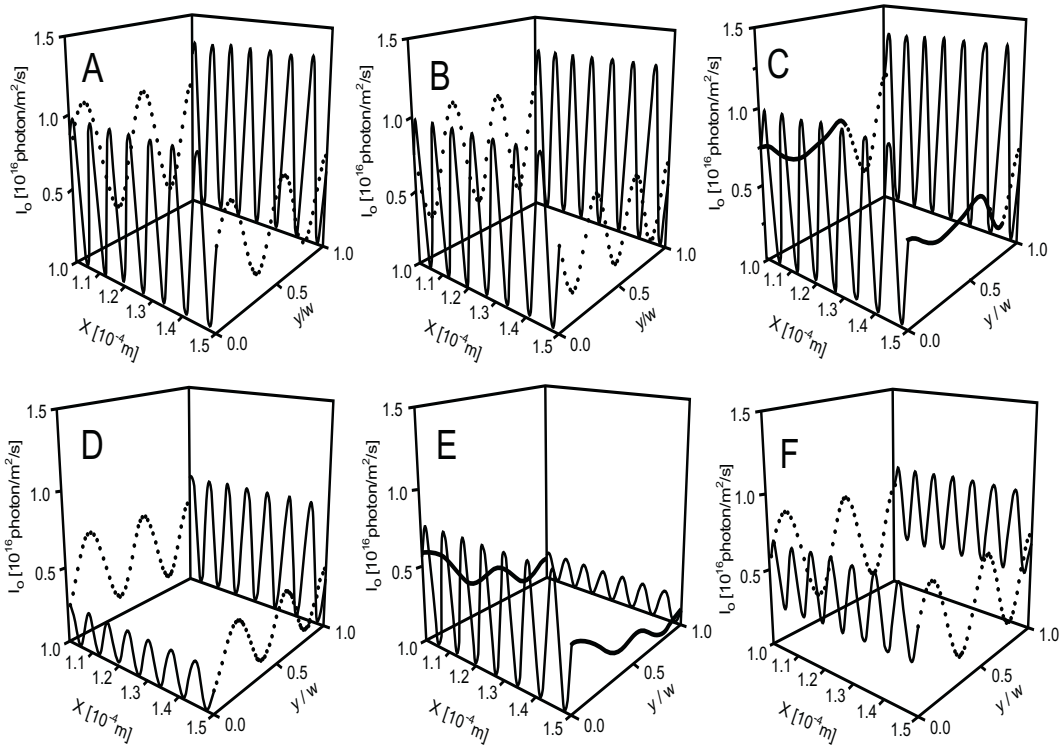


Figure 32: Influence of optical and geometrical parameters of a thin semiconductor film on spatial distribution of radiation intensity in a sample examined with the SSPG method in the case of interference of radiation internally reflected in a semiconductor film [76] (values of parameters essential for different sections of the figure are given in Table 5; s polarized radiation, λ= 633nm, Δλ=0, ϕ=5°, I_2=10^{16} photons/(m^2s), $\boldsymbol{N_{r2}}$=$\boldsymbol{N_{f2}}$=$\boldsymbol{N_{a2}}$=1.51, w_2=1 mm, $\boldsymbol{N_{r0}}$=$\boldsymbol{N_{f3}}$=1).

Fig. **32** shows the influence of the optical and geometrical parameters of a thin semiconductor film on spatial distribution of radiation intensity in a sample examined with the SSPG method in the interference example. The steady light wave is well recognized. To make the figure clearer, the thickness of a semiconductor film was assumed relatively small. The period of this steady light wave and consequently the number of extrema depends on the semiconductor thickness (compare Figs. **32A** and **32B**) and obviously the real part of the refractive index (compare Figs. **32A** and **32D**). The position of maxima or minima of the steady light wave at the semiconductor interface should be especially important if the surface recombination of electrons and holes is faster than the bulk recombination process. The last case is important for photoconductivity [5].

Table 5: Values for the curves in Fig. **32**.

Figure Section	**A**	**B**	**C**	**D**	**E**	**F**
w [μm]	0.2	0.25	0.2	0.2	0.2	0.2
σ_w [μm]	0	0	0.05	0	0	0
n	3.5	3.5	3.5	3.8	3.5	3.5
α [m^{-1}]	10^6	10^6	10^6	10^6	10^7	10^6
I_1/I_2	1	1	1	1	1	0.05

The steady light wave vanishes with the increase of the standard deviation σ_{w1} of the thickness of semiconductor film (Fig. **32C**) as well as with the increase of the absorption of light (Fig. **32F**). However, in the first case the decrease of the characteristic spatial oscillations of radiation intensity is stronger near the front surface of a semiconductor (Fig. **32C**). The periodicity of the spatial oscillations remains essentially the same as for ideal interference. For greater values of σ_{w1} the amplitudes decrease with increasing distance from both film surfaces. In this case the spatial distribution of radiation intensity in the *Y* direction becomes relatively smooth in the middle of the film. Yet, even for large σ_{w1} there are relatively large changes of $I_G(x, y)$ with increasing distance from the semiconductor surfaces, especially near the back surface (Fig. **32C**). This is a consequence of the accumulation of electric fields of incident and reflected waves close to the surface. This effect cannot be described by the formula derived for the case of negligible interference of radiation internally reflected in a thin film.

An increase of the real part of refractive index of a semiconductor affects the change in intensity of radiation that enters the semiconductor film (compare Fig. **32A** and **32D**). The same is observed in the case of the increase of absorption coefficient for the semiconductor (compare Fig. **32A** and **32F**). In both cases a lower photoconductivity is expected. The spatial distribution and magnitude of radiation intensity in a semiconductor film examined with the SSPG method is sensitive to the ratio of radiation intensities in the two beams that illuminate the sample (compare Fig. **32A** and **32F**). Therefore, the polarization of the oblique illumination beam is also important.

Fig. **33** presents the influence of polarization and angle of incidence ϕ on the spatial distribution of radiation intensity in a sample examined with the SSPG method. Comparing Figs. **32A** and **33C** one recognizes the influence of the high reflection support of the sample (see description of the figures) on the spatial distribution of radiation intensity in a semiconductor film. The increase of α_{a3} must also consider the shadow of the electrode for x=115.6 μm. Such a shadow is more

important in cases where there is no interference of the two beams of perpendicular polarization (Fig. **33B**). The position (in *X* dimension) of this shadow depends on the angle of incidence of radiation upon the sample (compare Fig. **33A** and **33C**) as well as on the thickness of the semiconductor film substrate [76] and its refractive index. An increase of the angle between the two beams incident upon a sample decreases the period of the steady-state light grating in the *X* dimension (compare Figs. **32A** and **33A**). This is an essential feature of the SSPG measurement [74-77].

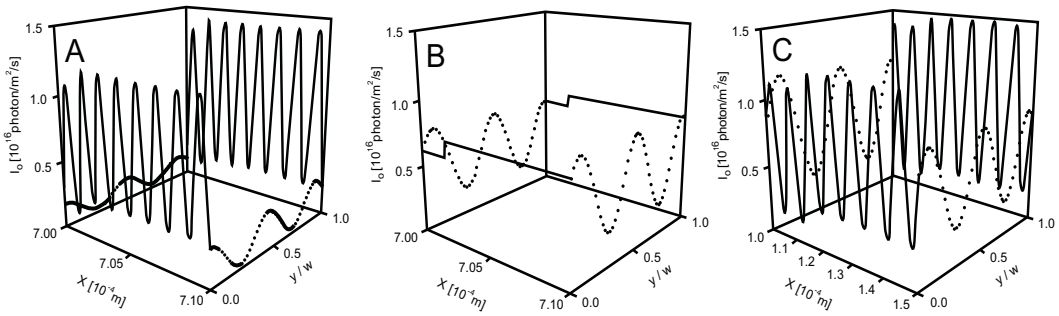


Figure 33: Influence of polarity and angle of radiation incidence ϕ on spatial distribution of radiation intensity in a sample examined with the SSPG method [76] (values of parameters essential for different sections of the figure are given in Table 6; $I_1=I_2=10^{16}$ photons/(m^2s), n=3.5, $\alpha=10^6$ m^{-1}, w=0.2 μm, $\sigma_w=0$, $n_3=1$, $\alpha_3=5\bullet10^7$ m^{-1}; other parameters are the same as for Fig. **32**).

Table 6: Values for the curves in Fig. **33**.

Figure Section	**A**	**B**	**C**	**D**
polarities	s-s	p-s	s-s	s-s
ϕ	30^o	30^o	5^o	30^o

It should be emphasized that even in cases of different polarizations of illumination beams, the spatial distribution of radiation intensity in a semiconductor film can be inhomogeneous both in the *X* and *Y* dimensions (Fig. **33B**). It is worth noting that the steady light wave occurring in homogeneously illuminated film is important for the magnitude of the observable photoconductivity (*e.g.* [70]). The increase of substrate thickness influences the spatial distribution of the radiation intensity in both the *X* direction (Fig. **33A**) and in the *Y* direction. Obviously the wavelength determines the values of optical parameters of the examined material and also strongly affects the interference phenomenon. Therefore the spatial distribution of radiation intensity in a semiconductor film is also strongly dependent on λ.

5. PHOTOGENERATION OF FREE CARRIERS

One can describe the ambipolar transport of photocarriers in a semiconductor in a phenomenological manner [4-6]. In this approach the concept of drift mobility is used, which is an average mobility of all carriers involved in the transport and is thus model independent. The phenomenological theory is based upon the solution of Maxwell's equations, the Poisson equation, the continuity equations and the transport equations. The solution can be obtained analytically only

for special cases. To simplify the consideration one assumes that: a homogeneous semiconductor is placed in a uniform, steady magnetic field; the magnetic field induction $\vec{B}$ is so weak that in the dependence of electrical conductivity on $\vec{B}$, the terms with second and higher orders of $\vec{B}$ are negligible; all parts of the semiconductor have the same temperature and the carriers are described by the Boltzmann statistics. The aforementioned assumptions are justified in most of the experiments on PEM effect. Some exceptions have been discussed in detail in [6].

The transport through a semiconductor in the presence of a static electric field intensity $\vec{E}$ and steady $\vec{B}$ under bulk photogeneration is described by the following equations

$$\vec{j}_e = e\mu_e n_e \vec{E} + eD_e grad(n_e) - \mu_{He}\left(\vec{j}_e \times \vec{B}\right) \quad \textbf{(70a)}$$

$$\vec{j}_h = e\mu_h n_h \vec{E} - eD_h grad(n_h) + \mu_{Hh}\left(\vec{j}_h \times \vec{B}\right) \quad \textbf{(70b)}$$

$$\frac{\partial n_e}{\partial t} = G_e - R_e + \frac{1}{e} div(\vec{j}_e) \quad \textbf{(71a)}$$

$$\frac{\partial n_h}{\partial t} = G_h - R_h - \frac{1}{e} div(\vec{j}_h) \quad \textbf{(71b)}$$

where $\vec{j}_e$ and $\vec{j}_h$ represent the electron and hole current densities, μ_e, μ_{He}, μ_h and μ_{Hh} are drift and Hall mobilities of electrons and holes, respectively, n_e and n_h are concentrations of electrons and holes, D_e and D_h are the diffusion constants for electron and holes, e is the electronic charge, G_e, R_e, G_h, and R_h are photogeneration and recombination rates of electrons and holes.

In Eq. (70), phenomenological distinction is made between Hall and drift mobilities of electrons and holes, scattering models not considered. In case of degenerate energy bands in the investigated semiconductor, the same equations still apply; however, the Hall and drift mobilities as well as diffusion coefficients for holes are certain weighted averages, as used, for example, in Refs. cited in [6]. It is worth mentioning that relatively few fast holes can make a large contribution to the PEM current or voltage.

The photogeneration rates are given by:

$$G_e = \beta_e \alpha_e I_{\mathrm{v}}(y) \quad \text{and} \quad G_h = \beta_h \alpha_h I_{\mathrm{v(y)}} \quad \textbf{(72)}$$

where $I_{\mathrm{v}}(y)$ represents the local intensity of radiation (in photons). Such intensity is described, *e.g.*, by Eqs. (54) and (61). The other parameters are the same as in Eq. (15).

In the so-called small-signal approach, a simple model for the recombination mechanisms states that R_e and R_h are proportional to the excess carrier density. It acknowledges the fact that no recombination takes place if the carrier density equals the thermal equilibrium value. The resulting expressions for the recombination rates of electrons and holes are given by:

$$R_e = \frac{\Delta n_e}{\tau_e} \quad \text{and} \quad R_h = \frac{\Delta n_h}{\tau_h} \quad \textbf{(73)}$$

where $\Delta n_e = n_e - n_{e0}$ and $\Delta n_h = n_h - n_{h0}$ are concentrations of the excess carriers, and n_{e0} and n_{h0} are equilibrium concentrations of electrons and holes, respectively. The electron and hole lifetimes τ_e and τ_h can be interpreted as the average times after which excess minority carriers recombine.

In the cases of arbitrary illumination intensities, the recombination rates are represented by much more complicated formulae different for various recombination mechanisms, *e.g.*, for the Auger recombination and for the trap-assisted Shockley-Hall-Read recombination (*e.g.* [4,5]). Additionally, recombination at semiconductor surfaces and interfaces can have a significant impact on the photoelectric and PEM effects. This is because surfaces and interfaces typically contain a large number of recombination centers because of the abrupt termination of the semiconductor crystal which leaves a large number of electrically active dangling bonds. In addition, the surfaces and interfaces are more likely to contain impurities since they are exposed during the device fabrication process.

For cases of small, steady illumination, the boundary conditions at the front and back semiconductor surfaces must be taken into consideration to solve the transport equations. For a parallel-sided sample, which is infinite in the XZ plane, the boundary conditions are:

$$j_{ey} = es_{1e}\Delta n_e = es_{1h}\Delta n_h \quad \text{for } y = 0 \tag{74}$$

$$j_{ey} = -es_{2e}\Delta n_e = -es_{2h}\Delta n_h \quad \text{for } y = w_j \tag{75}$$

where s_{1e}, s_{1h}, s_{2e}, and s_{2h} represent recombination velocities for electrons and holes at the front and back surfaces of the j semiconductor film, j_{ey} is the y component of electron current density.

When the semiconductor sample is placed in a magnetic field $\vec{B}$(0,0,B), the radiation propagates in the XY plane, and if the sample ends in X-direction are short-circuited externally, the so-called short-circuit PEM current which flows through the sample is given by:

$$i_{PEM} = (\mu_{He} + \mu_{Hh})Bl_z \int_0^{w_j} j_{ey} dy \tag{76}$$

where l_z is the width of a sample.

The PC of the sample is described by

$$\sigma_{PC} = el_z \int_0^{w_j} [\mu_e \Delta n_e(y) + \mu_h \Delta n_h(y)] dy \tag{77}$$

One can find the solutions for the PEM and PC responses solving Eqs. (70)-(73) with the boundary conditions (74) and (75) after assuming an adequate spatial distribution of light in the investigated sample. For example, in [29] the PEM and PC responses have been analysed in the double layer structure of a single, parallel-sided homogeneous, and isotropic semiconductor film of thickness w_1 on transparent, parallel-sided substrate of thickness $w_2 \gg w_1$ (the conditions (33) have been assumed, too). In this case, for normal illumination of a sample, the distribution of radiation in the

semiconductor film is given by Eq. (59). Hence, the following formulae have been derived (for $K_1 L \neq 1$):

$$i_{PEM} = (\mu_{He} + \mu_{Hh}) B e w_1 l_z \beta_{PEM} I_{s0} \left[\frac{g_1}{(K_1^2 - W^2) R_P} \{ [W + S_2 + (W - S_2) e^{-2W} - 2W e^{-W}](K_1 + S_1) + [W + S_1 + (W - S_1) e^{-2W} - 2W e^{-W}](K_1 - S_2) e^{-K_1} - (1 - e^{-K_1}) R_P \} - \frac{g_2 K_1 e^{-K_1}}{(K_1^2 - W^2) R_P} \{ [W_{s1}(K_1 + S_2) + W_{s2}(K_1 - S_1) e^{-K_1}](1 - e^{-W}) - (1 - e^{-K_1}) R_P \} - \frac{g_3 K_1 e^{-K_1}}{(K_1^2 - W^2) R_P} \langle (1 - e^{-W}) \{ [\Gamma_1 \sin(\Gamma_1 - \psi) - S_2 \cos(\Gamma_1 - \psi)] W_{s1} + (S_1 \cos\psi - \Gamma_1 \sin\psi) W_{s2} + R_P [\cos(\Gamma_1 - \psi) - \cos\psi] \} \rangle \right] \quad \textbf{(78)}$$

$$\sigma_{PC} = (\mu_{He} + \mu_{Hh}) e l_z \beta_{PC} \tau_{PC} I_{s0} \left[\frac{W K_1 (1 - e^{-W})}{(K_1^2 - W^2) R_P} \{ g_1 [W_{s2}(K_1 + S_1) - W_{s1}(K_1 - S_2) e^{-K_1}] + g_2 [W_{s1}(K_1 + S_2) - W_{s2}(K_1 - S_1) e^{-K_1}] \} - \frac{K_1^2 (1 - e^{-K_1})}{K_1^2 - W^2} (g_1 + g_2 e^{-K_1}) + \frac{g_3 K_1 e^{-K_1}}{(\Gamma_1^2 + W^2) R_P} \langle W (1 - e^{-W}) [\Gamma_1 \sin(\Gamma_1 - \psi) - S_2 \cos(\Gamma_1 - \psi)] W_{s1} - (S_1 \cos\psi - \Gamma_1 \sin\psi) W_{s2} \rangle - R_P \Gamma_1 [\sin(\Gamma_1 - \psi) + \sin\psi] \right] + (\mu_{He} + \mu_{Hh}) e l_z \beta_{PC} \tau_{PC} I_{s0} \left\{ (1 - e^{-K_1})(g_1 + g_2 e^{-K_1}) + \frac{g_3 K_1 e^{-K_1}}{2\Gamma_1} [\sin(\Gamma_1 - \psi) + \sin\psi] \right\} \quad \textbf{(79)}$$

where $R_P = (W + S_1)(W + S_2) - (W - S_1)(W - S_2) e^{-2W}$, **(80a)**

$W_{s1} = W + S_1 - (W - S_1) e^{-W}$, **(80b)**

$W_{s2} = W + S_2 - (W - S_2) e^{-W}$, **(80c)**

the ambipolar carrier diffusion constant is given by

$$D = \frac{(n_e + n_h) D_e D_h}{(1 + \mu_{Hh}^2 B^2) D_e n_e + (1 + \mu_{He}^2 B^2) D_h n_h} \quad \textbf{(80d)}$$

the effective carrier lifetime deduced from the PEM is represented by

$$\tau_{PEM} = \frac{n_e \tau_h + n_h \tau_e}{n_e + n_h} \quad \textbf{(80e)}$$

the effective carrier lifetime deduced from PC is given by

$$\tau_{PC} = \frac{\mu_e \tau_e + \mu_h \tau_h}{\mu_e + \mu_h} \quad \textbf{(80f)}$$

$W = w_1 / L_{PM}$ is the dimensionless thickness of a sample, $L_{PM}^2 = D \tau_{PEM}$ is the square of effective ambipolar carrier diffusion length that is determined in PEM investigations, and $S_1 = s_{1e} \tau_e w_1 / L_{PM}^2$ and $S_2 = s_{2e} \tau_e w_1 / L_{PM}^2$ are dimensionless front and back surface recombination velocities. All the other symbols retain their previous meanings.

The spectra of photoconductivity reported in [29] depicted correlation with the interference fringes observed in transmittance of the same sample (Fig. **34**). Therefore, formulae (78) and (79) have

been used in [29] to determine the spectral dependences of QECs (Fig. **3**) and to determine the spectral distributions of different components of absorption coefficient of a-Si:H,F (Fig. **2**). Values of carrier lifetime, diffusion length, and surface recombination velocity have been estimated, too. However, the influence of radiation intensity on optical and recombination parameters of the material has been observed [29]. The same situation has been observed in many experimental cases. For example, Fig. **35** presents the typical amorphous silicon non-linear dependencies of PC on illumination intensity. Fitting of $\sigma_{PC}(I_0)$ with the semi-empirical power-law formula (19) allows one to determine the power coefficients (Fig. **35**). Usually, the ζ depends on photon energy (Figs. **36** and **37**).

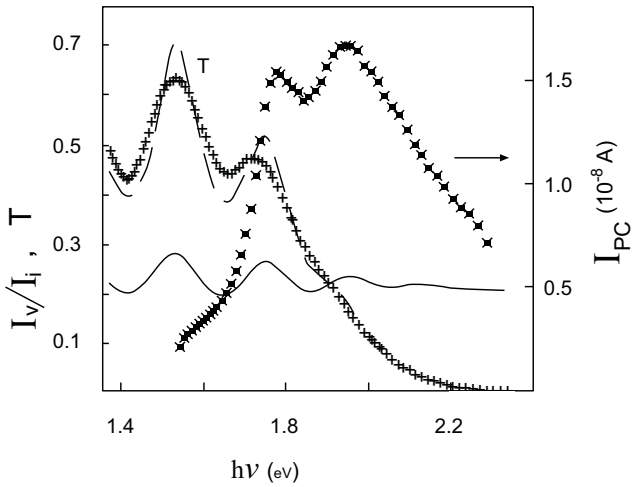


Figure 34: Optical transmittance (+) and PC current (×) of a 0.76 μm thick film of a-Si:H,F *vs.* photon energy (PC responses measured for I_0=10^{18} photons/m^{2}s). Dashed curve-theoretical transmittance calculated for $\sigma_{\Gamma 1}$=0, n_{f1}=n_{r1}=$n_{a1}(\lambda)$ and α_{f1}=α_{r1}=$\alpha_1(\lambda)$ determined in [29]. Solid curve-effective intensity of radiation which enters the semiconductor.

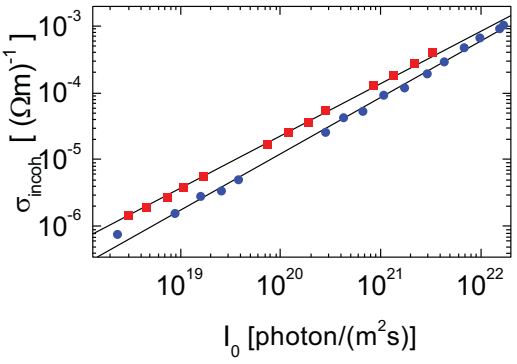


Figure 35: Photoconductivity *vs.* illumination intensity for λ=632.8 nm (■) and λ=488 nm (●); solid curves represent semi-empirical relation (19) with $\boldsymbol{\zeta}$=0.806(6) for λ=632.8 nm and $\boldsymbol{\zeta}$=0.859(9) for λ=488 nm [74].

Knowledge of ζ is necessary not only in the standard approach to SSPG measurements (*e.g.* [75]) but also in any investigations of photoconductivity. Usually, the PC responses measured for

various photon energies correspond to different illumination intensities (Fig. **36**). Therefore, the PC responses are normalized to different values of constant illumination intensity. The normalized PC can have different spectral characteristics (Fig. **37**). Such differences suggest the influence of illumination intensity and photon energy on values of surface recombination velocities and on carrier lifetimes (Fig. **38**). It is because the recombination rate is a nonlinear function of concentration of the excess carriers; simultaneously the penetration of light into a semiconductor changes with increasing hν. In general, the values of $\zeta \neq 1$ proof the necessity of using non-linear description of PC (*e.g.* the next Section).

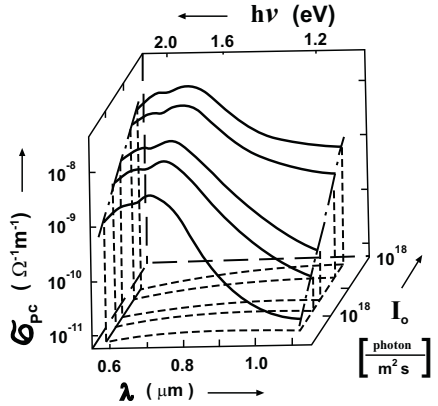


Figure 36: Photoconductivity of a 5.694 μm thick film of sputtered a-Si:H *vs.* wavelength and intensity of illumination [32].

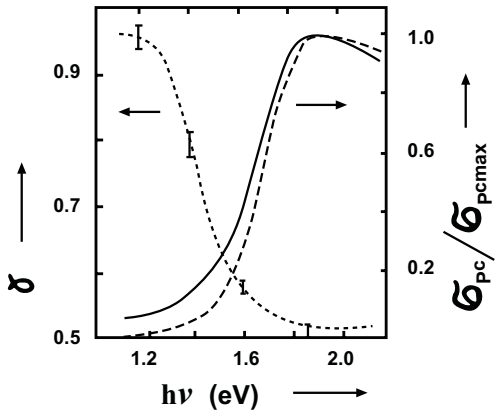


Figure 37: The power coefficient from the power-law dependence (19) and normalized photoconductivity *vs.* photon energy [32] (pointed curve, ζ; solid curve, σ_{PC} for I_0=3·10^{17} photons/m^{2}s, σ_{PCmax}=1.89·10^{-8} Ω^{-1}m^{-1}; broken curve, σ_{PC} for I_0=5·10^{15} photons/m^{2}s, σ_{PCmax}=2.5·10^{-9} Ω^{-1}m^{-1}).

6. SSPG METHOD OF DETERMINING ELECTRONIC STATES PARAMETERS OF AMORPHOUS SEMICONDUCTORS

In SSPG investigations of electronic states parameters in semiconductors [74,77], it is convenient to describe the PC of a sample in the form

$$\sigma_{PC} = \frac{e}{w_1}\int_0^{w_1} \frac{\Lambda}{\int_0^{\Lambda} \frac{dx}{\mu_e \Delta n_e(x,y) + \mu_h \Delta n_h(x,y)}} dy \tag{81}$$

where $\Lambda = \lambda / \sin\phi$ represents the grating period.

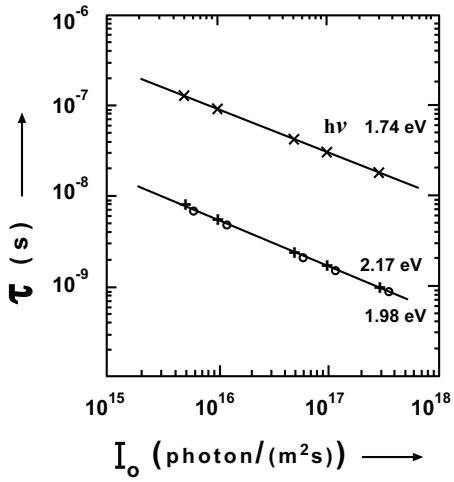


Figure 38: Carrier lifetime *vs.* illumination intensity for different photon energies [32].

The concentrations of excess electrons and holes can be found by solving numerically the set of charge-neutrality condition and the generation-recombination equality. In steady state the following simplification of latter equality is adopted [74]

$$D_e\left[\frac{\partial^2 \Delta n_e(x,y)}{\partial x^2} + \frac{\partial^2 \Delta n_e(x,y)}{\partial y^2}\right] + G_e = \sum\nolimits_l \int_{E_v}^{E_c} \{n_e K_{leA}(E)[1 - f_{lA}(E)] - e_{leA} f_{lA}(E)\} N_{lA}(E) dE + \sum\nolimits_k \int_{E_v}^{E_c} \{n_e K_{keD}(E)[1 - f_{kD}(E)] - e_{keD} f_{kD}(E)\} N_{kD}(E) dE \tag{82}$$

where G_e is given by Eq. (72), $N_{lA}(E)$ is the density of states (DOS) per unit energy of the *l*-th species of acceptor-like states at energy E, and $N_{kD}(E)$ is the DOS per unit energy of the *k*-th species of donor-like states at energy E, as measured upward from the valence-band edge E_v to the conduction-band edge E_c. The acceptor-like state can be electrically neutral or negatively charged when it is occupied by electron. The donor-like state can be electrically neutral or positively charged when it is empty for electron.

The coefficients $K_{leA}(E)$ and $K_{keD}(E)$ in (82) are the energy-dependent capture-rate constants for electrons to the *l*-th and *k*-th donor species, respectively. Sometimes the capture rates are represented by multiplication of thermal velocity v_e or v_h of electrons and holes and the capture cross sections σ_{ieS} and σ_{ihS} of the traps for electrons and holes (where idex *i* should be replaced with *l* and *k*, and index *S* must be replaced with *A* and *D* for the acceptor-like and donor-like states, respectively).

For example

$$K_{leA}(E) = \mathrm{v}_e \sigma_{leA} \quad \textbf{(83a)}$$

$$K_{lhA}(E) = \mathrm{v}_e \sigma_{lhA} \quad \textbf{(83b)}$$

where K_{lhA} is the rate constant of free hole recombination with captured electron at the *l*-th acceptor-like state.

The coefficients e_{ieS} in (82) are the thermal-emission rates for electrons at *i*-th species (where index *i* should be replaced with *l* and *k*, and index *S* must be replaced with *A* and *D* for the acceptor-like and donor-like states, respectively). For example, the probability of electron emission from the *l*-th acceptor-like trap equals

$$e_{leA} = K_{leA}(E) N_C exp\left(\frac{E-E_c}{k_B T}\right) \quad \textbf{(84)}$$

where N_C is the effective density of states at the conduction-band edge.

Under nonequilibrium steady-state conditions, the trap-occupancy function $f_{iS}(E)$ (*i.e.* the probability of occupation of the *i*-th acceptor-like or donor-like trap by electron, for *S* replaced with *A* or *D*, respectively) is given by the Simmons-Taylor statistics [78,79]

$$f_{iS}(E) = \frac{n_e K_{ieS}(E) + e_{ihS}(E)}{n_e K_{ieS}(E) + n_h K_{ihS}(E) + e_{ieS}(E) e_{ihS}(E)} \quad \textbf{(85a)}$$

where

$$e_{ihS}(E) = K_{ihS}(E) N_V exp\left(\frac{-E}{k_B T}\right) \quad \textbf{(85b)}$$

represents the thermal-emission rate for holes at *i*-th species, N_V is the effective density of states at the valence-band edge.

In [79] it was shown that (85) is mostly a general statement and is independent of the energy distribution of the traps. It was shown that $f_{iS}(E)$ can be multivalued at a particular energy without being irregular. For example, if we have three traps positioned at the same energy having different cross sections, then clearly $f_{iS}(E)$ will take three different values.

The total concentrations of free electrons and holes are given by

$$n_e(y) = N_C exp\left[\frac{E_{Fe}(y) - E_c}{k_B T}\right] \quad \textbf{(86a)}$$

$$n_h(y) = N_V exp\left[\frac{E_V - E_{Fh}(y)}{k_B T}\right] \quad \textbf{(86b)}$$

where $E_{Fe}(y)$ and $E_{Fh}(y)$ are quasi-Fermi levels for free electrons and holes at the depth *y* in the semiconductor, respectively. Thus, the conduction and valence bands may be regarded, to this

approximation, as single levels with degeneracy N_C and N_V placed at the bottom of the conduction-band and at the top of valence-band, respectively.

The equilibrium concentrations of electrons and holes are given by

$$n_{e0} = N_C exp\left(\frac{E_{F0}-E_c}{k_B T}\right) \quad \textbf{(87a)}$$

$$n_{h0} = N_V exp\left(\frac{E_v-E_{F0}}{k_B T}\right) \quad \textbf{(87b)}$$

where E_{F0} is the equilibrium Fermi energy.

Simultaneously, the charge-neutrality condition is given by

$$n_h(y) - n_e(y) = \sum\nolimits_l \int_{E_v}^{E_c} f_{lA}(E)\, N_{lA}(E) dE - \sum\nolimits_k \int_{E_v}^{E_c} [1 - f_{kD}(E)] N_{kD}(E) dE \quad \textbf{(88)}$$

In the case of discrete trap levels, the DOS per unit energy $N_{lA}(E)$ and $N_{kD}(E)$ must be replaced by $N_{lA}(E) = N_{lA0}\delta(E)$ and $N_{kD}(E) = N_{kD0}\delta(E)$, where $\delta(E)$ represents the Dirac function, N_{lA0} and N_{kD0} are the total numbers of states in the *l*-th acceptor-like and in *k*-th donor-like state, respectively.

The set of generation-recombination (82) and charge-neutrality (88) equations can be solved at least numerically for the assumed model of the state distributions in mobility gap of a semiconductor. The most generally accepted DOS for undoped or lightly doped a-Si:H includes two exponential band tails arising from the disorder of the continuous random network and the correlated states associated with the dangling bonds (DB) states situated around midgap. The DB center plays an essential role in the recombination of excess carriers in a-Si:H because of its amphoteric nature and its location in energy around midgap. The peculiarity of this defect is that, at equilibrium, it may be neutral, or positively or negatively charged according to the position of the Fermi level. The effective correlation energy of the DB in a-Si was shown to be positive (*e.g.* [80]).

Fig. **39** presents the model structure of energetic gap (so-called mobility gap) of an amorphous semiconductor [81,82]. In [74] it was assumed after [82] that the total density of states *N(E)* consists of:

exponential tails from conduction and valence bands

$$N_{1A}(E) = N_{ct}(E) = \frac{N_{ct0} exp[(E-E_c)/E_{ct}]}{E_{ct}[1-exp(-E_g/E_{ct})]} \quad \textbf{(89a)}$$

$$N_{1D}(E) = N_{vt}(E) = \frac{N_{vt0} exp[(E_v-E)/E_{vt}]}{E_{vt}[1-exp(-E_g/E_{vt})]} \quad \textbf{(89b)}$$

where N_{ct0} and N_{vt0} are total densities of acceptor– and donor-like states in exponential tails, E_{ct} and E_{vt} are characteristic energies of exponential decays of distribution of these states, and $E_g = E_c - E_v$ is energy gap.

Gaussian distributions of localized states of donor-like and acceptor-like states of *e.g.*, dangling bonds

$$N_{2D}(E) = \frac{N_{2D0}}{E_{2D}\sqrt{2\pi}} exp\left[-\frac{(E-E_{2D0})^2}{2{E_{2D}}^2}\right] \quad \textbf{(90a)}$$

$$N_{2A}(E) = \frac{N_{2A0}}{E_{2A}\sqrt{2\pi}} exp\left[-\frac{(E-E_{2A0})^2}{2{E_{2A}}^2}\right] \quad \textbf{(90b)}$$

where N_{2D0} and N_{2A0} are the integrated DOS in the Gaussian distribution of donor-like and acceptor-like states, E_{2D} and E_{2A} are standard deviations of the Gaussian distributions, and E_{2D0} and E_{2A0} represent energies to that the Gaussian distributions are pinned.

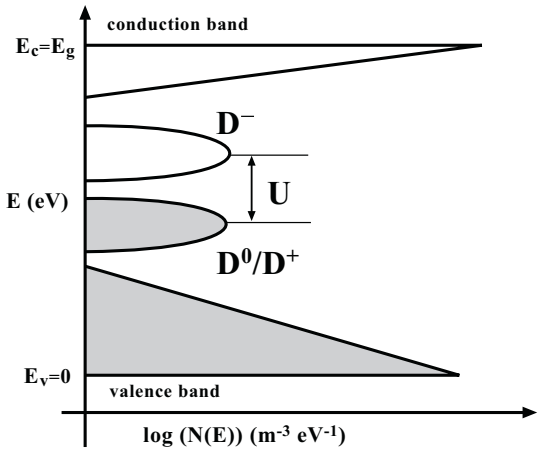


Figure 39: Model of density of electronic states in the mobility gap of a-Si:H (D^-, D^0, D^+ and U have the same meaning as in [81]).

According to [82] one can assume that capture-rate constants for trapping of free carriers in band tail regions are given by

$$K_{ct}(E) = \mathrm{v}_e \sigma_{ct0} exp[(E - E_c)/E_{ct}] \quad \textbf{(91a)}$$

$$K_{\mathrm{vt}}(E) = \mathrm{v}_e \sigma_{\mathrm{vt}0} exp[(E_{\mathrm{v}} - E)/E_{\mathrm{vt}}] \quad \textbf{(91b)}$$

where σ_{ct0} and $\sigma_{\mathrm{vt}0}$ are maximum capture cross-sections of the traps for electrons in the tail of conduction band and valence band, respectively.

The solution of Eqs. (82) and (88) was found in [74] using iterative method of numerical calculations [83,84] assuming the following boundary conditions

$$\Delta n_e(x,0) = const \quad \text{for } y = 0 \quad \textbf{(92a)}$$

$$eD_e grad[n_e(x,w_1)] = 0 \quad \text{for } y = w_1 \quad \textbf{(92b)}$$

$$\Delta n_e(x, y) = \Delta n_e(x + \Lambda, y) \quad \textbf{(92c)}$$

The value of $\Delta n_e(x, 0)$ has been estimated by solving for $y = 0$ the set of Eqs. (82), (88) and

$$\int_0^{\Lambda} \Delta n_e(x, 0) dx = const \quad \textbf{(93)}$$

The ratio $\sigma_{coh}/\sigma_{incoh}$ of photoconductivities is essential for the SSPG technique because fitting its dependence on angle ϕ between the incident beams allows one to determine the carrier diffusion length [75,76] or DOS parameters of electronic states in semiconductors [74,77]. The numerical calculations were done in [74] to analyze the influence of DOS parameters as well as experimental conditions on $\sigma_{coh}/\sigma_{incoh}$. The optical parameters of a-Si at *T*=293 K [51] have been used to describe the semiconductor film. The value of n_{a2}=1.51 was assumed as the refractive index of the substrate. Table **7** presents the values of DOS parameters taken after [82] to the calculations.

The evident influence of N_{cto}, N_{vto}, E_{ct}, and E_{vt} of the exponential tails of electronic states in energy gap of the semiconductor on the angular dependence $\sigma_{coh}/\sigma_{incoh}(\phi)$ was reported in [74]. Each of these parameters affects the range $\phi \in (0, \phi_M)$ of angles ϕ such that the nonlinear changes of $\sigma_{coh}/\sigma_{incoh}(\phi)$ are observed. Values of these parameters also affect the nearly constant $\sigma_{coh}/\sigma_{incoh}$ observed in the wide range of medium ϕ.

Table 7: Parameters of the DOS distributions of a-Si:H [82].

Name of Parameter	Value of Parameter
σ_{cto}= σ_{vto} (10^{-18} m^2)	2
σ_{2eA}= σ_{2eD} (10^{-20} m^2)	1
σ_{2hA}= σ_{2hD} (10^{-21} m^2)	1
E_{ac}= E_{av} (meV)	27
N_c (10^{25} m^{-3})	2.5
N_v (10^{25} m^{-3})	0.8
μ_e (10^{-4} m^2/(V·s))	13
μ_h (10^{-4} m^2/(V·s))	1
N_{cto} (10^{25} m^{-3})	3
N_{2A0} =N_{2D0} (10^{21} m^{-3})	11
N_{vto} (10^{25} m^{-3})	5
E_{2A} (meV)	80
E_{2A0} (eV)	1.35
E_{vt} (meV)	60
E_{2D} (meV)	80
E_{2D0} (eV)	0.85
E_{ct} (meV)	30
E_g (eV)	1.72

One can recognize (Fig. **40**) that changes of σ_{2hA} and σ_{2hD} evoke variations of $\sigma_{coh}/\sigma_{incoh}(\phi)$ similar to those evoked by N_{cto}, N_{vto}, E_{ct}, and E_{vt}. Above all, changing σ_{2hD} produces a relatively wide range of angles ($\phi_M = 10°$) so that the $\sigma_{coh}/\sigma_{incoh}$ ratio increases with the increase of ϕ. Meanwhile the two orders of magnitude changes of σ_{2eA} and σ_{2eD} do not effect significant variations in the $\sigma_{coh}/\sigma_{incoh}(\phi)$ characteristics. Comparing influences of N_{2A0} and E_{2A0} on $\sigma_{coh}/\sigma_{incoh}(\phi)$, the dominant significance of N_{2A0} has been found. Fig. **41** shows the evident influence of both N_{2D0} and E_{2D0} on $\sigma_{coh}/\sigma_{incoh}(\phi)$.

Fig. **42** presents the strong influence of illumination intensity on angular dependence of ratio $\sigma_{coh}/\sigma_{incoh}$. The parameter ϕ_{Mi} (where i=1,2,.) in this figure represents the angle for which $\sigma_{coh}/\sigma_{incoh}$ equals 95% of its saturation value. Therefore, magnitude of this parameter describes the range of strong dependence of SSPG results on the angle ϕ. The value of ϕ_{Mi} increases with increasing illumination intensity (Figs. **42** and **43**). The influence of the illumination intensity on ϕ_{Mi} depends on the DOS parameters (Fig. **43**).

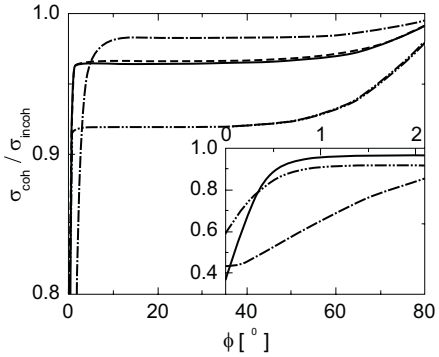


Figure 40: The influence of the capture cross sections of the traps for electrons and holes σ_{2eA}, σ_{2hA}, σ_{2eD}, σ_{2hD} on angular dependence of ratio $\sigma_{coh}/\sigma_{incoh}$ [74] (▬, $\sigma_{2eA}=10^{-20}$ m^2, $\sigma_{2eD}=10^{-20}$ m^2, $\sigma_{2hA}=10^{-21}$ m^2, $\sigma_{2hD}=10^{-21}$ m^2; ▪ ▪ ▪, $\sigma_{2eA}=10^{-18}$ m^2, $\sigma_{2eD}=10^{-20}$ m^2, $\sigma_{2hA}=10^{-21}$ m^2, $\sigma_{2hD}=10^{-21}$ m^2; ▪ ▪ ▪ ▪, $\sigma_{2eA}=10^{-20}$ m^2, $\sigma_{2eD}=10^{-18}$ m^2, $\sigma_{2hA}=10^{-21}$ m^2, $\sigma_{2hD}=10^{-21}$ m^2; ▪ ▪ ▪ ▪ ▪, $\sigma_{2eA}=10^{-20}$ m^2, $\sigma_{2eD}=10^{-20}$ m^2, $\sigma_{2hA}=10^{-19}$ m^2, $\sigma_{2hD}=10^{-21}$ m^2; ▪ ▪ ▪ ▪, $\sigma_{2eA}=10^{-20}$ m^2, $\sigma_{2eD}=10^{-20}$ m^2, $\sigma_{2hA}=10^{-21}$ m^2, $\sigma_{2hD}=10^{-19}$ m^2; values of other parameters are given in Table 7).

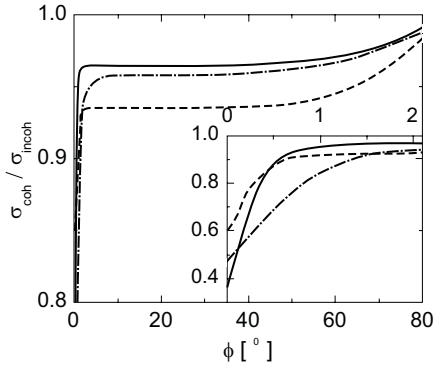


Figure 41: The influence of density N_{2D0} of DOS in Gaussian distribution, energy E_{2D0}, to which the distribution is pinned and standard deviation E_{2D} on angular dependence of ratio $\sigma_{coh}/\sigma_{incoh}$ [74] (▬,

$N_{2D0}=11\cdot10^{21}$ m^{-3}, E_{2D0}=0.85 eV, E_{2D}=80 meV; ▪ ▪ ▪, $N_{2D0}=11\cdot10^{21}$ m^{-3}, E_{2D0}=1.15 eV, E_{2D}=80 meV; ▪ ▪ ▪ ▪, $N_{2D0}=11\cdot10^{21}$ m^{-3}, E_{2D0}=0.85 eV, E_{2D}=40 meV; ▪ ▪ ▪ ▪ ▪, $N_{2D0}=11\cdot10^{22}$ m^{-3}, E_{2D0}=0.85 eV, E_{2D}=80 meV; values of other parameters are given in Table 7).

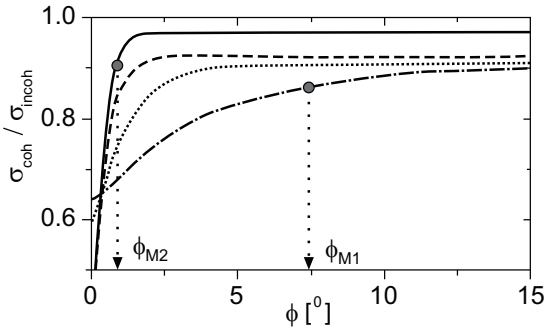


Figure 42: The influence of illumination intensity on angular dependence of ratio $\sigma_{coh}/\sigma_{incoh}$ [74]: ▬▬, 10^{16} photon/(m^{2}s); ▪ ▪ ▪, 10^{18} photon/(m^{2}s); ▪▪▪▪▪, 10^{20} photon/(m^{2}s); ▪ ▪ ▪ ▪ ▪, 10^{22} photon/(m^{2}s); values of parameters describing DOS are given in Table 7; description in the text.

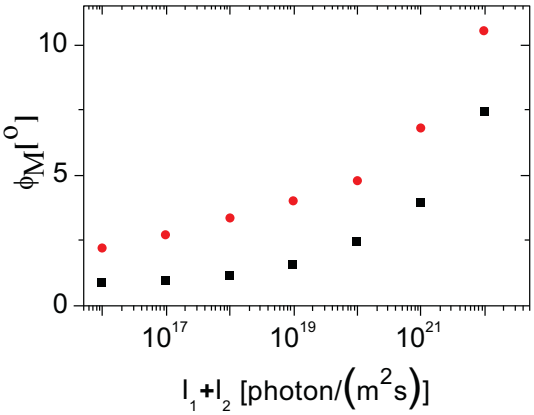


Figure 43: Upper limit of range of the angles for that the SSPG results strongly change *vs.* illumination intensity for different values of the integrated DOS in the Gaussian distribution of donor-like states [74] (■-$N_{2D0}=11\cdot10^{21}$ m^{-3}; ●-$N_{2D0}=11\cdot10^{22}$ m^{-3}; values of other parameters are given in Table 7).

Analyzing the results of SSPG measurements one should take into serious consideration the influence of the values of energy gap of the investigated amorphous material (see [74]). In addition, the higher mobility of one type of carrier can have substantial impact on the observed $\sigma_{coh}/\sigma_{incoh}(\phi)$ dependence. The results of performed calculations did not show evident influence of N_c, N_v, σ_{cto}, σ_{vto}, E_{ac} and E_{av} on the angular dependence of $\sigma_{coh}/\sigma_{incoh}(\phi)$.

6.1. Method of Experimental Data Treatment

Fig. **44** presents the diagram of the apparatus used in [74] for SSPG measurements. Direct current measurements were performed using the Keithley 617 electrometer at room temperature. The samples were illuminated with HeNe (λ=632.8 nm) or Ar^+ (λ=488 nm) lasers. The laser light intensity was changed using neutral filters.

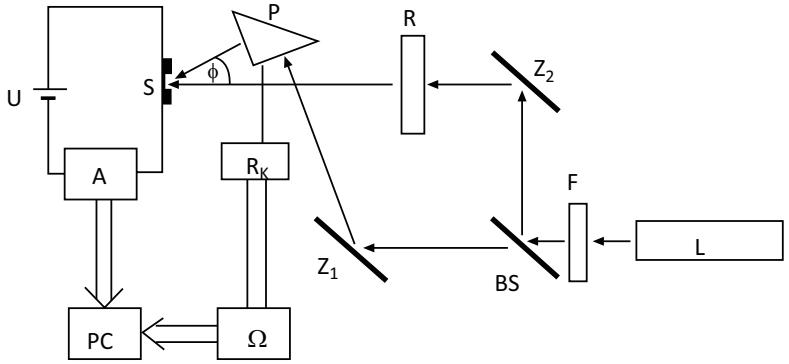


Figure 44: Experimental set-up for measuring the diffusion length using SSPG technique [74]: L-laser, F-neutral density filter, BS-beam splitter, R-half wavelength retardation plate, Z_1, Z_2-mirrors, P-prism, S-sample, U-voltage source, A-electrometer Keithley 617, R_K-resistor coupled mechanically with prism, Ω-multimeter Keithley 196, PC-computer IBM PC with IEEE-488 card.

Obviously a large number of parameters describing the investigated material cannot be determined using data obtained from one experiment alone. Therefore, taking into account the conclusions presented above, fitting of the angular dependence of the results of SSPG measurements with appropriate theoretical formulae has been used [74] to determine energy levels and densities of acceptor and donor-like states (N_{2A0}, N_{2D0}, E_{2A0}, E_{2D0}) in a-Si:H. Other parameters describing optical properties, recombination and mobilities of carriers, and DOS have been be taken in [74] from other experiments performed on the same semiconductor, *e.g.*, from investigations of optical transmittance and reflectance. Some parameters have been determined by standard investigations of the dependence of PC in uniformly illuminated samples on temperature, wavelength and intensity of radiation [85]. In some cases it was necessary to use typical values of semiconductor parameters measured by other investigators. In [74] the values of parameters given in [82] and [85] have been used.

Fig. **45** presents the evident influence of the optical properties of the back surface of the investigated sample on SSPG results. When radiation was relatively weakly absorbed in the investigated a-Si:H (for λ=632.8 nm, α_{a1}=1.9·10^6 m^{-1}, $\alpha_{a1}w_1$=2.69), the metallic foil covering the back side of the sample had reflected the radiation traversing a-Si:H film and the BK-7 substrate. This reflection has an important impact on the measured $\sigma_{coh}/\sigma_{incoh}(\phi)$. For strongly absorbed radiation (λ=488 nm, α_{a1}=10.6·10^6 m^{-1}, $\alpha_{a1}w_1$=14.84) this effect was not observed. Results shown in Fig. **45** prove that the suggested [74,76] spatial distribution of radiation internally reflected in the sample must be taken into account.

The number of fitted parameters depends on the non-linearity of the measured signal on controlled, independent variables. To obtain relatively strong non-linearity of the $\sigma_{coh}/\sigma_{incoh}(\phi)$ characteristics, all SSPG results (see Fig. **46**) have been simultaneously least-square fitted with the theoretical dependence

$$\chi^2 = \sum_j \sum_k \sum_i \left[\frac{\sigma_{Ecoh}(I_{1kj},I_{2kj},\lambda_k,\phi_i)}{\sigma_{Eincoh}(I_{1kj},I_{2kj},\lambda_k,\phi_i)} - \frac{\sigma_{coh}(I_{1kj},I_{2kj},\lambda_k,\phi_i,\eta_{0k},DOS)}{\sigma_{incoh}(I_{1kj},I_{2kj},\lambda_k,\phi_i,\eta_{0kj},DOS)} \right]^2 \quad \textbf{(94)}$$

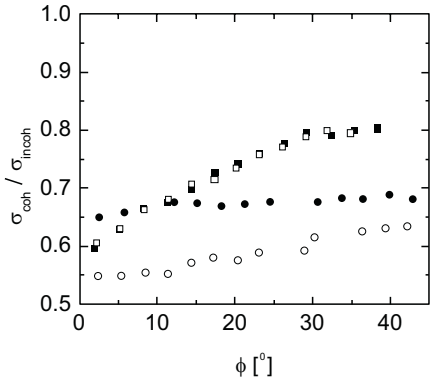


Figure 45: The influence of illumination wavelength on angular dependencies of $\sigma_{coh}/\sigma_{incoh}$ of a-Si:H samples with different back support [74] (■, λ=488 nm, back≡Al foil, L=79(5) nm; ●, λ=632.8 nm, back≡Al foil, L=26(3) nm; □, λ=488 nm, back≡air, L=81(4) nm; ○, λ=632.8 nm, back≡air, L=44(2) nm).

where index *i* represents different angles ϕ_i between the two beams incident on the sample, index *k* represents different wavelengths λ_k of radiation incident upon the sample, and index *j* describes various illumination intensities I_{1kj} and I_{2kj} of these parts of radiation that illuminates the sample perpendicularly and obliquely. σ_{Ecoh} and σ_{Eincoh} represent the measured photoconductivities for cases of the same and different polarizations of the beams incident upon the sample. σ_{coh} and σ_{incoh} represent the ratio of the photoconductivities (with and without interference of radiation incident upon the sample) calculated using the theoretical model presented above. The theoretical calculations are performed for the suitable values of I_{1kj}, I_{2kj}, ϕ_i, λ_k, $\alpha_{a1}(\lambda_k)$, $n_{a1}(\lambda_k)$, w_1 as well as values of parameters describing DOS. Using η_0 (see description of Eq. (67)) the corrected radiation intensity was described as [74]

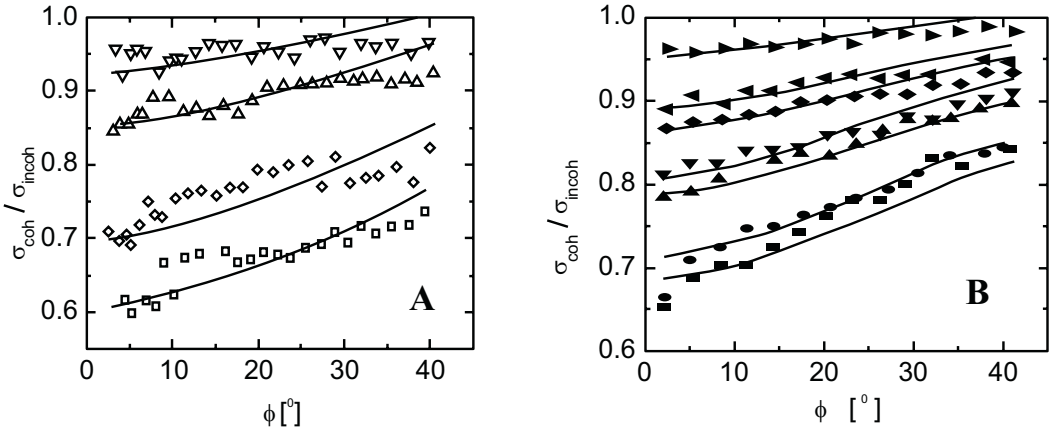


Figure 46: Influence of wavelength and intensity of illumination on angular dependencies of $\sigma_{coh}/\sigma_{incoh}$ for a-Si:H sample [74] (A, λ=632.8 nm; B, λ=488 nm; □, $I_1+I_2=4.64\cdot10^{21}$ photon/(m^{2}s); ○, $I_1+I_2=4.08\cdot10^{20}$ photon/(m^{2}s); Δ, $I_1+I_2 = 2.66\cdot10^{19}$ photon/(m^{2}s); ∇, $I_1+I_2=4.64\cdot10^{18}$ photon/(m^{2}s); ■, $I_1+I_2=6.5\cdot10^{21}$ photon/(m^{2}s); ●, $I_1+I_2=1.72\cdot10^{21}$ photon/(m^{2}s); ▲, $I_1+I_2=7.34\cdot10^{20}$ photon/(m^{2}s); ▼, $I_1+I_2=1.36\cdot10^{20}$ photon/(m^{2}s); ◆, $I_1+I_2=8.2\cdot10^{19}$ photon/(m^{2}s); ✚, $I_1+I_2=6.04\cdot10^{19}$ photon/(m^{2}s); ×, $I_1+I_2=1.02\cdot10^{19}$ photon/(m^{2}s); Solid curves: the fitted theoretical dependence, the values of the fitted parameters are given in Tables 8 and 9).

$$I_D(x,y) = I_a(y) + \eta_0[I_G(x,y) - I_a(y)] \quad \textbf{(95)}$$

$$\text{where } I_a(y) = \frac{1}{l}\int_0^l I_G(x,y)\,dx \quad \textbf{(96)}$$

Minimization of χ^2 was done in [74] numerically using the stepping method in a multidimensional space [86]. The appropriate calculations were done using the HP-UX Zeus B. 10.20 C 9000/800 machine. The success of using the least square method for non-linear problems depends on the choice of good starting points. In the described case [74], the information about some of the material parameters obtained from other measurements mentioned above were used. Table **8** presents the used initial values of the fitted parameters. Solid curves in Fig. **46** represent theoretical dependencies $\sigma_{coh}/\sigma_{incoh}(\phi)$ calculated for the fitted values of semiconductor parameters presented in Table **8**, too. Table **9** includes the fitted values of η_0 that decrease with decreasing illumination intensity. It can be interpreted as follows: For weak illumination, the ratio of signal to noise decreases.

Table 8: Values of DOS parameters determined in the presented SSPG measurements.

Parameter	Initial Values Taken from [30]	Values of the Fitted Parameters
E_{2A0} (eV)	1.32	1.15
E_{2D0} (eV)	0.96	0.79
N_{2A0} (10^{24} m^{-3})	3.41	18.5
N_{2D0} (10^{23} m^{-3})	0.97	5.26

Table 9: Values of empirical parameters η_0 obtained from simultaneous fitting of all the experimental results represented in Fig. **46** with theoretical dependences described in the text.

λ [nm]	I_1+I_2 [photon/(m^{2}s)]	η_0
632.8	$4.64\cdot10^{21}$	0.867
	$4.08\cdot10^{20}$	0.814
	$2.66\cdot10^{19}$	0.636
	$4.64\cdot10^{18}$	0.493
488	$6.5\cdot10^{21}$	0.800
	$1.72\cdot10^{21}$	0.800
	$7.34\cdot10^{20}$	0.700
	$1.36\cdot10^{20}$	0.697
	$8.2\cdot10^{19}$	0.611
	$6.04\cdot10^{19}$	0.561
	$1.02\cdot10^{19}$	0.433

The values from Table **8** have been used to calculate the energetic distribution of electronic states in mobility gap of the investigated a-Si:H (Fig. **47**). Such calculated DOS (solid curve in Fig. **48**) is somehow different from the DOS evaluated from the standard photoconductivity measurements [85] (*i.e.*, the measurements of PC as a function of temperature, wavelength and intensity of

radiation). However, it should be noted that the last DOS parameters (used as initial values in our minimization procedure) give $\sigma_{coh}/\sigma_{incoh}(\phi)$ characteristics different from the experimental data (Fig. **49**).

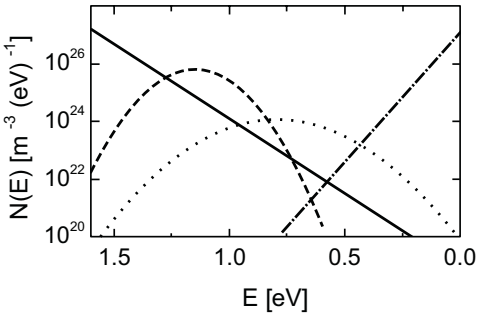


Figure 47: The energetic spectrum of density of electronic states in the mobility gap of a-Si:H obtained from SSPG measurements [74]: (▬▬, the exponential acceptor-like conduction-band tail, ▪ ▪ ▪, the Gaussian distribution of acceptor-like states, ▪ ▪ ▪ ▪ ▪, the Gaussian distribution of donor-like states, ▪ ▪ ▪ ▪ ▪, the exponential donor-like valence-band tail).

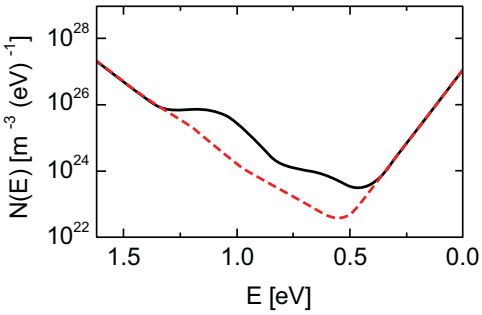


Figure 48: Total energetic spectrum of electronic states in the investigated a-Si:H [74] (▬▬, density of electronic states determined using SSPG methods; ▪ ▪ ▪, density of electronic states determined using the standard PC method of investigations [85]).

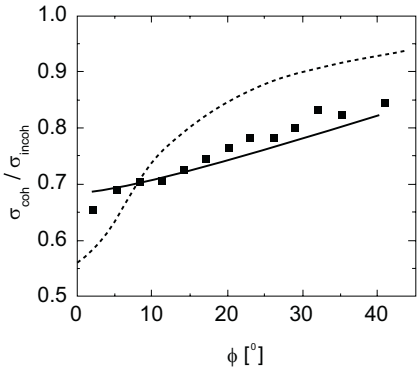


Figure 49: Comparison of the experimental (■) angular dependencies of $\sigma_{coh}/\sigma_{incoh}$ for sample of a-Si:H with the theoretical dependencies calculated for different parameters [74] (▬▬, the fitted parameters that values are given in Tables 8 and 9; ▪ ▪ ▪, the initial values of parameters presented in Table 8 and η_0=0.97; $I_1+I_2=6.5\cdot10^{21}$ photon/(m^2s); λ=488 nm).

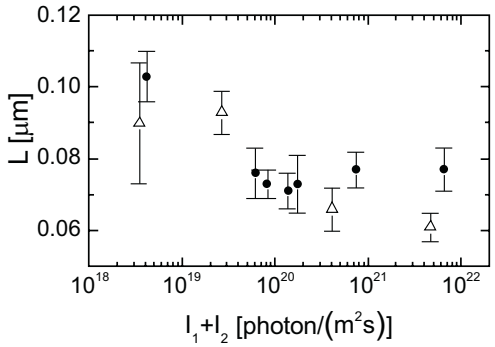


Figure 50: Diffusion length of excess carriers *vs.* illumination intensity for different wavelengths of the radiation incident upon the a-Si [74] (λ = 632.8 nm (△) and λ = 488 nm (●); description in the text).

Fig. **50** presents values of the diffusion lengths evaluated using Eq. (66) applied in the standard method of SSPG measurements. This evaluation is possible because in [87] it has been shown that the dc measurements can be applied in the SSPG technique.

It should be underlined that values of L calculated using the standard SSPG technique differ even more than 40% when the a-Si:H sample has different supports (see the results for λ=632.8 nm in Fig. **50**). The obtained decrease of L with increasing illumination intensity is rational and can be easily explained by the increase of recombination processes with the increase of excess carrier concentration.

Therefore, the spatial distributions of light intensity in semiconductors used in solar cells as well as inhomogeneities of their optical parameters as mentioned above should be taken into consideration.

ACKNOWLEDGEMENT

The author is indebted to Dr. M. Kępińska of the Silesian University of Technology, Katowice (Poland) for helpful discussions and her aid in preparing this paper.

CONFLICT OF INTEREST

The author(s) confirm that this chapter content has no conflict of interest.

REFERENCES

[1] Born M, Wolf E. Principles of optics: Electromagnetic theory of propagation, interference and diffraction of light. New York: Pergamon Press 1964.
[2] Heavens OS. Optical properties of thin solid films. New York: Dover Publ 1965.
[3] Pankove JI. Optical properties of semiconductors. Englewood Cliffs: Prentice-Hall Inc 1971.
[4] Sze SM, Kwok Kwok Ng. Physics of semiconductor devices. 3rd ed. New York: John Wiley and Sons 2007.
[5] Bube RH. Photoelectronic properties of semiconductors. Cambridge: Cambridge University Press 1992.

[6] Nowak M. Photoelectromagnetic effect in semiconductors and its applications. Progress in Quantum Electronics 1987; 11(3/4): 205-346.
[7] Azzam RM, Bashara NM. Ellipsometry and polarized light. Amsterdam: North-Holland 1992.
[8] Kortüm G. Reflectance Spectroscopy. Berlin: Springer-Verlag 1969.
[9] Dahm DJ, Dahm KD. Interpreting diffuse reflectance and transmittance: A theoretical introduction to absorption spectroscopy of scattering materials. Chichester: IM Publications 2007.
[10] Applied Spectroscopy: A Compact Reference for Practitioners, Workman Jr J, Springsteen AW, Eds. New York: Academic Press 1998.
[11] Woggon U. Optical properties of semiconductor quantum dots. Berlin: Springer-Verlag 1997.
[12] Tsakalakos L, Balch J, Fronheiser J, *et al.* Strong broadband optical absorption in silicon nanowire films. J Nanophotonics 2007; 1: 013552 (pp. 1-10).
[13] Lannin JS. Raman Scattering of Amorphous Si, Ge, and Their Alloys. In: Pankove JI, Ed. Hydrogenated amorphous silicon Part B: Optical properties. Semiconductors and Semimetals vol 21. New York: Academic Press 1984; pp. 159-95.
[14] Zanzucchi PJ. The vibrational Spectra of a-Si:H. In: Pankove JI, Ed. Hydrogenated amorphous silicon Part B: Optical properties. Semiconductors and Semimetals vol 21. New York: Academic Press 1984; pp. 113-40.
[15] Street RA. Luminescence in a-Si:H. In: Pankove J I, Ed. Hydrogenated amorphous silicon Part B: Optical properties. Semiconductors and Semimetals vol 21. New York: Academic Press 1984; pp. 197-244.
[16] Hamakawa Y. Electroreflectance and Electroabsorption. In: Pankove J I, Ed. Hydrogenated amorphous Silicon Part B: Optical Properties. Semiconductors and Semimetals vol 21. New York: Academic Press 1984; pp. 141-58.
[17] Simon JM, Simon MC, Presa VA. Thin anisotropic films: an alternative method. Optik 1993; 94: 137-42.
[18] Haiming Wang. Reflection/transmission measurements of anisotropic films with one of the principal axes in the direction of columnar growth. J Modern Optics 1995; 42: 497-505.
[19] Pokrovsky YaE, Ed. Radiative Recombination in Semiconductors. Moscow: Nauka 1972.
[20] Balucani M, Bondarenko V, Franchina L, Lamedica G, Yakovtseva VA, Ferrari A. A model of radiative recombination in n-type porous silicon–aluminum Schottky junction. Appl Phys Lett 1999; 74: 1960-2.
[21] Stroud D, Pan HP. Self-consistent approach to electromagnetic wave propagation in composite media: application to model granular metals. Phys Rev B 1978; 17: 1602-10.
[22] Poruba A, Fejfar A, Remeš Z, *et al.* Optical absorption and light scattering in microcrystalline silicon thin films and solar cells. J Appl Phys 2000; 88: 148-60.
[23] Cheong Wai-Fung, Prahl SA, Welch AJ. A review of the optical properties of biological tissues. IEEE J Quantum Electronics 1990; 26: 2166-85.
[24] Philips-Invernizzi B, Dupont D, Caze C. Bibliographical review for reflectance of diffusing media. Opt Eng 2001; 40: 1082-92.
[25] Nowak M, Kauch B, Szperlich P. Determination of energy band gap of nanocrystalline SbSI using diffuse reflectance spectroscopy. Review of Scientific Instruments 2009; 80**:** 046107-1-3.
[26] Tauc J, Grigorovici R, Vancu A. Optical properties and electronic structure of amorphous germanium. Phys Stat Sol 1966; 75: 627-37.
[27] Cody GD, Tiedje T, Abeles B, Brooks B, Goldstein Y. Disorder and the optical-absorption edge of hydrogenated amorphous silicon. Phys Rev Let 1981; 47: 1480-3.
[28] Macfarlane GG, McLean TP, Quarrington JE, Roberts V. Fine Structure in the absorption-edge spectrum of Si. Phys Rev 1958; 111: 1245-54.
[29] Augelli V, Murri R, Nowak M. Interference photoconductivity and photoelectromagnetic effect in amorphous silicon. Phys Rev B 1989; 39: 8336-46.

[30] See EPAPS Document No. E-RSINAK-80-007904 for the complete set of figures that present elaboration of the experimental data using different methods. More information on EPAPS at http://www.aip.org/pubservs/epaps.html.
[31] Moore AR. Photoelectromagnetic effect in amorphous silicon. Appl Phys Lett 1980; 37: 327-30.
[32] Grabowski A, Nowak M, Tzanetakis P. Determination of recombination and photogeneration parameters of a-Si:H using photoconductivity measurements. Thin Solid Films 1996; 283: 75-80.
[33] Szałajko M, Nowak M. Quantum efficiency coefficient for photogeneration of carriers in gallium sulphide single crystals. J Phys C 2007; 19: 196210-1-14.
[34] Amer NM, Jackson WB. Optical properties of defect states in a-Si:H. In: Pankove JI, Ed. Hydrogenated amorphous silicon Part B: Optical properties. Semiconductors and Semimetals vol 21. New York: Academic Press 1984; pp. 83-112.
[35] Vanêček M, Kočka J, Stuchlik J, Triska A. Direct measurement of the gap states and band tail absorption by constant photocurrent method in amorphous silicon. Solid State Commun 1981; 39**:** 1199-202.
[36] Vanêček M, Kočka J, Poruba A, Fejfar A. Direct measurement of the deep defect density in thin amorphous silicon films with the "absolute" constant photocurrent method. J Appl Phys 1995; 78: 6203-10.
[37] Moddel G, Anderson DA, Paul W. Derivation of the low-energy optical-absorption spectra of *a*-Si:H from photoconductivity. Phys Rev B 1980; 22: 1918-25.
[38] Kozlovsky SI, Moin MD. Transversal photovoltaic effect under laser illumination of Ge due to thermal change of energy gap. Fiz Tekh Poluprovodn [Sov. Phys. Semicond] 1984; 18: 1772-7.
[39] Nowak M. The dependence of the photomagnetoelectric effect on the angle of incidence of radiation. Phys Stat Sol A 1982; 74: 603-13.
[40] Nowak M, Łoś S, Kończak S. Refractive index of silicon oxide surface films determined by polarization method of photomagnetoelectric investigation. Surface Sci 1984; 140: 446-54.
[41] Loncierz B, Murri R, Nowak M. Determining carrier lifetime using frequency dependence in contactless photoelectromagnetic investigations of semiconductors. Thin Solid Films 1995; 266: 274-7.
[42] Nowak M, Solecka M. Application of high-frequency contactless method of PEM investigations to examine near-surface layer of Si and GaAs. Vacuum 2000; 57: 237-42.
[43] Jacobson J. Light reflection from films continuously varying refractive index. In: Wolf E, Ed. Progress in Optics. Amsterdam: North-Holland 1972.
[44] Pisarkiewicz T, Stapiński T, Czternastek H, Rava P. Inhomogeneity of amorphous silicon thin films from optical transmission and reflection measurements. J Non-Cryst Solids 1991; 137/138: 619-22.
[45] Cerdeira F. Optical properties. In: Hull R, Bean JC, Eds. Germanium Silicon: Physics and materials. Semiconductors and semimetals vol 56. New York: Academic Press 1999.
[46] Eberl K, Brunner K, Schmidt OG. $Si_{1-y}C_y$ and $Si_{1-x-y}Ge_xC_y$ alloy layers. In: In: Hull R, Bean JC, Eds. Germanium Silicon: Physics and materials. Semiconductors and semimetals vol 56. New York: Academic Press 1999.
[47] Kępińska M, Murri R, Nowak M. Surface and bulk values of real part of refractive index of GaSe. Vacuum 2002; 67: 143-7.
[48] Kępińska M, Nowak M. Comparison of optical constants and average thickness of inhomogeneous rough thin films obtained from special dependences of optical transmittance and reflectance. NDT&E International 1998; 31: 105-10.
[49] Kępińska M, Nowak M, Duka P, Kauch B. Spectro-goniometric determination of refractive indices of GaSe. Thin Solid Films 2009; 517: 3792–96.
[50] Swanepoel R. Determination of surface roughness and optical constants of inhomogeneous amorphous silicon films. J Phys E 1984; 17: 896-903.
[51] Nowak M. Determination of optical constants and average thickness of inhomogeneous-rough thin films using spectral dependence of optical transmittance. Thin Solid Films 1995; 254: 200-10.

[52] Michalewicz A, Nowak M, Kępińska M. Differences between surface and bulk refractive indices of a-In_xSe_{1-x}. Appl Surf Sci 2006; 252: 7743-7.
[53] Manual of the Double Grating GDM-1000 Monochromator. Carl Zeiss Jena.
[54] Manual of the SPM-2 Monochromator. Carl Zeiss Jena.
[55] Refractive index of BK-7 glass, http://refractiveindex.info.
[56] Jarząbek B, Jurusik J, Cisowski J, Nowak M. Roughness of amorphous Zn-P thin films. Optica Applicata 2001; 31: 93-101.
[57] Mahanty S, Basak D, Merino JM, Leon M. Determination of interference free optical constants of thin solid films. Mat Sci & Eng B 1999; 68: 72-5.
[58] Jaglarz J, Nowak M. Determination of optical constants and average thickness of thin films on thick substrates using angular distribution of intensity of reflected radiation. Thin Solid Films 1996; 278: 124-8.
[59] Nowak M. Linear distribution of intensity of radiation reflected from and transmitted through a thin film on a thick substrate. Thin Solid Films 1995; 266: 258-62.
[60] Petykiewicz J. Wave Optics. Warsaw: PWN 1986; p. 5.
[61] Grabowski A, Jaglarz J, Nowak M. Angular distribution of reflected radiation investigations of the influence of CO_2 laser treatment on optical properties of hydrogenated amorphous silicon. Optics & Laser Technology 1998; 30: 183-7.
[62] Jaglarz J, Nowak M. New technique of VAR investigations of thin films on thick substrates. NDT&E International 1998; 3: 341-7.
[63] Jaglarz J, Nowak M. Investigations of spatial distributions of intensity of radiation reflected from thin films which are inhomogeneous over thickness. J Modern Optics 1998; 45: 2451-60.
[64] Nowak M. The photomagnetoelectric effect and photoconductivity for non-normal incidence of radiation. Phys Stat Sol A 1983; 80: 691-702.
[65] Nowak M. The possible exestence of the interference photomagnetoelectric effect. Phys Stat Sol A 1982; 74: 313-22.
[66] Merz JL, Logan RA, Sergent AM, Loss measurements in GaAs and ALGaAs dielectric waveguides between 1.1 eV and the energy gap. J Appl Phys 1976; 47: 1436-50.
[67] Augelli V, Nowak M. Distribution of radiation intensity in a thin semiconductor film on a thick substrate. Thin Solid Films 1999; 338: 188-96.
[68] Wiener O. Stehende lichtwellen und die schwingungsrichtung polarisirten lichtes. Ann Physik u Chemie 1890; 40: 203-43.
[69] Djuric Z. Quantum efficiency of photoconductivite detectors-influence of reflection and surface recombination velocity. Infrared Phys 1987; 27: 407-10.
[70] Nowak M. Distribution of radiation intensity in a semiconductor film. Optical Engineering 1994; 33: 1501-10.
[71] Ryvkin BS. Oscillation in the current and the light intensity in laser irradiation of a plane-parallel photoconducting plate. Fiz Tekh Poluprovod [Sov Phys Semicond] 1979; 13(2): 367-70.
[72] Nowak M. Oscillatory dependence of the interference photomagnetoelectric effect and photoconductivity on magnetic field. Phys Stat Sol A 1984; 82: 249-56.
[73] Jóźwikowski K, Nowak M, Piotrowski J. Interference photoelectromagnetic effect in graded-gap semiconductors. Infrared Phys 1984; 24: 371-80.
[74] Nowak M, Starczewska A. Steady-state photocarrier grating method of determining electronic states parameters in amorphous semiconductors. J Non-Crystal Sol 2005; 351: 1383-92.
[75] Ritter D, Weiser K, Zeldov E. Steady-state photocarrier grating technique for diffusion-length measurement in semiconductors: Theory and experimental results for amorphous silicon and semi-insulating GaAs. J Appl Phys 1987; 62: 4563-70.
[76] Nowak M, Starczewska A. Influence of spatial distribution of radiation on steady-state photocarrier grating measurement. J Non-Crystal Solids 1999; 260: 41-53.

[77] Schmidt JA, Budini N, Ventosinos F, Longeaud C. Theoretical analysis and experimental results on the modulated photocarrier grating technique. Phys Stat Sol A 2010; 207: 556-60.
[78] Simmons G, Taylor GW. Theory of photoconductivity in amorphous semiconductors containing relatively narrow trap bands. J Phys C 1974; 7: 3051-66.
[79] Simmons G, Taylor GW. Nonequilibrium steady-state statistics and associated effects for insulators and semiconductors containing an arbitrary distribution of traps. Phys Rev B 1971; 4: 502-11.
[80] Vaillant F, Jousse D. Recombination at dangling bonds and steady-state photoconductivity in *a*-Si:H. Phys Rev B 1986; 34: 4088-98.
[81] Wang F, Schwarz R. Comprehensive numerical simulation of defect density and temperature-dependent transport properties in hydrogenated amorphous silicon. Phys Rev B 1995; 52: 14586-97.
[82] McMahonan J, Xi JP. Photoconductivity and light-induced change in a-Si:H. Phys Rev B 1986; 34, 2475-81.
[83] Polozy GN, Pahariewa NA, Stiepanienko IZ. Methods of approximate calculations. Warsaw: WNT 1966.
[84] Panow DJ. Numerical methods of solving of partial differential equations. Warsaw: PWN 1955.
[85] Grabowski A, Nowak M. Influence of CO_2 laser annealing on optoelectronical parameters of a-Si:H. Electron Technol 1997; 30: 145-8.
[86] James R. Function minimization. In: Proceedings of the 1972 CERN Computing and Data Processing School. Pertisau 1972.
[87] Balberg I, Delahoy AE, Weakliem HH. Ambipolar diffusion length measurements on hydrogenated amorphous silicon *p-i-n* structures. Appl Phys Lett 1988; 53: 1949-51.

Send Orders of Reprints at reprints@benthamscience.net
Silicon Based Thin Film Solar Cells, 2013, 243-276

CHAPTER 8

Electrical Properties of Semiconductors

Nicola Pinto*, Marco Ficcadenti+ and Lorenzo Morresi

University of Camerino, School of Science and Technology, Physics Division, Via Madonna delle Carceri 9, Camerino, 62032, Italy

Abstract: The accurate measure of semiconductor electrical properties is a fundamental step for the design and the correct operation of any electronic device. The electrical performance of any device will depend on how the carriers move inside the semiconductor lattice. The measure of the resistivity, the concentration of shallow and deep states, the charge carrier mobility, *etc.*, allow for the design of new and advanced functionalities and for improvement in current device technology. In this chapter we will give a brief overview of the main electronic transport coefficients and experimental techniques used to investigate semiconductor materials and the main solar cell parameters. We have limited our attention to the most common and reliable techniques. Our work has been organised into seven sections. The first and second sections define the conductivity and the mobility of any material in terms of its band structure and looks at some semiconductor properties and the material doping. The third and fourth sections illustrate the main scattering mechanisms of charge carriers in a semiconductor and several experimental techniques to measure thin film resistivity, respectively. The fifth section introduces the Hall effect and defines the Hall coefficient and the Hall mobility, with a description of an experimental method to measure these. In the sixth section we report a brief analysis of deep state defects and we describe the DLTS technique to reveal them in a semiconductor lattice. Finally, in the seventh section we describe the current-voltage technique commonly used to measure the main solar cell parameters.

Keywords: Electrical Conductors, Resistance measurement, Conductivity tensor, charge carrier scattering, Hall mobility, Hall coefficient, van der Pauw geometry, Deep Level Transient Spectroscopy, Current-voltage, Solar cell electrical parameters.

1. INTRODUCTION

One of the main physical properties of any material is its ability to conduct an electrical current. Depending on the nature of the material, its temperature, dimension and shape, applied electric field, *etc.* the current can span several orders of magnitude.

A parameter used to classify the attitude of materials to conduct a current is the electrical conductivity, σ, ($\Omega^{-1}cm^{-1}$ or Scm)$^{\Diamond}$ expressed as a function of the charge carrier density, n, (cm^{-3}) the electron charge, e, (C) the effective electron mass, m^*, by the relation [1]:

$$\sigma = ne^2 \langle \tau_m \rangle / m^* = ne\mu \quad \textbf{(1.1)}$$

***Address correspondence to Nicola Pinto:** University of Camerino, School of Science and Technology, Physics Division, Via Madonna delle Carceri 9, Camerino, 62032, Italy; Tel: +48 0737 402515; Fax: +48 0737 402853; E-mail: nicola.pinto@unicam.it

+Now at CESI SpA, Via Rubattino 54, 20134 Milan, Italy.

◊This unit is preferentially used instead of $(\Omega m)^{-1}$ or Sm, this last being the unit of measure in the SI.

Roberto Murri (Ed)
All rights reserved-© 2013 Bentham Science Publishers

where $\langle \tau_m \rangle$ is the average value of the momentum relaxation time of the carrier, and μ (cm^2/Vs) is the so called drift mobility, related to the above mentioned quantities by:

$$\mu = e\langle \tau_m \rangle / m^* \tag{1.2}$$

The mobility represents the average velocity gained by a charge carrier in an applied electric field of 1 V/cm. The mobility is another relevant electronic transport coefficient which may provide important physical information about the scattering mechanisms active in the semiconductor material, as will be detailed in the section 3.

According to the value of the conductivity, materials are conventionally divided into three groups: conductors, semiconductors, and insulators (or dielectrics). The room temperature conductivity of different kinds of materials spans more than 25 orders of magnitude. In fact, taking into account the conductivity of superconductors, measured at low temperatures, the conductivity can cover about 40 orders of magnitude[1]. This is the largest known variation in a physical property.

The electrical behaviour exhibited by the three classes of materials can be explained in terms of their band structure [2]. In particular, according to quantum theory, an electric current can flow thorough a material if it has a partially filled electron band (the so called conduction band). Electrons can then be lifted slightly above the Fermi energy into an allowed and unfilled energy state. This permits them to be accelerated by an electric field, thus producing a current. However, only those electrons that are close to the Fermi energy can participate in the conduction process. The number of electrons near the Fermi energy depends on the density of available electron states. In terms of a quantum mechanic description, the conductivity yields the following equation:

$$\sigma = \frac{1}{3} e^2 v_F \tau N(E_F) \tag{1.3}$$

where v_F is the velocity of the electrons at the Fermi energy (the so called Fermi velocity) and $\tau N(E_F)$ is the density of filled electron states (called the population density) at the Fermi energy.

1.1. Behaviour of Insulators and Semiconductors

Insulators and semiconductors at very low temperatures (ideally at 0 K) have a completely filled valence band (VB) and a completely empty conduction band (CB), which results in a virtually zero population density (Fig. **1**).

Thus, in insulators, the conductivity is virtually zero at all but very high temperatures. A similar result holds for semiconductors near absolute zero.

Focussing attention on the behaviour of semiconductors, their unique and technologically relevant properties can be deduced by their band structure (Fig. **1**).

[1]For superconductors conductivity a value of 10^{20} Scm has been assumed.

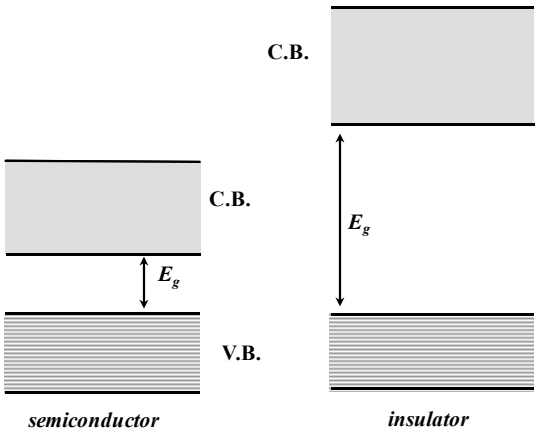


Figure 1: Schematic of a band diagram showing the energy levels filing for a semiconductor, near 0 K, and for an insulator. E_g represents the amplitude of the energy gap of the material.

At 0 K, the VB, completely filled with valence electrons, is separated by a gap, E_g, (called energy gap or forbidden band) from the completely empty conduction band. Quantum mechanics prevents electrons from residing in the gap between these bands.

The E_g values range from few tenths of eV (*e.g.* for compound materials of groups IV-VI) to more than 3 eV (*e.g.* GaN, ZnS, ZnO, *etc.*) depending on the semiconductor material.

Since at 0 K the valence band is completely filled (electrons are not allowed to move in empty energy states), while the conduction band contains no electrons at all (empty states), the semiconductor material behaves as an insulator.

Raising the semiconductor temperature above 0 K causes a sizeable change in conductivity. In fact, some electrons may be thermally excited across the band gap, passing from states near the edge (top) of the VB to empty states available in the CB. The number of these electrons is generally extremely small and will depend exponentially on the temperature and energy gap values of the semiconductor. Specifically, about one out of every 10^{13} atoms contributes an electron at room temperature. Nevertheless, this number is large enough to cause some conduction and the conductivity increases according to the relation (1.1). The mobility of electrons is substantially impaired by interactions with impurity atoms, crystallographic defects and phonons.

Hence, the conductivity for semiconductors increases exponentially with rising temperature due to the exponential increase of the charge carrier concentration in both bands. This is in marked contrast to metals and alloys, for which the conductivity decreases with temperature.

However, the conduction process in semiconductors is not uniquely due to electrons. In fact, as a consequence of thermal excitation of valence electrons from the VB to the CB, some empty states have been left behind, which allows additional conduction to take place in the valence band. The empty states are called electron holes or simply holes. From a quantum mechanical point of view

these holes are considered, and indeed effectively behave like, positively charged carriers. They can freely move in the VB providing there is some conduction. This hole current is directed in the opposite direction with respect to the electron one.

The total conductivity is a sum of both contributions and the process is called intrinsic conduction. The material involved is termed an intrinsic semiconductor since no foreign (impurity) elements are involved.

The Fermi energy of intrinsic semiconductors is located near the centre of the gap since it can be considered the average of the electron and the hole Fermi energies.

1.2. Semiconductor Doping

For the useful and correct operation of any electronic device based on a semiconductor material, a relatively high charge carrier concentration (either electrons or holes) is required. This can be achieved by adding impurity atoms to the semiconductor lattice host. For example, very few atoms of Group-V elements, called donors, added to the silicon can significantly lower its conductivity. Donor dopants such as phosphorous (P) or arsenic (As) are commonly utilized as substitutional atoms in a ratio of about 1 dopant every $10^5 \div 10^7$ atoms of the host semiconductor (Fig. **2**).

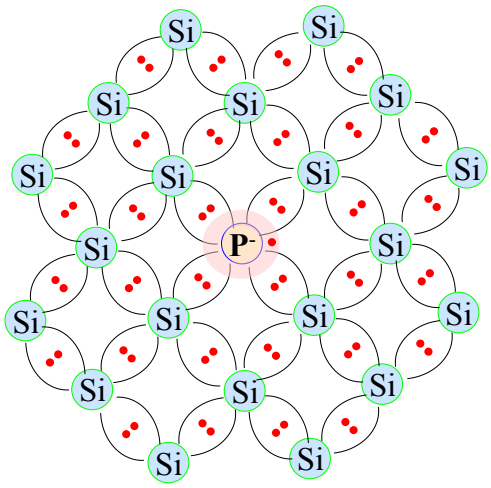


Figure 2: Two-dimensional representation of a silicon lattice (covalent bonds) with a phosphorus atom substituting a regular lattice atom.

Since phosphorous has five valence electrons, that is, one more than silicon, the extra electron called the donor electron is only loosely bound. The binding energy of an electron of a dopant element will depend on the semiconductor host material [3]. For example, phosphorous donor electrons in a silicon matrix have a binding energy of about 0.045 eV. Thus, the donor electrons can be disassociated from their nuclei by only a slight increase in the thermal energy. In fact, at room temperature all donor electrons have already been excited into the conduction band.

Similar arguments can be used to explain the *p*-type doping in a semiconductor. For example adding a Group-III element (B, Al, Ga, *etc.*) to silicon or germanium will cause an excess of free holes in the material and then an increase of the semiconductor conductivity. The *p*-type dopant, called acceptor, will introduce empty energetic levels just above the VB edge. At RT the acceptor levels, occupied by thermally excited electrons coming from the VB, will leave empty states in the VB. These last will behave as positively charged carriers (*i.e.* electron holes) which can contribute to the conduction process.

It is worthwhile noting that electrons and holes differ not only for the sign of the electric charge. In fact, their effective mass[2]:

$$m^* = \hbar^2 \Big/ \frac{d^2 E(k)}{dk^2} \tag{1.4}$$

will depend on the semiconductor band structure, with electrons having an effective mass generally lighter than that of holes. Hence, the mobility of electrons will be generally higher than that of holes in the same material.

For example, the gallium arsenide (GaAs) is a compound semiconductor, made of Group-III and Group-V elements, exhibiting interesting properties with respect to the Group-IV materials like silicon or germanium. In fact, its larger electron mobility aids in high-speed applications. Moreover, GaAs is of some technological interest since it is a direct band gap material, with a wider band gap than Si and Ge, allowing for the fabrication of optoelectronic devices like LED, lasers, *etc.*

Further, the ionization energies of donors (acceptors) impurities in GaAs are one order of magnitude smaller than in silicon, which ensures complete electron (hole) transfer from the donor (acceptor) levels into the conduction (valence) band even at relatively low temperatures. However, GaAs is about ten times more expensive than Si and its thermal conductivity is smaller. Other compound semiconductors include II-VI combinations, such as ZnO, ZnS, ZnSe, or CdTe, and IV-VI materials such as PbS, PbSe, or PbTe. Silicon carbide, a IV-IV compound with a band gap of about 3 eV, can thus be used in devices operating at high temperatures (up to 700°C) before intrinsic effects set in.

2. CONDUCTIVITY TENSOR

If we consider a weak electric field applied to a semiconductor, with or without a magnetic field, the current density, $\vec{j}$, induced in the material [4, 5] will follow the microscopic relationship:

$$\left|\vec{j}\right|_l = \sum_m \sigma_{lm}\left(\vec{B}\right)\left|\vec{E}\right|_m \tag{2.1}$$

[2]Strictly speaking, the effective mass is a tensor with components $m_{ij} = \hbar^2 \big/ \partial^2 E(k) \big/ \partial k_i \, \partial k_j$.

where σ_{lm} are the components of the electrical conductivity tensor, $\underline{\underline{\sigma}}$, depending on the magnetic field $\vec{B}$ eventually applied. The electrical conductivity $\underline{\underline{\sigma}}$ is a second-rank tensor, symmetric since its components σ_{lm} obey the Osanger relation [6]:

$$\sigma_{lm}\left(\vec{B}\right) = \sigma_{lm}\left(-\vec{B}\right) \tag{2.2}$$

However, for semiconductors with a cubic symmetry, and at low fields, the conductivity tensor $\underline{\underline{\sigma}}$ reduces to the form [1]:

$$\underline{\underline{\sigma}} = \begin{pmatrix} \sigma_{xx} & \sigma_{xy} & 0 \\ \sigma_{yx} & \sigma_{yy} & 0 \\ 0 & 0 & \sigma_{zz} \end{pmatrix} \tag{2.3}$$

assuming that $\vec{B}$ has been applied in the z direction. We note that the conductivity component in the z direction is unaffected by the field $\vec{B}$, as it does not generate any force in its own direction. The other two diagonal components σ_{xx} and σ_{yy} are equal to each other due to symmetry. Also, the non diagonal components σ_{xy} and σ_{yx} would be odd functions of the magnetic field because the forces in the cross directions due to the magnetic field are proportional to it. Considered that σ_{xy} and σ_{yx} are odd functions of $\vec{B}$ and holding the Osanger relation (2.2), it follows that:

$$\sigma_{xy} = -\sigma_{yx} \tag{2.4}$$

The current density $\vec{j}$ may be expressed as follows:

$$\begin{aligned} j_x &= \sigma_{xx}E_x + \sigma_{xy}E_y \\ j_y &= -\sigma_{xy}E_x + \sigma_{yy}E_y \\ j_z &= \sigma_{zz}E_z \end{aligned} \tag{2.5}$$

where E_x, E_y and E_z are the components of the electric field in the three directions. Since, in an actual experiment the sample is generally rectangular in shape, with the current flowing along one direction (*e.g. x* direction), we can assume that $j_y = 0$. Hence from the (2.5) we get:

$$E_y = \sigma_{xy}\, E_x / \sigma_{yy} \tag{2.6}$$

However, considering that the current direction is more easily measured than the field direction (*e.g.* by means of a long thin sample with leads at the ends), the resistivity is another physical quantity of interest. The resistivity tensor, $\underline{\underline{\rho}}$, is the inverse of the conductivity tensor $\underline{\underline{\sigma}}$:

$$\underline{\underline{\rho}} = \underline{\underline{\sigma}}^{-1} \tag{2.7}$$

whose components are defined by:

$$E_l = \sum_m \rho_{lm} j_m \tag{2.8}$$

An exception is the Corbino disk geometry [7] in which the components of the conductivity tensor are measured directly.

In general, for several practical reasons it is not always possible to identify the different components of the conductivity of a semiconductor material. Therefore, the experimental measure of the conductivity (or resistivity) is an average value characteristic of the investigated material under well-defined parameters of measure (temperature, voltage o current applied, *etc.*) In these cases, the sample conductivity (or resistivity) is considered as a scalar quantity and holds the following relations:

$$j = \sigma E \tag{2.9}$$

$$\sigma = 1/\rho \tag{2.10}$$

with the relations (1.1) and (1.2) are still valid.

In real semiconductors, electrons and/or holes can contribute to the conduction process simultaneously.

If this condition is present, and we assume that both the charge carriers in different bands do not interact with each other and that the magnetic field eventually applied has a weak intensity, the conductivity is independent of the magnetic field intensity and is expressed by the relation:

$$\sigma = ne\mu_e + pe\mu_h \tag{2.11}$$

where n, p, μ_e and μ_h are the electron and hole concentration, and electron and hole mobility, respectively. The general relations accounting for the thermal effects and the magnetic field are reported in the reference [8].

3. SCATTERING MECHANISMS OF CHARGE CARRIERS

In any conducting material, the motion of charge carriers is hampered by several collision processes with crystalline "imperfections" [9-11] which will limit their average drift velocity and then the carrier mobility. The collision process (also known as scattering mechanism) is the result of an interaction between the carrier wave function and the potential associated with the imperfections.

The nature of these collision processes can be very different and their contribution to the overall mobility will be generally dependent, among other factors, on the temperature range considered. Hence, a measure of the charge carrier mobility as a function of the temperature affords greater knowledge of the electronic transport mechanisms active in the semiconductor material. In the following sections a summary of the main scattering mechanisms will be briefly outlined.

3.1. Neutral Impurity Scattering

Collisions of charge carriers with impurity atoms are those most commonly found in a semiconductor. The presence of impurities in the material lattice must be considered an

unavoidable consequence of their growth process. In fact, any growth or deposition process creates imperfections in the lattice structure such as crystallographic defects (dislocations, stacking faults, point defects, *etc.*) and impurities (neutral or ionized). These last can be formed either as substitutional (*i.e.* in a crystal position of the host lattice) or interstitial atoms (*i.e.* in any place inside the lattice structure).

From an energy point of view, defects and impurities will introduce energy levels in the energy gap of the material. At very low temperatures (around liquid helium temperature) these impurities are neutral and the carrier mobility is independent of the temperature [12]:

$$\mu = \frac{e}{20 a_B \hbar \varepsilon N^{\varepsilon}} \frac{m^*}{m_0} \tag{3.1}$$

where a_B is the Bohr radius, ε the dielectric constant and N the impurity atom density, m^* the effective electron mass (see Eq. 1.4) and m_0 the electron mass.

The scattering mechanism caused by neutral impurities is difficult to detect experimentally because it is generally accompanied by other collision processes, such as ionized impurity scattering and phonon scattering. The cyclotron resonance technique is generally used to get information by this scattering mechanism [1].

3.2. Ionized Impurity Scattering

Above few Kelvin of temperature, the atoms of impurities have a finite probability for ionization and the carrier concentration will increase with the temperature increase. An electron approaching a charged impurity will be deflected from its trajectory, *i.e.* it will undergo a scattering process caused by ionized atoms.

Depending on the model used, several expressions for mobility have been found [1]. In any case, independently of the model used, the temperature dependence of the mobility is always the same and expressed by the relation:

$$\mu_i = a T^{\frac{3}{2}} \tag{3.2}$$

where a is a quantity almost independent of the temperature but inversely dependent on the total ionized impurity concentration [1].

At impurity concentration values ranging from 10^{17} to 10^{18} atoms/cm^3, the different theoretical expressions can differ markedly [1]. A review of the collision processes by ionized impurities scattering can be found in reference [13].

3.3. Scattering by Phonons

Charge carriers can also be subject to another relevant scattering mechanism produced by lattice vibrations. As we know from quantum mechanics [14], the lattice vibration can be described as lattice particles called phonons whose nature will depend on vibration types. The scattering of charge carriers by phonons will differ depending on the phonon types.

The phonons are quasi particles which follow Bose-Einstein statistics and are divided into two branches, acoustical and optical. They interact with electrons as particles obeying the principles of momentum and energy conservation.

For the acoustical branch, both longitudinal (LA) and transverse (TA) acoustic vibrations can set; these phonons are called acoustic phonons. Similarly, in the optical branch both longitudinal (LO) and transverse (TO) optical vibrations can be found; the corresponding phonons are called optical phonons.

3.4. Acoustic Deformation Potential Scattering

In this specific interaction of acoustic phonons with electrons, phonons generate a perturbing potential, changing the distance among the lattice atoms and then affecting both the energy gap and the edges of the conduction and valence bands. These changes from site to site of the crystal will produce a potential discontinuity, called deformation potential, whose magnitude is proportional to the lattice strain caused by the phonons. Consequently, the interaction of the charge carriers with phonons will be called acoustic deformation potential scattering.

The temperature dependence of the electron mobility is expressed by the relation:

$$\mu = A\left(m^*\right)^{-\frac{5}{2}}\left(k_{\mathrm{B}}T\right)^{-\frac{3}{2}} \tag{3.3}$$

where A is constant quantity, depending on the semiconductor material considered. The relation shows a mass dependence of the mobility. Hence, high mobility values will be obtained by semiconductors with smaller effective mass. For example, in an *n*-type Ge sample at 100 K, the mobility attains a value of 3×10^4 cm^2/Vs. In any case, at higher temperatures the contribution to the collision processes by optical deformation potential scattering (see the next subsection) modifies the exponent of the temperature in the mobility expression. It has been found on experimentation that the mobility is proportional to $T^{-1.67}$ [9].

Even if acoustic deformation potential scattering is essentially an elastic process, at high intensity electric fields the mobility becomes field strength dependent [9, 11].

3.5. Piezoelectric Scattering Mechanism

The second perturbing potential caused by acoustic phonons involves compound semiconductors having different atoms (*e.g.* SiC) with a partial or a complete ionization. In this case, a piezoelectric field will be created by the periodic displacement of the lattice atoms. Field intensity, depending on both the position of the atoms in the crystal and the system symmetry, will be stronger in lower symmetry systems. This kind of collision process is called piezoelectric scattering and is relevant for compound semiconductors, below RT in the low-medium range of temperature (Fig. **3**).

The mobility for non degenerate thermal carriers is expressed by [15]:

$$\mu = A'\left(m^*\right)^{-\frac{3}{2}}\left(k_{\mathrm{B}}T\right)^{-\frac{1}{2}} \tag{3.4}$$

where A' is a quantity depending on the semiconductor material.

In a temperature range of around 100 K, piezoelectric scattering competes with the acoustic (non-polar) collision process, this last being the main scattering mechanism in semiconductors with partly ionic bonds.

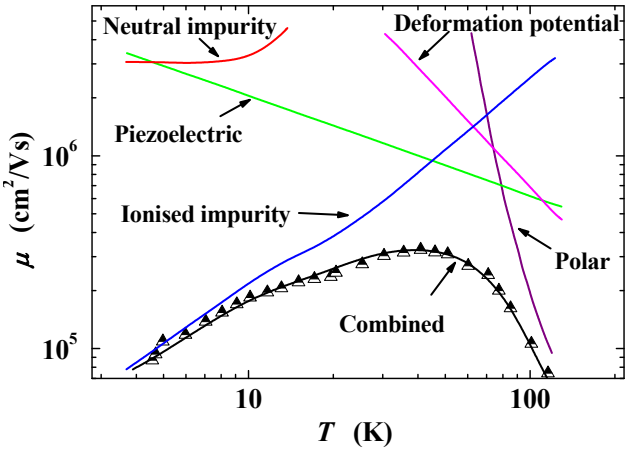


Figure 3: Mobility as a function of the temperature for a sample of *n*-type GaAs. Triangles: experimental data; continuous line: theoretical contributions to the overall (combined) mobility taking into account different scattering mechanisms (After [16]).

In a pure polar semiconductor, such as GaAs with a very low density of dislocation and crystallographic defects, the piezoelectric scattering may be the dominant process at low temperatures (about 10 K) resulting in a mobility value about five times lower than that dominated by acoustic deformation potential scattering (Fig. **3**).

3.6. Optical Deformation Potential Scattering

In non-polar semiconductors, charge carriers may be scattered by longitudinal optical phonons. Due to the higher values of the phonon energies which are comparable to the thermal carrier energies, this kind of collision process must be treated as inelastic. Therefore, scattering rates for transitions from a state $\vec{k}$ to a state $\vec{k}-\vec{q}$ or to a state $\vec{k}+\vec{q}$ must be considered different.

In general, the expression for the mobility will depend on different parameters such as the electric field intensity and a function of the ratio between the Debye temperature and the sample temperature [9, 11].

3.7. Polar Optical Scattering

The scattering process between carriers and optical phonons takes place in polar semiconductors (*e.g.* GaAs), similar to piezoelectric scattering for acoustical phonons. As mentioned above, the inelastic nature of the electron-phonon interaction should not allow for a momentum relaxation

time. However, using an approximation [9, 11] it is possible to derive an expression for μ depending on the Debye temperature, Θ:

$$\mu = A'' e^{\frac{\Theta}{T}} \tag{3.5}$$

where A'' is a constant quantity for a given material. The computed values of the mobility are comparable to the experimental values, although at temperatures lower than 100 K, the main scattering mechanisms in GaAs, and in general in compound materials, is still due to impurity scattering, making it difficult to check the equation (3.5).

The experimental behavior of the mobility *vs. T* for a GaAs crystal has been reproduced in the Fig. **3**, in the range from about 4 K to about 100 K. The figure also reproduces the contribution to the overall mobility of several different scattering mechanisms as outlined in the previous subsections.

4. METHODS OF MEASUREMENT

The measurement methods for electrical conductivity can be divided into two main classes: methods that use contacts and those that do not (contactless).

Reviews of the electrical characterization of semiconductors, both for majority and minority carriers, can be found in [17-19].

In general, contact methods require suitably prepared samples with ohmic contacts fabricated on the sample surface or the use of point probes.

The contactless methods do not generally require electrical contacts. However, each method presents advantages and drawbacks. Although electrical characterization is considered a non destructive technique, ohmic contacts and probe methods may render the sample unsuitable for further use. This is especially the case with ohmic contacts, which require a very good mechanical adhesion of the metallic alloy onto the sample surface. Such adhesion is frequently assured by thermal treatment of the contacted specimen. The contactless methods have no deleterious effects.

Among the probe methods, spreading resistance has a much higher spatial resolution (≈ 10 μm) than the four-point probe techniques (~ 1 mm), but is not an absolute method (*i.e.* it requires calibration using standard samples) [18]. In several cases, the resistivity and the Hall effect measurements are combined in the same experimental set up, allowing for the evaluation of different physical parameters of the investigated material.

By extending the measurements over a wide temperature range, from few Kelvin to about several hundreds of Kelvin above RT, sample parameters can be derived, such as the concentration of electrically active donor, N_D, and acceptor, N_A, dopants and their energy levels, ε_D and ε_A, respectively. One common assumption concerns the spatial uniformity of the electrical properties. In practice, considerable attention must be devoted to the methods of measuring the spatial variation of carrier density and mobility, establishing their "profiles".

Depending on the application, the measurement techniques involve different sample geometry and/or experimental approaches. The bar geometry (Fig. **4**) (or bridge samples) and the van der Pauw geometry [20] belong to a first group. The four-point probe and the spreading resistance methods [18] belong to a second group.

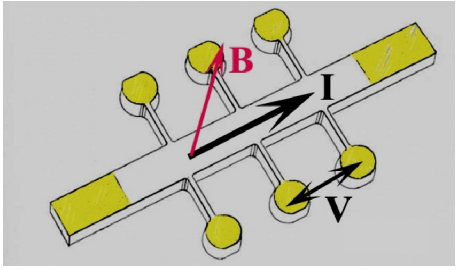


Figure 4: Schematic of a Hall bar samples. Current is sourced along the bar length while the voltage is measured along the side arms. The six arms Hall bar geometry allows for annuling the voltage offset eventually measured in absence of any current applied. The same bar geometry allows to measure the Hall coefficient by applying a magnetic field orthogonal to the sample surface.

Finally, a third group involves contactless methods using power dissipation from radio frequency or microwave sources [18].

On measurements and data interpretation involving thin epitaxial films careful consideration must be given to corrections for conduction in the substrate, while the interpretation of the probe measurements requires a reconstruction of the current distribution [21].

"Ohmic" contacts are required when one is using two terminals, but even with four terminals, it is advisable to use good ohmic contacts wherever possible. A comprehensive review of ohmic contacts is given in [22].

Finally, it is worthwhile mentioning that cracks and voids in the material lead to a local change in conductivity which can be detected by conductivity probes.

4.1. Contact Methods

4.1.1. Bar Geometry

A geometry to directly measure the semiconductor resistivity makes use of a bar sample (Fig. **4**) having a uniform cross-section along its length. A constant current, I, is supplied through the bar length by way of ohmic contacts covering the two ends of the bar and, under the assumption of uniform current distribution, the voltage drop, V, is measured between two facing side arms. This geometry avoids arithmetical corrections in converting measured resistance into resistivity, using Ohm's law.

The resistance R is then calculated according to Ohm's law:

$$R = V/I \tag{4.1}$$

The semiconductor material conductivity is determined by the measured value of R and its dimensions (length l, width w, and thickness t_s). From these data the value of σ can be directly obtained [1]:

$$\sigma = l/Rwt_s \tag{4.2}$$

4.1.2. Van der Pauw Geometry

Several steps are required for the preparation of bar-shaped samples. The theorem published by van der Pauw [20] provides resistivity measurements in an arbitrarily shaped, uniform and plane sample, with four line contacts placed on its edge. The location of the contacts along the sample border is arbitrary. The theorem also assumes a uniform thickness and a homogeneous doping level. Moreover, the material must not contain holes.

With reference to Fig. **5**, the sample resistivity can be obtained by supplying a constant current between two adjacent contacts (*e.g.* 1 and 2) and then measuring the voltage V between another two contacts (*e.g.* 3 and 4). To obtain a more accurate value and minimize contribution from non perfectly ohmic contacts, up to 8 measures are collected (Fig. **5**) [23]. The voltage is measured twice on the same couple of contacts considering the two possible current directions for the same contact set (Fig. **5**). The current supplied and the measure voltage configuration are cycled around "90°" (Fig. **5**).

Two values of resistivity, ρ_A and ρ_B are then computed as follows:

$$\rho_A = \frac{\pi}{\ln 2} f_A t_s \frac{V_2 + V_4 - V_1 - V_3}{4I} \tag{4.3}$$

$$\rho_B = \frac{\pi}{\ln 2} f_B t_s \frac{V_6 + V_8 - V_5 - V_7}{4I} \tag{4.4}$$

where: t_s is the sample thickness; $V_1 \div V_8$ represents the voltages measured by the voltmeter; I is the current intensity through the sample; f_A and f_B are geometrical factors based on sample symmetry. The f_A and f_B values are related to the two voltage ratios Q_A and Q_B, whose values depend on the measured voltages, as follows:

$$Q_A = \frac{V_2 - V_1}{V_4 - V_3} \quad \text{and} \quad Q_B = \frac{V_6 - V_5}{V_8 - V_7} \tag{4.5}$$

For perfect symmetry: $f_A = f_B = 1$. In the other cases the f value can be computed by solving the implicit function relating Q to f:

$$\frac{Q-1}{Q+1} = \frac{f}{0.693} \operatorname{arccos h}\left(\frac{e^{\frac{0.693}{f}}}{2} \right) \tag{4.6}$$

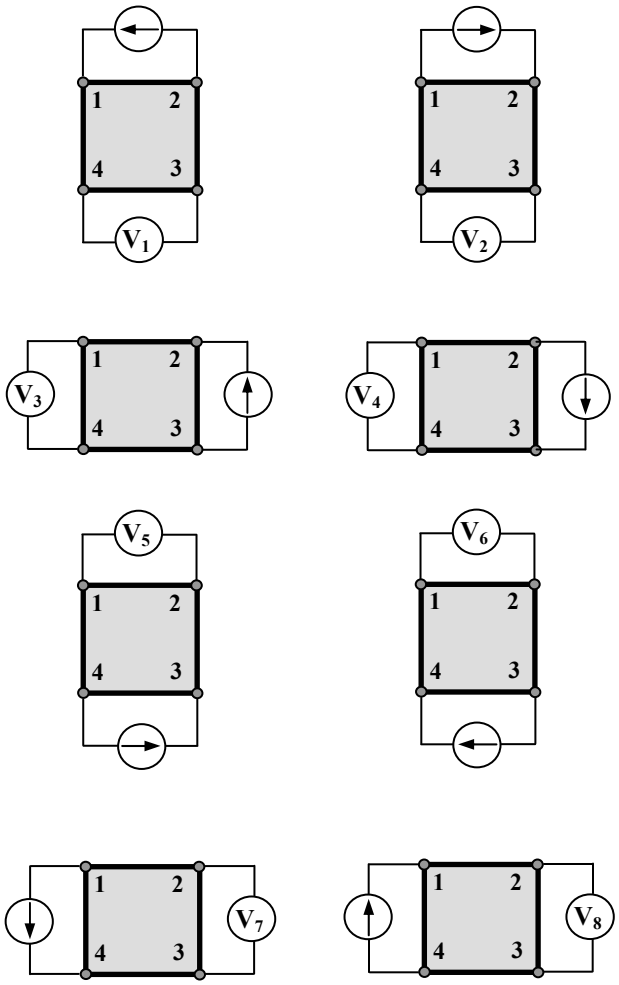


Figure 5: Schematic of a van der Pauw geometry for the resistivity measurement. The numbers in the squares represents the 4 ohmic contacts on the sample border. For each combination of contacts, the current is reversed (After [23]).

It is worthwhile noting that if ρ_A and ρ_B are not within 10% of one another, the sample is not sufficiently uniform to determine an accurate value of the resistivity, and their values should be discarded [23].

Once ρ_A and ρ_B are known, the average resistivity (ρ_{AVG}) can be determined as follows:

$$\rho_{AVG} = (\rho_A + \rho_B)/2 \quad \textbf{(4.7)}$$

The van der Pauw geometry can also be used to determine the Hall coefficient by applying a magnetic field orthogonal to the sample surface. The measured values of the sample resistivity and Hall coefficient provide the Hall mobility (as will be explained in the section 5). Therefore, this

kind of geometry has been used extensively for several semiconductors such as III-VI layered materials, amorphous silicon and amorphous gallium arsenide [24-29].

A differential measurement may be required if the sample resistance is of the same magnitude as the isolation of the voltmeter. Electronic equipment has been specifically designed to measure the resistivity and Hall coefficient of semiconductor materials applying the van der Pauw and Hall bar geometry [23]. The current source and the voltmeter are automatically switched to all sides of the sample by using a high isolation card controlled by a PC. Special features, such as built-in unity-gain buffers, allow differential measurements on high resistivity samples. The addition of a magnetic field, whose insertion and field reversion is PC controlled, provides the measure of the Hall coefficient for the same sample [23].

Equations (4.3) and (4.4) are essentially concerned with the sheet resistance of the sample, defined as the resistance between opposite edges of a square of size, L. This resistance is independent on L and is therefore a property of the sheet. Its dimensions are simply "ohms", even if, to avoid confusion, they are commonly referred to as "ohms per square". The concept of sheet resistance is important for thin films where typical lateral dimensions are much greater than the film thickness, t_s.

To obtain a van der Pauw measurement, samples can be rapidly contacted by spring-loaded tips. However, in many cases this form of contact may show resistance that is too high and it then becomes necessary to use planar contacts deposited on the sample surface. However, due to a non-ideal van der Pauw geometry, alternative contact geometries are generally taken into account [1, 17].

Errors can also arise from a number of causes in addition to the sample non-uniformity and contact problems: Joule heating, photo-effects, current leakage through the substrate and surface; interface depletion effects (for epitaxial films). The first two can be eliminated by taking measurements in the dark as a function of the measuring current. The latter two are more difficult to control. For example, a semi-insulating substrate may conduct significantly at elevated temperatures showing activation energy of half the band gap. Possible *p-n* junction substrate break-down can be eliminated by reducing the measured voltage with a reduction of the supplied current. Surface leakage can introduce serious errors in these measurements and requires strong control [1].

4.1.3. Four Points Probe

A local determination of the DC conductivity can be obtained by the so-called four-point probe technique. The four-point probe technique represents a development of the "bar" method.

The technique uses four-point electrodes (probes) pressed on the semiconductor material surface. In this technique, the voltage measuring arms are replaced by point-contact probes. The need for ohmic contacts is no longer critical since no current flows in the voltage arms. A resistivity in the range of about $10^{-1} \div 10^{3}$ Ωcm can be easily measured with a standard accuracy of less than 1% [1, 18, 21].

A typical implementation is the linear four-point probe configuration (Fig. **6**) [18, 21]. Four spring-loaded needles, at an equal distance, s, (*e.g.* s = l mm), are pressed onto the semiconductor surface. The system head applies enough pressure to ensure good near-ohmic contacts, but soft

enough to avoid sample damage. In the two outer probes (Fig. **6)** the measurement current, I, is supplied by a constant current generator, with a high impedance output, while the voltage, V, is read between the inner pair of probes by a high impedance input voltmeter.

The resistivity is computed from the Ohm's law, introducing a right proportionality constant, c, dependent on the sample dimensions and the distance among the needles:

$$\rho = cV/I \tag{4.8}$$

Practical problems concern the type of probe, the spring loading, the accuracy of probe spacing, the contact between probes and the material surface, its preparation, *etc.* Several sources of error and various factors can affect the accuracy of the sample resistivity such as: minority carrier injection, heating by the measurement current, leakage current in the voltmeter circuit, sample geometry, *etc.* [1].

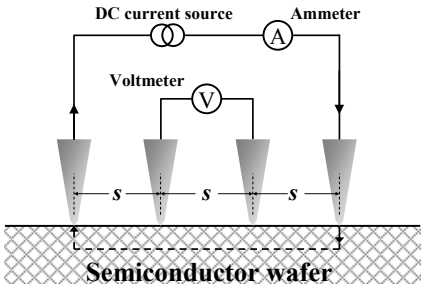


Figure 6: Four point probe on a semi-infinite semiconductor wafer, with a resistivity ρ.

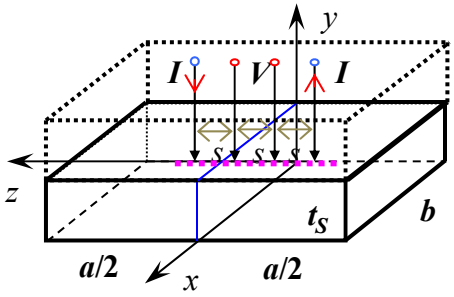


Figure 7: Linear four point probes technique applied to a sample of finite dimensions, on a semi-insulating substrate. The sample must be isolated from the substrate.

Experimentally, four point probe measurement on thin films is no different from that on bulk materials. Practical expressions for the bulk and thin film cases are reported in the reference [18, 21], while some specific cases will be detailed in the next sections.

An additional complication arises when the film is supported by a substrate of high resistivity which, because it is thicker, has a sheet resistance similar to that of the layer. A correction factor

depending both on the ratio (t_s/s) and the substrate resistivity must be used to calculate the actual resistivity of the layer [18]. In practice, there are many possible combinations of resistivity and layer thickness.

Despite the practical difficulties mentioned above, the method is widely used and the correction factor, c, has been calculated for different sample geometries, some of which are reported in the next paragraphs.

4.1.4. Thin Film on an Insulating Substrate

In this case, it is assumed that a thin layer of thickness, t_s, extended infinitely in the other two dimensions, is deposited on a semi-insulating substrate. The semiconductor film should be homogeneous with a specific resistance, ρ.

The film resistivity can be computed by using the following relation:

$$\rho = \frac{V}{I} t_s \frac{\pi}{\ln 2} \tag{4.9}$$

A typical error of about 1% in the ρ value is obtained when t_s is about one half of the probe distance s. For higher values of t_s, the error would increase and in the case of $t_s = s$, it is ≈ 8 %. For typical layer thicknesses ($1 \div 10$ μm) and probe distances (≈ 1 mm) the error can be neglected.

The previous relation is also applicable in all cases where the sample lateral dimensions are much larger than s and the probes are distant from the sample border.

4.1.5. Bulk Material

Finally, we should mention the case of a homogeneous bulk semiconductor such as an ingot of silicon with a planar surface. The technique provides the resistivity value by using:

$$\rho = 2\pi d \frac{V}{I} \tag{4.10}$$

if the condition $d > 3.5s$ if fulfilled, where d represents, in this case, the radius of a hemispherical volume centred in the middle of the inner probes and extending in the bulk semiconductor volume.

4.1.6. Small Sample of Rectangular Shape

For a small slab of rectangular shape with finite dimensions a and b (see Fig. **7**), different approaches and solutions have been proposed. The equation relating the specimen resistivity to the sample dimensions (a, b and t_s) and to the probe spacing, s, has been found by *Hansen* [30] by an analytical approach, solving the Laplace equation and applying standard boundary conditions on the doubled sample (see dotted lines in Fig. **7**) without changing the field and current line conditions in the original sample. The resulting expression is:

$$\rho = \frac{V}{I}\left(\frac{s}{bt_s} + \frac{8}{bd} \sum_{m=0}^{\infty} \sum_{n=0}^{\infty} F \right)^{-1} \tag{4.11}$$

where:

$$F = \frac{\cosh\beta\left(l - \frac{3s}{2}\right)\sinh\left(\frac{\beta s}{2}\right)}{\left(1+\delta_{0,m}\right)\left(1+\delta_{0,n}\right)\beta\cosh\left(\beta l\right)}$$

(m, n) is unequal to (0, 0);

$$\beta = \frac{2\pi}{b}\left[m^2 + \left(\frac{nb}{2t_s}\right)^2\right]^{\frac{1}{2}}$$

and $\delta_{0,m} = 1$ (if $m = 0$) and $\delta_{0,m} = 0$ (for $m > 0$).

4.2. Contactless Methods

These methods are based on the physical absorption of power from a radiation field by free charge carriers in the semiconductor material. Depending on the frequency radiation excitation, three bands are generally involved: radio frequency (RF; ≈ 10^7 Hz); microwave (MW; ≈ 10^{10} Hz) and optical (≈ 10^{14} Hz). The experimental methods as well as the spatial resolution will depend on the frequency band considered.

The RF methods provide an average resistivity value over the area of the investigated film up to a thickness of the order of the skin depth. Examples of experimental setup are reported in literature [31-33].

The MW methods are based on waveguide techniques and generally require well-shaped specimens since the wavelengths used are comparable to the sample size. Several approaches in different frequency bands have been proposed [19, 34-39].

Finally, the optical techniques may offer some advantages with respect to those previously considered because they allow for investigation of local properties of the sample, such as inhomogeneity, focusing the beam on area of order the 10 μm. For a general review and experimental details see the reference [19].

All these methods have in common the problem of deriving the theoretical relationships between the sample resistivity and the measured parameters. In practice, a reliable value of the resistivity requires calibration of the experimental setup. Further drawbacks are the possible non linearity between resistivity and measured parameters and the reduced range of resistivity that can be measured. The above-mentioned difficulties and range of applications make contactless methods suitable only for specific applications.

5. HALL EFFECT

The Hall effect was discovered for the first time in 1879 by E.H Hall [40] in a conducting material. It is largely used to measure important electronic transport coefficients such as charge carrier concentration and Hall mobility, this last in conjunction with the measurement of the sample resistivity.

The mathematical relationships involving the main physical quantities of the Hall effect can easily be found by considering a slab of a conductor, in the shape of a parallelepiped.

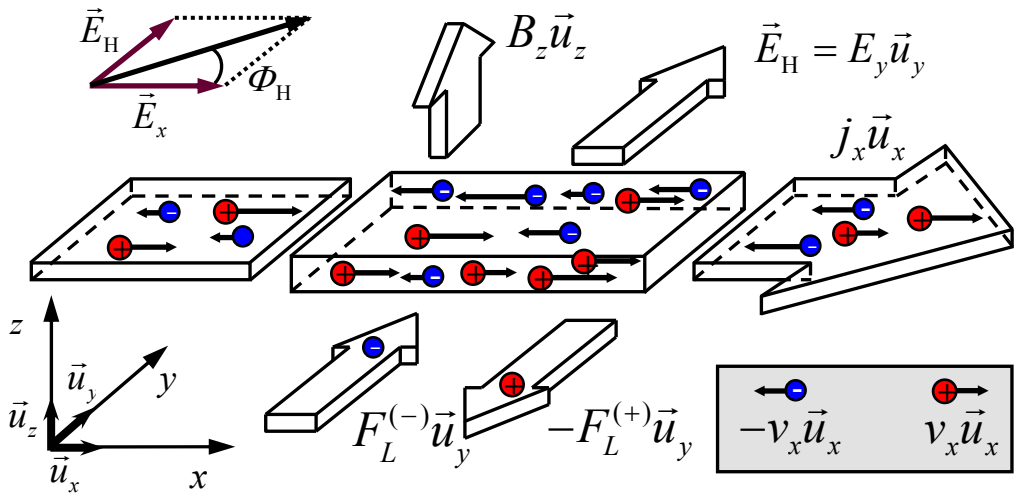


Figure 8: The classical Hall effect. Both electrons and holes are deflected by the Lorentz force ($F_L^{(-)}\vec{u}_y, -F_L^{(+)}\vec{u}_y$ respectively) in two opposite direction as shown by the large arrows. The Hall field, $\vec{E}_H = E_y\vec{u}_y$, has the direction of the positive *y* axis.

In a cartesian system (see Fig. **8**), if a current density $\vec{j}_x = j_x\vec{u}_x$ flows along the *x* axis direction and an induction magnetic field $\vec{B}_z = B_z\vec{u}_z$ is applied parallel to the z axis, orthogonal to the current flow direction, an electric field $\vec{E}_y = E_y\vec{u}_y$ (called Hall field) is set up, mutually perpendicular to the directions of $\vec{j}_x$ and $\vec{B}_z$. The intensity of $\vec{E}_y$ is proportional to j_x and B_z by a quantity *R*, called Hall coefficient:

$$E_y = Rj_xB_z \qquad \textbf{(5.1)}$$

The Hall effect can be physically explained by considering that charge carriers, forming the electrical current, $\vec{j}_x$, will experience a Lorentz force $\vec{F}_L = ev\vec{u}_x \wedge \vec{B}_z$ in a direction orthogonal to the plane formed by the vectors $\vec{B}_z$ and $\vec{j}_x = nqv\vec{u}_x$, where *n* is the concentration of the charged particles.

This force will deflect the charge carriers towards the edges of the slab and will create an electric field, $\vec{E}_H = E_y\vec{u}_y$, whose force, $e\vec{E}_y\vec{u}_y$, will counterbalance the Lorentz force and, then, the further build up of charge:

$$e\vec{v}_x \wedge \vec{B}_z = e\vec{E}_H \qquad \textbf{(5.2)}$$

With reference to Fig. **8** and considering the definition of the current density, the (5.2) can be written:

$$v_xB_z = E_y \qquad \textbf{(5.3)}$$

Hence, the magnitude of the field $\vec{E}_y$ can be expressed as:

$$E_y = \frac{1}{ne} B_z j_x \tag{5.4}$$

The expression for *R* can be derived by comparing the (5.4) with the (5.1):

$$R = \frac{E_y}{B_z j_x} = \frac{1}{ne} \tag{5.5}$$

The convention governing the sign of *R* is to take it as negative when the electric charge, *e*, is negative.

The measure unit of *R* in the SI is m^3/C but generally the unit cm^3/C is preferred.

The Hall coefficient is a powerful investigative tool for the study of the transport properties of conductors and semiconductors due to its simple relationship to the electric charge concentration, *n*. The measurement of *R* provides a direct estimate of the carrier concentration contributing to the transport process.

A more general expression for the Hall coefficient for a simple isotropic band can be found in reference [1].

5.1. Hall Mobility

Another relevant electronic transport coefficient can be obtained by combining the Hall coefficient with the resistivity (or conductivity) of the material. This coefficient is known as Hall mobility, μ_H, and is related to the other two quantities as follows:

$$\mu_H = \left|\frac{R}{\rho}\right| = |R\sigma| \tag{5.6}$$

In general, for the same material, the Hall mobility and drift mobility (see equation (12)) assume different values. A more correct expression for the Hall coefficient is [1]:

$$R = -\frac{\mu_H}{\mu}\frac{1}{ne} = -\frac{r_H}{ne} \tag{5.7}$$

where the adimensional ratio of the Hall mobility to the drift mobility is called the Hall factor, r_H. This quantity is of great interest in a discussion of the electronic transport properties of semiconductors; its theoretical and experimental determination is extremely difficult, r_H depending on the temperature and band structure of the semiconductor. Its value ranges from about 1 to about 2, for most semiconductors [18]. Knowledge of the r_H value is important because from a direct measure of *R* the carrier concentration, *n*, can be derived from the equation (5.7).

Where there is doubt as to the most probable value of r_H, setting it equal to unity is not likely to introduce an error greater than 20 ÷ 30 % in the *n* value [18].

In the presence of electrons and holes, with concentration n_e and n_h respectively, the Hall coefficient can be rearranged in the following way:

$$R = \frac{r_{\mathrm{H}}}{e} \frac{n_h - n_e \left(\frac{\mu_e}{\mu_h} \right)^2}{\left(n_h + n_e \frac{\mu_e}{\mu_h} \right)^2} \tag{5.8}$$

Finally, another useful quantity can be derived by observing Fig. **8.** In fact, in the presence of a magnetic field, the direction of the electric field, $\vec{E}$, ($\vec{E} = \vec{E}_x + \vec{E}_{\mathrm{H}}$, see the Fig. **8**) and the current density, $\vec{j}$, differ. In fact, considering the (5.4), the expression of j_x and $\sigma = \frac{j_x}{E_x}$, it follows:

$$E_y = \frac{1}{nq} B_z j_x = \frac{1}{nq} B_z \sigma E_x = R B_z \sigma E_x$$

then:

$$R B_z \sigma = \frac{E_y}{E_x} = \tan \Phi_H \tag{5.9}$$

The equation (5.9) is valid in the limit of small Φ_{H}, *i.e.* if the intensity of $\vec{B}$ is so low that σ does not depend on $\vec{B}$ [1].

5.2. Experimental Measure of the Hall Effect

The Hall effect can be measured in a semiconductor by a DC method using different geometries. One possibility is the bar (see the Fig. **4**).

A requirement for a correct determination of the Hall coefficient value is that the side arms for the four or six contacts must be narrow enough to ensure a uniform voltage drop along the bar. The ratio of the bar length to its width must be at least 4, to avoid the end contacts shorting the Hall voltage. These end contacts must also be either non-injecting or sufficiently far from the other side arms to avoid injected minority carriers recombining before reaching them. Experimentally, the voltages measured for both directions of current are generally averaged to minimize errors arising from misalignment of the facing Hall side arms and from thermo-electric effects due to temperature gradients within the bar [1]. A uniform current distribution and a well-defined electric field are assured by the geometrical regular bar sample.

Ultrasonic cutting for bulk material, or "sandblasting" with alumina powder for epitaxial films, is commonly used to prepare samples. Epitaxial films must be isolated either by growth on semi-insulating substrates or by using a *p-n* junction. In this last case, attention must be paid to the effect of the depletion regions on the effective sample thickness.

An alternative approach to the bar geometry is van der Pauw's [20]. With respect to the resistivity, the Hall coefficient measurement requires the additional application of a magnetic field, orthogonal to the sample surface, while a constant current must be sourced by using diagonal pairs of contacts (see Fig. **9**).

A total of eight voltage values are measured to obtain two values of the Hall coefficient for a better control of the homogeneity of the film properties [23]. These are the result of the two permutations of the diagonal contacts and the reversal of the current direction for each set and of the magnetic field direction (see Fig. **9**).

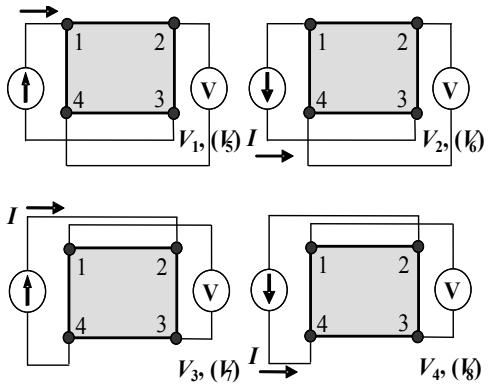


Figure 9: Schematic of the van der Pauw geometry for the Hall coefficient measurement. The numbers in the corners represent the 4 ohmic contacts on the sample border. For each combination of contacts, the current is reversed. The magnetic field, not shown in the figure, is orthogonal to the sample surface. The sequence shown, is repeated again with the magnetic field applied in the reverse direction. The corresponding measured voltages are shown in the brackets.

The average of the two measured Hall coefficient values is taken as the best estimate of R for the sample. The Hall coefficient is measured using diagonal pairs of contacts rather than adjacent pairs:

$$R_a = \left(2.5\times10^7 t_s / IB_z\right)\left(V_2 - V_1 + V_5 - V_6\right)$$
$$R_b = \left(2.5\times10^7 t_s / IB_z\right)\left(V_4 - V_3 + V_7 - V_8\right) \quad \textbf{(5.10)}$$

where R_a and R_b are two independent Hall coefficient values and the V_i (i = 1÷ 8) are the measured voltages (see the Fig. **9**).

The Hall coefficient for the sample is the average of R_a and R_b. Finally, the Hall mobility is then given by the equation (5.6) if the sample resistivity has been measured.

An accurate knowledge of sample thickness is necessary when measuring carrier density, while the value derived for Hall mobility is independent of sample thickness, if the electric field inside the material is uniform. The importance of the Hall effect as a characterization method lies in its ability to measure the free carrier density, (see the Eq. 5.7), when current is carried by a single type of carrier.

6. DEEP STATES IN A DEPLETION LAYER

Impurity and defect levels in semiconductors are usually classified as shallow and deep. To the first classification belong the so called hydrogenic impurities such as the substituitional atoms used for semiconductor doping. These states are located in the forbidden gap near the CB or the VB edge. On the contrary, deep states are energetically located in the forbidden gap at several tens or hundreds of meV from band edges.

Deep states are important because they affect some material properties such as forward and reverse current in devices, reduce minority charge carrier recombination lifetime (*e.g.* in photovoltaic cells), increase the noise in photodiodes and transistors, or can quench the storage time in charge coupled devices.

Deep states can be intentionally introduced in the semiconductor host matrix to control some properties[3] or more frequently are the unwanted result of the preparation technique (growth, deposition and/or post deposition processing) of the semiconductor material. Thus, the study of deep state properties is important both to evaluate their influence on carrier recombination and as a means of identifying and labeling defects.

Deep states are also referred to as deep levels and traps depending on their electrical behavior. In detail, deep levels generally may interact with both the conduction and valence band, while traps exchange their carriers mainly with one of the two bands. This fact is evident in a different energy position of deep states in the semiconductor gap. In fact, deep levels are located closer to the midgap, while the trap states are shifted from the midgap towards one of the two bands.

Due to their position, deep levels act as recombination centers to extract charge carriers from both bands under non-equilibrium excitation conditions. Conversely, traps will capture carriers from the band which they are closer to, in a very short time constant (of the order of few ns), re-emitting carriers to the same band after a delay time (emission time constant of the order of ms or more).

From an experimental point of view, deep states properties cannot be accessed directly. In fact, it is not infrequent that their concentration is several orders lower than that of shallow impurities which control the density of free charge carriers and the Fermi level position in the semiconductor. Therefore, in this case, the Hall effect measurement will be inadequate to determine the energy position and concentration of deep states because the Hall coefficient value will be affected only by charge carriers coming from the shallow levels [18].

The study of deep states requires measurement techniques which are both sensitive to very low concentration of these centers (in presence of a great concentration of shallow impurities), and are capable of revealing recombination processes at deep level centers. These techniques are based on the observation of transient phenomena related to charge carriers capture and emission only at deep states. The time constant of transient is controlled by the rate of the capture or emission process, while its amplitude provides information about the concentration of the deep traps.

---

[3]For example, Au is introduced in the Si matrix to control the lifetime in thyristors.

One of the most sensitive techniques for investigation of deep states properties in a semiconductor is the Deep Level Transient Spectroscopy (DLTS) [41].

The technique uses a diode structure to investigate the time dependent change of the depletion region capacitance due to the capture and emission of charge carriers after the application of a suitable pulse to charge the deep states. Monitoring this capacitance change as a function of time will produce trap states properties. Several different techniques have been developed, known as capacitance spectroscopy [42].

Different possibilities can be found for trap location in a semiconductor material, as shown in Fig. **10**.

Looking at Fig. **10**, if a trap is located closer to the CB than to the VB (top left and bottom right) the electron emission rate, e_n, will be higher than the hole emission rate, e_h. Likewise for traps located closer to the VB.

A further distinction is made in majority or minority carrier traps depending on the main trap interaction with the majority or minority carrier band[4].

The electron capture rate, c_n (c_h for the holes), is related to other characteristic trap parameters such as the capture cross section, σ_n (σ_h), the electron thermal velocity, v_{th}, and the electron concentration, n (p), by the following relation:

$$c_n = n\sigma_n v_{th} \qquad \textbf{(6.1)}$$

and $c_h = p\sigma_h v_{th}$

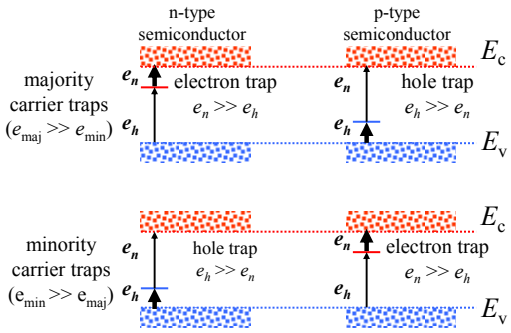


Figure 10: Energy location of main processes for majority and minority carrier traps in a *n* and a *p* type semiconductor. The thick arrows indicate the dominant transition process.

for the holes. The electron emission rate, e_n (e_h), process, following the carrier capture, is also related to the trap level position with respect to the CB edge, *i.e.,* E_C - E_T (E_T - E_V, for the VB) by the equation:

[4]A trap interacting mainly with the conduction band is called an electron trap. Similarly, a hole trap will interact dominantly with the VB.

$$e_n = \sigma_n v_{th} N_C g \exp\left[-\left(E_C - E_T / k_B T\right)\right] \quad \textbf{(6.2)}$$

where N_C and g are the effective density of states of the CB and the trap degeneracy, respectively. A similar relation holds for e_h.

According to the Shockley, Read, Hall theory [43, 44], the minority carrier lifetime, $\tau_{eff,}$ can be deduced from the generation rate, U, and the intrinsic carrier concentration in the semiconductor:

$$\tau_{eff} = n_i / U \quad \textbf{(6.3)}$$

$$U = n_i \frac{\sigma_h \sigma_n v_{th} N_T}{\sigma_n \exp\left(E_{trap} / k_B T\right) + \sigma_h \exp\left(-E_{trap} / k_B T\right)} \quad \textbf{(6.4)}$$

where E_{trap} is the energy position of the trap with respect to the intrinsic energy $E_i \approx \left(E_C + E_V\right)/2$ of the semiconductor.

It is worthwhile noting that deep levels located around the midgap cause large U values (see eq. 6.4) and then lower τ_{eff} values (see eq. 6.3) with respect to trap states.

All the above reported relations can be used to obtain the main trap parameters, *i.e.,* N_T, $E_T \approx E_i$, σ_n and σ_h.

6.1. The DLTS Technique

The exploitation of the DLTS technique requires a *p-n* junction, or a Schottky structure (of the semiconductor to be investigated), kept in a state of reverse biasing. A repetitive pulse is applied to the structure (see Fig. **11**a) resulting in a capacitance transient due to the capture and subsequent emission of charge carriers from the traps (see Fig. **11**b). This transient is induced in the structure by applying a slight forward bias (a short duration pulse of few μs) into deep depletion for a longer time (duration from ms to s), see the Fig. **11**a.

The pulse fills the traps repetitively and the resulting series of emission transients are processed to generate a "spectrum" as the sample is slowly heated, with peaks in the system output corresponding to each trap species. The pulse repetition allows for the collection of more transients to be averaged, since their amplitudes are generally low.

Hence, the process is carried out at several fixed temperatures in a wide range, from about 77 K to about 400 K in order to detect trap states with energy levels ranging from near band edge to mid-gap.

The principle of the DLTS technique can be explained considering the case of a majority electron trap.

The diode structure is held under reverse biasing by applying a voltage V_r. Then a pulse, of duration t_f, reduces the reverse bias almost to zero causing traps to be filled by majority electrons. This pulse is repeated with a t_r interval (see the Fig. **11**a).

Between two consecutive pulses (interval t_m, see the Fig. **11**a) the trapped electrons will be emitted at a rate e_n and an exponential transient will be observed in the recorded capacitance $C(t)$:

$$C(t) = A\sqrt{b\left\{N_D^+ + N_T\left[1-\exp\left(-t/\tau\right)\right]\right\}} \tag{6.5}$$

where A is the area of the diode structure; $b = \dfrac{q\varepsilon_0\varepsilon_r}{2\left(V_{bi}+V_r\right)}$; V_{bi} is the built-in voltage and N_D^+ the concentration of the ionized shallow donors. The transient is shown in the Fig. **11**b.

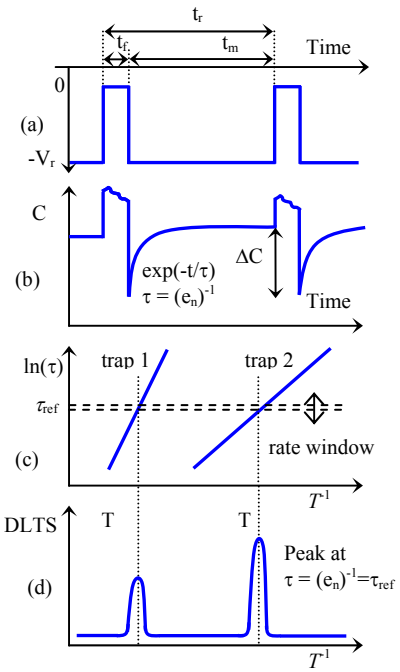


Figure 11: Working principle of the DLTS technique. (a) Repetitive pulse sequence for filing (duration t_f) and reverse biasing (duration t_m). (b) Diode structure capacitance transient as a function of time. (c) Variation of the transient time constant $t_t = e_n^{-1}$ vs T^1 for two different traps. (d) Deep level spectrum obtained by a reference time constant, τ_{ref}, considering the capacitance transient shown in (b).

For practical reasons, due to the need to observe emission rates covering many orders of magnitude (more than 10) by using standard electronic equipments[5], the transient is analyzed in a given time window, called rate window, r_w ($r_w = t_2 - t_1$). For a given r_w value, the capacitance variation will be maximum when the time constant, $t_t = e_n^{-1}(T)$, is equal to a known reference time constant, τ_{ref}, related to r_w. This condition is fulfilled at a given temperature value, T_{pk}, while at low and high temperatures the capacitance transient in r_w will be practically constant. In fact, for low T the emission process will be low and the capacitance change will be negligible during the

[5]A fast response electronics is required, with enough resolution to appreciate very small change in the capacitance value.

observation time window (r_w). For high temperatures the transient is almost complete even before the first sampling time t_1, and then the capacitance remains constant during the interval r_w. However, within the temperature range used for the investigation, there will be a narrow T region where the capacitance transient will be highest. In this state, the electron trap emission rate will fit the selected rate window (t_2 - t_1), *i.e.* the condition $t_t = e_n^{-1}(T) = \tau_{ref}$ will be satisfied (Fig. **12**). The quantity τ_{ref} is related to r_w. In case of a shallow trap, relatively low temperatures are requested to obtain a maximum DLTS signal.

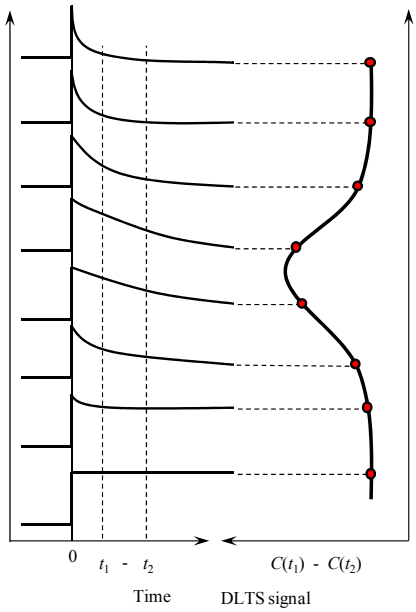


Figure 12: Capacitance transients collected at different temperatures. The abscissa shows the t_1 and t_2 sampling times (rate window) for the construction of the DLTS signal $C(t_1)$ - $C(t_2)$ (right curve) (after [21]).

It is not infrequent to find semiconductors containing two different traps, each characterized by a clear trap signature in the form of a linear dependence of $\ln\left(e_n^{-1}\right)$ *vs.* T^{-1}, with different values of E_{trap} and σ_n. Increasing the system temperature, a peak will occur (at T_{pk}), as $\tau = e_n^{-1}(T)$ passes through τ_{ref}, for each trap (see the Fig. **11**d).

For a given τ_{ref} the T_{pk} values (*e.g.* T_1 and T_2) are characteristic of each trap.

Repeating the scan with different values of the rate window (and then of τ_{ref}), sets of e_n and T_{pk} values can be obtained.

An Arrhenius plot of $\ln(e_n^{-1}T^2)$ vs T^{-1} allows to get the E_{trap} and σ_n values for each trap. However, great care must be taken in the physical interpretation of the results [18].

Typical DLTS signals for an Au donor trap in *n*-type Si is shown in Fig. **13**. The DLTS peaks shift towards higher T with the increase of the rate window. The trap concentration can be determined

from the DLTS signal amplitude. An Arrehnius plot of $\ln(e_n^{-1}T^2)$ *vs.* $1000/T$ provides the trap activation energy while the extrapolation of the line to $1000/T \rightarrow 0$ allows for the extraction of the capture cross section, see Fig. **14**.

A more detailed treatment of the physics of deep states in a depletion region and the DLTS technique is reported in reference [18].

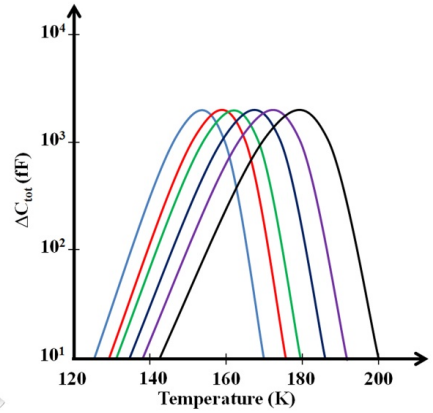


Figure 13: DLTS measurement of the Au trap in *n*-type Si doped with 3.5×10^{17} cm^{-3} atoms. The structure is reversed biased at 13.3 V. The rate windows of the shown curves are (from left to right): 20/s, 50/s, 80/s, 200/s, 400/s and 1000/s. The depletion capacitance is 100 pF (after [21]).

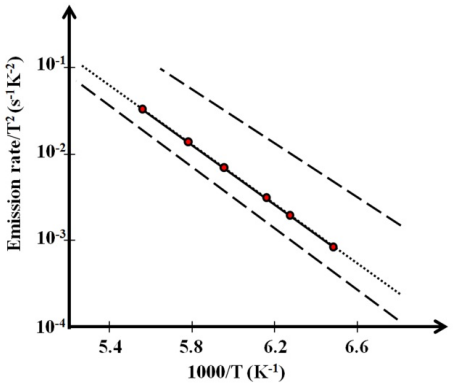


Figure 14: Arrhenius plot of the DLTS signal reported in the Fig. **13**. The measurement is the full line. Dashed lines are data from a trap library for Au in *n*-type Si. The measured activation energy is 340 meV. The dotted lines are used for extrapolation of the capture cross section for $1000/T \rightarrow 0$ (after [21]).

7. CURRENT- VOLTAGE CHARACTERIZATION OF SOLAR CELLS

Solar cells performance can be measured by several electrical characterization techniques which are performed as part of research and development of photovoltaic materials and cells, as well as a standard test tool during the manufacturing process.

Electrical tests usually performed on PV cells, involve measuring capacitance and/or current as a function of several parameters such as an externally applied DC voltage; the illumination intensity; the wavelength of a monochromatic illumination; the illumination position; device temperature, *etc.* [45]. Relevant device parameters, such as output current and voltage; energy conversion efficiency; maximum power output; doping density; resistivity, *etc.* can be extracted from current-voltage (I-V) and capacitance-voltage (C-V) measurements, carried out either in DC or in pulsed mode. Additional information can be derived by the measurement of the device impedance as a function of frequency or voltage, by applying alternating voltages [45].

Among the available characterization methods a fundamental one is the measurement of the illuminated current - voltage (I-V) curves carried out under standard conditions, *i.e.* at 25°C and by using an AM1.5G spectrum.

A simplified equivalent electrical circuit of a single *p-n* junction solar cell (see Ficcadenti and Murri in the chapter 1) is represented in Fig. **15**, which consists in a light-induced current source (I_L), a diode that generates a saturation current, a series resistance, r_s, and a shunt resistance, r_{sh}.

The series resistance is due to the resistance of the metal contacts, ohmic losses in the front surface of the cell, impurity concentrations, and junction depth. The r_s limits both the maximum short-circuit current and the maximum power output of a cell. The ideal value for r_s should be zero. The shunt resistance represents the loss due to the surface leakage along the edge of the cell or to the crystal defects. The ideal value for the shunt resistance should be infinite.

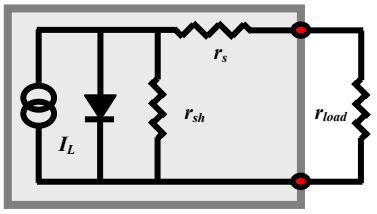


Figure 15: Simplified equivalent electrical circuit of a bulk or a thin film solar cell.

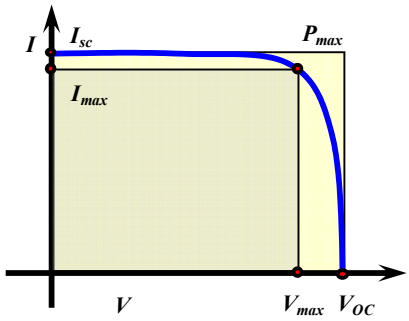


Figure 16: Typical current – voltage curve of a solar cell, having a reversed current sign (see the text). The figure shows the main cell parameters: short-circuit current (I_{SC}); maximum output current (I_{max}) and voltage (V_{max}) on an external load; maximum output power (P_{max}); open circuit voltage.

The total current flowing through an illuminated solar cell, when a load resistor (r_{load}) is connected to its output terminals, can be approximated by the following relation:

$$I = I_S\left[\exp\left(qV/k_{\mathrm{B}}T\right)\right] - I_L \tag{7.1}$$

Fig. **16** illustrates a typical I-V curve of a forward biased solar cell under illumination. We note that in an actual I-V characteristics, the curve passes through the fourth quadrant and allows power to be extracted from the device (V^+, I^-). For convention, considered that a PV cell is an active device, the measured current is reversed in sign and the I-V curve is plotted in the first quadrant, as in the Fig. **16**.

The electrical parameters commonly used to characterize the solar cell efficiency are: the short circuit current, I_{SC}; the maximum current, $I_{\max}$; the open circuit voltage, V_{OC}; and the maximum voltage, $V_{\max}$.

The maximum power point, $P_{\max}$, is the product of the $I_{\max}V_{\max}$ and it represents the knee of the I-V curve. The $P_{\max}$ value corresponds to the area of the largest rectangle (whose sides are $I_{\max}$ and V_{max}) under the I-V curve. Another important parameter of a PV cell is the fill factor (*FF*), defined as:

$$FF = \frac{P_{\max}}{I_{SC}V_{OC}} = \frac{I_{\max}V_{\max}}{I_{SC}V_{OC}} \tag{7.2}$$

The *FF* represents how far the I-V characteristics of an actual solar cell differs from that of an ideal one. The *FF* is always lower than one, due to the losses from series and shunt resistances. From a geometrical point of view the *FF* is also equal to the area ratio between the two rectangles shown in the Fig. **16**.

Finally, the conversion efficiency, η, is defined as the ratio of the maximum power output, $P_{\max}$, to the power input, P_{inc}, this last being the total radiant energy incident on the surface of the PV cell:

$$\eta = \frac{P_{\max}}{P_{inc}} \tag{7.3}$$

7.1. Experimental Measure

In general, the measurement is carried out under standard testing conditions, *i.e.,* usually keeping constant the cell temperature at 25 °C and illuminating the cell by means of a AM1.5G spectrum (for non concentrating solar cells) that resembles the solar spectrum as much as possible [46]. This kind of spectrum is usually realized combining a W-halogen lamp with a Xe-lamp to get a close match to the solar spectrum. Details about the measurement of I-V characteristics under illumination of solar cells can be found in references [47, 48].

To extract the solar cell parameters, the I-V characteristics is measured with a load resistance connected to the cell, under illumination with a standard AM1.5G spectrum. The voltage and current are measured during the voltage sweep with a four-point probe technique (see the section

4) in order to eliminate the lead resistance. By using a set of leads, a voltage sweep, ranging from 0 V to V_{OC}, will source the PV cell with a current ranging from I_{SC} to 0, respectively. The voltage drop across the cell is measured by a second set of leads, allowing to calculate all the characteristic solar cell parameters [45].

Several apparatus are now commercially available in order to simplify electrical testing and analysis of material and PV cell parameters. These last can be measured sourcing and measuring both current and voltage, (four-quadrant source capability), *i.e.* the measuring instrument can sink the cell current as a function of the applied voltage.

A method for the determination of the series resistance in PV cells, with a voltage-independent charge carrier collection in the *p-n* junction, is the comparison between dark and illuminated I-V curves, since the difference between dark and illuminated I-V curves is not a constant, when $r_s > 0$, even when the actual charge carrier collection process is not voltage dependent [45].

Now, if the I-V curve measured under illumination by the AM1.5G spectrum, I_L, is shifted by the short-circuit current I_{SC} (at exactly this AM1.5G illumination) the resulting current ($I_L + I_{SC}$) voltage characteristics will show the same voltage behaviour as the unshifted one.

The value of r_s can be obtained by the following relation:

$$r_S = \frac{V_d - V_L}{I_{SC}} \tag{7.4}$$

where V_d and V_L are the dark and under illumination voltages at a given current intensity, respectively, while *Isc* is the short circuit current intensity measured under AM1.5 G spectrum. V_L is the voltage value obtained by the (I_L + *Isc*) - V curve [45].

However, this method is only suitable as long as the series resistance is independent on illumination conditions. For this situation, Aberle *et al.* [49] proposed to use the V_{OC} measured at different illumination conditions yielding the so-called *Isc* - V_{OC} curve. Then the r_s value can be derived by the following relation:

$$r_S = \frac{V_{OC} - V_L}{I_{SC} - I_{SC}^{AM1.5}} \tag{7.5}$$

where V_L and I_{SC} are the variable voltage and short circuit current at various illumination intensities.

It is worthwhile mentioning that V_L is the value measured at a given current intensity, in the far forward region of the I-V curve, while V_{OC} is completely independent on r_s because no current flows at open-circuit conditions. Then the *Isc* - V_{OC} curve is a series-resistance free I-V curve [45].

The value of shunt resistance r_{sh} and leakage current can be derived from the reverse-biased I-V characteristics carried out in the dark. A voltage sweep applied to the cell is sourced from 0 V, up to a value near the break down of the device. The resulting current is measured and plotted as a

function of the voltage. The r_{sh} is determined from the slope of the reverse-biased I-V curve of a PV cell, as shown in Fig. **17**. From the linear region of this curve, the shunt resistance can be calculated as:

$$r_{Sh} = \frac{\Delta V_{RB}}{\Delta I_{RB}} \tag{7.6}$$

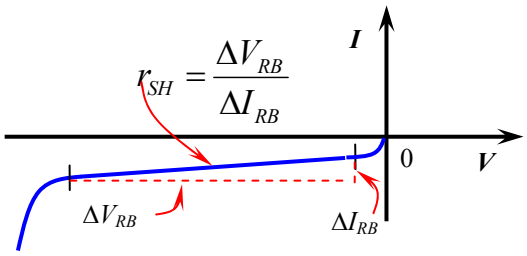


Figure 17: Current – voltage characteristics of a reverse polarized solar cell. The curve allows to calculate the value of the shunt resistance, r_{sh}, as shown in the figure.

ACKNOWLEDGEMENT

Declared none.

CONFLICT OF INTEREST

The author(s) confirm that this chapter content has no conflict of interest.

REFERENCES

[1] Pinto N, Murri R, Nowak M. Magnetotransport effects in semiconductors. In: Nalwa HS, Eds Handbook of Thin Films, Vol 5, Chap 9. New York: Academic Press 2002; pp. 439 – 494.
[2] Ashcroft NW, Mermin ND, Eds. Solid State Physics. USA: John Wiley & Sons 2005.
[3] Sze SM, Kwork KN, Eds. Physics of Semiconductor devices. USA: John Wiley & Sons 2009.
[4] Ziman J, Eds. Electrons and Phonons. Oxford: Oxford University Press 1960.
[5] Butcher PN. The theory of electron transport in crystalline semiconductors. In: Crystalline Semiconducting Materials and Devices. New York: Plenum Press 1986; pp. 131 – 163.
[6] Callen HB. The Application of Onsager's Reciprocal Relations to Thermoelectric, Thermomagnetic and Galvanomagnetic Effects. Phys Rev 1948; 73: 1349 –1358.
[7] Beer AC. Galvanomagnetic Effects in Semiconductors. Solid State Physics 1963; 4: 256 –263.
[8] Putley EH, Eds. The Hall Effect and Related Phenomena. London: Butterworths 1960.
[9] Seeger K, Eds. Semiconductor Physics 4th ed. Berlin: Springer-Verlag 1989.
[10] Nag BR. Electron Transport in Compound Semiconductors. Berlin: Springer-Verlag 1980.
[11] Roth LM. In: Landsberg PT, Eds. Handbook on Semiconductors. Amsterdam: North Holland 1992; pp. 489 –581.
[12] Erginsoy C. Neutral Impurity Scattering in Semiconductors. Phys Rev 1950; 79: 1013-1014.
[13] Chattopadhyay D, Queisser HJ. Electron scattering by ionized impurities in semiconductors. Rev Mod Phys 1981; 53: 745-768.
[14] Madelung O, Eds. Introduction to Solid State Theory. Berlin: Springer-Verlag 1981.

[15] Hutson AR. Piezoelectric Scattering and Phonon Drag in ZnO and CdS. J Appl Phys 1961; 32: 2287-2293.
[16] Stillman GE, Wolfe CM. Electrical characterization of epitaxial layers. Thin Sol Films 1976; 31: 69-88.
[17] Beer AC. Galvanomagnetic Effects in Semiconductors. Solid State Physics. In: Seitz F, Turnbull D, Beer AC, Eds. Advances in research and applications suppl. 4. New York: Academic Press 1963.
[18] Blood P, Orton JW, Eds. The electrical characterization of semiconductors: Majority carriers and electron states. London: Academic Press 1992, pp. 1 – 217.
[19] Blood P, Orton JW, Eds. The electrical characterization of semiconductors: Measurement of minority carriers properties. London: Academic Press 1990.
[20] van der Pauw LJ. A method for measuring specific resistance and Hall mobility of disc of arbitrary shape. Philips Res Rep 1958; 13: 1-9.
[21] Bach H-G. In: Czichos H, Saito T, Smith L, Eds. Springer Handbook of Materials Measurement Methods. Berlin: Springer-Verlag 2006, pp. 453 – 472.
[22] Sharma BL. In: Willardson RK, Beer AC, Eds. Semiconductors and Semimetals. New York: Academic Press 1981; vol 15, pp. 1-42.
[23] Low level Measurements Handbook, 6th ed. Cleveland (Ohio): Keithley Instruments Inc 2004.
[24] Augelli V, Manfredotti C, Murri R, *et al.* Influence of iodine doping on the electrical properties of GaSe. Il Nuovo Cimento (B) 1977; 38: 327-31.
[25] Manfredotti C, Mancini AM, Rizzo A, *et al.* Electrical properties of $GaS_xSe_{(1-x)}$ solid solutions. Phys Stat Sol (a) 1978; 48: 293-6.
[26] Augelli V, Murri R. Dark conductivity in amorphous undoped silicon films. J Non-Cryst Solids 1983; 57: 225-40.
[27] Augelli V, Ligonzo T, Murri R, *et al.* Effects of dopants on the electrical conductivity and hall mobility in Si:H,Cl films. Thin Solid Films 1985; 125: 9-16.
[28] Murri R, Pinto N, Ambrosone G, *et al.* Electrical resistivity of a-SiC:H as a function of temperature: evidence for discontinuities. Phys Rev B 2000; 62: 1801-5.
[29] Pinto N, Ficcadenti M, Morresi L, *et al.* Electrical transport properties of microcrystalline silicon grown by PECVD. J Appl Phys 2004; 96: 7306-11.
[30] Hansen BH. On the influence of shape and variations in conductivity of four point measurements. Appl Sci Res 1960; B8: 93-104.
[31] Bryant CA, Gunn JB. Noncontact technique for the local Measurement of Semiconductor Resistivity. Rev Sci Inst 1965; 36: 1614 – 1621.
[32] Miller GL, Robinson DAH, Wiley JD. Contactless measurement of semiconductor conductivity by radio frequency free carrier power absorption. Rev Sci Inst 1976; 47: 799 – 806.
[33] McElroy RGC. Use of capacitively coupled marginal oscillator for contactless transient conductivity measurements. Rev Sci Inst 1980; 51: 1374 – 1380.
[34] Brodwin ME, Pao-Sun Lu. A precise cavity technique for measuring low resistivity semiconductors. Proc IEEE 1965; 53: 1742 – 1743.
[35] Bichara MRE, Poitevin JPR. Resistivity Measurement of Semiconducting Epitaxial layers by the reflection of a Hyperfrequency Electromagnetic Wave. IEEE Trans Instrum Meas 1964; IM13: 323 – 28.
[36] Beck G, Kunst M. Contactless scanner for photoactive materials using laser induced microwave absorption. Rev Sci Inst 1986; 57: 197 – 204.
[37] Srivastava GP, Jain AK. Conductivity Measurements of Semiconductors by Microwave Transmission Technique. Rev Sci Inst 1971; 42: 1793 – 1800.
[38] Hasegawa H, Ohno H, Shimizu H, *et al.* Non-destructive characterization of electrical uniformity in semi-insulating GaAs substrates by microwave photoconductive technique. J Electron Mat 1984; 13: 931 – 948.
[39] Cummings KD, Pearton SJ, Vella-Colleiro GP. Characterization of GaAs and Si by a microwave photoconductance technique. J Appl Phys 1986; 60: 1676 – 1683.

[40] Hall EH. On a New Action of the Magnet on Electric Currents. Amer J Math 1879; 2: 287 – 290.
[41] Lang DV. Deep level transient spectroscopy. J Appl Phys 1974; 45: 3023 – 3032.
[42] Miller GL, Lang DV, Kimerling LC. Capacitance transient spectroscopy. Ann Rev Mater Sci 1977; 7: 377 – 448.
[43] Hall RN. Electron-hole recombination in Germanium. Phys Rev 1952; 87: 387 – 394.
[44] Shockley W, Read WT. Statistics of the recombinations of holes and electrons. Phys Rev 1952; 87: 835 – 842.
[45] Kirchartz T, Ding K, Rau U. Fundamental electrical characterization of thin-film solar cells. In: Abou-Ras D, Kirchartz T, Rau U, Eds. Advanced Characterization Techniques for Thin Film Solar Cells. Weinheim Germany: Wiley-VCH Verlag GmbH & Co KGaA 2011; pp. 36 – 44.
[46] ASTM G173 (2010) Standard Tables for Reference Solar Spectral Irradiances: Direct Normal and Hemispherical on 37° Tilted Surface West Conshocken, PA, USA: American Society for Testing and Materials, 2010.
[47] Osterwald CR. In: Markvart T, Castañer L, Eds. Practical Handbook of Photovoltaics. Kidlington Oxford: Elsevier 2003; p. 793.
[48] Emery K. Measurement and characterization of solar cell modules. In: Luque A, Hegedus S, Eds. Handbook of Photovoltaic Science and Engineering. Chichester UK: John Wiley & Sons Ltd 2003; pp. 701-752.
[49] Aberle AG, Wenham SR, Green MA. A new method for accurate measurements of the lumped series resistance of solar cells. In: Proc of the 23rd IEEE Photov Spec Conf. Louisville. Kentucky New York 1993; pp. 133-36.

SECTION III - PHOTOVOLTAIC DEVICES

Send Orders of Reprints at reprints@benthamscience.net
Silicon Based Thin Film Solar Cells, 2013, 277-358

CHAPTER 9

Heterojunction for Silicon Photovoltaics

Mario Tucci[1,*], Luca Serenelli[1], Massimo Izzi[1], Enrico Salza[1], Simona De Iuliis[1], Pietro Mangiapane[1], Giampiero de Cesare[2] and Domenico Caputo[2]

[1]ENEA, Research Center Casaccia, via Anguillarese 301, 00123 Roma Italy and [2]DIIET, University "Sapienza", Via Eudossiana 18 00184 Rome, Italy

Abstract: The amorphous/crystalline silicon heterojunction solar cell fascinated the researchers since the beginning as a way to improve the efficiency of silicon based solar cell and to reduce the cost of the PV. Indeed with the aid of a heterojunction it is possible to achieve higher built-in voltage and higher cell open circuit voltage with respect to the homojunction. Moreover thin amorphous film technology, using low temperature processes (below 300°C), in principle allows the use of thinner silicon wafer that could suffer of high temperature step required in the homojunction approach to the cell efficiency. Many efforts have been spent by several research groups to address the main problems of the HJ device related to the silicon surface cleaning, defects at the interface, thin film doping, metal contact and device architecture. From '90 years the progresses of SANYO results have driven the scientific community to achieve higher cell efficiency. Actually SANYO has demonstrated the possibility to fabricate heterojunction cell on c-Si wafer thinner than 100 μm, leading the amorphous crystalline silicon heterojunction concept toward thin film solar cell.

In this chapter we overview the heterojunction cell concept out lighting the problems encountered and the current understanding of the fundamental device physics to achieve highest efficiency.

Keywords: Amorphous silicon, cleaning, doping, heterojunction, lifetime, numerical model, plasma treatment, screen printing, solar cell, silicon, texturing, thin film, transparent conductive oxide.

1. INTRODUCTION

Basically the amorphous/crystalline silicon (a-Si:H/c-Si) heterojunction solar cell cannot be considered as a thin film cell, since, up to now, the silicon wafer act as a base. Nevertheless all the technologies involved in the HJ cell fabrication are more related to the thin film than to the conventional silicon based cell. This allows in the near future reducing the silicon wafer thickness thus approaching the thin film cell. Therefore in this chapter we propose a brief overview of the HJ cell.

Hydrogenated amorphous/crystalline silicon (a-Si:H/c-Si) heterojunction (HJ) has been widely studied since 70 years [1]. Even though a stacked a-Si:H/c-Si tandem junction has been reported in 1983 [2] and several years have been spent on understanding transport mechanism and band

[*]**Address correspondence to Mario Tucci:** ENEA, Research Center Casaccia, Via Anguillarese 301, 00123 Rome Italy; Tel: +39 630484095; Fax: +39 30486405; E-mail: mario.tucci@enea.it

Roberto Murri (Ed)
All rights reserved-© 2013 Bentham Science Publishers

discontinuity at the heterointerface [3-9], the first efficient cell comparable with the c-Si based top cell [10] has been demonstrated in 1992 when the HIT cell [11] has been presented to the scientific community. A cross section of the HIT cell first release is depicted in Fig. **1**. The thin intrinsic layer between the doped a-Si:H film and the c-Si base works as an effective silicon surface passivation that strongly reduces the interface recombination, leading to an efficiency of 18.1% using temperature lower than 200 °C in the cell manufacturing process. In particular that cell had not only the a-Si:H front side emitter, but also the rear side a-Si:H base contact. Due to a-Si:H emitter poor conductivity the front side contact has been formed by TCO deposition and the rear side contact has been ensured by Al evaporation. In 1994, SANYO ltd. overcame 20% efficiency with heterojunction solar cell based on a n-type Czochralski silicon textured absorber [12, 13]. In 2009 SANYO achieved 23% efficiency on practical size of 100 cm^2 and 22.8% on c-Si wafer thinner than 100 μm [14, 15]. Even though SANYO patent on HIT cell has limited the industrial application from other solar cell manufacturing companies, many research groups worldwide have investigated HJ approach to achieve silicon based solar cell using low temperature processes needed for the a-Si:H film deposition as well as TCO fabrication. Indeed the possibility to reduce the thermal budget in cell manufacturing has been considered as a way to reduce the solar cell cost. A qualitative comparison of the thermal budget needed for the homojunction c-Si conventional and a-Si:H/c-Si heterojunction cell fabrication processes in Fig. **2** are reported. Actually the SANYO patent has been expired therefore a growing interest on this technology is rising up from solar cell manufacturing companies [16].

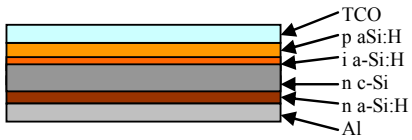


Figure 1: Schematic cross section of the HIT cell first release.

All the other research groups involved in the HJ investigation have reached lower efficiency with respect to the impressive SANYO results, despite to their strong efforts. Fig. **3** shows the SANYO progress in conversion efficiency with respect to the other competitors.

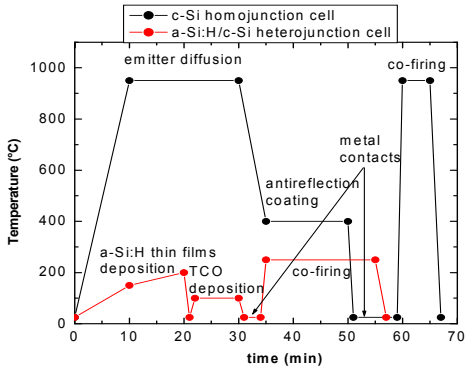


Figure 2: Qualitative comparison of the thermal budget needed for the homojunction c-Si conventional and a-Si:H/c-Si heterojunction cell fabrication processes.

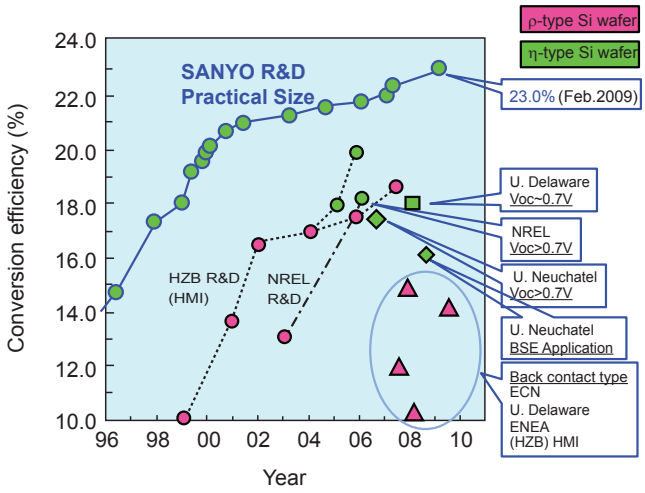


Figure 3: Progress in conversion efficiency of HIT and other institutions' results for heterojunction solar cells.

We can summarize a series of advantages and related to the HJ technology:

1) high open circuit voltage due to the potentiality of HJ and due to the good silicon surface passivation promoted by the a-Si;H layer that reflects in high cell efficiency as demonstrated not only by SANYO but also from other competitors [14];

2) excellent stability with respect to amorphous thin film cells since the a-Si:H layer in the HJ technology are extremely thin thus escaping from the Staebler-Wronski degradation effect that still affect the a-Si:H thin film solar cells [17];

3) better response with operating temperature with respect to conventional silicon based cells. This represents a great advantage in operating conditions since the cell are packaged by glass and plastic and leaved under sunlight with low possibility to dissipate the thermal excess [13];

4) low cost related to the lower thermal budget and less time needed in the cell manufacturing. This allows the use of very thin c-Si wafer [18] that can strongly reduce the PV cost.

Nevertheless several drawbacks still affect the market breakthrough of this technology:

1) difficulties to setup the cleaning procedure for the c-Si wafer as well as the a-Si:H passivation layer. These issues strongly affect the device performances.

2) n-type c-Si wafer actually are not at the same price level of p-type c-Si. HJ on p-type c-Si does not reach the same efficiency level of n-type based c-Si HJ to justify the investment in a production line.

2. DEFECTS AT THE HETEROJUNCTION

The heterointerface is the heart of the HJ device; the photogenerated carriers within the c-Si absorber material have to cross the interface to be collected by the emitter and during this path they survive only if recombination at interface is lower than collection probability. This general concept becomes critical when one of the two materials is amorphous. Indeed, the crystalline silicon edge represents a strong discontinuity of atoms network that in the well known Tham-Shockley theory can be represented by a defect density distribution laying around one third of energy gap from the valence band. The number of states has been estimated as two third fraction of the atomic density within the volume [19, 20]. A schematic picture of p-type doped c-Si edge discontinuity is depicted in Fig. **4(a)**. The Fermi level moves toward mid gap since a pinning occurs on the defect distribution. On the other side a-Si:H is a well known defective atom network even if hydrogen introduction helps to reduce the defect density amount [21]. The defect density is so high that the energy band theory, based on the crystal network periodicity and the thigh binding model, can be approximated on a short range periodicity and still survives introducing a pronounced density distribution along the forbidden gap as depicted in Fig. **4(b)** for an intrinsic material. Due the high defect density the edge of a-Si:H layer not differ too much from the bulk material in terms of energy band distribution. Therefore it is likely imaging that the probability of an electron to recombine crossing the interface formed jointing the two band diagrams and their density distributions, is high as depicted in Fig. **4(c)**. The decision to immediately escape from this game could be understandable, but the challenge in finding a strategy to overcome the difficulties and then producing low cost solar cells still based on c-Si absorber fascinated many research groups for long time and still now several aspects are under debate.

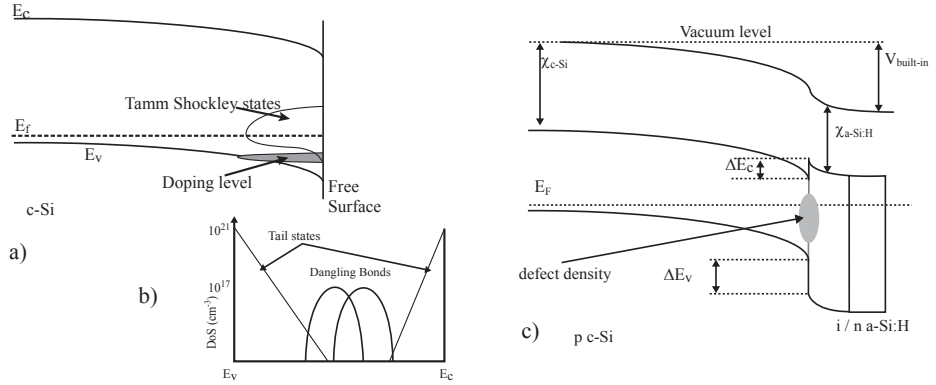


Figure 4: (a) Band bending at the c-Si surface due to Tamm Shokley states. (b) Schematic band diagram of a-Si:H material. (c) Energy band distribution at c-Si/a-Si:H interface.

2.1. Nature of Defects in a-Si:H

In this paragraph we focus on the nature of the interface defect density and the possibility to reduce their impact on the recombination by introducing the silicon surface passivation concept. In c-Si when N tetravalent atoms combine into solid they modify their orbitals to four hybrid sp3 disposing in a tetrahedral shape. Taking into account Pauli principle they form 2N bonding orbitals (valence band) and 2N anti-bonding orbitals (conduction band), as depicted in Fig. **5(a)**, where the bandgap between the two bands is empty. When the atom network is disordered and a great

amount of bonds are weak and stressed, as in a-Si:H, two tails of states appear in the forbidden bandgap. If the bonds are not saturated but dangling within the network, then a distribution of states appears at midgap of the forbidden bandgap. They determine the position of Fermi level and act as recombination centres. Hydrogen, introduced during the a-Si formation in order to reduce the dangling bond density, alters the tetrahedral structure of Si and modifies the energy band distributions. If a Si atom is bonded to three Si atoms and to one H atom a distribution as depicted in Fig. **5(b)** is obtained. Since the Si-Si bonding energy is 3.4 eV while the Si-H that is 2.4 eV, a wider separation between bonding and anti-bonding orbitals occurs. The 1s H orbital is at energy lower than that sp3 therefore the resulting bonding orbital lies within valence band, while the anti-bonding, due to the wider separation, lies at the bottom of conduction band. This reduces the density of states (DoS) close to the band edge, thus increasing the energy bandgap of the semiconductor (1.72eV). A more precise description of the localized states should include the Coulomb effect between electrons.

If two electrons with opposite spin are on the same energy state they repulse each other inducing an energy variation U (correlation energy) of the state [21, 23]. If the state is in the extended bands, U can be neglected and the one-electron approximation is still valid. If the state is localized (gap), the average distance between the two electrons can so short that U cannot be neglected since it assumes value of tens meV. This means that the density of states depends on their occupation. The most common defect in a-Si network is the dangling bond (DB), denoted as T_z^q in which z is the coordination number and q is the state of charge. Therefore the Si atom tetrahedric bonded in the network is T_4^0, while a T_3^0 is a neutral DB. This atom still assumes a tetrahedric configuration, but introduces two states within the gap: one empty at higher energy and one filled at lower energy as depicted in Fig. **4(c)**. These states are separated by the energy U. If T_3^0 loses an electron it becomes T_3^+ thus altering the hybridization orbitals from sp3 to sp2 and forming planar molecules having 120° angles between each other. As a result an increment of energy related to the DB occurs. In other words, if the centre T_3^0 captures a hole has a more stable energetic situation. On the contrary, if T_3^0 captures an electron, becomes T_3^- and a de-hybridization occurs towards p orbitals, having 95° between each other. Also this effect produces an energy reduction of the DB. Therefore both cases produce bond relaxation leading to correlation energy U_{eff} lower than U that can also assume negative values [24]. A schematic view of the density of states with $U_{eff} > 0$ and $U_{eff} < 0$ is reported in Fig. **5(d)**. If $U_{eff} > 0$ the states under the Fermi level are occupied with one electron and then a strong Electron Spin resonance signal appears. If $U_{eff} < 0$ the states under the Fermi level are occupied with electron pair having opposite spin and then there is no evidence from ESR measurements. Therefore if the ESR signal is lower with respect of expected DoS; this probably means that states with $U_{eff} < 0$ and $U_{eff} > 0$ are simultaneously in equilibrium [23].

This DB behaviour is referred as amphoteric nature and the resulting defect density distribution is referred as defect pool model [25, 26]. The model proposes the existence of a pool of defect from which the density of dangling bond states are determined by a chemical equilibrium process, leading to a minimum of the system free energy. In the different presented defect pool models, the equilibration process involves breaking of weak Si-Si bonds, diffusion of hydrogen as well as reformation of Si-H bonds. Winer [25] developed a suitable framework for the description of the defect pool model, where the chemical equilibrium between dangling bonds and weak Si-Si bonds is similar to the equilibrium between vacancies and interstitial defects in crystalline silicon. In particular, the neutral defect formation in intrinsic a-Si:H is described by the reaction:

$$SiH + SiSi \leftrightarrow D^0 + SiHSi \quad \textbf{(1)}$$

where SiSi are the weak Si-Si bonds (valence band tails), SiH group provides that hydrogen atom that enables the equilibration, D^0 are the neutral (*i.e.* occupied by one electron) dangling bonds and SiHSi group traps the hydrogen released by the SiH. This equation establishes that the system free energy minimum is determined by the equilibrium between the entropy produced by defect creation and the enthalpy cost of transferring hydrogen atoms from SiH group to trapping H sites.

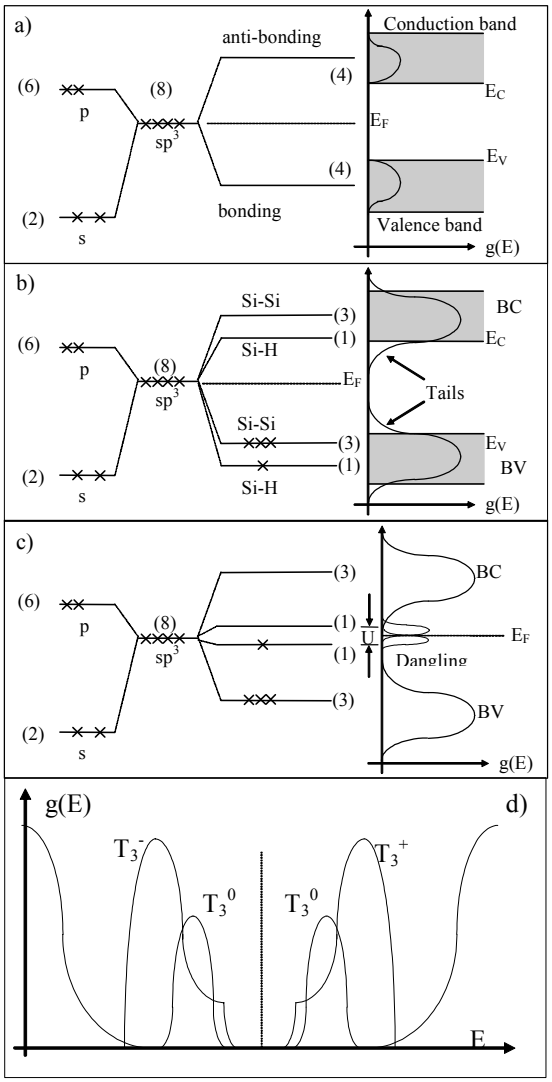


Figure 5: (a) Si bonding and antibonding; (b) tails formation in a-Si:H energy gap due to H; (c) DB related states within energy gap; (d) simultaneously presence of states with $U > 0$ and $U < 0$ within a-Si:H energy gap.

Applying the law of mass action and assuming that the pool of defect energies is expressed by a Gaussian distribution with peak at E_p, Winer derives a defect density with Gaussian shape with width equal to σ and centered at $E_p-\sigma^2/E_0$ if $kT<E_0$ or at $E_p-\sigma^2/kT$ if $kT>E_0$. σ is the standard deviation of the Gaussian defect pool distribution that can be identified with the concentration of bonded hydrogen, whose variable back bond strain determines the broad distribution of potential defect sites. σ therefore is a measure of the disorder of a-Si:H material as well as E_0 that represents the slope of the valence band tail states.

The shift of the defect distribution with respect to the defect pool means that the free energy system minimum does not coincides with the energy at which the potential defect sites are most numerous.

In the Winer's theory these considerations apply to undoped a-Si:H materials. In order to take into account the effect of dopant atoms, Winer considers that in a n-type material, the following reaction occurs:

$$D^0 + e^- \leftrightarrow D \quad \textbf{(2)}$$

where D^- is the concentration of defects that have captured one electron from the conduction band. An analogous reaction involving holes has to be considered for p-type materials. From a qualitative point of view, the above equilibrium equation says that the presence of electrons determines a larger defect concentration in reaction 1 and that in n-type films the most likely defect are D^-states. Mathematically speaking, the increase of defect concentration is caused by the reduction of the enthalpic cost to form a defect due to the difference between the energy gained in dropping an electron from the Fermi level to the defect level and the energy spent (correlation energy U) in bringing two electrons in the same defect state. This energy variation determines a variation of the defect chemical potential that becomes Fermi level dependent and shifting of the maximum defect distribution that now occurs at $E_p+U-2\sigma^2/E_0$. From this equation derives that if σ is sufficiently large, *i.e.* the defect pool is sufficiently wide, D^- in a-Si:H material lies deeper than D^0 in undoped materials even though the correlation energy is positive. These results are summarized in Fig. **6**, where the gap-state distribution for n-type, intrinsic and p-type a-Si:H materials are calculated basing on the above theoretical considerations. Powell and Deane [26] improved the defect pool model proposed by Winer, including in their theory the simultaneous presence of defects in all three charge states in all material types, the weak bond depletion due to defect formation and the hydrogen entropy. The microscopic model assumed by these authors for the defect formation is described by the following three chemical reactions:

$$WB \leftrightarrow (2D) \quad \textbf{(3)}$$

$$SiH + WB \leftrightarrow (D + Si\text{-}H) + D \quad \textbf{(4)}$$

$$2SiH + SiSi \leftrightarrow (D + Si\text{-}H\text{-}H\text{-}Si) + 2D \quad \textbf{(5)}$$

As a starting point for the calculation of the defect density they determined a general expression for the defect chemical potential taking into account the energy of electron (or electrons) of the defect, the entropy associated with the electron occupancy of the defect and the entropy associated with the location of the defect on alternative hydrogen sites. For the calculation of the defect density D(E) at energy Et from weak bond states they derive the following expression:

$$D(E) = \int \frac{P(E)D(E_t)}{1+\exp\left\{2\left[E_f(E)-Et\right]/kT\right\}}dE \quad \textbf{(6)}$$

where $P(E)g_t(E_t)$ is the density of weak bonds at energy E_t that lead to potential defect sites at energy E, μd is the defect chemical potential and the integral is extended over the all weak bond energies. Assuming that $D(E_t)$ is given by the valence band tail states with an exponential behavior and that P(E) has a Gaussian distribution with pool width σ and maximum E_p, they calculated the density of positive (D^+), neutral (D^0) and negative (D^-) defect distribution by:

$$D^+(E) = D(E)f^+(E)$$

$$D^0(E) = D(E)f^0(E)$$

$$D^-(E) = D(E)f^-(E)$$

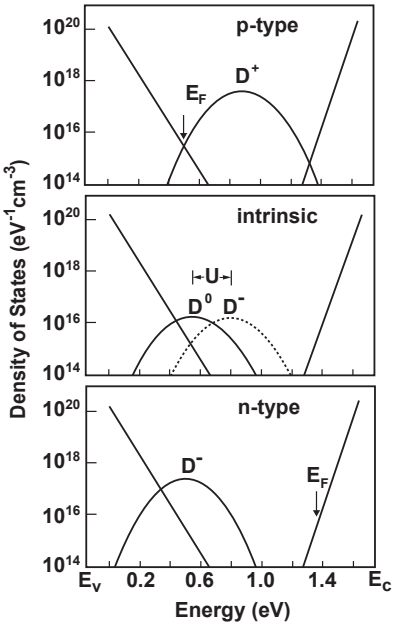


Figure 6: Gap state defect distribution for n-type, intrinsic an p-type doped a-Si:H with the appropriate defect chemical potentials (U = 0.25eV) [25].

where f^+, f^0 and *f*-are respectively the occupancy functions of the amphoteric dangling bonds occupied by zero, one or two electrons, respectively and D(E) is calculated from equation.

The main results are reported in Fig. **7** for intrinsic material, and in Fig. **8(a)**, **(b)** for n-type and p-type respectively.

As for the Winer model the Gaussian distribution are shifted with respect to the pool of potential sites by energy dependent on σ for the neutral defect and by a linear combination of s and U for

charged defect states. However, it is important to underline that both charged states are present even for undoped material and that their density is approximately four times higher than density of neutral defects.

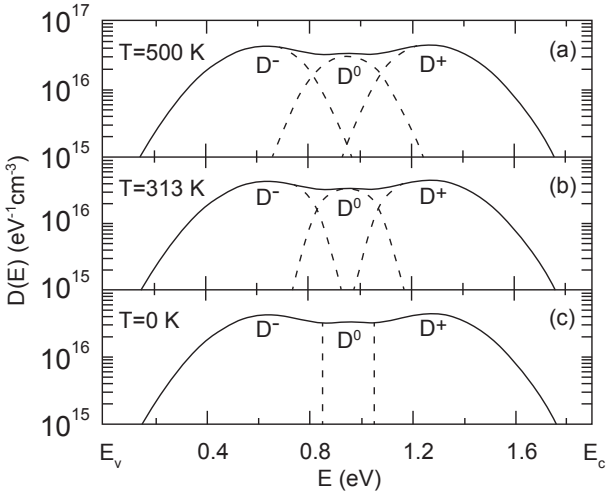


Figure 7: Defect pool in intrinsic a-Si:H at different temperatures [26].

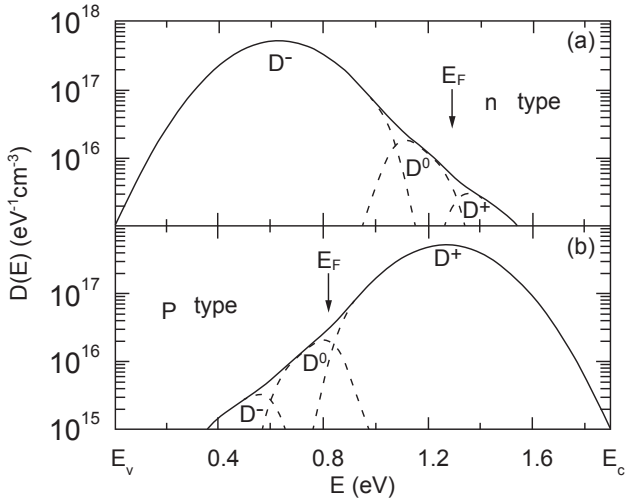


Figure 8: Defect pool in n-type (a) and p-type (b) doped a-Si:H [26].

3. RECOMBINATION *VIA* DEFECTS

As pointed out in section 2, the carrier transport in the HJ is dominated by the defect density distribution at the interface. Surface recombination has to be considered to evaluate the junction quality. Shockley-Read-Hall theory is always used to describe bulk recombination *via* defects [27], [28] even if it considers defect as discrete level in the gap having two states: neutral or charged. This concept can be extended to continuous distribution in disordered semiconductors, as in a-

Si:H, as suggested in [29]. Moreover the states located between the quasi Fermi levels work as recombination centers and their re-emission probability is almost negligible. In turn, the states between quasi Fermi levels and bandgap edges act as trap centres with a re-emission probability toward the band edge. Concerning the DB, Olibet *et al.* [30] showed that the recombination rate through defect density within the a-Si:H is linearly dependent on density of states at the interface:

$$R_{DB} = \frac{n\sigma_n^0 + p\sigma_p^0}{\frac{p\sigma_p^0}{n\sigma_n^+} + 1 + \frac{n\sigma_n^0}{p\sigma_p^-}} v_{th} N_{DB} \quad \textbf{(7)}$$

where n and p are the free carriers, N_{DB} is the total density of DB, v_{th} is the thermal velocity, $\sigma^0_{p,n}$ are the capture cross section for neutral states and σ^+_n,σ^-_p are the capture cross section for charged states. Of course to reduce the recombination a neutralization of the N_{DB} is needed, but the equation (7) also states that recombination *via* DB can be determined by the largest free carrier density. This is opposite to the SHR recombination rate which is limited by the lowest carrier density [27, 28]:

$$R_{SHR} = \frac{np}{\frac{p}{\sigma_n} + \frac{n}{\sigma_p}} v_{th} N_{DB} \quad \textbf{(8)}$$

If doped a-Si:H is considered, the equation (7) reduces to SHR case since one type of charged dangling bond is dominant. Indeed in n-type doped a-Si:H the majority of DB are negatively charged. To describe the surface recombination rate a similar approach in HJ, as in equation (7), can be followed since the a-Si:H dominates the defect density:

$$U_{Sur} = \frac{n\sigma_n^0 + p\sigma_p^0}{\frac{p\sigma_p^0}{n\sigma_n^+} + 1 + \frac{n\sigma_n^0}{p\sigma_p^-}} v_{th} N_S \quad \textbf{(9)}$$

where N_S is the density of states at the c-Si surface. Then it is possible to calculate the effective surface recombination velocity S_{eff} [31]:

$$U_{Sur} = S_{eff} \Delta n_s \quad \textbf{(10)}$$

Δn_s is the carrier density at the edge of space charge region within the c-Si, formed by the band bending that neutralizes the built-in potential at the junction. Calculated S_{eff} on c-Si lightly p-doped (130 Ωcm) surface as a function of the charge generation for different values of N_s and surface charge distribution Q_s and different ratio between capture cross sections are reported in Fig. **9**. The proposed model has been validated on both n-type and p-type doped c-Si surface passivated by different kind of passivation layers. a-Si:H passivation is due to the low N_S and the symmetrical neutral capture cross section for both carriers. Moreover a-Si:H passivation performs better on n-type c-Si surface with respect to p-type, because holes have a larger capture cross section than electrons $\sigma^0_p > \sigma^0_n$.

In c-Si the effective carrier lifetime τ_{eff} can be determined by recombination in the bulk and at the surfaces according to [32]:

$$\frac{1}{\tau_{eff}} = \frac{1}{\tau_{bulk}} + 2\frac{S_{eff}}{W_{eff}} \tag{11}$$

Therefore we can summarize that two mechanism can be used to passivate the silicon surface: 1) reducing the density of states; 2) induce a field effect able to deplete one carrier in c-Si close to interface by varying the state of charge of the DB

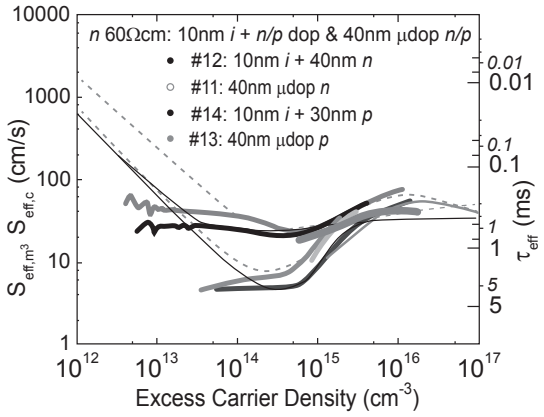


Figure 9: Measured and calculated S_{eff} for the lightly n-type doped c-Si surface passivated by stacks of intrinsic plus doped layers. Empty symbols and dotted lines replicate the microdoped layers passivation for comparison purpose. The symbols show the measurements, and the lines the fits [30].

being at the a-Si:H/c-Si interface. This effect causes a repulsion of electrons or holes from the surface states. The first may be accomplished by hydrogenation of silicon dangling bonds at the c-Si surfaces [33] that can be easily performed and monitored by flash test while dipping the c-Si substrate into HF bath [34]. Intrinsic *a*-Si:H films are known already for some decades to yield good *c*-Si surface passivation [35-37] Experimentally, such films are commonly prepared by plasma-enhanced chemical vapor deposition (PECVD) with SiH_4 as precursor gas, possibly diluted in H_2. For the plasma-excitation frequency 13.56 MHz is often chosen [38, 41], although the successful use of very high frequencies (*e.g.*, 40 MHz [42, 43] or 70 MHz is reported too [44]). For device-grade films, usually the deposition temperatures are about 200°C and the system is kept at a relatively low pressure (0.1-1 Torr). Other techniques reported to give good results are direct-current PECVD [44] and hot-wire or catalytic CVD [46, 47].

4. HYDROGEN AND THERMAL ANNEALING

It has been well established that hydrogen plays a role in the c-Si surface passivation. From infrared attenuated total reflection spectroscopy (ATR) [48], the authors have found that for a-Si:H thickness lower than 20 nm the SiH_2 content is higher with respect to the SiH. This indicates a poor network formation and islands growth. After 4 nm of a-Si:H growth, a certain steady state equilibrium is reached in which the amount of both SiH_2 and SiH species is roughly similar, as

reports in the upper side of Fig. **10**. From that point the DB amount becomes lower. Then, as reported in lower part of Fig. **10** the best thickness for the buffer intrinsic layer in HJ solar cell can be defined. a-Si:H thinner than 5 nm reduces the HJ cell efficiency due to defect while a-Si:H thicker than 5 nm introduce just a filtering effect.

It has been found that low-temperature annealing is beneficial for the passivation quality. It has been observed that annealing can yield an extremely low interface recombination activity, even at temperature below 180°C [44]. Carrier injection dependent recombination calculations suggest that the origin of this phenomenon is related to dangling bond reduction at the interface instead of to a field effect. This behaviour is similar to the SiO_2/c-Si passivation [49].

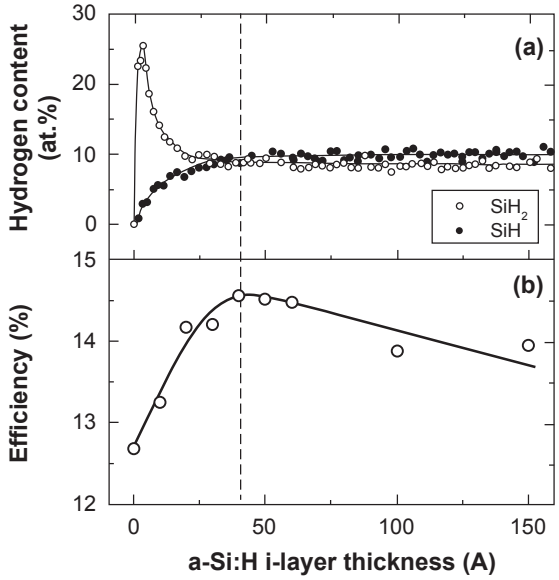


Figure 10: (a) Depth profile of hydrogen contents; (b) HJ solar cell efficiency, as a function of a-Si:H buffer layer thickness [48].

To evaluate the effect of thermal annealing several HJ samples have been prepared starting from 300 mm thick 3Ωcm n-type doped (100) FZ c-Si with mirror polished surface. After a cleaning in HF 4% bath for 45s the a-Si film has been deposited in a RF 70MHz PECVD system in the following conditions: 300mTorr, 15mW/cm^2, 11 sccm SiH_4 and 29 sccm H_2. Before a-Si:H deposition 50 sccm H_2 has been fluxed over the substrate to stabilize its temperature [44]. 50 nm thick a-Si:H layers have been deposited on both side of the c-Si wafer to evaluate the surface passivation quality. Minority carrier effective lifetime τ_{eff} changes over thermal annealing time of bifacial a-Si:H passivated c-Si wafers is reported in Fig. **11**. It is quite surprising to note that low temperature deposited sample (T = 130 °C) shows an as grown poor lifetime τ_{eff} = 12.2 μs (measured with a flash lifetime Sinton Consulting WCT100 tester at injection level of 1x10^{15} cm^{-3} [50]) that, after prolonged thermal annealing reach a lifetime value of 4 ms. The experimental data can be fitted by the stretched exponential function helpful to describe the relaxation of disordered systems towards equilibrium [51, 53]. Hydrogen diffusion, arising from a distribution of energies for trap states and barrier heights, was argued to assume the stretched-exponential relaxation [54].

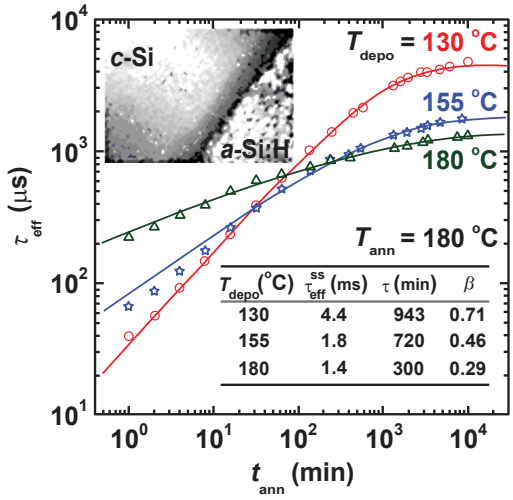


Figure 11: Minority carrier effective lifetime as a function of thermal annealing time. Symbols refer to measurements, curves refer to stretch exponential fit. In the inset an HRTEM picture is reported for a-Si:H deposited at 200°C, over (100) 3Ωcm FZ c-Si [44].

$$\tau_{eff}\left(t_{ann}\right) = \tau_{eff}^{SS}\left[1-\exp\left[-\left(\frac{t_{ann}}{\tau}\right)^{\beta}\right]\right] \tag{12}$$

where τ^{ss}_{eff} is the saturation value for τ_{eff}, β and τ the dispersion parameter ($0 < \beta < 1$) and effective time constant, respectively.

Fig. **12** shows in detail the evolution of τ_{eff} related to the sample deposited at 130°C during the thermal annealing time as a function of injection level. The uppermost curve represents the maximum bulk lifetime based on Auger recombination [55]. The experimental data curves can be explained with the model expressed before, in which the recombination mechanism at the HJ is due to DB having amphoteric nature. To fit the data at different thermal annealing time (solid line in Fig. **12**), it is sufficient to vary N_S in the recombination mechanism reported in equation (7) (σ^0_p/σ^0_n=20 and σ^+_n/σ^0_n= σ^-_p/σ^0_p = 500). Q_s has been kept constant at-2.2x10^{10}cm^{-2} [55]. This assumption means that the charge does not vary during the thermal annealing exposure leading to the conclusion that the a-Si:H passivation is not promoted by any field effect at the interface. Hydrogen passivation of DB at c-Si surface is a more convincing explanation for the observed improvement. For bulk a-Si:H, relaxation is governed by release of hydrogen from trap sites [54]. In case of few nm a-Si:H thinner films, typically higher DB densities are measured, compared to thicker layers [56]. This is related to the hydrogen content within the first layer of the growth. The most relevant condition for the improvement under annealing of the intrinsic a-Si:H(*i*)/c-Si interface passivation is to avoid epitaxial film as depicted in the inset of Fig. **11** [44]. In this experiment several 50 nm thick a-Si:H films have been grown at different temperatures on HF 5% oxide free (100) p-type 3Ωcm FZ c-Si wafer, by RF 13.56MHz PECVD system using the following conditions: 20sccm SiH_4, 500mTorr, 12 mW/cm^2. The imaginary part of the pseudo dielectric function $\langle\varepsilon_1\rangle + i\,\langle\varepsilon_2\rangle$, as obtained from spectroscopic ellipsometry, for thin a-Si:H layers deposited at different temperature on c-Si is reported in Fig. **13**.

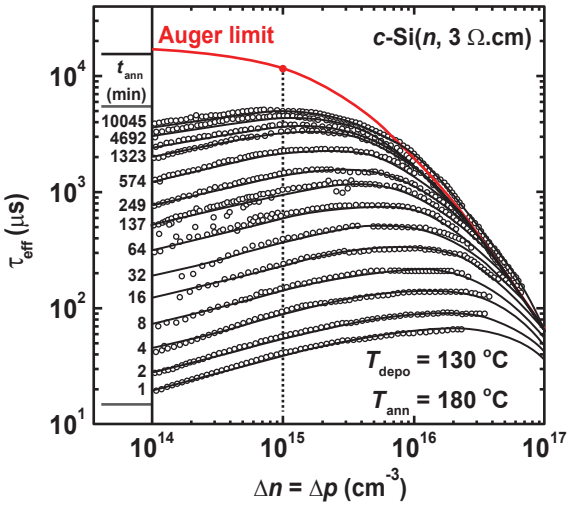


Figure 12: Measured (symbols) values for τ_{eff} as function of the carrier injection level for films deposited at 130 °C. Each curve is measured at different thermal annealing time exposure. Solid lines represent the calculated recombination-model [44].

Since samples deposited at T > 200 °C show the crystalline signature, they can be considered epitaxial. In turn samples deposited at lower temperature are more amorphous. Films deposited at very low temperatures show initial poor τ_{eff} value that increase after thermal annealing. The c-Si surface passivation quality improves for samples deposited at higher temperature up to 180°C. After 30 min of thermal annealing al temperature of 260 °C the τ_{eff} rises up to 1ms. Sample deposited at 205°C has higher τ_{eff} as grown value and is not affected by the annealing. Samples deposited at higher temperature show a strong detrimental of τ_{eff} after annealing procedure. Therefore 200 °C as the deposition temperature can be used to discriminate the two phases of the deposited a-Si:H layer: below amorphous, upper epitaxial. Epitaxial material grown at such low temperatures is known to be defective at the interface. Clustered H-related defects such as H-platelets [57] may be present at the interface with increasing density as decreasing deposition temperature [58]. For deposition temperature below 550 °C, breakdown of the epi-Si into an amorphous phase often occurs, which depends on the precise deposition conditions [59]. At the brink of epi-breakdown, these films are usually very defective [60]. At breakdown itself, a mixed-phase transition region consisting of a-Si:H cones embedded in a c-Si matrix exists [61]. The detrimental effect of low-temperature annealing on the passivation quality can be related to the low hydrogen content of the interfacial epitaxial layer. Indeed, this contains about 30-100 times less hydrogen than a-Si:H [62]. During thermal annealing, hydrogen effuses from higher hydride states, leaving a dehydrogenated DB at the a-Si:H/c-Si interface. In turn, when the amorphous phase is dominant at the a-Si:H/c-Si interface, a larger hydrogen source is present to guarantee re-passivation of the interface states. Several deeper investigations concerning the buffer layer deposition conditions, remarked the role of the silane depletion fraction in the plasma [43], rather than film deposition-rate or ion-bombardment before a-Si:H deposition [11, 63, 64]. High-quality interface passivation has been associated with highly-depleted plasmas, close to the microcrystalline silicon (μc-Si) growth regime [43]. These observations show that even though epi-Si is undesired, the film growth conditions that guarantee highly quality passivation are quite

related to those yielding epi-Si interfaces. Deposition temperatures lower than 150 °C in the initial amorphous layer growth are also suggested in [65, 66] to avoid detrimental epilayer formation. However the epilayer can be completely avoided reducing the deposition temperature down to 70°C [67].

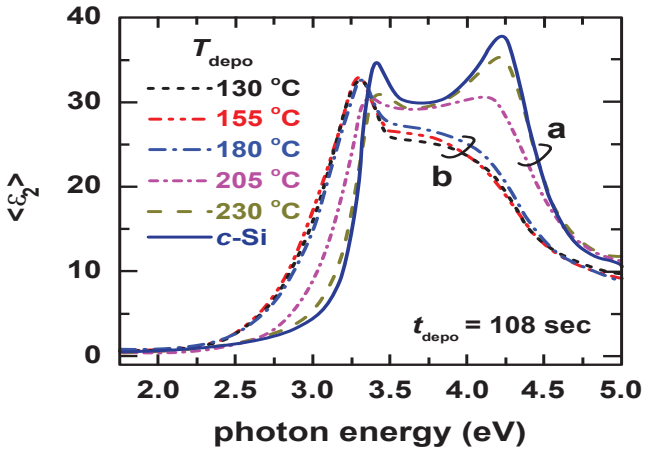


Figure 13: Imaginary part of the pseudo dielectric function $\langle\varepsilon_1\rangle + i\langle\varepsilon_2\rangle$, as obtained from spectroscopic ellipsometry, for thin a-Si:H layers deposited at different temperature on c-Si [38].

To complete the overview on the intimate interface between a-Si:H and c-Si we report on the use of epilayer instead of amorphous at the interface. According to [68] epitaxial growth has been obtained depositing a-Si:H layer over 14 Ωcm p-type doped (100) c-Si deoxidized by HF dip wafer, in the following conditions: 200 °C substrate temperature; 10 mW/cm^2 RF power density; $H_2/SiH_4 = 2$. Then n-type a-Si:H has been deposited and the top contact has been ensured by ITO. From HRTEM reported in Fig. **14** the presence of the epi-Si at the c-Si edge is evident. After 6nm a mixed phase appears and a completely amorphized phase is formed close to ITO layer. Quite high open circuit voltage of 664 mV and a cell efficiency of 17% have been reached. Therefore the authors argued that the loss in Voc is not due to the presence of epilayer. Moreover the epilayer itself deposited on c-Si wafer did not perform a good surface passivation. Since this Voc value is lower than that reported in [30] it is possible to conclude that amorphous phase show better performances to passivated the c-Si surface with respect to epi-layer but the epi-layer can be used too in solar cell application. The relevant point is that mixed phase must be avoided and the abrupt junction must be preferred and performed to fabricate an effective HJ solar cell. To complete the concerning on thermal annealing of a-Si:H layer to enhance the c-Si surface passivation, it is interesting to introduce a particular technical procedure proposed in literature that differs from the commonly used quartz tube or hot plate in nitrogen environment. In practical the authors of [69] suggested to expose the HJ sample to a commercial 2.45GHz magnetron generated microwave (MW) radiation. They operated the MW at 700W also controling the power transferred to the sample by inserting a defined quantity of water (200 ml) as additional absorber. The MW heating coefficient of the sample has been used as 114 ±1.6 K/s. To evaluate the effectiveness of this technique a comparison is reported with respect to a hot plate (HP) procedure settled at 210°C. Two reported with respect to a hot plate (HP) procedure settled at 210°C. Two nominally identical samples have been respectively exposed to MW for 1.6 s and HP for 10 s to reach the same peak

temperature as reported in the inset a) of Fig. **14**. Several cycles have benn performed and compared in terms of lifetime τ_{eff} and reported in the inset c) of Fig. **15**. Moreover it is worth to note that using deposition temperature of 130°C for the HJ formation S_{eff} lower than 3 cm/s corresponding to a τ_{eff} > 4 ms has been achieved. As expected the MW resulted much faster, indeed after 2 cycles the passivation saturation has been achieved, while the same results needed 20 cycles with HP. This effect is due to MW absorption mechanism in a-Si:H, which selectively affects the polar Si-H bonds thus enhancing the release of H from the reach hydrogenated surface leading a better surface passivation. From FTIR measurements performed on the samples after several annealing cycles it has been observed an enhancement of Si-H on the c-Si surface as a consequence of reconfiguration and decrease of both Si-H peaks at 2000 cm^{-1} and H-Si-H peak at 2090 cm^{-1} in a-Si:H layer thus resulting in a surface passivation enhancement. Of course the prerequisite for this is a hydrogen rich a-Si:H layer at the interface, even if very low hydrogen relocation would be needed to reduce the defect density at the interface [70].

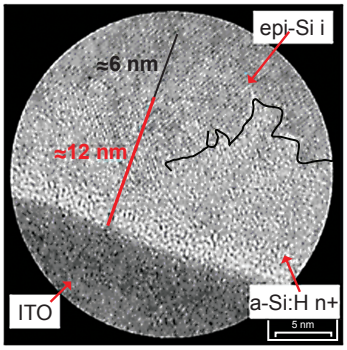


Figure 14: HRTEM image of a mixed phase silicon layer (c-Si and a-Si:H) grown on p-type 14Wcm (100) c-Si [68].

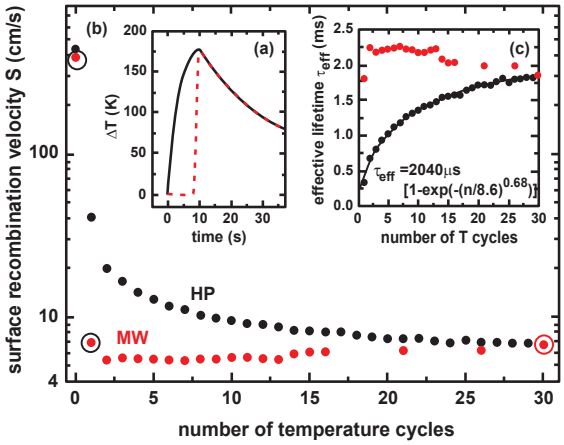


Figure 15: Passivation of nominally identical samples being pulse-annealed with similar temperature profiles. (a) T profiles for a 10 s contact with the HP at 210 °C (black line) and for a 1.6 s MW exposure [gray (red) dashed line]. (b) Comparison of S upon successive pulse annealing steps with T profiles shown in (a) on the HP (black) and in the MW [gray (red)]. (c) Linear plot of S_{eff} with stretched-exponential fit for HP data [69].

5. DOPING AND DEFECTS

While post-deposition thermal annealing has a beneficial effect on c-Si/a-Si:H interface passivation, this may not be the case for a few nanometers thin a-Si:H/p^+ a-Si:H stacked structures deposited on c-Si surfaces. Indeed the H transfers from a-Si:H film into H_2 state creating defects within the material. Moreover presence of such doped layers may result in lowered Si–H bond rupture energies in underlying a-Si:H buffer. Both effects are attributed to the particular energetic position of the Fermi level in the amorphous material rather than on the actual dopants [71]. The same mechanism has been attributed as well to doping dependent hydrogen desorption in such material [72]. Since the a-Si:H layer is only a thin buffer before doped film growth, it is relevant to evaluate the effect of doping layer deposited over this film to form the emitter layer of the HJ solar cell. Indeed it has been demonstrated that boron doped a-Si:H film deposited on top of intrinsic a-Si:H promotes a hydrogen effusion even at low temperature [73]. According to [74], different τ_{eff} have been obtained using different stacked structure on c-Si wafer as reported in Fig. **16**. For a-Si:H/c-Si interface passivation, doping has been observed to produce very similar trends: post-deposition annealing of p-type passivation layers yielded at much lower temperatures already losses in passivation, compared to their n-type counterparts. Hydrogen effusion occurs at higher temperature for i/n-type a-Si:H stacked layer with respect to the i/p-type a-Si:H stacked layer, and this reflects to the c-Si passivation as reported in Fig. **16**. The hydrogen diffusion energy E_D^*, defined by $D_H = D_0^* \exp(-E_D^*/kT)$, in *a*-Si:H and μc-Si is displayed as function of E_F in Fig. **17** [75]. The diffusion coefficient, D_H, describes the motion of hydrogen in the silicon matrix, where $D_0^* = 10^{-3}$ cm^2s^{-1} is the theoretical diffusion coefficient unaffected by traps [76], k is the Boltzmann constant and T is the temperature. The diffusion activation energy E_D^* equals E_S-μ_H, where E_S is the saddle point for interstitial H migration and μ_H the chemical potential of H atoms [77, 78].

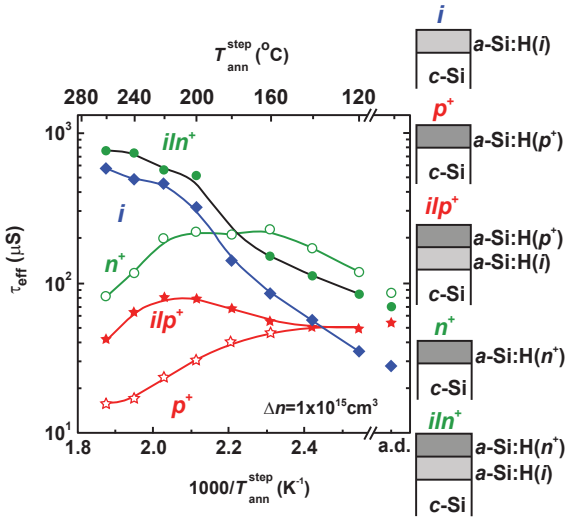


Figure 16: Influence of stepwise annealing treatment on the c-Si surface passivation quality, expressed by τ_{eff} (evaluated at 1.0 x10^{15} cm^{-3}), for doped a-Si:H stacks as shown in the inset sketches. Open symbols represent doped single films, closed symbols represent stacks, featuring an intrinsic buffer layer. Symmetric structures have been deposited on both wafer surfaces. Results for as deposited material are indicated in the abscissa by the label a.d. Symbols represent experimental data; the lines are guides for the eye [74].

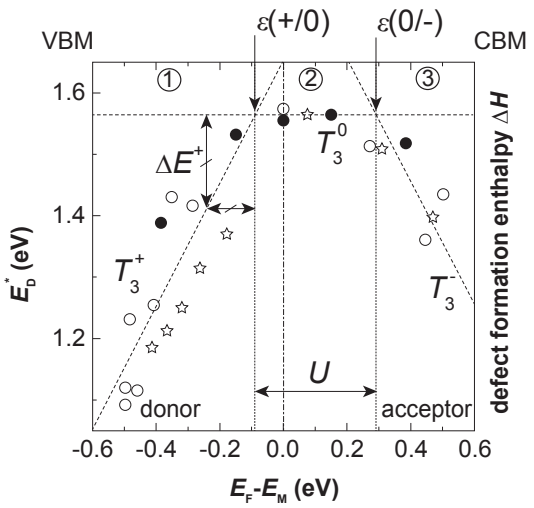


Figure 17: H diffusion energy E_D^* in *a*-Si:H (stars), μc-Si:H (open circles) or *c*-Si:H (closed circles) as a function of E_F, at T_{ann} = 350°C. The superposed straight lines represent the dependence of the formation enthalpy ΔH of defect α in the respective charge states q = +, 0 and-on E_F. E_M represents the middle of the bandgap [74].

When E_F is closer to the VB maximum (VBM, *i.e. p*-type doping) this results in decreasing values for E_D^* (see region with label (1)). For *n*-type doping, E_F must be brought relatively closer to the CB minimum (CBM) to yield a similar drop (region with label (3)). Since doping of a-Si:H films occurs by incorporation of substitutional impurities [79], it may induce additional localized states in the film [80].

A schematic model of donor and defect bonding states is depicted in Fig. **18**. The sp3 hybridized states of P4 donor are split into bonding and antibonding donor levels, while the silicon defect has three bonding states and a DB at midgap (the antibonding is not shown). The transfer of the electron from the donor onto the DB gives energy of E_p-E_{d2} that is 0.5-1eV. This energy transfer leaves the both the defect and dopant pair to lower energy configuration. Therefore in a-Si:H defect and DB are not independent consequence of the doping, but are intrinsically linked. Substitutional doping in a-Si:H does not occur without defect.

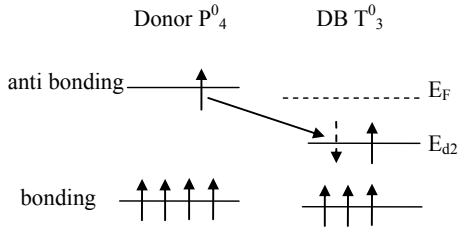


Figure 18: Schematic energy diagram of the donor and DB, showing the energy gain by the transfer of an electron from donor to DB.

The defect-formation in a semiconductor mainly depends on the energetic position of its Fermi level rather than on the physical nature of a dopant. Therefore dangling bond formation enthalpy can change in the intrinsic absorber layer depending on its position within the gap [81]. When intrinsic is grown close to doped material E_f has the maximum deviation from midgap moving toward energy position where larger T3 density is expected. Due to the asymmetry in U energy, larger density of $T3^+$ is generated when E_f is close to VBM with respect to the $T3^-$density generated when E_f shifts toward to CBM, as evident from Fig. **17**. This reflects in hydrogen effusion at lower temperature when i a-Si:H is a buffer sandwiched between doped materials whit respect to the bulk intrinsic [74]. This means that the doped layer plays a role in defect creation in the intrinsic layer underneath. Also this suggests the reason for poorer passivation of i/p a-Si:H with respect to i/n a-Si:H. Indeed in this last the shift of E_F in the buffer layer towards CBM is not sufficient to overcome the energy barrier U (see Fig. **18**). Therefore i/n a-Si:H is able to passivated the c-Si surface at the same level of the intrinsic alone. Then we can conclude that doping of a-Si:H films may result in Fermi-energy dependent defect generation in the layer, detrimentally affecting its passivation properties. p-type films passivate worse than their n-type counterparts due to positive correlation energy of DB in a-Si:H. Therefore an intrinsic buffer layer is needed to decoupling passivation and doping properties. p-type films may still generate defects in the intrinsic buffer layers underneath promoting hydrogen effusion. For optimal device performance, a careful assessment of the deposition conditions of doped films is thus strongly needed. Directly deposit doped a-Si:H on c-Si substrate has been not the best suggestion since, as we detailed discuss in the following paragraphs, the first layers of doped a-Si:H result highly defected due to the presence of dopant atoms at the beginning of the a-Si:H layer growth [11, 82]. The poor c-Si surface passivation of doped a-Si:H film suggested the insertion of few nanometres of intrinsic a-Si:H layer before doped layer [11].

6. MEASURING THE $D_{IT}(E)$

Constant final state yield spectroscopy CFSYS is interesting way to investigate the a-Si:H/c-Si interface as proposed in [67]. The technique is based on the photoemission of a semiconductor irradiated by monochromatic photons (*i.e.* generated by UV light of a Xenon lamp filtered by a monochromator) having energy in the range 4-7 eV, keeping 0.1-0.2 eV higher than the material under test vacuum level. Nevertheless some limitation in the accuracy [83], the photoemission provides a signal directly proportional to the DoS, under the assumption that it is constant. Since the escape depth of an electron increases at low kinetic energies, a thicker layer (4-5 nm) under the surface can be investigated. The photoemitted electrons can be collected as a function of the photon energy.

The valence band edge can be determined by the slope of a straight line in a plot of $\sqrt{Y(E)}$ as a function of E, Y(E) being the photoelectron quantum yield. The number of occupied states at the valence band, evaluated as 2×10^{21} $cm^{-3}eV^{-1}$ [84], can be used as reference in the photoemitted electron numbers at different energies. A comparison of DoS for p-type (10^4 ppm B_2H_6), n-type doped ($2x10^4$ ppm B_2H_6) and intrinsic a-Si:H films growth at 180 °C on p-type doped c-Si substrate is reported in Fig. **19** [85].

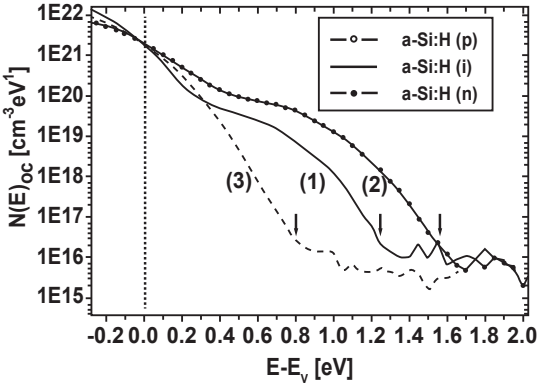


Figure 19: N(E) distribution in the bandgap of p-type (10^4 ppm B_2H_6), n-type doped ($2x10^4$ ppm B_2H_6) and intrinsic a-Si:H films growth at 180°C on p-type doped c-Si. The arrows remark the position of the Fermi level. The vertical line is the valence band edge [85].

The position of Fermi level from the valence band edge can be evaluated as follows: 1.22 eV for undoped a-Si:H (confirming the n-type behavior of the intrinsic film); 1.56 eV for n-type doped a-Si:H (0.18 eV from conduction band if 1.74 eV is assumed as a-Si:H bandgap); 0.8 eV for p-type doped a-Si:H film (confirming the difficulties to reduce the E_{att} in p-type doped a-Si:H). If n-type a-Si:H thin films (~10 nm) are grown at 170°C directly on c-Si wafer, even at different PH_3 dilution ratio with respect to SiH_4, the defect density is one order of magnitude higher with respect to intrinsic film as evaluated by near ultraviolet photoemission spectroscopy in the constant final state yield mode (NUV-PES-CFSYS) and reported in Fig. **20**. From the data it is evident the shift of Fermi level toward the conduction band with increasing dopant concentration [86].

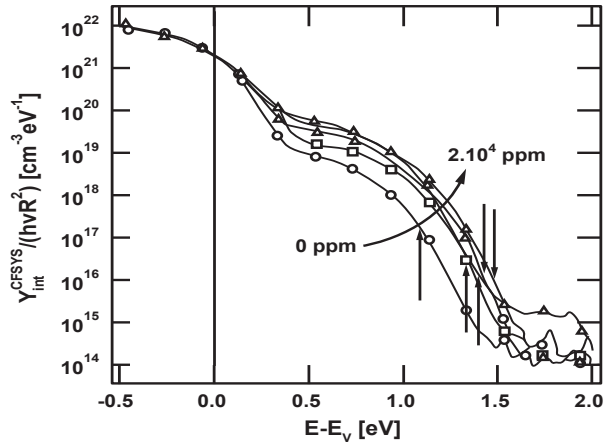


Figure 20: CFSYS measurements, normalized to a density of states, on a-Si:H layers with varying gas phase doping $[PH_3]/[SiH_4]$ = 0, 0.1, 0.3, 1 and 2 $x10^4$ ppm. a-Si:H film thickness 10 nm, T_{dep} = 170 °C. Arrows mark the Fermi level, the vertical line is the valence band mobility edge [86].

The CFSYS method has been also used to evaluate the effect of deposition temperature, in the range between 65°C and 300°C, of 10 nm thick undoped a-Si:H layers grown on 1Ωcm p-type doped c-Si wafer. Urbach energy dependence of valence band edge, Fermi level position and

integrated defect density are reported in Fig. **21** as a function of deposition temperature [87]. From the data it is observed an order of magnitude enhancement of defect density in these thin film layer with respect to bulk a-Si:H [88]. The shift of Fermi level toward valence band for sample deposited near 200°C is indicating a less pronounced pinning of Fermi level close to midgap resulting in a better a-Si:H quality material with respect to other deposition temperature. Moreover N(E) is not correlated to the Urbach energy E_{0V} due to the constrain imposed by the c-Si substrate that can alter the film growth as expected and previously mentioned. Indeed voids and large hydrogen content (SiH_2) at the interface degrade the network formation thus resulting in higher defect density due to dangling bonds enhancement [39]. In this frame the thinner the a-Si:H film the higher the occupied defect density [86]. As suggested in [89], this is due to incomplete annealing of the thin film during short growth. Indeed the growth of thicker layer induces a prolonged thermal annealing on the first layers that, since at beginning, are more defected than the bulk material.

Surface photovoltage (SPV) is an helpful tool to determine the surface states D_{it} by measuring the photovoltage of a MIS structure formed by a TCO, a dielectric transparent mica foil and a a-Si:H/c-Si HJ sample back contacted with a metal, [90, 91]. A scheme of SPV measuring set-up is depicted in Fig. **22**. The surface potential can be shifted through the gap applying an external field. When a pulsed light with energy lower than a-Si:H gap crossing through the TCO/mica/a-Si:H window hit the c-Si surface, an excess of carriers is generated close to the c-Si surface that can recombine *via* defect density at the a-Si:H/c-Si interface. If the short light pulse flattens the band, the related surface photovoltage pulse can be capacitively measured at each applied bias voltage. Then it is possible to obtain the surface potential-field voltage relation, even subtracting the Dember voltage [90], from which the distribution of surface states can be evaluated [90], under the hypothesis that the defects do not change their charge state during the light pulse. It is worth to note that $D_{it,min} = 10^{11} cm^{-2} eV^{-1}$ can be assumed as the lowest density of states of thermally oxidized well passivated c-Si surface [91].

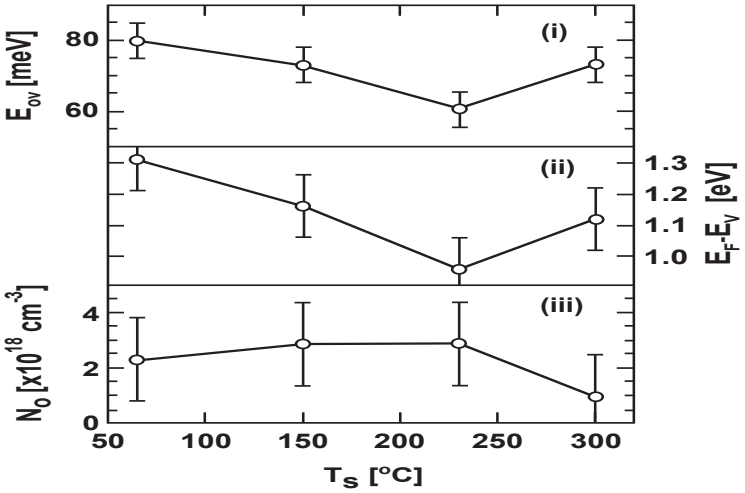


Figure 21: Urbach energy dependence of valence band edge, Fermi level position and integrated defect density as a function of deposition temperature [87].

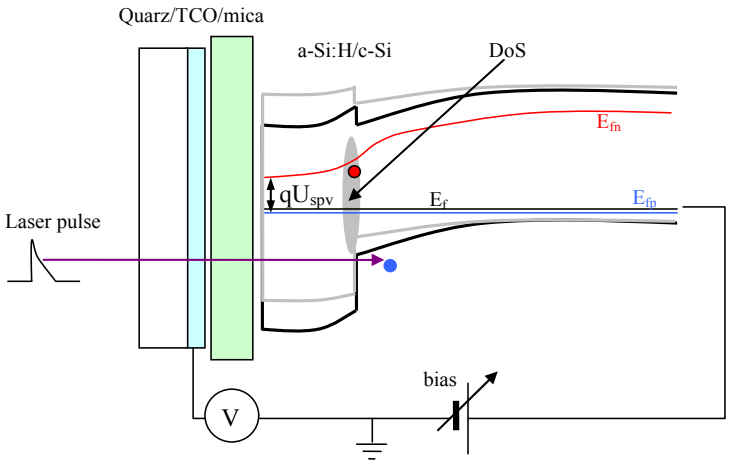


Figure 22: Scheme of surface photovoltage measuring set-up. When the laser pulse with photon energy lower than a-Si:H energy gap, hit the c-Si the band bending at the a-Si:H/c-Si interface become flat and a photovoltage pulse can be detected.

A comparison of the $D_{it}(E)$ on c-Si/SiO_2 and a-Si:H/c-Si on both n-type and p-type doped c-si wafer interfaces is shown in Fig. **23**. In particular the SiO_2 is a thermally oxide grown at 1100°C in dry O_2 followed by 30 min forming gas annealing procedure at 450°C. It is worth to note that sample temperature during the SPV measurements has been kept as low as 120 K to reduce recharging effect of the a-Si:H layer during the laser pulse excitation, therefore the measure $D_{it}(E)$ can be assumed as the upper limit of the interface density distribution [92]. Starting from a flat DoS at interface, independent from energy position within the gap and able to reproduce a $10^{11}cm^{-2}eV^{-1}$ $D_{it}(E)$, the HJ n^+a-Si:H/p-c-Si/p^+a-Si:H cell structure has been simulated with the aid of numerical program [93] to evaluate the photovoltaic performances. The simulations verified that increasing the $D_{it}(E)$ both the Voc and Isc reduce as well as the cell efficiency as reported in Fig. **24** [94].

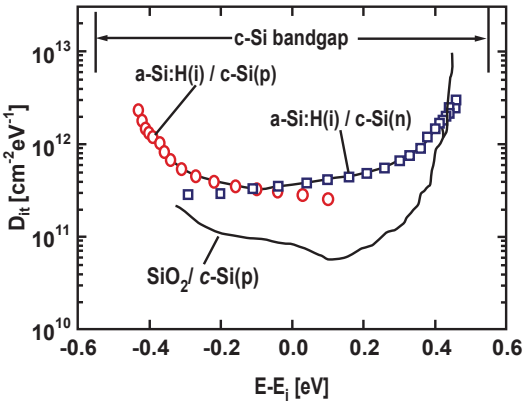


Figure 23: $D_{it}(E)$ for 10 nm a-Si:H(i)/c-Si(p,n, (111)) structures resulting from SPV measurements, carried out at 118 K. For comparison $D_{it}(E)$ of 100 nm thermally grown oxide (1000 °C) on c-Si(n, (100)) measured at 295 K is reported [92].

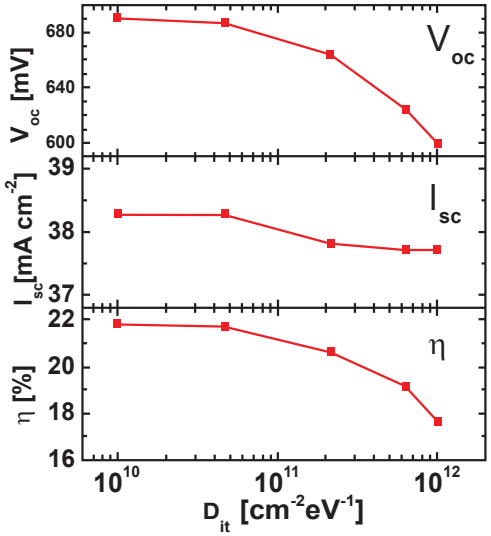


Figure 24: Photovoltaic parameters evolution as a function of $D_{it}(E)$ at the interface of n^+a-Si:H/p-c-Si/p^+a-Si:H cell structure as obtained by numerical simulations [94].

7. CLEANING

Open circuit voltage values over 740 mV can be obtained by using the HIT™ structure [14], which permits to drastically reduce the defect level at the crystalline silicon surface by implementing a high quality intrinsic amorphous silicon layer [13]. By inserting a buffer layer the tunneling effect due to the presence of many localized defect states in the doped layer can be suppressed and an excellent interface properties can be obtained. To attain a high quality intrinsic layer and excellent a-Si/c-Si interfaces has to be implemented [95].

The electronic interface properties of Si devices are strongly influenced by the chemical integrity and morphological structure of the substrate surface prior to the preparation. Conventional wet-chemical treatments were developed decades ago to remove particles, organic and metallic contaminants from the polished wafer surface [96]. However, the fabrication of efficient HJ requires not only extremely clean and undamaged interfaces but also a surface texture to enhance antireflection properties. Furthermore the textured surface directly becomes part of the electronic interface because the *a-Si:H/c-Si* interface is used to form the emitter junction. Additionally, due to the texturing, the interface area is increased and consequently interface defects become more critical for the quality of subsequent processing. The recombination losses are mainly controlled by surface charge, and interface trap densities D_{it} [97, 98]. These electronic interface states result from dangling bond defects localised in a very small interlayer extended over only a few Å. Therefore, the density of these states is strongly related to the surface morphology and micro-roughness. Different approaches have been investigated to reduce interface recombination losses: (i) wet-chemical smoothing of the silicon surface after saw damage removal and texturing [99], (ii) the saturation of dangling bonds at the surface and near surface region by hydrogen (H-termination) [100] or other substituent's [101, 102], and (iii) the engineering of the surface band

bending to separate the electronic junction from the crystallographic interface [103]. The final aim of the wafer cleaning and surface conditioning is the removal of damaged regions and the defect passivation at the interface/surface.

The relevance of clean substrate surfaces in the fabrication of semiconductor devices has been recognized since the dawn of solid state device technology in the 1950s. It is now well known that the device performance, reliability, and product yield of Si devices are critically affected by the presence of chemical contaminants and particulate impurities on the wafer surface. As a consequence, the preparation of ultraclean Si wafers has become one of the key technologies in the fabrication processes. The term *"ultraclean"* may be defined in terms of the concentration of both chemical contaminants and particles on the wafer surface. The term *"surface conditioning"* may need some clarification. In recent years one has become to realize that the process of cleaning may do more than just remove impurities from the surface. It can prepare the surface chemically for the next process step. For example, immersing a Si wafer with a contaminated native (ambient) SiO_2 layer in dilute HF (DHF) solution not only removes the contaminants with the oxide film but also leaves a hydrogenated Si surface, an important prerequisite for subsequent thin film layer growth from the gas phase. Thus, the cleaning step has also conditioned the Si surface by a chemical reaction in preparation for the next process step.

Surface micro-contamination detection is an important topic to address. If we can prevent contamination during the entire device manufacturing process by creating and maintaining super-clean conditions in equipment, materials, and environment, there would be little need for wafer cleaning. Therefore, avoiding contamination must be the first priority, and strict contamination control should be exercised throughout device manufacturing. Methods for the analysis of trace impurities on Si surfaces are available to monitor the results of cleaning processes [104, 105], [105]. Wafer cleaning and surface conditioning processes are based on the use of aqueous chemicals, organic solvents, or mixtures of the two. If aqueous chemicals are used the process is properly called *"wet-chemical"*. The mechanism of liquid cleaning can be purely physical dissolution and/or chemical reaction dissolution. Chemical etching occurs when materials are removed by a chemical transformation to soluble species. Traditionally, chemical etching is expected to remove substantial quantities of a material, however, certain chemical cleaning processes may result in the removal of only a few atom layers of material and by above definition should also be considered chemical etching; perhaps the term "*micro-etching"* would be a more appropriate description.

7.1. Hydrofluoric Acidic Solutions

Silicon dioxide, silicate glasses and silicon nitride have been widely etched using HF, either diluted with DIW, or pH buffered using NH_4F, known as buffered HF (BHF) or buffered oxide etch (BOE). Concentrated HF is actually a 49 wt% solution of HF in DIW. Dilutions ranging from 5:1 to 200:1 are commonly used in the industry. The chemical dissolution reactions have been identified and described in the literature [106]. The etching rate increases with temperature and concentration. Typically room temperature is used, while time and concentration determine the amount of film removal. The thin layer of native oxide on Si, typically 1.0–1.5 nm thick, is removed by dipping the wafers in ultrapure and filtered DHF solution at room temperature. The change of the wetting characteristics of the initially hydrophilic to a hydrophobic surface, which

strongly repels aqueous solutions, can visually indicate when the oxide dissolution is complete. The effect is due to the H-passivated Si surface that results from exposure to HF. The resulting oxide-free, H-terminated Si surface strongly attracts oppositely charged particles and is very sensitive to organic contaminants from DIW and ambient air. Therefore, etching with HF solutions that leave the Si surface bare must be carried out with very dilute, ultrapure (Fe-free), and ultra-filtered HF solution in a very low-particle atmosphere. In addition to etching, HF solutions can desorb metallic impurities from the Si surface. If desired, a pure SiO_2 film can be re-grown by surface exposure to an oxidizing solution.

Mixtures of DHF and 40 wt% NH_4F solutions, results in a more stable etch rate. The NH_4F dissociates to provide F^- ions that stabilise etch rate by replacing ions consumed in the SiO_2 etch reaction. Surfactants may be added to the solution to improve the wettability and to prevent Si attack, namely in preventing surface micro-roughness [104]. Whereas the free acid is the major etching species in DHF, the ionized F species $HF_2^-$is the major etchant component in BHF. Commonly used BHF volume ratio of (7:1=NH_4F:HF) has a pH of about 4.5 and appears to contain only HF_2^- and F^-, with very little free HF. The SiO_2 etching rate of HF_2^- is four to five times as fast as that for free HF in DHF [104]. Addition of NH_4F increases the pH, maintains the F concentration, stabilizes the etching rate, and produces the highly reactive HF_2.

7.2. Sulphuric Acid/Hydrogen Peroxide Mixtures

Removal of gross organic materials from Si wafers can be accomplished by using mixtures of 98 wt% H_2SO_4 and 30 wt% H_2O_2. Volume ratios of 2:1–4:1 are used at a temperature of 100–130 °C for 10–15 minutes. Organics are destroyed and eliminated by wet-chemical oxidation, but inorganic contaminants, such as metals, are not desorbed. What is worse, the Si surface after this cleaning step is strongly contaminated with sulphur residues [104]. These *"sulphuric-peroxide mixture"* (SPM), which is also known as *"piranha etch"* is extremely dangerous to handle and is not commonly used in the fabrication process. Anyway it would have been employed it should be the first cleaning process to prepare grossly contaminated Si wafers for subsequent treatments. Vigorous rinsing with DIW is required to completely remove the viscous liquid. Finally, it is advantageous to strip the impurity-containing formed oxide film on Si by dipping the wafers for 15 seconds in 1:50 DHF, followed by a DIW rinse. By adding a small amount of HF to the SPM several beneficial can be obtained: better removal of sulphur compounds, shorter rinsing times, and improved particle removal [104]. Some alternative oxidants are sometimes used instead of H_2O_2 to improve the mixture stability. These alternative additives include $(NH_4)_2SO_4$; $H_2S_2O_8$; and DIW/O_3 [106].

7.3. RCA Cleaning Process

The first successful process for wet-cleaning Si wafers was systematically developed at Radio Corporation of America, (RCA), and published in 1970 [107, 110]. The process consists of two, SC-1 and SC-2, consecutively applied hot solutions known as *"RCA Standard Clean"*. The SC-1 solution consists of a mixture of NH_4OH, H_2O_2, and H_2O; also known as *"APM"* for *"ammonia/peroxide mixture"*. The SC-2 solution consists of a mixture of HCl, H_2O_2, and H_2O; also known as *"HPM"* for *"hydrochloric/peroxide mixture"*. The originally specified composition for the SC-1 solution ranges from 5:1:1 to 7:2:1 parts by volume of: H_2O:H_2O_2:NH_4OH. Filtered DIW or quartz distilled H_2O is used. The 30 wt% H_2O_2 is electronic grade and un-stabilized (to exclude contaminating stabilizers).

The NH_4OH is 27 wt%. The originally specified composition for the SC-2 solution ranges from 6:1:1 to 8:2:1 parts by volume of: H_2O:H_2O_2:HCl; the H_2O and H_2O_2 are as noted above, while the HCl concentration is 37 wt %. Cleaning in either mixture is carried out at 75–85 °C for 10–20 minutes followed by a quench and overflow rinse in running DIW. After rinsing the wafers are spun dried and immediately transferred to an enclosure flushed with pre-filtered inert gas for storage, if they cannot be processed immediately. The SC-1 solution was designed to remove from Si, oxide and quartz surfaces organic contaminants that are attacked by both the solvating action of the NH_4OH and the powerful oxidizing action of the alkaline H_2O_2. The NH_4OH also serves to remove by complexing some periodic group IB and IIB metals such as Cu, Au, Ag, Zn, and Cd, as well as some elements from other groups such as Ni, Co, and Cr. SC-1 dissolves the thin native oxide layer on Si at a very low rate and forms a new oxide on the Si surface by oxidation at approximately the same rate. This oxide regeneration is now believed to be an important factor in the removal of particles and chemical impurities [111]. The SC-2 solution was designed to dissolve and remove from the Si surface alkali residues and any residual trace metals (such as Au and Ag), as well as metal hydroxides, including $Al(OH)_3$, $Fe(OH)_3$, $Mg(OH)_2$, and $Zn(OH)_2$. The solution does not etch Si or SiO_2 and does not have the beneficial surfactant activity of SC-1 for removing particles. SC-2 has better thermal stability than SC-1 so that the treatment temperature does not need to be as closely controlled. The thermal instability of H_2O_2 in SC-1 (and to a lesser extent in SC-2) necessitates the use of freshly prepared mixtures. The effects of H_2O_2 depletion and of fluoride ion addition were also investigated in terms of Si and SiO_2 etch rates. Several improvements to the original RCA cleaning procedure were employed during the last 20 years. The most influential of these changes was the introduction of the RCA mega-sonic cleaning system for cleaning and rinsing of wafers [112]. Mega-sonic treatment in an SC-1 bath is especially advantageous for physically dislodging particles from the wafer surface due to the high level of kinetic energy. It allows a substantial reduction in solution temperature and offers a much more efficient mode of rinsing than immersion tank processing. Other important improvements include the simplification of the composition ratios for both SC-1 and SC-2 to 5:1:1 and a reduction of treatment temperature and time to 70–75 °C for just 5–10 minutes. The use of fused silica vessels instead of Pyrex glassware was introduced to eliminate contamination from leached glass components. The separation of SC-1 from SC-2 processing stations in two dedicated exhaust hoods was recommended to avoid contamination from airborne colloidal NH_4Cl generated from NH_3 and HCl vapours. No gross etching of Si or SiO_2 was shown to occur with SC-1 even if the H_2O_2 concentration is reduced by a factor of ten. Finally, an optional process step was introduced by stripping the hydrous oxide film formed after SC-1 with high-purity particle-free, 1:50 DHF-dipping for 10 seconds so as to re-expose the Si surface for the subsequent SC-2 step. The employment of surfactant additives to aqueous solutions has become widely accepted. Surfactants increase the Si wafers wettability, can prevent surface micro-roughness generation, and improve the overall cleaning efficiency [107].

7.4. Wafer Rinsing, Drying and Storing

The last steps in wet-chemical wafer cleaning are rinsing and drying, both are extremely critical because clean wafers can become re-contaminated very easily. Rinsing should be done with flowing high-purity and ultra-filtered high-resistivity DIW at room temperature. *Mega-sonic rinsing* is advantageous and is the most effective technique for reducing the critical boundary layer between the wafer surface and the rinse H_2O. Wafer drying after rinsing must be done by physical removal of the H_2O, rather than by allowing it to evaporate, which would leave residues. *Spin drying* accomplishes this and has been one of the most widely used techniques, although

recontamination tends to occur. *Forced air or N_2 drying* using warm and filtered gas is a preferred technique with less chance for particle recontamination. *Solvent vapour drying* starts with wet wafers being moved into the hot vapour of a pure, H_2O-miscible solvent, usually IPA, which condenses and thereby displaces the H_2O. The wafers dry particle-free when the cassette is withdrawn above the vapour zone. IPA vapour drying in its various modifications has become the preferred method in batch processing. Extreme care must be taken to avoid recontamination of clean wafers during storage if immediate continuation of processing is not possible. Wafers should be placed ideally in chemically cleaned, closed glass containers or stainless steel enclosures, while being flushed with high-purity filtered N_2 in a clean room. However, this is rarely feasible in a production line; the usually used plastic containers will always cause organic surface contamination. Metal tweezers must never be used to handle wafers since they will invariably cause contamination by traces of metals. The final criteria of the success of all wafer cleaning operations are the purity of the wafer surface after the last treatment and eventually the device yield. No matter how effective the various cleaning steps may be, improper rinsing, drying, and storing can ruin the best results. Wafer carriers are an integral part of all wafer processing operations due to the need of handling and transfer of wafers in batches. Wafer carriers are designed to hold wafers in slots of 25 or more wafers. A variety of plastic materials are available for their manufacturing. They can be a critical source of particle contamination, their proper use and specialized cleaning are very important for preserving wafer cleanliness.

7.5. Saw Damage Etching, Texturing and Cleaning

Wet-chemical surface preparation is used in solar cell manufacturing mainly for three purposes: (*i*) saw damage etching, (*ii*) texturing and (*iii*) wafer cleaning/surface conditioning for the subsequent passivation and/or junction and contact formation.

So far in HJ manufacturing alkaline wet-chemical etching procedures are preferred to remove saw damage and texture the as-cut wafers. A well-established process in Si solar cell fabrication is the anisotropic etching of <100>Si in KOH/IPA solution at 80°C to obtain randomly distributed pyramids, thus improving the light trapping properties [113, 114]. To reduce manufacturing expense it should be advantageous to combine saw damage removal and texture formation in a single step process by using KOH/IPA solution at 80°C and extending the etching time or by using an acidic texturing process [115, 116]. The completed removal of saw damage is a crucial pre-condition to reduce recombination losses on solar cell substrates. SEM micrographs show saw damaged regions (Fig. **25(a)**) and cracks (Fig. **25(b)**) typically observed on as-cut Si substrates. The thickness of the damaged surface layer is dependent on the wafer saw technology. Fig. **26** depicts the energetic distributions of interface states $D_{it}(E)$, obtained by field depended SPV measurements [92], [93] of commercial p-type CZ wafers after standard alkaline saw damage etch and texture. For comparison the $D_{it}(E)$ of a neighbouring as-cut substrate is also shown. The very high $D_{it,min}$ ($\geq 2 \cdot 10^{13} cm^{-2} eV^{-1}$) is drastically reduced to a value $\leq 2 \cdot 10^{12} cm^{-2} eV^{-1}$ by employing a typical saw damage etching due to removal of crystallographic defects in the near surface range of about 30 μm. The KOH etched surface is characterised by flat, extended (20 to 50 μm) <100>Si structures (see Fig. **25(c)**). Once the random pyramids are formed the $D_{it,min}$ rise up to value $\leq 25 \cdot 10^{12} cm^{-2} eV^{-1}$ due to the texturing process that generates randomly distributed pyramids on <111>Si crystal facets (see Fig. **25(d)**), thus increasing the surface roughness, namely the interface traps density. The anisotropic etching in KOH/IPA changes the initial surface orientation of the <100>Si substrate to <111>Si orientation to well-ordered pyramid facets.

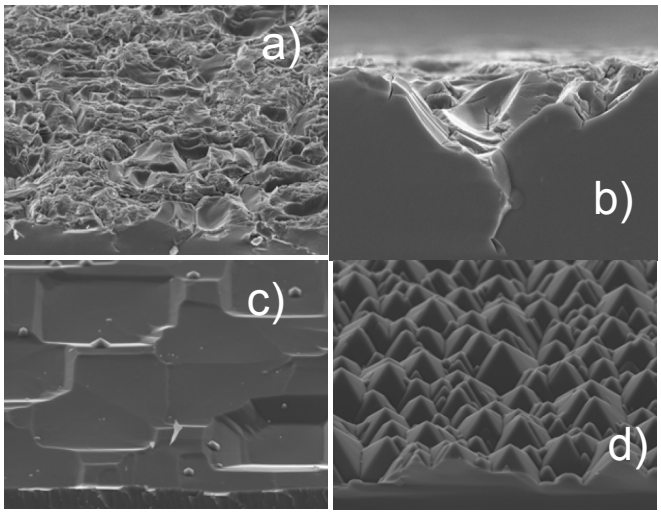


Figure 25: Scanning electron micrographs (tilted view) of: (a) as-cut wafer, (b) cracks on as-cut wafer surface, (c) saw damage etched wafer in KOH solution (d) textured wafer in KOH/IPA solution [119].

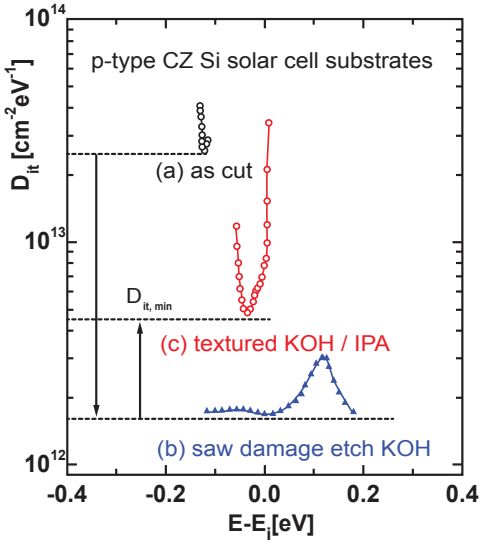


Figure 26: Interface state density comparison for CZ wafers obtained by SPV measurements on (a) as-cut wafers, (b) after saw damage etch in KOH solution and (c) after texturization by anisotropic etching KOH/IPA [119].

The formation of pyramids increases $D_{it,min}$ and results in significantly narrowed energetic distributions by additional appearance of states near the band edges and in the lower half of the gap, *i.e.* closer to the valence band edge. These states, typically observed on microscopically rough surfaces, are related to strained bond defects and defects on Si atoms of lower stage of oxidation, Si^{+1} ($Si_2O{\equiv}Si^{-}$) *e.g.* formed by hydroxyl groups [117]. It was demonstrated [118] that the strongest decrease in surface reflectance can be achieved by anisotropic etching of in KOH/IPA solution.

Moreover, surfaces texturisation by acid solutions, generally lead to higher light reflectance and interface state densities, compared to the alkaline etched substrates. Up to now, the acid based texture etch yields a roughened surface by isotropic etching that exhibits less light absorption than the alkaline process and produce higher surface micro-roughness, resulting in high recombination losses. Further investigations are required to optimize the isotropic texturization process and subsequent wet-chemical treatments, to make it possible to combine saw damage removal and surface texturization. Therefore, for high efficient HJ, normally anisotropic etched substrates with random pyramids should be preferred.

7.6. Wafer Cleaning and Surface Conditioning

Values of $D_{it,min}$ as well as that obtained after the texturing process (see above Fig. **26**) do not allow to deposit a high quality buffer layer needed to produce high efficiency solar cells. It is evident that a wafer cleaning followed by a surface conditioning has to be applied prior to the thin film layer growth.

Several groups are hardly working trying to reproduce HIT^{TM} performance. One of the technological keys is the wafer cleaning combined with a surface conditioning. Comparing standard RCA cleaning with others wet-chemical treatments once again confirmed that the better is the standard one. However a wet-chemical surface conditioning has to be applied prior to the *a-Si:H* growth to obtain D_{it} values suitable for high efficiency HJ. Wet-chemical surface conditioning consists of wet-chemical oxide formation followed by an oxide removal step to smooth the surface roughness; thus avoiding microscopical irregularities that would otherwise represent fertile spots acting as recombination centres. The effect of different combination of wet-chemical wafer cleaning and surface conditioning on the interface state density and minority carrier lifetime has been extensively studied and recently published by Laades *et al.* [119]. They reported that the wet-chemical surface conditioning has to be carefully optimised with respect to the different substrate configurations by means of μW-PCD [120] and SPV measurements [92, 93] to determine the spatially resolved effective minority carrier lifetime and the energy distribution of the interface states respectively. They fabricated several samples starting from commercial (3-6 Ωcm) p-type CZ wafers, and investigated the interface properties of two surface morphology (saw damage etched and textured surfaces) when different wet-chemical surface conditioning are applied soon after a standard RCA cleaning. To measure and compare the τ_{eff} the samples have been passivated by iodine/ethanol (I/E) solution. Because of passivation by I/E is based on saturation of dangling bond defects, the choice has been taken to obtain similar results for n-and p-type substrates. Fig. **27** depicts results of lifetime measurements. For almost all pre-treatments, as expected, the KOH etched surface shows higher values of effective lifetime. On KOH etched surfaces using just DHF for oxide removal (RCA+HF) higher values of lifetimes were obtained compared to the cleaning procedure (RCA+HF+DIW). In contrast, on textured surfaces the omission of DIW rinsing leads to lower lifetimes. Both can be explained by the counteracting effects of two processes caused by DIW rinsing: (*i*) the removal of chemical reaction products, which leads to a clean, hydrogen-terminated surface and (*ii*) the subsequent initial oxidation of this clean surface. On the pyramids of textured substrates, a clean surface with higher lifetime can only be achieved by employing DIW rinsing. On the comparatively flat surface of KOH etched substrates however, the rinsing leads to oxidation-induced defects, higher density of states and

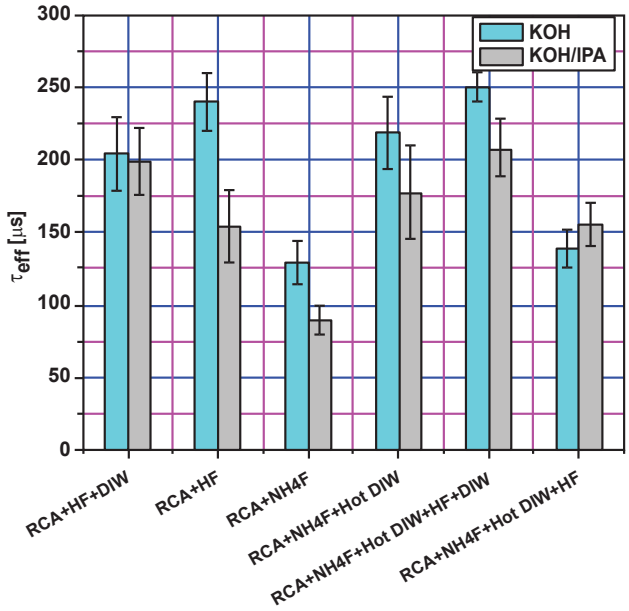


Figure 27: Lifetime distribution over the area of representative p-type samples obtained on wafer with the two surface structures, saw damage etched and textured, after different sequences of wet-chemical steps and subsequent passivation with iodine ethanol solution [119].

lower lifetime values. In order to decrease surface micro-roughness at atomic scale, for the first oxide removal step the DHF-dip was replaced by NH_4F treatment. Without rinsing in DIW this treatment results in a drastic decrease of the lifetime probably due to surface contamination by ammonium salts [121]. To dissolve these contaminations the substrates have been subsequently treated in hot water for 6 min followed by a DHF-dip to remove the water-induced surface oxide. The highest lifetime values have been obtained applying these treatments followed by a final short DIW rinsing at room temperature: (RCA+NH_4F+Hot DIW+HF+DIW).

The influence of different combination of wafer cleaning and surface conditioning has been extensively investigated for randomly pyramids textured surfaces, obtained from polished p-type FZ samples in order to eliminate bulk effects, by means of $D_{it}(E)$ measurements [122]. As demonstrated, the microscopic surface roughness, typically obtained after alkaline texturing (KOH/IPA) and standard cleaning (RCA+DHF-dip) treatments, can be stepwise reduced by wet-chemical smoothing applying sequences of oxidation in H_2SO_4/H_2O_2 and oxide removal in (1%)DHF or in (48%)NH_4F solutions.

NH_4F containing solutions are commonly used to passivate atomically flat smooth <111>Si surfaces by H-termination, on the other hand also produce various compositions of ammonium salts by the reaction with Si and SiO_2 [100]. This reaction results surface irregularities, which seems to start particularly on surface particle contaminations, or on crystallographic irregularities of the structured surfaces (Fig. **28(a)**). These contaminations cannot be removed even by intensive water rinse, because of the poor solubility of $(NH_4)_2SiF_6$ in water. As expected this behaviour leads to a strong increase in $D_{it,min}$ compare to the minimum value obtained for the initial rough

RCA treated surface as shown in Fig. **29** curve 1. The application of NH_4F solution after formal smoothing in H_2SO_4/H_2O_2 leads to a reduction in $D_{it,min}$, mainly in the lower half of the gap. Best results were obtained by smoothing in NH_4F solution with a subsequent wet-chemical oxidation step in H_2SO_4/H_2O_2, followed by DHF-dip (120 s), which obviously dissolves these contaminations, as shown in Fig. **28(b)**. When (1%) DHF was used as final etching solution, the D_{it} near the band edges and in the lower half of the gap, *i.e.*, closer to the valence band edge, were found to be significantly reduced. These states, typically on microscopically rough surfaces, are related to strained bond defects and defects on silicon atoms of lower stage of oxidation, $Si^{+}(SiO_2{\equiv}Si{-})$ formed by hydroxyl groups [123]. Wet-chemical smoothing procedures using H_2SO_4/H_2O_2 subsequent to NH_4F treatment (Fig. **29** curve 4) or DHF-dip (Fig. **29** curve 5) results result in lower densities of these states, with respect to the standard RCA process plus DHF-dip (Fig. **29** curve 2,3). The density of states in the upper half of the gap, *i.e.* closer to the conductivity band edge, results from dangling bond of the next higher stage of oxidation $Si^{+2}(SiO_2{\equiv}Si{-})$ and were found to be strongly related to the stage of Si surface oxidation [123]. In order to further elucidate the influence of wet-chemical oxide removal, the HF treatment times were systematically stepped up after RCA as well as after H_2SO_4/H_2O_2. The extension of the HF treatment time from 60 s to 90 s and to 120 s leads to a stepwise reduction in D_{it} in the upper half of the gap, and to a $D_{it}(E)$ broadening. The chemical and physical conditions of the Si substrate surfaces can be modified by dry or wet specific process steps. For example, remote hydrogen-plasma *in situ* cleaning and surface conditioning of the Si surface to produce smooth and atomically clean surfaces with controlled Si H-termination-bonds immediately prior to Si growth can be achieved by activated hydrogen plasma processing in a remote plasma reactor [124]. Wet-chemical cleaning processes for Si wafers can be classified according to the final surface condition into two groups: the surface passivation (i) by H-passivation (H-terminated surface) or (ii) by thin wet-chemical oxide layers, resulting in hydrophobic and hydrophilic surfaces, respectively [125, 127]. Which substrate surface conditioning can successfully be applied to Si solar cells largely depends on the details of the device structure and the kind of subsequent layer deposition.

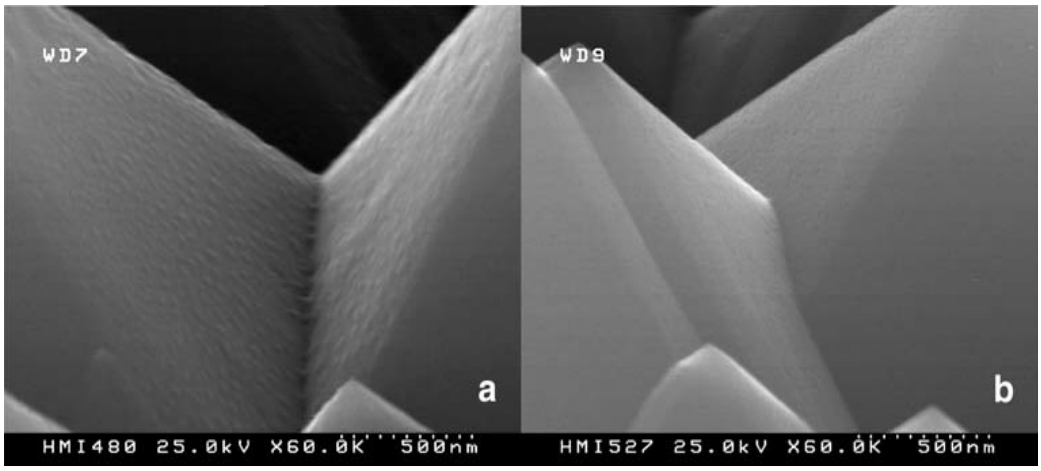


Figure 28: Scanning electron micrographs (tilted by 30°) of silicon substrates with randomly distributed pyramids: (a) after H-termination by NH_4F and (b) after subsequent wet-chemical oxidation and oxide removal in H_2SO_4/H_2O_2+HF-dip (120 s) [122].

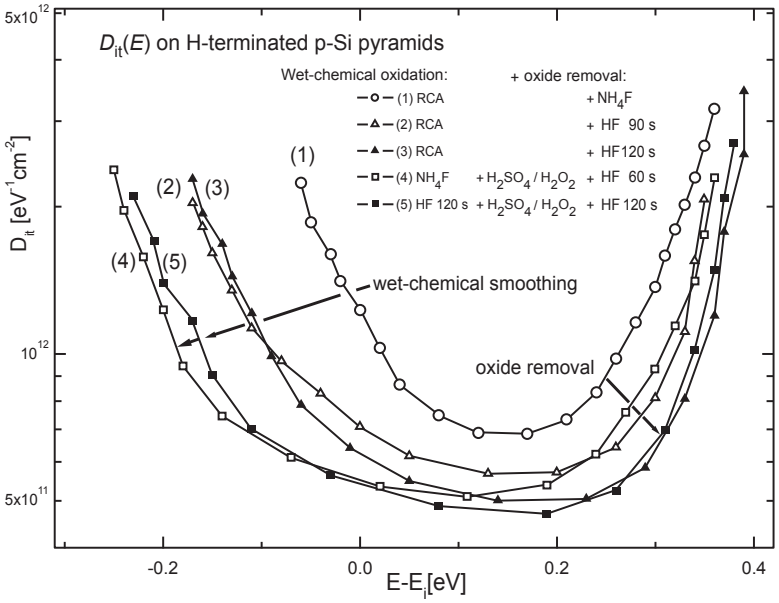


Figure 29: *$D_{it}(E)$* of p-type Si substrates with randomly distributed pyramids, obtained after two types wet-chemical pre-treatment: (i) standard RCA process and subsequent oxide removal by NH_4F (curve 1), or HF-dip for 90 and 120 s (curves 2,3) and (ii) wet-chemical smoothing by H_2SO_4/H_2O_2 and subsequent oxide removal by HF-dip for 60 s (curve 4) and 120 s (curve 5), respectively [122].

7.7. Surface Passivation Stability

The stability of surface passivation on wet-chemically treated wafers with the time of the subsequent layer preparation step is an important parameter in the technological process. The H-terminated Si surface predominantly limits oxidation in clean room air but does not completely inhibit native oxidation. The stability of hydrogen passivation was shown to be influenced mainly by substrate morphology and the employed wet-chemical preparation method. A strong influence of various etching and smoothing procedures on the stability of the H-terminated vicinal <111>Si surfaces under ambient atmosphere was recently shown by M. Kolibal *et al.* [128]. Highest stability (48 h) was found on the atomically smooth mono-crystalline surface. Thereby a completed removal of RCA oxides was achieve after 3 min treatment time on polished p-type <111>Si substrates, compared to 6 min on alkaline textured substrates. A rapid decrease in the effective minority carrier lifetime was observed during the initial phase of oxidation in air, corresponding to an increase in surface states. A significantly shorter duration of the initial phase of oxidation in air was found on the polished <100>Si surfaces in contrast to that observed on textured surfaces [129]. These experimental results indicate a strong influence of surface morphology on native oxidation growth in air. The initial oxidation reactions start on atomic defects and steps, because various species of $Si(-H)_2$, Si−OH and dangling bond defects are localised there. Oxidants, such as oxygen and water in air, are expected to preferentially break the Si back-bonds on atomic defects and polarised back-bonds of the silanol groups Si≡Si−OH, on the atomically rough surface, rather than the Si≡Si−H bonds on the atomically flat <111>Si terraces. Thus, the insertion of oxygen, results in a strong polarization of Si≡Si−O back-bonds, which leads

to further nucleophilic reactions with their neighbouring Si atoms forming the first monolayer of native oxide. Whether all Si atoms of the top layer are oxidized, the $Si_{bulk}{\equiv}Si_{bulk}{-}O$ back-bonds of the second monolayer are broken by subsequent insertion of oxygen and a layer-by-layer growth of native oxide films takes place on Si surfaces exposed to air at room temperature. In this way, a layer-by-layer growth of native oxide films takes place on Si surfaces exposed to air at room temperature. The over-layer structure converts to the amorphous phase. The remaining $O{-}Si_s(-H)_2$ bonds on the top-layer cause the hydrophobic behaviour of the surface, which can be observed during the initial phase of native oxidation in air. The Si−H bonds on the surface are oxidized only after completion of the back-bond oxidation, resulting in the formation of silanol groups Si−OH. By this oxidation mechanism, the dependence of the first oxide monolayer growth rate on the initial density of interface states can be explained. To inhibit native oxide growth, H-terminated substrates are often stored in dry nitrogen atmosphere. A very slow initial native oxidation, however was also observed in N_2 atmosphere, probably due to the fact that water molecules adsorbate or not completely H-terminated surface defects [130]. Summarising these results the duration of initial phase of oxidation, which can be used as measure for the stability of H-terminated Si surfaces in ambient atmosphere, was found to be not only influenced by the clean room conditions and the handling procedures, but also by the substrate bulk properties, surface morphology and the preparation-induces surface micro-roughness and surface coverage. The re-oxidation of H-terminated Si surfaces can be slowed down for a short time by excellent smoothing and complete saturation of the dangling bonds by hydrogen or by storage in dry N_2 atmosphere until subsequent layer deposition. Other surface passivation methods, however, are required to inhibit completely the native oxidation of substrate surface for longer time duration as recently published by organically modified Si surfaces [131, 132].

7.8. Influence of Optimised Wet-Chemical Treatment on Test HJ Solar Cells

Several groups are hardly working to individuate the effect best wet-chemical pre-treatment to improve HJ solar cells performances. One recent work [133] showed the influence of optimised surface pre-treatment for amorphous/crystalline heterojunction solar cells (ZnO/*a*-Si:H/*c*-Si/BSF/Al) prepared on p-type substrates with random pyramids texturing. Two groups of samples, consisting of 24 cells of 1 cm^2 each, were processed and characterised. Both groups received a standard RCA cleaning followed by a DHF-dip to etch the silicon oxide. For the second group a subsequent wet-chemical smoothing by H_2SO_4/H_2O_2+(1%)DHF-dip was applied. Fig. **30** shows the distribution of the obtained solar cell characteristics. In addition to the histograms, the results of fitting normal (Gaussian) distributions to the data are shown. The histograms over cells demonstrate that the samples with the smoothened *a*-Si:H/*c*-Si interface shows much narrower distributions of the respective parameters around the mean value. Further a pronounced increase in efficiency was achieved by the group with optimised surface conditioning. The increase in efficiency is mainly due to a higher J_{sc} (mean improve 5.0%) and to a less pronounced extent, an increased fill factor (2.2%), while the change in the V_{oc} is rather small (0.5%). Because of a previous simulation studies [134], have shown that the increasing front side interface state density from 10^{10} cm^{-2} to 10^{12} cm^{-2} leads to a reduction in V_{oc} of 90 mV, and the rear side recombination acts as a loss mechanism on J_{sc} and reduces V_{oc} by 40 mV at maximum additional investigations are under way to clarify the reason for this behaviour. Similar results were also obtained for test solar cells prepared on textured n-type substrates [135]. Those results indicate not just a better

performance but also a better reproducibility when textured substrates are processed by an additional smoothing step and optimised wet-chemical oxide removal.

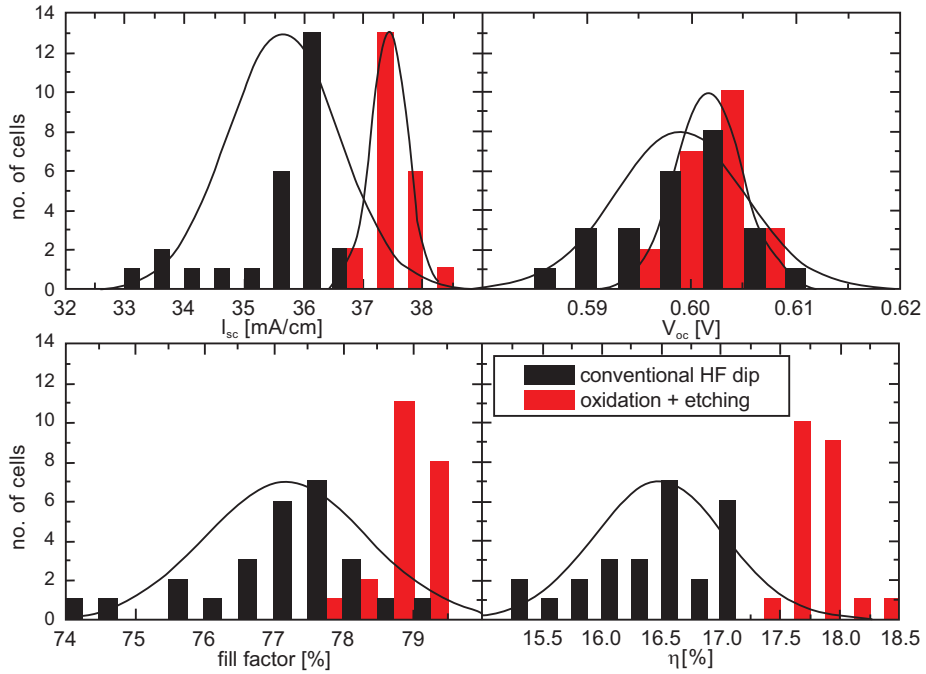


Figure 30: Histogram of the basic solar cell parameters: short cut current density J_{sc}, open circuit voltage V_{oc}, fill factor and efficiency η, for two groups of 1 cm^2 (n)*a*-Si:H/(p)*c*-Si solar cells The black bars denote conventional HF treatment after cleaning of the c-Si substrate; red bars: additional smoothening of the textured substrate surface; lines: normal distributions fitted to the data [134].

8. ELECTRICAL TRANSPORT AND TRAPPING IN A-SI:H/C-SI

In general the current voltage in HJ solar cell can be expressed using the common double diode expression plus series and shunt resistances (R_s, R_{sh}):

$$J(V) = J_d(V) - J_{ph} = J_{01}\left(e^{\frac{q(V-JR_S)}{n_1 kT}} - 1\right) + J_{02}\left(e^{\frac{q(V-JR_S)}{n_2 kT}} - 1\right) + \frac{V - JR_S}{R_{sh}} - J_{ph} \quad \textbf{(13)}$$

where J_d is dark current; J_{ph} is photogenerated current; R_s, R_{sh} are series and shunt resistance respectively; $n_{1,2}$ are ideality factors; T is the temperature; k is the Boltzmann constant.

However in a-Si:H/c-Si HJ device the carrier transport can be affected by several issues as defect density at interface, barriers due to band alignment mismatch and defect within bulk material. Therefore the use of the diode model with recombination in the space charge region, commonly used in homojunction diode [136, 137] should be reconsidered [5, 6, 138, 139] taking into account tunneling mechanisms.

Basically the current voltage still follows the high forward regime written above (J_{01} diode), of course affected by the series resistance for forward bias. According to the Shockley theory [95] and with the assumption of single side junction, J_{01} can be expressed as the prefactor of the diffusion current within c-Si base:

$$J_{01} = \frac{qn_i^2 D_{p/n}}{L_d N_{D/A}} \tag{14}$$

where $D_{p/n}$ is the c-Si minority diffusion coefficient, $N_{D/A}$ is the c-Si doping type and concentration; L_d is the diffusion length. This last can be evaluated from lifetime measurements performed on passivated c-Si wafer before HJ device fabrication [140] or from quantum efficiency when the device is completed [141, 142]. Commonly for a very good HJ cell J_{01} should be in the order of 10^{-13} A/cm^2 as for the Sanyo HIT cell [11] in which the S_{eff} is lower than 5 cm/s after a-Si:H deposition on both sides of the c-Si wafer. This of course reflects in open circuit voltage:

$$V_{oc} = \frac{n_1 kT}{q} \ln\left(\frac{J_{sc}}{J_{01}} + 1\right) \tag{15}$$

that is weakly affected by the low forward bias regime. Instead at low bias voltage (< 0.5V) regime, the current flowing through the device can be written as follows:

$$J_d(V) = J_0 e^{AV} \tag{16}$$

where A is constant.

Current voltage measurements in dark condition of n-type a-Si:H/a-Si:H/c-Si p-type HJ sample for different temperature is reported in Fig. **31**.

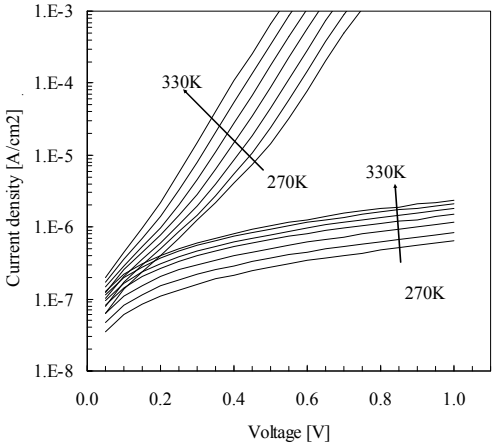


Figure 31: Current voltage measurements in dark condition of n-type a-Si:H/a-Si:H/c-Si p-type HJ sample for different temperatures.

According to [143] most of tunneling take place at peak of conduction band mismatch (path A of Fig. **32**).

Since the density of states is high at the energy below that peak, by the a-Si:H layer side, also path B of Fig. **32** should occur. J_0 is:

$$J_0 = Be^{(-\Delta E/kT)} \tag{17}$$

where B is constant. Now the energy related to the tunneling ΔE should be lower than the pick height, but experimentally has been found the opposite [4, 7]. Path C in Fig. **32** can be considered small with respect to path D and E due to large amount of DoS within the a-Si:H. Path D is a multi-step tunneling that can be expressed as follows according to [4, 145]:

$$J_0 = Be^{bT} \tag{18}$$

If hopping mechanism through the defects [146] at energy E_t close to the Fermi level density could prevail then J_0 becomes [7]:

$$J_0 = B\left[\sigma_p v_{th} N_v \exp\left(-\frac{E_t - E_v}{kT}\right) + \sigma_n v_{th} N_c \exp\left(-\frac{E_c - E_f}{kT}\right)\right] \tag{19}$$

or

$$J_0 = B\left[\sigma_n v_{th} N_c \exp\left(-\frac{E_c - E_t}{kT}\right) + \sigma_n v_{th} N_c \exp\left(-\frac{E_f - E_v}{kT}\right)\right] \tag{20}$$

where $\sigma_{p,n}$ are the capture cross sections, E_f, E_t,E_c,E_v are the Fermi level, the trapping level, the valence band and the conduction band respectively. The use of (17) or (18) depends on the c-Si doping type choice on which the HJ is formed.

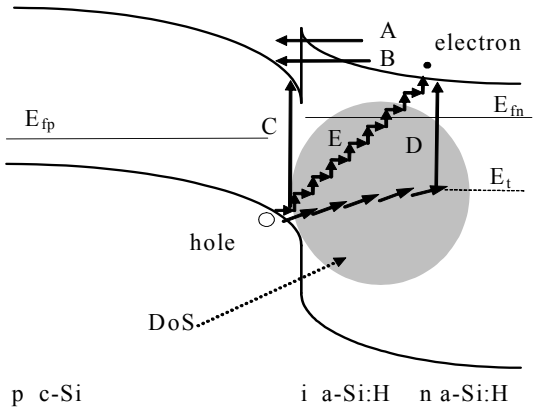


Figure 32: Schematic overview of HJ band bending in low forward bias regime and tunneling mechanisms.

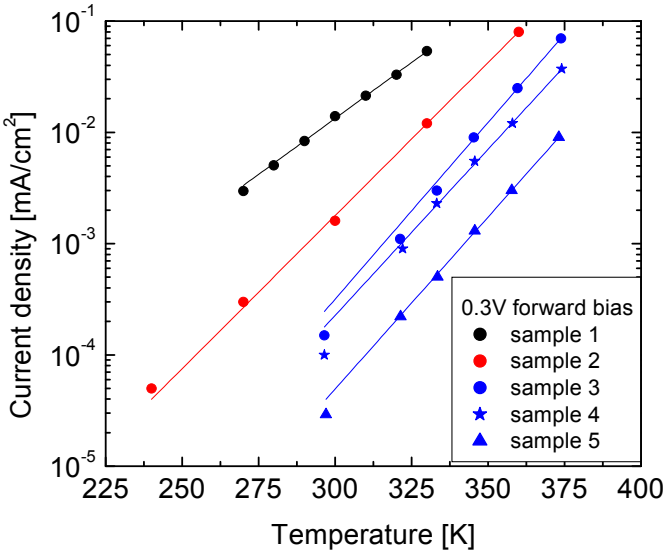


Figure 33: Exponential dependence of the current from T, in dark condition, for different samples listed in Table **1**. Note that the current of samples 3-5 have been scaled 100 times to be comparable with the other samples.

Now it is interesting to note that J_0 expressed as (18) or (19, 20) for low forward bias such as 0.3V are quite similar in a certain range of temperature as evident from the IV data of different samples collected from different references [7, 147, 148] and reported in Figs. **33, 34**. The structure of the different samples are listed in Table **1**. In general current voltage characteristics under sunlight exposure are the common way to evaluate solar cell performances. Since in these measurements all carrier transport mechanisms and recombination phenomena are averaged, it is very difficult to extract detailed information on specific part of the cell from these characteristics. Quantum efficiency and current voltage profiles in dark condition can help to this aim, but also from them it is critical to select the details. The amphoteric nature of DB within the a-Si:H and their not homogeneous distribution along the energy gap and along the interface make difficult to evaluate in details. The generation mechanism within depletion region seems to dominate the current in reverse bias condition as reported in Fig. **35**, in which the dependence of current on the square root of reverse bias is highlighted (V_{bi} refers to built-in voltage) [7]. Details on transport mechanism are widely discussed and a complete analytical model is under construction in [148].

Table 1: Sample structures of Figs. **33** and **34**.

Sample	**References**	**HJ**
Sample 1	[147]	n aSiH/a-SiH/p c-Si
Sample 2	[148]	p aSiH/a-SiH/n c-Si
Sample 3	[7]	Mg/a-SiH/p c-Si
Sample 4	[7]	Mg/a-SiH/p c-Si
Sample 5	[7]	Mg/a-SiH/p c-Si

Capacitance voltage measurements as a function of frequency (CVf) have been used as a tool to evaluate defect density distribution in a-si:H either solar cell p-i-n structures [149, 150] or in stacked photo-detectors [151], since capacitance is highly sensitive to the trapping kinetics depending on the trap state position in the gap close to the junction and test signal frequency. Capacitance indeed depends on the variation of state occupancy around the Fermi level, for each temperature the lower the test signal frequency, the higher the number of states involved in the trapping kinetics process and the higher the exchanged charge and then the capacitance value [152]. The dependence of the capacitance on the bias voltage is related to different position of Fermi levels in the space charge region of the junction and to different minority carrier density. Moreover the temperature parameter can be introduced to further improve the capacitance measurements sensitivity (CVfT). Indeed the dependence of capacitance on temperature is related to the freezing of trapping kinetics that occurs by lowering the temperature described by the steeping of the Fermi function.

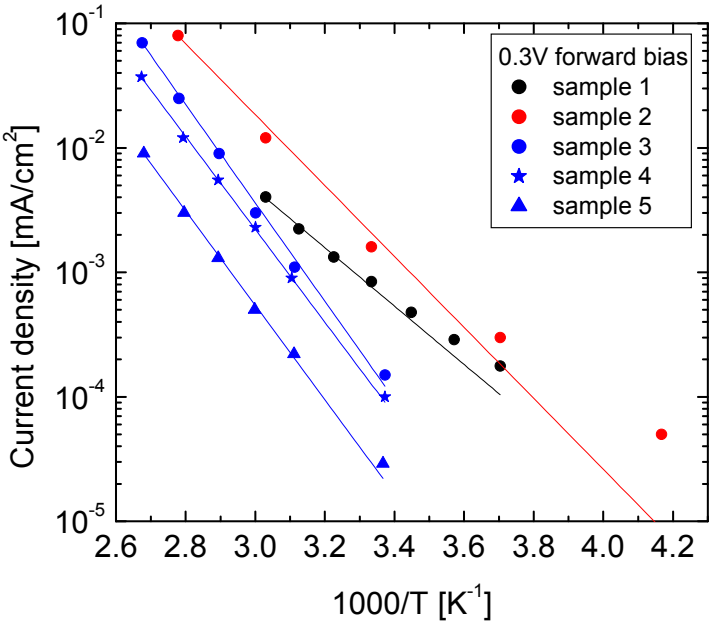


Figure 34: Exponential dependence of the current from-1/T, in dark condition, for different samples listed in Table **1**. Note that the current of samples 3-5 have been scaled 100 times to be comparable with the other samples.

The amplitude of the capacitance variation from low to high temperature is related to the number of states involved in the trapping kinetics and to their distribution along the thickness of the involved layers. Even though the capacitance measurements are relatively easy to perform, their interpretation requires a carefully analysis that cannot be performed by analytical models. To this aim, numerical simulations of the device structure under measurements can be helpful to reproduce the measurements, even if sometimes it is difficult to rightly establish the values of a large number of free parameters within the model.

Here we report the CVfT measurements used to evaluate the defect density at interface of two HJ p-type c-Si based in which dry cleaning wafer treatment before the a-Si:H layer deposition have been applied:

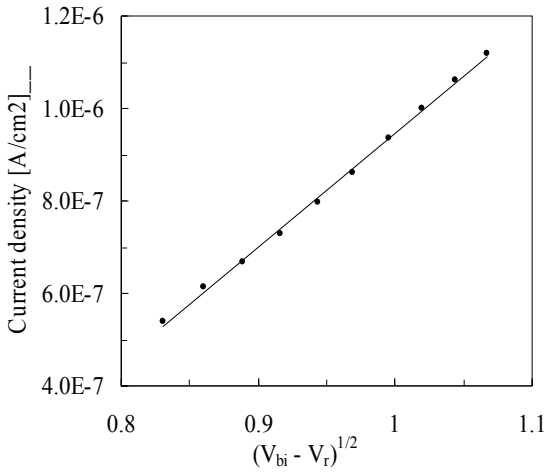


Figure 35: Current voltage measurements of n-type a-Si:H/a-Si:H/c-Si p-type HJ sample for different temperature in dark condition [148].

H_2 plasma in the following conditions: 200 mTorr working pressure, 100 sccm gas flow, 28 mW/cm^2 RF 13.56MHz power density, and 280°C substrate temperature for 5 minutes;

CF_4/O_2 with 8% oxygen content with the follow parameters: 200 mTorr working pressure, 30 sccm gas flow, 98 mW/cm^2 RF 13.56 MHz power density, and 240 °C substrate temperature for 90 seconds [153].

We compared the capacitance values with the output of numerical simulation able to solve both the DC and AC problem in the stacked structure. We used one dimensional approximation dividing the structure in a grid of points, each characterized by a set of parameters [154]. Comparing Fig. **36(a)**, **36(b)** we noted also an increase of defect density in number and extension in the crystalline silicon side in case of H_2 treatment. This was absolutely needed to model the experimental capacitance values. We related this behavior to damages in crystalline layer during plasma treatments. Then we can argue that, due to high mobility of hydrogen atoms, H_2 plasma treatment on p-type crystalline silicon induced hydrogen diffusion inside crystalline wafer.

In Fig. **37** current voltage measurements performed at room temperature and dark conditions were reported as dot. They highlight that sample treated with H_2 plasma was strongly affected by recombination mechanism.

In Fig. **37** line curves refers to simulations obtained starting from the same defect density and distribution as used in capacitance calculation were reported. The good agreement of the measurements and the simulation remarked the validity of parameters chosen in numerical model.

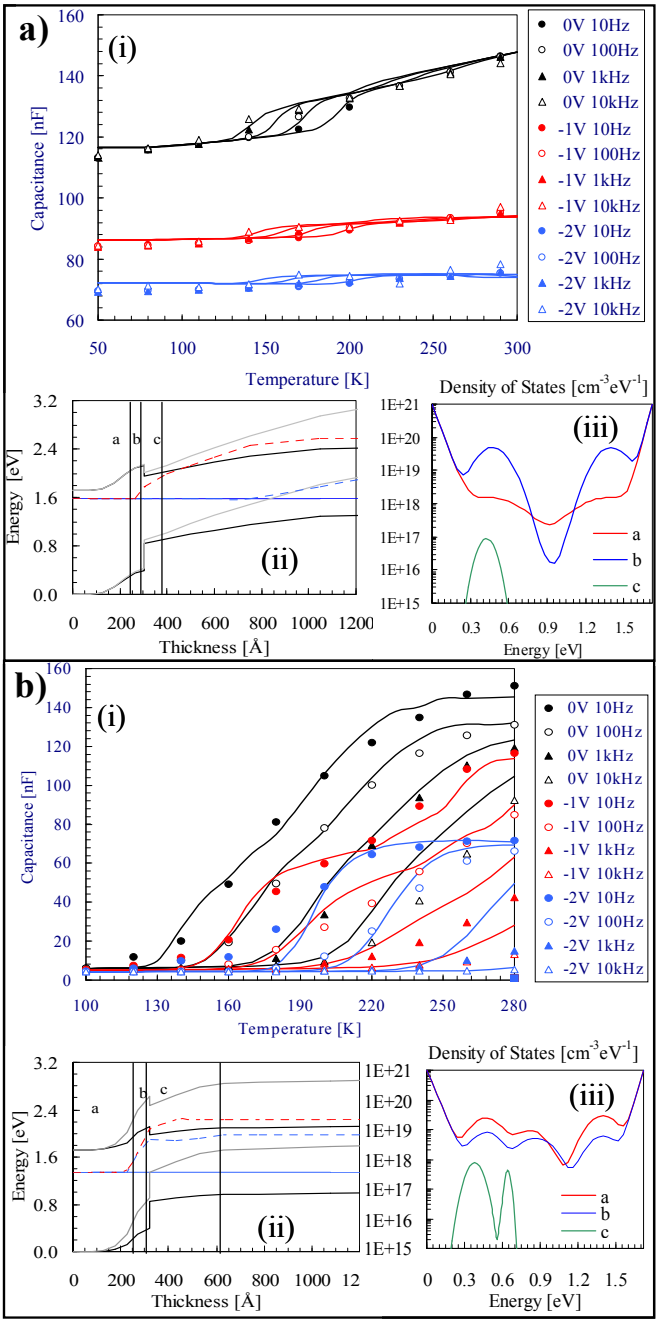


Figure 36: (i) CVfT measurements (symbols) and model (lines); (ii) band bending at 0V (dark) and-1V (grey) as obtained by the simulation of the CVfT values; (iii) defect distributions in the three region of the HJ used to fit the experimental data. (a) HJ treated with plasma dry etching of CF_4/O_2 before a-Si:H layer depositions: (b) HJ treated with plasma dry etching of H_2 before a-Si:H layer depositions.

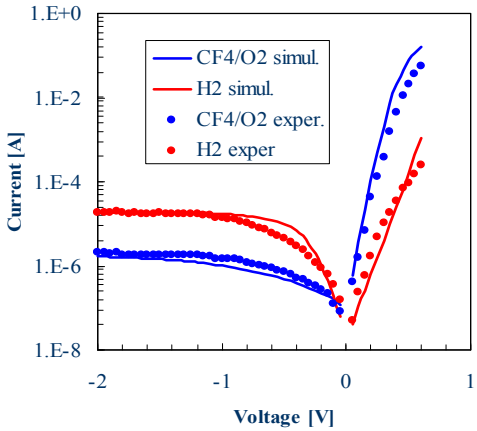


Figure 37: Measured (symbols) and simulated (lines) current voltage characteristics in dark and room temperature conditions of HJ p-type c-Si base 1cm^2 area.

9. DEVICE DESIGN

The cell structure of a-Si:H/c-Si solar cell is basically fabricated starting from a c-Si wafer (Floating Zone FZ; Chocralsky CZ; multicrystalline mc-Si) which needs a previously saw damage removal and texturing that are commonly used in c-Si based solar cell manufacturing. Before a-Si:H deposition particular care must be paid to clean the silicon surface in order to reduce contamination. Then thin doped a-Si:H can be deposited by plasma enhanced chemical vapour deposition (PECVD) or hot-wire chemical vapour deposition (HW-CVD). Even if the emitter layer has higher bandgap (1.7eV) with respect to the c-Si base (1.124eV) and then it should work just as a window layer for the c-Si absorber, it shows strong a-Si:H absorption in the short wavelengths spectrum. Since the emitter layer is a doped a-Si:H film, does not contribute to the carrier generation due to the high recombination within the material that strongly limits the diffusion length [155, 156]. Therefore the emitter thickness should be optimized to reduce its filtering effect to the c-Si base absorber. The choice of doping type of c-Si base is crucial for the device configuration. In principle, since the c-Si is an absorber thicker than the depletion region that can be formed on one side of the wafer, most of carriers are generated inside the neutral region where they move by diffusion mechanism. Therefore electron should be preferred as minority carriers and then p-type doped c-Si should be adopted (electron diffusivity in 1Ωcm p-type doped c-Si: D_n = 26.88cm^2/s; hole diffusivity in 1Ωcm n-type doped c-Si: D_p = 11.64 cm^2/s at room temperature). Also industrial considerations can support this choice such as the abundance of p-type doped c-Si in the PV market historically driven by microelectronic in which the p-type doped is commonly used. But for the HJ solar cell this choice has several drawbacks:

1) the p-type doped c-Si degrades under sunlight exposure mainly due to B-O pairs [157, 158];

2) the n-type doped emitter layer has a bandgap (1.65-1.68 eV) lower with respect to the p-type a-Si:H (1.7-1.72 eV) and then it can reduce the cell photocurrent due to filtering effect;

3) the band diagram of the HJ shows a higher mismatch in valence band with respect to the conduction band [159], therefore the p-type c-Si/p-type a-Si:H base contact not easily forms a ohmic junction as well as back surface field (BSF) as, in turn, the counterpart n-type c-Si/n-type a-Si:H junction.

To evaluate the valence band discontinuity offset between a-Si:H and c-Si several methods have been proposed in literature [7, 160, 163]. The most interesting is once again the constant final state yield spectroscopy CFSYS proposed in ref [67]. The evolution of the CFSYS for several HJ with different a-Si:H thicknesses is reported in Fig. **38**. The progressive reduction of the substrate signal increasing the a-Si:H layer is clearly visible and it is also possible to evaluate the DoS from a clean hydrogenated p-type c-Si surface to thicker a-Si:H layer. 0.44 eV offset in valence band with a standard deviation of 0.02 eV has been evaluated from the data reported in Fig. **38**.

The basic band diagram of the HJ cells is depicted in Figs. **39, 40** for p-type and n-type c-Si base respectively. These band bending distributions are plotted on the base of finite difference simulation program able to describe the carrier transport in stacked structure by solving Poisson, continuity and current equations in each layer described by a set of parameters imposed to define semiconductor properties [164]. In particular these simulations have been performed taking into account the energy gap: E_g, electron affinity: χ and the activation energy: E_{att} of each material. The lowest E_{att} that doped a-Si:H films can achieve [11] is reported in Table **2**.

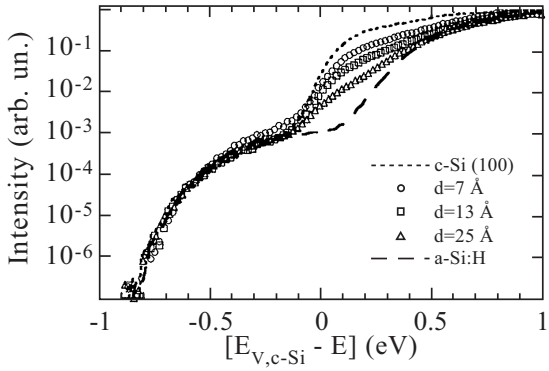


Figure 38: CFSYS spectra of HJ at different a-Si:H thicknesses, starting from c-Si wafer.

Table 2: Dopant activation energy E_{att}, electron affinity χ, energy gap E_g.

Materials	**E_{att}(eV)**	**χ(eV)**	**E_g(eV)**
n-type c-Si	0.21	4.05	1.12
p-type c-Si	0.19	4.05	1.12
i a-Si:H	0.86	3.9	1.72
n-type a-Si:H	0.2	3.9	1.67
p-type a-Si:H	0.34	3.9	1.72
n^+-type a-Si:H	0.017	3.9	1.67
p^+-type a-Si:H	0.14	3.9	1.72

Higher built-in potentials and then higher cell efficiency can be obtained with the HJ structure with respect to the c-Si based homojunction with the same doping concentration in the c-Si bulk, but defect density can strongly affect and reduce this potentiality [165].

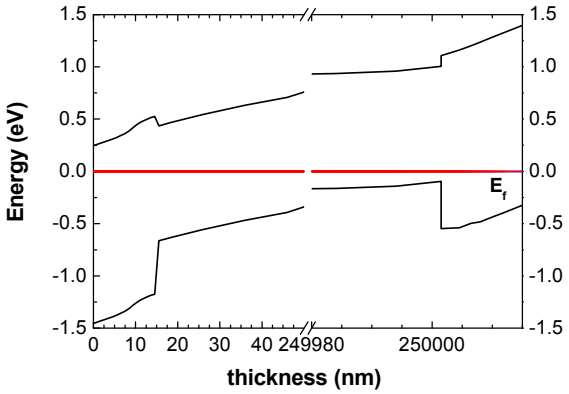


Figure 39: Band bending simulations in dark and 0V. p-a-Si:H/i-a-Si:H/n-type-c-Si/i-a-Si:H/n-aSi:H double heterostructure cell.

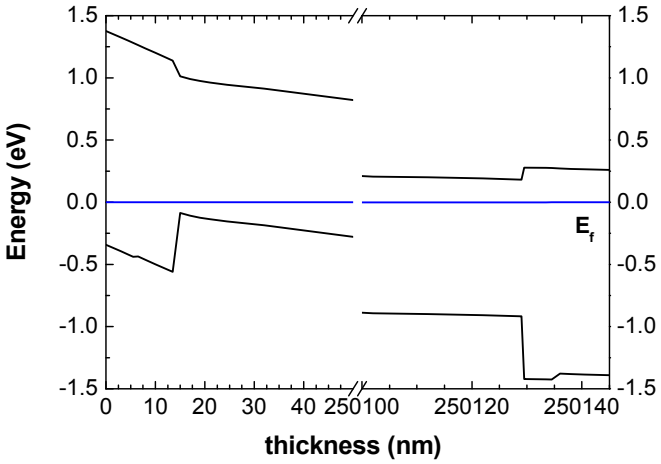


Figure 40: Band bending simulations in dark and 0V. n-a-Si:H/i-a-Si:H/p-type-c-Si/i-a-Si:H/p-aSi:H double heterostructure cell.

If same defect density is chosen at the interface both HJ structure on p and n-type doped c-Si show the same built-in potential value of 1.03V.

If HJ not affected by defect density at the interface are simulated without BSF, simply taking into account the E_{att} of doped a-Si:H emitters, as reported in Table **2**, and the E_{att} = 0.2 eV of 1Ωcm doped c-Si (p on n-type), a built in potential of 0.94V and 0.79V for n-and p-type c-Si based is respectively obtained. This is merely due to the band alignment between the two semiconductors. In turn the higher valence band offset with respect to the conduction band offset affects the carriers collection as evident from Fig. **41**, in which the sun lighted IV characteristics of HJ, not affected by defect density at the interface, and simulated without BSF, are reported. While the p-type c-Si HJ is not affected by the band offset, in turn the n-type c-Si HJ is strongly dominated by barrier

against the hole flow toward the emitter layer and an undesired S shape appears. Moreover the depletion region is more pronounced within HJ on p-type c-Si than in HJ on n-type c-Si. Indeed the simulations report that capacitance values at 100 kHz and 0V are higher in HJ on n-type c-Si (660 nF/cm^2) with respect to that on p-type c-Si (125 nF/cm^2). If defect density at the interface is introduced the S shape in HJ on n-type c-Si would be more pronounced. This unwanted effect almost disappears if microcrystalline silicon (μc-Si) emitter is used instead of a-Si:H [166]; in that case the valence band offset is reduced due to narrow E_{gap} of μc-Si, but the unwanted epilayer that forms during microcrystalline growth reduces the cell performance as already discussed.

9.1. n-Type Doped c-Si

On n-type doped c-Si substrate several studies have been reported in literature to evaluate the potentiality of this heterostructure, but the efficiency obtained were always much lower than the Sanyo results. This was mainly due to the choice of the device architecture. One of the relevant part of the cell as the rear side contact was always neglected by the authors, since they mainly focus on the front junction of the cell to investigate the transport and the role of the intrinsic a-Si:H buffer layer [167, 169]. In that approach part of the built-in potential of the entire structure proposed by Sanyo is lost due to the lack of back surface field. Increasing the doping of the c-Si base the S shape seen in Fig. **41** become less pronounced and almost disappear if a n^+ c-Si (1x10^{19} cm^{-3}) is added to the rear side of HJ cell. Better situation is achieved introducing i/n a-Si:H as BSF. The lighted IV characteristic reported in Fig. **41** reveals a very high efficiency (almost fitting the Sanyo's best results). Then it is quite surprising that the same emitter that produced S shape lighted I-V characteristic now is working almost perfectly.

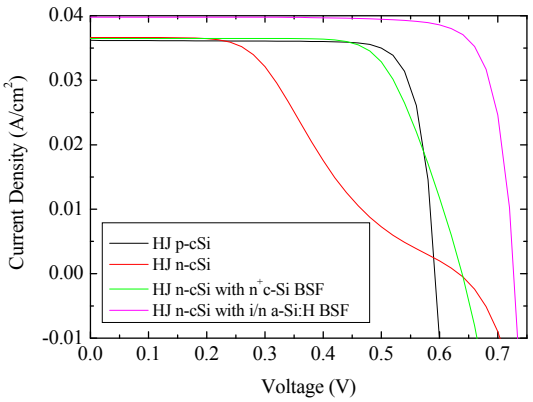


Figure 41: Comparison of simulated lighted IV characteristics of HJ on p-(black) and n-type doped c-Si (red) without BSF and defects at the interface.

This effect is described in Fig. **42** comparing the band bending and the quasi Fermi levels, at 0.4V and sunlight exposure, related to the two structure with and without n a-Si:H BSF. It is worth to note that all the material involved in the simulation are the same and the defect densities at the interfaces have been chosen very low to affect the quasi Fermi level distribution along the structure. Indeed also now the valence band offset is still working as a barrier against hole collection from the emitter side. But now the end point of the entire carrier equilibrium is fixed by

the i/n a-Si:H BSF. The hole quasi Fermi level is almost free within the c-Si (no defects have been added yet that could pin it) assuming a value closer to the valence band almost everywhere along the c-Si. This effect is due to the edge condition at the surface from which the carriers are extracted. Indeed at that surface the mass law ($np = n_i^2$) must be always satisfied. This condition implies a reduction of hole in the semiconductor underneath the surface as well described by the jointing of the two quasi Fermi levels at the surface. If this happens on n a-Si:H (as in case of n c-Si/n a-Si:H BSF) the n c-Si is safe and there the hole amount can remain higher with respect to the case in which the carrier extraction is performed from directly from the n c-Si surface. The quasi Fermi levels are indeed more splitted at the c-Si surface than in c-Si BSF. Then if the hole amount in the c-Si is higher the hole collection from the emitter side is less affected by the valence band offset thus enhancing the total current as evident from lighted IV curves in Fig. **41**. Moreover the splitting of quasi Fermi levels during sunlight exposure is larger along the c-Si and thus the cell V_{oc} value is higher. This has another relevant consequence: wider the Fermi levels splitting lower the sensitivity to the interface defects. The right dopant amount and thickness, as well as the choice of metal work function of this layer have needed an optimization process. Indeed the n-type a-Si:H should be sufficiently thin to avoid series resistance enhancement and sufficiently doped to avoid depletion by the metal contact due to its work function.

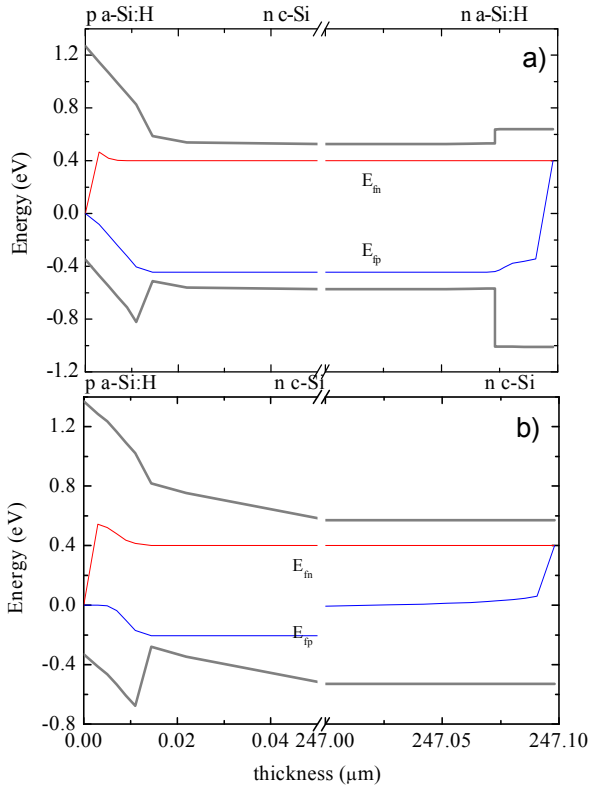


Figure 42: Comparison of simulated band bending at 0.4V under sun light exposure related to the two HJ structure with (a) and without n a-Si:H BSF (b).

To better evaluate this concept a comparison of band bending distributions at the rear side of the cell is reported in Fig. **43**, as obtained by numerical simulations, in which two different work function 4.2 eV and 4.6 eV have been applied at the rear side metal contact keeping the same doping and density of state distribution within the n a-Si:H layer. The W_f has been simulated fixing the Fermi level at the edge of the n a-Si:H layer where the metal contact would be. The thickness of the n a-Si:H layer has been fixed at 27 nm. As evident from Fig. **43**, depletion occurs in the n-type c-Si and this reflects in a barrier formation for the electrons being collected by the metal contact. This barrier reflects again in a "S shape" in the sun-lighted current voltage characteristic as reported in Fig. **44** as continuous lines. This unwanted effect has been experimentally observed on sample with TCO rear contact (see Fig. **44** red dots) and has been almost recovered by TCO removal and subsequent Al contact evaporation (see Fig. **44** black dots). The good agreement between simulation and experiments can be considered as proof of the effect of metal contact W_f on thin n-type a-Si:H layer. Indeed the rear side c-Si/a-Si:H interface refers to the same sample. But the use of Al to ensure an ohmic contact at the rear side of the n-type c-Si wafer, even if suggested by the Al work function (W_f) able to align the Fermi level close to the conduction band, is not the best choice since also small amount of Al diffusion into c-Si wafer enhance the recombination process. Indeed Al is a p-type dopant for c-Si and, therefore no BSF can be formed in any way.

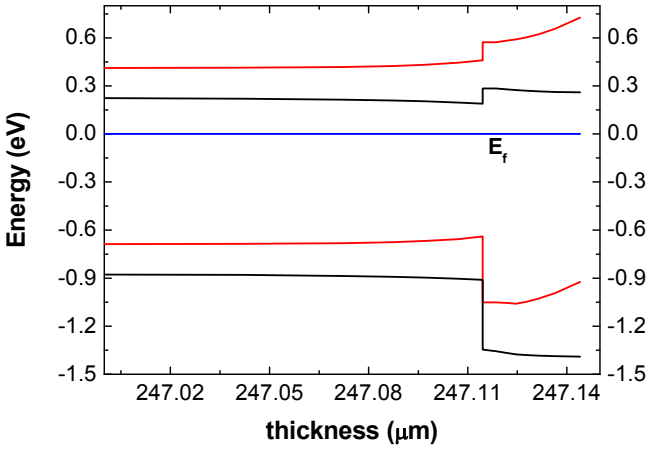


Figure 43: Numerical simulations of band bending distributions of n c-Si/n aSi:H rear side of HJ solar cell, in which the work function of the metal contact to the n a-Si:H has been varied from 4.2 eV (black) to 4.6 eV (red).

Now it is intuitive that reducing the doping density within the n-a-Si:H layer the current voltage sun-lighted characteristics will assume a behaviour similar to that reported in Fig. **44**. To confirm the effectiveness of the a-Si:H BSF, two similar HJ cells have been compared: the first with a-Si:H BSF and the latter with P diffused BSF (n^+ region). Different Voc values have been obtained: 690 mV and 630 mV respectively. Inserting an intrinsic a-Si:H buffer layer 710 mV of V_{oc} value has been achieved [170]. Actually Sanyo has two best results on HJ n type doped c-Si based cell [171]. Their photovoltaic parameters are listed in Table **3**.

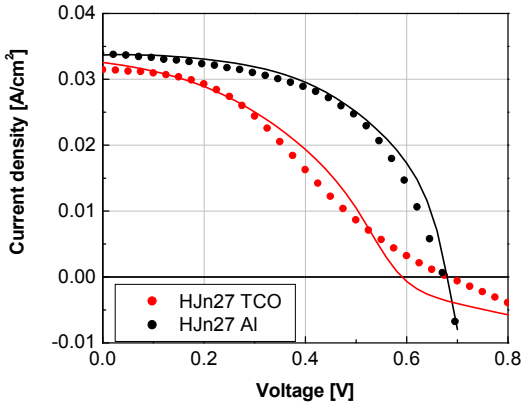


Figure 44: Comparison between experimental and numerically simulated IV characteristics under sun-light of n c-Si/n aSi:H rear side of HJ solar cell in which the workfunction of the metal contact to the n a-Si:H has been varied from TCO = 4.6 eV (red) to Al = 4.2 eV (black).

Table 3: Photovoltaic parameters of the actually Sanyo's best HJ cell.

Thickness (μm)	V_{oc} (mV)	J_{sc} (mA/cm^2)	FF %	Eff %	Area (cm^2)
180	729	39.68	80	23	100.4
60	743	38.96	79.1	22.8	100.3

Starting from the simulation of the best cell produced by Sanyo, reported as black curve in Fig. **45**, and introducing defects within the c-Si up to 1x10^{18} cm^{-3} in a thin layer close to the interface, the shape of the current-voltage lighted characteristic shows an S shape that strongly reduces the cell Fill Factor as already seen in [172]. If the defect density is introduced at both side of the cell very similar results occur.

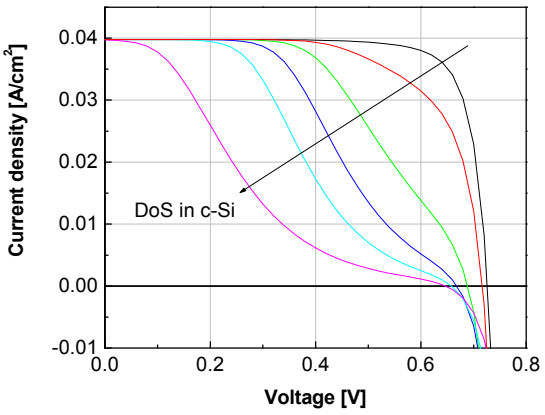


Figure 45: Numerically simulated IV characteristics under sun-light of n c-Si/n aSi:H rear side of HJ solar cell in which the DoS has been increased up to up to 1x10^{18} cm^{-3}.

As discussed in the previous paragraphs, the introduction of 5 nm thin intrinsic buffer layer at beginning only at the front side interface and then at both the interfaces of the HJ, resulted in higher silicon surface passivation and then in higher cell performance mainly due to a Voc enhancement. The thicknesses of p-type a-Si:H emitter layer and n-type a-Si:H BSF have been fixed at 5 nm and 15 nm respectively [173] even if thicker n-type a-Si:H and n-type μc-Si has also been reported in literature [174].

In [94] high efficiency on n-type c-Si base has been reported with the following performances: V_{oc} = 639 mV, J_{sc} = 39.3 mA/cm^2, FF = 78.9%, eff = 19.8% on 1cm^2 area FZ 1-2Ωcm n-type c-Si.

V_{oc} as high as 713mV has also been obtained using 70 MHz VHF-PECVD, as reported in [175].

9.2. p-Type Doped c-Si

In the past, to form the back surface field, various groups have used diffused junctions [175], [177]. Currently, an a-Si:H BSF also formed by PECVD/HWCVD has to be considered as state of the art, both because the diffused BSF diffusion is not in line with the low temperature approach, and due to the excellent passivation of the c-Si surface that can be obtained by a-Si:H. Surface recombination velocities as low as 3 cm/s have been reported [178].

The main advantage in the use of n-type doped a-Si:H emitter is due to its conductivity that is two order of magnitude higher with respect to the p-type a-Si:H layer as shown in Fig. **46** in which the dark and light conductivities as well as the doping activation energies of both n-type and p-type doped a-Si:H films as a function of PH_3 and B_2H_6 dilution in SiH_4 are respectively reported [179]. These conductivity have been measured on 500 nm thick a-Si:H films deposited on 7059 corning glass using 13.56 MHz RF glow discharge with a power density of 28 mW/cm^2, SiH_4 flow of 40 sccm, gas pressure of 300 mTorr, substrate temperature of 200 °C and dopant gas concentrations ranging between 0% and 1%. On the other hand the optimum n-type doping concentration should be carefully considered in order to also form a good ohmic contact with a metal avoiding Schottky barrier formation. Fig. **47** reports the current-voltage characteristic for the n-a-Si:H/Al junction for two different doping concentrations of the amorphous film. In particular, open and dark symbols correspond to a dopant/silane ratio equal to the saturation value 10^{-2} %, and 1%, respectively. It is evident that doping ratio equal to 10^{-2} % interface induces a rectifying Schottky barrier at the metal interface. Then higher dopant concentration is needed to have a good ohmic contact [82]. It is worth to note that the a-Si:H film conductivity decrease as the film thickness reduces as remarked in [180] and reported in Fig. **48**. This effect cannot be compensated introducing more dopant during the thin layer deposition since higher defect density would be formed strongly affecting the electronic transport within the doped layer as previously discussed.

Therefore the emitter thickness and the dopant amount is a compromise between conductivity, filtering effect and recombination. An example of this trade-off is reported in ref [82] and summarized in Fig. **49 (a**), **(b)** in which are reported photovoltaic performances of several HJ cells fabricated on p-type doped c-Si base with same thickness of n-type doped a-Si:H emitter deposited at different PH_3 doping concentration. Nor TCO neither antireflection coating has been used as a top contact. The maximum efficiency value was obtained at a ratio equal to 0.12% (1700

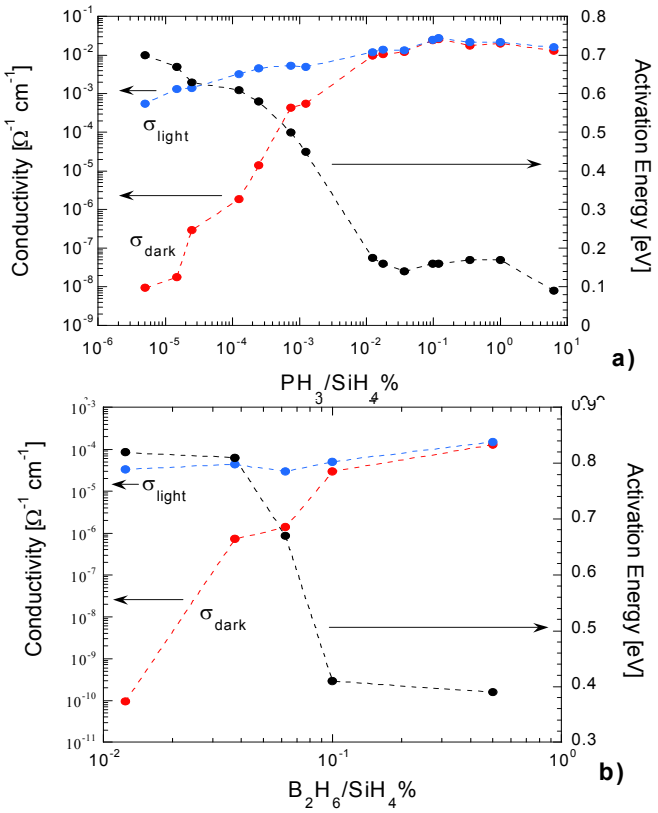


Figure 46: (a) Dark and lighted conductivities, activation energy for n-doped films *vs.* phosphine percentage in the gas mixture. (b) Dark and lighted conductivities, activation energy for p-doped films *versus* diborane percentage in the gas mixture [179].

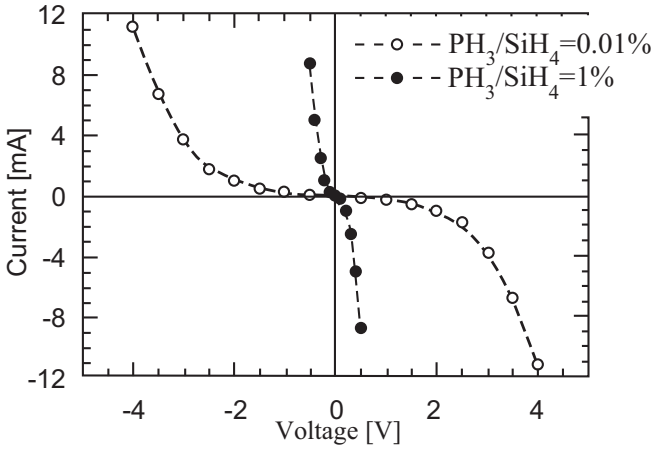


Figure 47: Current *vs.* voltage characteristics of n-doped a-Si:H/Al contact for two different dopant concentrations in the amorphous layer [82].

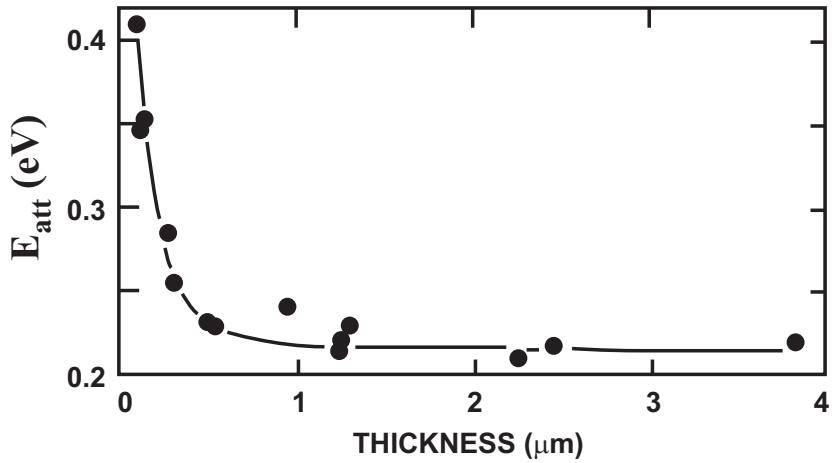


Figure 48: Electrical activation energy of n-type doped a-Si:H as a function of film thickness. Same PH_3 amount is used during the deposition of each sample [180].

$[PH_3]/[SiH_4]$ ppm), corresponds to the conductivity saturation value found for the single doped layer as reported in Fig. **46**. A reduction of the doping concentration in the buffer layer determines a shift of the Fermi level toward midgap and thus a reduction of the electric field at the interface. On the other hand at higher doping concentration the increase of defect density at the interface layer causes recombination and a reduction of the conversion efficiency of the device. This effect is also confirmed in Fig. **49(c)** in which the HJ external quantum efficiency is reported at 460 nm of wavelength as a function of doping dilution in the emitter layer. This wavelength has been chosen since it is absorbed mainly at the heterointerface [82]. Quite similar results, in terms of $[PH_3]/[SiH_4]$ ppm, are reported in [181]. Also the depletion region within the crystalline side of the HJ follows the same trend as a function of doping dilution as demonstrated in Fig. **49(d)** by the capacitance measurements performed at frequency of 10 kHz where there is no contribute to the capacitance value from the capture-emission kinetic of the defects present at heterojunction and the device behaves as a capacitor in which the depletion region is the dielectric [149]. V_{oc} improvement up to 635 mV has been obtained by introducing an intrinsic buffer layer on front side interface. Then a compromise of 5 nm thick n-type emitter and 5 nm thick intrinsic buffer layer has been reached [182].

Photoluminescence (PL) measurements, reported as I_{PL} (PL-intensity) as the transient PL signal over time, can be used to evaluate the a-Si:H/c-Si interface quality. Indeed the higher the defect density at the interface the lower is the I_{PL} signal due to higher recombination [92]. A comparison between HJ cell efficiencies and I_{PL} as a function of deposition temperature and a comparison between HJ cell efficiencies and I_{PL} as a function of $[PH_3]/[SiH_4]$ doping ratio are respectively reported in Figs. **50, 51**. In both comparisons the I_{PL} can be considered as the signature of the lowest defect density at the interface, thus suggesting 210-230°C as the best temperature deposition range and the doping ratio of 2000 ppm as the best choice to enhance the built-in voltage taking into account the interface defect density. Even if lower doping ratio should reduce the defect density, in this case the position of Fermi level moves toward the midgap at the a-Si:H/c-Si interface where the defect density is more effective in recombination mechanism.

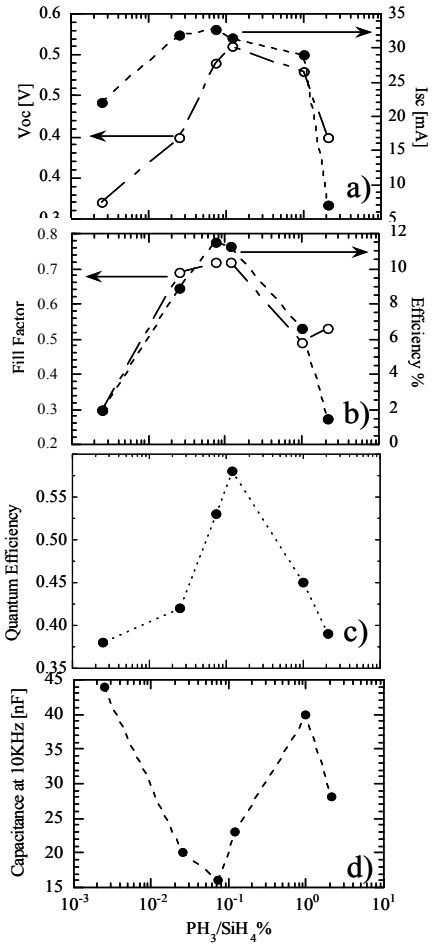


Figure 49: (a) V_{oc}, I_{sc} (sample area 1cm^2); (b) FF, Eff; (c) Quantum Efficiency at 460 nm; (d) Capacitance of n-aSi:H/p-cSi HJ solar cell [82].

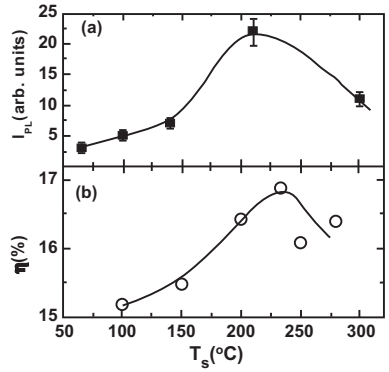


Figure 50: (a) IPL of a-Si:H/c-Si HJ and (b) HJ cell efficiency, both as a function of deposition temperature [92].

In order to fabricate a full low temperature HJ cell on p-type doped c-Si wafer the base contact cannot be formed by high temperature diffusion process.

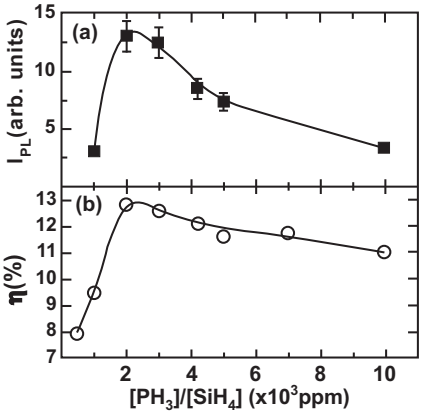


Figure 51: (a) I_{PL} of a-Si:H/c-Si HJ and (b) HJ cell efficiency, both as a function of emitter doping ratio[92].

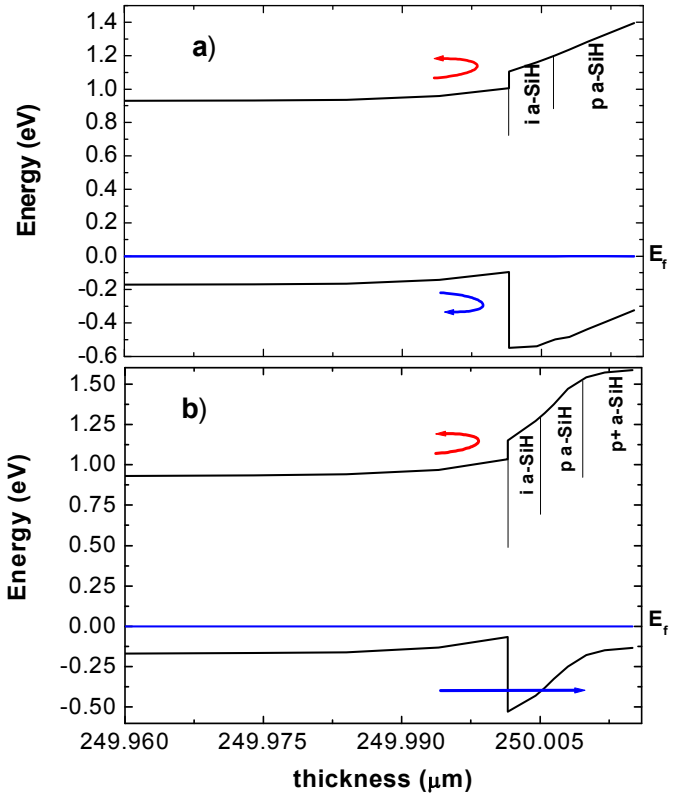


Figure 52: Band bending simulations in dark and 0V. (a) p-type-c-Si/i-a-Si:H/p-aSi:H heterostructure; (b) p-type-c-Si/i-a-Si:H/p-aSi:H/p^+-aSi:H heterostructure.

The use of heterojunction on the rear side of the cell, as suggested in Fig. **39**, needs particular care. The valence band discontinuity between p-type c-Si and p-type a-Si:H reduces the hole collection at the rear side contact. Moreover the high E_{att} in p-type a-Si:H does not allow a strong bending of valence band. On the other hand it is very difficult to reduce the p-type a-Si:H E_{att} by simply adding more dopant gasses in the gas mixture during the plasma deposition [183]. Indeed the more the B_2H_6 the more the defect density [184].

The numerical simulations performed on this heterostructure remark that, if the E_{att} of p-type a-Si:H layer is chosen on the base of data reported in Table **2**. If the p-type a-Si:H is high doped (p^+), the band bending at the heterointerface changes from that reported in Fig. **52(a)** into a more helpful configuration, as reported in Fig. **52(b)** and this reflects in a better hole collection as evident in Fig. **53(a)** (red curves). Indeed the hole collection is dominated by recombination process, as evident in Fig. **53(b)** (blue curves).The IV simulated characteristics related to the two band distribution of Fig. **52** are reported in Fig. **54**. The S shape that strongly affects the cell FF can be almost removed by the p^+ a-Si:H introduction [185]. In neither these simulations nor hopping at the Fermi level, neither tunneling through the barrier mechanisms are included. In principle they can help the hole collection from the p-type c-Si toward the rear side electrode, but are difficult to control of course.

A way to enhance the p-type a-Si:H conductivity thus producing a kind of p^+ is represented by the formation of CrSi thin layer on top of the p-type a-Si:H. This can be accomplished by Cr evaporation and subsequently wet removal [186]. CrSi layer results in lowering the p-type a-Si:H E_{att} as reported in Table **2** as p^+ layer. This approach has been successfully used also in HJ fabricated on p-type multicrystalline silicon (mc-Si) wafer [187, 188]. The CrSi has been applied successfully also on front side of the cell to enhance the n-type a-Si:H conductivity, thus reducing the E_{att} as reported in Table **2** as n^+ a-Si:H. With this approach HJ cell efficiency as high as 17% has been achieved [177].

The problem of the BSF formation on p-type c-Si has been almost solved as follows:

1) Increasing the $[B_2H_6]/[SiH_4]$ up to 10000 ppm and the layer thickness up to 35 nm as reported in Fig. **55** [181].

2) Using HWCVD and increasing the B_2H_6 (2.5% B_2H_6 in H_2) flux from 2 sccm to 18 sccm with H_2 dilution in the gas mixture (B_2H_6 + 100 sccm H_2 +2.5 sccm SiH_4) during the p-type a-Si:H layer deposition as suggested in [189]. Very high efficiency as high as 18.83% with V_{oc} of 670 mV and J_{sc} of 36.71 mA/cm^2 has been obtained on CZ p-type c-Si wafer, and efficiency of 19.3% with Voc of 678 mV, Jsc of 36.2 mA/cm^2 on FZ p-type c-Si wafer 1cm^2 area as reported in [190]. Also in [94] high efficiency on p-type c-Si base has been reported with the following performances: Voc = 633.7 mV, Jsc = 36.8 mA/cm^2, FF = 79.1%, eff = 18.5% on 1cm^2 area FZ p-type c-Si.

To confirm the effectiveness of the a-Si:H BSF, two similar HJ cells have been compared: the first with a-Si:H BSF and the latter with Al diffused BSF (p^+ region). Different V_{oc} values have been obtained: 680 mV and 650 mV respectively [170]. Concerning the doping of the p-type c-Si wafer

several simulations have been performed and reported in [191]. The authors suggested better performances if 0.5 Ωcm substrate resistivity is adopted as p-type doped base wafer.

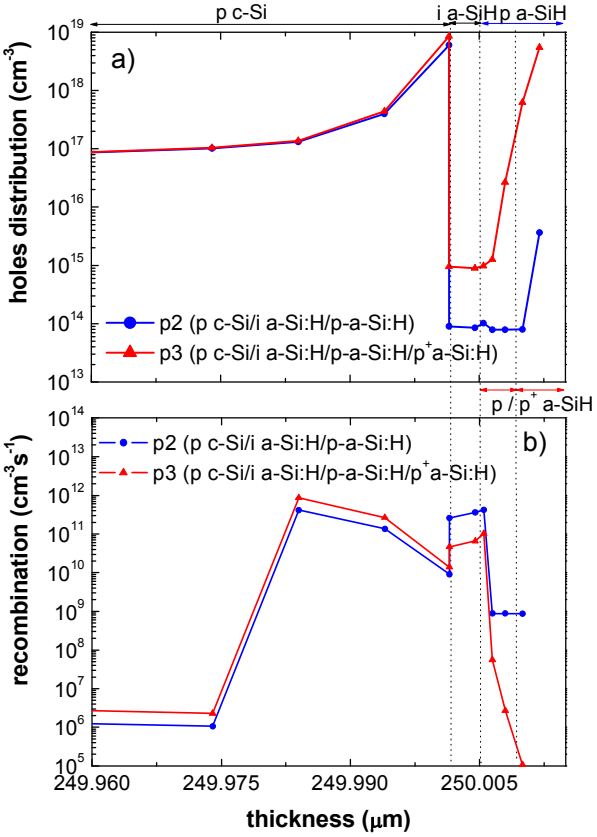


Figure 53: Holes and recombination distributions at the heterojunction at 0.65 V in dark condition.

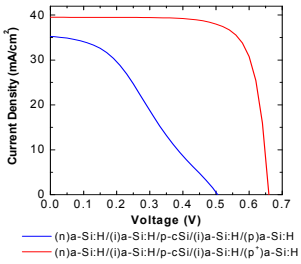


Figure 54: Simulated current voltage characteristics under AM1.5G sunlight conditions.

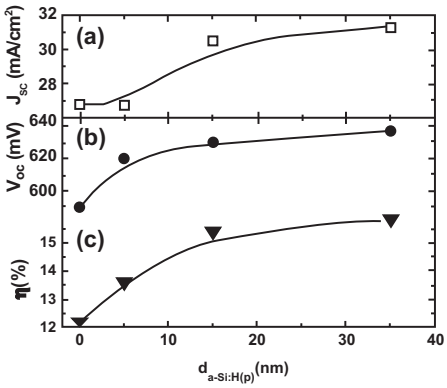


Figure 55: Solar cell parameters, short-circuit current (a), open-circuit voltage (b) and efficiency (c), as a function of the thickness of the a-Si:H(p) layer, $d_{a\text{-}Si:H(p),}$ in a-Si:H(n)/c-Si(p)/a-Si:H(p) cell structure [181].

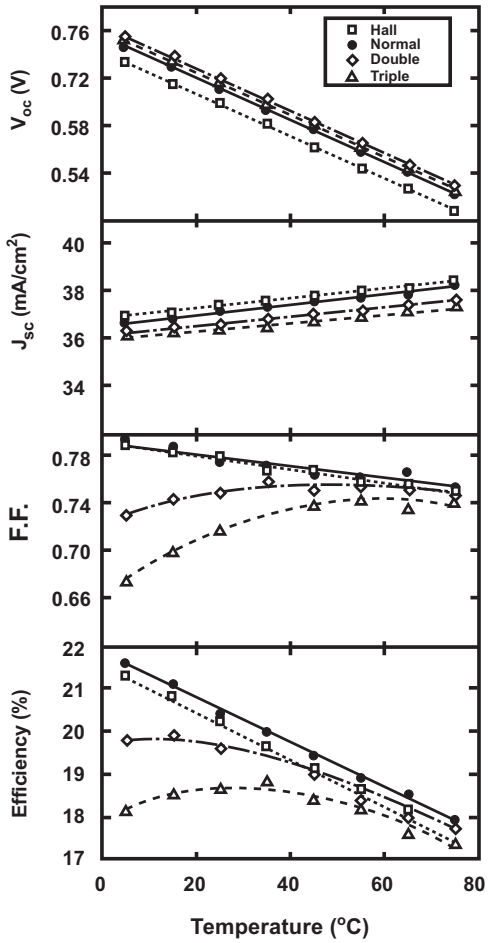


Figure 56: Temperature dependence of PV parameters of the HIT cell with different a-Si:H buffer layer thicknesses [192].

9.3. Temperature Coefficient

One of the most particular features of the HIT solar cell is its temperature dependence. Indeed the temperature coefficient is lower than c-Si base homojunction, thus reducing the detrimental effect on the photovoltaic performance due to heating under sunlight exposure. This temperature dependence is mainly characterized by the high Voc due to the lower J_0, with respect to the c-Si based homojunction, and by FF dependence related more to the a-Si:H layer conductivity. The temperature dependence of the photovoltaic parameters of the HIT cell fabricated with different a-Si:H buffer layer thickness (half, normal, double, triple) is reported in Fig. **56**. The temperature coefficient can be summarised as -1.78 mV/°C. It increases in absolute value increasing the a-Si:H buffer layer thickness [192].

9.4. TCO

These best performance of HJ solar cells have been achieved by a continuous effort in a-Si:H quality, interface quality, in terms of cleaning and pre-treatment before a-Si:H deposition, dopant optimization and TCO optimization. In particular this last has allowed enhancing cell efficiency in the near infrared region of the sunlight spectra as reported in Fig. **57**.

Details about the TCO used by Sanyo are not completely discloused, but some ideas are maturing to establish its role within the HJ cell. As seen before concerning the a-Si:H doping efficiency as well as the metal contact, it is relevant to use particular care to chose the correct contact having the right W_f to avoid built-in potential reduction as well as S-shape formation.

In general the need of TCO is mainly due to the poor conductivity of the a-Si:H layer. Moreover the possibility to deposit it at low temperature (< 300°C) forming at the same time an antireflection coating for the impinging sunlight, has made the TCO material one of the relevant part of the HJ cell. The electrical and optical properties of TCO films are critically process dependent. Transparency and conductivity of this highly degenerate and wide band-gap oxide semiconductor film can be varied by adjusting the deposition conditions. To obtain the best solar cell performances the ability of depositing highly conductive and transparent ITO films is crucial. However, the optical and electrical properties of this material are inversely related so that a larger conductivity in the ITO film is accompanied by a larger light absorption and opacity. For this reason, a compromise in performance must be made for the intended application.

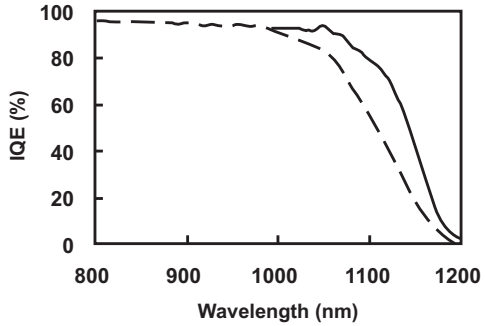


Figure 57: IQE spectra of HIT cell, with optimized TCO (solid line) and not optimized TCO (dashed line) [171].

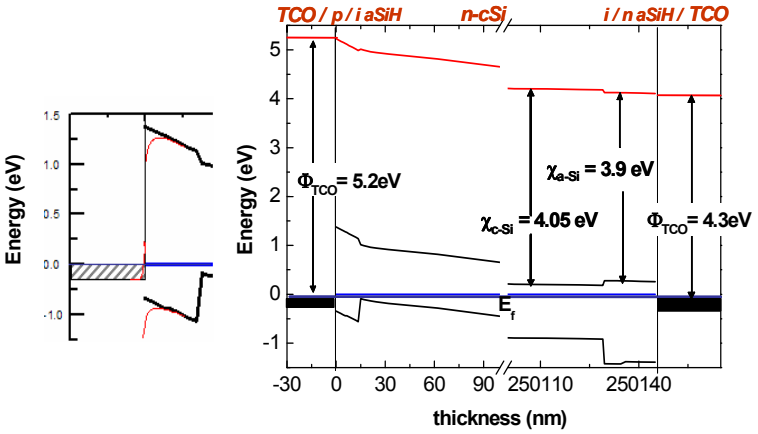


Figure 58: Band bending simulation of the n-type c-Si doped based a-Si:H/c-Si heterojunction cell with two different TCO work functions: 5.2 eV for front and 4.2 eV for the back side. At the left side the band bending at the edge between TCO and p-type doped a-Si:H is magnified to remark the undesired band bending distribution (red) when TCO work function lower than 5.2 eV is used for the cell front side.

Actually the majority of TCO are n-type doped, as indium thin oxide, (ITO) ZnO:Al (AZO), SnO_2; while very few p-type doped TCO are under development. However their resistivity is almost one order of magnitude lower than their n-type counterpart. The physical mechanism for the contact formation at the TCO/p-a-Si:H interface is a tunneling effect, as shown in the Fig. **58**. By modeling the bifacial heterojunction device using numerical simulator [164], the band bending at the amorphous/crystalline silicon interfaces and the electronic affinity distribution can be evaluated, and the minimum value of the TCO work function can be estimated as 5.2 eV for the emitter side of the cell, while 4.3 eV are sufficient for the rear side of the heterostructure cell.

Thus we can conclude that to avoid a built-in reduction due to the presence of the TCO/p-a-Si:H contact a TCO with an associated work function more than 5 eV should be designed as suggested by literature [193, 194]. If this rule is neglected and a TCO work function lower than 5eV is used for the front side of the heterostructure cell a band bending at the TCO/p type doped a-Si:H interface can reduce the built-in potential as shown in left side of Fig. **58**. One of the most used in the HJ fabrication process is the ITO film [196]. It is used as both front and back contacts and has been optimized by combining experimental and computer simulation results, determining also which deviation from the optimal ITO thicknesses can be tolerated. The ITO films useful for heterostructure solar cells have been deposited using a low temperature RF 13.56 MHz magnetron sputtering. The sputtering process temperature has been chosen after several trials varying the temperature from 50°C to 300°C. In Fig. **59** are reported, as points, the values of resistivity and effective transmittance (T_{eff}) from 350 nm to 1200 nm. In this graph T_{eff} is defined as:

$$T_{eff} = \frac{\int_{350nm}^{1200nm} T(\lambda) \cdot AM1.5G(\lambda) d\lambda}{\int_{350nm}^{1200nm} T(\lambda) d\lambda} \quad \textbf{(21)}$$

where T (λ) is the transmittance and AM1.5G(λ) is the number of photons per unit wavelength (λ).

The deposition process parameters have been optimized in order to obtain a good compromise between the film conductivity and transmittance. Nevertheless the ITO is not sufficient to collect the photo generated current without introduce a great amount of series resistance. Indeed, to reduce this power lost mechanism the HJ cell still needs a front metal grid. In the HJ solar cell technology high temperature steps are detrimental for the cell, due to the low temperature process used to deposit a-Si:H films. Specific silver pastes have been developed from different screen printable paste manufacturers, able to be sintered at temperatures ranging from 120°C to 250°C.

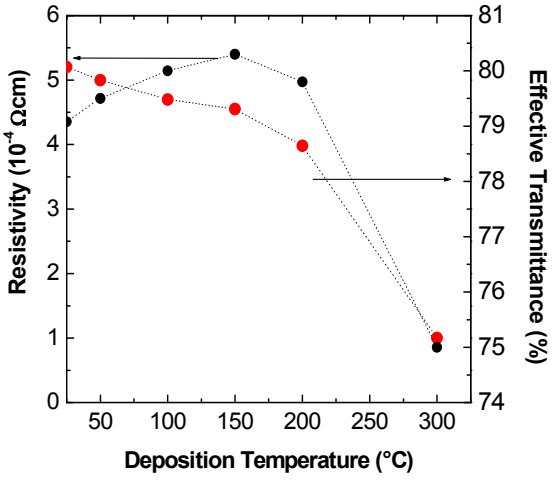


Figure 59: Sputtered ITO resistivity and transmittance as a function of deposition temperature.

Longer thermal annealing time and higher temperatures improve adhesion and bulk resistivity [197, 198]. The actual application of this kind of pastes requires an accurate optimization of printing parameters to obtain a fine-line printing, aspect ratio, non-interrupted fingers. At the same time adequate curing in air atmosphere has to be chosen to obtain good conductivity of front grid without damaging the cell performances or modifying the TCO properties. The best condition we have used in the HJ cell manufacturing for the screen printing process has been settled as follows: low temperature sintering Ag paste (Dupont PV410); double wet printed through a 350 mesh screen; drying in a conveyor IR belt furnace at 250°C for 15 minutes; 15 micron thick fingers. A resistivity of $2.92 \cdot 10^{-5}$ Ωcm has been determined on screen printed silver after this curing process [188]. It has to be mentioned that the ITO sheet resistance increases from 45 Ω/ϒ up to 60 Ω/ϒ during the procedure while ITO reflectance and transmittance have been almost unaffected. Also the rear side of the cell has been formed by a screen printed metal grid in order to reduce the amount of Ag and thus the cost as well as to perform bifacial cell configuration cell. Actually ZnO is one candidate to replace the ITO due to difficulties in managing the ITO W_f to obtain a good material for front and back contact, as well as availability and cost. Indeed boron doped ZnO has been used for the rear side of the cell followed by an Al foil. This approach is justified by the lower workfunction of the ZnO (around 4.1 eV) with respect to the sputtered ITO (around 5 eV).

Indeed a work function of 4.1 eV aligns better with the Fermi level of n-type doped a-Si:H layer as indicated in Fig. **58**. In Fig. **60** the sun-lighted I-V characteristic of the best cell is reported together with the photovoltaic parameters. Series resistance of 0.95 Ωcm^2 and shunt resistance higher than 1 $M\Omega cm^2$ have been evaluated. Reducing the edge effects by cutting the cell area to 100 cm^2 the efficiency has been raised up to 20% as reported in Fig. **60**.

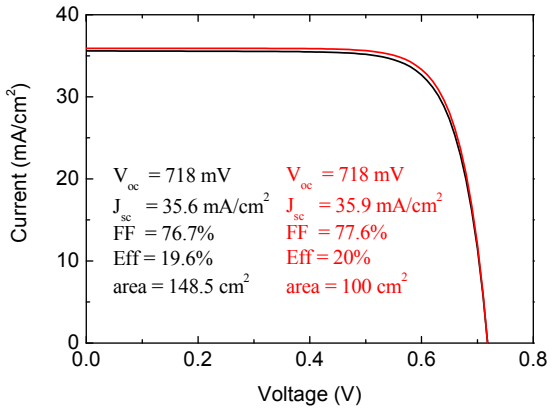


Figure 60: Current Voltage characteristic of the a-Si:H/c-Si heterostructure best cell under AM 1.5G sunlight simulator before and after the area reduction from 148.5 cm^2 to 100 cm^2 [195].

Amorphous P-I-N Solar cells have poor stability under sunlight exposure, due to a-Si:H light induced degradation by the Staebler-Wronski effect [17]. Thus using a-Si:H in heterojunction solar cells could be detrimental to the stability of such devices. Instead of heterojunction cells have shown good stability to light-soaking and high temperature exposure tests measured over periods of hours [200, 201]. The performance of HJ cells have been evaluated stable on both p-and n-type [199] even with light soaking of few months.

10. INTERDIGITATED BACK CONTACT HJ CELL

Once the recombination processes have been limited, the main limitation to the short circuit current is the front grid shadowing which is, in average, 8-10% of the cell area. This issue has been overcame by Sunpower which developed the Interdigitated Back Contact (IBC) solar cells, initially proposed by Lammert and Schwartz [202] in which the sunward side is completely exposed, so maximising the absorption. Both the emitter and base contact, produced with alternate diffusing processes at high temperature, are located at the back side following an interdigitated pattern. The Sunpower record cell, based on n-type FZ wafer, shows 24.2% efficiency, having Voc above 720 mV [203]. In Fig. **61** is illustrated the schematic of an IBC solar cell.

The idea to apply the IBC concept to the HJ cell, to take advance of low temperatures budget process and high V_{oc} together with a fully exposed sunward side proposed a new challenge. Taking into account the high FF that can be obtained by IBC cells, it is possible to consider an IBC-HJ cell as one of the most attracting and promising technology for Silicon solar cell production to reach up to 26% efficiency.

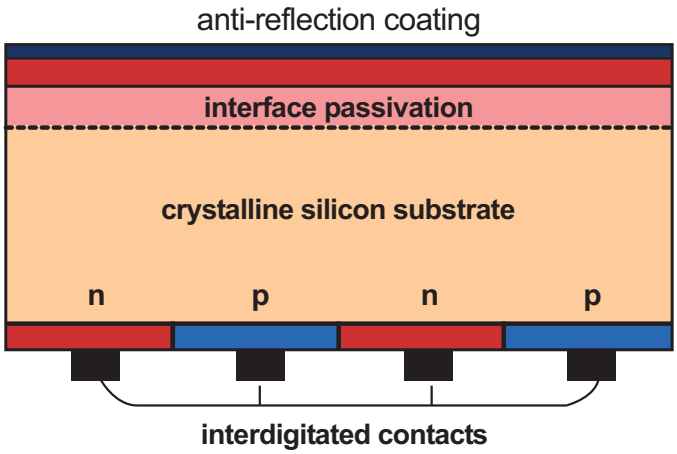


Figure 61: General schematic of an Interdigitated Back Contact solar cell.

On this considerations basis, several research groups have recently started to find the best approach to produce IBC-HJ. In this section we report an overview of different approach as well as results obtained by different groups: University of Delaware (USA); University of Toronto (Canada); Helmholtz Zentrum (Germany); IMEC (Belgium); CEA-INES (France); ENEA (Italy). Several patents have been deposited in Europe [205-207]. Actually the highest efficiency result to date for IBC-HJ, it is still on small area (1 cm^2) and involves photolithography steps as well as high temperature steps like diffusion for FSF and oxidation for passivation. Nevertheless we will show two IBC-HJ structures produced all at low temperature and avoiding photolithography, even if their efficiencies are still lower than the expectation.

10.1. University of Delaware

The earlier publication on IBC-HJ solar cells from university of Delaware, by Lu *et al.* are dated 2007 [208]. The developed cells are based on polished 2.5 Ωcm n-type FZ 300 μm thick wafer. Both emitter (p-type a-Si:H) and base contact (n-type a-Si:H) are placed at the back side of the cell, in an interdigitated structure, separated by a narrow non-diffused and non-passivated region.

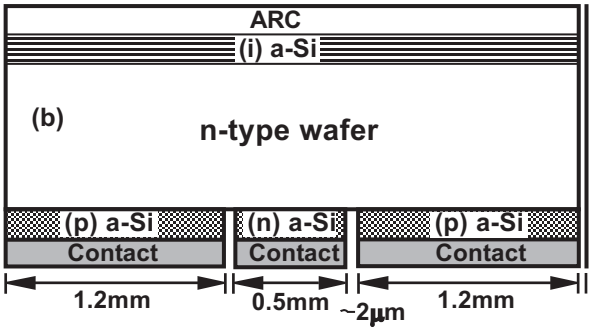


Figure 62: IBC HJ at University of Delaware [208].

Both doped layers, 20 nm thick each, are deposited in a multi-chamber PECVD system at temperature of 200°C, followed by 200 nm thick e-beam evaporated Al layer. The interdigitated

pattern, consisting of 1.2 mm wide strips for emitter and 0.5 mm for base contact, is produced by a two-step photolithography processing; the 2 μm wide separation region is the natural product of the etching processes undercutting.

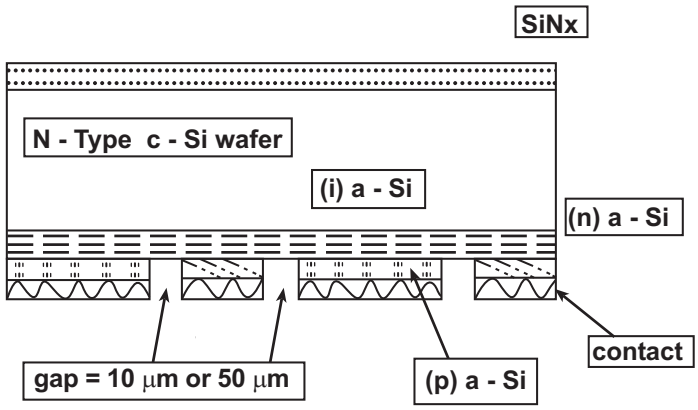


Figure 63: Schematic of IBC-SHJ cell having the i-a-Si buffer layer between substrate and doped layers.

The sunward side is passivated with 20 nm intrinsic a-Si:H layer, finished with Indium Tin Oxide (ITO) and MgF_2 double layer as antireflection coating (ARC).

It has been found the current and the IQE strongly affected by front surface recombination S_{eff}. Reducing the S_{eff} from 300 to 82 cm/s by means of thermal annealing, the overall response of the cell enhanced in the range of 600-900 nm from an average of 0.55 to 0.8, thus ramping up the efficiency to 11.8% on 1.32 cm^2 area, having a V_{oc} of 602 mV.

Numerical simulations have shown the possibility to get device over 24% [204] if: 1) the V_{oc} is enhanced up to 700 mV inserting an intrinsic a-Si:H layer between doped amorphous layer and crystalline base; 2) the J_{sc} is enhanced up to 26.7 mA/cm^2 by applying Silicon Nitride (SiN_x) to the front surface substituting the used structure for both passivation and antireflection purpose; 3) the Fill Factor (FF) is improved by optimizing the doped amorphous layers, their covering fractions and the metallization process. While the introduction of (i) a-Si:H buffer helps to enhance the cell V_{oc}, in turn has detrimental effect in cell FF resulting in a "S shape" in the lighted I-V characteristic, as shown in Fig. **64**. The "S shape" curve, similar to those of standard HJ when intrinsic buffer is too thick, is assumed to be not dependent by shunting between p and n regions because of the flat behaviour in reverse bias condition. From Fig. **63** can be noted that the interspacing between doped regions are larger than that in Fig. **62**, and it is formed with an additional photolithography step. Since the front i-a-Si:H passivation/ARC structure resulted not effective, it has been replaced by 75 nm thick Silicon Nitride, to improve both passivation and optical properties. Two dimensional (2D) simulations have been performed [209] with the aid of Sentaurus software from Synopsys. A particular care have been spent in considering the (i) a-Si:H buffer layer properties and the interface with c-Si. It has been found the lower the thickness the higher the FF. Moreover the simulations have evidenced a monotonically dependence between FF and increasing B dopant concentration (*i.e.* the p-type a-Si:H conductivity), without affecting the V_{oc}. In particular moving the concentration by one order of magnitude, 78% FF without any "S shape" is achievable. However both V_{oc} and J_{sc} are lower in this case. Simulations suggest the

increased recombination velocity at the rear side is due to high doping level, both under emitter and in the gap region: increasing S_{eff} by 30 times lead to decrease of 30 mV and 3 mA/cm^2 on V_{oc} and J_{sc} respectively, without affective the FF, neither in negative nor in positive. From simulations it has been shown also the E_{gap} has its influence. When using intrinsic amorphous silicon with decreasing E_{gap}, the FF is enhanced, due to modification in band alignment and offsets. The reason is the less the barriers for the minority carrier (hole) for the lower bandgap, the more the Fill Factor.

Following simulations suggestions, new cells have been fabricated with narrower bandgap back surface buffer layer by decreasing the RF power in the (i) a-Si:H plasma deposition process, obtaining a thickness of 5 nm. Cell efficiency of 13.5% has been reached with V_{oc} and J_{sc} values lower than the expected.

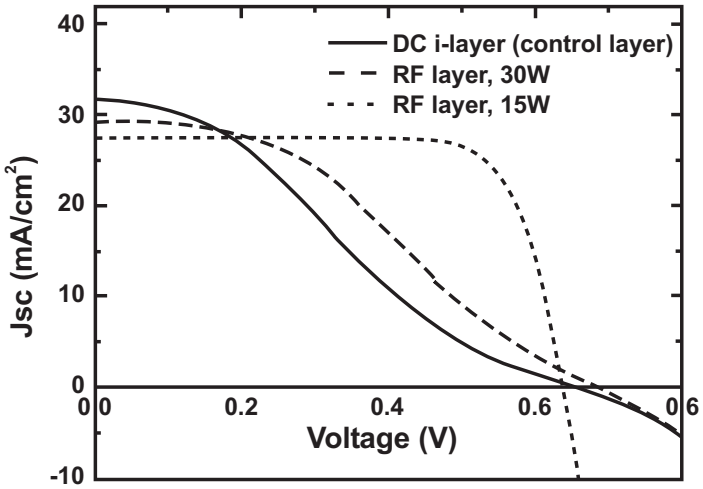


Figure 64: I-V characteristic of previous IBC-SHJ cell (straight line) and with reduced bandgap (*via* reduced RF power) a-Si:H buffer layer [209].

However from simulations it is possible to evaluate the potentiality of this structure. If the front surface recombination velocity is limited to 5 cm/s, the base contact width is reduced to 200 μm with simultaneous emitter enlargement, and a light trapping scheme is adopted it is possible to achieve 26%.

10.2. BACH Cell

Recently at University of Toronto has been presented the Back Amorphous-Crystalline silicon Heterojunction (BACH) cell, based on n-type 300 μm thick FZ wafer having resistivity around 20 Ω cm. Also in this case the fabrication process consists of different photolithographic steps with at least 4 photo masks. The process sequence comprises also initial oxidation of the n-type wafer to have surface passivation and electrical isolation between emitter and base contacts at the back side. The efficiencies of IBC cells having area of circa 1 cm^2 are quite low, with a maximum of 8.1%, having V_{oc} below 600 mV, and low short circuit current density below 20 mA/cm^2, nevertheless the front textured surface. However Fill Factors are appreciably higher than 75% [210]. The major limiting factor for both V_{oc} and J_{sc} is recognized to be surfaces passivation.

10.3. Helmholtz Zentrum

The first papers published by this group talking about RECASH (Rear Contacted Amorphous/crystalline Silicon Heterojunction) cells are dated to 2007 [211].

This device is a particular kind of heterostructure, which is not a proper interdigitated heterojunction, but an heterojunction with interdigitated. It consists of a base contact on p-type (FZ, 240 μm thick, 1 Ωcm resistivity) silicon substrate made by an e-beam evaporated Al grid (structured by photolithography) covered by an insulator, such as PECVD deposited SiO_2. The structuring of this oxide is done by HF etching, assisted with photolithography step.

Over the whole back surface but the busbar of the base contact, the a-Si:H n-type doped emitter, 30 nm thick, is deposited, followed by an e-beam Al evaporation to make the emitter contact. A 3rd photolithography step has been used to isolate the cells, to a final size is 1 cm^2. The sunward side, alkaline textured, is passivated by Silicon Nitride, which also acts as ARC.

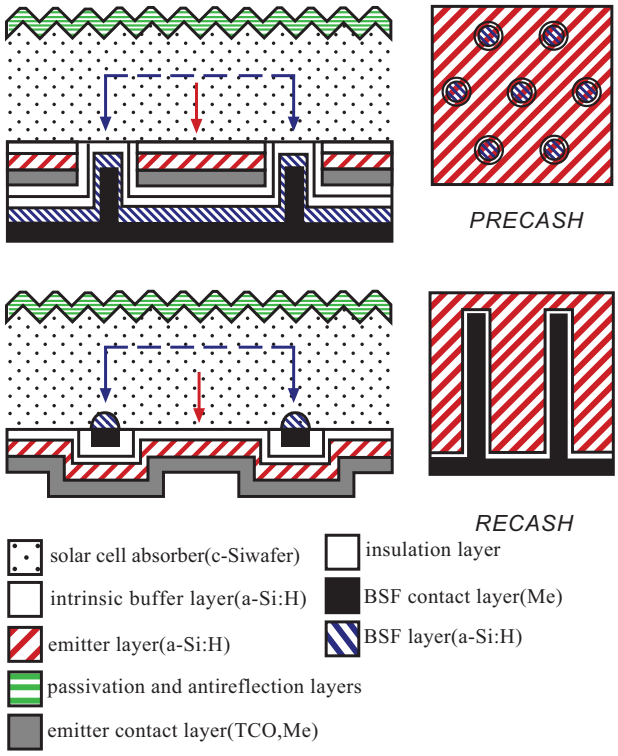


Figure 65: Sketch of RECACH and PRECACHcells in cross-section (left) and in longitudinal section (right), The inner arrows sketch the average traveling path of the absorber minority/majority excess carriers towards the contacts [213].

The point contacted version (PRECASH) instead consists of a textured front surface passivated by means of SiN_x. The whole back surface is instead covered by the a-Si emitter layer (n-type doped) contacted by e-beam evaporated Aluminium. Then a structuring with point-like opening is

produced by photolithography and electrically insulated by using SiO_2. Then p-type a-Si is deposited and contacted by e-beam evaporated Aluminium. In this way the most back surface is covered by the emitter, while the point contacts are just for the base [212]. In Fig. **65** the scheme of both cell structures are shown.

The authors (Stangl *et al.)* remark the photolithography has been used to provide a proof of concept and other technologies for base grid burying and patterning can be used, like Oxides growth by electrochemical oxidation or screen printing or inkjet. However, at the moment none of this technologies have applied to the RECASH cells [214].

The cells optimization and limits understanding have been done comparing the PRECASH structure with a reference cell having front emitter, with the aid of AFORS-HET software simulation [93]. The model is in 1D, with an approximation: the base back contact Al grid is modelled with a fictive front contact with S=30 cm/s due to SiN_x passivation. The BSF p-type layer is similar in both cell structures chosen to give a similar passivation level. The main differences are the side of minority carrier collection (front for reference, back for RECASH) and the absence of TCO front absorption and front shadowing for the back contact cell. Depending on the wafer quality in terms of diffusion length, the RECACH cell has higher efficiency if $\tau > 130$ μs for 275 μm wafer thick. In particular if the diffusion length higher than 2 mm then 24% is achievable. However, using wafers with 1 ms bulk lifetime, and the n-a-Si:H actual parameters (as measured from deposited layers) this limit does not exceed 21% [211]. The efficiencies obtained so far, with I-V characteristics reported in Fig. **66**, are of 8.1% for PRECASH and 13.9% for RECACH [214].

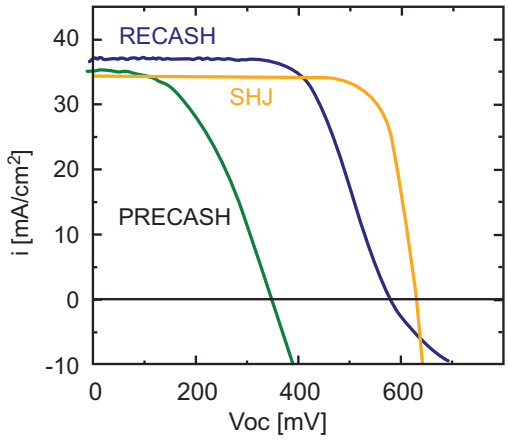


Figure 66: Measured I-V characteristic under AM1.5 of PRECASH and RECACH cell compared to a standard SHJ cell [213].

Very recently, in early 2011, a group form the same institute together with ISFH group have reached a 20.2% IBC-SHJ cell [215] based on the same structure proposed by Lu *et al.* [208] on n-type 3 Ωcm FZ substrate. The front side is textured and phosphorous diffused to form a Front Surface Field, then passivated by means of Silicon Oxide and SiN_x. The back side has 60% area coverage by emitter strips (p-type), 28% BSF strips (n-type) and 12% of gap space between these,

passivated by a SiO_2/SiN_x stack, with pitch in the range of millimetres. The metal contact is Aluminium for both emitter and BSF regions.

Two different approaches have been considered: with or without intrinsic buffer layer just under the emitter, obtaining in both cases nearly 20% efficiency. In the first case V_{oc} is 40 mV higher (673 mV), but he FF is nearly 3% absolute less (75.7%); due to the short circuit current density (39.7 mA/cm^2) the efficiency s 20.2%. Without any buffer the V_{oc} is less (633 mV) but the FF of course is higher (78.8%) with the same current, so that the efficiency is 19.8%. Both cell structures and I-V curves are depicted in Fig. **67**.

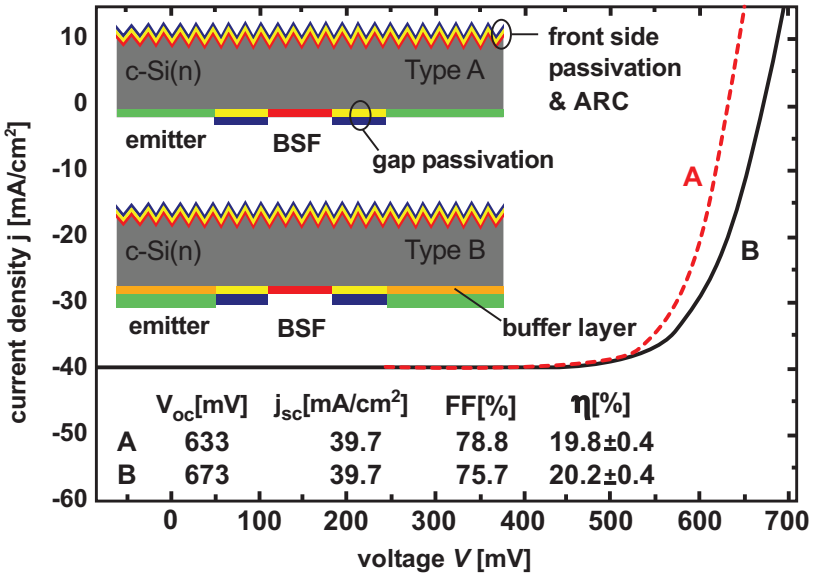


Figure 67: New cell structure produced at Helmholtz Zentrum and their results in term of I-V curves and PV parameters [215].

10.4. IMEC

They started from CZ n-type, 3-4 Ω.cm (100) silicon, with thickness of either 150 or 280 µm.

Different front side passivation have been adopted: n^+ diffusion ($POCl_3$) and HJ on both textured and flat surface. Then on the rear side of the wafer the (i) a-Si:H passivation layer, and doped (p+) emitter have been deposited by PECVD at temperatures less than 200°C. An indium tin oxide (ITO) transparent conductive oxide has been deposited on the a-Si:H layers. Photoresist has been spun on both sides of the wafer, and patterned on the rear side, before etching through the ITO. Openings through the a-Si:H have been performed by wet etching, and immediately prior to Al base deposition, an HF dip has been performed. Aluminium base contacts has been deposited by e-beam evaporation, and following Al lift off/resist removal (in acetone and IPA), the emitter contact Ti/Pd/Ag has been deposited on the ITO layer using shadow masks during e-beam evaporation. A final anneal has been performed in N_2 at low temperature. In Fig. **68** the schematic cross section of the cell is reported in Fig. **68** together with the photovoltaic sunlighted I-V characteristic of each cell.

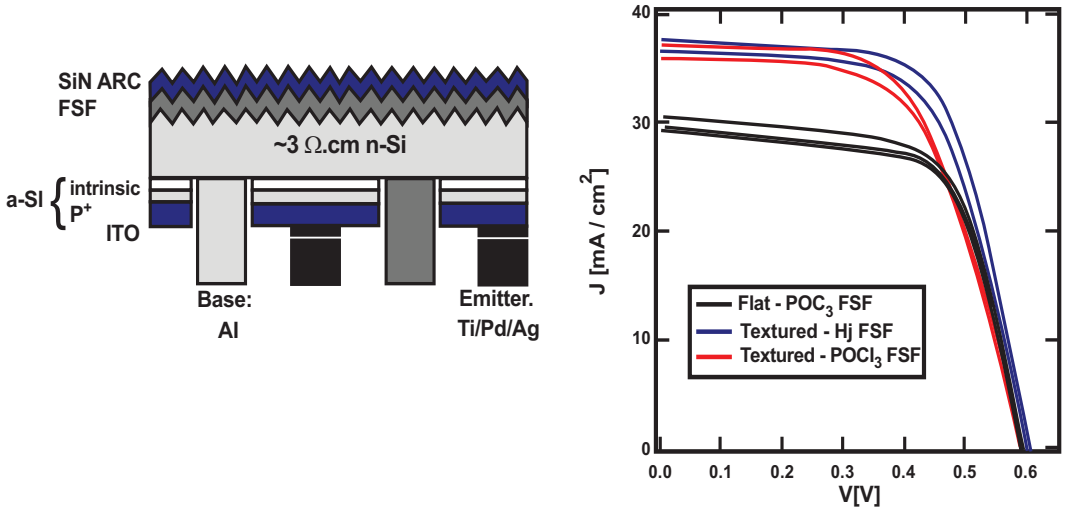


Figure 68: Schematic cross section of the cell (left) and relative I-V characteristic (right) [216].

Textured front side has ensured higher J_{sc} of course, but the V_{oc} as well as the FF are quite low to reach the expected high efficiency, maybe due to poor c-Si surface passivation by low quality a-Si:H layer. Nevertheless 15.2% efficiency has been achieved on 1cm^2 area [216].

10.5. CEA-INES

The earlier publications of CEA-INES about this topic are dated to 2008 [217, 218]. The solar cell architecture is very similar to those illustrated for University of Delaware. It is based on n-type wafers, with back interdigitated heterojunction and contacts. The difference is in the cell size (25 cm^2) and of course in the processing which completely avoid both high temperature and photolithography steps.

Before producing solar cells, the structure, illustrated in Fig. **69**, has been numerically simulated by means of ATLAS software from Silvaco [217, 219, 220]. It has been found a series of relationships between absorber and amorphous silicon properties and geometries and the final performances. As the base doping concentration increases (*i.e.* less resistive substrate) the short circuit current decreases because of the degradation of carrier lifetime. On the contrary, the Fill Factor increases because of the higher conductivity. Then an optimum doping concentration lays between $5x10^{16}$ and $1x10^{17}$ cm^{-3}. The bulk lifetime has a strong influence mainly to the J_{sc} and V_{oc} so that passing from 1.8 ms to 0.36 the efficiency drop is from 23.6 to 14%, keeping all other parameter fixed. The front surface passivation is the most critical parameter even for p-type substrates, having detrimental effect on both J_{sc} and V_{oc}. The BSF width (in the case of p-type substrate a p-type doped a-SI) is related to the Jsc, which increases when the BSF region decreases. The gap region between emitter and BSF strongly influences the current: the larger the gap, the lower the J_{sc}. Of course this effect is more pronounced for the lower passivation level achieved on this area. The coverage fraction of the emitter affects the FF linearly, so that the whole emitter area should be covered by the metal, and the contact resistance has to be, of course, as low as possible. Indeed decreasing from 1 to 0.1 Ω/cm^2 the FF can increase of 30% absolute.

Passing to a n-type substrates the picture is similar. In this case several difficulties have to be considered in the device design essentially due to the poor lateral conductivity of the emitter, since is p-type doped a-Si:H. Therefore in this case the use of high conductive layer on top of amorphous emitter, such as TCO, is mandatory to achieve cell efficiency.

Simulations with the ATLAS software have been performed also on a structure based on 300 μm n-ype wafer, with p-type a-Si:H emitter and n-type a-Si:H base contact/BSF with a gap region between them of circa 100 μm, as sketched in Fig. **69**. The results are similar to those obtained for p-type c-Si based cell. The V_{oc}'s, higher for higher bulk quality, increases with decreasing c-Si resistivity, but with a lower limit of 0.5 Ωcm. J_{sc} slightly decrease with increasing c-Si doping, but dramatically reduces, as also $V_{oc,}$ below 0.5 Ωcm. The FF shows an opposite behaviour, but the decrease for higher bulk resistivity is not so pronounced as for V_{oc} and J_{sc}. The result is that Efficiency, depending on the bulk material quality, can stay well above 20% for substrate resistivity in the range 0.6-30 Ωcm.

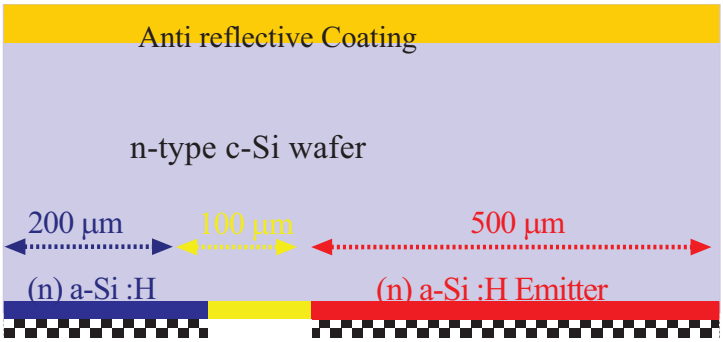


Figure 69: Device structure used in simulations with ATLAS software [221].

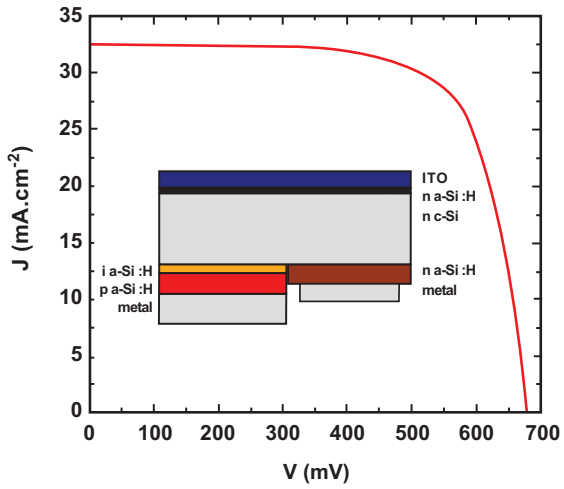


Figure 70: Cross section and sun lighted I-V characteristic of the IBC cell based on n-type c-Si wafer [223].

It is mandatory the $D_{it}(E)$ at interface between c-Si and doped a-Si:H stays below $5x10^{11}cm^{-2}$ to avoid any strong reduction in all photovoltaic parameters [221].

The presence of a Front Surface Field, produced with a Front diffusion or either a n-a-Si deposition is very important. It allows to obtain 20% efficient IBC-HJ cells even if the front surface recombination velocity S is up to hundreds cm/s [222]. Based on the simulations, the fabricated solar cells [223] started from high quality FZ 300 μm n-type wafers. Front ITO as ARC over a Front Surface Field produced by a n-type a-Si:H layer, reduces the S_{eff} down to 20 cm/s. On the back side an interdigitated pattern has been produced, with the base contact formed by a n-type a-SI:H layer directly deposited on the n-type c-Si and followed by a stack of 80 nm ZnO and 3 μm of Al. The emitter consists of an intrinsic a-Si:H as buffer layer and p-type doped a-Si:H layer, deposited at temperature around 200°C. To reduce the problem of poor lateral conductivity of p-type doped a-Si layer an emitter stack consisting in a-Si:H (i)/a-Si:H (p)/ZnO/Al has been chosen for the IBC structure. Then the emitter layer has been patterned in an interdigitated comb shape configuration using a screen-printing etching step, followed by a n-type a-Si:H base contact deposition. Finally a mask assisted process has been used to deposit a metal sheet on top of n-type a-Si:H base contact. This patterning process has not completely reduced the wafer surface passivation. On a 25cm^2 area an efficiency of 15.7 % (V_{oc} = 678 mV and J_{sc} = 32.4 mA/cm^2) has been achieved as reported in Fig. **70**. In the same figure the scheme of the device cross section is reported on the left side, together with the photovoltaic parameters of the IBC.

10.6. BEHIND Cell

At ENEA the work on interdigitated back contact heterojunction cells has started in 2006 and presented for the first time in 2007 [224]. The novel scheme for heterojunction has been named BEHIND: Back Enhanced Heterostructure with INterDigitated contact solar cell. What makes BEHIND cell different from other IBC-HJ is the fabrication method which do not involve chemical step for the patterning, neither photolithography nor etching. The back contact structuring is formed by using metallic mask assisted process, in which the alignment is self-mechanically achieved by adopting a specifically designed holder for the substrate and the masks. In principle this kind of concept can be scaled up in area and volume so that it has more appealing for industrial application with respect to other IBC approach reported above. The BEHIND concept can be applied to both p- and n-type substrates, however it has been optimized on the first one, renouncing on the benefits of n-type silicon, but taking advance of higher lateral conductivity of n-a-Si:H emitter, allowing to avoid TCO. While the earlier BEHIND cell used just one metallic mask to produce the interdigitated pattern after a rotation of 180 degrees within the holder [224], the best results have obtained employing two masks, one for the depositions and one for the metallization, with narrower finger [224]. It has been fabricated starting from a 200 μm thick, 1 Ωcm p-type, one side polished CZ mono-crystalline silicon wafer. After front side alkaline texturing and cleaning, the front side antireflection and passivation coating and the rear side emitter and back contact have been deposited in a 13.56 MHz direct Plasma Enhanced Chemical Vapour Deposition (PECVD) system. In particular for the front side a double layer stack of a-Si:H/SiN_x has been deposited [226] because of its demonstrated good passivation level, despite to a small absorption in the UV part of the sun spectrum. Then on the whole polished backside of the wafer, the emitter n-type doped a-Si:H layer has been deposited over an (i) a-Si:H buffer layer. A Chromium evaporation and following removal has been used to increase the emitter conductivity by formation of CrSi [227].

At this stage part of the emitter has been removed by using a plasma assisted dry etching procedure using NF_3 gas through the apertures of a metallic mask, fabricated from a 100 μm thick

Molybdenum foil. Subsequently, keeping the mask in the same position, the cell base contact has been formed by an intrinsic a-Si:H buffer and a p-type a-Si:H layers, followed by a δn-a-Si:H deposition useful to increase the conductivity of the a-Si layer [227]. Both doped a-Si have been deposited in a three-chamber having each chamber devoted to a specific doping type. Then another comb shaped aperture mask, having narrower fingers (halved) with respect to the previous mask, has been held and fixed on the rear side of the device. Through these apertures, a 30 nm thick Cr layer followed by 4 μm Al layer have been e-beam evaporated. Finally, the mask has been rotated 180 degrees and 4 μm of Ag have been evaporated to contact the emitter region, creating the interdigitated shape with respect to the base contact. The total area of the solar cell is 6.25 cm^2. A schematic cross section of the BEHIND cell is depicted in Fig. **71**, together with the experimental I-V characteristic measured at room temperature, under Class A calibrated to 100 mW/cm^2 AM1.5G sun simulator.

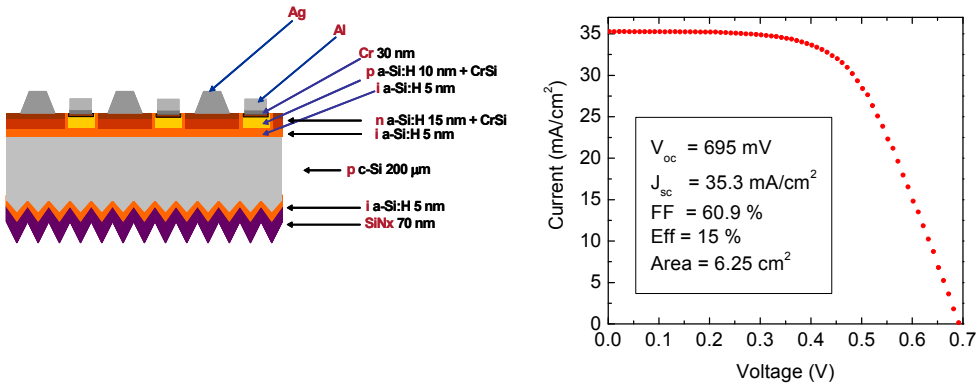


Figure 71: Schematic cross section of the BEHIND cell (left) and relative I-V characteristic (right) [228].

The solar cell efficiency, 15%, is the highest known at the moment on p-type based IBC-HJ. However it is limited by a low Fill Factor. The very high open circuit voltage V_{oc} = 695 mV confirms the effectiveness of the a-Si:H/c-Si heterojunction as the way to improve the silicon based solar cell efficiency. This result also confirms that the uniformity of the deposited amorphous silicon layers is not influenced by the mask-assisted deposition process even when multiple masks are used in the fabrication process. Indeed the alignment between masks and substrate is feasible and the regions where the doped layers can unfortunately overlap are isolated by the intrinsic a-Si:H. The key issues to obtain high J_{sc} depends on diffusion length, L_d, and front surface recombination velocity, $S_{n,p}$. In particular L_d and $S_{n,p}$ have been respectively estimated of 680 μm and 80 cm/s from a fitting procedure of the IQE reported in Fig. **72** [228] together with reflectance and EQE of the cell.

The weak point of this technology is the relatively high number of steps required to complete the cell.

Therefore a new simplified version of the BEHIND cell has been investigated in order to reduce the number of steps needed in the cell fabrication procedure and presented recently as BEHIND 2.0 [229]. This kind of structure also avoids the dry etching steps through masks, which are critical

in terms of reliability and reproducibility. The new scheme is based on the idea to deposit both the emitter and base amorphous contact on the same passivating intrinsic amorphous layer. The absorber is a p-type 1Ωcm CZ 200 μm thick double side polished c-Si wafer, having on the sunward side the same a-Si:H/SiN_x double layer shown before, having thicknesses of 10 nm and 65 nm respectively. After the deposition of 7 nm thick intrinsic a-Si:H buffer layer on the whole rear side of the wafer the interdigitated structure have been deposited in two steps by using two different metal (Molybdenum foil based) masks: "n-mask" for the emitter and "p-mask" for the base contact on purpose designed. The masks are in turn ensured in contact to the rear side of the wafer by using a specific designed holder. To form the n-type emitter it has been deposited the amorphous emitter layer and evaporated 100 nm of Cr to form the CrSi. Then, after un-set the "n-mask", the "p-mask" is used to deposit the amorphous base contact layer, an amorphous delta-n layer and finally evaporated the Cr to form the CrSi. To enhance the metallization thickness, instead of metal evaporation, a low temperature sintering (250°C for 15 minutes) Ag screen printing process for both contacts has been developed. The mask alignment is not critical since the n-type a-Si:H emitter width is three times wider than the p-type a-Si:H region. Finally a SiN_x layer has been deposited over the entire rear side (except the two cell bus bars) to enhance the of the region not covered by emitter or base contact [199] A sketch of the new structure, together with picture of the screen printed interdigitated metal electrodes is reported in Fig. **73**. Despite of the simplified process, two main point has to be addressed:

1) The a-Si:H rear surface passivation layer thickness should be sufficiently thin to avoid a barrier effect against carrier transport, but sufficiently thick to ensure crystalline surface passivation in the region not covered by doped amorphous layers.

2) The distance between the two patterns, which cannot be in intimate contact, to avoid strong recombination, but at a feasible distance, to avoid photolithographic steps.

To exploit these two points 2D numerical simulation have been performed with ATLAS software [219]. In particular the doping density of each layer has been chosen taking into account the activation energies of doped amorphous films as already mentioned in Table **1**. The intrinsic layer thickness has been varied in the range from 3.5 nm to 14 nm. It has been found that increasing the i-a-Si:H layer thickness the lighted I-V characteristics, simulated under standard AM1.5G condition, has been strongly affected resulting in a fill factor reduction. This effect is related to the recombination at the a-Si:H/c-Si interface. Indeed when the (i) a-Si:H layer becomes thicker, the p-type a-Si:H base contact is not able to collect the holes due to the valence band offset at the edge of a-Si:H/c-Si interface These holes can recombine through a-Si:H/c-Si interface defects with electrons generated in the c-Si side of the device and diffusing also toward the rear side of the device. This reflects in a barrier against carrier collection from the base contact that can be regarded as a double diode (in anti-series) [229]. From the simulated lighted I-V characteristics as a function of intrinsic layer thickness it has been understood that increasing the (i) a-Si:H layer thickness an S shape curve in the I-V characteristic occurs. Indeed also several interdigitated structures have been simulated having different distance between the two doped contacts, varied from 4 μm to 90 μm. These simulations remarked that to achieve the best efficiency the distance between doped contacts should be as short as possible; otherwise a reduction of fill factor occurs. This effect is due to the absence of electric field in crystalline region covered only by the intrinsic a-Si:H layer which favorites the recombination Indeed if the density of states in the i-a-Si:H layer

were increased from 10^{17} cm^{-3} to 10^{18} cm^{-3} the recombination would be stronger and its effect on the I-V characteristic would be dramatic with the presence of a S shape. Unfortunately in practice it is evident the difficulty to obtain a distance between the two doped contacts as short as 4 μm without any photolithographic process.

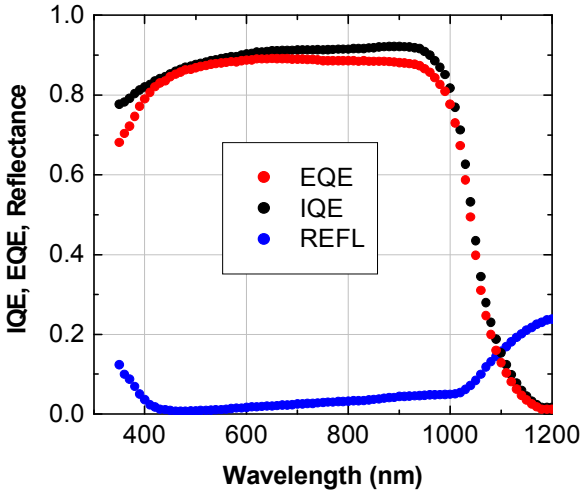


Figure 72: Reflectance, Internal and External Quantum Efficiency of the BEHIND Cell [228].

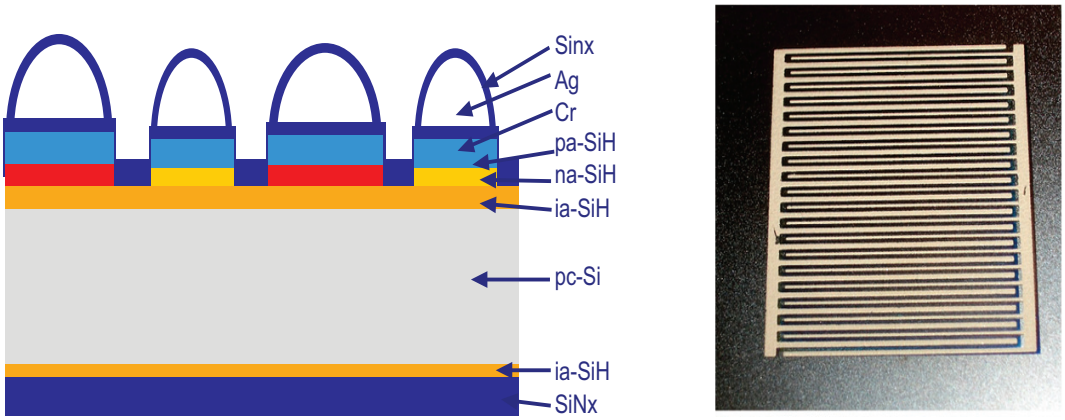


Figure 73: BEHIND 2.0 structure, with a picture of interdigitated screen printed silver electrodes.

Nevertheless several experiments have been performed to evaluate the proposed structure and to validate the simulations. The experimental I-V characteristic in this study have been measured at room temperature, calibrated to 100 mW/cm^2 and AM1.5G illumination and are shown in the Fig. **74**. The difference between the two samples consists of spacing width between the n and p type

regions, in case of A-sample this width is 100 μm, while for the B-sample this distance is 200 μm. Moreover the SiN_x deposition over the rear side of the structure, proposed to enhance the surface passivation in the gap region, even if is able to enhance the V_{oc} of 10 ÷ 15 mV with respect to the values measured before the SiN_x deposition, is not sufficient to recover the S shape of the I-V characteristic, probably due to its positive charges that recall electrons close to the c-Si/a-Si:H interface.

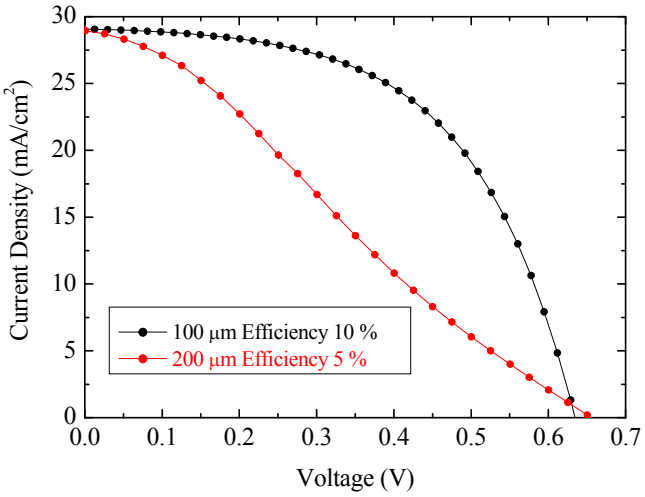


Figure 74: Sun lighted I-V as a function of distance between base and emitter contacts. Front side of the cell is not textured [229].

I-V characteristic of sample A seems not affected by the barrier against carrier collection and thus is free from the S shape, but the fill factor of sample A is far from the ideality. This effect can be related to two main reasons. The first to the a-Si:H/c-Si interface defects that affect the transport mechanism toward the doped contacts. The latter to shunt effect arising from screen printing process not perfectly aligned with the underneath Cr contacts. Nevertheless the cell efficiencies have not exceeded the 12%, so it can be concluded that the gap between the base and emitter contact is the main limitation of the simplified cell design.

ACKNOWLEDGEMENT

Declared none.

CONFLICT OF INTEREST

The author(s) confirm that this chapter content has no conflict of interest.

REFERENCES

[1] Fhus W, Niemann K, Stuke J. Heterojunctions of amorphous silicon and silicon single crystals. Proceedings of AIP Conference; 1974 Mar 20-22; Yorktown Heights, NY, USA 1974; pp. 345-350.

[2] Okuda K, Okamoto H, Hamakawa Y. Amorphous Si polycrystalline Si stacked solar cell having more than 12 percent conversion efficiency. Jpn J Appl Phys 1983; 22/9: L605-L607.

[3] Rahman MN, Furukawa S. Preparation and electrical properties of an amorphous SiC/crystalline Si p^+-n heterostructure. Jpn J Appl Phys 1984: 23(5); 515-524.

[4] Matsuura H. Hydrogenated amorphous silicon/crystalline silicon heterojunctions: properties and applications, IEEE Trans El Dev, 1989; 36: 2908-2914.

[5] Mimura H, Hatanaka Y. Carrier transport mechanisms of p-type amorphous-n-type crystalline silicon heterojunctions. J Appl Phys 1992; 71(5): 2315-2320.

[6] Matsuura H, Okuno T, Okushi H, *et al.* Electrical properties of n-p amorphous-crystalline silicon heterojunctions. Extended Abstract of 15th Conf on Solid State Devices and Materials, 1984; pp.185-188.

[7] Matsuura H., Okuno T, Okushi H, *et al.* Electrical properties on n-amorphous/p-crystalline silicon heterojunctions. J Appl Phys 1984; 55(4):1012-1020.

[8] Matsuura H, Matsuda A, Okushi H, *et al.* Metal-semiconductor junctions and amorphous-crystalline heterojunctions using B-doped hydrogenated amorphous silicon. Appl Phys Lett 1984;45(4):433-435.

[9] Patella F, Evangelisti F, Fiorini P, *et al.* Photoemission studies of amorphous silicon heterostructures. Proceedings of AIP Conference 1984 Ed. P.G. Taylor and S.G. Bishop 1984; No.120, pp. 402-409.

[10] Zhao J, Wang A., Green, MA. 24.5% Efficiency Silicon PERT Cells on MCZ Substrates and 24.7% Efficiency PERL Cells on FZ Substrates. Prog in Photovol 1999; 7: 471-474.

[11] Tanaka M, Taguchi M, Matsuyama T, *et al.* Development of new a-Si/c-Si heterojunction solar cells: ACJ-HIT (Artificially Constructed Junction-Heterojunction with intrinsic layer). Jpn J Appl Phys, 1992; 31:3518-3522.

[12] Sawada T, Terada N, Tsuge S, *et al.* High-efficiency a-Si/c-Si heterojunction solar cell. Proceedings of the 1st WCPEC, 1994; Hawaii, USA 1994. pp. 1219-1232.

[13] Taguchi M, Kawamoto K, Tsuge S, *et al.* HIT cells-high efficiency crystalline Si cells with novel structure. Prog Phototovolt Res Appl 2000; 8: 503-510.

[14] Sakata H, Tsunomura Y, Inoue H, *et al.* R&D Progress of Next-Generation Very Thin HITtm Solar Cells. Proceedings of the 25th EUPVSEC 2010 Sept 6-10; Valencia, Spain 2010; pp. 1102-1106.

[15] Taguchi M, Tsunomura Y, Inoue H, *et al.* High-Efficiency HIT Solar Cell on Thin (< 100 μm) Silicon Wafer. Proceedings of the 24th EUPVSEC 2009 Sept 21-25; Hamburg, Germany 2009: pp. 1690-1693.

[16] Available from: http://www.roth-rau.de

[17] Staebler DL, Wronski CR. Reversible conductivity changes in discharge produced amorphous Si. Appl Phys Lett, 1977; 31: 292-294.

[18] Henley F, Lamm A, Kang S, *et al.* Direct film transfer (DFT) technology for kerf-free silicon wafering. Proceedings of the 23rd EUPVSEC 2008 Sept 6-9; Valencia, Spain 2008; pp.1090-1093.

[19] Tamm IE. Phys Z. Sowjetunion 1932; 1: 733.

[20] Shockley W. On the Surface states associated with a periodic potential. Phys Rev 1939; 56: 317-323.

[21] Brodsky MH, Dohler GH, Steinhard PJ. On the measurement of the conductivity density of states of evaporated amorphous silicon films. Phys Status Solidi B 1975; 32: 420-440.

[22] Bar-Yam Y, Joannopoulos JD. Dangling bond in a-Si:ZZH. Phys Rev Lett, 1986; 56: 2203-2206,

[23] Madan A, Shaw MP. The physics and application of amorphous semiconductors. Hartcourt Brace Jovanovich, Publishers, Accademic Press Inc. 1988; p.165.

[24] Branz HM, Silver M. Potential fluctuations due to inhomogeneity in hydrogenated amorphous silicon and resulting charged dangling bond defects. Phys Rev B 1990; 42: 7420-7428.

[25] Winer K. Defect formation in a-Si:H. Phys Rev B 1990; 41: 12150-12161.

[26] Powell MJ, Deane SC. Improved defect-pool model for charged defects in amorphous silicon. Phys Rev B 1993; 48: 10815-10827.

[27] Shockley W, Read WT. Statistic of the recombination of holes and electrons. Phys Rev 1952; 87: 835-842.

[28] Hall RN. Electron-Hole Recombination in Germanium. Phys Rev B 1952; 87: 387-387.

[29] Simmons JG, Taylor GW. Nonequilibrium Steady-State Statistics and Associated Effects for Insulators and Semiconductors Containing an Arbitrary Distribution of Traps. Phys Rev B 1971; 4: 502-511.

[30] Olibet S, Vallat-Sauvain E, and Ballif C. Model for a-Si:H/c-Si interface recombination based on the amphoteric nature of silicon dangling bonds. Phys Rev B 2007; 76: 035326.

[31] Aberle AG, Glunz S, Warta W. Impact of illumination level and oxide parameters on Shockley-Read-Hall recombination at the Si-SiO2 interface. J Appl Phys 1992; 71: 4422-4431.

[32] Schroder DK. Semiconductor Material and Device Characterization, Wiley-Interscience, Hoboken, NJ, 3rd ed. 2006; p. 250.

[33] Pankove JI, Lampert MA, and Tarng ML. Hydrogen passivation of dislocations in silicon. Appl Phys Lett 1978; 32: 439-441.

[34] Yablonovitch E, Allara DL, Chang CC, *et al.* Unusually Low Surface Recombination Velocity on Silicon and Germanium Surfaces. Phys Rev Lett 1986; 57: 249-252.

[35] Pankove JI, Tarng ML. Amorphous silicon as a passivant for crystalline silicon. Appl Phys Lett 1979; 34: 56-58.

[36] Tarng ML, Pankove JI. Passivation of p-n junction in crystalline silicon by amorphous silicon. IEEE Trans Electron Dev 1979; 26: 1728-1734.

[37] Weitzel R, Primig R, and Kempter K. Preparation of glow discharge amorphous silicon for passivation layers. Thin Solid Films 1981; 75: 143-150.

[38] De Wolf S, Kondo M. Abruptness of a-Si:H/c-Si interface revealed by carrier lifetime measurements. Appl Phys Lett 2007; 90: 042111.

[39] Fujiwara H, Kondo M. Real-time monitoring and process control in amorphous/crystalline silicon heterojunction solar cells by spectroscopic ellipsometry and infrared spectroscopy. Appl Phys Lett 2005; 86: 032112.

[40] Schulze TF, Beushausen HN, Hansmann T, *et al.* Accelerated interface defect removal in amorphous/crystalline silicon heterostructures using pulsed annealing and microwave heating. Appl Phys Lett 2009; 95: 182108.

[41] Strahm B, Andrault Y, Bätzner D, Lachenal D, *et al.* Amorphous and Polycrystalline Thin-Film Silicon Science and Technology. Proceedings of the Mater Res Soc Symp 2010 San Francisco CA, USA; 1245 A01-04.

[42] Damon-Lacoste J, Fesquet L, Olibet S, *et al.* Ultra-high quality surface passivation of crystalline silicon wafers in large area parallel plate reactor at 40 MHz. Thin Solid Films 2009; 517: 6401-6403.

[43] Descoeudres D, Barraud L, Bartlome R, *et al.* Optimization of high efficiency heterojunction solar cell using silane-plasma diagnostic. Proceedings of the 25th EUPVSEC 2010 Sept 6-10; Valencia, Spain 2010; pp. 2069-2073.

[44] De Wolf S, Olibet S, Ballif C, Stretched-Exponential a-Si:H/c-Si interface recombination decay. Appl Phys Lett 2008; 93: 032101.

[45] Das UK, Burrows MZ, Lu M, *et al.* Surface passivation and heterojunction cells on Si (100) and (111) wafers using dc and rf plasma deposited Si:H thin films. Appl Phys Lett 2008; 92: 063504.

[46] Gielis JJH, Van den Oever PJ, Hoex B, *et al.* Real-time study of a-Si:H/c-Si heterointerface formation and epitaxial Si growth by spectroscopic ellipsometry, infrared spectroscopy, and second-harmonic generation. Phys Rev B 2008; 77: 205329.

[47] Wang Q, Page MR, Iwaniczko E, *et al.* Efficient heterojunction solar cells on p-type crystal silicon wafers. Appl Phys Lett 2010; 96: 013507.

[48] Fujiwara H, Kondo M. Interface structure in a-Si:H/c-Si heterojunction solar cells characterized by optical diagnosis technique. Proceedings of the 4th WCPSEC 2006, May 7–12 Waikoloa, Hawaii, USA; pp.1443-1448.

[49] Biegelsen DK, Johnson NM, Stutzmann M, *et al.* Native defects at the Si/SiO_2 interface-amorphous silicon revisited. Appl Surf Sci 1985; 22/23: 879-890.

[50] Sinton RA, Cuevas A. Contactless determination of current–voltage characteristics and minority carrier lifetimes in semiconductors from quasi-steady-state photoconductance data. Appl Phys Lett 1996; 69: 2510-2512.

[51] Kohlrausch R, Pogg H. Theorie des elektrischen Rückstandes in der Leidener Flasche. Ann Phys Chem 1854; 167(2): 179-214.
[52] Williams G, Watts DC. Non-symmetrical dielectric relaxation behaviour arising from a simple empirical decay function. Trans. Farad. Soc. 1970; 66: 80-85.
[53] Cardona M, Chamberlin RV, Marx W. The history of the stretched exponential function. Ann Phys 2007; 16: 842-845.
[54] Kakalios J, Street RA, Jackson WB. Stretched-exponential relaxation arising from dispersive diffusion of hydrogen in amorphous silicon. Phys Rev Lett 1987; 59: 1037-1040.
[55] Kerr MJ, Cuevas A. General parameterization of Auger recombination in crystalline silicon. J Appl Phys 2002; 91: 2473-2480.
[56] Korte L, Conrad E, Angermann H, *et al.* Advances in a-Si:H/c-Si heterojunction solar cell fabrication and characterization. Sol En Mat Sol Cells 2009; 93: 905-910.
[57] Johnson NM, Ponce FA, Street RA, *et al.* Defects in single-crystal silicon induced by hydrogenation. Phys Rev B 1987; 35: 4166-4169.
[58] Tsai CC, Anderson GB, Thompson R. Low temperature growth of epitaxial and amorphous silicon in a hydrogen-diluted silane plasma. J Non-Cryst Solids 1991; 137: 673-676.
[59] Eaglesham J, Gossmann HJ, Cerullo M. Limiting thickness h_{epi} for epitaxial growth and room-temperature Si growth on Si(100). Phys Rev Lett. 1990; 65. 1227-1230.
[60] Schwarzkopf J, Selle B, Bohne W, *et al.* Disorder in silicon films grown epitaxially at low temperature. J Appl Phys 2003; 93: 5215-5222.
[61] Teplin CW, Iwancziko E, To B, *et al.* Breakdown physics of low-temperature silicon epitaxy grown from silane radicals. Phys Rev B 2006; 74: 235428-33.
[62] Tsai CC, Anderson GB, Thompson R. Low temperature growth of epitaxial and amorphous silicon in a hydrogen-diluted silane plasma. J Non-Cryst Solids 1991; 137: 673-677.
[63] Tucci M, De Rosa R, Roca F, CF_4/O_2 dry etching of textured crystalline silicon surface in a-Si:H/c-Si heterojunction for photovoltaic applications. Solar Energy Materials and Solar Cells; 2001; 69/2: 175-178.
[64] Carabe J, Gandia JJ, Influence of interface treatments on the performance of silicon heterojunction solar cells. Thin Solid Films 2002; 403-404: 238–241.
[65] Wang Qi, Page MR., Iwaniczko E, *et al.* Efficient heterojunction solar cells on *p*-type crystal silicon wafers. Appl Phys Lett 2010; 96: 013507.
[66] Wang TH, Iwaniczko E, Page MR, *et al.* Effect of emitter deposition temperature on surface passivation in hot-wire chemical vapor deposited silicon heterojunction solar cells. Thin Solid Films 2006; 501: 284-287.
[67] Sebastiani M, Gaspare LD, Capellini G, *et al.* Low Energy yield spettroscopy as a novel technique for determining band offsets: application to the c-Si (100)/a-Si:H heterostructure. Phys Rev Lett 1995; 75: 3352-55.
[68] Damon-Lacoste J. Roca i Cabarrocas P. Toward a better physical understanding of a-Si:H/c-Si heterojunction solar cells. J Appl Phys 2009; 105: 063712.
[69] Schulze TF., Beushausen HN, Hansmann T *et al.* Accelerated interface defect removal in amorphous/crystalline silicon heterostructures using pulsed annealing and microwave heating. Appl Phys Lett 2009; 95: 182108.
[70] Burrows MZ, Das UK, Bowden S *et al.* Improved Passivation of a-Si:H/c-Si Interfaces Through Film Restructuring. Proceedings of Mater Res Soc Symp 2008 San Francisco CA, USA; 1066, 1066–A02–05.
[71] Street RA, Tsai CC, Kakalios J *et al.* Hydrogen diffusion in amorphous silicon. Philos Mag B 1987; 56: 305-320.
[72] Beyer W. Hydrogen effusion: a probe for surface desorption and diffusion. Physica B 1991; 170: 105-114.
[73] De Wolf S, Kondo M. Boron-doped a-Si:H/c-Si interface passivation: Degradation mechanism. Appl Phys Lett 2007; 91: 112109.

[74] De Wolf S, Kondo M. Nature of doped a-Si:H/c-Si interface recombination, J Appl Phys 2009; 105: 103707.
[75] Beyer W, Zastrow U. Dependence of H Diffusion in Hydrogenated Silicon on Doping and the Fermi Level. Proceedings of Mat Res Soc Symp 2000 San Francisco CA USA; 609, A20.4.1.
[76] Beyer W. Semicond. and Semimetals. 61 Academic, San Diego, 1999 p.165.
[77] Street RA. Hydrogen diffusion and electronic metastability in amorphous silicon. Physica B 1991; 170: 69-81.
[78] Van de Walle CG, Street RA. Silicon-hydrogen bonding and hydrogen diffusion in amorphous silicon. Phys Rev B 1995; 51: 10615-18.
[79] Spear WE, Le Comber PG. Substitutional doping of amorphous silicon. Solid State Comm 1975; 17: 1193-1196.
[80] Street RA. Localized states in doped amorphous silicon. J Non-Cryst Solids 1985; 77&78: 1-16.
[81] Branz HM, Crandall RS. Defect equilibrium thermodynamics in hydrogenated amorphous silicon: Consequences for solar cells. Solar Cells 1989; 27: 159-168.
[82] Tucci M. Optimization of n-doping in n-type a-Si:H/p-type textured c-Si heterojunction for photovoltaic applications. Solar Energy Materials and Solar Cells, 1999; 57: 249-257.
[83] List RS, Spider WE. Can photoemission measure valence-band discontinuities? J Vac Sci Technology B 1988; 6: 1228-1234.
[84] Jackson WB, Kelso SM, Tsai CC *et al.* Energy dependence of the optical matrix element in hydrogenated amorphous and crystalline silicon. Phys Rev B 1985; 31: 5187-98.
[85] Schmidt M, Schoepke, Korte L, *et al.* Density distribution of gap states in extremely thin a-Si:H layers on crystalline silicon wafers J of Non-Cryst Solid 2004; 338–340: 211–214.
[86] Korte L, Schmidt M. Investigation of gap states in phosphorous-doped ultra-thin a-Si:H by near-UV photoelectron spectroscopy. J of Non-Cryst Solids 2008; 354: 2138–2143.
[87] Korte L, Laades A, Schmidt M. Electronic states in a-Si:H/c-Si heterostructures. J of Non-Cryst Solids 2006; 352: 1217–1220.
[88] Stutzmann M. The defect density in amorphous silicon. Phylos Mag B 1989; 60: 531-546.
[89] Hata N, Wagner S, Roca y Cabarrocas P, *et al.* Deposition induced defect profile in amorphous hydrogenated silicon. Appl Phys Lett 1990; 56: 2448-2450.
[90] Lam YW. Surface-state density and surface potential in MIS capacitors by surface photovoltage measurements. J Phys D: Appl Phys 1971; 4: 1370-1375.
[91] Fussel W, Schmidt M, Angermann H, *et al.* Defects at the Si/SiO_2 interface: Their nature and behaviour in technological processes and stress. Nucl Instrum Methods Phys Res B 1996; 377: 177-183.
[92] Schmidt M, Korte L, Laades A, *et al.* Physical aspects of a-Si:H/c-Si hetero-junction solar cells. Thin Solid Films 2007; 515: 7475–7480.
[93] Available from: www.helmholtz-berlin.de/forschung/enma/si-pv/projekte/asicsi/afors-het/index_en.html
[94] Korte L, Conrad E, Angermann H, *et al.* Overviev on a-Si:H/c-Si heterojunction solar cells Physics and technology. Proceedings of the 22nd EUPVSEC Milan Italy 2007; pp. 859-865.
[95] Taguchi M, Terakawa A, Maruyama E, *et al.* Obtaining a Higher Voc in HIT Cells. Prog Photovolt: Res Appl 2005; 13:481-8.
[96] Kern W. The Evolution of Silicon Wafer Cleaning technology. J Electrochem Soc 1990; 137(6):1887-92.
[97] Eades W, Swanson R. Improvements in the determination of interface state density using deep level transient spectroscopy. J Appl Phys 1984; 56(6):1744-51.
[98] Eades W, Swanson R. Calculation of surface generation and recombination velocities at the Si-Si02 interface. J Appl Phys 1985; 58(11): 4267-76.
[99] Angermann H, Rappich J, Korte L, *et al.* Wet-chemical passivation of atomically flat and structured silicon substrates for solar cell application. Appl Surf Sci 2008; 254: 3615-25.

[100] Chabal Y, Higashi G, Raghavachari K, *et al.* Infrared spectroscopy of Si(111) and Si(100) surfaces after HF treatment: Hydrogen termination and surface morphology. J Vac Sci Technol 1989; A7(3): 2104-9.
[101] Intelmann C, Hinrichs K, Syritski V, *et al.* Recombination Behaviour at the Ultrathin Polypyrrole Film/Silicon Interface Investigated by *In situ* Pulsed Photoluminescence. Jap J Appl Phys 2008; 47(1): 554-7.
[102] Rappich J, Fahoume M. Nonradiative recombination and band bending of p-Si(100) surfaces during electrochemical deposition of polycrystalline ZnO. Thin Solid Films 2005; 487: 157-61.
[103] Aberle A. Surface passivation of crystalline silicon solar cells: a review. Prog Photovolt: Res Appl 2000; 8(5): 473-87.
[104] Kern W. Handbook of Silicon Wafer Cleaning Technology, Edited by Reinhardt KA, Kern W, 2nd Edition. William Andrew Inc. 2008; pp. 3-92.
[105] Bearda T, Martens PW, Beaudoin SP. Handbook of Silicon Wafer Cleaning Technology, Edited by Reinhardt KA, Kern W, 2nd Edition. William Andrew Inc. 2008; pp. 93-164.
[106] Nishi Y, Doering R. Handbook of Semiconductor Manufacturing Technology. New York: Marcel Dekker Inc 2000.
[107] Gale GW, Small RJ, Reinhardt KA. Handbook of Silicon Wafer Cleaning Technology, Edited by Reinhardt KA, Kern W, 2nd Edition. William Andrew Inc. 2008; pp. 201-65.
[108] Kern W, Puotinen D. Cleaning solutions based on hydrogen peroxide for use in silicon semiconductor technology. RCA Review 1970; 31(6): 187-206.
[109] Kern W. Radiochemical study of semiconductor surface contamination, I. Adsorption of reagent components. RCA Review 1970; 31(6): 207-33.
[110] Kern W. Radiochemical study of semiconductor surface contamination, II. Deposition of trace impurities on silicon and silica. RCA Review 1970; 31(6): 234-64.
[111] Hiemenez P, Rajagopalan R. Principles of Colloid and Surface Chemistry. 3rd ed. New York: Marcel Dekker Inc 1997.
[112] Schwartzman S, Mayer A, Kern W. Megasonic Particle Removal from Solid State Wafers. RCA Review 1985; 46: 81-105.
[113] Bailey WL, Coleman MG, Harris CB, Lesk IA. Texture etching of silicon: method. US 4137123. 1979 Jan.
[114] Holdermann K. Method for the wet chemical pyramidal texture etching of silicon surfaces. US 6451218 B1. 2002 Sep.
[115] Inomata Y, Fukui K, Shirasawa K, *et al.* Surface texturing of large area multicrystalline silicon solar cells using reactive ion etching method. Sol Energy Mater Sol Cells 1997; 48: 237-42.
[116] Einhaus R, Vazsonyi E, Szlufcik J, *et al.* Isotropic texturing of multi-crystalline silicon wafers with acidic texturing. Proceedings of the 26th IEEE PVSEC; 1997: Anaheim, California: 1997, pp. 167-70.
[117] Angermann H. Characterization of wet-chemically treated silicon interfaces by surface photovoltage measurements. Anal Bioanal Chem 2002; 374: 676-80.
[118] Angermann H, Rappich J, Klimm C. Wet-chemical treatment and electronic interface properties of silicon solar cell substrates. Cent Eur J Phys 2009; 7(2): 363-70.
[119] Laades A, Brauer J, Stürzebecher U, *et al.* Wet-chemical treatment of solar grade CZ silicon prior to surface passivation. Proceedings of the 24th EUPVSEC; 2009: Hamburg, Germany: WIP Renewable Energies, pp. 1640-4.
[120] Lauer K, Laades A, Ubensee H, *et al.* Detailed analysis of the microwave-detected photoconductance decay in crystalline silicon. J Appl Phys 2008; 104: 104503-9.
[121] Yang S, Peter S, Takoudis C. Fundamentals of two-step etching techniques for ideal silicon-hydrogen termination of silicon(111). J Appl Phys 1994; 76(7): 4107-12.
[122] Angermann H, Rappich J, Sieber I, *et al.* Smoothing and passivation of special Si(111) substrates: studied by SPV, PL, AFM and SEM measurements. Anal Bioanal Chem 2008; 390: 1463-70.
[123] Angermann H. Characterization of wet-chemically treated silicon interfaces by surface photovoltage measurements. Anal Bioanal Chem 2002; 374: 676-80.

[124] Gale GW, Small RJ, Reinhardt KA. Handbook of Silicon Wafer Cleaning Technology, Edited by Reinhardt KA, Kern W, 2nd Edition. William Andrew Inc 2008; pp. 201-65.

[125] Rentsch J, Ackermann R, Birmann K, *et al.* Wet chemical processing for c-Si solar cells-status and perspectives. Proceedings of the 24th EUPVSEC; 2009: Hamburg, Germany: WIP Renewable Energies, pp. 1113-7.

[126] Angermann H, Henrion W, Rebien M, *et al.* H-terminated silicon: spectroscopic ellipsometry measurements correlated to the surface electronic properties. Thin Solid Films 1998; 313-314: 552-6.

[127] Angermann H, Kliefoth K, Flietner H. Preparation of H-terminated Si surfaces and their characterisation by measuring the surface state density. Appl Surf Sci 1996; 104-105: 107-12.

[128] Kolibal M, Cechal J, Bartosik M, *et al.* Stability of hydrogen-terminated vicinal Si(111) surface under ambient atmosphere. Appl Surf Sci 2010; 256(11): 3423-6.

[129] Zhao L, Zhou C, Li H, *et al.* Characterization on the Passivation Stability of HF Aqueous Solution Treated Silicon Surfaces for HIT Solar Cell Application by the Effective Minority Carrier Lifetime Measurement. Chinese Journal of Physics 2010; 48(3): 392-9.

[130] Angermann H, Henrion W, Rebien M, *et al,* Wet-chemical passivation and characterization of silicon interfaces for solar cell applications. Sol Energy Mater Sol Cells 2004; 83: 331-46.

[131] Rappich, Hartig P, Nickel N, *et al.* Stable electrochemically passivated Si surfaces by ultra thin benzene-type layers. Microelectronic Engineering 2005; 80: 62-5.

[132] Aureau D, Rappich J, Moraillon A. *et al. In situ* monitoring of the electronic properties and the pH stability of grafted Si(111). Journal of Electroanalytical Chemistry 2010; 646 (1-2): 33-42.

[133] Angermann H, Henrion W, Rebien M, *et al.* Optimisation of electronic interface properties of a-Si:H/c-Si hetero-junction solar cells by wet-chemical surface pre-treatment. Thin Solid Films 2008; 516: 6775-81.

[134] Conrad E, Korte L, Maydell K, *et al.* Development and optimization of a-Si:H/c-Si heterojunction solar cells completely processed at low temperatures. Proceedings of the 21st EUPVSEC; 2006: Dresden, Germany, pp. 784-7.

[135] Angermann H, Schulze T, Conrad E. *et al.* Cleaning and passivation of structured n-type Si substrates preparation and interface properties of a-Si:H/c-Si heterojunction solar cells. Proceedings of the 23rd EUPVSEC; 2008: Valencia, Spain: WIP Renewable Energies, pp. 1422-6.

[136] Shockley W. Electrons and holes in semiconductors Van nostrand, Princeton, 1950 p.309.

[137] Sah CT, Noyce RN, Shockley W. Carrier Generation and Recombination in p-n Junction and p-n Junction Characteristics. Proceedings of the IRE, 1957, 45: pp. 1228–1243.

[138] Anderson RL. Experiments on Ge-GaAs heterojunctions. Solid-State Electron 1962; 5: 341-344.

[139] Rahman MN, Furukawa S. Preparation and electrical properties of an amorphous SiC/crystalline Si p+-n heterostructure. Jpn J Appl Phys 1984; 23(5): 515-524.

[140] Schaper M, Schmidt J, Plagwitz H, *et al.* 20.1%-Efficient crystalline silicon solar cell with amorphous silicon rear-surface passivation. Prog in Photov 2005; 13 5: 381-386.

[141] Jjensen N, Rau U, Hausner RM, *et al.* Recombination mechanisms in amorphous silicon/crystalline silicon heterojunction solar cells. J Appl Phys 2000; 87: 2639-2645.

[142] Parretta A, Grillo P, Tucci M. Investigation of minority carrier diffusion length in shallow junction by angle resolved illumination technique. Materials Science and Engineering B 2002; 102: 179-184.

[143] Riben AR, Feucht DL. nGe-pGaAs Heterojunctions Solid-State Electronics. 1966; 9: 1055-1065.

[144] De Vos A, Pauwels, HJ. Collection efficiency of heterojunction solar cells. IEEE Trans Elect Dev, 1977; 4: 388-392.

[145] Fonash SJ. Solar cell device physics. Harcourt Brace Jovanovich, Publishers, Accademic Press, Inc. 1981.

[146] Street RA. Hydrogenated amorphous silicon. Cambridge solid state science series, 1991.

[147] Tucci M. Amorphous crystalline silicon heterojunction for solar cell applications. Ph.D. thesis National Library Rome-Florence Italy 1996.

[148] Schulze TF, Korte L, Conrad E, *et al.* Electrical transport mechanism in a-Si:H/c-Si heterojunction solar cells. J Appl Phys 2010; 107: 023711.

[149] Caputo D, de Cesare G, Irrera F, *et al.* Characterization of intrinsic a-Si:H in P-I-N devices by capacitance measurements: theory and experiment. J of Appl Phys, 1994; 76: 3534-3541.
[150] Caputo D, Irrera F, Palma F, Tucci M. Monitoring of photodegradation and recovery of a-Si:H P-I-N solar cells by capacitance measurements. Physica Scripta, 1994; l.49: 724-728.
[151] Tucci M, Caputo D. Study of capacitance in hydrogenated amorphous silicon phototransistors for image arrays. J of Non-Cryst Solids 2004; 338: 780-783.
[152] Cohen JD. Semiconductor and Semimetal. JI Pankove Editor, Accademic Press Inc. Orlando, 1984; 21C,: p. 9.
[153] Tucci M, De Rosa R, Roca F. CF_4/O_2 dry etching of textured crystalline silicon surface in a-Si:H/c-Si heterojunction for photovoltaic applications. Sol En Mat Sol Cells; 2001; 69/2: 175-185.
[154] Tucci M, Salurso E, Roca F, *et al.* Dry cleaning process of crystalline silicon surface in a-Si:H/c-Si heterojunction for photovoltaic applications. Thin Solid Films 2002; 403-404: 307-310.
[155] Balberg I, Weisz SZ. State distribution and ambipolar diffusion length in n-type hydrogenated amorphous silicon. J Appl Phys. 1989; 66: 215-218.
[156] Faughnan B, Moore A, Crandall R. Relationship between collection length and diffusion length in amorphous silicon. ppl Phys Lett 1984; 44: 613-615.
[157] Schmidt J, Cuevas A, Rein S, *et al.* Impact of light-induced recombination centres on the current-voltage characteristic of Czochralski silicon solar cells. rog Photovol 2001; 9 4: 249-255.
[158] Schmidt J, Cuevas A. Electronic properties of light-induced recombination centers in boron-doped Czochralski silicon. J Appl Phys 1999; 86: 3175-3180.
[159] Evangelisti F. Photoemission studies of amorphous semiconductor heterojunctions. J Non-Cryst Solids 1985; 77 & 78: 969-978.
[160] Mimura H, Hatanaka Y. Energy-band discontinuities in a heterojunction of amorphous hydrogenated Si and crystalline Si measured by internal photoemission. Appl Phys Lett 1987; 50: 326-328.
[161] Cuniot M, Marfaing Y. Energy band diagram of the a-Si:H/c-Si interface as determined by internal photoemission. Philos Mag B 1988; 57: 291-300.
[162] Essick JM, Cohen JD. Band offset and deep defect distribution in hydrogenated amorphous crystalline silicon solar cells. Appl Pgys Lett 1989; 55: 1232-1234.
[163] Eschrich H, Bruns J, Elstner L *et al.* The Dependence of a-Si:H/cSi Solar Cell Generator and Spectral Response Characteristics on Heterojunction Band Discontinuities. J Non-Cryst Solids 1993; 164-166: 717-722.
[164] Caputo D, Forghieri U, Palma F. Low-temperature admittance measurement in thin film amorphous silicon structures. J Appl Phys 1997; 82: 733-741.
[165] Rubinelli FA. Amorphous-crystalline silicon anisotype heterojunctions: built-in potential, its distribution and depletion widths. Solid state electronics 1987; 30: 345-351.
[166] Van Cleef MWM, Rath JK, Runinelli FA *et al.* Performance of heterojunction p+ microcrystalline silicon n crystalline silicon solar cells. J Appl Phys 1997; 82 (12): 6089-95.
[167] Pallares J, Schroop REI. Role of the buffer layer in the active junction in amorphous crystalline silicon heterojunction solar cells. J Apll Phys 2000; 88(1): 293-299.
[168] Van Cleef MWM, Runinelli FA *et al.* Amorphous-crystalline heterojunction silicon solar cells with an a-SiC:H window layer. Proceedings of the 13th EUPVSEC 1995 Nice, France; pp.1303-1306
[169] Summonte C, Rizzoli R, Iencinella D, *et al.* Silicon heterojunction solar cells with microcrystalline emitter. J of Non-Cryst Solids 2004; 338-340: 706-709.
[170] Page MR, Iwaniczko E, Xu Y, *et al.* Well Passivated a-Si:H Back Contacts for Double-Heterojunction Silicon Solar Cells. Proceedings of the 4th WCPSEC 2006, May 7–12 Waikoloa, Hawaii, USA; pp.2012-2015.
[171] Sakata H, Tsunomura Y, Inoue H, *et al.* R&D Progress of Next-Generation Very Thin HITtm Solar Cells. 25th EUPVSEC Sept 6-10 2010, Valencia, Spain; pp.1102-1105
[172] Froitzheim AM, R Stangl, L Elstner, *et al.* Interface recombination in amorphous/crystalline silicon solar cells, a simulation study. Proceeding of the IEEE PV Conf. 2002; pp. 1238-1242.

[173] Taguchi M, Kawamoto K, Tsuge S, *et al.* HIT cells-High efficiecy crystalline Si cells with novel structure. Prog Photovolt: Res Appl 2000; 8: 503-513.

[174] Iencinella D, Centurioni E, Zebaze Kana MG, *et al.* Proceedings of the 20th EUPVSEC, June 6–10 2005 Barcelona, Spain, 992. 998.

[175] Fesquet L, Olibet S, Vallat-Sauvain, *et al.* High Quality surface passivation and heterojunction fabrication by VHF-PECVD deposition of amorphous silicon on crystalline Si: theory and experiment. Proceedings of the 22nd EPVSEC 2007 Milan, Italy; pp. 1678-1681.

[176] Froitzheim A, Brendel K, Elstner L, *et al.* Interface Recombination in Heterojunctions of Amorphous and Crystalline Silicon. J Non-Cryst Solids 2002; 299-302: 663-667.

[177] Tucci M, de Cesare G. 17% efficiency heterostructure solar cell based on p-type crystalline silicon. J Non-Cryst Solids 2004; 338-340: 663-667.

[178] Dauwe S, Schmidt J, Hezel R. Very low surface recombination velocities on p-and n-type silicon wafers passivated with hydrogenated amorphous silicon films. Proceedings of the 29th IEEE Photovoltaics Specialists Conference, New Orleans, Louisiana, USA, 20–24 May 2002, pp. 1246–1249.

[179] Caputo D, de Cesare G, Palma F, Tucci M *et al.* Investigation of amorphous silicon compensated materials over a wide range of dopant concentration. Thin Solid Films 1997; 303: 269-273.

[180] Brodsky MH, Evangelisti F, Fischer R, *et al.* Tickness-dependent conductivity and photoconductivity of hydrogenated amorphous silicon. Solar Cells, 1980; 2: 401-406

[181] Maydell KVY, Conrad E, Schmidt M. Efficient Silicon Heterojunction Solar Cells Based on p-and n-type Substrates Processed at Temperatures < 220 °C. Prog Photovolt: Res Appl 2006; 14:289–295

[182] Froitzheim AM, Scherff MLD, Ulyashin A, *et al.* Amorphous/crystalline silicon heterojunction solar cells with intrinsic buffer layer. Proc. of 3rd WCPVEC May 18-22 Osaka, Japan, 2003; pp. 180-183.

[183] Tsai CC. Characterization of amorphous silicon-boron alloys prepared by plasma decomposition. Phys. Rev. B 1979; 19: 2041-2055.

[184] Caputo D, de Cesare G, Palma F, *et al.* Interaction of phosphorus and boron in compensated amorphous silicon films. J Non-Cryst Solids 1998; 227: 380-383.

[185] Tucci M, Serenelli L, De Iuliis S *et al.* Back contact formation for p-type based a-Si:H/c-Si heterojunction solar cells. Phys Status Solidi C 2011; 8 (3): 932–935.

[186] Caputo D, de Cesare G, Ceccarelli M, *et al.* Characterization of chromium silicide thin layer formed on amorphous silicon films. J Non-Cryst Solids 2008; 354: 2171-2175

[187] Tucci M, Serenelli L, De Iuliis S, *et al.* Amorphous/crystalline silicon heterostructure solar cell based on multi-crystalline silicon, Proceedings of the 21st EUPVSEC; 2006: Dresden, Germany; pp.902-906

[188] Tucci M, Serenelli L, De Iuliis S *et al.* Heterojunction solar cells on multicrystalline silicon: surface treatments. Phys Status Solidi C 2011; 8 (3) : 928–931.

[189] Wang TH, Iwaniczko E, Page MR, *et al.* High efficiency silicon heterojunction solar cells by HWCVD. Proceedings of the 4th WCPSEC 2006, May 7–12 Waikoloa, Hawaii, USA; 2006; pp. 1439-1443.

[190] Wang Q, Page MR, Iwaniczko E, *et al.* Efficient heterojunction solar cells on *p*-type crystal silicon wafers. Appl Phys Lett 2010; 96: 013507.

[191] Zhao L, Li HL, Zhou CL, *et al.* Optimized resistivity of p-type Si substrate for HIT solar cell with Al back surface field by computer simulation. Solar Energy 2009; 83(6): 812-816.

[192] Taguchi M, Maruyama E, Tanaka M. Temperature Dependence of Amorphous/Crystalline Silicon Heterojunction Solar Cells. Jpn J Appl Phys 2008; 47: 814-818.

[193] Centurioni E, Iencinella D. Role of front contact work function on amorphous silicon/crystalline silicon heterojunction solar cell performance. IEEE El Dev Lett, 2003; 24(2): 177-179.

[194] Rubinelli FA, Arch JK, Fonash SJ. Effect of contact barrier heights on P-I-N detector and solar cell performance. J Appl Phys 1992; 72 (4) 15: 1621-1630.

[195] Muñoz D, Ozanne AS, Harrisson *et al.* Toward high efficiency on full wafer a-Si:H/c-Si heterjunction solar cells: 19.6% on 148cm^2. Proceedings of the 35th IEEE PVSC, (2010)Hawaï USA; pp.39-43.

[196] Plà J, Tamasi M, Rizzoli R, *et al.* Optimization of ITO layers for applications in a-Si/c-Si heterojunction solar cells. Thin Solid Films 2003; 425: 185-192.

[197] Available from: DuPont:http://www2.dupont.com/Photovoltaics/en_US/news_events/article20090325.html

[198] Ferro: LF33-series pastes. Available from: http://www.ferro.com/non-cms/ems/Solar_2009/, LF33-701.pdf, LF33-750.pdf

[199] Bowden S, Das U, Herasimenka S, *et al.* Stability of amorphous/crystalline silicon heterojunctions Proceedings of the IEEE PVSEC May 11-16 2008 San Diego, CA, USA; pp. 1641-7.

[200] Sawada T, Terada N, Tsuge S, *et al.* High-efficiency a-Si:H/c-Si heterojunction solar cell. Proceedings of the 1st WCPEC, Hawaii, USA; 1994, pp.1219-1223.

[201] Stiebig H, Zastrow U, Scherff MLD, Ulyashin A. Medium Production of Concentrator Silicon Solar Cells: Approaching the Industrialisation. Proceedings of the 20th EPVSEC 2005 June Barcellona, Spain; pp.1048-1052.

[202] Lammert MD, Schwartz RJ. The interdigitated back contact solar cell-a silicon solar cell for use in concentrated sunlight. IEEE Trans El Dev 1977; 24: 337-342.

[203] Cousins PJ, Smith DD, Luan HC *et al.* Generation III: improved performance at lower cost. Proceedings of 35th IEEE PVSC; 2010 Hawaii, USA; 275-278.

[204] Lu M, Bowden S, Das U, *et al.* a-si/C-Si heterojunction for interdigitated back contact solar cell. Proceedings of the 22nd EUPVSEC; 2007: Milan, Italy: pp 924-927.

[205] Tucci M, Pirozzi L, Salza E, Serenelli L. Italian Patent: BO2007A000717 2007

[206] Bettinelli A, Desrues T. Patent application number: 20100032014 which claims priority of French Patent Application 07 54107, 2007.

[207] Scherf, MLD, Fahrner, W. Patent WO 2008/040273 A3.

[208] Lu M, Bowden S, Das U, Birkmire R. Interdigitated back contact silicon heterojunction solar cells and the effect of front surface passivation. Appl Phys Lett 2007; 91: 063507.

[209] Lu M., Das U., Bowden S., *et. al.* Optimization of interdigitated back contact silicon heterojunction solar cells: tailoring hetero-interface band structure while maintaining surface passivation. Progress in photovoltaics: Res Appl; 2011;19(3): 326-338.

[210] Honggang L. Yeghikyan D, Rayaprol BG, *et al.* Back Amorphous-Crystalline Silicon heterojunction (bach) photovoltaic device.Proceedings of the 34th IEEE PVSEC 2009, June 7-12, 2009, Philadelphia, PA, USA; pp.1767-1770.

[211] Stangl R, Bivour M, Conrad E, *et al.* RECASH a novel high efficiency buried grid rear contact amorphous/crystalline silicon heterojunction solar cell concept. Proceedings of the 22nd EUPVEC; 2007: Milan, Italy: pp. 870-874.

[212] Stangl R., Haschke J., Bivour M., *et al.* Planar rear emitter back contact amorphous/crystalline silicon heterojunction solar cells (RECASH/PRECASH). Proceedings of 33rd IEEE Photovoltaic Specialists Conference; 2008: San Diego: pp 1-6.

[213] Stangl R, Haschke J, Bivour M, *et al.* Planar rear emitter back contact silicon heterojunction solar cells. Sol Energy mater Sol Cells 2009; 93: 1900-1903.

[214] Haschke J, Stangl R, Bivour M, *et al.* New rear contacted amorphous/crystalline silicon heterojuncn solar cells. Proceedings of the 23rd EUPVSEC 2008 Sept 6-9; Valencia, Spain 2008: pp 1652-1656.

[215] Mingirulli N, Haschke J, Gogolin R, *et al.* Efficient interdigitated back-contacted silicon heterojunction solar cells. Phys. Status Solidi RRL 2011; 5-4: 159-161.

[216] O'Sullivan BJ, Bearda T, Qiu Y, *et al.* Interdigitated rear contact solar cells with amorphous silicon heterojunction emitter. Proceedings of the IEEE PVSEC 2010; pp. 3549-3553.

[217] Diouf D, Kleider JP, Desrues T, *et al.* Interdigitated back contact a-Si:H/c-Si Heterojunction solar cells modeling: limiting parameters influence on device efficiency. Proceedings of the 23rd EUPVEC; 2008, Valencia: Spain; pp.1949-1953.

[218] Desrues T, Ribeyron PJ, Vandeneynde A, *et al.* New process integration for interdigitated back contact (IBC) a-Si :H/c-Si heterojunction solar cells. Proceedings of the 23rd EUPVEC 2008 Sept 6-9; Valencia: Spain; pp.1673-1676.

[219] Available from: http://www.silvaco.com/products/device_simulation/atlas.html
[220] Diouf D, Kleider JP, Desrues T, *et al.* Study of interdigitated back contact silicon heterojunction solar cells by two-dimensional numerical simulations. Mater Sci Eng B 2009; 159-160: 291-294.
[221] Diouf D, Kleider JP, Desrues T, *et al.* 2D Simulations of interdigitated back contact heterojunction solar cells based on n-type crystalline silicon. Phys Status Solidi 2010; 7: 1033-1036.
[222] Diouf D, Kleider JP, Desrues T, *et al.* Effects of the front surface field in n-type interdigitated back contact silicon heterojunction solar cells. Energy Procedia 2010; 2: pp. 59-64.
[223] Desrues T., Souche F., Vandeneynde A., *et al.* Emitter optimization for interdigitated back contact (IBC)Silicon heterojunction (Si-HJ) Solar cells. Proc. of the 25th EUPVEC; 2010: Valencia, Spain; pp.2374-2377.
[224] Tucci M, Serenelli L, Salza E, *et al.* Innovative design of amorphous/crystalline silicon heterojunction solar cell. Thin Solid Films 2007; 515: 7625-7629.
[225] Tucci M, Serenelli L, Salza E, *et al.* BEHIND (Back Enhanced Heterostructure with INterDigitated contact) solar cell. Proceedings of the 23rd EUPVSEC 2008 Sept 6-9; Valencia, Spain 2008; pp. 1749-1752.
[226] Tucci M and Serenelli L. Metastability of SiNx/a-Si:H crystalline silicon surface passivation for PV application. Thin Solid Films 2008; 516: 6939-6942.
[227] Caputo D, de Cesare G, Tucci M. Built-in Enhancement in a-Si:H Solar Cell by Chromium Silicide Layer IEEE Electron Dev Lett, 2010; 31-7: 689-691.
[228] Tucci M, Serenelli L, Salza E, *et al.* Back Enhanced Heterostructure with INterDigitated contact-BEHIND-solar cell. Proceedings of the IEEE Conference on Optoelectronic and Microelectronic Materials and Devices, COMMAD 2008: pp 242-245.
[229] Tucci M, De Iuliis S, Serenelli L, *et al.* BEHIND 2.0: the Back Enhanced Heterostructure with INterDigitated contact solar cell evolution. Proceedings of the 25th EUPVSEC 2010 Sept 6-10; Valencia, Spain 2010; pp. 2089-2094.

Send Orders of Reprints at reprints@benthamscience.net
Silicon Based Thin Film Solar Cells, 2013, 359-394

CHAPTER 10

Micromorph Cells

Maurizio Acciarri*

Department of Materials Science and Solar Energy Research Center (MIB-SOLAR), Università degli Studi Milano Bicocca, Via Cozzi, 53-20125 Milan, Italy

Abstract: The photovoltaic (PV) industry is growing, with rates well in excess of 30% a year over the last decade. World solar photovoltaic market installations are expected to reach 17.5 Gigawatt in 2010; however, PV contribution to global electricity generation is still negligible. The main challenge for a major contribution demands incremental reductions in €/Wp costs of PV modules. The traditional development of photovoltaics was based on crystalline-silicon wafer technology. However, the early 1970's witnessed a new approach based on the possibility of growing silicon in the form of a thin-film on a given substrate. Several techniques are currently used to achieve this deposition, and they are mainly based on the chemical vapour deposition (CVD) technique. While amorphous silicon-based PV modules have dominated the thin-film market for over 20 years, recent industrial developments include tandem solar cells based on stacks of amorphous (a-Si:H) and microcrystalline silicon (μc-Si:H) film ("micromorph cells"). A basic question that already awaits an answer concerns the link between the microstructure of the material, transport properties of the intrinsic absorbing layers, as well as the electrical performance of solar cells. μc-Si:H is a complex material with a wide range of microstructures, depending both on deposition conditions and on the substrate material. This chapter will report on the state of the art and several aspects of material properties. Device physics will also be presented.

Keywords: Absorption coefficients, amorphous superconductors, impurity and defect levels, chemical vapor deposition, electronic structure, electrical conductivity, optical properties, photovoltaic thin films, semiconductors and insulators, thin films.

1. INTRODUCTION

The photovoltaic market has grown quickly in recent years at a rate well in excess of 30% a year. The market is dominated by bulk mono-and multi-crystalline silicon (c-Si) solar cells, which account for about 85% of the total production. However, the wafer-based technology has still not proven its capability of making the cost of electricity produced by PV competitive against that produced by fossil fuels. One reason for this, though not the only one, is the high cost of raw material (silicon). PV industries are making an intensive effort to reduce consumption of the material by diminishing the thickness of solar cells. Thin-film technologies allow for important reductions in semiconductor thickness through the capacity to absorb most of the incident sunlight within a few microns of thickness. In addition, thin-film technology has an enormous potential in terms of cost reduction by offering the opportunity to use large area monolithic modules with a fully automated manufacturing procedure. The GBI Research [1] recently reported the increase in

*Address correspondence to Maurizio Acciarri: Department of Materials Science and Solar Energy Research Center (MIB-SOLAR) Università degli Studi Milano-Bicocca, Via Cozzi, 53-20125 Milan, Italy; Tel: +390264485136; Fax: +390264485400; E-mail: maurizio.acciarri@unimib.it

Roberto Murri (Ed)
All rights reserved-© 2013 Bentham Science Publishers

thin-film production from 14 MW in 2001 to 2141 MW in 2009. Considering production in 2009, thin-film technologies represented 25% of total global production and were expected to increase their share to 38% by 2020. However, silicon thin-film technology lost its leadership in the thin-film PV market because of the steep rise of CdTe modules. In 2010 the market share for silicon-based thin-film technology dropped to 32% *vs.* 60% in 2005 [1]. This reduction may also be associated with the inability of the modules based on amorphous silicon to overcome certain limitations in their photovoltaic performance. In particular, the efficiency of an amorphous silicon module is considerably less than levels reached by crystalline silicon modules. This means that, despite the lower production cost of amorphous silicon modules, the market is dominated by crystalline silicon, and interest is growing in new materials like CdTe or Cu (In, Ga)Se2. But the recent use of microcrystalline silicon for tandem junctions with amorphous silicon has aroused interest in enhancing construction efficiency while maintaining low costs. This chapter will discuss the deposition methods of microcrystalline silicon thin-film, its structural and electrical properties and photovoltaic devices based on this material.

2. MICROCRYSTALLINE SILICON THIN-FILM: AN OVERVIEW

Reducing material consumption by diminishing thickness was one of the reasons that triggered the introduction of thin-film technology in the PV market. However, the low absorption coefficient of crystalline silicon limits this solution. Therefore new materials were studied in view of their potential use as an active layer in solar cells. Amorphous silicon was the first to draw the interest of researchers.

Amorphous silicon PV history [2, 3] starts in 1965, when Sterling *et al.* [4] reported deposition of silicon onto a substrate using a silane glow discharge. In 1969, Chittick *et al.* [5] obtained an intrinsic amorphous silicon film of acceptable quality through plasma Enhanced Chemical Vapor Deposition (PECVD).

The PE-CVD technique consists in gas decomposition by plasma. Gases used for the deposition of intrinsic silicon thin-films are silane (SiH4) and hydrogen (H2). The amorphous or microcrystalline nature of the deposited material depends on the various deposition parameters that have to be adjusted.

Another important date is 1975 when Spear and LeComber [6] demonstrated the possibility of doping (both n-and p-type) amorphous silicon. This paved the way for solar cell development.

In 1976 Carlson and Wronski announced the first experimental a-Si:H solar cell made at the RCA Laboratory [7]. This single junction p-i-n a-Si:H solar cell deposited on a glass substrate exhibits 2.4% conversion efficiency. It took some years to realize that plasma-deposited amorphous silicon contains a significant percentage of hydrogen atoms bound to the amorphous silicon structure. Hydrogen is essential to increase the electrical quality of the amorphous growth film. Due to the presence of hydrogen, this amorphous silicon film was named hydrogenated amorphous silicon (a-Si:H). The development of a monolithically integrated type of a-Si:H solar cell was of the utmost importance for industrial production [8]. Integration of the monolithic series made it easy to achieve the desired output voltage from a single substrate. In 1980, the integrated type a-Si:H solar cells were commercialized by Sanyo and Fuji Electric, and used in consumer electronics such as

calculators and watches. In the 1980s the initial cell efficiency was increased to around 11-12% [3], which dropped to 7-8% after stabilization. Three decades later, the highest confirmed stable efficiency for a single-junction a-Si:H cell at lab level is 10% obtained in 2010 at the Oerlikon Solar Lab, Neuchatel [9].

Always in the 1980s, industry addressed its interest to off-grid power generation. Modules chosen for this application were single junction p-i-n a-Si:H solar cells. The typical area of the modules ranged from 0.1 to 0.3 m2 and they were designed to deliver a power of around 14 W with up to 5% stabilized efficiency. However, the strong interest in a-Si:H modules cooled down owing to certain limitations that were detected at the time.

The main problem was light-induced degradation known as the Staebler–Wronski effect [10]. This effect is responsible for a typical 15–30% decrease in the initial performance of an a-Si:H solar module. Moreover, inadequate protection and framing of these modules against moisture resulted in the corrosion of contacting electrodes. These problems and the difficulty in further increasing cell (module) efficiency directed researchers to pursue new paths.

In 1983, Matsuda [11] produced both p-and n-type microcrystalline silicon (μc-Si). This new material was used in 1987 by Hattori *et al.* [12] to make the first thin-film silicon solar cell that had microcrystalline-silicon emitters (μc-Si). μc-Si cells attracted general interest mainly because they presented no light-induced degradation. The interest in microcrystalline silicon continued in the 1990s as the market demanded more stable absorbing material, higher output power modules and lower manufacturing costs for thin-film silicon solar cells. New deposition techniques were explored and in 1992 Faraji *et al.* [13] used very-high-frequency PECVD (VHF-PECVD), and in 1997 Rath *et al.* [14] proposed the hot-wire CVD (HW-CVD).

In the 1990s it became quite clear that a-Si:H single junction alone could not compete with low cost crystal silicon and, more recently, with CIS and CIGS-based solar cells. In fact, single-junction technology is expected to hit its practical efficiency peak (8% to 8.5%) for many producers by 2012, and it will phase out thereafter [1].

To overcome the efficiency limit of amorphous single junction solar cells, industries developed tandem and even triple layer devices containing p-i-n cells stacked one on top of the other. Several a-Si:H based alloys were tested for a better match of the solar spectrum. Hydrogenated amorphous silicon carbide (a-SiC:H) was used as top cell (window layer) [15]. Hydrogenated amorphous silicon germanium (a-SiGe:H) became an attractive low bandgap material for stacked solar cells [16]. Surface textured substrates were also introduced to enhance optical absorption [17].

Some industries transferred these new materials and devices to production lines. For example, a-SiGe:H alloy was used in a tandem solar cell structure by BP Solar [18], Sanyo [19] and Fuji Electric [20], and in a triple junction by United Solar [21]. However, better performances are expected if a higher electrical quality material like μc-Si is used.

In 1994 [22, 23] the “micromorph tandem cell” concept was introduced at the “Institut de Microtechnique” in Neuchatel (Switzerland). It was a new promising thin-film solar cell that used the same deposition technology as amorphous silicon-based devices. The use of the a-Si:H cell

combined with microcrystalline silicon (μc-Si:H) leads to the so-called "micromorph" (microcrystalline/amorphous) tandem solar cells.

Because of the difference in bandgap, a-Si layer is suitable for the use of shorter wavelengths and a μc-Si:H layer is suitable for the use of longer wavelengths (Fig. **1**). Therefore a-Si:H/μc-Si:H tandem structure absorbs the sunlight effectively. This technology makes a 30% or more increase possible in output power.

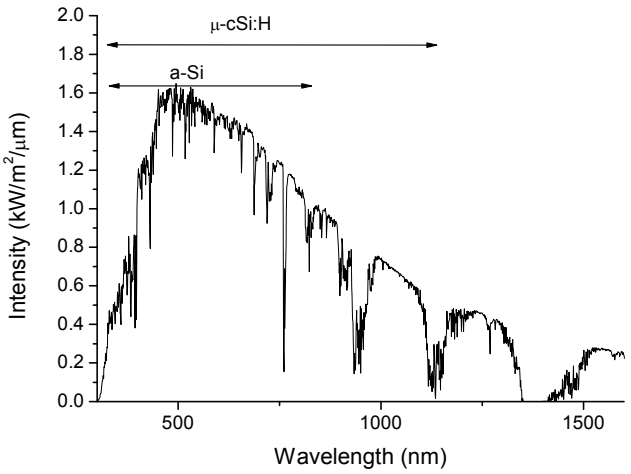


Figure 1: Spectral distribution of the AM1.5 solar spectrum incident on the Earth's surface. The spectral ranges which are absorbed by a-Si:H and μc-Si:H, respectively, are indicated.

Moreover, compared to other thin-film technologies currently under development and industrialization (CIGS, CdTe), silicon thin-films have the key advantage of using silicon as raw material which is non-toxic and widely available.

Although the first microcrystalline thin-film was introduced into solar cell fabrication something like 20 years ago, these cells/modules have still not achieved an important increase in conversion efficiency. However, the amorphous/microcrystalline silicon solar cells are still a topic of research and new progress is expected.

3. MICROCRYSTALLINE SILICON THIN-FILM DEPOSITION

Considering that the principal techniques used nowadays for microcrystalline deposition are the same as those used for amorphous deposition, and that they have already been mentioned in this eBook, the easy deposition process will be briefly described below along with the evolution from amorphous silicon to the “micromorphous” concept.

Starting from the initial amorphous silicon deposition and then from the evolved family of semiconductors based on different forms of silicon alloys or crystallinity (nano, micro or poly), all

the various deposition techniques have in common deposition in the form of thin-film at low temperatures (below 600°C and often around 300°C). The general idea of research on µc-Si:H deposition is to understand and control the deposition process in order to achieve the best material quality at the lowest feasible preparation cost. A broad range of vacuum techniques has been employed to work towards this goal.

The three methods commonly used for manufacturing a-Si are electron beam evaporation, rf sputtering and deposition from silane (SiH_4) in a radio frequency discharge. Electrical and optical properties of the resulting film depend on the method of deposition.

In these deposition techniques, film growth takes place through sequential sticking of reactive silicon-containing species called growth precursors, which may originate either from a source gas or from a solid target. A common feature of all µc-Si:H deposition techniques is that H_2 gas is present to tune the material ranging from a-Si:H to highly crystallized µc-Si:H, as illustrated in Fig. **2**. Crystalline growth starts at nucleation centers near the film/substrate interface. The columnar grains can be several 100 nm wide and several µm long. Atomic hydrogen is believed to play the decisive role in structuring the Si-Si bonds to form a more crystallized matrix [24, 25]. The crystallization process evolves in a transient way, giving rise to a substrate-dependent structural evolution ranging from an initial amorphous incubation zone to the more crystalline thicker parts of the film [26, 27] (Fig. **2**).

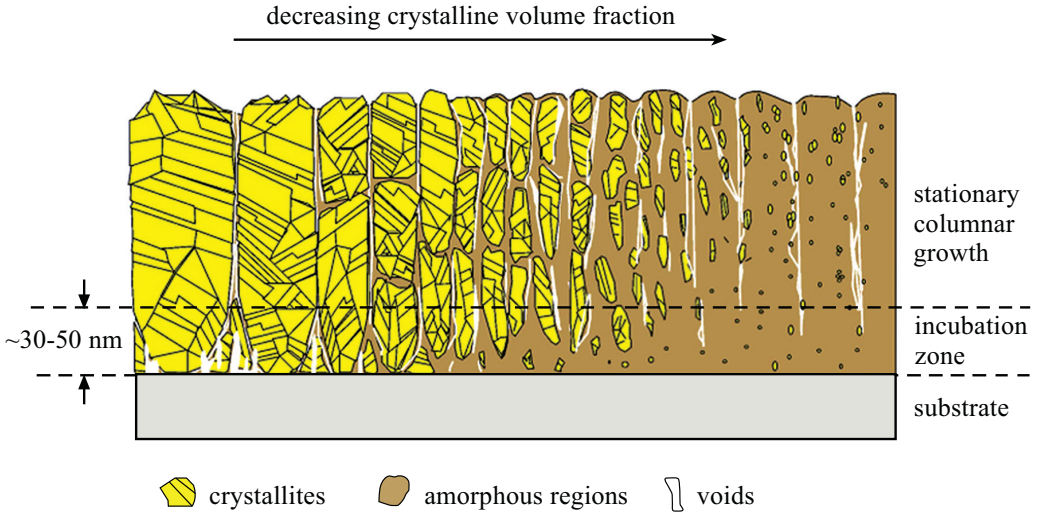


Figure 2: Schematic diagram showing the prominent microstructural characteristics of µc-Si:H, after Vetterl *et al.* [28]. The left-most region corresponds to highly crystallized material deposited in hydrogen-rich conditions whereas the right-most region corresponds to highly amorphous material deposited in hydrogen-poor conditions (reproduced with permission of Elsevier).

The space between these crystalline grains is filled with amorphous silicon and/or voids. The crystalline volume content of the film depends on deposition conditions, in particular on the silane concentration in the gas mix. The regime around 6% silane concentration is called the "transition region" and yields the best µc-Si:H solar cells [29].

The terms 'micro-crystalline silicon' (μc-Si:H) or, alternatively 'nano-crystalline silicon' (nc-Si:H) are usually adopted to indicate layers that are deposited at low temperatures (below 400°C). The low deposition temperature allows the application of flexible substrates (stainless steel or polymer) that are useful for building integration [29].

Industry was initially drawn to the a-Si:H PV technology as it is a low-T silicon deposition process and the material deposited does not require any post-deposition treatments (such as hydrogenation). This cuts down the thermal budget and saves time.

However, the limited efficiency obtained with amorphous silicon in the 1990s pushed research along new paths which, maintaining these features, could produce solar cells with higher stable efficiency.

Hydrogenated microcrystalline silicon was prepared by Veprek and Marecek for the first time in 1968 by chemical transport method [30]. The fabrication of μc-Si:H using PECVD was introduced in 1980 [31]. The first application of the PECVD technique in microcrystalline deposition was limited to the p type window layers in p-i-n type amorphous silicon solar cells [32]. Hydrogen dilution ratio $r = H_2/SiH_4 > 15$ was conventionally used to form μc-Si:H.

The introduction of microcrystalline silicon (μc-Si:H) as i-layer in the 1990s by Wang *et al.* [33] initiated the production of solar cells that possessed higher and more stable efficiency. This material is a heterogeneous blend of a-Si:H, voids and 10 nm c-Si grains. Regardless of the deposition technique used, the resulting material had a very high density of defects.

In 1994 Meier *et al.* prepared solar cells with μc-Si:H i-layer that suffered no light-induced degradation. Later, Klein *et al.* demonstrated that μc-Si:H may show some light-induced degradation with significant a-Si:H volume fractions of 40% or more [34]; however, this degradation is much less pronounced than in a-Si:H and shows improved electronic properties. For this issue, the crystalline volume fraction is a crucial property for materials. Vetterl *et al.* demonstrated in 2000 that there is an optimum in solar cell performance for material consisting of about 60% c-Si grains, 40% a-Si:H and a minimum amount of voids [28].

The PECVD deposition of silane (SiH_4) and silane-containing mixtures ensured better material quality as the result of the incorporation of hydrogen in the silicon matrix that diminishes defects [39]. These features have made PECVD the most widely used preparation technique for thin-film silicon.

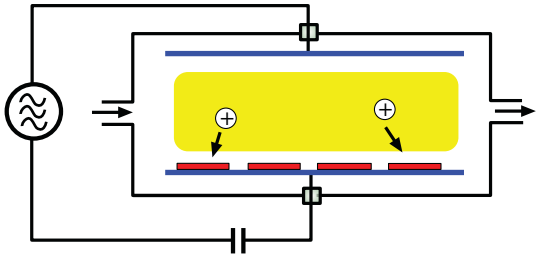


Figure 3: Diagram of a parallel plate capacitively coupled plasma deposition set up.

The most widespread preparation CVD configuration is parallel plate capacitively coupled plasma deposition using an $SiH_4 + H_2$ gas mixture. The parallel plate plasma source consists of two planar electrodes (Fig. **3**). One of the electrodes is the substrate itself on which the silicon film is to be deposited. The other electrode is supplied with an oscillating voltage signal at a typical frequency of 1-100 MHz. The breakdown voltage for plasma ignition strongly depends on the pressure and electrode gap.

For H_2 the breakdown voltage shows a minimum of approximately 100 V (about 1 Torr cm). For voltages above the breakdown voltage, ionization reactions ensure the creation of free electrons with a temperature in the range of 104 K and a density in the range of 1010 cm^{-3}. Due to the inefficient thermal coupling between electrons and the much heavier neutral atoms and molecules, the substrate and background gas temperatures are hardly affected by the hot electrons. The fast electrons create plasma potential compared to grounded walls and substrate over which positively charged ions can gain energy amounting to several tens of eV leading to ion bombardment of the substrate. Moreover, the hot electrons induce chemical reactions that create the reactive precursors involved in film growth. The general growth mechanism and the contribution of the various precursors to μc-Si:H growth is an active area of research.

More details about CVD deposition can be found in dedicated literature but the brief description given here has the sole purpose of underscoring the fact that material properties like crystalline volume fraction are a result of precursor fluxes during deposition. Plasma properties such as electron density and temperature are the result of complex processes like RF power dissipation, inelastic collisions, gas-phase chemistry and surface chemistry. These processes can be empirically influenced by changing process parameters, such as pressure, substrate temperature, RF power, RF frequency, electrode gap, electrode area, gas flow and gas mixture.

Considering the experience developed, it became clear that the guidelines for forming high quality microcrystalline silicon from plasma CVD are very simple as long as a sufficient quantity of hydrogen atoms can be supplied to the substrate during crystallization without causing any damage (most of it is ion damage). Then film fabrication speed can be improved without deteriorating cell characteristics.

Throughput is an important parameter to be considered for mass-production, and it is, therefore, essential to develop a method for high speed film deposition over large areas.

In the case of μc-Si:H, the deposition rate is definitely an issue regarding industrialization as, at present, the thickness of μc-Si:H solar cells is about 5 to 10 times higher than that of a-Si:H solar cells. μc-Si:H solar cells require a thick intrinsic layer (2.0–3.5 μm) to absorb a sufficient amount of sunlight because of its indirect optical transition.

However, thin-film silicon solar cell technology works at relatively low deposition rates, and a high hydrogen dilution condition can limit the growth rate of μc-Si at some A/s. The deposition of a 2 μm thick μc-Si:H film might take 5 h in “standard conditions”.

Therefore, high-rate-growth of μc-Si:H film is a crucial matter for low-cost production of thin-film solar cells.

The introduction of very-high-frequency (VHF) PECVD techniques (*i.e.* plasma excitation frequencies well above the standard industrial frequency of 13.56 MHz) has increased growth rates and offers high-quality materials.

The use of plasma excitation frequencies in the Very High Frequencies (VHF) range (70 to 130 MHz) was pioneered by Curtins *et al.* in 1987 [35].

The VHF-PECVD method enabled researchers at the University of Neuchatel to manufacture the first hydrogenated microcrystalline silicon (μc-Si:H) cells at 200°C with reasonable efficiency indexes [36]. These new cells presented maximum efficiency levels of 4.6% and were stable under light soaking conditions. This last feature convinced researchers that it could be possible to produce modules with more stable efficiency levels than the a-Si:H modules.

When a higher excitation frequency is used (typically in the range of 30-300 MHz), electrons in plasma have a much higher thermal velocity than positive ions. This induces a positive potential in the bulk plasma to maintain charge neutrality. The plasma sheath near the substrate leads to the acceleration of positive ions and also to electron confinement within plasma with enhanced dissociation of silane and reduced energy of ions impinging on the growing surface [37]. The use of VHF plasma is a consequence of the improved formation of microcrystalline silicon and higher deposition rate as compared to conventional plasma deposition at 13.56 MHz [38].

In the VHF-PECVD deposition technique the quality of film growth can be controlled by adjusting some deposition parameters.

The thermal budget is another crucial point in crystalline silicon solar cell production. An advantage of PE-CVD is that it allows relatively low deposition temperatures (below 400°C).

During the plasma gas phase, pressure and Silane Concentration (SC):

$$SC = SiH_4/(SiH_4+H_2)$$

strongly affect the crystalline and electrical properties of the μc-Si:H film. The structure of the deposited layer changes from amorphous (at high SC-values) to microcrystalline (at low SC-values). The most efficient solar cells are grown near the μc-Si:H/a-Si:H transition point (SC= 4-9%).

However, high-rate deposition of device grade μc-Si:H has been generally difficult because of such problems as ion bombardment and powder formation that are often encountered during the high-rate plasma process [40]. In fact, high efficiency μc-Si:H solar cells reported so far can be achieved at limited deposition rates, typically as low as 0.5 nm/s.

An alternative promising deposition technique for the parallel plate plasma deposition of μc-Si:H is the so-called “high pressure depletion” (HPD) regime, [38, 40, 41]. Using this regime, the maximum efficiency of 9.13% has been achieved at an i-layer deposition rate of 2.3 nm/s [42] without important material quality deterioration, and up-scaling to ~m^2 substrate sizes [43] has been demonstrated. Key aspects of the regime are a “small” electrode gap (~1 cm or less), “high”

pressure (~5 Torr or more), "high" power density (~0.5 W/cm^2 or more) and "high" H_2 dilution (~10% SiH_4 in H_2 or less). A qualitative view of the μc-Si:H deposition process has been developed to describe the HPD deposition regime. According to this view, dilution in H_2 produces sufficient atomic hydrogen for the crystallization process. A high RF power and corresponding high degree of dissociation in the plasma allows high deposition rates to be obtained, but too high RF power gives rise to energetic ion bombardment inducing defects in the deposited material. A high pressure and corresponding short mean free path ensures multiple collisions of ions as they are accelerated towards the substrate, thereby reducing ion energy and preventing defect formation. A small electrode gap is required for plasma operation at high pressure.

Besides the parallel plate plasma deposition, several other deposition methods are being studied.

Growth rates of 3–5 nm/s, which are compatible with industrial applications, can be obtained with the Low Energy Plasma Enhanced Chemical Vapor Deposition [44] techniques see Fig. **4**. This technique is based on a low-voltage, high-current arc discharge which has been so far very successfully applied, in terms of material quality, in the field of Si–Ge hetero-structures grown epitaxially on Si [45].

Preparation of μc-Si:H from a solid silicon target has been reported using reactive sputtering from an Ar + H_2 gas mixture [46] or etching and re-deposition (chemical transport) using H_2 plasma [30]. Preparation from an SiH_4 + H_2 gas mixture has been reported using various methods to dissociate the gas, *e.g.* hot wire [47], expanding thermal plasma [48], inductively coupled RF plasma [49], microwave plasma [50-52] and a DC arc [53]. Preparation of μc-Si:H from source gases besides SiH_4 + H_2 has been reported for *e.g.* $SiCl_4$ + H_2 [54], SiH_2Cl_2 + H_2 [55] and SiF_4 + H_2 [56].

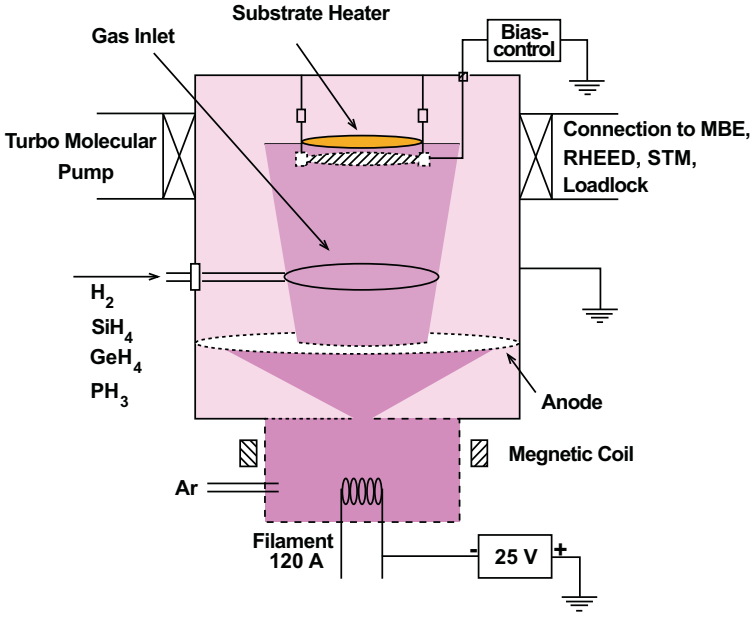


Figure 4: Diagram of a LEPECVD deposition system.

Recently, Shinohara [57] reported a variation implemented to the CVS technique, the so-called Localized Plasma Confinement CVD (LPC-CVD) method [58]. The concept of LPC-CVD is to generate a large amount of small plasma by using pyramidal nozzles under very high-pressure conditions, instead of generating uniform large plasma through parallel plane electrodes under conventional conditions. This concept makes it easier to deposit uniform μc-Si:H film with a high deposition rate, because the overlap of the localized plasma can form uniform high-density silane radicals even under high-pressure conditions (>1,000Pa). A maximum deposition rate of 4.1 nm/s was obtained. This feature also helps to increase gas utilization. An a-Si:H/μc-Si:H solar panel with a conversion efficiency of 11.1% (Voc=161.7 V, Isc=1.46 A, F.F.=72.4%, Pmax=171 W), and stabilized efficiency corresponding to 10.0%, was obtained with this technique. The size was 1,100 mm x 1,400 mm and the deposition rate of μc-Si:H was 2.4 nm/s.

However the advantages and disadvantages compared to parallel plate plasma deposition are not clear to date, and more work on these preparation techniques is necessary.

In the laboratory, deposition rates up to 10 Å/s can be obtained for state-of-the-art solar cells with some of these methods, and regular large scale production at such high rates has not been reported as yet, with the exception of Kaneka Corp.

4. STRUCTURAL, OPTICAL AND ELECTRICAL PROPERTIES

The intrinsic layer of a p-i-n (or n-i-p) silicon thin-film solar cell plays two important roles in the functioning process of the device. On the one hand, it must have good light absorption properties in order to generate as many electron-hole pairs as possible for a given incident light intensity and, on the other hand, it must have good electrical transport properties in order to enable the free electron and holes to exit the device before recombining.

Only under certain conditions microcrystalline silicon is suitable for solar cell applications. For instance, it is claimed that favorable conditions for high efficiency pin solar cells are obtained by depositing the μc-Si film at growth conditions near the μc-Si:H/a-Si:H phase transition [62] or close to the transition to amorphous silicon [34].

Other conditions, which must be complied with for high efficiency, are described below:

- in addition to a p-and n-doped material, a truly intrinsic material should also be deposited for efficient pin cells [62],

- the potential role of unwanted oxygen contamination, which causes an n-type behavior, must be suppressed by proper use of cleaning and purification procedures for the UHV system and the gas inlet systems,

- grain boundaries and other defects should be well passivated by hydrogen, resulting in sub-bandgap (defect) absorption at 0.8 eV of less than 3 cm^{-1} [62] or, better, less than 1 cm^{-1} [34],

- the layer surface should be rough for better light trapping properties,

- the growth rate should be around 1–3 nms^{-1} to be compatible with industrial applications [40].

In the following paragraph we shall describe the main physical characteristics of undoped and doped μc-Si:H layers in view of their incorporation into solar cell devices.

For such μc-Si:H material, the microstructure varies while the growth of the film proceeds: an amorphous incubation layer has frequently been observed at the bottom (*i.e.* in the initial growth stage) of layers grown with deposition conditions close to the μc-Si:H/a-Si:H transition. Thereafter, the microcrystalline phase follows, consisting of conical conglomerates made of nanocrystals the size of a few tens of nanometers (See Fig. **5**) [59].

The microstructure of μc-Si:H is actually a "mix" between that of amorphous silicon (*i.e.* no periodicity and no long-range order) and that of crystalline silicon (*i.e.* fully regular network of atoms). In fact, three main length scales for disorder can be identified in microcrystalline silicon (see Fig. **5**):

- Local disorder: μc-Si:H contains a more or less large part of amorphous material, *i.e.* of material that consists of an arrangement of atoms without any long-distance order and that also contains a substantial density of defects (dangling bonds),

- Nanometrical disorder: nanocrystals consist of small crystalline (c-Si) grains of random orientation and a few tens of nanometers in size; they can be observed on Transmission Electron Microscopy (TEM) micrographs; their average size (d) can be evaluated from X-Ray Diffraction (XRD) spectra; the grain boundaries of the nanocrystals, consisting of a certain form of amorphous tissue are between the nanocrystals,

- Micrometrical disorder: conglomerates are formed by a multitude of nanocrystals and generally have a conical shape (see Fig. **5**). The size of the conglomerates (D) emerging on the free surface of the layers can be evaluated with Atomic Force Microscopy (AFM) scans and is roughly half a micrometer. Between the conglomerates one also finds a kind of amorphous tissue that forms the conglomerate boundaries.

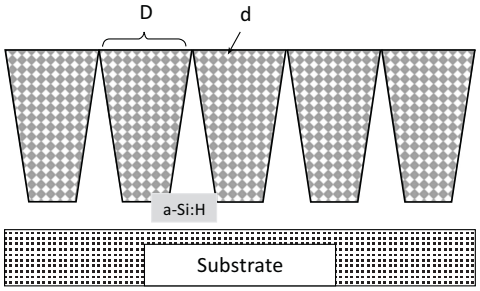


Figure 5: Hydrogenated microcrystalline silicon (μc-Si:H). Schematic illustration of a μc-Si:H layer: pencil-like conglomerates (D) formed by a multitude of nanocrystals (d), plus their corresponding boundaries.

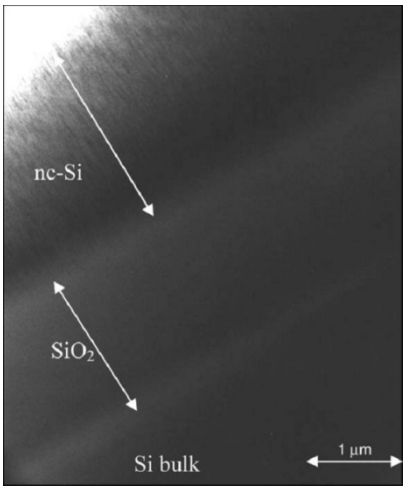


Figure 6: Cross-sectional TEM image of the µc-Si/SiO2/Si region.

Experimental methods allowing the evaluation of i-layer crystallinity are, therefore, of practical importance for the characterization of µc-Si:H. Transmission electron microscopy (TEM) is a very powerful technique that allows for direct observation of the presence of amorphous and microcrystalline phases.

Figs. **6** and **7** show the typical microstructural features of films deposited at low temperature, as obtained from TEM. They present a typical columnar structure that is orthogonal to the substrate surface and a distribution of elongated nanocrystals, with a section of about 5–6 nm, inside the amorphous phase.

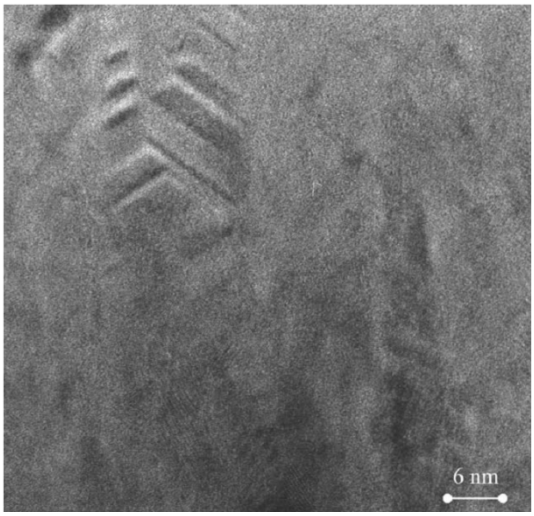


Figure 7: Cross-sectional HRTEM image of a particular region of µc-Si film. Some stacking faults and some crystalline regions with different crystallographic orientation can be noticed.

Information about the orientation and size of the nanocrystals can be obtained from XRD measurements. Some typical XRD spectra of μc-Si:H samples at different dilutions are reported in Fig. **8**.

In an XRD spectrum of randomly oriented Si powder, a peak intensity ratio of 1:0.55:0.3 among the (111), (220) and (311) peaks is observed.

In this example, the (220) peak intensity is, like the (111) peak intensity, indicative of a preferred (220) orientation of nanocrystallites.

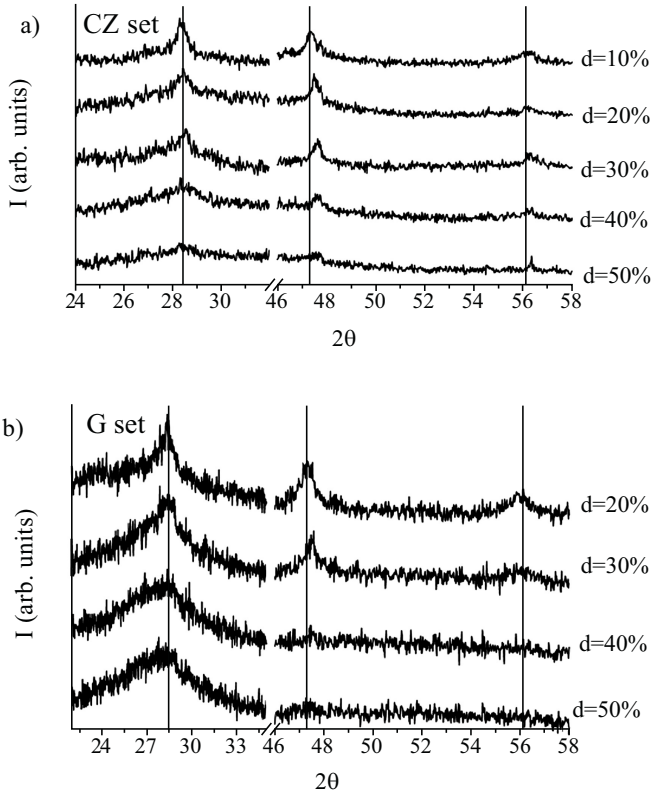


Figure 8: X-ray diffraction spectra obtained for a series of μc-Si:H layers deposited on silicon (a) and glass (b) substrates at various silane, d percentage, dilutions. The curves are shifted for clarity. The three main diffraction peaks corresponding to the (111), (220) and (311) silicon crystallographic planes are indicated [60].

The grain size φ along different crystallographic directions can by calculated using the Debye–Scherrer equation:

$$\varphi = (0.9)\,\lambda/[K\cos(2\theta)]$$

where λ is the X-ray beam wavelength and K is the broadening of the X-ray diffraction line expressed in radiants.

Raman spectroscopy measurements do provide additional information about the microstructural features of the films [61]. Fig. **9** gives an example of the Raman spectrum of sample growth at different dilutions.

By their deconvolution, one could detect the presence of two bands of which the one at about 520 cm^{-1} is the position of the transverse optical mode in monocrystalline silicon, and the integrated area is associated with the crystalline fraction (I_C).

The peak at about 480 cm^{-1} is associated with the amorphous phase. The integrated intensity of this peak I_A is proportional to the amorphous volume fraction in the excited volume.

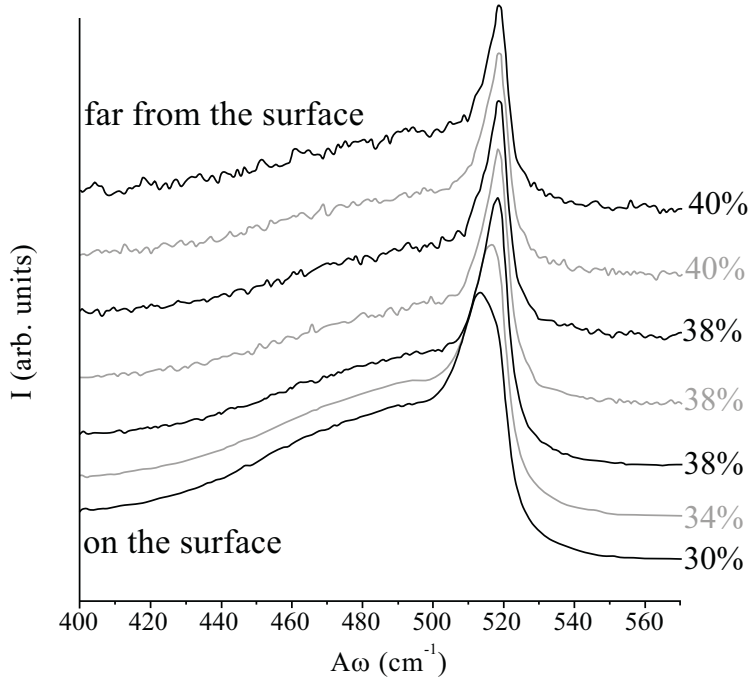


Figure 9: Raman depth profile of a typical CZ set sample grown at d>30%. The crystallinity obtained from each spectrum is reported on the right side. The spectra are vertically shifted for better clarity [60].

The crystalline phase volume fraction χ_c could be obtained from the Raman spectrum by using the equations:

$$\chi_c = I_C/(I_C + \sigma I_A)$$

where σ is the ratio between the cross-sections of c-Si and a-Si.

Structural properties have a strong impact on the electrical and optical properties of μc-Si:H films which, again, are closely related to hydrogenated amorphous silicon (a-Si:H), as both materials are deposited by similar techniques. As previously reported, a-Si:H or μc-Si:H material can be

obtained by working on the deposition parameters (such as temperature, silane concentration, power, frequency, pressure…).

µc-Si:H can be considered as something like a (complex) mixture between crystalline silicon (c-Si) and a-Si:H. So it is useful to consider the basic electronic characteristics of a-Si:H before studying µc-Si:H.

As reported in other chapters of this eBook, a-Si:H is a solid-state material made of silicon atoms which are arranged on a lattice that has a certain short range order, but no long range order. Compared to crystalline silicon (c-Si), the average bond angles between neighboring atoms are distorted. Some bonds are even broken and result in so-called "dangling bonds". The presence of hydrogen during the fabrication of amorphous silicon material enables one to passivate a large part of these dangling bonds. These two main "defects" of the lattice of a-Si:H-bond distortion and dangling bonds-give rise to an electronic band structure containing localized states within the so-called "mobility" bandgap (see Fig. **10**). Note that the value of the "optical" bandgap, which is extrapolated from optical measurements, can be slightly different from that of the resistivity or mobility gap.

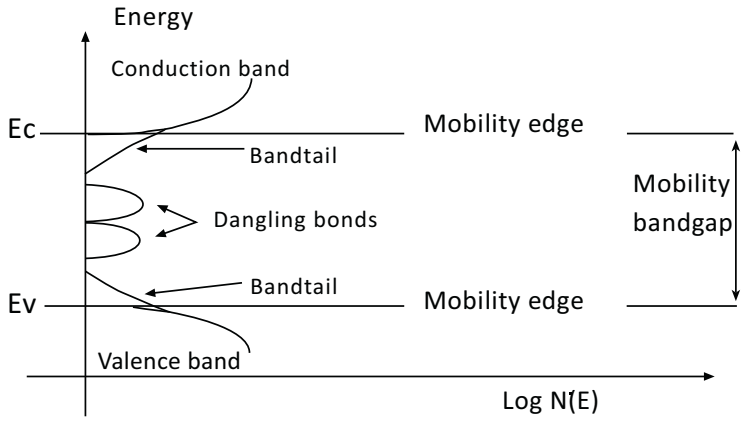


Figure 10: Density of states N(E) for intrinsic a-Si:H. The states are localized (dangling bonds and band-tails) within the mobility bandgap (delimited by EC and EV).

The bond distortion results in band-tails near the valence and conduction bands. In these band-tails, the electrons (or holes) are localized in space and do not participate (directly) in electron transport. The (non-passivated) dangling bonds create deep states near the middle of the bandgap. They can either be positively charged (*i.e.* absence of electron), neutral (*i.e.* one electron) or negatively charged (*i.e.* two electrons). The dangling bonds act as recombination centers for the free electrons and holes. They can also affect electron transport by influencing the total electric charge. In a-Si:H as well as in µc-Si:H, hydrogen has the important role of reducing the number of dangling bonds, or "defects" and, therefore, of making the material "device-grade", *i.e.* suitable for use in optoelectronic devices like solar cells and detectors.

Coming to µc-Si:H films, the co-presence of amorphous and crystalline silicon is mirrored by electrical and optical properties which are a mix of the two materials.

The difference in the absorption range of a-Si:H and μc-Si:H is due to different bandgap energy (Eg) values. For a-Si:H material, Eg ≈ 1.75 eV, whereas for highly microcrystalline silicon Eg ≈ 1.1 eV, similarly to c-Si. Due to its indirect gap, the absorption of μc-Si:H is lower than that of a-Si:H (Fig. **11**).

In addition to the enhanced light absorption, related to its lower bandgap, microcrystalline silicon has an enhanced scattering property due to the natural texture of its surface, which increases effective absorption.

We have already reported that one of the main advantages of μc-Si:H was its stability under light exposure. Works are reported in literature which confirm no light-induced degradation in the transport properties of μc-Si:H layers [63] as well as in the efficiency of μc-Si:H solar cells [22]. In the past, mainly "highly microcrystalline" material, *i.e.* material deposited far from the μc-Si:H/a-Si:H transition, was studied.

However, solar cells exhibiting the highest efficiencies are fabricated near the μc-Si:H/a-Si:H transition. Therefore, light-induced degradation is an important argument for this material and contrasting data can be found in literature. In 1986 Liu [64] reported a light-induced degradation effect for μc-Si:H films containing grain sizes smaller than 120 Å [64]. On the other hand, Fonrodona *et al.* [65] reported the different behavior of nanocrystalline solar cells deposited by HW (hot wire)-CVD at different silane concentrations. In fact, a variation in dangling bond density under illumination was detected for a solar cell deposited at a SC-value of 6.2%. Conversely, they obtained stable solar cells at SC-values of 5 and 5.6%.

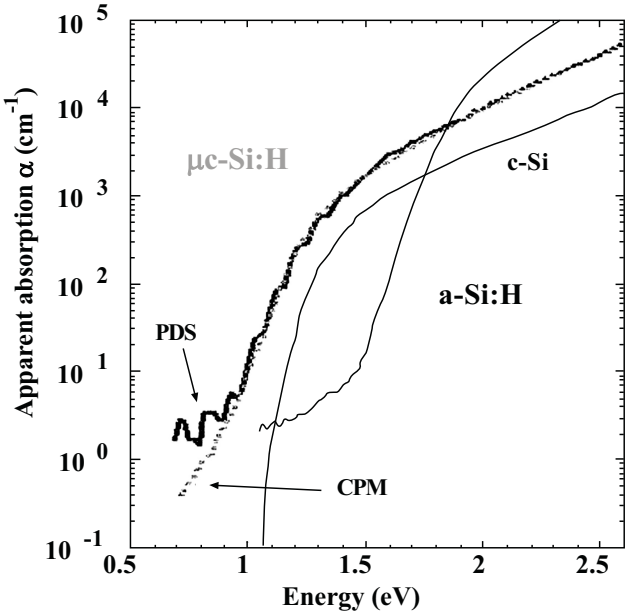


Figure 11: Typical curves for the optical absorption coefficient of photon energy, for (mono)crystalline silicon (c-Si), as well as for hydrogenated amorphous silicon (a-Si:H) and hydrogenated microcrystalline (mc-Si:H) silicon thin-films [62] (reproduced with permission of Elsevier).

Klein *et al.* [34] have reported up to 10% relative degradation in the efficiency of μc-Si:H HW-CVD solar cells containing a high amorphous volume fraction, after 1000 hours of exposure to light at an intensity of 100 mW/cm2 and a temperature of 50°C.

However, if it seems that the μc-Si:H films are more stable compared to light degradation, on the other hand, μc-Si:H is very sensitive to the incorporation of oxygen, both during deposition and after deposition (post-oxidation). This is why a gas purifier must be used during deposition in order to get "device-grade" microcrystalline silicon material [66]. Fortunately, once incorporated into complete solar cells, μc-Si:H is usually not subjected to post-oxidation. On the other hand, the electrical properties of single intrinsic layers can be dramatically affected by post-oxidation [67], the latter depending on the deposition conditions (especially on the power applied to the plasma). Therefore, the interpretation of transport measurements performed on layers can be a problem.

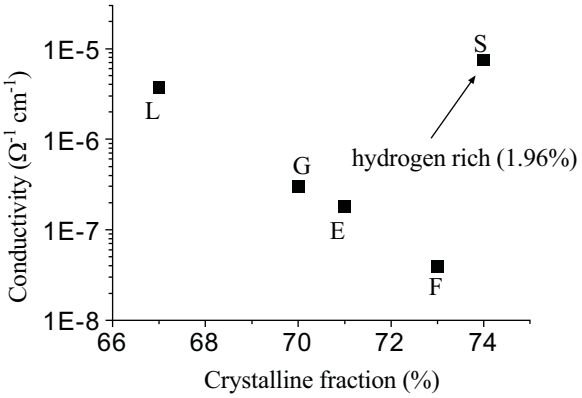


Figure 12: Conductivity as a function of the crystalline volume fraction.

Charge transport in microcrystalline silicon is strongly influenced by its heterogeneous microstructure composed of crystalline grains and amorphous tissue. An even bigger effect on transport is their arrangement in grain aggregates or possibly columns, separated by grain boundaries, causing transport anisotropy and/or depth profile of transport properties.

An example of the impact of crystalline fraction and hydrogen can be seen in (Fig. **12**). Low conductivity values are requested for p–i–n junction fabrication. A decrease in conductivity with increasing crystallinity can be clearly noticed in the figure. This behavior can be explained by the increased presence of grain boundaries inside the film.

Instead, the increase in hydrogen content induces a conductivity increase. This last behavior can be explained assuming a passivation effect of grain boundaries induced by dissolved hydrogen.

Indeed, unlike a-Si:H, where transport models have been successfully developed (see *e.g.* [68]), no simple generally accepted transport model is so far available for mc-Si:H.

Kocka *et al.* [69] recently analyzed electron transport in microcrystalline silicon thin-film and proposed a transport model which considers the columnar structure of this film [70]. A schematic picture of a microcrystalline film is given in Fig. **13**.

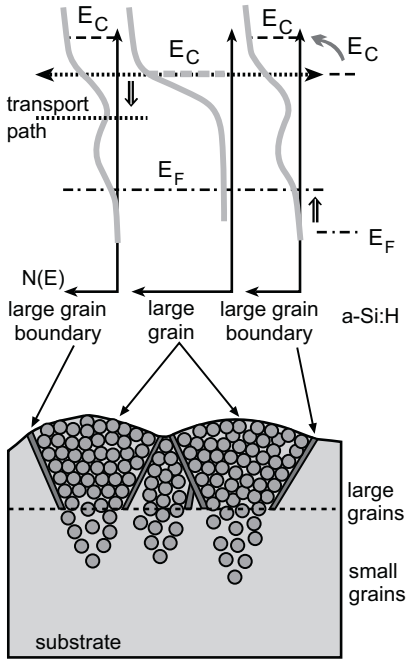


Figure 13: Schematic drawing of the uc-Si:H film structure and the density of states [69]. (reproduced with permission of Elsevier).

Authors concluded that it is necessary to know the transport path inside the film in order to correctly interpret conductivity. The microstructure of mc-Si:H, namely of the grain boundaries, plays an important role in electron transport. They also formulated a transport model that is based on the idea that there are at least two kinds of c-Si grains, small and LGs. Whenever potential barriers related to "LG boundaries" are formed, the transport properties deteriorate. The detrimental role of LG boundaries on transport stands in contrast with the beneficial optical effect of light trapping *via* scattering on the column heads. This raises the question about what kind of mc-Si:H microstructure is optimal for solar cells, LGs and/or columns. The question is still open.

5. SOLAR CELLS

5.1. Microcrystalline Silicon Solar Cells

Just like amorphous solar cells, microcrystalline silicon solar cells are usually designed with a p-i-n structure. The p-i-n structure is necessary as μc-Si:H films have a shorter lifetime than single-crystal cells. The three layers are a very thin (typically 20 nm) p-type layer, a much thicker undoped intrinsic (i) layer and a very thin n-type layer.

We have already seen that there are, however, some main important differences between μc-Si:H and a-Si:H solar cells; they are summarised below:

- The bandgap of μc-Si:H is about that of monocrystalline silicon (≈1.1 eV at room temperature) whereas that of a-Si:H is significantly higher, *i.e.* around 1.75 eV;

- μc-Si:H films have a lower absorption coefficient in the visible range compared to a-Si:H due to its indirect bandgap; therefore, thicker i-layers (around 1 μm or more) are required for μc-Si:H solar cells; this compares with typical values of 0.3 μm for a-Si:H;

- The light-induced degradation effect (or Staebler–Wronski effect) is either not present in μc-Si:H or considerably reduced.

Although μc-Si:H films have these advantages on amorphous silicon material, the higher conversion efficiency so far reached by single junction μc-Si:H solar cells in the laboratory is comparable with that reached by the best single junction a-Si:H cells after degradation (stabilized efficiency) [71].

Moreover, due to the reduced absorption coefficient of μc-Si:H films, a higher thickness is required for optimal light absorption but the deposition of μc-Si:H solar cells takes much longer than that of a-Si:H solar cells and is, therefore, more expensive.

The introduction of the micromorph tandem cell concept [36] has opened new potential. The 1.1 eV (microcrystalline Si) and 1.75 eV (amorphous Si) bandgap combination is very near to the ideal 'theoretical' bandgap combination needed to obtain maximum efficiency under AM1.5 illumination [72, 73].

Single junction μc-Si:H solar cells will be described in the following sections, giving the state of the art for this technology. Then the application of μc-Si:H films in silicon hybrid solar cells will be presented with a tandem structure made of microcrystalline and amorphous silicon thin-films.

Single junction microcrystalline silicon solar cells. Thin-film μc-Si:H solar cells can be divided into p-i-n and n-i-p types according to the film deposition order, although the window layer of the solar cell is the p-type layer in both cases. This is done in order to enhance the collection of holes, which are collected at the p-layer, and whose mobility is smaller than that of electrons. A detailed analysis of the transport process in thin-film amorphous silicon solar cells is reported by Deng and Shiff [74]. The asymmetrical drift of electrons and holes explains why amorphous silicon–based pin solar cells are more efficient when illuminated through their p-layers.

Fig. **14** (pin) also reports the two totally different designs for the solar cells involved, corresponding to transparent and opaque substrates connected to the use of the p-i-n or n-i-p configuration.

The n-i-p substrate configuration processing starts with the n-layer, which is normally grown on a metallic back contact. The first n-i-p cells were developed at Kaneka PV Research Division [75] in 1994. These cells had an initial conversion efficiency of 10.1% [75] for a film thickness of 2 μm (surface area 1 cm^2).

The characteristics of a cell which has a p-i-n structure prepared with the very high frequency glow discharge method were first reported by researchers at Neuchatel University [22]. An initial efficiency of 4.6% and short circuit current densities of up to 21.9 mA/cm^2 were obtained.

A typical diagram for a p-i-n cell is given in Fig. **14**.

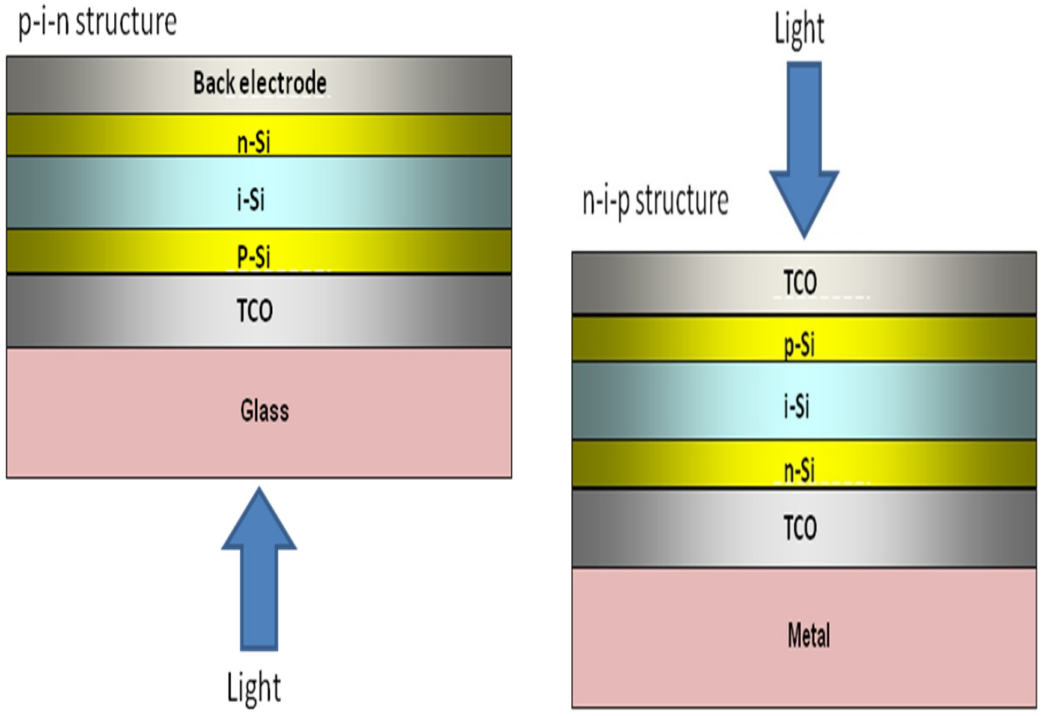


Figure 14: Schematic illustration of the structure of p-i-n (a) and n-i-p (b) solar cells.

In the "superstrate" design (Fig. **14(a)**), sunlight enters through the transparent substrate, which is usually glass or a transparent plastic. A conducting layer, typically a "transparent conductive oxide" (TCO) such as SnO_2, is deposited on the insulating substrate. The thin-film silicon layers are then deposited on the TCO, starting with a p-type window layer. Finally, a "back" reflector is deposited, which acts as an electrode for the n-type film layer. The "superstrate" configuration is adopted for the p-i-n structure. PV thin-film module manufacturers use soda-lime glass substrates coated with transparent conductive oxide. Soda-lime glass is used for its low cost but this glass has a negative impact on overall cell efficiency due to its absorption in the near infrared. In this spectral region μc-Si:H solar cells still have significant conversion efficiency. A solution could be the introduction in the production line of the more expensive low iron content glass.

In the "substrate" (n-i-p) design (Fig. **14b**), sunlight enters the cell before it reaches the substrate. Starting with the substrate, the cell is manufactured in reverse order, compared to the superstrate design: first a back reflector, then the film layers (starting with an n-type layer), and finally a TCO layer to act as an electrode to the topmost, window layer of the cell.

The main difference between the two configurations is that the underlying layer of a p-i-n cell is the transparent electrode, whereas the underlying layer of a n-i-p cell is the back electrode.

These two designs allow a very wide range of applications for amorphous silicon solar cells. The superstrate design (light enters through the substrate) is particularly suited for building-integrated solar cells in which a glass substrate can be used as an architectural element. The "substrate" design has generally been applied to solar cells using flexible, stainless steel (SS) substrates. The detailed construction of a deposition facility of course depends on whether the substrate is rigid or flexible. Finally, it turns out that the substrate has a profound effect on the properties of the first layers deposited upon it; this effect has led to fairly different cell structures for the "superstrate" and "substrate" designs.

In the thin-film deposition process, the need to keep the device at temperatures not higher than the highest temperature attained during the previous steps is of particular importance throughout the manufacturing process. This means that the "superstrate" configuration allows cheap deposition of SnO_2:F by spray pyrolysis (involving temperatures of 600°C to 800°C) at the beginning, so that the 200 to 300°C PECVD process is performed afterwards.

Moreover, the "superstrate" geometry includes an easy encapsulation process and, usually, higher conversion efficiency. In this case, enhanced η values are a common consequence of the relatively simple application of light confinement strategies [76].

Generally, transparent electrodes are made of oxides and there is a risk of these oxides being reduced by the hydrogen atoms used during growth. In the p-i-n structure the oxide window process must be thinner but the reduced film thickness increases contact resistance. The "superstrate" configuration adopted for p-i-n cells has the advantage that cell integration into the modules can be achieved with well consolidated techniques resembling those used for amorphous silicon.

For n-i-p cells, it should be possible to make integrated structures with methods that are equivalent to those used for Cu(In,Ga)Se_2-based solar cells [77]. At present, it is hard to determine which is better.

Historically the n-i-p configuration is connected to flexible substrates because it was used on opaque substrates or poorly transparent substrates like steel foils or high temperature polymers. However, the configuration is not limited to this choice. It is, in fact, compatible with any kind of substrates, such as rigid or flexible, transparent or opaque. Nevertheless, flexible substrates are still the main application for n-i-p cells because roll-to-roll processing makes them highly attractive for cutting down production costs as well as energy payback time, particularly when low cost substrates like polyethylene are used. Use of metal substrate requires substrate insulation as, for example, SiO_2 films, and this topic is still the focus of research [78, 79].

The schematic band diagram of a p-i-n device is illustrated in Fig. **15**. As with the a-Si:H-based solar cell, a particularly important conclusion that must be drawn is that the absorber layer, the intrinsic one, is indeed the space-charge zone. This means that:

- carrier transport is performed by drift, and not by diffusion; the mobility-lifetime product ($\mu\tau$) is now the key parameter that determines effective carrier recombination; the average distance covered by a carrier before recombining is given by $\mu\tau E$, where E is the electric field present,

- the usual hypothesis (in wafer-based PV) of a negligible recombination in the space-charge zone is not valid.

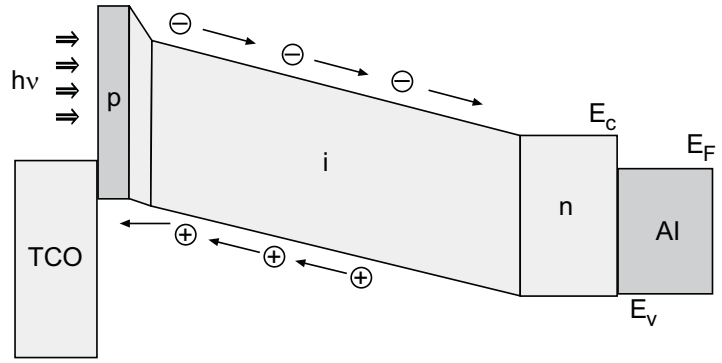


Figure 15: Band diagram of a p-i-n thin-film silicon solar cell.

As already mentioned, by using the AMPS-1D computer program [80] and a set of optimized parameters to describe a-Si:H [81], Schropp demonstrated that it is possible to design electronic levels such as band edges and to gain insight into device physics.

The electric field E(x) within the device causes all electron level energies such as E_C and E_V to vary in space in the same way. When the device is assembled, these Fermi energies must be equalized to create thermal equilibrium. Electrons are donated from the n-layer to the p-layer, which generates a built-in electric field; while level positions such as E_C and E_V now vary. The Fermi energy level remains constant.

Carriers are mainly generated in the intrinsic layer, where incoming light generates electron/hole pairs. Both electrons and holes are separated by the internal electric field (drift current), which is built by the doped layers (p-and n-type) on each side of the intrinsic material. Electrons are drifted to the n-type layer, whereas holes, which exhibit lower mobility, are driven towards the p-type one. The geometry presented favors an increased production of electron-hole pairs near the p-i interface, so that hole collection is facilitated by reducing their mean collection distance. It is important to note that carriers generated in the doped layers do not contribute toward the measured current, as the doped material density of defects is too large to allow carrier transport. As a consequence, light absorption in the p-type is to be minimized.

Thus, the electrical, optical and structural properties of the intrinsic layer strongly influence the PV performance of the cell.

Although short circuit current, open circuit voltage and fill factor are all important parameters to be optimized in terms of IV cell characteristics, the open circuit voltage is used here as a guide to overall cell characteristics as it is directly related to the lifetime of the cell. The current is mainly related to light trapping effects and cell film thickness.

In μc-Si:H-based thin-film solar cells, improved performance is achieved [82, 83] when i-layers contain a substantial amount of amorphous tissue but are still in the microcrystalline regime [84]

(a-Si:H/μc-Si:H transition). Bailat *et al.* [59] clearly demonstrated the correlation between the open circuit voltage (Voc) and crystallinity.

Nath *et al.* [85] have reported the dependence of open-circuit voltage (Voc) on crystallinity. Precisely, open-circuit voltage diminishes as the crystalline volume fraction (Fc) increases (Fig. **16**). Authors have identified three contributing factors to the decrease in Voc with increasing Fc, namely an increase in both mid-gap and tail defects as well as a decrease in the mobility gap.

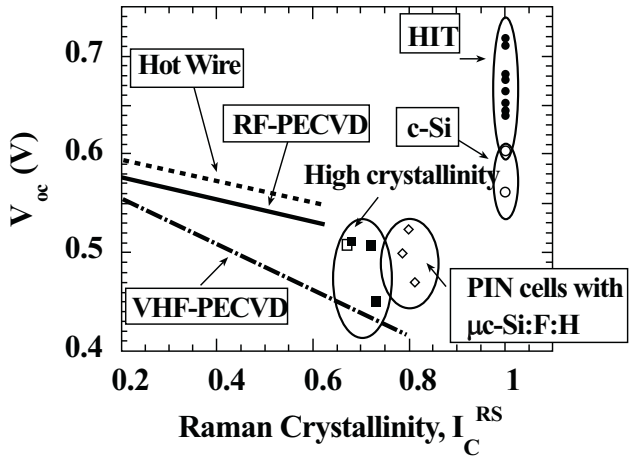


Figure 16: The Voc of silicon solar cells with varying Raman crystallinity [86] (reproduced with permission of Elsevier).

The same authors have also [86] reported a deviation to this general rule in fluorinated μc-Si:H solar cells when grain dimensions increase. The large grain fluorinated films grown with high crystalline volume fraction and large grain exhibit an increased performance. They explained this behavior with a reduction in midgap defects and effective density of states at band edges.

The impact of grain dimension was already studied by Werner *et al.* [87]. According to Werner *et al.* the reason why a microcrystalline silicon cell exhibits a typical 10% or more regardless of its small grain size is because of the very low recombination speed at its grain boundaries. This low recombination speed originates from the small barrier height at the grain boundaries, which is guaranteed by (a) the passivation of hydrogen at grain boundary defects, (b) uncharged intrinsic grains (low oxygen density), and (c) the (110) orientation of crystal grains. These hypotheses are in agreement with results obtained by Nath *et al.*

By the close of the 1990s, low-T fabricated μc-Si:H solar cells on glass had reached stable efficiencies of up to 8.5%. However, due to the low deposition rate (<40 nm/min) of the μc-Si:H film and technical difficulties with the development of industrial-scale VHF PECVD systems, μc-Si:H single-junction solar cells do not seem to be commercially viable at present. The same conclusion appears to apply to the 2 μm thick, 10% efficient μc-Si:H STAR solar cell developed at Kaneka using intermediate-T (~550 °C) and standard 13.56-MHz PECVD [88]. Nevertheless, these results showed that a c-Si thickness of merely 2 μm is all that is needed for obtaining a short-circuit current density Jsc of >24 mA/cm^2.

5.2. Contact Layers

Generally, all thin-film silicon solar cells use a transparent conductive oxide (TCO) layer as front contact, whereas a reflective contact material is needed at the back.

Various transparent conducting oxides have been reported for their solar cell applications. Among the reported TCOs, ZnO [89], ITO [90], and SnO2 [91] are most widely used in the PV area. The PV market requires low-cost solar cells for the widespread use of PV, which can be achieved by introducing low-cost materials and processes for solar cell production. ZnO has been considered as the most promising TCO material in view of cost and properties. Several deposition techniques, such as spray pyrolysis [92], CVD [93] and sputtering [94], have been successfully employed to produce ZnO films. Sputtering has been the preferred method for its production. The window layer in solar cells must be well optimized so that it has low absorption and critical resistivity. The interface properties with underlying layers have to be carefully considered in preparing the window layer.

Very high quality transparent and back reflecting films can reduce the total thickness required for the absorbing layer and, subsequently, the cell cost.

TCO films are strongly affected by deposition parameters (argon ambient pressure and substrate temperature).

For thin-film solar cells based on amorphous (a-Si:H) or microcrystalline silicon (μc-Si:H) with absorber layer(s) in the micrometer range, efficient light trapping is of the utmost importance. Light trapping and effective light incoupling are important aspects for optimized utilization of the solar spectrum. The use of transparent conductive oxides (TCO: ZnO) with a randomly textured surface is a common approach to meet both requirements [95].

As previously reported, two basic cell configurations are used, in practice, for thin-film silicon solar cells: substrates and the p–i–n or ‘superstrate’ configuration. We shall now see which solution has been proposed to form contact layers for the two configurations.

p–i–n or ‘superstrate’ configuration

In the case of a p–i–n deposition sequence, light enters the cell through the glass substrate on which the TCO layer has been deposited as contact layer. We have seen that the p-layer is the first film crossed by incoming light. However we have also seen that the electrical and optical properties of this layer are low. So, this layer should be relatively thin (about 10 nm) and have a low absorption coefficient in order to allow light to reach more efficient layers. The light then crosses the much thicker i-layer (the active layer) and, finally, the relatively thin n-layer (20 nm typical thickness), and reaches (if not yet absorbed) the reflective back contact layer. This last reflective back contact can be a TCO and/or a metal layer. Actual reflectivity is determined by the combination of the TCO interlayer and the metal.

In this ‘superstrate’ configuration, not only are the electrical and optical properties of the TCO film important, but it is also essential to ensure that it remains chemically stable during plasma

deposition of the other layers. The use of SnO2:F is quite common for a-Si:H solar cells, but must be avoided for single-junction μc-Si:H cells, as it is partly chemically reduced in the H_2-rich plasmas that are necessary in this case. Current research also focuses on ZnO, deposited either by sputtering [96] or by low-pressure CVD (LPCVD) [97].

The higher electrical and optical property quality indium-tin-oxide (ITO) film cannot be used in this application as it can be chemically reduced, even without any hydrogen dilution, *i.e.* already by hydrogen formed by silane decomposition during the PECVD process.

A very important aspect for the back contact is its capacity to reflect whatever light reaches this far back into the intrinsic absorber layer. An appropriate combination of a thin TCO layer with a thicker metallic layer (Al or Ag) provides both the desired optical properties (high value of reflectivity) and high electrical conductivity.

n–i–p or 'substrate' configuration

This configuration has the advantage of using lightweight, unbreakable substrates, such as stainless steel, polyimide or PET. These are generally either opaque, as in the case of stainless steel, or, if they are transparent, they are often easily damaged by ultraviolet light, like most plastics.

Therefore, the substrate/n–i–p configuration is generally used in this case, and lets light enter the device through the semiconductor layer deposited as last layer, *i.e.* still through the p-layer. The top TCO layer is the critical layer, and both ITO and ZnO are used in this case.

Although the deposition sequence differs from the superstrate configuration, the electrical and optical properties required for these films remain stringent.

Electrical TCO properties Electrical properties are determined by the sheet resistance of the TCO film, which is related to specific resistivity ρ and film thickness d, *i.e.* $R_{sheet} = \rho/d$. Sheet resistance is practically important for integrated serial connection of cells to a solar panel; it gives rise to a series resistance and, hence, to electrical losses.

Obviously, sheet resistance should be minimized; this is achieved by:

- reducing the specific resistivity of the TCO material, which can be preferentially done by increasing carrier mobility, rather than carrier concentration; in fact, an increase in carrier concentration enhances the optical absorption in the near-infrared region (so-called free carrier absorption);

- increasing the TCO thickness, which, unfortunately, enhancing TCO absorbance, too.

Thus, TCO sheet resistance is inherently related to the absorption of near-infrared light within the TCO film. In fact, increasing carrier mobility is the only way to decrease sheet resistance without

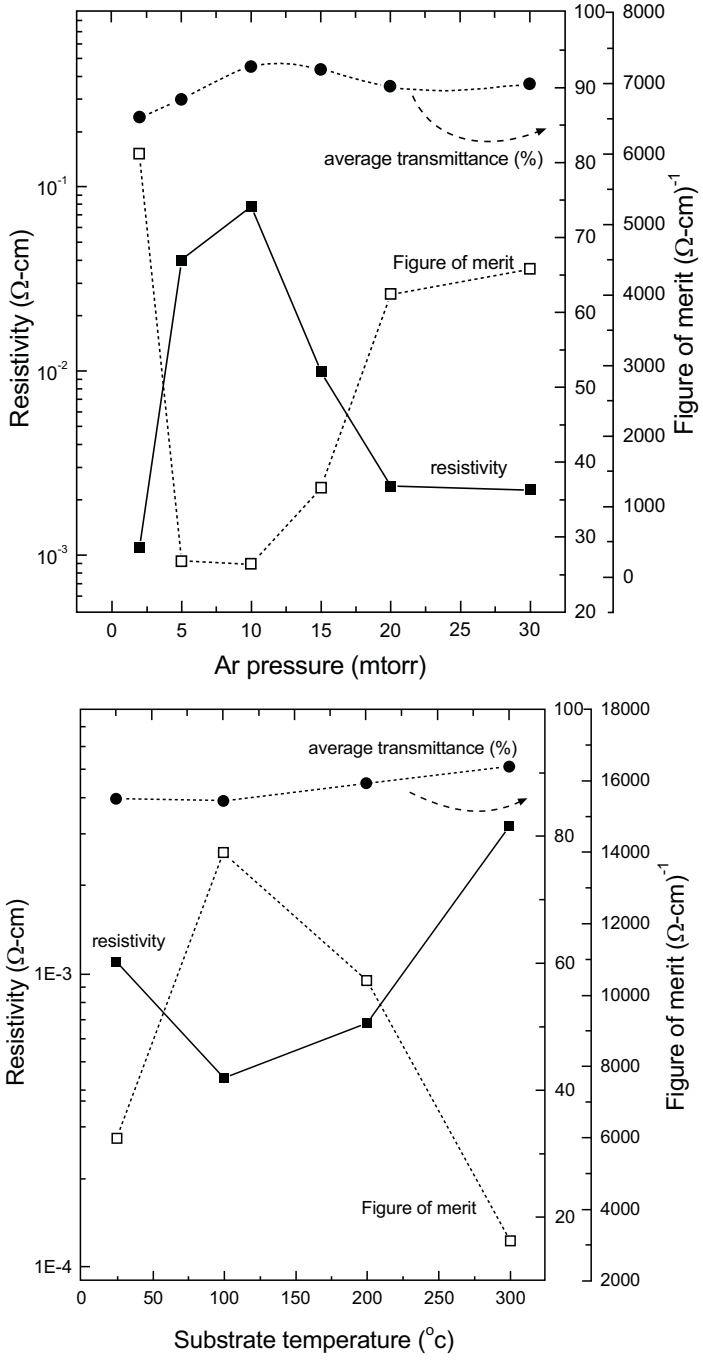


Figure 17: Example of the impact of Ar pressure and substrate temperature on TCO resistivity. More details about the deposition procedure can be found in the reference [98] (reproduced with permission of Elsevier).

generating a rise in optical absorption of the TCO layer in the near-infrared. The latter may, on the other hand, significantly contribute toward TCO-related optical losses (see below) already at cell level, while sheet resistance causes electrical losses practically only at module level, as a consequence of the integral serial connection of cells.

Considering the mentioned relationship between sheet resistance and TCO absorbance, it follows that efficiency considerations imply a trade-off between these two TCO quantities.

As mentioned, deposition parameters can have a strong effect on the electrical properties of the film. For example, Lee *et al.* [92] have reported the effect of temperature and Ar pressure on film resistivity (See Fig. **17**).

Optical TCO properties Apart from the optical absorption that is directly related to sheet resistance, the TCO should have additional optical properties:

- reduced reflection due to refractive index grading; this effect applies to the entire wavelength range of the spectral cell response;

- light scattering and subsequent light trapping in the silicon absorber; this second effect applies to weakly absorbed light that penetrates up to the reflective back contact of the cell. The effect is absolutely essential for thin-film silicon solar cells and, especially, for μc-Si:H cells. Without light trapping, short-circuit current densities Jsc would remain unreasonably low.

Both functions may be achieved by a suitable surface texture of the TCO, with feature sizes comparable to the wavelengths (divided by the refractive index of the corresponding layer).

For shorter wavelengths, the difference in reflectance is due to index grading at the front TCO/p-layer interface. For longer wavelengths penetrating to the back contact, the reduced reflectance stems from both index grading and light trapping.

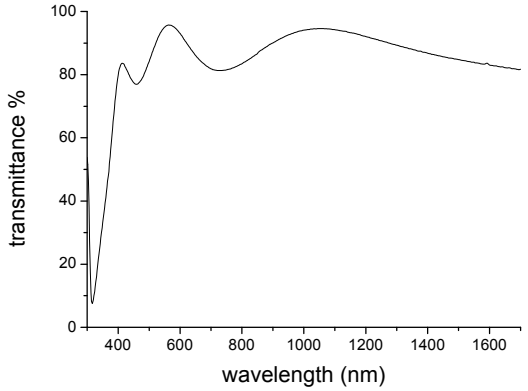


Figure 18: Typical transmission spectrum of TCO film.

A typical transmission spectrum of TCO film is reported in Fig. **18**.

An important aspect should be mentioned here. During the multiple passes of trapped light, light goes through the TCO several times and is reflected by the back contact. Hence, all absorption losses will accumulate, and this makes the need for very low light absorption in contact layers more severe. It is in this field of contact layers and light trapping that most progress is to be expected in cell research, whereas the photoactive absorber layer, the i-layer, has been well optimized.

5.3. Micromorph Tandem Silicon Solar Cells

Although microcrystalline silicon cells formed at low temperatures have a potential for high efficiency, their efficiency in single-cell structures is much lower than that of bulk mono or multi-crystalline cells. New concepts have been researched to achieve a substantial improvement in efficiency. In an attempt to achieve this, different groups introduced the concept of two-stacked (hybrid) structures (Fig. **19**) in which multiple cells with different light absorption characteristics are stacked together.

This device structure, as already mentioned, was pioneered by the University of Neuchatel in the 1990s [22].

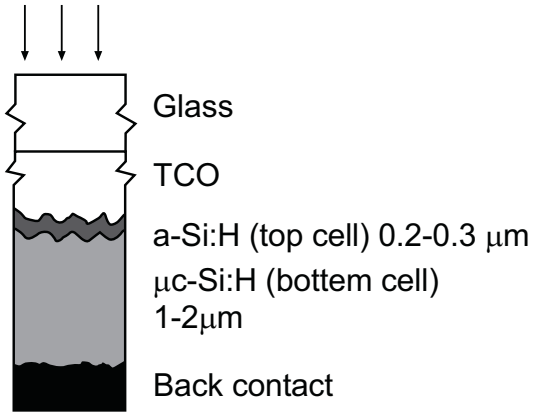


Figure 19: Schematic device structure of the micromorph tandem cell in the 'superstrate' configuration, *i.e.* in the configuration glass/TCO/p-i-n a-Si:H/p-i-n μc-Si:H.

This approach allows better characteristics to be obtained with existing materials and processes. There are different advantages in using a layered structure: it enables a much better use of the solar spectrum; it enables to obtain a higher open-circuit voltage and, it allows, to some extent, suppression of the rate of reduction in cell performance, which is caused by optical degradation phenomena that are observed when using amorphous silicon-based materials (Staebler–Wronski effect). Hence, in principle, higher PV efficiency can be achieved.

Microcrystalline and amorphous silicon are quite good for tandem cells. It can be proven that the bandgap combination of 1.1 eV with 1.75 eV to is very near the ideal combination for tandem solar cells (See Fig. **20**).

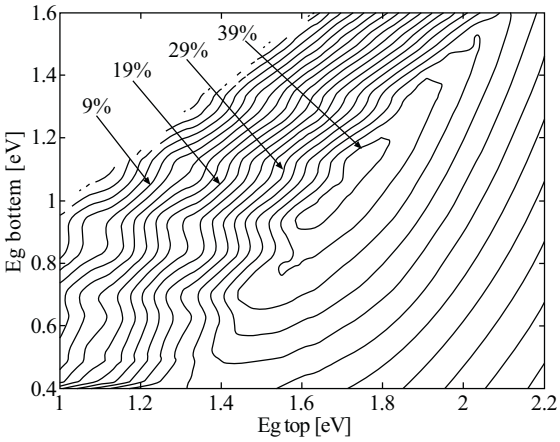


Figure 20: Semi-empirical upper limit of efficiency g as a function of the energy gap Eg of the bottom and top cells of a tandem solar cell [99] (reproduced with permission of Elsevier).

Practically speaking, the double layer thickness must be optimized in order to match the current of the two sub cells.

The preliminary structure studied was composed of stacked (tandem) cells in which an amorphous silicon cell was combined with a microcrystalline silicon cell (Fig. **19**).

The low Jsc of stable a-Si:H cells ensures that the thickness of the μc-Si:H cell in the stack does not have to be increased significantly, compared to a stand-alone μc-Si:H cell. Thus, using PECVD, a high PV module efficiency can be achieved with an economic process.

The research team at the University of Neuchatel has coined the term "micromorph" for this tandem cell and reported initial (*i.e.* non-stabilized) efficiencies of up to 13.1% [22].

The "micromorph" concept has also been considered by various organizations, including Kaneka [100]. In 2001 this company started a pilot production of their so-called "hybrid" thin-film PV technology.

The production line is based on low temperature deposition (13.56-MHz PECVD) onto a large (~0.85 m^2) TCO-coated soda lime glass. The μc-Si:H cell is about 2 μm thick, whereas the a-Si:H top cell is about 5 times thinner.

This company introduced an intermediate thin TCO layer between the amorphous silicon layer of the top cell and the microcrystalline silicon layer of the bottom cell [101].

In this configuration, a transparent intermediate layer reflects part of the light that has not been absorbed while passing through the amorphous silicon layer of the top cell.

As a result, the effective light sensitivity of the top cell is higher than that of a top cell with the same thickness in a conventional hybrid structure. Hence, an improvement can be expected in the

short-circuit current Jsc of the overall hybrid cell. The cell with a transparent intermediate layer is more sensitive at shorter wavelengths (top cell).

The presence of the transparent intermediate layer enables to reduce the top cell thickness needed to obtain the same current compared with a conventional hybrid cell. If the thickness of the amorphous silicon film in the top cell can be reduced, then it should also be possible to reduce photo-degradation of the cell.

Quite good initial efficiency rates (aperture area) of over 12% were reported for these large ($0.41m^2$) all-silicon modules. The best cell (area 1 cm^2) made so far has an initial efficiency of 14.5% [102].

Due to the thinness of the a-Si: H cell in the stack, micromorph (or hybrid) PV devices are expected to decay very weakly in the field. The best stable efficiency confirmed as yet is 11.7% for a sub-module [103] produced by Kaneka in 2004 [104], and 11.9 for a cell manufactured by the Neuchatel group in collaboration with industrial partner Oerlikon [105].

These technologies promise high stable average efficiency of about 10% for large-area mass-produced modules using large-area low-T processing equipment from the LCD industry.

However, they require a textured TCO layer and a high capital cost of the deposition tool for the ~2 μm thick μc-Si:H cell, which can be a limitation for high throughput production lines.

CONCLUSIONS

The introduction of microcrystalline silicon in thin-film silicon solar cells is relatively recent. The interest in microcrystalline silicon issued from the need to overcome some intrinsic limitations of amorphous solar cells. However the results so far obtained are still unsatisfactory and, in fact, incorporating μc-Si:H is, thus, still a topic of research.

Several deposition techniques have been tested, and the PE-CVD ones have achieved the best results so far. PE-CVD equipment is already used for a-Si:H deposition with a mixture of silane and hydrogen, and increasing the hydrogen to silane ratio in the feed gas easily obtains microcrystalline growth with reduced variation of equipment.

This technique has many advantages, such as low temperature deposition, use of non-toxic materials and deposition on large substrates. All these features offer the potential for future cost reduction of photovoltaic modules based on this material. Hydrogenated microcrystalline silicon is a complex material composed of a mixture of crystalline and amorphous silicon that can be more easily doped than a-Si:H. On the other hand, it is also more sensitive to contaminants than a-Si:H (for example, oxygen). This material exhibits a wide range of microstructures that depend both on deposition conditions and on the substrate material.

It is quite clear that the best solar cells are obtained when the deposition conditions (hydrogen dilution, temperature,) are tuned in order to approach the microcrystalline/amorphous transition.

The strong interest in μc-Si:H also comes from the quite different optical properties of μc-Si:H compared to a-Si:H. Although μc-Si:H has an indirect optical bandgap at 1.1 eV and has, therefore, a relatively low optical absorption, this optical gap matches the higher bandgap of a-Si:H (about 1.75 eV) for a tandem cell quite well.

The electron transport properties of μc-Si:H resemble those typical of a-Si:H but with increased conductivity. The carrier transport mechanism can be explained considering the amorphous/disordered material present in μc-Si:H layers.

Although the electronic properties are quite better, lifetime is reduced and a p-i-n type or n-i-p type device structure is used also for microcrystalline silicon-based devices. In such devices, carrier collection is enhanced by drift, *i.e.* by the internal electric field that prevails in the i-layer. Currently, the conversion efficiency of the best single junction μc-Si:H solar cell is around 10%.

Microcrystalline silicon was initially introduced in single junction μc-Si:H solar cells due to the reduced electrical performance degradation associated with the Staebler–Wronski effect. However, the conversion efficiency achieved so far by the best single junction μc-Si:H solar cell is around 10%.

One expects a further increase in the efficiency of μc-Si:H single junction solar cells mostly by implementation of improved light trapping schemes and by a corresponding increase in short circuit current density. Improved light trapping will be based on the development of new and better suited transparent conductive oxides, structured substrates (periodic gratings or rough random substrates).

More improvements are expected using microcrystalline silicon in tandem cells consisting of a stack with a top a-Si:H cell and a bottom μc-Si:H cell. This combination of materials can be shown theoretically to possess bandgaps that are very near to the best combination of bandgaps for optimum conversion of the AM1.5 spectrum. For reaching maximum efficiency, an intermediate reflector is used between the bottom and the top cell. Such tandem devices generally suffer less from light-induced degradation in the amorphous top cell. In general, the microcrystalline bottom cell inside the tandem is stable (as it is only exposed to the long wavelength part of the solar spectrum). In order to gain both in conversion efficiency and in device stability, one should reduce the thickness of the amorphous top cell and further optimize light trapping. This may hopefully lead to solar cells with stabilized efficiencies of 13–14%. The industrial production of tandem modules has currently been started by a Japanese module manufacturer.

Several other firms (mainly Japanese) are carrying out research on this subject and a few of them have even developed prototype modules.

Thin-film silicon offers interesting applications in building-integrated photovoltaics through its esthetical appearance and the versatility provided in the choice of a substrate material. On the other hand, the ‘micromorph’ tandem concept allows for an increase in module efficiency towards a stabilized value above 10%. Because of these factors, one may reckon that the industrial development of thin-film silicon tandem modules based on a combination of amorphous and

microcrystalline silicon will be intensified during the next few years, leading to a clear reduction in module costs, probably down to values below 1$/Wp.

ACKNOWLEDGEMENT

Declared none.

CONFLICT OF INTEREST

The author(s) confirm that this chapter content has no conflict of interest.

REFERENCES

[1] Thin-Film Photovoltaic (PV) Cells Market Analysis to 2020-CIGS (Copper Indium Gallium Diselenide) to Emerge as the Major Technology by 2020. Report on ReportsandReports July 2010
[2] Carabe J, Gandia JJ. Thin solid silicon solar cell. Opto-Electronics Rev 2004; 12(1): 1-6.
[3] Zeman M. Advanced Amorphous Silicon Solar Cell Technologies. In: Poortmans J, Arkhipov V, Eds. Thin Film Solar Cells Fabrication, Characterization and Applications. Edit by, West Sussex England John Wiley and Sons Ltd 2006; pp. 173-230
[4] Sterling HF, Swann RCG. Chemical vapour deposition promoted by r.f. discharge. Solid State Elect 1965; 8: 653-8.
[5] Chittick RC, Alexander JH. The preparation and properties of amorphous silicon. Journal of Electrochemical Society 1969; 116: 77-81.
[6] Spear WE, Le Comber PG. Substitutional doping of amorphous silicon. Solid State Communication 1975; 17(9): 1193-8.
[7] D.E. Carlson and C.R. Wronski. Amorphous silicon solar cell. Applied Physics Letter 1976; 28: 671-3.
[8] Kuwanov Y, Imai T, Ohnishi M, Nakano S. Microcrystalline silicon solar cells deposited at high rates by combination of VHF-PECVD. Proceedings of the 14th IEEE Photovoltaic Specialist Conference; 1980; San Diego, USA: pp. 1408-11.
[9] Benagli S, Borrello D, Vallat-Sauvain E, *et al.* High-Efficiency Amorphous Silicon Devices on LPCVD-ZnO TCO Prepared in Industrial KAI TM-M R&D Reactor Proceedings of the 24th European Photovoltaic Solar Energy Conference; 2009; Hamburg, Germany: pp. 1245-8.
[10] Staebler DL, Wronski CR. Reversible conductivity changes in discharge-produced amorphous Si. Applied Physics Letter 1977; 31(4): 292–4.
[11] Matsuda A. Formation kinetics and control of microcrystallite in uc-Si:H from glow discharge plasma. Journal Non-Crystal Solids 1983; 59-60: 767-75.
[12] Hattori Y, Kruangam D. High efficiency amorphous heterojunction solar cell employing ECR-CVD produced p-type microcrystalline SiC film. Tech Dig PVSEC-3, 1987; pp. 171-8.
[13] Faraji M, Gokhale S, Choudhari SM, Takwale MG, Ghaisas SV. High mobility hydrogenated and oxygenated microcrystalline silicon as a photosensitive. Applied Physics Letter 1992; 60: 3289-92.
[14] Rath JK, Galetto M, van der Werf CHM. Hot Wire CVD: A One-Step Process to Obtain Thin Film Polycrystalline Silicon at a Low Temperature on Cheap Substrates. Proceddings of the 9th International Photovoltaic Science and Engineering Conference 1996; Miyazaki, Japan: pp. 227-31.
[15] Tawada Y, Okamoto H, Hamakawa Y. a-SiC:H/a-Si:H heterojunction solar cell having more than 7.1% conversion efficiency. Applied Physics Letter 1981; 39(3): 237-9.
[16] Nakamura G, Sato K, Yukimoto Y, Shirahata K. Proceedings of the 3rd EC Photovoltaic Solar Energy Conference 1980; Cannes, France: pp. 835-9.
[17] Deckman HW, Wronski CR, H. Witzke, Yablonovitch E. Optically enhanced amorphous silicon solar cells. Applied Physics Letter 1983; 42(11): 968-75.

[18] Arya RR, Carlson DE. Amorphous silicon PV module manufacturing at BP Solar. Progress in Photovoltaic's: Research and Application 2002: 10; 69–76.

[19] Maruyama E, Okamoto S, Terakawa A, Shinohara W, Tanaka M, Kiyama S. Toward stabilized 10% efficiency of large-area (>5000 cm2) a-Si/a-SiGe tandem solar cells using high-rate deposition. Solar Energy Materials & Solar Cells 2002; 74: 339–49.

[20] Ichikawa Y, Yoshida T, Hama T, Sakai H, Harashima K. Production technology for amorphous silicon-based flexible solar cells. Solar Energy Materials & Solar Cells 2001; 66: 107–15.

[21] S. Guha, Yang J, Banerjee A. Amorphous silicon alloy photovoltaic research—present and future. Progress in Photovoltaic's: Research and Application 2000; 8: 141–50.

[22] Meier J., Dubail S, Fluckiger R, Fischer D, Keppner H, Shah A. Intrinsic microcrystalline silicon (mc-Si:H) a promising new thin film solar cell material. Proceedings of the 1st World Photovoltaic Solar Energy Conference, 1994; Amsterdam, The Netherlands: 476–9

[23] Vallat-Sauvain E, Shah A, Bailat J. Advances in Microcrystalline Silicon Solar Cell Technologies. In: Poortmans J, Arkhipov V, Eds. Thin Film Solar Cells Fabrication, Characterization and Applications Edit by, West Sussex England John Wiley and Sons Ltd 2006; pp.134-71

[24] Matsuda A. Microcrystalline silicon: Growth and device application. Journal Non-Crystal Solid 2004; 338-340: 1-12

[25] Sriraman S, Agarwal S, Aydil ES, Maroudas D. Mechanism of Hydrogen-induced crystallization of amorphous silicon. Nature 2002; 418: 62-5

[26] Collins R, Yang B. High rate low kinetic energy gas-flow-sputtering system. Journal Vacuum Science and Technology 1989; B7: 155-68

[27] Collins RW, Ferlauto AS, Ferreira G.M, *et al.* Evolution of microstructure and phase in amorphous, protocrystalline, and microcrystalline silicon studied by real time spectroscopic ellipsometry. Solar Energy Materials & Solar Cells 2003; 78; 143-50

[28] Vetterl O, Finger F, Carius R, *et al.* Intrinsic microcrystalline silicon: A new material for photovoltaics. Solar Energy Materials & Solar Cells 2000; 62; 97-108

[29] Pernet P. Proceedings of the 14th European Photovoltaic Solar Energy Conference; 1997: Barcelona, Spain; pp. 2339-42.

[30] Veprek S, Marecek V. Reactivity of solid silicon with a dydrogen. Solid State Electronics 1968; 11: 683-705.

[31] Tsu R, Izu M, Ovshinsky SR, Pollack F H. Electroreflectance and Raman scattering investigation of glow-discharge amorphous Si:F:H. Solid State Communication 1980; 36: 817–22

[32] Uchida Y, Ichimura T, Ueno M, Haruki H. Microcrystalline Si: H Film and Its Application to Solar Cells Japanese Journal of Applied Physics 1982; 21: L586–8.

[33] Wang C, Lucovsky G. Plasma Deposition of Microcrystalline Silicon Solar Cells. Proceedings of 10th IEEE Photovoltaic Specialists Conference; 1990: Kissimmee, USA; pp. 1614-9

[34] Klein S, Finger F, Carius R, *et al.* Intrinsic microcrystalline silicon prepared by hot-wire chemical vapour deposition for thin film solar cells. Thin Solid Films 2003; 430: 202-7

[35] Curtins H, Wyrsch N, Favre M, Shah AV. Plasma enhanced chemical vapor deposition (PECVD) of amorphous silicon thin films Plasma Chemical Proc 1987; 7(3): 267-73.

[36] Meier J, Flückiger R, Keppner H, Shah A. Complete microcrystalline p-i-n solar cell. Applied Physics Letters 1994; 65: 860–2.

[37] Howling AA, Dorier JL, Hollenstein C, Kroll U, Finger F. Frequency effects in silane plasmas for plasma enhanced chemical vapor deposition. Journal Vacuum Science Technology 1992; A10: 1080-6.

[38] Heintze M, Zedlitz R, Bauer GH. Analysis of high rate a-Si:H deposition in VHF plasma, Journal of Physics D: Applied Physics 1993; 26: 1781–6.

[39] Guo L, Kondo M, Fukawa M, Saitoh K, Matsuda A. High Rate Deposition of Microcrystalline Silicon Using Conventional Plasma-Enhanced Chemical Vapor Deposition. Japanese Journal of Applied Physics 1998; 37: L1116-8

[40] Kondo M, Fukawa M, Guo L, Matsuda A. Plasma Composition by Mass Spectrometry in a Ar-SiH4-H2. Journal Non-Cryst Sol 200; 84: 66-9.

[41] Niikura C, Kondo M, Matsuda A. High rate growth of microcrystalline silicon films. Proceedings of the 3rd World Conference on Photovoltaic Solar Energy Conference; 2003; Osaka, Japan; pp. 1710–3

[42] Matsui T, Matsuda A, Kondo M. High-rate microcrystalline silicon deposition for p–i–n junction solar cells. Solar Energy Materials & Solar Cells 2006; 90: 3199–204

[43] Meier J, Kroll U, Spitznagel J, *et al.* Plasma deposition of microcrystalline silicon. Proceedings of the 31st IEEE Photovoltaic Specialist Conference; 2005: Barcelona, Spain; pp. 1464-7

[44] Binetti S, Acciarri M, Bollani M, Fumagalli L, von Kanel H, Pizzini S. Nanocrystalline silicon films grown by Low Energy Plasma Enhanced Chemical Deposition for optoelectronic application Thin Solid Films 2005; 487: 19-23

[45] Rosenblad C, Deller HR, Dommann A, Meyer T, Schroeter, von Kanel H. Low energy plasma enhanced chemical vapor deposition. Journal Vacuum Science Technology Vac Surf Films 1998; 16: 2785-92.

[46] Moustakas TD, Paul H, Friedman R. Properties and photovoltaic applications of microcrystalline silicon films prepared by rf reactive sputtering. Journal of Applied Physics 1985; 58: 983-88

[47] Klein S, Finger F, Carius R, Stutzmann M. Deposition of microcrystalline silicon prepared by hot-wire chemical-vapor deposition: The influence of the deposition parameters on the material properties and solar cell performance. Journal of Applied Physics 2005; 98: 024905-12

[48] Smit C, Hamers EAG, Korevaar BA, van Swaaij RA, van de Sanden MCM. Fast deposition of microcrystalline silicon with an expanding thermal plasma. Journal Non-Crystal Solid 2002; 299-302: 98-102.

[49] Kosku N, Kurisu F, Takegoshi M, Takahashi H, Miyazaki S. High-rate deposition of highly crystallized silicon films from inductively coupled plasma. Thin Solid Films 2003; 435: 39-44

[50] Schellenberg JJ, Mcleod RD, Mejia SR, Card HC, Kao KC. Microcrystalline to amorphous transition in silicon from microwave plasmas. Applied Physics Letter 1986; 48: 163-9.

[51] Shirai H, Sakuma Y, Yoshino K, Uemaya H. Proceedings of the Materials Research Society Symposium; 2001; 609: A.4.4.1–6

[52] Yan B, Yue G, Yang J, Lord K, Banerjee A, Guha S. Microcrystalline silicon solar cells made using RF, MVHF. Proceedings of the 3rd World Conference on Photovoltaic Solar Energy Conference; 2003; Osaka, Japan; pp. 2773–8.

[53] Acciarri M, Binetti S, Bollani M, *et al.* Nanocrystalline silicon film grown by lepecvd for photovoltaic applications. Solar Energy Materials & Solar Cells 2005; 87; 11-4

[54] Lejeune M, Beyer W, Carius R, Muller J, Rech B. Silicontetrachloride based microcrystalline silicon for application in thin film silicon solar cells. Thin Solid Films 2004; 451-2: 280-5

[55] Platz R., Wagner S. Intrinsic microcrystalline silicon by plasma-enhanced chemical vapor deposition from dichlorosilane. Applied Physics Letter 1998; 73: 1236-42

[56] Cicala G, Capezzuto P, Bruno G. From amorphous to microcrystalline silicon deposition in SiF4–H2–He plasmas: *in situ* control by optical emission spectroscopy. Thin Solid Films 2001; 383: 203-5

[57] Shinohara R, Aya Y, Hishida M, *et al.* Recent Progress in Thin-Film Silicon Photovoltaic Technologies Proceedings of 25th European Photovoltaic Solar Energy Conference and Exhibition/5th World Conference on Photovoltaic Energy Conversion; 2010; Valencia, Spain; pp. 2735-9.

[58] Kunii K, Murata M, Matsumoto K, *et al.* Proc. 33rd IEEE Photovoltaic Science and Engineering Conference; 2008; San Diego, USA: pp. 259-64.

[59] Bailat J, Vallat-Sauvain E, Feitknecht L, Droz C, Shah A. Microstructure and open-circuit voltage of n−i−p microcrystalline silicon solar cells. Journal of Applied Physics 2003; 93(9): 5727-33

[60] Le Donne A, Binetti S, Isella G, *et al.* Advances in Structural Characterization of Thin Film Nanocrystalline Silicon for Photovoltaic. Solid State Phenomena 2008; 131-3; 33-38

[61] Smit C, van Swaaij R, Donker H, Petit A, Kessels W, van de Sanden M. Determining the material structure of microcrystalline silicon from Raman spectra. Journal of Applied Physics 2003; 94: 3582-9

[62] Shah A, Meier J, Vallat-Sauvain E, *et al.* Microcrystalline silicon and 'micromorph' tandem solar cells. Thin Solid Films 2002; 403-4; 179–87

[63] Goerlitzer M, Beck N, Torres P, *et al.* Structural properties and electronic transport in intrinsic microcrystalline silicon deposited by the VHF-GD technique. Journal of Non-Crystalline Solids 1998; 227–230; 996-1000.

[64] Liu HN, Xu MD. The Staebler-Wronski effect in microcrystalline silicon films. Solid State Communication 1986; 58-9: 601-7.

[65] Fonrodona M, Soler D, Asensi JM, Bertomeu J, Andreu J. Proceedings of the 3rd World Conference on Photovoltaic Solar Energy Conference; 2003; Osaka, Japan; pp. 2010-4.

[66] Torres P, Meier J, Fluckiger R, *et al.* Device grade microcrystalline silicon owing to reduced oxygen contamination. Applied Physics Letter. 1996; 69(10); 1373-6.

[67] Goerlitzer M, Torres P, Beck N, Wyrsch N, Keppner H, Pohl J, Shah A. Structural properties and electronic transport in intrinsic microcrystalline silicon deposited by the VHF-GD technique. Journal Non-Crystal Solids 1998; 230: 996-9.

[68] Hubin J, V. Shah A, Sauvain E, Pipoz P. Consistency between experimental data for ambipolar diffusion length and for photoconductivity when incorporated into the ''standard'' defect model for a-Si:H. Journal of Applied Physics 1995; 78(10): 6050-4

[69] Kocka J, Fejfar A, Stuchlkova H, *et al.* Basic features of transport in microcrystalline silicon Solar Energy Materials & Solar Cells 2003; 78; 493–512

[70] Kocka J, Mates T, Stuchlkova H, Stuchlk J, Fejfar A. Characterization of grain growth, nature and role of grain boundaries in microcrystalline silicon—review of typical features. Thin Solid Films 2006; 501: 107-12

[71] Green MA, Emery K, Hishikawa Y, Warta W. Solar cell efficiency tables (version 37). Progress in Photovoltaic: Research Application 2011; 19: 84–92

[72] Coutts TJ, Emery KA, Ward JS. Modeled performance of polycrystalline thin-film tandem solar cells. Progress in Photovoltaics: Research and Applications 2002; 10: 195–203.

[73] Mitchell K. uc-SiC/poly-Si heterojunction solar cell. Technical Digest 1st International Photovoltaic Solar Energy Conversion; 1984; Kobe, Japan: pp. 691–94.

[74] Deng X, Schiff EA. Amorphous Silicon–based Solar Cells. In: Handbook of Photovoltaic Science and Engineering Edit by Luque A, Hegedus S, John Wiley & Sons Ltd London press 2003; pp. 505-60

[75] Yamamoto K. Microcrystalline Silicon Solar Cells. In: Solar Cells: Materials, Manufacture and Operation. Edited by Markvart T, L. Castañier L, Elsevier Ltd. The Boulevard, Langford Lane, Kidlington, UK 2005; pp. 254-66

[76] Rech B, Wagner H. Potential of amorphous silicon for solar cells. Applied Physics A 1999; 69: 155-9.

[77] Powalla M, Cemernjak M, Eberhardt J, *et al.* Large-area CIGS modules: Pilot line production and new developments. Solar Energy Materials & Solar Cells 2006; 90; 3158–64

[78] Guillen C, Martınez MA, San Vicente G, Morales A, Herrero J. SiO2 coatings onto metallic foil substrates. Surface and Coatings Technology 2001; 138: 205-10

[79] Kupich M, Grunsky D, Kumar P, Schroder B. Separation of microcrystalline silicon nip solar cells and amorphous–microcrystalline nipnip tandem solar cells entirely by hot-wire CVD. Thin Solid Films 2006; 501: 268-71.

[80] Schropp R, Zeman M. Amorphous and Microcrystalline Silicon Solar Cells: Modeling Materials, and Device Technology. Kluwer, Boston, USA 1998. pp.340-56

[81] Jiang L, Rane S, Schiff E, Wang Q, Yuan Q. Open-Circuit Voltage Physics in Amorphous Silicon Solar Cells. Proceedings of the Materials Research Society Symposium; 2000; San Francisco, USA: pp. A18.3.1–11.

[82] Kocka J, Fejfar A, Mates T, *et al.* Model of electronic transport in microcrystalline silicon. Physics State Solid (c) 2004; 1(5); 1097–114.

[83] Vetterl O, Carius R, Houben L, *et al.* Microcrystalline silicon films material prepared by hot-wire. Proceedings of the Materials Research Society Symposium; 2000; San Francisco, USA: pp. A15.2-6.

[84] Houben L, Luysberg M, Hapke P, Carius R, Finger F, Wagner H. Structural properties of microcrystalline silicon. Philos Mag 1998; A 77(6): 1447-52.

[85] Johnson EV, Nath M, Roca i Cabarrocas P, Abramov A, Chatterjee P. Why does the open-circuit voltage in a micro-crystalline silicon PIN solar cell decrease with increasing crystalline volume fraction? Journal Non-Crystal Solids 2008; 354: 2455–9.

[86] Nath M, Chakraborty S, Johnson EV, Abramov A, Roca i Cabarrocas P, Chatterjee P. Performance of microcrystalline silicon single and double junction solar cells of different degrees of crystallinity. Solar Energy Materials & Solar Cells 2010; 94: 1477–80

[87] Werner J, Bergmann R. Technical Digest 12th Int. Photovoltaic Science and Engineering Conference; 1999; Sapporo, Japan: pp. 2041-7

[88] Yamamoto K. Very thin film crystalline silicon solar cells on glass substrate fabricated at low temperature. IEEE Trans Electron Devices 1999; 46: 2041–7.

[89] Martinez MA, Herrero J, Gutierrez MT. Deposition of transparent and conductive Al-doped ZnO thin films for photovoltaic solar cells. Solar Energy Materials & Solar Cells 1997; 45: 75-81.

[90] Davis L. A simple model for the formation of compressive stress in thin films by ion bombardment. Thin Solid Films 1993; 226: 30-4.

[91] Schade H, Smith ZE. Optical properties and quantum efficiency of a-Si1−xCx@B:H/a-Si@B:H solar cells. Journal Applied Physics 1985; 57: 568-74.

[92] Lee CH, Lim KS, Song J. Highly textured ZnO thin films doped with indium prepared by the pyrosol method. Solar Energy Materials & Solar Cells 1996; 43: 37-45.

[93] Yoshino M, Wenas WW, Yamada A, Konagai M, Takahashi K. Large-Area ZnO Thin Films for Solar Cells Prepared by Photo-Induced Metalorganic Chemical Vapor Deposition. Japanese Journal Applied Physics 1993; 32: 726-30.

[94] Bose S, Swati AK, Barua R. Textured aluminium-doped ZnO thin films prepared by magnetron sputtering. Journal Physics D 1996; 29: 1873-5

[95] Kambe M, Fukawa M, Taneda N, *et al.* Proceedings of the 3rd World Conference on Photovoltaic Solar Energy Conference; 2003; Osaka, Japan; pp. 1812-6

[96] Kim SK, Jung Lee C, Dutta V. The Effect of ZnO:Al Sputtering Condition on a-Si:H/Si Wafer Heterojunction. Solar Cells. Solid State Phenomena, 2007; 124-126: 1015-9

[97] Bailat J, Dominé D, Schlüchter R, *et al.* High-efficiency p-i-n microcrystalline and micromorph thin film silicon solar cells deposited on LPCVD ZnO coated glass substrates. Proceedings of the Photovoltaic Energy Conversion, Conference Record of the 2006 IEEE 4th World Conference; 2006; Hawaii, USA: pp. 1533-6.

[98] Lee JC, Kang KH, Kim SK, Yoon KH, Park IJ, Song J. RF sputter deposition of the high-quality intrinsic and n-type ZnO window layers for Cu(In,Ga)Se2-based solar cell applications. Solar Energy Materials & Solar Cells 2000; 64: 185-95

[99] Shah AV, Vanecek M, Meier J. Basic efficiency limits, recent experimental results and novel light-trapping schemes in a-Si:H, μc-Si:H and `micromorph tandem' solar cells. Journal of Non-Crystalline Solids 2004; 338-40: 639–45

[100] Yamamoto K, Nakajima A, Yoshimi M, *et al.* Single junction amorphous and microcrystalline p–i–n-type solar cells. Proceedings of the 29th IEEE Photovoltaic Specialists Conference; 2002; New Orleans, USA: 2002, p. 1110-4.

[101] Yamamoto K, Yoshimi M, Tawada Y, *et al.* Large area thin film Si module. Solar Energy Materials & Solar Cells 2002; 74: 449–55.

[102] Tawada Y, Yamagishi H, Yamamoto K. Mass productions of thin film silicon PV modules. Solar Energy Materials & Solar Cells 2003; 78: 647–62.

[103] Green MA, Emery K, Hishikawa Y, Warta W. Solar cell efficiency tables (version 37). Progress in Photovoltaic: Research Application 2011; 19: 84–92

[104] Yoshimi M, Sasaki T, Sawada T, *et al.* High efficiency thin film silicon hybrid solar cell module on 1m2 class large area substrate. Proceedings of the 3rd World Conference on Photovoltaic Solar Energy Conference; 2003; Osaka, Japan; pp. 1566–9

[105] Bailat J, Fesquet L, Orhan J, *et al.* Recent Developments of High-Efficiency Micromorph® Tandem Solar Cells in KAI-M PECVD Reactors. Proceedings of the 25th European Conference on Photovoltaic Energy Conversion; 2010; Valencia, Spain: pp.650-4.

Send Orders of Reprints at reprints@benthamscience.net
Silicon Based Thin Film Solar Cells, 2013, 395-473

CHAPTER 11

Light Trapping in Thin Silicon Solar Cells

Mario Tucci[1,*], Luca Serenelli[1], Simona de Iuliis[1], Domenico Caputo[2] and Giampiero de Cesare[2]

[1]ENEA, Research Center Casaccia, Via Anguillarese 301, 00123 Roma Italy and [2]DIIET, University "Sapienza", Via Eudossiana 18 00184 Rome, Italy

Abstract: Light trapping plays a key role in solar cell to enhance light confinement and then light absorption within the cell. The reduction of the optical losses reflects in photovoltaic solar cell efficiency enhancement. To this aim different and combined strategies can be adopted. Firstly a reflectance reduction of sunlight impinging on the cell is mandatory. Then a cell surface texturing can be very helpful to reduce the reflection by increasing the chances of reflected light bouncing back onto the surface rather than surrounding air. To this purpose different approach can be followed such as substrate and/or single layer texturing. Moreover particular care should be paid to the rear side of the cell where the introduction of a reflecting mirror can produce an optical path length enhancement over a wide wavelength spectrum. Rightly combining the front side texturing and the rear side mirroring it is possible to enhance this pathlength up to 50 times the device thickness indicating that light bounces back and forth within the cell many times performing a light confinement. To this purpose Bragg reflector formed using thin film technology is one of the most promising approach to the back side reflector. Also multi-junction cell, such as tandem micromorph, can receive benefit to the light management by the introduction of inner reflector within the two cells to enhance the spectral separation between the two cells and reduce the front cell thickness where the metastability problem still remain an open request.

In this work we overview all these concepts as applied to thin film cell and to silicon based cell that actually are speedily moving toward thinner substrate making the light confinement a key point to cell efficiency enhancement and PV cost reduction.

Keywords: Amorphous silicon, antireflection coating, heterojunction, lifetime, numerical model, optical properties, reflector, scattering, solar cell, texturing, thin film, transparent conductive oxide, plasma process, light trapping, thin wafer, quantum efficiency, bragg reflector, haze, reactive ion etching, laser treatment, silicon.

1. INTRODUCTION

To enhance the solar cell efficiency in recent years, researchers have experimented with approaches to capture the sunlight photon impinging on the device and forcing it to collaborate instead of being reflected away. This is done by changing the basic structure of solar cells, so that photons become trapped when they arrive in contact with the cell, thus providing a greater chance that they will be absorbed and converted into electrons. To this aim a light-trapping scheme introduction is mandatory. Light trapping allows cell to absorb sunlight using an active material

***Address correspondence Mario Tucci:** ENEA, Research Centre Casaccia, *Via* Anguillarese 301, 00123 Rome Italy; Fax: 0044 1740 644146; E-mail: mario.tucci@enea.it

Roberto Murri (Ed)
All rights reserved-© 2013 Bentham Science Publishers

layer thinner than the material's intrinsic absorption length. This can reduce the amount of materials used in PV cells, cutting cell cost that are mainly based on less abundant or expensive purified materials. It is well known that the largest part in cost production of industrial silicon solar cells is actually referred to the base silicon substrates. Hence reducing the amount of involved silicon, by means of thinner wafer, is a key point in limiting the overall PV cost, making the price of energy from solar cells competitive with the conventional production systems [1]. Moreover, light trapping can improve cell efficiency, since thinner cells provide better collection of photo-generated charge carriers [2]. Historically the theory of light trapping was developed for conventional cells in which the optical path length is several times the actual device thickness, where the optical path length of a device refers to the distance that an unabsorbed photon may travel within the device before it escapes out of the device [2, 3]. For example, a solar cell with no light trapping features may have an optical path length of one device thickness, while a solar cell with good light trapping may have an optical path length of 50 times the device thickness, indicating that light bounces back and forth within the cell many times. Basically conventional light trapping exploits the effect of total internal reflection between the semiconductor material, such as silicon, and the surrounding medium commonly assumed to be air. Simply by texturing the semiconductor surface it is possible to couple light obliquely into the medium, thus giving a longer optical path length than the physical device thickness and also it is possible to randomize the light propagation directions inside the material. Achieving a total internal reflection results in a much longer propagation distance inside the material and hence a considerable absorption enhancement. Indeed the light can be trapped inside the cell and make multiple passes through the cell, thus allowing even a thin solar cell to maintain a high optical path length. The standard theory for this light-trapping scheme was developed by Yablonovitch [3] and applied to silicon based solar cell several years later [4]. To further enhance the absorption of light penetrated into the device a rear side reflector is needed to avoid light escape from the rear side of the cell. This allows the light to bounce back into the cell for possible absorption. This allows an optical path length of approximately 50 times the physical devices thickness and thus is an effective light trapping scheme. For thin film cells with thicknesses comparable or even smaller than wavelength scale, the ray-optics representation and some of the basic assumptions adopted in the conventional theory are no longer applicable. Recently in literature several numerical [5-8] and experimental [9-17] works reported considerable improvement beyond the Yablonovitch limit.

In this chapter a description of light management at the front and rear side of the solar cell is reported. In this description not only thin film cell are considered, but also silicon base cells that are going beyond thinner silicon wafer to reduce PV cost. Indeed in this case several approaches can be helpfully transferred from thin film technologies to wafer based technology. In this direction the best silicon based cell candidate is the amorphous/crystalline heterostructure. To exploit this argument a particular section is dedicated to a dielectric reflector and its related manufacturing technology helpful to improve thin solar cell performances. All the technologies that can be proposed to the light confinement must fit with industrial manufacturing facilities otherwise can only represent academic speculations not useful to reduce the cost per watt produced by the sunlight photovoltaic conversion. Therefore the use of sophisticated technology such as photo-lithographic steps, not easy to transfer to very large area device, used to produce particular features on front or rear side of the cell to enhance the light confinement are not extensively exploited in this overview.

In this chapter a detailed description of cell design is reported concerning the use of antireflection coating and texturing of both thin films and silicon wafer based device in order to manage at the best the light impinging on a solar cell. After an overview of light scattering promoted by texturing a detailed description is proposed on rear side reflector in which a Bragg scheme is detailed and experimented.

2. ANTIREFLECTION COATING

Optical losses are responsible for the short circuit lowering in solar cells. They are mainly caused by the parts of incident light escaping from the cell and the part reflected from the cells surface or metal front contacts. To maximise the percentage of light to be converted in electron-hole pairs it is important to maximise the light penetrating into the cell. This can be done modifying the surfaces morphology producing the so-called texturing and applying to the front surface an Anti Reflection Coating (ARC) [18]. The idea behind anti-reflection coatings is that the creation of a double interface by means of a thin film gives you two reflected waves.

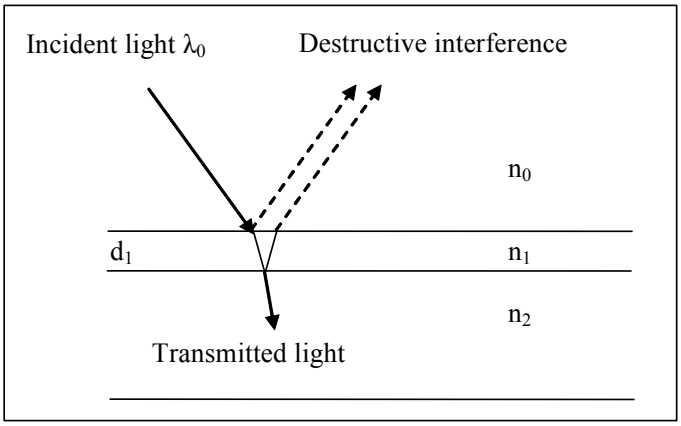


Figure 1: Schematic of Anti Reflection Coating principle of operation for a single layer ARC.

If these waves are out of phase, they partially or totally cancel. In practice a thin layer of dielectric material having a precise refractive index is deposited with a specific thickness on a substrate, so that interference effects in the coating cause the wave reflected from the anti-reflection coating top surface to be out of phase with the wave reflected from the semiconductor surfaces. In particular when the light reflected from the second interface arrives back at the first interface 180° out of phase with that reflected from the first interface, there is no net light coming out, at least for a chosen wavelength. The schematic situation is sketched in Fig. **1**, where n_0, n_1 and n_2 are surrounding ambient, dielectric film and semiconductor refractive index respectively. The expression for the fraction of the energy in a normally incident beam of light reflected from the surface of a material covered by a transparent layer of thickness d_1 is [19, 20]:

$$R = \frac{r_1^2 + r_2^2 + 2r_1 r_2 \cos 2\theta}{1 + r_1^2 r_2^2 + r_1 r_2 \cos 2\theta} \quad \textbf{(1)}$$

with:

$$r_1 = \frac{n_0 - n_1}{n_0 + n_1} \quad r_2 = \frac{n_1 - n_2}{n_1 + n_2} \quad \theta = \frac{2\pi n_1 d_1}{\lambda} \tag{2}$$

In this case the reflectance has its minimum value:

$$R_{\min} = \left(\frac{n_1^2 - n_0 n_2}{n_1^2 + n_0 n_2} \right)^2 \tag{3}$$

which can be driven to zero when $n_1^2 = n_0 n_2$, for a specific wavelength λ_0, due to the dependence of the refraction index on wavelength.

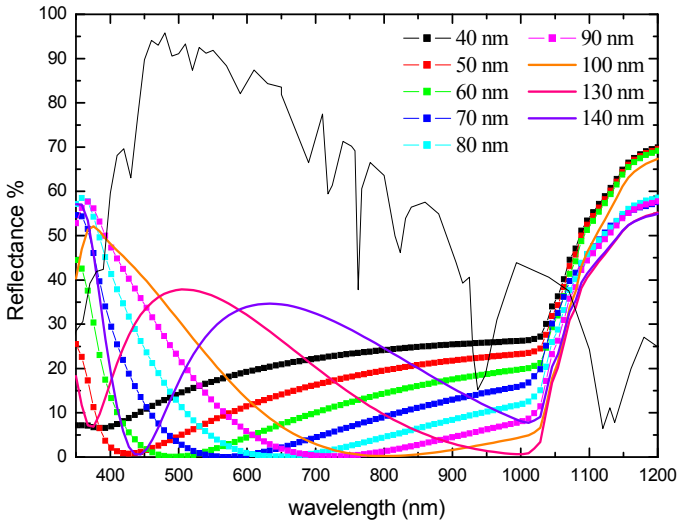


Figure 2: Reflectance profiles simulations of Silicon Nitride on flat silicon as a function of silicon thin film thickness. The Black continues line is the AM 1.5 G spectrum, expressed in arbitrary units.

However the sun spectrum is of course made by multiple wavelength photons, so the choice of material, refractive index and thickness of the dielectric film needs to be done considering the best reflection reduction around the wavelength corresponding to the maximum of the sun spectrum intensity. For photovoltaic applications, the refractive index and thickness are chosen in order to minimise reflection for a wavelength of 600 nm [21]. At the present one of the most widely used material is Silicon Nitride deposited *via* Plasma Enhanced Chemical Vapour Deposition (PECVD) which refractive index can be varied from 1.5 and 2.3 circa, evaluated at 633 nm [22]. In Fig. **2** we show simulations made with the aid of NKDGEN software [23] of how the reflectance profile (in term of % of incident light) varies with the thickness of a silicon nitride film (as deposited on a flat

silicon surface) having a refractive index of 2 at 633 nm. It is appreciable the best profile giving the lower reflectance around 600 nm is around 60-70 nm thickness.

Such a kind of behaviour can be enhanced with the introduction of a multi-layer as ARC (see Fig. **3**), varying the refractive indexes and thicknesses to obtain a low reflectance profile over a wider range of wavelengths. The equations for multiple antireflection coatings are more complicated than that for a single layer [20]. Any film combination composed of two dielectric layers on a semi-infinite substrate has a reflectance given by:

$$R = \frac{r_1^2 + r_2^2 + r_3^2 + r_1^2 r_2^2 r_3^2 + 2r_1 r_2 (1 + r_3^2)\cos 2\varphi + 2r_2 r_3 (1 + r_1^2)\cos 2\psi + 2r_1 r_3 \cos 2(\varphi + \psi) + 2r_1 r_2^2 r_3 \cos 2(\varphi - \psi)}{1 + r_1^2 r_2^2 + r_1^2 r_3^2 + r_2^2 r_3^2 + 2r_1 r_2 (1 + r_3^2)\cos 2\varphi + 2r_2 r_3 (1 + r_1^2)\cos 2\psi + 2r_1 r_3 \cos 2(\varphi + \psi) + 2r_1 r_2^2 r_3 \cos 2(\varphi - \psi)} \quad \textbf{(4)}$$

with:

$$r_1 = \frac{n - n_1}{n + n_1},\ r_2 = \frac{n_1 - n_2}{n_1 + n_2},\ r_1 = \frac{n_2 - n_3}{n_2 + n_3},\ \varphi = \frac{2\pi n_1 d_1}{\lambda},\ \psi = \frac{2\pi n_2 d_2}{\lambda} \quad \textbf{(5)}$$

where n is the refractive index, d the film thickness and λ the wavelength. This expression is quite cumbersome and can be solved only by approximate numerical methods, unless the two layers are restricted to be of equal optical thickness at 550nm. In this case the above equation can be simplified to:

$$R = \frac{r_1^2 + r_2^2 + r_3^2 + r_1^2 r_2^2 r_3^2 + 2r_2 (r_1 + r_3)(1 + r_1 r_3)\cos 2\varphi + 2r_1 r_3 \cos 4\varphi}{1 + r_1^2 r_2^2 + r_1^2 r_3^2 + r_2^2 r_3^2 + 2r_2 (r_1 + r_3)(1 + r_1 r_3)\cos 2\varphi + 2r_1 r_3 \cos 4\varphi} \quad \textbf{(6)}$$

For the equal optical thickness of quarter-wavelength coatings (*i.e.* $n_1 d_1 = n_2 d_2 = \lambda_0 / 4$) and in terms of the indices media n_0 of ambient, n_1 and n_2 for two coatings and n_3 for substrate, R at λ_0 becomes

$$R = \left(\frac{n_1^2 n_3 - n_2^2 n_0}{n_1^2 n_3 + n_2^2 n_0} \right)^2 \quad \textbf{(7)}$$

and it can be found that zero reflectance can be obtained in this case with a double quarter-wave coating if the refractive indexes of the two layer satisfy the following relation:

$$\frac{n_2}{n_1} = \sqrt{\frac{n_3}{n_0}} \quad \textbf{(8)}$$

In Fig. **4** is shown an experimental reflectance profile of a double ARC made by MgF_2 and ZnS over a flat silicon surface, having effective reflectance equal to 8.1%, good if compared to the one of a single SiN ARC, which is around 13%. However, this treatment is usually too expensive for most commercial solar cells, but it finds application in very high efficiency solar cells designed to operate in concentration. The ARC concept illustrated till now for silicon solar cells is actually

totally general and can find application on thin film cells and modules. For instance it is possible to use Silicon Nitride as ARC for thin film cells CdS/$CuInSe_2$ [24].

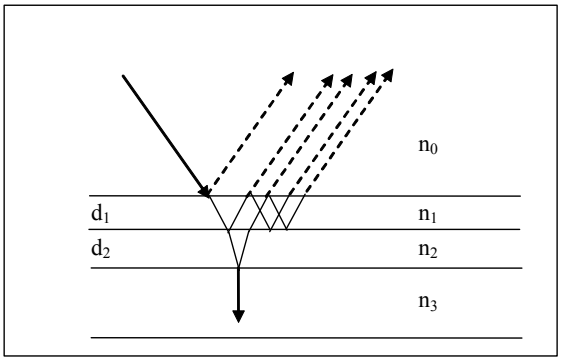


Figure 3: Schematic of Anti Reflection Coating principle of operation with two equal thickness coating.

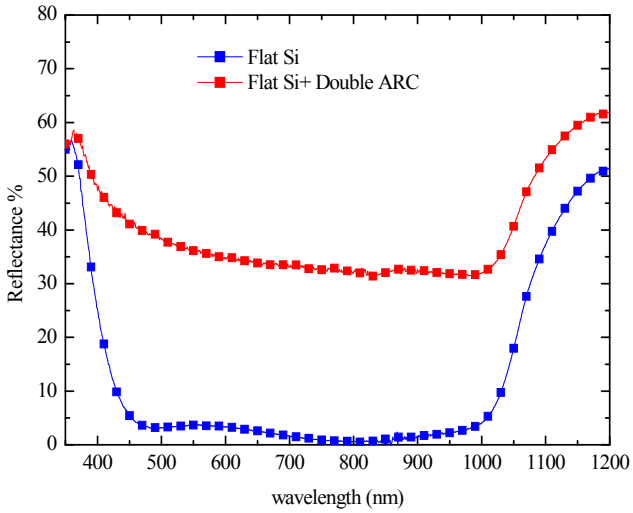


Figure 4: Experimental reflectance profile of double ARC (blue) compared with flat silicon (red).

2.1. Dielectric Layers

Dielectric layers have wide applications in photovoltaics due to their different optical and electrical properties useful for passivation, antireflection and even masking purposes.

The former two are keys to increase solar cell performances since the passivation level strongly influences the Voc, the Jsc, and in minor part the FF, while according to paragraph above the antireflection coatings are very important to drastically reduce the optical losses, and so influence the Jsc. However, not all dielectrics employed in PV are appropriate to both purpose, or suitable on all kind of processes.

Before the wide diffusion of Silicon Nitride (SiNx) deposition *via* remote plasma [25], leading the overall silicon solar cell processing throughput at the present level, the main way to passivate the front of silicon solar cells was Silicon Oxide (SiO2) grown by thermal wet or dry oxidation in which ultra clean water vapour or oxygen respectively are entered in a quartz tube at high temperature (in the range 800-1200 °C) to oxidise the Silicon wafers. Such high temperatures are one of the drawbacks of using SiO_2 in solar cells processing. Indeed metallization of cells when using silicon oxide would involve low throughput steps of lithography, since metal contacts cannot be deposited prior to high temperatures step because of the consequent lifetime degradation in the base wafer and metal contacts extra-penetration through the formed emitter [26]. Moreover since the hardness of SiO_2 films, common firing through processes are not effective in this case, so an opening procedure (*via* laser or chemical processing) is mandatory. Of course silicon oxide is not suitable for thin film applications.

Sputtered or evaporated dielectric films, like Titanium Oxide (TiO_2) [27] or Magnesium Fluoride (MgF_2), or Zinc Sulphide (ZnS) are suitable for antireflection purpose and have been used previously in photovoltaic industry but with poor passivation quality. Plasma deposited films, like non-stoichiometric Silicon Oxide (SiO_x) [28], Silicon Nitride (SiN_x) also coupled with amorphous silicon (a-Si) [29] have shown both good passivation quality and optical characteristic suitable to be employed as ARC. Also they are such to be easily penetrated by common Silver screen printable paste to perform good firing through during metallization processes.

Finally, due to their low process temperatures, they are suitable also in low temperature application, like thin film [24] and heterojunction [30].

In the following paragraph we will focus on silicon nitride, which is at the present the most widely diffused dielectric employed in solar cell processing.

2.2. Silicon Nitride

The application of Silicon Nitride, deposited *via* Plasma Enhanced Chemical Vapor Deposition (PECVD), to photovoltaic represents an important step toward the enhancement of conversion efficiency, especially for c-Si based cells. Indeed its electric properties make it an excellent passivating dielectric, due to the relevant surface recombination velocity reduction, while it is a natural good candidate for Anti Reflection purpose because it is possible to continuously move the refractive index from 1.7 to 2.3 (evaluated at 633 nm), depending on deposition condition [31]. These are the main reasons to adopt this material in solar cells processing, giving a double contribute in a single step deposition. For historical reasons we report that Silicon Nitride can be deposited using high temperature process approach, but the one utilized for photovoltaic applications is deposited by the low temperature techniques (< 400 °C), like PECVD, suitable to be industrially adopted, because of low cost of ownership, high throughput and high reliability. One of the mostly interesting characteristics is the possibility of good interfacing in terms of electrical and optical properties of Silicon Nitride with different materials, like amorphous silicon [29], or Silicon Oxides [32]. Depending on deposition conditions it is possible to vary the stoichiometry composition and the Hydrogen content, that affect the fixed and mobile charge content, which are responsible of the film passivation properties. Indeed there are two main mechanisms to passivate silicon surface: the dangling bonds saturation by means of Hydrogen

atoms and a field effect due to the charge present in the film [33], better explained in the following.

Silicon Nitride can be grown in different ways that we can group in three classes:

- deposition by means of sputtering or silicon laser ablation in nitrogen atmosphere;
- direct nitridation or N atom implantation on a silicon wafer;
- deposition of reaction solid products in gas (Chemical Vapour Depositions-CVD).

In the two former cases the obtained film are perfectly stoichiometric (Si_3N_4) but, despite a long deposition process and at high temperature (circa 900 °C), very thin (< 10 nm). This low deposition rate is the main reason for abandoning this growth method toward other techniques using reaction in gas phase [34].

CVD deposition happens in a pressure and temperature controlled chamber, called reactor, because of the dissociation of gas species molecular bonding after an excitation. Depending on gas mixture, excitation source, pressure and process temperature, it can be distinguished between different CVD types [35].

- Atmospheric Pressure Chemical Vapour Deposition (APCVD);
- Low Pressure Chemical Vapour Deposition (LPCVD);
- Hot Wire Chemical Vapour Deposition (HWCVD);
- Plasma Enhanced Chemical Vapour Deposition (PECVD);
- Remote Plasma Enhanced Chemical Vapour Deposition (RPECVD).

Generally all these techniques use reactant gases containing Hydrogen, easily incorporated in the film. Moreover the particular deposition condition of a single solid phase from a gas one, in condition far from the thermodynamic equilibrium lead to the formation of an amorphous and non-stoichiometric material. This is the reason why, referring to silicon nitride deposited in CVD systems, they are defined as amorphous and hydrogenated silicon nitride, a-SiN_x:H, (or simply SiN_x) where *x* is the atomic ratio N/Si [36], equal to 1.33 for perfectly stoichiometric nitride. Both APCVD or LPCVD are based on the reaction of silane (SiH_4) and ammonia (NH_3) happening at the substrate surface due to the high temperature (700-1000 °C) or the low pressure in the reactor (0.01-1 Torr), with a deposition rate of around 2.5-5 Å/min [26]. Both methods are quite obsolete, due to the low growth rate and process conditions, not suitable for high throughput production in industrial environment, especially when compared to plasma assisted CVD. Similar drawbacks are typical of HWCVD, in which the gas mixture is excited by a wire kept at high temperature by current flow, which does not ensure a homogenous deposition on large area wafer surface, even with low deposition rate [37]. The main advantage of plasma assisted CVD (Plasma Enhanced CVD-PECVD) compared to the APCVD or LPCVD is the low process temperature, since the

reaction is started by means of an external source, like an electric field in radiofrequency. In this case the electric field gives energy to electrons in the external shells of reactant gases atoms in the reactor, ionizing them, while electrons are free to travel into the gas mixture. In this way the collisions they experience with other molecules lead to new ions and radicals formation, which are then free to combine with other reactant species. During these collisions, electrons loose kinetic energy, with light emission. All this complex of ions, radicals, light and free electrons in gas phase is the so-called plasma [26]. The second strength of PECVD is the high deposition rate, which allows to grow hundreds nanometres thick film in few minutes. In summary PECVD is a fast and low temperature process, allowing the deposition of different kind of materials controling both optical and electrical properties by means of deposition parameters. PECVD systems differ by working frequencies (Low Frequency, High frequency, Very High Frequency [38], and microwave [39]), and applied plasma (direct or remote [25]). The system choice is mainly related to the application and required final properties.

As reported before, silicon Nitride properties depend strongly on the deposition method.

In APCVD and LPCVD cases the film is purely stoichiometric, very strong and poor of Hydrogen content. The material structure is made by Silicon atoms in tetrahedral coordination with Nitrogen atoms, in turn placed on a plane.

In PECVD case, instead, the ratio N/Si and the Hydrogen content are strongly dependent on the process parameters, like the precursor gases flux ratio, the RF power, the substrate temperature. Despite the non-stoichiometric and amorphous nature of the so obtained film, experiments show the tetrahedral coordinated structure for silicon and trivalent for Nitrogen is still valid [26]. The Hydrogen content increases with deposition temperature decreasing, and this is the reason why Silicon Nitride produced *via* PECVD has higher Hydrogen content with respect the ones deposited *via* APCVD or LPCVD. This phenomenon is correlated with the cross linking between Si and N atoms, because of the correspondence between the Hydrogen content and film density, in turn related to the Si-N bonding. Such a kind of behaviour can be confirmed by means of IR absorbance spectra, where depending of peaks position and intensity it can be estimated both Hydrogen content and structural properties of film, such as refractive index, related to Si-N bonds. Moreover depending on the stoichiometry of deposited material, SiN_x can be classified in Silicon rich (N/Si<1.2) or Nitrogen rich (N/Si>1.4). In the former, Si-Si and Si-N bonds are definitely prevalent with respect to N-H bonds,; while in the latter, or even near the stoichiometry, Silicon can form several bonding and Nitrogen is able to establish bonds with both H and Si. N-N bonds are very difficult to be formed, even for Nitrogen rich film, due to the bonding energy (38.4 kcal/mol), lower with respect to both Si-N (50 kcal/mol) and N-H (93.4 kcal/mol). This suggests, for Nitrogen rich films, more N-H bonding than Si-H, since bonding between N atoms are less favourite, obtaining higher Hydrogen contents [40], which increases with N/Si ratio. The stoichiometric silicon nitride (Si_3N_4) electronic structure was calculated by Robertson [41] and shows the non-saturated bonds of trivalent Silicon (≡Si•) introduce a paramagnetic state in the middle of its bandgap (estimated to be 5.3 eV), while the defects introduced by nitrogen dangling bonds (=N•) are located just above the valence band edge. This is still valid for silicon rich SiN_x (x<1.1), where trivalent silicon bonding can be saturated with different configurations, like Si_3≡Si•, Si_2N≡Si•, SiN_2≡Si•, N_3≡Si•. The bonding density is controlled by the equilibrium with weak Si-Si bonding, forming states near the band edges, while the level caused by Nitrogen

dangling bonds are not present. This happens because the high silicon content in SiN_x moves the conduction and valence band edges toward midgap, reducing its value till 1.7 eV. Silicon induced defects still remain around midgap, while those due to Nitrogen disappear into Valence band. Actually the more the Silicon content, the more SiN_x behaves like a-Si:H, where Nitrogen atoms act as donors, when they are less than 2%, and SiN_x is, in practise, n-type a-Si [42]. From FTIR spectra it is possible to obtain an absorption spectrum as function of IR radiation wave number (expressed in cm^{-1}) where peaks or distribution are related to the energy corresponding a particular vibration or stretching mode of a molecule, whose values are reported in literature [22, 43] and the most important indicated in Fig. **5**.

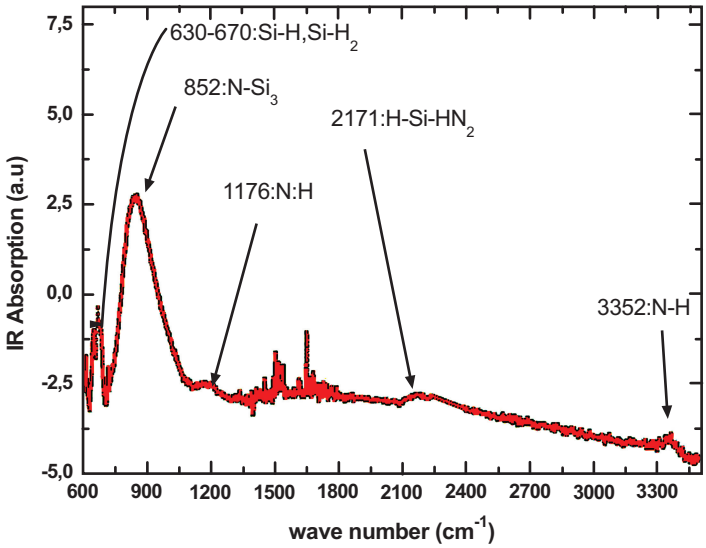


Figure 5: Example of FTIR spectrum for Silicon Nitride, with most important explicit peaks.

Analysing such spectra is possible to understand the material composition. In particular it can be found a relation between the presence of certain bonds with the optical and electrical material, like the refractive index and the charge inside the film [40]. The eventual peaks related to CO_2 presence, around 653 and 2340 cm^{-1} have been reduced by software interpolation. If in silicon rich Nitride the only states at midgap are due to Silicon, different is for Nitrogen rich Silicon Nitride. In this case, also the states due to Nitrogen dangling bonds are inside the gap, and the prevalent effect is due to $N_3{\equiv}Si\bullet$ groups, the so-called K centres of recombination.

They are diamagnetic and neutral, but introduce a large amount of instable charge in the film, since they are able to capture both electron and holes, becoming positively or negatively charged (K^+, K^-). This charge state formation can happen also after the film exposure to high energy radiation, like UV, which breaks some Si-H and SiN-H bonds around the K centre, forming new radicals and mobile charges inside the Nitride film [44]. Of course the silicon or nitrogen rich behaviour is determined by the deposition parameter, like the reactant gas flux ratio $R{=}\Phi_{NH3}/\Phi_{SiH4}$. The correspondence between deposition parameter, film properties, and atoms bonding can be appreciated in Fig. **6(a)**. We report the

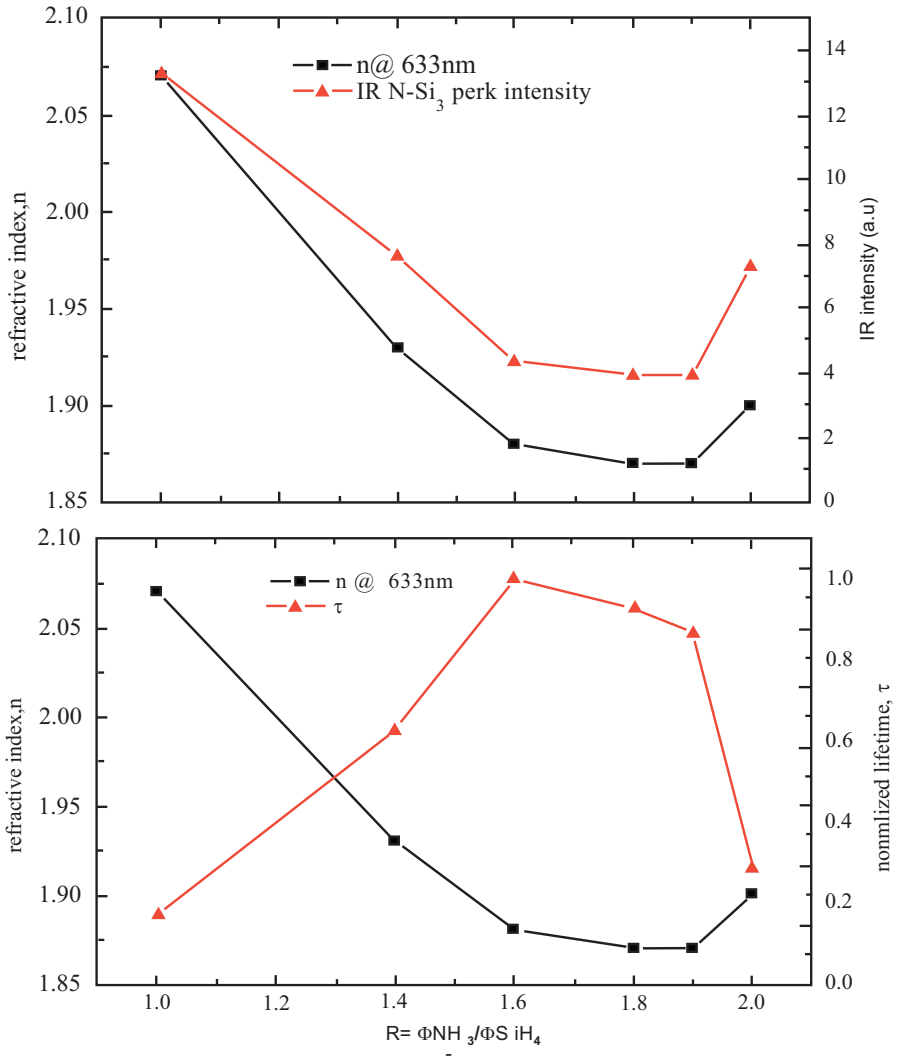


Figure 6: a) Comparison of refractive index and N-Si_3 peak intensity in FTIR spectra of Silicon Nitride deposited with different Ammonia/Silane gas flux ratio. b) comparison of refractive index and lifetime of Silicon Nitride deposited with different Ammonia/Silane gas flux ratio.

variation of refractive index (evaluated at 633 nm) as a function of R. When the film is deposited with less Silane the refractive index start to reduce, because the equilibrium between Silicon and Nitrogen atom content move their availability to form bonds with Hydrogen. Then N-Si bonding is less favourite and the film become less dense, with lower n. This behaviour is confirmed measuring IR spectra. In particular the intensity of peak located around 850 cm^{-1} shows the same trend of refractive index. At the same time the opposite trend in N-H and Si-H bonds is reflected in lifetime trend, as reported in Fig. **6(b)**. Indeed the higher charge content due to K centres and hydrogen is responsible of Field effect passivation on crystalline silicon: the charge inside the film can accumulate electrons near

the silicon wafer surface avoiding recombination or also inverting the silicon locally, obtaining an effective passivation. For instance in case of SiNx with high positive charge in the film, when deposited on p-type silicon, there are electrons recalled from the substrate close to the surface. This causes a band bending which moves the Fermi Level away from midgap, where the most important defects (through which electrons and holes can recombine, lowering the overall lifetime) are located [32]. This effect together with the saturation of dangling bonds at the surface defect state density can led to very high effective lifetime, in the order of milliseconds [26] both for mono and multicrystalline silicon.

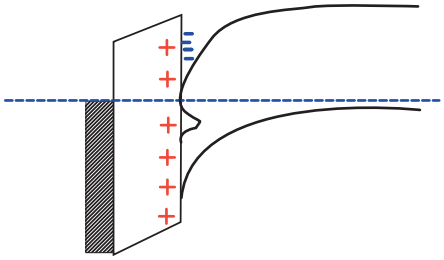


Figure 7: Field effect: the positive charge in the SiN_x recalls electron from the substrate close to the surface, avoiding recombination *via* midgap defects.

3. TCO AND SURFACE SCATTERING

In thin film silicon solar cells and modules incorporating amorphous (a-Si:H) or microcrystalline (μc-Si:H) silicon as absorber materials, light trapping, *i.e.* increasing the path length of incoming light, plays a decisive role for device performance. All these cells commonly have a Transparent Conductive Oxide (TCO) as top electrode deposited on low cost glass substrate. In Fig. **8** schematic sketch of the cross section of thin film solar cell is reported. The light trapping is illustrated by the arrows representing incoming/reflected and scattered sun light at different interfaces: glass/TCO, TCO/absorber layers, absorber/TCO and TCO/back reflector.

Not all device configurations include the TCO before the metal electrode but often this layer is introduced to enhance the chemical compatibility between thin films and metal electrode. In a particular kind of silicon wafer based solar cell, TCO is also applied on both sides of the cell, such as the a-Si:H/c-Si/a-Si:H heterostructure cell [45].

When TCO is applied at the cell front side, it needs high transparency in the spectral region where the solar cell is operating. Therefore refractive indexes are relevant and have to be well designed for coupling of light into the absorber materials. TCO also should have high carrier mobility and high electrical conductivity properties to reduce electrical losses. This last property is mandatory due to the poor lateral conductivity of doped emitter thin films composing the front junction. Of course the minimum requirements for the optical and electrical properties of the TCO depend on the structure and the absorber material adopted to fabricate the solar cell. Typically values of 10 Ω/sq as a sheet resistance and a transmittance around 93-94% in the range 350-1100 nm are valuable for solar cell applications. A high transparency for visible light (wavelength from 350 nm up to 750 nm) is sufficient for amorphous silicon absorber layers [46], while for solar cells integrating μc-Si:H or a-Si:H/c-Si the TCO has to be highly transparent up to the near infrared (NIR) region (1100 nm). This reflects in certain restrictions on the carrier density n of the TCO

material. Indeed higher the free carrier absorption, lower is the IR transmittance [47, 48]. However the success of the TCO films is mainly determined by the physical-chemical properties for the growth of the thin film material on top of it. For example it has to be inert to hydrogen-rich plasmas or act as a good nucleation layer for growth of nano-or microcrystalline material. A brief summary of the relevant properties of the most common TCO for photovoltaic applications, such as ZnO, SnO_2 and ITO is listed in the following section.

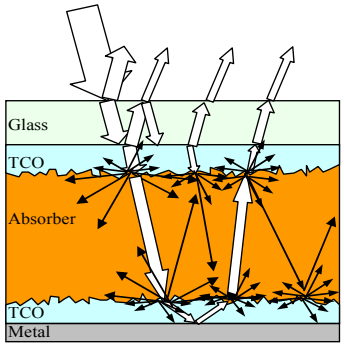


Figure 8: Schematic cross section (not in scale) of thin film cell with rough interfaces. The light trapping is remarked by the arrows representing impinging and scattered sun light at the rough interfaces.

3.1. ZnO

ZnO films is n-type semiconductor due to oxygen deficiencies with an energy gap of 3.3eV, commonly doped by adding aluminium, gallium, boron or indium [49].

In Fig. **9** resistivity as a function of impurities is reported on the base of [50]. In the same work it is shown that a film with low resistivity ($5.10^{-4}\Omega$ cm) and high optical transmission (greater than 85% between 400 and 800 nm) can be produced on low-temperature substrates with a relatively high deposition rate in particular RF magnetron sputtering configuration. The sheet resistance and Hall mobility of the film are 10 Ω/square and 120 cm^2/Vs respectively [50].

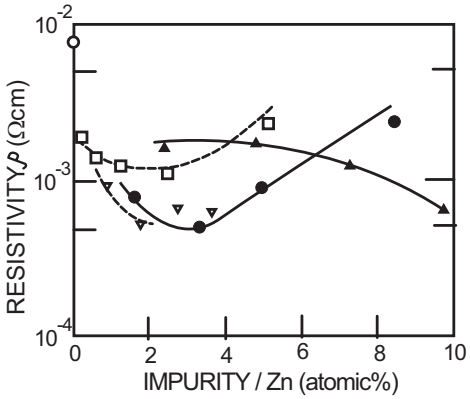


Figure 9: Dependence of ZnO resistivity (ρ) on impurity/Zn ratio in the target. Film with B(▲), Ga (Δ), Al(●), In(□) have been experimented [50].

Theoretical work [51] has identified also hydrogen as a possible n-type dopant although an enhancement of conductivity by hydrogen treatment has been known for long time [52].

Various methods are commonly used for TCO preparation. The methods involve spray pyrolysis, vapour and liquid phase or sol–gel deposition, pulsed laser deposition and sputtering. Zinc oxide is often prepared by CVD processes (using, *e.g.*, $Zn(C_2H_5)_2$ as a precursor gas) or sputter deposition [53]. Substrate temperatures differ quite significantly in these two deposition techniques. Indeed, for ZnO prepared by CVD, temperatures near 150 °C are applied [53, 54], while for ZnO prepared by sputtering, typical process temperatures are near 300 °C.

Recently doped ZnO has been established as a successful alternative to the ZnO also on large area module as demonstrated by Oerlikon [55]. Examples are boron doped ZnO prepared by low-pressure chemical vapour deposition (LPCVD) [56, 57] or aluminium-doped films deposited by expanding thermal plasma CVD [58]. A very helpful approach is the use of magnetron sputtering together with a post-deposition chemical etching step. The sputtering process leads to highly conductive and transparent but smooth ZnO:Al films. Typical sheet resistance values of 5–8 Ω/sq for film of 650 nm thicknesses and absorption of only 5–6% in the wavelength range from 350 nm to 1100 nm proof the high quality of these films. A surface texturing can be performed by a simple chemical etching step in diluted hydrochloric acid (typically 0.5% HCl) to improve the light scattering as well as the light trapping of the ZnO film. This etch yields a textured surface which can be adjusted to give optimal light scattering over a wide wavelength range. Fig. **10** shows scanning electron microscope (SEM) images of an (a) as deposited and (b) etched ZnO:Al film. Sputtered ZnO:Al is initially smooth. With increasing etch time, the roughness of the surface increases from 7 nm to 162 nm [49].

ZnO electrical properties are sensitive to the working pressure and the deposition temperature as demonstrated in Fig. **11** [48].

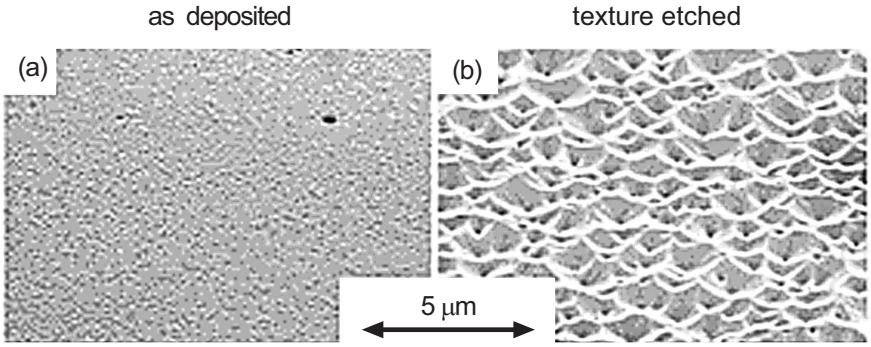


Figure 10: SEM images of RF sputtered ZnO:Al surface before (a) and after wet chemical texturing (b) [49].

It should be noted that film properties depend also strongly on film thickness. In Fig. **12** the Hall mobility, carrier densities and conductivities of Al doped ZnO films are reported according [48] as a function of deposited thicknesses and for different doping density related to the concentration of Al_2O_3 in the target (referred as TAC).

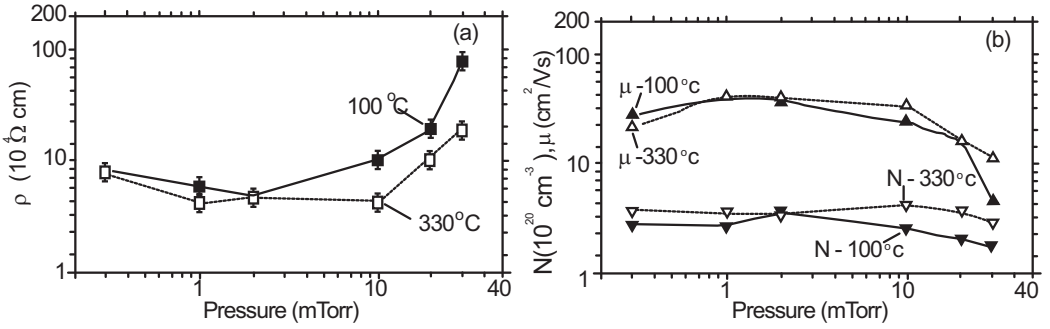


Figure 11: (a) resistivity (ρ), (b) carrier concentration (N) and mobility (μ), of Al:ZnO layers as a function of working pressure during film deposition [48].

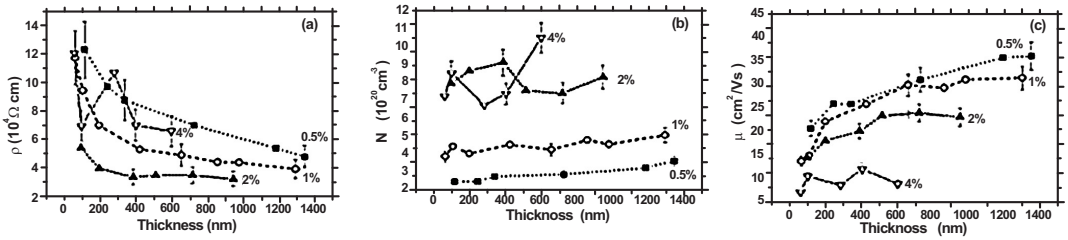


Figure 12: (a) Resistivity (ρ), (b) mobility (μ), (c) carrier concentration (N) of Al:ZnO layers as a function of film thickness [48].

Also the optical properties can be affected by the deposition temperature as evident from the transmittance spectra of ZnO films deposited at different temperature and different doping densities reported in Fig. **13**.

Electronic transport parameters such as sheet resistance R_{sh}, resistivity ρ, carrier concentration N, mobility μ, and the optical gap for ZnO:Al films deposited with different target doping concentration TAC and deposition temperature are listed in Table **1**.

Table 1: Thickness; Sheet resistance, Rsh; Resistivity, ρ; Carrier concentration, N; Mobility, μ and Optical gap, E_{Gap} for ZnO:Al films deposited with different target doping concentration (TAC) and deposition temperature, T.

TAC %	T (°C)	Thickness (nm)	Rsh (Ω/sq)	ρ.10^{-4} (Ωcm)	μ (cm^2/Vs)	N. 10^{20} (cm^{-3})	E_{Gap} (eV)
0.5	100	726	16	7	31	2.9	3.41
1	100	657	10.1	4.9	29.9	4.2	3.51
2	100	718	7.5	3.5	24	7.4	3.69
4	100	600	18	6.6	8.9	10.5	3.69
0.5	330	640	9.6	4.3	41.3	3.6	3.69
4	330	582	96	44.1	3.7	3.9	3.69

When viewing the electrical parameters it can be seen that the lowest resistivities and the highest mobilities have not changed in the last 15 years, despite a lot of technological effort in this period [53]. The lowest resistivities reported are in the range of 1.4 to $2\times10^{-4}\,\Omega$ cm, independently of the deposition method. Carrier concentration of 5.10^{20} cm^{-3} and mobility of about 40 $cm^2V^{-1}s^{-1}$, can be considered as an upper limit. It seems reasonable to suppose, that resistivities less than $1.10^{-4}\Omega$cm for doped polycrystalline zinc oxide films are hard to achieve, due to a general limitation by ionized impurity scattering. This assumption is further supported by the fact that heavily n-doped single crystalline silicon also exhibits mobilities in the same range as polycrystalline ZnO films [59].

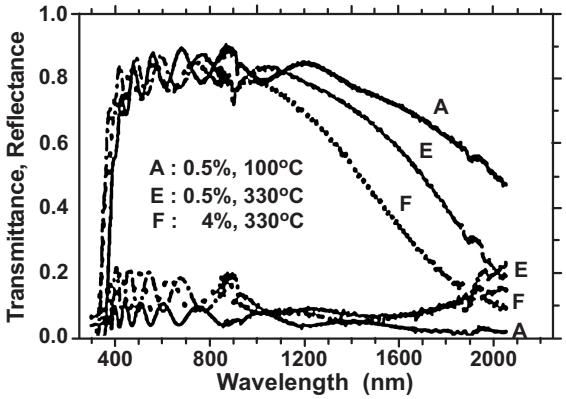


Figure 13: Transmittance and reflectance of different doping films (Ts =100°C and film thickness d=600-725 nm) deposited from different percentage Al content in the target [48].

Conducting p-type ZnO has recently been realized [60]. Even if the conductivity still remains on open request (ρ around 300 Ωcm), a promising way to enhance the light trapping in thin film cell using ZnO film, concerns the formation of surface nanostructures. They exhibit a high crystalline quality. Fig. **14(a)** shows a tilted SEM image of the ZnO nanorods synthesized on the fluorine thin oxide substrate by chemical solution deposition (CSD). The SEM image in the inset of Fig. **14(a)** shows a cross-sectional view of the ZnO nanorods. The length and average diameter of the ZnO nanorods were about 1.5 μm and 80–90 nm, respectively. Each ZnO nanorod has a hexagonal shape. The SEM images of Al n-doped p-type ZnO thin film coated ZnO nanorods are depicted in Fig. **14(b)**. The thickness of the ZnO thin film coating the nanorod is about 200 nm [61].

Very helpful ZnO nanorods for antireflection coating in solar cell application is also reported in ref [62] where the authors achieved a weighted global reflectance of 6.6% on silicon surface.

3.2. SnO_2

As a front transparent conducting oxide (TCO) layer for thin-film solar cells, ZnO:Al has a lot of advantages over the conventional SnO_2:F, *e.g.*, high stability under the hydrogen plasma environment and high electro-optical properties [63]. In turn, due to the higher contact potential of ZnO:Al/p a-SiC:H compared with SnO_2:F/p a-SiC:H, the contact properties of n-type ZnO:Al with adjacent p-type a-SiC:H can be limiting factors for a-Si:H solar cell performances, since the a-Si:H solar cells prepared on ZnO:Al suffer from reduced fill factor and Voc [64].

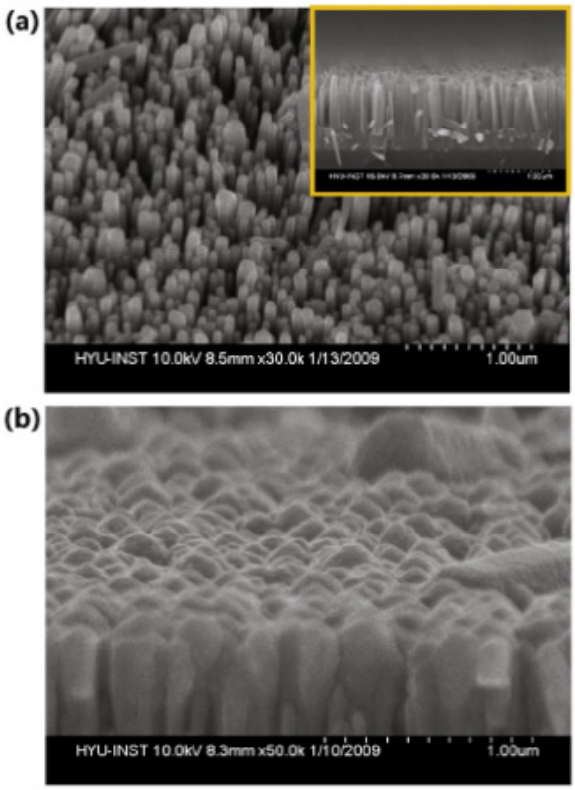


Figure 14: (a) SEM image of ZnO nanorod synthesized on F:SnO_2 substrate. Inset shows the cross sention view. (b) Tilted SEM image of the p-type ZnO thin film coated ZnO nanorod [61].

Fluorine-doped tin oxide films (SnO_2:F), which fulfil these requirements up to a large extent, have been developed by Asahi Glass (Asahi Type U, [65]) by chemical vapour deposition CVD process using $SnCl_4$ precursor gas [56, 57]. It is also the most commonly used TCO material for thin film Si solar large area module manufacturing [65].

Accurate optical constants (n and k) of textured SnO_2 films have been reported in the range of 0.85–4.6 eV using spectroscopic ellipsometry on Ashai U type SnO_2 on glass substrate [66]. In Fig. **15** is reported the transmission spectrum of the SnO_2 film deposited on glass substrate.

In Fig. **16** are reported the refractive index n as well as the extinction coefficient k of the textured SnO_2 on glass measured at different angles. For comparison the n and k of SnO_2 flat surface are also reported.

SnO_2:F can also be fabricated by spray pyrolysis technique as referred in [67]. In that experience SnO_2:F films were deposited from a solution comprising 23 ml of $SnCl_4$, 7 ml of H_2O, and 920 ml of methanol solution 6. Fluorine was added in the form of HF, instead of NH_4F, to give the solution a doping level of F/Sn in the range of 0–180 atomic per cent.

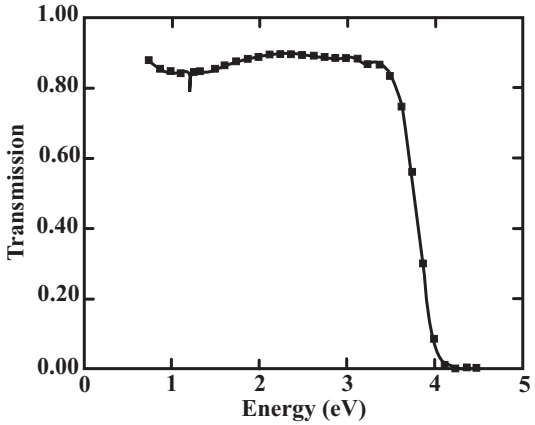


Figure 15: Measurements and fit of the transmission measured on SnO_2 deposited on glass substrate [66].

Deposition was performed on borosilicate glass substrates at a temperature of 490 °C-525 °C and from a distance of approximately 18 cm using a spray bottle with a nozzle diameter of 0.5 mm. The carrier gas was nitrogen and the spray rate was 12 ml/min. ρ, μ, N as a function of doping level expressed as F/Sn atomic percentage are reported in Fig. **17**.

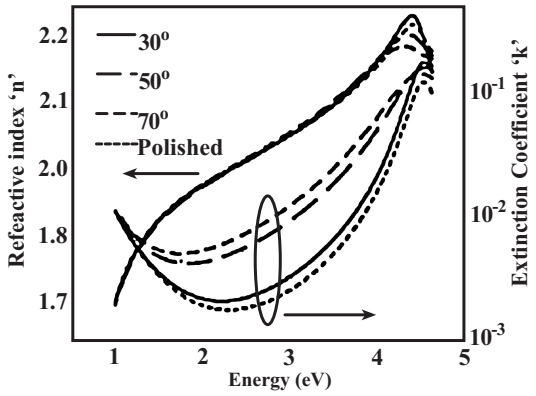


Figure 16: Refractive index n and extinction coefficient k of the textured SnO_2 on glass measured at different angles. For comparison dashed line refers to n and k of SnO_2 flat surface [66].

The transmission spectra of doped ($n = 7.2.10^{20}cm^{-3}$, $\rho = 4.7\ 10^{-4}\Omega cm$ thickness = 0.25 μm) and undoped ($n = 3.2.10^{20}cm^{-3}$, $\rho = 63.4\ 10^{-4}\Omega cm$ thickness = 0.28 μm) SnO_2 films are reported in Fig. **18**.

3.3. ITO

Basically the ITO is a degenerate n-type doped semiconductor that can be fabricate by thermal evaporation [68] or by sputtering system [69, 70]. Here we briefly report on the ITO films as fabricated by the authors for amorphous crystalline heterojunction solar cell solar cell applications.

Concerning the first technique, the ITO was deposited using a Balzers BA510 electron gun system starting from a self-made target of Indium and Tin alloy. Films of 150 nm thickness have been deposited on Corning 7059 in oxygen atmosphere setting a chamber pressure of $2 \cdot 10^{-4}$ mbar. Temperature was measured directly on the substrate using a K thermocouple. Sn/(Sn+In) (wt%) target ratio and substrate temperature were varied to obtain minimum resistivity and best transmittance in the visible range.

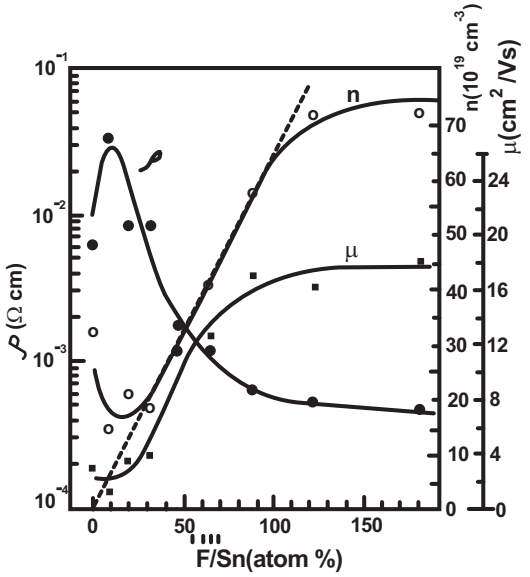


Figure 17: ρ, μ, N as a function of doping level expressed as F/Sn atomic percentage [67].

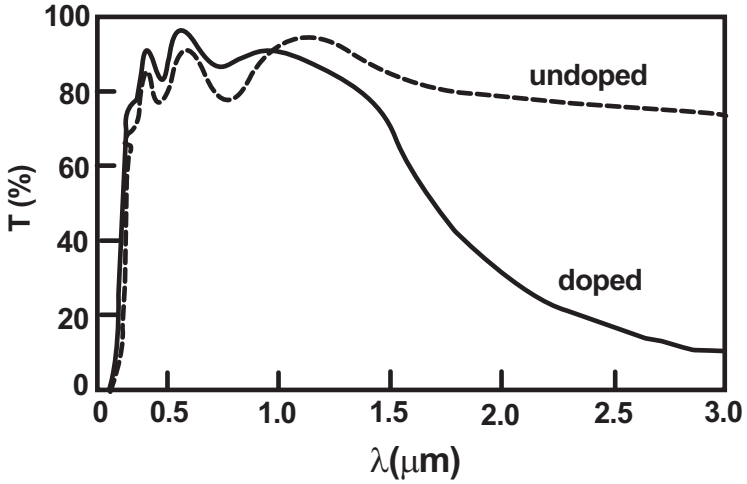


Figure 18: The transmission spectra of doped and undoped SnO_2 films [67].

The variation of resistivity and averaged transmittance from 400 to 800 nm as a function of Sn/(Sn+In) ratio for a fixed substrate temperature are reported in Fig. **19**. The variation of

resistivity and averaged transmittance from 400 to 800 nm as a function of substrate temperature for a fixed Sn/(Sn+In) ratio are reported in Fig. **20**.

The ITO films useful for a-Si:H/c-Si heterostructure solar cells [71, 72] have been deposited using a low temperature RF 13.56 MHz magnetron sputtering. In Fig. **21** are reported, as a function of deposition temperature, the values of resistivity and effective transmittance from 350 nm to 1200 nm defined as:

$$T_{eff} = \frac{\int_{350nm}^{1200nm} T(\lambda) \cdot AM1.5G(\lambda) d\lambda}{\int_{350nm}^{1200nm} T(\lambda) d\lambda} \quad \textbf{(9)}$$

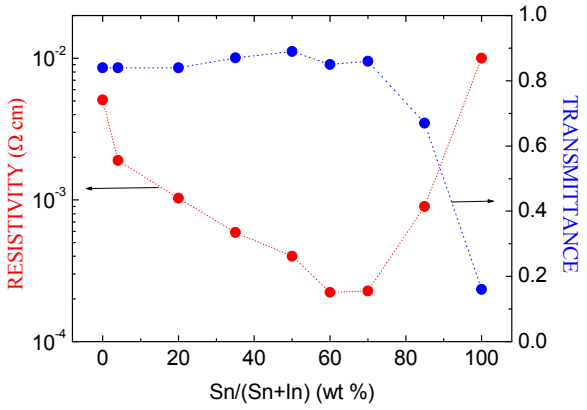


Figure 19: Resistivity and optical averaged transmittance (400-800 nm) of ITO *vs.* percent of Tin in the Tin+Indium solid source for films deposited at 260°C of temperature substrate [68].

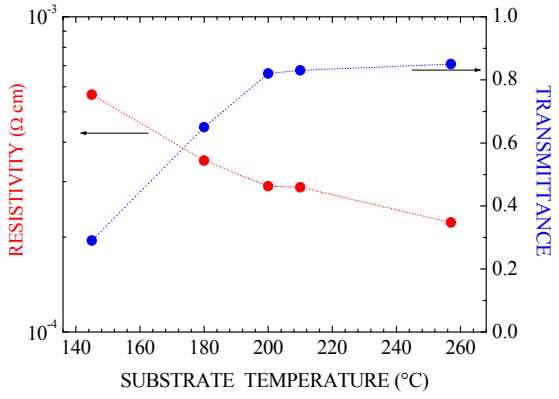


Figure 20: Resistivity and optical averaged transmittance (400-800 nm) of ITO *vs.* substrate temperature of deposition for fixed target composition (60% Sn content) [68].

where T(λ) is the transmittance and AM1.5G(λ) is the number of photons per unit wavelength (λ).

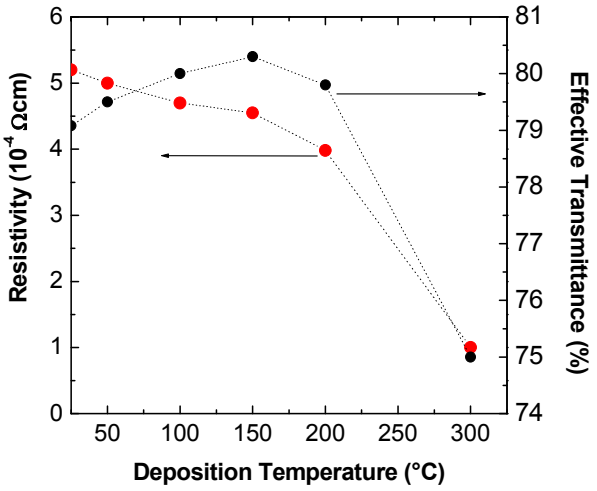


Figure 21: Sputtered ITO resistivity and transmittance as a function of deposition temperature.

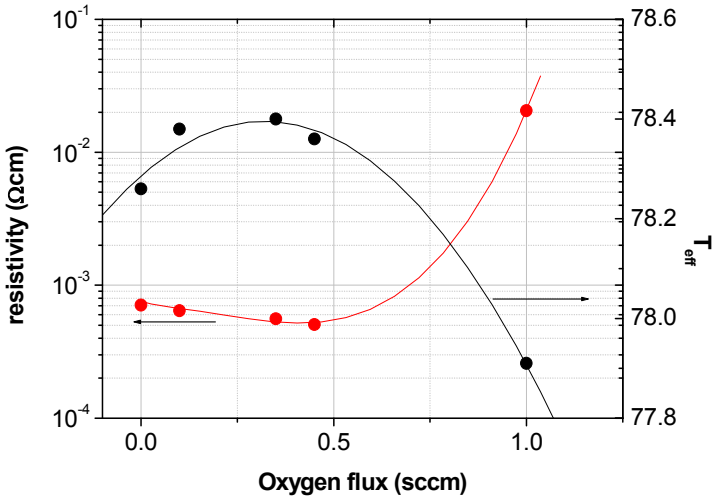


Figure 22: Sputtered ITO resistivity and transmittance as a function of oxygen flux at a deposition temperature of 80°C.

The deposition process parameters have been optimized in order to obtain a good compromise between the film conductivity and transmittance. In particular, the sputtering conditions have been fixed as follows: the RF power to 200 W, the process pressure to 2.25 mTorr, the Ar content to 25 sccm. It is worth to note that no oxygen has been used in order to reduce the film resistivity. For comparison the effective transmittance and resistivity as a function of oxygen flux during the sputtering process at a fixed temperature of 80°C are reported in Fig. **22**.

3.4. Texturing

Basically light trapping is an interesting technique to increase absorption of the incident light in the active layers of solar cells. This is particularly true in all thin film cells where the absorber layer thickness is chosen on the base of the orthogonal light absorption. To enhance the optical path of the refracted light impinging onto the cell, a texturing technique is commonly adopted producing roughness on the window layer of the device. Moreover to further enhance the internal absorption a rear side textured reflector is used, thus producing several light round trip within the absorber layer. These concepts can be successfully extended also to solar cell involving thicker absorber layer, such as silicon wafer based cell, even more when wafer thinning is mandatory to reduce the PV cost. In this paragraph we focus on texturing techniques used in thin film and in c-Si based solar cell also going toward thinner silicon wafer.

Thin film cells are commonly based on different kind of architecture depending on the choice of mechanical support as substrate. If a hard substrate such a glass is used, then a top down configuration is adopted in the cell manufacturing, thus the glass is the cell window layer [73]. On the other hand if a flexible substrate is preferred such as stainless steel, then the cell fabrication process has a bottom up development during the growth [74]. These are the most common configurations, even if mixed approach are possible such as flexible transparent plastic foil [75] or hard metallic substrates. Except for the CdTe and CIS/CIGS cells, in which the TCO is used just for the front side contact, the other device commonly use TCO for both front and rear side contacts. In Fig. **23** a schematic overview of the different configuration is reported. To enhance the cell absorption by the texturing technique, two strategies can be adopted and eventually merged: TCO texturing and substrate texturing. Both introduce light scattering at the rough interfaces in the solar cell. In this way the average length of the optical light path in a layer is increased and the light absorption enhanced. Scattering at rough interfaces not only leads to enhancement of the absorption in the active layer of the cell but also influences the absorption in all other layers.

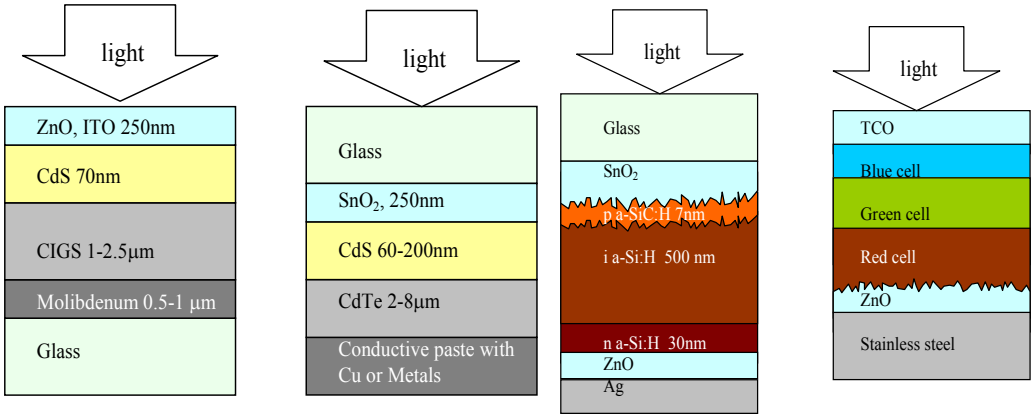


Figure 23: Different thin film cell configurations.

Now we will consider the scattering promoted by a rough surface of TCO deposited on flat glass surface as depicted in Fig. **24**.

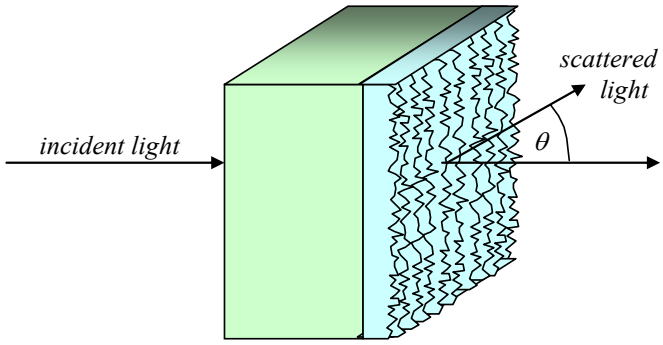


Figure 24: Light scattering at a thin film with one roughly textured surface deposited on glass surface.

For an optimal optical design of thin film solar cells it is important to know the light absorption profile in the whole solar cell. Since it is not easy to determine this profile experimentally, computer modeling has often reported in literature to study the absorption in thin film solar cells [76-78]. The model is based on the first order Born approximation [79] and on Fraunhofer scattering. A rough interface can be described taking into account the root mean square (rms) roughness,σ_{rms} and the scattering data including the haze parameter and the angular distribution of diffuse light. The σ_{rms} is defined as follows:

$$\sigma_{rms} = \sqrt{\frac{1}{N}\sum_{i=1}^{N}\left(\eta_i - \bar{\eta}\right)^2} \quad \textbf{(10)}$$

Where η is the height of the i-th scanned point, $\bar{\eta}$ the average height of the scanned point and N is the total number of point collected during an atomic force microscopy (AFM) scan.

The haze for transmitted light normally incident to the glass side and crossing a rough surface as depicted in Fig. **24** is defined:

$$H_T = T_{dif}/T_{tot} \quad \textbf{(11)}$$

where T_{tot} is the total and T_{dif} is the diffused optical transmittance measured by a photo-spectrometer equipped with an integrating sphere. The total and diffused transmittance of a fluorine doped tin oxide (FTO) SnO_2 glass coated, deposited using atmospheric pressure chemical vapour deposition APCVD, commonly available on market as Ashai U-type [65], having σ around 40 nm, is reported in Fig. **25**.

To simulate the haze of TCO it is possible to use the following equation:

$$H_T(\lambda) = 1 - \exp\left[-\left(4\pi\sigma_{rms}C_T\left|n_1(\lambda)\cos\theta_{inc} - n_2(\lambda)\cos\theta_{out}\right|/\lambda\right)^{\beta}\right] \quad \textbf{(12)}$$

where n_1 and n_2 are the refractive indices of the two media (incident and refracted) respectively, θ_1 and θ_2 are the angle of the incident specular beam and the outgoing beam respectively and C_T, β are fitting parameters. While a square dependence ($\beta = 2$) is reported by the scalar scattering theory [80], other research group found better agreement for large wavelength λ as cubic dependence [76].

The meaning of C_T is quite controversial: it is dependent from λ and it is strongly needed to have reasonable results. Physically might be related to the shadowing effect of scattered light [81]. Power factors larger than 3 for ZnO:Al layers textured by post-etching in HCl is also reported in [82, 83].

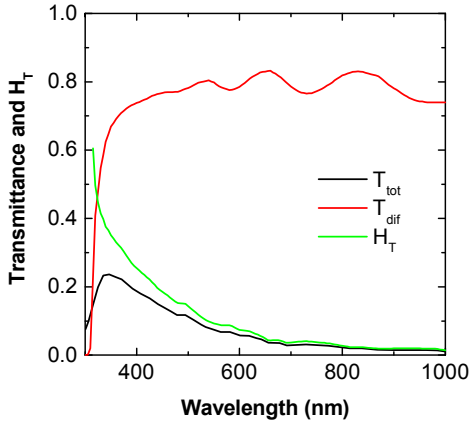


Figure 25: Total and diffused transmittance together with haze of FTO Asahi U-type.

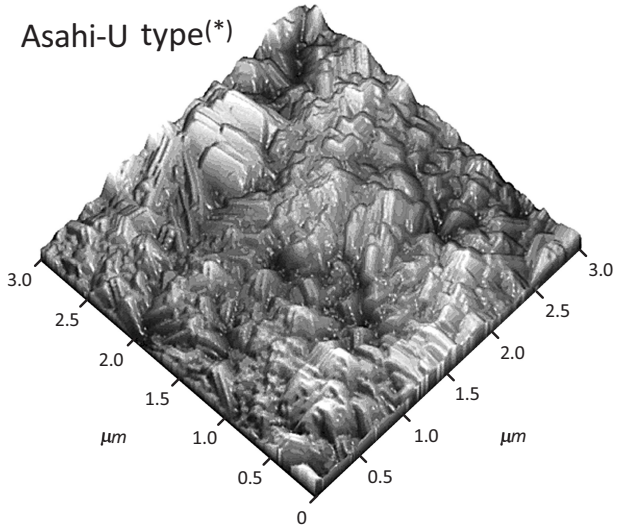


Figure 26: AFM scan image over a 3x3 μm^2 of F:SnO_2 Ashai U-type.

Moreover is not easy to evaluate the σ_{rms} because, if atomic force microscopy (AFM) is used, the σ_{rms} can depend on the scanned area, becoming higher for larger scanned area. This would indicate that the roughness varies more than the range of one micron as a typical AFM scan. Therefore large area should be investigated with AFM to estimate reasonable σ_{rms} values.

After deposition of absorber layer on rough TCO surface a smoothening occurs that reduces the σ_{rms}. Indeed, in case of P-I-N amorphous silicon solar cell deposited onto Asahi U-type covered corning glass, while the very short p-type doped layer almost does not affect the TCO roughness, after 300 nm intrinsic layer deposition the σ_{rms} reduces to 33 nm [77]. An AFM scan image over a 3x3 μm^2 of F:SnO_2, Ashai U-type is reported in Fig. **26** [83]. A SEM picture remarking the pyramidal surface of this textured TCO is reported in Fig. **27** [76].

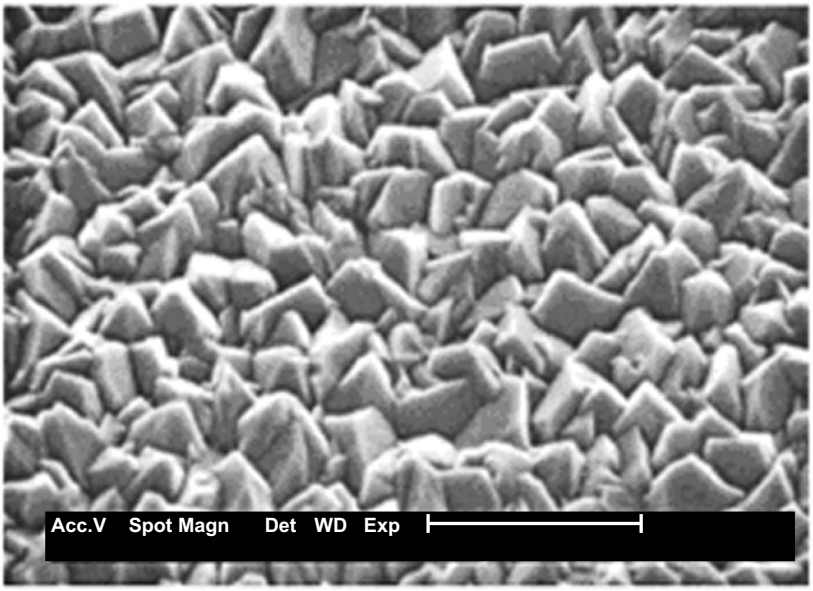


Figure 27: The SEM picture of the rough surface of the glass/SnO2 Asahi U-type substrate [76].

A haze comparison of three different ZnO textured surfaces in case of ZnO/air and ZnO/c-Si interfaces are respectively reported in Fig. **28(d), (e)**, together with the simulations obtained using equation (12). The thicknesses, the σ_{rms} and the shape of these Al doped TCOs are listed in Table **2**. Moreover the shape of the three different Al ZnO textured surfaces are depicted in SEM images reported in Fig. **28(a), (b), (c)** [84].

Table 2: Parameters related to the Al doped textured ZnO.

Al ZnO	**A**	**B**	**C**
Thick (mm)	1.9	4.8	4.8
Srms (nm)	66	178	165
Morphology	V shape	V shape	U shape

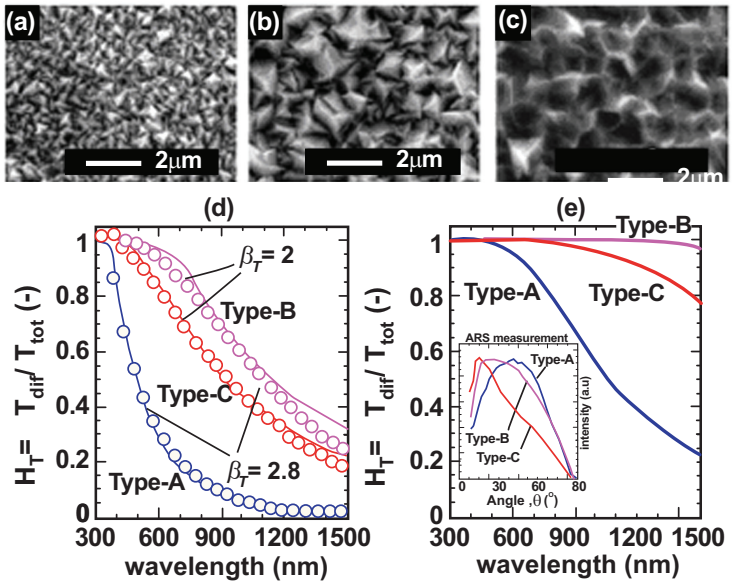


Figure 28: SEM pictures (a), (b, (c) of typical type-A,-B and-C ZnO layers respectively. Experimental (symbols) and calculated (lines) haze in transmission in air (d) and at the ZnO/Si interface for the type-A,-B and-C front ZnO layers (e) [84].

Basing on the experience reported in [77], now we report about the use of model related to the equation (12) to evaluate the reflectance and transmittance of a Ashai U-type F:SnO_2 used for p-i-n a-Si:H solar cell.

In case of rough interface, having σ_{rms} smaller than λ/n of the medium incidence, the scalar scattering theory is applicable to determine the specular reflectance of an interface. The total reflectance R_s can be modelled using the following equation reported in [77]:

$$R_S(\lambda) = R_0(\lambda)\exp\left[-\left(4\pi\sigma_{rms}n_0/\lambda\right)^2\right] \quad \textbf{(13)}$$

where R_0 is the reflectance of a flat surface. Assuming that:

$$R_0(\lambda) = R_s(\lambda) + R_d(\lambda) \quad \textbf{(14)}$$

where $R_d(\lambda)$ is the diffused reflectance, we obtain

$$R_d(\lambda) = R_0(\lambda)\left(1-\exp\left[-\left(4\pi\sigma_{rms}n_0/\lambda\right)^2\right]\right) \quad \textbf{(15)}$$

Fig. **29(a** and **b)** show the ratio R_d/R_0 as calculated from equation (15) for light incident at a rough interface through Asahi U-type TCO and n-type a-Si:H, respectively, for several values of σ_{rms}. It

is important to note in Fig. **29** that the back contact interface acts as a nearly perfect diffuser for the reflected light in the wavelength range of interest when $\sigma_{rms}$is larger than 30 nm [77].

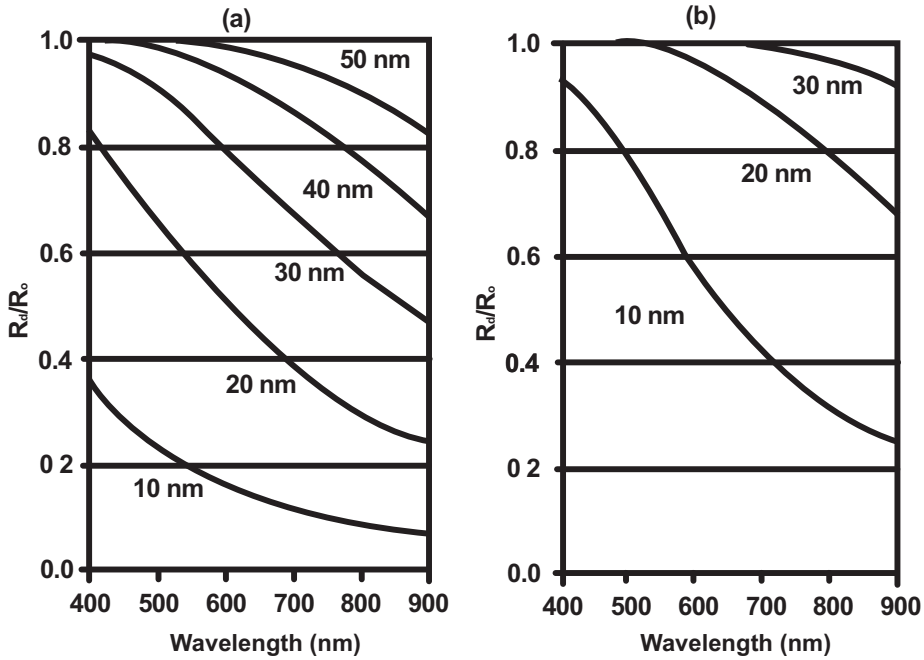


Figure 29: The R_d/R_0 ratio as a function of wavelength for several values of the σ_{rms} roughness of the rough interface: a) Asahi U-type TCO material and b) *n*-type *a*-Si:H [77].

To evaluate the diffused transmittance $T_d(\lambda)$ of the rough Ashai U-type TCO it is possible to use a relation similar to equation (15):

$$T_d(\lambda) = T_0(\lambda)\left(1 - \exp\left[-\left(4\pi\sigma_{rms} C\ \left|n_0(\lambda) - n_1(\lambda)\right| / \lambda\right)^3\right]\right) \quad \textbf{(16)}$$

where C depends on the two media and in particular when $|n_0\text{-}n_1|$ increases C tends to 1. Fig. **30** shows the ratio of T_d to T_0 for TCO/p and p/i interfaces for different values of σ_{rms} assuming C = 1.

By using the modelled transmittance and reflectance and the values of σ_{rms} at each interfaces it is possible to evaluate how the interfaces within the TCO/p/i/n/Ag structure affect the Quantum Efficiency of the solar cell. Indeed a Quantum Efficiency can be seen as the sum of optical and electrical contributes arising from each scattering interface and each layer respectively.

$$QE(\lambda) = \sum_{layers} QE_{op}(\lambda)\eta(\lambda)QE_{el}(\lambda) \quad \textbf{(17)}$$

QE_{op} is the optical quantum efficiency measuring the probability of a photon to be absorbed; $\eta(\lambda)$ is the carriers generation per photons; QE_{el} is the collection probability.

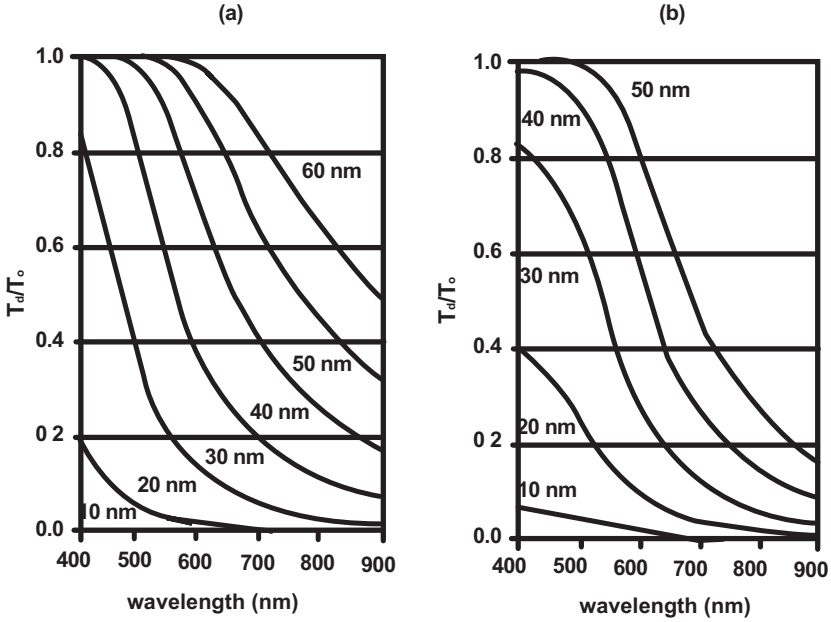


Figure 30: The T_d/T_0 ratio as function of wavelength for several values of σ_{rms} for: a) the TCO/*p* interface and b) the *p*/*i* interface [77].

The texturing effects on front and rear contact on experimental QE of four different TCO/p/i/n/Ag cells are reported in Fig. **31** as points. The cells have different intrinsic layer thicknesses. For each of them four different simulations are reported in the same figure as lines. Each of them refers to: (1) all interfaces are flat; (2) only TCO/p is a rough interface; (3) only n/Ag is a rough interface; (4) all interfaces are rough. For each case it is possible to evaluate the short circuit current (Jsc) integrating the QE values over the wavelength range from 350 nm to 900 nm and taking into account the photon number per wavelength of sunlight AM1.5G spectrum. This value is also reported in Fig. **31** for each simulation as Jph. The simulation clarifies that the scattering enhances the absorption in the intrinsic layer leading to a gain up to 2.3 mA/cm^2. This enhancement is slightly dependent on the intrinsic layer thicknesses. The simulation also states that the roughness close to the rear contact has a strong effect in the spectral region of wavelength higher than 650 nm and has no effect on front side of the cell then does not affect the QE in the spectral range from 350 nm to 550 nm. Moreover the front rough interface strongly affects the QE in the spectral range between 450 nm and 650 nm slight, while introduces a slight decrease of the QE below 450 nm.

Introducing a TCO layer with rough surface in between n/Ag interface it is possible to further enhance the QE in the spectral range above 650 nm, leading to a Jsc improvement up to 2.9 mA/cm^2.

As expressed before, the angular distribution of diffused light is a relevant parameter to evaluate the scattered light in transmission I_T and then to extract information on the surface roughness of the investigated medium. A very helpful tool to determine I_T is the Angular reflectance transmittance Analyzer (ARTA) [86] depicted in Fig. **31**. This instrument uses monochromatic

light coming from a spectrophotometer. The detector is located in a little integrating sphere and can be moved along the sphere for an angle between-165° and 165°. The sample under test is placed in the centre of the sphere and can be rotated with respect to the incident light from 0° (normal incidence) to 90° (parallel incidence). At normal incidence the reflected light cannot be collected due to restriction of the detector

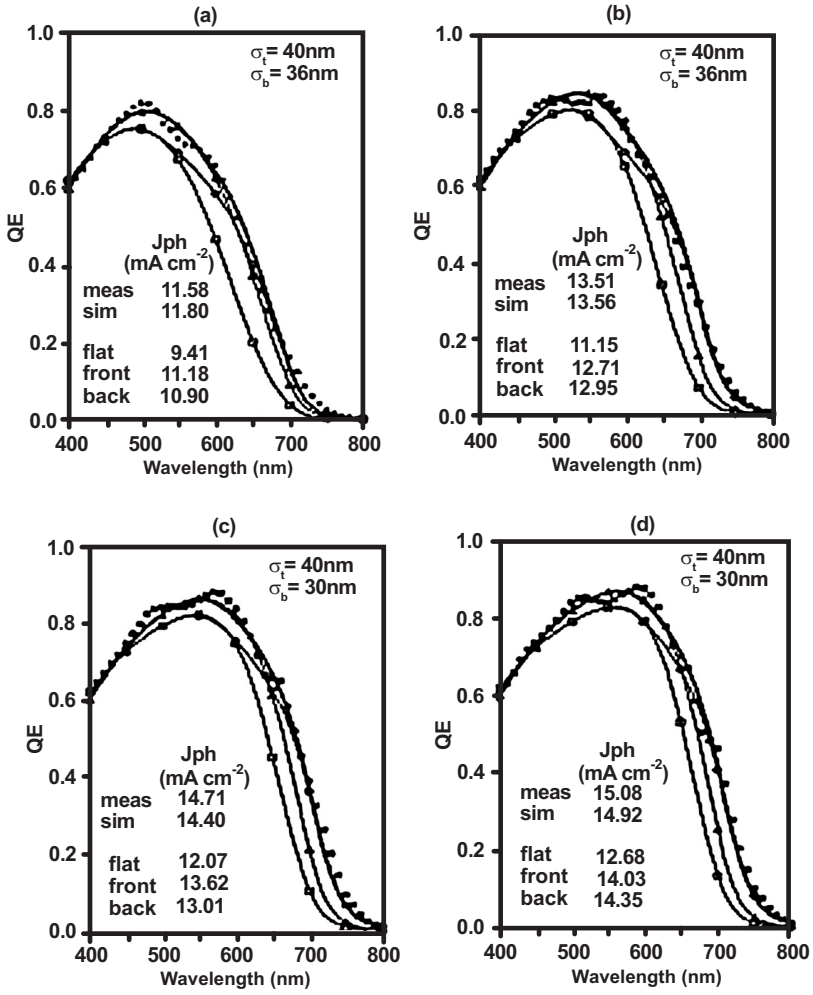


Figure 31: Experimental (■ points) and simulated (lines) QE of the four single junction *a*-Si:H solar cells each with a different thickness of the intrinsic layer: (a) 150 nm, (b) 300 nm, (c) 450 nm, and (d) 600 nm. The simulated QE curves refer to: (□) all flat interfaces; (Δ) only the front interfaces TCO/*p* and *p*/*i* are rough; (o) only the back interfaces (*i*/*n* and *n*/metal) are rough; (full line) all interfaces are rough. The σ_{rms} roughness of the front and rear interface of the cell and the J_{ph} values are reported for each cell [77].

The absorbance A of the sample is related to the incoming light intensity I_0 as follows:

$$I = I_0 10^{-A} \quad \textbf{(18)}$$

In this way the I_T can be measured over a wide range of wavelengths.

Several textured substrates have been evaluated as reported in Table **3** where the surface structure and the σ_{rms} values are listed. The FTO has been already described.

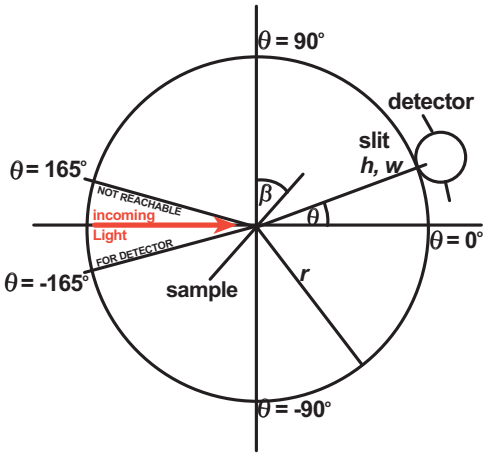


Figure 32: Schematic cross section of the ARTA [85].

Table 3: Morphology and σ_{rms} of different textured TCOs.

Material	**Morphology**	**σ_{rms}**
FTO	Pyramidal	40
AZO 40 sec	Crater like	100
BZO	pyramidal	220

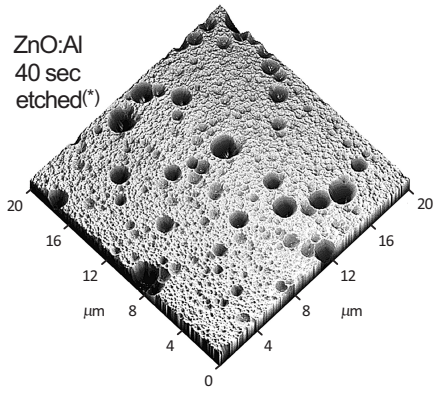


Figure 33: AFM scan image of Al:ZnO etched surface.

The Al:ZnO (AZO) has been deposited in condition so that it resulted flat after the deposition and then has been etched in 0.5% HCl bath for 40 s to form a crater like surface morphology as depicted by AFM scan image reported in Fig. **33** [87].

Boron depod ZnO (BZO) has been deposited by LP-CVD. The transmitted light angular distributions of samples listed in Table **4** are reported in Fig. **34(a),(b)** for 450 nm and 700 nm monochromatic incident light respectively. To compare these intensities each other they are normalized to the total transmittance $T_{tot}(\lambda)$. From the measurements reported in Fig. **34** it is evident that at 700 nm the higher the σ_{rms}, the stronger the scattering; moreover the AZO sample shows a stronger scattering at smaller angles than BZO. On the contrary, for both wavelengths, the specular part of the transmittance decreases with increasing σ_{rms}.

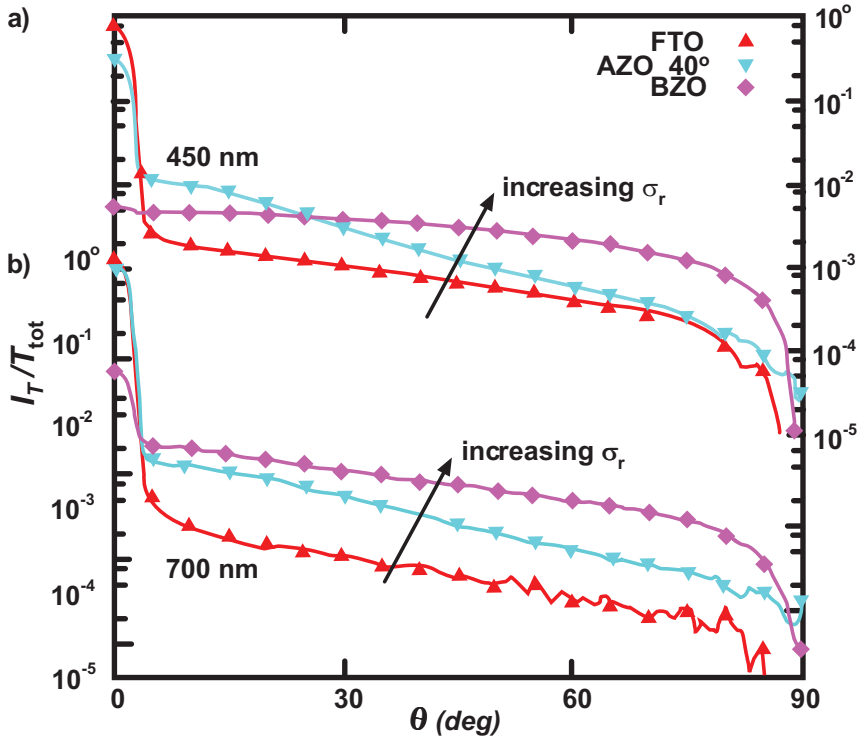


Figure 34: Scattered light angular distribution at λ = 450 nm (a) and 700 nm (b) for the samples listed in Table **3** [85].

Now we report about an interesting study on the scattering properties of ZnO useful for thin film solar cells [87]. They have used the most common way to fabricate ZnO films by 13.56MHz rf magnetron sputtering system using a $ZnO:Al_2O_3$ target. Four different kinds of ZnO films have been prepared on 1737 Corning glass by varying the Al_2O_3 weight percentage (TCA) of the target as: 0.2, 0.5, 1 and 2%. 0.3 Pa deposition pressure has been used for three kinds of film, while 1 Pa has been adopted in case of 2%. Different films have been deposited at different temperature in the range between 60 and 490 °C. After deposition a wet chemical etch in 0.5% HCl bath has been performed on top of the film initially smooth to texture the surface. By varying the deposition conditions the ZnO films can assume different optoelectronic properties. Briefly we summarize the most relevant, such as carrier concentrations-mobilities as a function of deposition temperature for different TAC, reported in Fig. **35**, and transmission-absorption in the wavelength range between 300 nm and 2500 nm, reported in Fig. **36**.

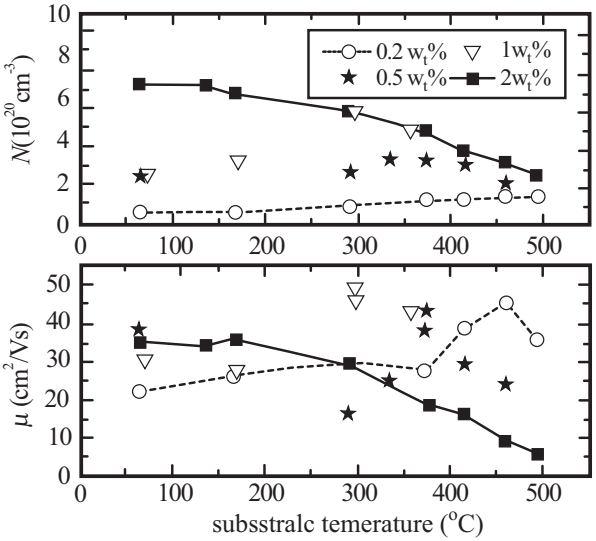


Figure 35: Carrier concentration and mobility of Al:ZnO films as a function of deposition temperature for different TAC. Reprinted with permission from [87]. Copyright (2007), American Institute of Physics.

To evaluate the roughness σ_{rms}, AFM scans have been performed after wet chemical treatment and the relevant results are depicted in Fig. **37**. From the data it is evident a certain activation temperature that increases with decreasing the TAC. Depending on the temperature and TAC, different surface morphologies appear. Three features can be found: (i) very rough surface with lateral feature size of about 300 nm and with rather steep edges, as in case of TAC = 0.2% and T = 290 °C; (ii) large craters that uniformly cover the surface, as in case of TAC = 0.5-1% and T =300-375 °C; (iii) shallow craters with diameters of 1-3 μm and depth of about 150-400 nm, as in case of TAC = 0.5-1%. Increasing the deposition temperature the surface changes from (i) toward (iii).

These data are useful to evaluate the haze of samples as reported in Fig. **38**. Also in this picture a transition temperature can be identified and it corresponds with the transition from feature (i) to (ii). To evaluate the PV performance of these TCO as top contact of thin film solar cell several μc-Si:H cells, with 1 μm of absorber layer, have been manufactured and different results have been obtained using different featured Al:ZnO films. In case of type (i) features (TAC = 0.2%, T = 290 °C) the cell reached only 22.1 mA/cm^2 due to poor electrical properties of Al:ZnO and relatively low scattering effect.With the same amount of TAC but increasing the deposition temperature up to 460°C a transition to features (ii) appears forming craters over the Al:ZnO surface able to enhance the light scattering thus increasing the Jsc to 22.9 mA/cm^2. Even though the features of type (iii), such as obtainable in case of TAC = 2%, T = 375 °C, produce less scattering effect resulting in 17.2 mA/cm^2, the relatively smooth surface, able to reduces the shunt effects together with better electrical properties, enhances the cell Voc. With the TAC of 2%, increasing the Al:ZnO deposition temperature the scattering effect strongly reduces toward non-textured front contact. Since features of type (ii) are the most interesting from the light scattering point of view, deeper investigation have been carried out in this direction [87]. With increasing the intrinsic μc-Si:H layer thickness up to 1.9 μm the influence of parasitic losses, produced using the ZnO surface features of type (ii), reduces at both top and bottom interfaces with doped p and n layers. This effect, together with absorption along the thicker intrinsic layer produces a strong enhancement of Js up to 26.8mA/cm^2 [87].

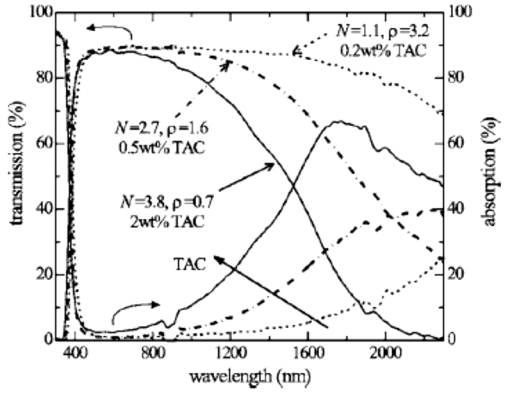


Figure 36: Transmission and absorption of Al:ZnO deposited at 370 °C for different TAC. Reprinted with permission from [87]. Copyright (2007), American Institute of Physics.

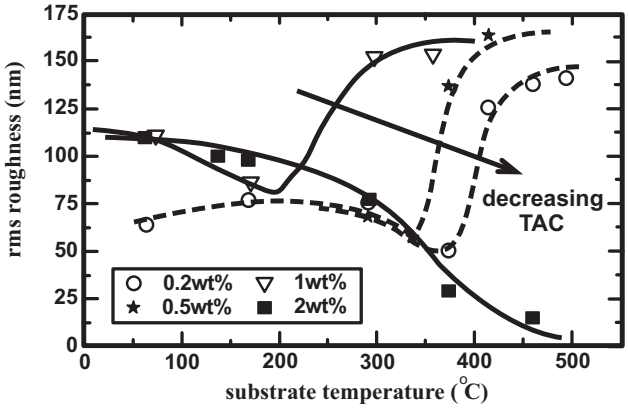


Figure 37: Calculated rms roughness data points using AFM measurements of texture-etched Al:ZnO films with different TACs. Lines are Guide-to-the-eye Reprinted with permission from [87]. Copyright (2007), American Institute of Physics.

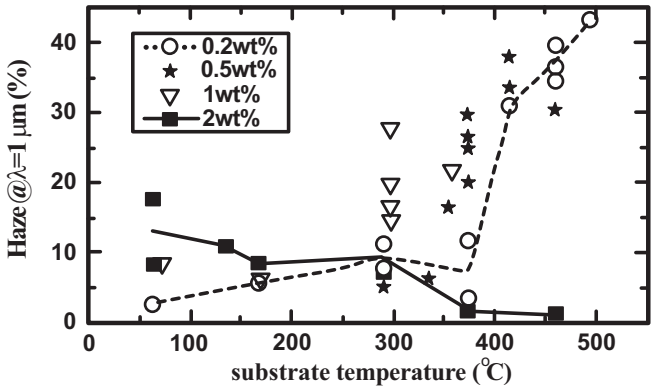


Figure 38: Haze values at wavelength of 1μm. Reprinted with permission from [87]. Copyright (2007), American Institute of Physics.

Using a similar approach it is possible to evaluate the role of the scattering at each interface of a micromorph tandem solar cells deposited on two different kinds of LPCVD textured TCO type A and C of Table **2**. In these cells a Silicon Oxide Intermediate Reflector (SOIR) has been introduced [88]. Four different cells have been deposited on type A and type C ZnO with and without SOIR. Their External Quantum Efficiencies are reported in Fig. **39(a)**. Taking into account that the top cell is the limiting factor of the total device, from the figure is evident that the gain in Jsc is larger when the SOIR is introduced and the cell is formed starting from type-A ZnO compared to type-C ZnO. Also the top cell is strongly affected by the presence of SOIR but is less affected by the ZnO substrate. ΔJsc, top *vs.* the thickness of the SOIR layer inserted in devices with top and bottom cell thicknesses of 180 nm and 1.8 μm, respectively, is plotted in Fig. **39(b)**. In turn a decrease of total reflectance of the cell is observed when SOIR is applied, as indicated by the Jsc values [88]. Nevertheless micromorph tandem cell deposited on type-C ZnO layer having a 3 μm thick bottom cell reached initial efficiency of 12.6% with Jsc of 12.7mA/cm^2,Voc of 1.38 V and FF of 72.2%. This efficiency is, up to now, the state of art of this tandem micromorph cells.

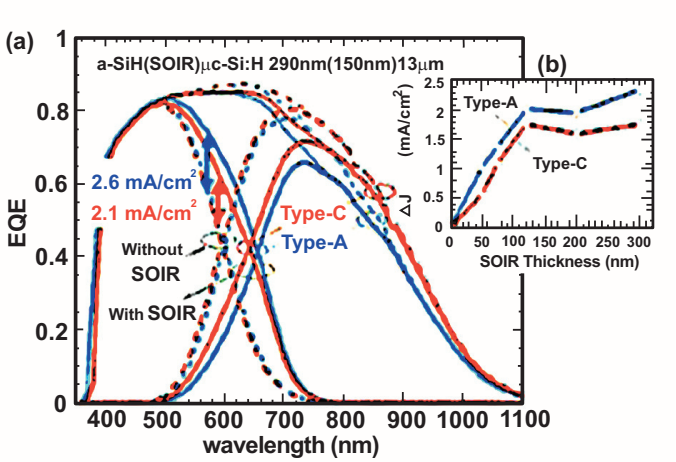


Figure 39: (a) EQEs of micromorph cells with and without a 150 nm thick SOIR deposited on type-A and type-C front ZnO layers; (b) Gains obtained in Jsc of top cell for a thickness series of SOIR layers [84].

The balance of scattering in micromorph tandem a-Si:H/mc-Si:H solar cell is quite critical since the two cells work as series of current generator. Then the tandem cell current is the lowest current generated by the two cells. This means that every kind of scattering enhancement introduced to the front will result in limited efficacy if also the rear cell is not sufficiently enhanced at the same time. On the other hand the top cell should be as thin as possible in order to reduce light induced degradation [89, 90]; therefore it limits the tandem cell current. To overcome this problem an intermediate reflecting layer (IRL) has been proposed [91]. To be effective this layer should have a refractive index lower than silicon (n_{Si} = 3.8 at 600 nm) to produce a step index at the interface able to reflect part of incident light. At same time this layer must be quite conductive to avoid series resistance enhancement. ZnO has been proposed [91, 92] and an increment of 2.8mA/cm^2 has been obtained using 110 nm thick ZnO with a80 nm thick top cell [93]. At the industrial scale this approach requires a significant trouble related to the deposition of ZnO layer in a different system with respect to the PECVD used to deposit the tandem cell layers. Recently a n-type doped

SiOx intermediate reflector layer (SOIR) has been proposed instead of ZnO [94]. It can be deposited by a 110 MHz RF PECVD using a $PH_3/SiH_4 = 0.024$ and $CO_2/SiH_4 = 2.7$ at 250°C using a power density in the range between 0.01 and 0.1W/cm^2. With reducing the CO_2/SiH_4 ratio from 6 to 0.5 it is possible to change the refractive index from 2 to 3. Moreover its conductivity grows from $10^{-14}\Omega^{-1}cm^{-1}$ up to 1 $\Omega^{-1}cm^{-1}$ reducing the CO_2/SiH_4 ratio from 3.2 to 1.6 and increasing the PH_3/SiH_4 ratio from 0.008 to 0.024. Nevertheless its conductivity still remains two order of magnitude lower than ZnO layer ($10^2\Omega^{-1}cm^{-1}$), even if when the SOIR is deposited in a tandem cell unexpected growth of microcrystalline Si grains appears from Raman measurements that penetrate through the SOIR thus enhancing its conductivity and suggests a percolation mechanism for the current flowing through is. The effect of SOIR introduced as IRL in a tandem cell is reported in Fig. **40** where both the EQE and absorbance are plotted for different SOIR thicknesses. Introducing this layer a relative enhancement of 8% in cell efficiency has been obtained reaching an efficiency of 12.2% [94].

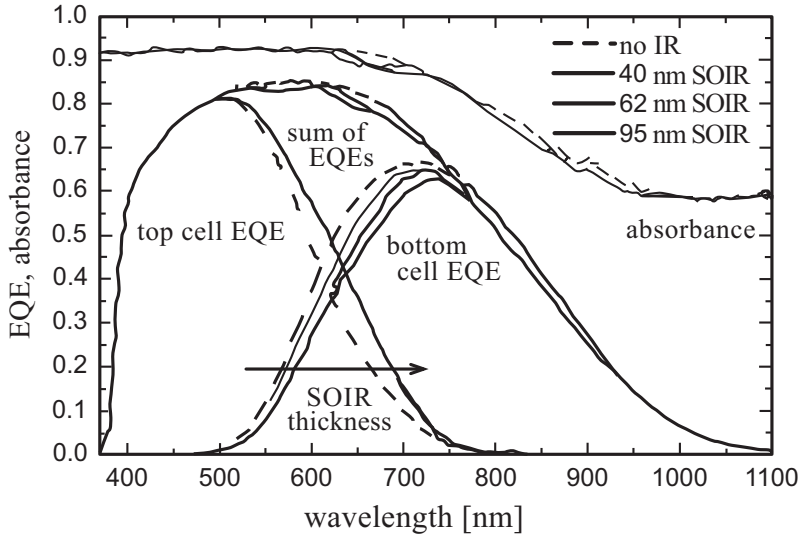


Figure 40: EQE and absorbance of tandem micromorph cell for different SOIR thicknesses [94].

An alternative approach to the texturing of window layer to enhance the light scattering effect is represented by the design of periodic surface texture on the substrate before contact deposition [95, 96]. To this aim the technology mutated from CD and DVD manufacturing can be really helpful. Here we briefly report an example of periodic pattern formed on top of polycarbonate substrate by embossing procedure [97] and covered by a thin Al layer (100 nm). Over this structure a single junction 200 nm thick a-Si:H cell has been deposited. The periodic structure, as monitored by AFM scan, together with the profile and the cell structure are depicted in Fig. **41**. The proposed structure induces optical interferences due to the periodic structure of the substrate. These interferences enhance the absorption in the a-Si:H layer and strongly reduce the total reflectance.

The cell has fabricated with the following structure and thicknesses: ZnO:Al (500 nm)/p-type a-SiC:H (10 nm)/intrinsic a-Si:H (300 nm)/n-typea-Si:H (20 nm)/ZnO (80 nm)/Ag (300 nm). Using a numerical simulator program (FEMOS [98]) it has been possible to find the optimum combination of the height h and the periodicity P of the periodic structure in terms of

interferences. In particular values of P = 300 nm and h = 300 nm are able to optimize the cell QE as well as the J_{sc}. The effect of pattern duty cycle on the cell Jsc values for two different couple of P and h parameters is reported in Fig. **42**. As evident from the data reported in Fig. **42** a duty cycle of 50% allows reaching the maximum Jsc of 15 mA/cm^2 that is 3.5 mA/cm^2 higher than the Jsc obtainable starting from flat substrate. A drawback of this approach is represented by the increasing absorption in the Ag layer with higher vertical features (h). No absorption within front side ZnO has been found in comparison with cell fabricated on flat substrate, since very less light is reflected back at the metal back contact.

The above texturing approach can be also performed on top of cell if the periodic pattern is transferred on a glass substrate. Further enhancement can be achieved if the glass substrate is subsequently covered by ZnO, later textured by wet chemical bath as demonstrated in [99].

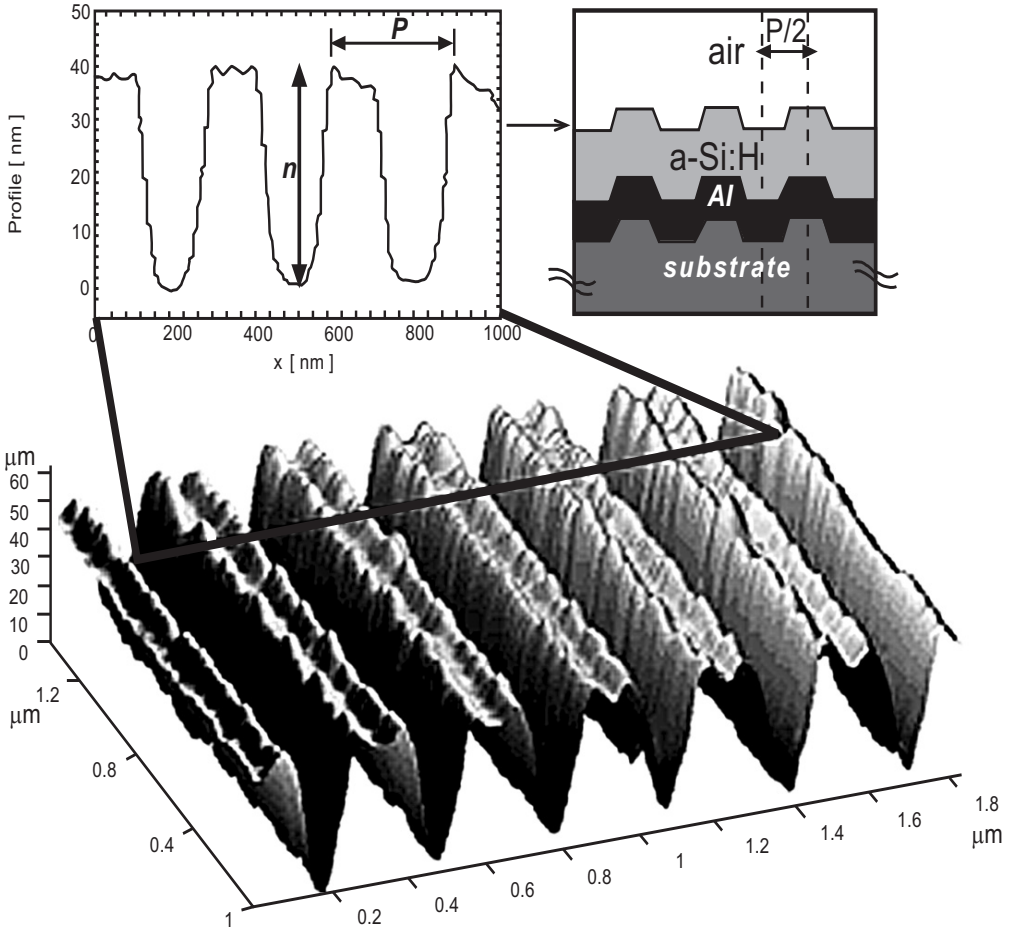


Figure 41: AFM scan of periodic texture formed by embossing procedure on a polycarbonate substrate and after covered by Al and a-Si:H layers [97].

4. SILICON SURFACE TEXTURING

Silicon is the most important of the available photovoltaic energy conversion materials. Crystalline silicon solar cells currently comprise more than 80% of all solar cells produced worldwide, with multi-and mono-crystalline approximately sharing the market. The solar cell industry currently obtains its silicon base material from the by-products of hyperpure poly-Si production and from re-melted Czochralski (CZ) and Float-Zone (FZ) material originating from the microelectronics industry. As-cut silicon substrates are typically 180 µm thick, with approximately 200 µm thick saw kerf losses, but significant cost and energy reduction can also be achieved if thinner wafers are used. For this reason, the general trend is towards the use of still thinner silicon wafers. An important consequence of reducing the cell thickness arises due to the low absorption coefficient of crystalline silicon. An increasing proportion of light of longer wavelengths will not be fully absorbed on its first passage through the cell thickness, so that very effective light trapping schemes have to be built in. A way to reducing reflectance is by applying a randomizing or geometrical surface texture to the front surface of the silicon. This can be done mechanically, by

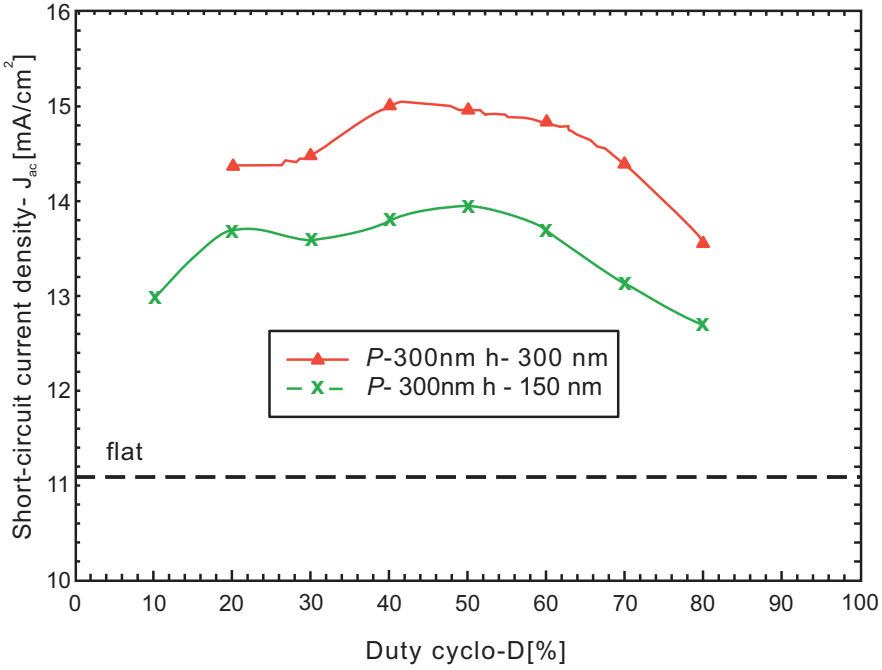


Figure 42: Effect of pattern duty cycle on the J_{sc} [97].

laser assisted processing, by plasma, or (electro-) chemically, by etching the silicon in an alkaline or acidic solution. Texturing the front surface of a solar cell generally results in improved performance, mostly due to an increase in the short-circuit current. This increase arises from three distinct mechanisms, all of which are related to the fact that the incident photons strike the cell surface at an angle. Firstly, some light rays will be reflected from one angled surface merely to strike another, resulting in an improved probability of absorption, and therefore reduced reflection.

Secondly, photons refracted into the silicon will propagate at an angle, causing them to be absorbed closer to the junction than would occur with a planar surface. This is especially relevant in material with diffusion lengths comparable to or less than the cell thickness, such as many multi-crystalline silicon wafers. Thirdly, long-wavelength photons which are reflected from the rear surface back to the front will encounter an angled silicon surface, improving the chance of being internally reflected, either at the silicon interface or at the glass surface, and providing another chance for absorption. This final process is referred to as light-trapping, and gives an improved response to infrared light. The anti-reflection properties pertaining to the geometry of the texture are demonstrated for a simple two-dimensional structure shown in Fig. **43**. Light incident normally to the silicon wafer falls upon the grooves at a point *a*. About 70% of this light is transmitted into the silicon and the rest is reflected. However, the reflected light is now angled downwards towards a neighboring groove, instead of away from the silicon surface as would be the case of a planar cell. Thus the light falls re-incident at the silicon surface for a second chance of transmission into the silicon at point *b*. In this way, light is more efficiently coupled into the silicon, leading to reflection reduction. The number of bounces upon the front surface for such a periodic symmetrical texture depends upon the facet angle of the texture with respect to the wafer surface. Minimal facet angles of 30° and 54° are required for double and triple bounce reflectance respectively. For the double bounce, case shown in Fig. **43**, the light reflected away from the silicon at *b* is lost. However, if the silicon is encapsulated under the glass, it is possible to totally internally reflect light arriving at the glass-air-interface at above the critical angle of 42°, whereby it will be re-directed towards the silicon yet again for possible incidence.

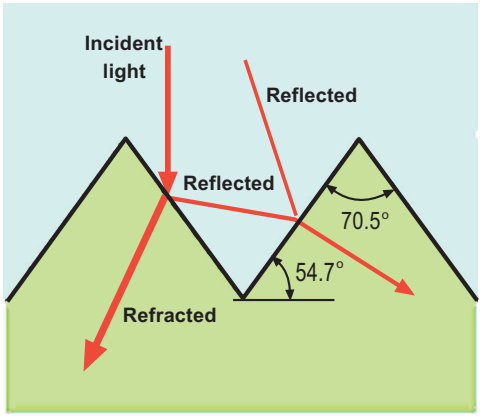


Figure 43: Reflection reduction and light trapping in geometrically textured silicon [100].

4.1. Texturing of Si Wafers

Texturing of crystalline silicon has been adopted for the development of high efficiency mono-crystalline silicon solar cells. Inverted pyramids (Fig. **44**) on the c-Si surface produced with photolithography and anisotropic wet etching steps have resulted in reflectance values as low as 8%, leading to a record efficiency of 25% in c-Si solar cells [101, 102]. The standard inverted pyramid scheme shown in Fig. **44** is non optimal in terms of its light trapping capabilities [103]. Specifically, as shown in Fig. **45**, weakly absorbed light incident on one face of the inverted pyramid will be reflected from the rear reflector upwards. From the symmetry of this situation, light, which then falls internally on a face of opposite orientation from that coupling it in, will exit immediately from the cell.

However, the light, resurfacing at the two other possible faces it can strike, will be totally internally reflected and trapped within the cell. To maximize this trapped component, the relative spacing between the inverted pyramid structures can be varied as indicated by the arrow on the plan view of the process in Fig. **45**. This component could be increased even further if the pyramid positioning in the perpendicular direction could also be varied. One way of doing this is to use the bi-dimensional screw structure shown in Fig. **46**. In this geometry, two different pyramid sizes have been incorporated which provides an additional degree of freedom in optimizing the overall design. Ideally, the difference in the two pyramid sizes would be very small to minimize the criticality in pyramid size to wafer thickness ratio. This scheme is a development of the idea originally proposed by Campbell and Green [103]. An example of a fabricated structure is shown in Fig. **47**.

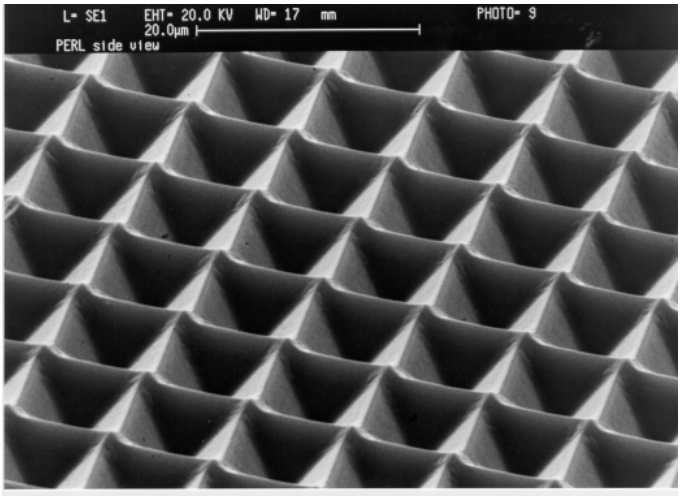


Figure 44: Scanning electron microscope of a textured silicon surface: "inverted pyramids" [100].

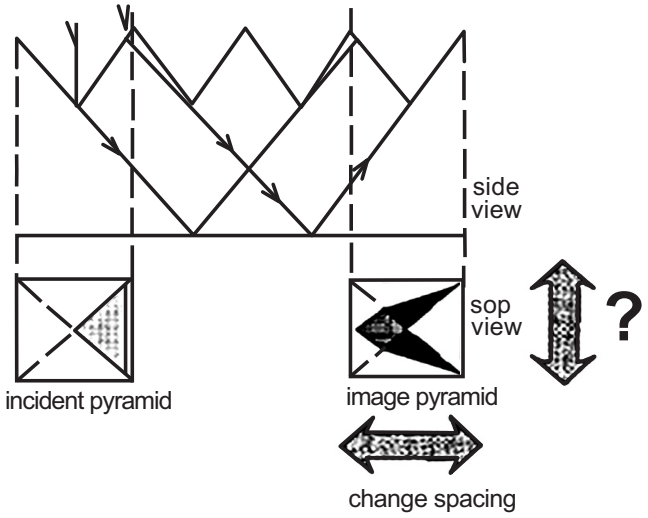


Figure 45: Path of rays in inverted pyramid structure [102].

Also by numerical three dimensional simulations it has been found that inverted pyramids with periodicity of around 1 mm resulted in high quantum efficiencies close to the theoretical limit [104]. However, the use of photolithography steps for producing such structures is a time consuming and costly process. Photolithography-free texturing processes are currently used by industry, employing wet chemical solutions such as KOH/IPA or NaOH/IPA among others. Random pyramids formation on the surface of (100) c-Si is a very effective way to reduce the reflectivity of the front surface of c-Si solar cells [105-107].

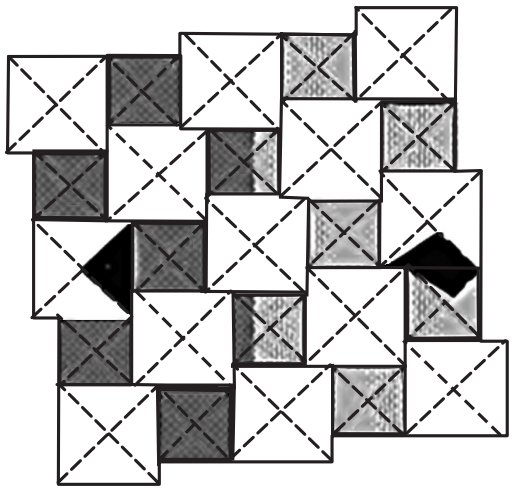


Figure 46: Improved light trapping scheme using a bi-dimensional screw caused by incorporating two different sizes of inverted pyramids [102].

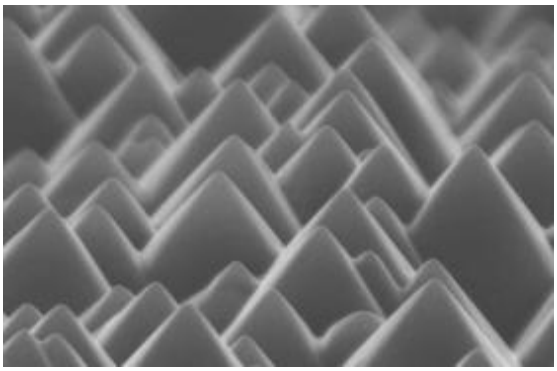


Figure 47: Scanning electron microscope of a textured silicon surface: "random pyramids" [100].

Potassium hydroxide combined with isopropyl alcohol (KOH/IPA) is widely used in order to obtain normal pyramid structures with reflectance values around 15%, however it produces contamination due to potassium, which causes a detrimental in the electrical characteristics of semiconductor devices and as a consequence an extensive wafer cleaning is required. Sodium hydroxide based etchants (NaOH/IPA) have also been investigated for obtaining pyramid structures without the use of KOH, however those processes are not cost-effective, because of the

use of IPA. Thus despite the low reflectance, due to pyramid structures, that is achieved with wet processes, they have several drawbacks. These processes cannot be performed just in the front wafer surface where required, since texture in the back surface reduces the quality of the dielectric rear surface passivation [108]. For large volume production in PV industry the relative high amount of chemicals and de-ionized water (DI), which are employed in wet processes, represent an important environmental and financial issue. Recently attention has been focused on dry texturing processes in order to obtain highly textured surfaces, without the use of photolithography steps, DI water, or chemicals. It is known that fluorine radicals easily etch silicon, and more over the addition of oxygen to fluorine enhances the plasma texturing [109]. In particular SF_6 and O_2 plasmas have been used for texturing silicon in a micro-wave (MW) reactor, obtaining reflectance values below 20%; however no details on the process parameters have been reported [110-112]. Reactive ion etching (RIE), which is a standard process in microelectronics industry, has been used for texturing c-Si, for solar cells fabricated by doping diffusion [113]. However the needle-like structures reported are not suitable for a reliable solar cell process. Thus, despite the efforts made so far on plasma texturing, to our knowledge, there are no reports in literature about obtaining of normal or inverted pyramids by a dry etching process until the work [114] was recently published. It reports important results on the study of texturing c-Si wafers using SF_6/O_2 plasma in a RIE system. They focused on the combined effects of the RF plasma power and the SF_6/O_2 ratio. They found that by varying the RF power with an optimized SF_6/O_2 ratio it is possible to produce normal or inverted pyramid-like structures, with very low reflectance values, as low as 6%. They also studied the evolution from normal to inverted pyramids by increasing the RF power. Texturing was performed using p-type c-Si (100), with resistivity s in the range of 14–22 Ω cm. For reliable texturing it was found that the gas ratio should be adjusted to 3 (SF_6/O_2=99sccm/33sccm). With an optimized gas ratio, the most interesting structures produced were obtained when the RF power was adjusted to 25, 50, 100, and 150 W. All the processes were performed for 15 min at a fixed pressure of 100 mTorr. Before each texturing process, an oxygen plasma was applied for 5 minutes. The addition of O_2 to SF_6 plays an important role on the plasma texturing process. It is believed that two opposite effects take place on the SF_6/O_2 plasma: an etching process due to fluorine radicals which are very efficient for etch silicon, and a deposition process due to residual SiO_xF_y radicals, which produce a masking effect [109]. Those micro-masks enhance the texturing of the c-Si surface. Experimentally, authors found that the SF_6/O_2 ratio determines the density of micro-masks, and a ratio equal to 3 improves the density of the structures produced on the c-Si wafers. On the other hand the RF plasma power determines the shape of the produced structures. By varying the RF power using an optimized gas ratio (SF_6/O_2=3), it is possible to produce very different structures such as pyramid-like or inverted pyramid-like structures. They found that the RF power has a critical effect on the c-Si texture. At low RF power the formation of normal pyramid-like structures is achieved, where texturing is governed by an anisotropic process, while at high RF power the inverted pyramid-like structures were obtained, where texturing is mainly governed by an isotropic ion assisted process. Normal pyramid-like structures in the c-Si surface resulted in an average reflectance around 18%, while inverted pyramid-like structures resulted in an average reflectance as low as 6%, without any anti-reflection coating. SEM images and reflectances of textured surfaces at different RF power are respectively reported in Figs. **48-50**.

The University of New South Wales has held the world record for silicon solar cell efficiencies for the last 15 years, initially with the Passivated Emitter solar cell (PESC) and more recently with the Passivated Emitter and Rear Locally diffused (PERL) solar cell. Despite the performance and achievements of these two technologies, neither has been used commercially, apart from for space cells, primarily due to the sophistication, cost and complexity of the processes involved. The photolithographic based processing is probably the main contributor to this. Recently the group has been developed inkjet printing techniques [115] for patterning low cost resist layers as a simple, much cheaper alternative to photolithographic based processing. Figs. **51** and **52** show images of the structures and reflectance results achieved with this new technology.

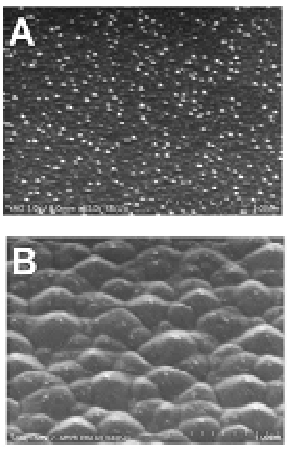


Figure 48: SEM images of textured c-Si surfaces, for different RF power: (A) P=25W; (B) 50W with SF_6/O_2=3 [114].

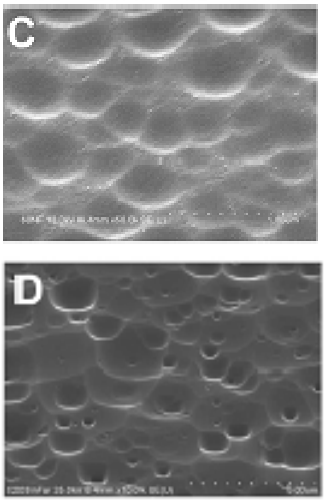


Figure 49: SEM images of textured c-Si surfaces, for different RF power: (C) 100W and (D) 150W with SF_6/O_2=3 [114].

These new approaches appear capable of achieving similar device performance levels but with the greatest challenge being to match the dimensions of features in the resist patterning achievable with photolithography. Test devices to date based on inkjet technology have achieved feature dimensions such as holes of 30-40 microns diameter. However, these dimensions need to be reduced to about 10 microns diameter to fully match the performance levels demonstrated with photolithographic based processing. New and innovative inkjet printing techniques have been recently developed for further reducing the resist patterning dimensions. This work is being greatly assisted by the recent availability of the new 1 picolitre inkjet heads. The described dielectric patterning capabilities *via* inkjet patterning can not only be used for defining localized diffusion regions and locations for metal contacts, but also for the formation of textured surfaces and light trapping schemes. Examples of the latter are shown below as well as corresponding reflectance curves.

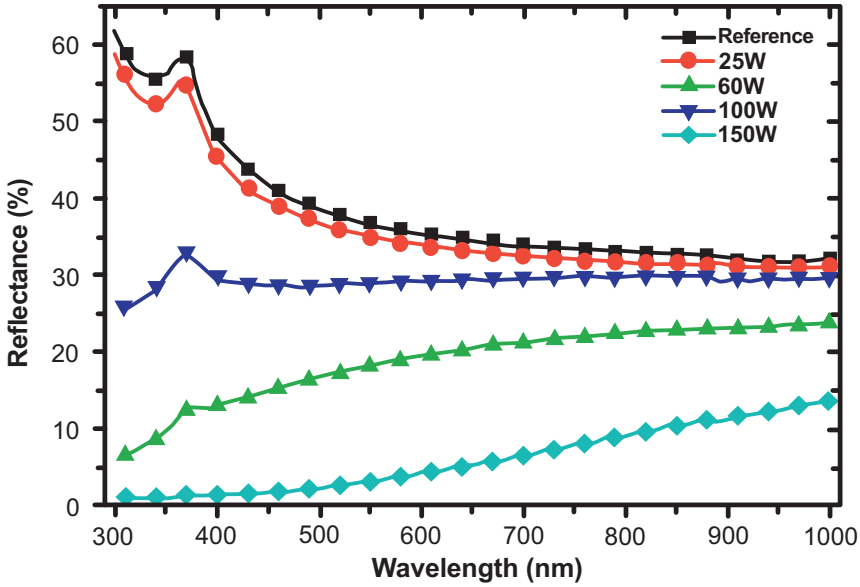


Figure 50: Reflectance of the textured c-Si surfaces without anti-reflection coating, when RF power is varied in 25, 50, 100 and 150 W, with SF_6/O_2=3. Also included as reference is the reflectance of a flat c-Si wafer, which was not exposed to plasma [114].

Commercial multicrystalline silicon cells have lower efficiencies than their single-crystal counterparts. One of the major performance limitations with the use of multicrystalline silicon is the inability to effectively texture the front surface, a process that is relatively straightforward in single-crystal cells. Anisotropic alkaline etching techniques, commonly used to texture monocrystalline wafers, are ineffective on the randomly oriented grains that make up a multicrystalline wafer. The random nature of the crystal orientation of multicrystalline silicon wafers makes such techniques much less effective for this material because only a handful of grains are properly orientated. It is therefore necessary to develop a texturing technique that will isotropically shape the front surface, regardless of crystallographic orientation. In addition, alkaline solutions can cause unwanted steps and crevasses between the grains. To be useful in the fabrication of solar cells, the texture must perform well both electrically and optically. There have

been many techniques proposed to texture multicrystalline silicon solar cells, masked and mask-less wet acidic texturing, masked and mask-less reactive ion etching, mechanical scribing and masked isotropic etching, laser texturing followed by wet etching, and the so called black silicon etching.

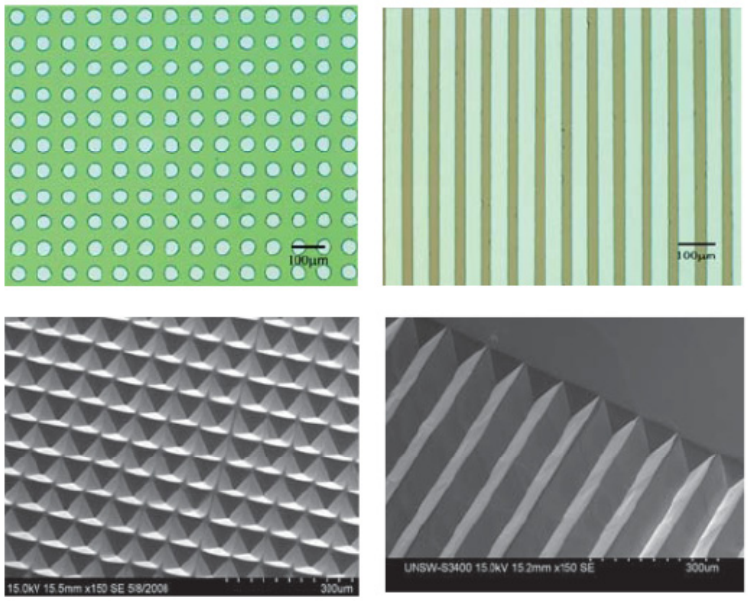


Figure 51: Top: optical Microscope photograph of ink jet patterned lines in a SiO_2 layer and bottom: Scanning Electron Microscope photograph of the inverted pyramids (left) and grooves (right) formed in the silicon surface following KOH etching of [115].

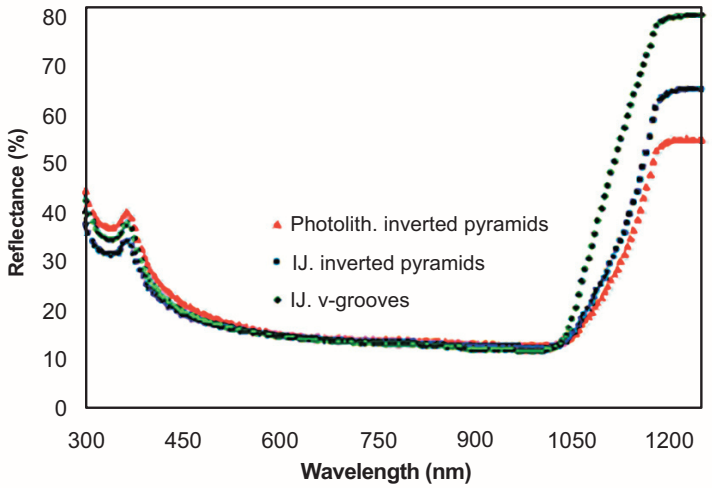


Figure 52: Reflectance of silicon wafers with different surface finish (i) inverted pyramids formed by photolithography, (ii) inverted pyramids patterned by ink jet printing and (iii) v-grooves patterned by ink jet printing [115].

4.2. Wet Acidic Texturing

Industrial multi-crystalline silicon solar cells are textured using a technique based on isotropic etching with acidic solutions [116, 117]. The acidic solution consists of a mixture of nitric acid, hydrofluoric acid and some additives. In the etching reaction of silicon, nitric acid acts as an oxidising agent, while the created silicon-oxides are removed from the surface by hydrofluoric acid. The additives reduce the initiation-time required to start the reaction, and ensure good wet ability, resulting in uniform surface etching. For example H_2SO_4, or $NaNO_2$ can be added to the etching solution, the role of the sulphuric acid is to stabilise the reaction, while by adding a tiny amount of $NaNO_2$ the reaction starts before and control the etch speed. The removal of saw damage from the wafer surface is part of the texture etching, thus it requires only one single short chemical step to create the surface texture, starting from as-cut wafers. Wet acidic texturing can result in features with rounded surfaces, as opposed to flat-sided features which arise from anisotropic etches [118]. These rounded features produce a scalloped surface that can have good antireflection properties. An important issue with this technique is that the feature growth needs to be 'seeded' in some way, otherwise a planar surface will result. This seeding can be provided by surface damage caused during wafer sawing (mask-less acidic etching), or, in more complex methods, by defined holes through protective layers such as oxides, nitrides or polymers (masked acidic etching). Such a technique does not provide the extremely low reflection of some other methods, but does have the advantages of being relatively easy to implement and low-cost.

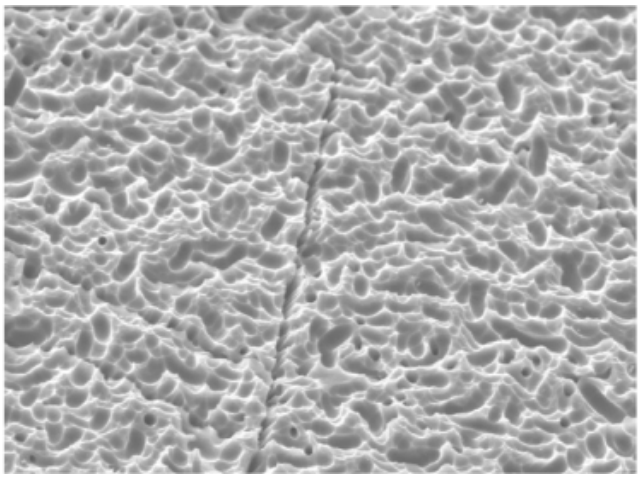


Figure 53: SEM photograph of an isotextured multi-crystalline silicon wafer [118].

On the other hand, this technique has some drawbacks such as making the substrates fragile (this can be avoid adding surfactants to the solution even though this increases the texturing process cost dramatically) and using a large amount of chemicals which is not good for the environment. During etching of silicon, the composition of the solution will change due to the ongoing chemical reaction: nitric acid and hydrofluoric acid are consumed while water is created, resulting in an expected decrease of the etch-rate. Furthermore, it should be noted that temperature-control during this exothermic reaction is desired as well, since a temperature rise drastically increases the etch-

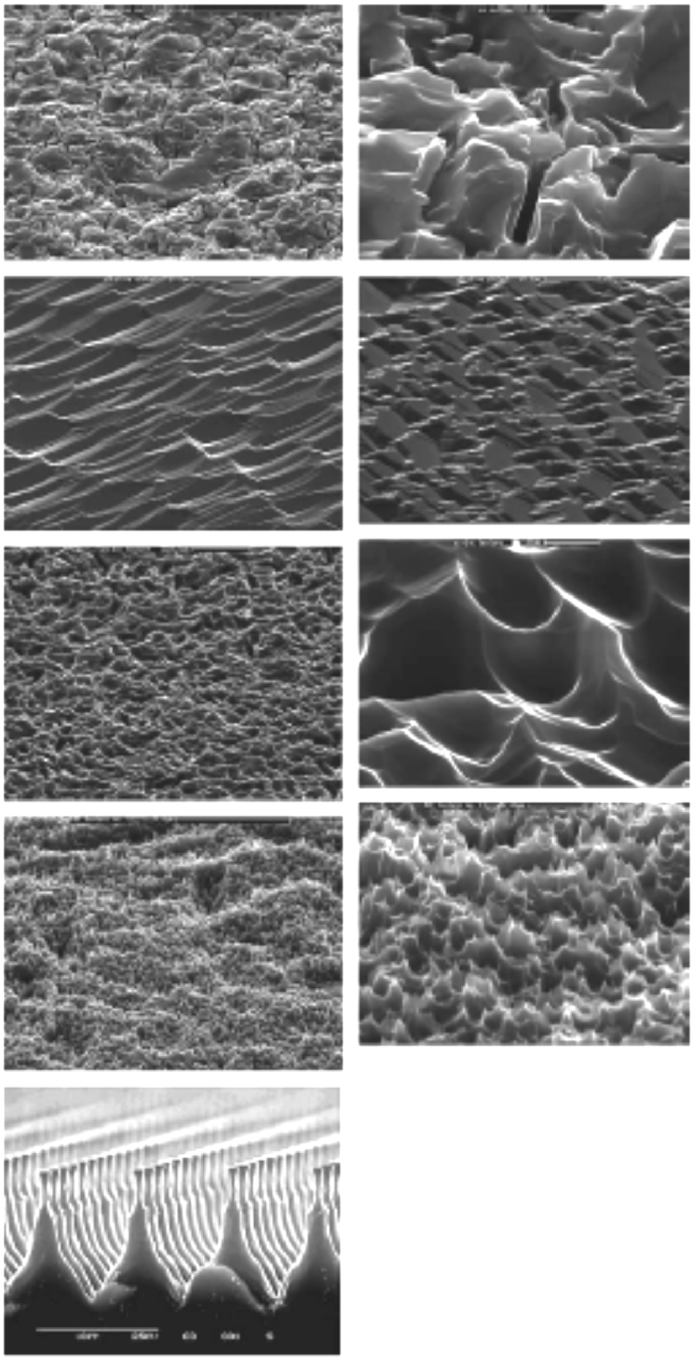


Figure 54: SEM images of various mc-Si surfaces with different magnifications. From top to bottom: as-cut (left 1000x·, right 5000x·), alkaline-etched (both 500x·, different grains), acidic textured (left 500x·, right 5000x·), maskless RIE textured (left 1000x·, right 5000x·) and masked RIE pyramids [122].

rate. Finally the isotexturing technique does not develop grain boundaries, but some dislocations are partially developed by increasing the etching rate (see Fig. **53**). For industrial application of the isotexturing technique some requirement need to be taken into account such as respecting the temperature-window in which the etching should take place by employing a temperature controlled etching bath and providing at regular intervals replenishments cycles to prevent depletion of the solution.

4.3. Plasma Texturing

Reactive ion etching (RIE) is a method for 'dry' etching of silicon without the use of large quantities of liquid solutions. It is based on placing wafers in a plasma of highly reactive ions. Under certain conditions, the etching dynamics produce deep surface features that have excellent antireflection properties. Like wet acidic etching, RIE can be performed in a mask-less fashion that produces somewhat randomly placed features, or in conjunction with a masking layer to produce more even features. Masked RIE texturing was created by etching through photo-lithographically defined holes in a metal layer which is subsequently removed [119]. The mask-less RIE texturing was performed at Sandia laboratories in the USA using a proprietary 'metal-assisted' process [120, 121]. Both of these techniques offer promise for very low reflectance surfaces with minimal chemical waste, an issue that will become increasingly important in the photovoltaic industry. However, they are likely to be more costly to implement than wet chemical methods.

Fig. **54** shows scanning electron micrographs (SEMs) of multi-crystalline silicon wafers with various surfaces. In the as-cut wafer (top two images), the heavy surface damage is evident as deep fissures and cracks, resulting in reasonable reflection control but high recombination. The next two images are of a standard industrial alkaline-etched wafer. It appears to have some texturing, but this is both shallow and highly grain-dependent, and when averaged over many grains is almost as reflective as a perfectly flat wafer. The following two images are of an acidic textured wafer, which was performed with a HF/HNO_3 solution. A wetting agent was added to produce more uniform texturing. Approximately 5–10 μm of silicon was removed from each surface. Although the surface damage is removed, its original presence is nevertheless critical, since it acts as a seeding layer for the texturing. The resulting surface contains smooth sided, bowl-like features. Fig. **54** also shows images of the mask-less RIE texturing performed at Sandia. These wafers have somewhat randomly placed but nevertheless deep features with steep sides, which provide very low reflection. Note that the features of these RIE textured wafers are much smaller than those of the acidic textured sample (the two images on the right have the same magnification, 5000·). Finally, a masked RIE textured wafer is also shown at the bottom Fig. **54**. These features are very regular and steep-sided, with a distance of 7 μm between pyramid peaks. The pyramids are approximately the same size as the features on the wet acidic textured wafer. Fig. **55** shows the results of reflectance measurements on the three types of textured wafers, plus alkaline etched and as-cut samples.

While the results of the bare wafers give a good indication of the effectiveness of the various texturing methods, in a real cell the surface will have an encapsulated antireflection coating (ARC), which will further change the overall reflection properties. Therefore, we have measured the reflectance of the textured surfaces coated with a plasma-enhanced chemical vapour deposited (PECVD) SiN_xfilm, both before and after encapsulation. A major advantage of PECVD SiN_xfilms

is that they also electronically passivate the surface, leading to reduced recombination losses. Hence there are two separate issues to consider here: firstly, the optical properties of the SiN_xcoated textured surfaces, and secondly, how well the SiN_x film passivates the textured surfaces. The quality of the surface passivation is revealed by lifetime measurements, which are presented in the next section. Firstly though, we present reflectance results on SiN_x coated wafers. The results for the un-encapsulated wafers show that the difference between the various textures

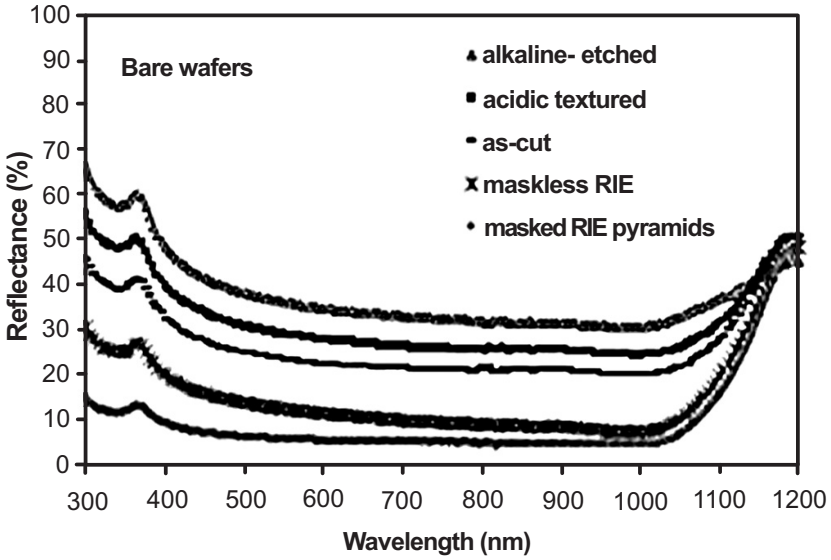


Figure 55: Reflectance measurements of bare alkaline-etched, as-cut acidic textured, masked RIE and mask-less RIE textured multi-crystalline silicon wafers [122].

and the alkaline etched surface has been reduced. Initially, this appears to diminish the relative benefit of the texturing processes. However, this does not accurately represent the real case of a finished solar cell inside a module. When encapsulated under glass, and with a rear reflector in place, the samples with more textured surfaces will have relatively improved reflectance values due to light-trapping. These encapsulated measurements were taken with a 90% reflective mirror behind the wafer. This reasonably closely simulates the case in a finished cell which has a rear reflectivity of about 70% due to the Al back surface field. At wavelengths greater than 1000 nm, the benefits of light-trapping in the textured wafers as opposed to the alkaline-etched sample are clear. The RIE textured wafer in particular exhibits good light-trapping. The reflectivity curves shown in the previous figures cannot be interpreted in this way, since no mirror at the rear was used, and there was no planar glass surface at the front. We found that the reduction in reflection in the UV region after encapsulation is caused by absorption within the encapsulating material. The results certainly show that both the mask-less RIE and wet acidic texturing methods give a significant reduction in reflectance in comparison to the alkaline-etched wafer after encapsulation. Comparable results for the masked RIE process were not available, but it is reasonable to assume that they would be lower even that the mask-less RIE value of 7.6%. One important observation is that the difference between the acidic and RIE process has been further reduced after encapsulation. In comparison to the alkaline-etched wafer, the acidic wafer gives a 3.7% reduction

in reflectance, while the mask-less RIE wafer yields a gain of 5.3%. It may be that the extra cost of RIE processes is warranted by this extra gain. All three texturing methods examined, wet acidic texturing, and masked and mask-less RIE texturing, significantly reduce reflection losses in solar cells. The reduction in reflection is greatest for masked RIE pyramids, followed by mask-less RIE, and then acidic texturing and this is likely to also be the order of greatest improvement in cell performance. However, the relative difference between the methods is substantially reduced after antireflection coating and encapsulation. Also, the cost of implementation is likely to be substantially less for acidic texturing then for either RIE process, especially masked RIE.

4.4. Laser Texturing

Laser ablation is an isotropic process that will sculpt the surface of a silicon wafer, regardless of its crystallographic orientation. When combined with isotropic etching techniques, the process is able to effectively texture the silicon surface. The technique of using a laser to texture multicrystalline silicon solar cells was first published by Zolper *et al.* [123]. Initial attempts employed overlapping grooves to create an approximation of an upright pyramid texture. This provided a reduction in reflection, a boost in current and a decrease in open-circuit voltage and fill factor. It was concluded that the technique was limited by excessively deep grooves at cross-over points and dislocations penetrating the junction region. It was speculated that these dislocations may have been caused either by laser damage of the front surface or generated during the oxidation occurring after re-crystallization process of the non-planar front surface. It was suggested that future work be done to develop a better post-scribe etching technique to remove the laser damage and further smooth the surface to reduce the oxidation-induced stress. A modified technique for the laser scribing was suggested that would incorporate the use of a matrix of individual laser-ablated pits, thereby removing the overlapping sections. A work of the UNSW group [124] demonstrates that laser texture is as good as the upright random pyramid technique and that the laser can be used to texture silicon solar cells and concludes that, if this process could be performed economically, it would be of benefit to the solar cell. Texture features are formed in a two-step process. The surface of the silicon is first sculpted by laser ablation, which removes the bulk of the silicon required for texturing. The laser ablation is performed using a Q-switched, Nd:YAG laser at a wavelength of 1064 nm. Pulse triggering is synchronized with the position of the sample stage, allowing the texture spacing to be easily controlled, regardless of the stage speed. A nitrogen shield gas protects the laser optics and removes some of the slag from the ablation pits. The ablated pits are arranged in the interlocking pattern shown in Fig. **57** by scanning the laser across the silicon surface. Next, the surface is chemically etched to remove the slag, smooth the surface and etch away any residual laser damage. The etching is performed in two stages. Initially a low-temperature, high-concentration NaOH etch is used to clear away surface slag blocking the holes. This is followed by an isotropic etch consisting of nitric, acetic and hydrofluoric acid that removes remaining slag from the holes and the layer of laser damaged silicon. The etching process is illustrated in Figs. **56-58**.

The optimum laser parameters were determined experimentally by creating textures with different laser settings and the optimal process parameters are illustrated in the reference [124]. Textures on high lifetime wafers were surface passivated with a phosphorus diffusion and dry thermal oxidation, then measured using the generalised photoconductance decay technique. This provided information on the effect the texture may have on the electrical properties of the cell. The carrier lifetime and implied open-circuit voltage after texturing are higher than 3 ms and 690 mV respectively, indicating the efficiency potential of laser textured surfaces for multi-crystalline silicon wafers.

4.5. Honeycomb Texturing

Record performance multicrystalline silicon cells have in the past benefited from photo-lithographically defined "honeycomb" texturing using an acidic isotropic etch. Such structures have also been demonstrated recently using inkjet technology as shown in Fig. **59**. Such techniques appear to have significant commercial appeal.

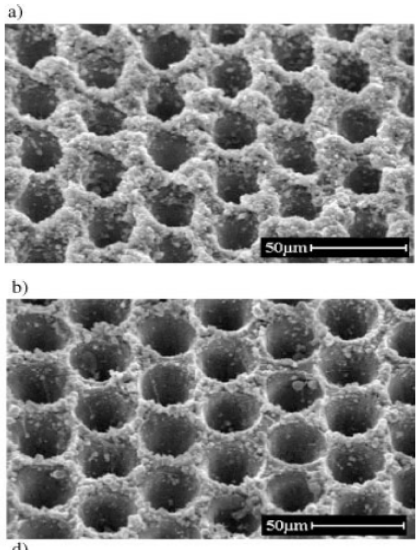


Figure 56: SEM Images of laser texture fabrication: (a) immediately after ablation; (b) after NaOH etch [124].

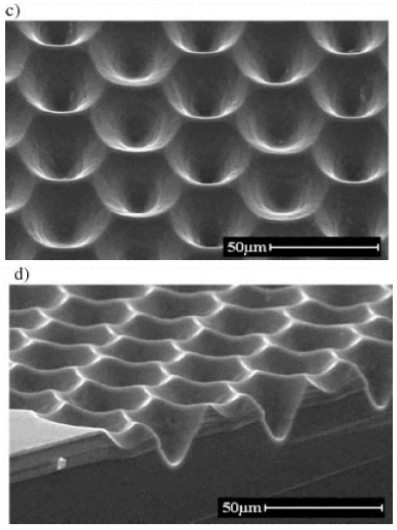


Figure 57: SEM Images of laser texture fabrication: (c) finished texture after isotropic etch; (d) cross-section of finished texture viewed at an angle [124].

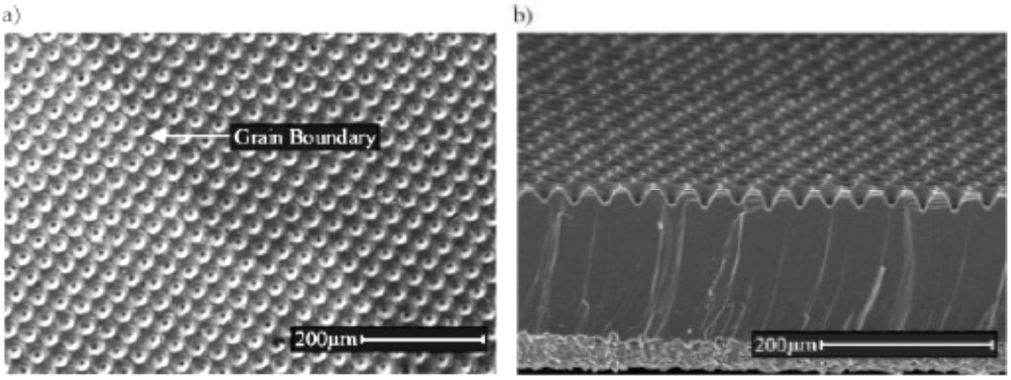


Figure 58: Laser texture on multi-crystalline wafers: (a) FIB image of surface; (b) SEM image of cross-section on an angle [124].

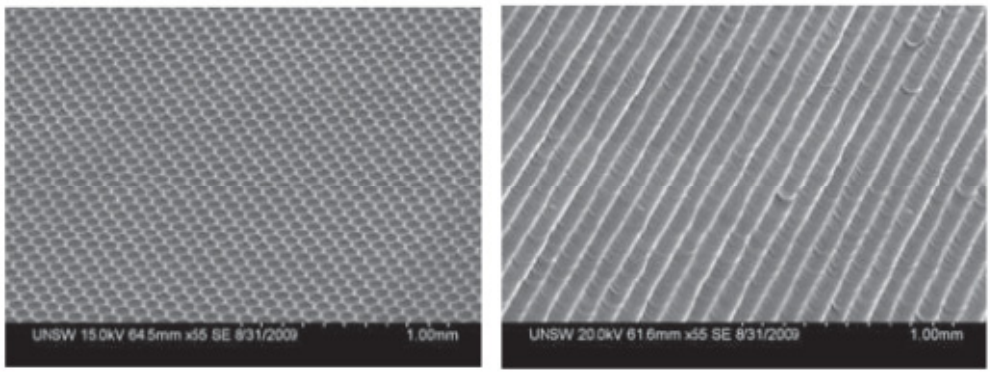


Figure 59: Honeycomb texturing (left) and macro-groove texturing (right) of multi-crystalline silicon wafers through the use of inkjet technology. Direct Etching Via Aerosol Jetting [115].

4.6. Black Si Etching

An appealing approach to minimize reflectivity utilizes a fine surface texture, comprising features on the nano-meter scale. Stephens and Cody [125] have proposed a model assuming that a textured surface with features smaller than the wavelength of light is an effective medium with gradually varying optical constants. The model predicts that the reflectivity of such a boundary layer is vanishing for wavelengths below a cut-off threshold, which depends on the complex refractive index of the bulk material as well as on the density profile and depth of the textured layer. Accordingly, the reflectivity cut-off for textured silicon surfaces with a linearly increasing density should appear at a wavelength four to six times larger than the depth of the textured layer, *i.e.*, a fine texture of only 200–300 nm in depth should be enough to suppress the reflectivity of a Si surface in the whole usable spectral range of photon energies above the band gap. These predictions have been confirmed experimentally *via* the preparation of randomly textured Si surfaces with nano-scale features by sputtering etching [126]. Similar techniques based on reactive ion etching RIE have been developed recently, employing selective etching through discontinuous SiO_2 micro-masks [127] or utilizing the catalytic action of various metals during the ion etch

process [128]. However, the ion damage associated with RIE, difficulties with obtaining a uniform texturing on area above 100 cm^2, and the complexity of the plasma processes involved are of concern regarding a large scale solar cell production. In 2006 Svetoslav Koynov *et al.* [129] presented a method for nano-scale texturing of silicon surfaces, which utilizes simple wet chemical etching, facilitated by the presence of small metal clusters. Three kinds of silicon samples were used to demonstrate the universality of the method with respect to surface structure and doping: n type single crystalline Si p type multi-crystalline Si, and thin films of intrinsic hydrogenated amorphous silicon (a-Si:H). They demonstrated that the optical losses due to surface reflection can be reduced to below 5% throughout the entire usable spectrum, from 350 to 1000 nm wavelength for crystalline Si. The samples are first cleaned in acetone and isopropyl alcohol, followed by a HF dip to remove the natural oxide from the surface. The texturing process, referred to as "black etch" in the following, is performed in three steps.

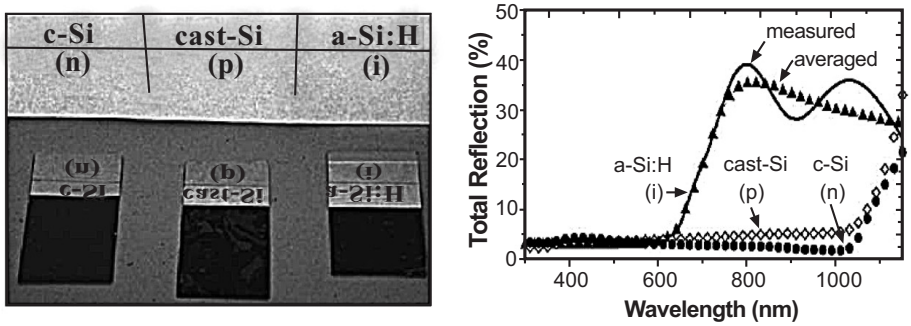
i. A tiny amount of metal is deposited in the form of nano-clusters onto the flat Si surface. The composition and structure of this initial coating determine the texture and optical properties obtained. A typical treatment starts from Au layers with a nominal thickness of 1–2 nm, deposited by thermal evaporation at a pressure of 10^{-5}–10^{-6} mbar. Such layers are discontinuous, comprising clustered grains of several manometer sizes with about 20%–40% of exposed Si surface between them. For other nominal layer thicknesses, no pronounced suppression of reflectivity has been achieved.

ii. A wet chemical etching of the Si substrate is performed as the second step of the texturing process. The etching is carried out at room temperature in an aqueous solution of hydrofluoric acid and hydrogen peroxide with volume ratio HF50%:$H_2O_2$30%:H_2O = 1:5:10. This solution etches clean Si surfaces very slowly etch rate below 1 nm/min, preserving the surface polish and not changing the reflectivity. An exception is heavily doped p-type Si, on which the formation of a thin porous silicon layer was observed. In contrast, dramatic modifications of the optical properties occur if the Si substrates are partially covered by Au clusters according to i. The duration of this etching step can be conveniently controlled visually, as an initially polished Si surface turns completely black within 50–90 s only.

iii. Finally, the remaining Au is removed from the textured Si surface by room temperature etching in aqueous solution of iodine and potassium iodide 25 g I and 100 g KI per 1liter H_2O.

Fig. **60** illustrates the ability of the black etch treatment to produce the desired optical antireflection properties on different silicon surfaces. Three silicon samples with different morphologies crystalline, multi-crystalline, and amorphous and doping n type, p type, and intrinsic are shown. Initially, all three samples had polished or smooth surfaces. The major part of each sample surface bottom parts in Fig. **60(a)** has been modified, while the rest remained untreated for direct comparison. The treated areas of all samples appear similarly black, even under non-normal incidence. Small differences in the reflectivity of the crystallites in the cast-Si sample are visible after treatment, indicating a slight variation in the textures obtained. In distinct contrast, all

untreated areas have a high reflectivity, as seen by the mirror images of the labels above them. The spectra in Fig. **60(b)** quantify the similar, uniformly suppressed reflectivity of as little as 2%–5% in the high absorption ranges of all three samples.The amount of absorbed light is significantly increased after the surface treatment. The increase at wavelengths below the absorption edge obviously originates from the suppressed reflection.



(a) (b)

Figure 60: (a) Photograph of black etched Si samples of different crystal structure and doping. "c-Si n" denotes a bulk single crystalline silicon sample with(100) orientation, n-type doping, and 2.5 Ω cm resistivity; "cast-Si p" a bulk multi-crystalline silicon, p-doped sample also with 2.5 Ω cm resistivity; and "a-Si:H i" a nominally un-doped thin film of amorphous hydrogenated a-Si:H on a glass substrate, with a thickness of 500 nm. For comparison with the initial surfaces, the upper part of each sample is left untreated. (b) Total hemispherical reflection spectra of the treated areas of the samples from a. The data for a-Si:H are shown as measured and after removal of the interference fringes [129].

5. REAR SIDE REFLECTOR

The rear side reflectance inward the absorber layer is very relevant to enhance the cell absorption and then the efficiency. High reflection of the rear cell surface reduces absorption in the rear cell contacts or transmission from the rear, allowing the light to bounce back into the cell for possible absorption. Randomising the direction of light allows much of the reflected light to be totally internally reflected. Light reaching the top surface at an angle greater than the critical angle for total internal reflection is reflected again towards the back surface. Light absorption can be considerably increased in this way, since the pathlength of the incident light can be enhanced by a factor up to $4n^2$ where n is the index of refraction for the semiconductor [130, 131]. This allows an optical path length of approximately 50 times the physical devices thickness even if a more realistic value of 10 is achievable [132]. This allows the use of thinner absorption layer and then, in case of c-Si wafer, PV cost reduction that is strongly related to the cost of silicon of course. Light impinging with angle less than the critical angle escapes the cell, but light having incident angle greater than the critical angle is totally internally reflected inside the cell. From the rear reflection point of view, the Lambertian reflector is the theoretically preferred scheme to enhance the internal light absorption as depicted in Fig. **61**.

Even with textured rear side surface, part of the light impinging the rear contact can be absorbed by the metal. With the aid of optical simulation software (XOP [133]) it is possible to evaluate the optical properties of different back reflecting scheme of the solar cell. Most of the actual rear side

contacts on p-type c-Si wafer are formed using single metal, such as Al in case of, or passivating coating, such as SiO_2 or SiNx followed by Al metal [131, 134, 135], in case of point contacts [136], or a-Si.H-ZnO/Al [137].

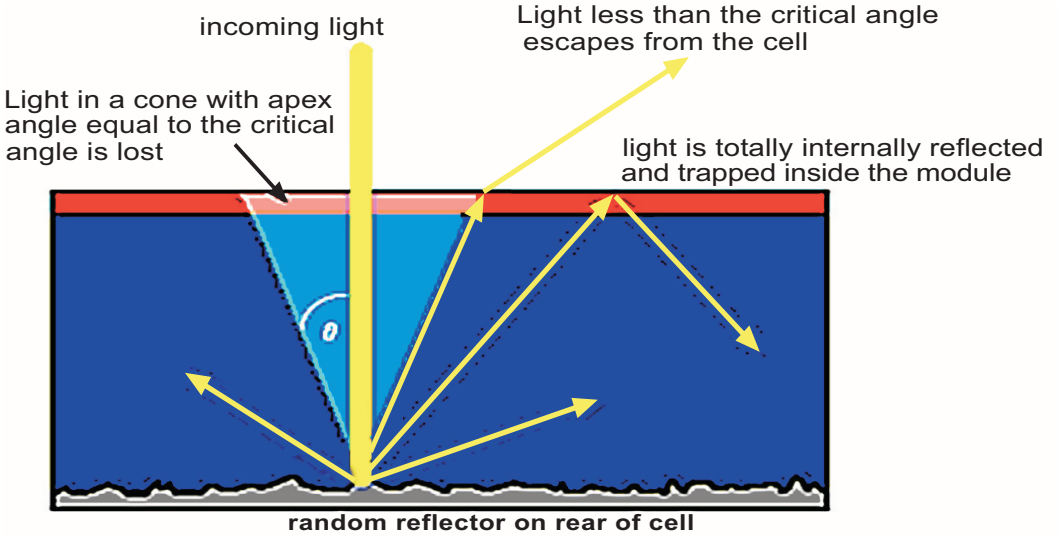


Figure 61: Randomize reflected rear side surface able to form a Lambertian reflector.

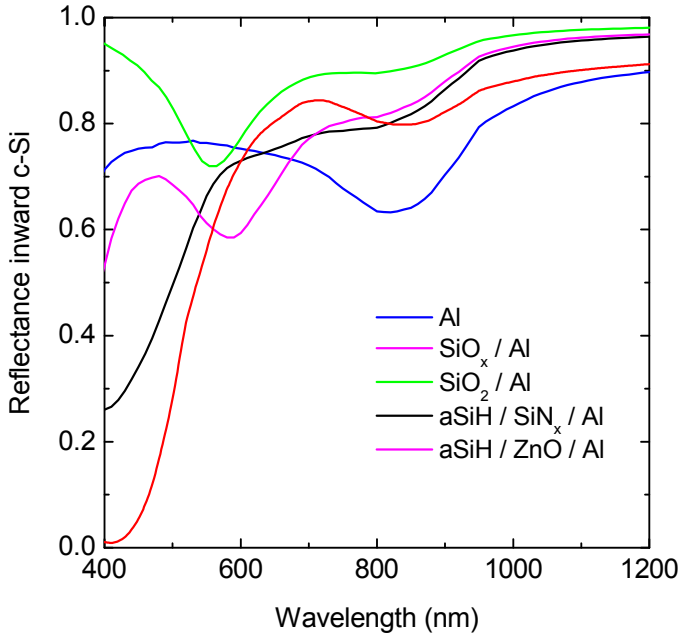


Figure 62: Reflectance inward the c-Si bulk for different kind of rear c-Si surface coating as simulated using XOP software.

A comparison of reflectances inward the c-Si bulk of the solar cell due to different kind of rear surface coatings are reported in Fig. **62**. As evident, the Al reflector shows a pronounced reduction of reflectance in the near infrared spectrum. Other schemes using passivating layers show less absorption. In the simulations reported in Fig. **64** the optimum thicknesses values for the thin films to ensure the maximum inner reflectances have been assumed.

5.1. Bragg Reflector

To enhance the reflectance (R) inward the Si substrate from the rear side of the cell it is possible to form a Dielectric Bragg Reflector (DBR) instead of the commonly adopted full Al contact. A DBR can be fabricated using a multilayer-stack of alternate high-and low-index films. Referring to our experiment, those films are respectively a-Si:H and SiNx and their thickness (t) can be dimensioned as one quarter wavelength thick: $t = \lambda /(4\ n)$ taking into account the refractive index (n) of a-Si:H and SiNx and the centre wavelength of the DBR (λ_0). Introducing the DBR in the rear side of our cell its scheme can be fabricated referring to Fig. **63**, in which a cross section scheme of the device is depicted.

Keeping in mind this structure we can evaluate the reflectance $R(\lambda)$ toward the Si substrate as [138]:

$$R(\lambda)=\left[\frac{n_{Si}\left(n_{a-Si:H}\right)^{2\#}-n_{Al}\left(n_{SiNx}\right)^{2\#}}{n_{Si}\left(n_{a-Si:H}\right)^{2\#}+n_{Al}\left(n_{SiNx}\right)^{2\#}}\right]^2 \quad \textbf{(19)}$$

where n_{Si}, $n_{a\text{-}Si:H}$, n_{SiNx}, n_{Al} are the refractive indexes of the materials respectively. # is the number of couples a-Si:H/SiNx.The bandwidth $\Delta\lambda$ of the photonic stopband can be calculated by:

$$\Delta\lambda=\frac{4\lambda_0}{\pi}\cdot\arcsin\left(\frac{n_{a\text{-}Si:H}-n_{SiNx}}{n_{a\text{-}Si:H}+n_{SiNx}}\right) \quad \textbf{(20)}$$

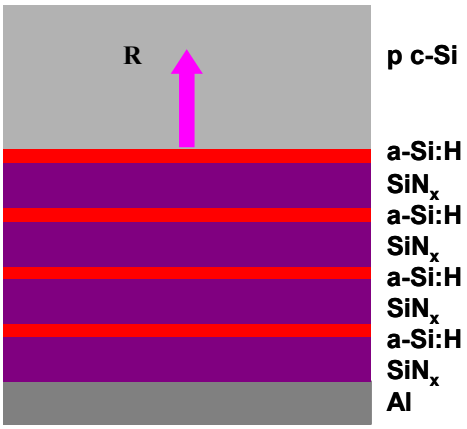


Figure 63: Schematic Cross section view, not in scale, of the cell with DBR.

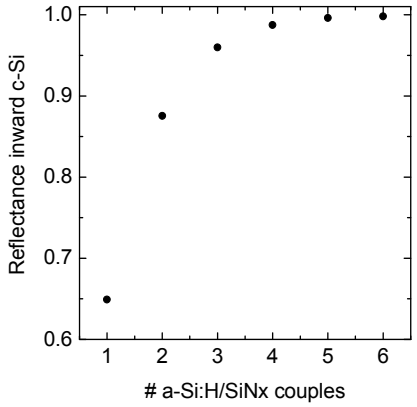


Figure 64: Reflectance at 1050 nm inward the c-Si bulk as a function of a-Si:H/SiNx couples number in DBR [17].

To obtain high reflection in the infrared region of the sun spectrum,1050 nm as the DBR centre wavelength can be chosen. At that wavelength the thicknesses of a-Si:H and SiNx films become 66 nm and 130 nm respectively, taking into account their refractive index as 3.65 and 2.01 respectively.

The higher the a-Si:H/SiNx couples number, the higher the mirror reflectance, as reported in Fig. **64** where the inward Silicon wafer reflectance, as expressed by equation (10), is exploited. As evident from this figure, four couples of a-Si:H/SiNx can be considered sufficient to obtain a reflection higher than 95%. A comparison of reflectances spectrum, in the range between 400 nm and 1200 nm, inward the c-Si bulk of the solar cell due to different number of a-Si:H/SiN_x couples forming the DBR is reported in Fig. **65**.

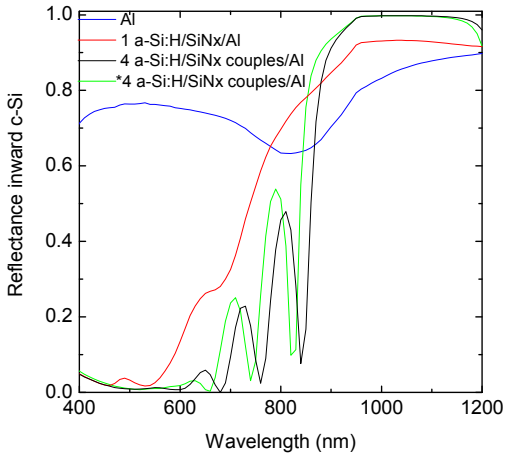


Figure 65: XOP numerical simulations of reflectance inward the c-Si bulk for single couple aSiH/SiNx/Al, 4 couples aSiH/SiNx/Al and 4 couples aSiH/SiNx/Al after fitting procedure of experimental data [17].

The four couple of DBR/Al shows higher reflectance values in the same spectral region with respect to single couple of a-Si:H/SiN_x/Al as well as simple Al contact used as reference.

To verify the presence and the consistence of the DBR structure after its growth on the rear side of c-Si wafer, we have measured the reflectance profile from the rear side of this multilayer before the SOD and Al deposition. To extract information from this measurement we have optically modelled our structure using XOP software [133] taking into account the sequence, the refractive index and the expected thicknesses of each layer in our stack over a c-Si substrate. We have fitted the reflectance experimental data using those thicknesses as free parameters as reported in Fig. **66**. From the good agreement between experimental data and simulation we have found several differences between the expected and the evaluated thicknesses of each layer in the DBR, as reported in Table **4**. Even if the deposition time has been set equal for each kind of film at the beginning of the PECVD process, an unpredictable enhancement of SiN_x growth rate occurs increasing the number of subsequent depositions. On the contrary the a-Si:H growth rate seems to be underestimated from the beginning of the process.

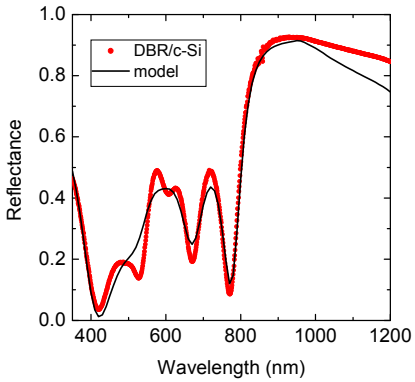


Figure 66: Experimental (symbols) and optical model of reflectance collected from the rear side of the DBR deposited onto a c-Si wafer [17].

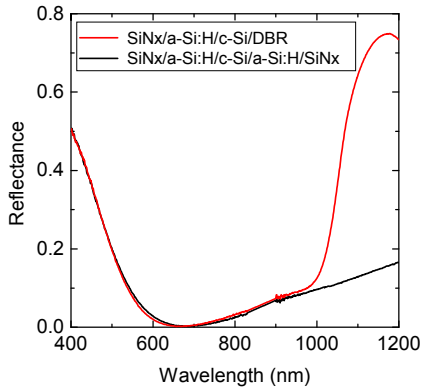


Figure 67: Effect of DBR on the reflectance in the infrared region of the impinging light spectrum [17].

Table 4: Comparison of expected and evaluated thicknesses of each layer inside the DBR.

Layer	Expected Thickness (nm)	Evaluated Thickness (nm)
SiNx	130	157
a-Si:H	66	58
SiNx	130	151
a-Si:H	66	56
SiNx	130	147
a-Si:H	66	60
SiNx	130	130
a-Si:H	66	60

Taking into account the evaluated thickness data we have calculated a new reflectance profile of the DBR inward the c:Si bulk, as reported in Fig. **65** as green line. Comparing the two curves of expected DBR and fabricated DBR* we can remark that even if the multi-layer deposited shows different thicknesses with respect to the expected one, only an helpful left shift of the reflectance curve occurs. This effect confirms that the DBR can be easily formed despite to its complexity.

To have a better vision of the DBR effect on rear side of the solar cell structure, a comparison of the front side reflectance of the two different structures: ARC/c-Si/DBR and ARC/c-Si is reported in Fig. **67**. From the reflectance in the near infrared region of the front side impinging spectrum the mirror effect imposed by the DBR is evident if compared with the a-Si:H/SiNx surface coating layer. Mirror like surface of the silicon wafer is used to remark the effectiveness of the DBR. The wafer front side is covered by SiNx thin film working as sunlight antireflection coating.

5.2. Bragg a-Si:H/c-Si Solar Cell

As an example of the reflector efficiency in solar cell, we have applied the DBR as a back side mirror in a-Si:H/c-Si heterojunction solar cell. The success of a-Si:H/c-Si hetero-structure has been first demonstrated by SANYO ltd, which have reported efficiency above 20% with very high open circuit voltage (V_{oc} = 746 mV) [139] on heterojunction solar cells based on n-type Czochralski silicon. In particular the good performances of this kind of cell relies on the introduction of a thin intrinsic buffer layer between the n-type a-Si:H layer and the c-Si absorber for the improvement of interface properties. a-Si:H/c-Si heterostructure solar cells have been also fabricated on commercial p-type substrates and on multicrystalline silicon (mc-Si) achieving 17% and 15% efficiency respectively [140, 141]. However heterostructure itself is not enough to ensure good performances on thin wafers. Indeed also back surface passivation and Back Surface Field (BSF) play a fundamental role in enhancing open circuit voltage. It has already been demonstrated the feasibility of BSF on n-type c-Si based a-Si:H/c-Si heterostructure using the n-c-Si/i-a-Si:H/n-a-Si:H/ITO structure [139]. Several difficulties, instead, occur in the p-c-Si/i-a-Si:H/p-a-Si:H/structure in the formation of the rear contact, due to a band offset in valence band between amorphous and crystalline materials. The band bending distribution of heterojunction rear contact formed on p-type heterojunction contact is reported in Fig. **68** in dark and short circuit conditions. The simulation, made using a finite difference numerical simulator [140] has been performed taking into account the energy band gaps E_{gaSiH} = 1.72eV, E_{gcSi} = 1.12eV the electron affinities

χ_{aSiH} = 3.9eV, χ_{cSi} = 4.05eV, the activation energies E_{att}= 0.2 eV of p-type 1 Ωcm c-Si, the lowest E_{att} that doped a-Si:H films can assume [141] of 3.4 eV and the density of states (DoS) within each layer (lower than $10^{17}cm^{-3}$). An intrinsic buffer layer has been introduced between the a-Si:H and c-Si doped materials in order to reduce defect density and thus the recombination at the interface [139].

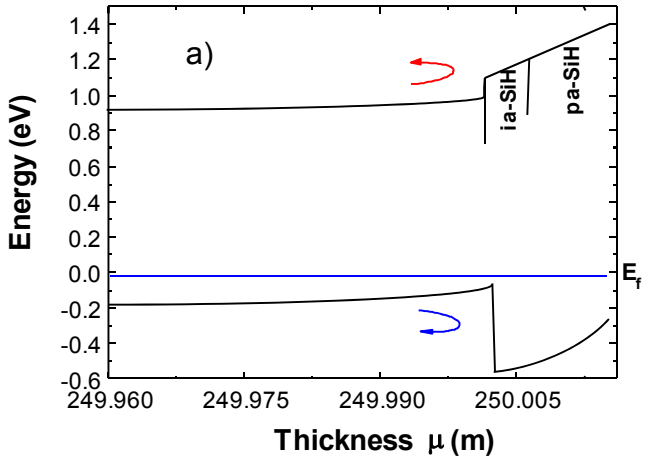


Figure 68: Band bending simulations in dark and 0V conditions of the p-type-c-Si/i-a-Si:H/p-aSi:H heterostructure.

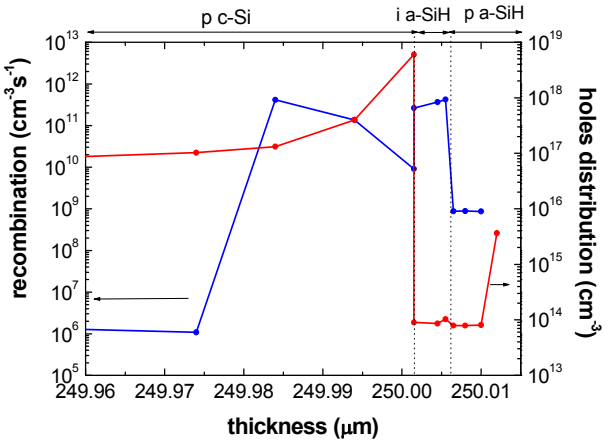


Figure 69: Holes and recombination distributions at the hetero-junction simulated at 0.65 V in dark condition.

As evident from the band diagrams, the pronounced valence band offset is a critical point for holes flowing toward the metal electrode. In the simulations the carrier collection at the amorphous silicon edge has been supposed not influenced by the metal electrode workfunction. Indeed any depletion within amorphous layer can be neglected due to the high defect density at the metal/a-Si:H interface. This unwanted effect is mainly due to the valence band offset at the edge of the c-

Si wafer that forms a barrier against the carrier collection from the metal electrode as can be deduced from Fig. **69**. In this figure the hole distribution along heterojunction p c-Si/i a-SiH/p a-Si:H at the cell rear side, simulated at 0.65 V in case of 5 nm and 10 nm of intrinsic buffer and doped p-type a-Si:H thicknesses respectively, strongly drops at the edge of the a-Si:H/c-Si heterojunction due to recombination, as reported in the same figure. As reported in literature, this problem can be overcome with a low temperature BSF formation process, which requires a back surface passivation, obtained depositing a-Si:H/SiN_x stacked layers. Then a Nd:YAG pulsed laser treatment, used to promote a local and simultaneous Al & B diffusion through the passivation layers [142], allowed to achieve V_{oc} higher than 630 mV [143, 144] on substrates having thicknesses in the order of 250-300 μm. The efficacy of this approach is also exploited in [145, 146].

Even though hetero-structure solar cells coupled with laser promoted BSF give the possibility to get a full low temperature process suitable to obtain high efficiency thin wafer solar cells, their performances can be still enhanced because the near infrared components of the sun spectrum is not completely absorbed in a thin wafers. This enhancement can be obtained using a mirror on the back side of the solar cell. Indeed merging a perfect dielectric mirror with an ohmic semiconductor metal contact on the rear side of a cell means to adopt a particular scheme in which the rear area of the cell would be divided in two regions where both mirror and contact would coexist. Different kind of point contact technologies have been reported in literature [147]. Even though some of them resulted in highest efficiency solar cells, often they adopt several technology steps merged from microelectronic, such as photolithography, that are not easy to transfer to mass production. A very promising technology, able to form effective metal contact on semiconductor material through dielectric film, is represented by Laser firing contact technology developed in the last few years [146]. Moreover different kinds of surface passivation layers have been reported in literature such as SiNx and/or SiOx [148] on which the laser process can be applied.

a-Si:H/SiN_x DBR and single couple of a-Si:H/SiN_x structures have been compared as back side mirror of identical hetero-structure solar cells fabricated on 250 μm thick FZ monocrystalline 0.5 Ω cm p-type wafers with one side polished. After RCA standard cleaning procedure and 1% HF bath, the front cell emitter has been deposited in a Plasma Enhanced Chemical Vapor Deposition (PECVD) system as an intrinsic-type a-Si:H/n-type a-Si:H stacked structure. Then a 30 nm thick chromium layer has been evaporated on the top of the heterostructure and subsequently wet removed to form a high conductive CrSi layer [141]. The four couples of the a-Si:H/SiN_x structure of the DBR has been formed on the rear side of the wafer after a 1% HF bath. The PECVD parameters of the emitter and of the DBR structure, together with the estimated thicknesses, are reported in Table **5**. Each material couple of the DBR has been deposited without interruption of the glow discharge process in order to reduce the stress at the a-Si:H/SiN_x interface. Between two subsequent couple depositions, a N_2 purge and adequate vacuum conditions have been recovered to avoid ammonia residua during the a-Si:H layer depositions.

Then the front side of the cell has been completed by an ITO layer, deposited in a sputtering system at 150 °C, 200 W RF power using 25 sccm of Ar. Its final thickness has been fixed at 65 nm, which is also ideal for antireflection purpose. After a Filmtronics B200 Boron spin-on dopant (SOD), spinned at 2000 round/min for 30 sec on the DBR, has been deposited and cured at 250 °C for 15 min. The SOD annealing temperature has been chosen as the one sufficient to hard the SOD avoiding at the

same time boron contaminations in the underneath amorphous layers. Subsequently a 2 μm thick Al layer has been e-beam evaporated on the whole rear surface of the mirror. To form the rear side contact of the solar cells a laser treatment has been locally performed by a Q-Switched Nd-YAG pulsed laser working at 1064 nm of wavelength in TEM_{00} mode with power 320 mW, pulse burst of 100 ms at 1kHz repetition rate, in order to induce a simultaneous diffusion of Al and B inside the silicon wafer, through the amorphous multilayer [144]. The front contact of the cell is ensured by a silver grid deposited by screen printing of low temperature sintering DuPont Ag paste. The paste has been then dried and simultaneously sintered at 200 °C for 10 minutes in a conventional IR dryer belt furnace. Finally the cell area has been limited to 4 cm^2 cutting the wafer with a dicing machine. An identical procedure has been followed for the fabrication of solar cells having only one couple of a-Si:H/SiN_x in the rear side. In particular the a-Si:H/SiN_x mirror has been deposited with the same parameters reported in Table **5** for the four couples of the DBR structure. To evaluate the efficacy of both the mirror and the Back Surface Field we have characterized the heterostructure solar cells measuring the Internal and External Quantum Efficiency (IQE, EQE) as well as the Reflectance profiles as a function of wavelength. Results are reported as symbols in Figs. **70**, **71** for the DBR and for the single a-Si:H/SiN_x respectively. As predicted by the simulation results, the reflectance values of the DBR, in the spectral range from 1000 nm to 1200 nm, are higher than in case of the a-Si:H/SiN_x. This effect immediately reflects on the IQE of both samples, leading to a higher IQE values when DBR is adopted as back reflecting mirror.

Table 5: PECVD parameters used in the deposition of the a-Si:H, and a-SiN_x layers of the emitter and DBR structures. P_D is the process pressure; P_{RF} is the power density of the plasma discharge; T_D is the substrate temperature.

EMITTER						
Material	**SiH_4 (sccm)**	**PH_3 (sccm)**	**P_D (Torr)**	**P_{RF} (mW/cm^2)**	**T_D (°C)**	**Thick (nm)**
n-a-Si:H	40	10	0.3	28	200	10
i-a-Si:H	40		0.3	25	180	5
DIELECTRIC BRAGG REFLECTOR						
Material	**SiH_4 (sccm)**	**NH_3 (sccm)**	**P_D (Torr)**	**P_{RF} (mW/cm^2)**	**T_D (°C)**	**Thick (nm)**
i-a-Si:H	120		0.75	31	200	66
SiN_x	120	10	0.75	264	200	130

To extract quantitative information from the quantum efficiency measurements, the experimental QE data have been modelled with the numerical program PC1D [149]. The heterostructure has been divided in three regions:

1. the amorphous emitter, in which the recombination effect due to defect density of the amorphous material is taken into account by the μτ product (μ is the mobility and τ is the minority carriers lifetime);

2. the c-Si base in which the diffusion length L_d is the parameter used in the fitting procedure;

3. a 5 μm thick region which considers the effect of Al laser diffusion in terms of band gap narrowing due to p^+ overdoping [150]. In this last region, the passivation quality of the back side mirror affects the rear side surface recombination velocity S_R.Results of modeling are reported as lines in Figs. **70** and **71**. The values of the fitting parameters are summarized in Table **6** for both kind of cells. We observe that the cell with the DBR structure shows higher L_d and lower S_R than the cell with the a-Si:H/SiN_x single back mirror structure. Moreover it is possible to reproduce the reflectance data considering a 70 nm thick front coating having 2 as refractive index and an internal reflectance due to mirror effect equal to 93% and 65% for the DBR/Al and a-Si:H/SiN_x/Al, respectively. The good agreement between experimental data and models have been reached in the spectral range from 800 nm to 1200 nm, as reported in the Figs. **70** and **71**. In the IQE and EQE simulations of a-Si:H/SiN_x/Al sample higher absorption is needed in the 5 mm thick rear side of cell model to fit the experimental data with respect to the DBR/Al sample. This choice can be related to the higher density of laser fired point contacts adopted in the former sample [146].

Table 6: Parameters used in PC1D simulations for fitting the experimental data of EQE, IQE and current voltage curves. The front coating and the back inner reflectances fit the reflectance curves in the range 800-1200 nm.

Layer	Parameters	DBR	aSi:H/SiNx
Coating	External Reflectance Thickness (nm)	70	70
	Reflectance Index	2	2
a-Si:H	Thickness (nm)	15	15
	Bandgap (eV)	1.7	1.7
	n_i concentration cm^{-3}	$1{\cdot}10^{7}$	$1{\cdot}10^{7}$
	$\mu\tau$ (cm^2/V)	$1{\cdot}10^{11}$	$1{\cdot}10^{11}$
	n-type doping (cm^{-3})	$1{\cdot}10^{18}$	$1{\cdot}10^{18}$
c-Si	thickness (μm)	245	245
	Bandgap (eV)	1.124	1.124
	mobility μ_n(cm^2/Vs) mobility μ_p (cm^2/Vs)	1417, 470	1417, 470
	n_i concentration cm^{-3}	$1{\cdot}10^{10}$	$1{\cdot}10^{10}$
	p-type doping (cm^{-3})	$3.2{\cdot}10^{16}$	$3.2{\cdot}10^{16}$
	L_d (μm)	750	500
c-Si + BSF	thickness (μm)	5	5
	Bandgap (eV)	1.0	1.0
	S_R(cm/s)	10	80
	Internal Reflect. %	93	65

These better performances have been confirmed by the measurement of the minority carriers lifetime τ_{eff}, that quantifies the effectiveness of the back side mirrors as surface passivation

structure. Measurement have been performed on two 0.5 Ωcm p-type silicon wafers, passivated on both side by the DBR or the single a-Si:H/SiN_x respectively, by monitoring the Quasi Steady State Photoconductance decay in a Sinton System [151]. The experimental values are reported in Table **7**. The higher τ_{eff} found in case of DBR is mainly due to the increase of the positive charge content at the a-Si:H/SiN_x interfaces of stacked structure with respect to the single couple of a-Si:H/SiN_x layers. Indeed higher the positive charge amount, stronger the field effect close to the a-Si:H/c-Si interface due to inversion layer formation that keeps away the minority carriers from the silicon surface [29].

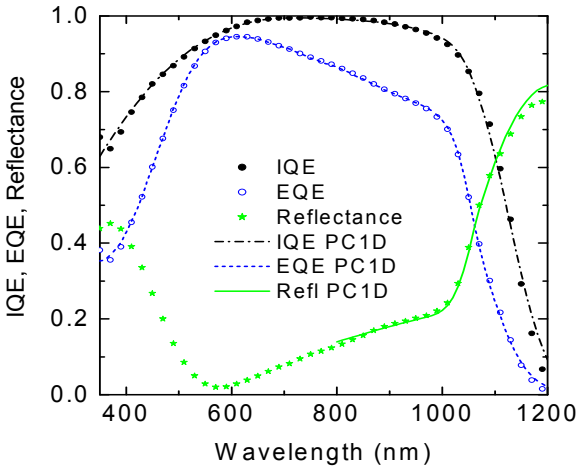


Figure 70: Reflectance profile (stars), External (open circles) and Internal (filled circles) Quantum Efficiencies for a-Si:H/c-Si heterojunction solar cell with the DBR/Al back structure. Lines refer to the simulation results obtained using PC1D software with the parameters reported in Table **6** [16].

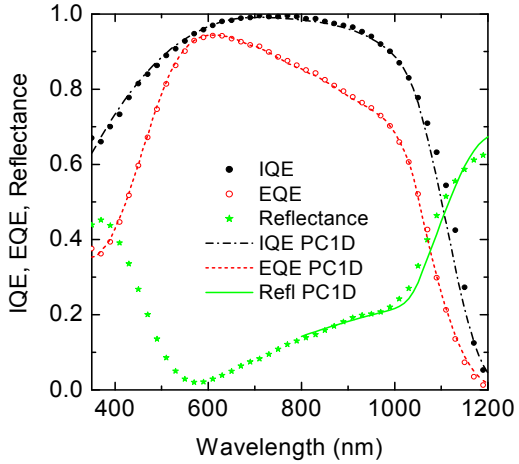


Figure 71: Reflectance profile (stars), External (open circles) and Internal (filled circles) Quantum Efficiencies for a-Si:H/c-Si heterojunction solar cell with the a-Si:H/SiNx/Al back structure. Lines refer to the simulation results obtained using PC1D software with the parameters reported in Table **6** [16].

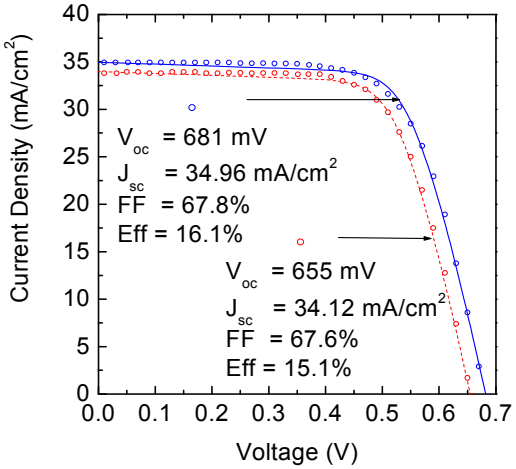


Figure 72: Measured (symbols) and modeled (lines) current-voltage characteristics measured under AM1.5G for solar cells with DBR/Al (filled symbols) and a-Si:H/SiN_x/Al (open symbols) as mirror [16].

Table 7: Minority carrier lifetime value of the c-Si surface passivation structures as measured from photoconductance decay method.

Structure	**τ_{eff} (μs)**
SiN_x/a-Si:H/c-Si/a-Si:H/SiN_x	310
DBR/c-Si/DBR	400

The photovoltaic performances of the solar cell with the DBR result once again better than the ones with the single couple. A high V_{oc} of 681 mV and a J_{sc} of 34.96 mA/cm^2 have been achieved, which confirm the DBR efficacy as rear side dielectric mirror in laser fired point contacted cell. The current voltage characteristics, measured under Class A AM1.5G sunlight simulator, of both kind of heterostructure solar cells is reported as points in Fig. **72**. In the same figure the lines are related to the PC1D numerical simulations. The same set of parameters, used to reproduce QE data, allow to accurately model the current voltage curves collected under standard AM 1.5G. The overall efficiency at 16.1% is limited by the Fill Factor (67.8%), which can be increased by an optimization of the screen printed front grid and of the pitch of laser point contact.

Taking into account the proposed model it is possible to apply the DBR idea to thinner silicon wafer to enhance the near IR cell response also choosing the centre wavelength of the DBR accordingly.

5.3. Thin c-Si Wafer

In order to reduce the PV cost the most promising approach concerns to the use of thinner silicon wafer, indeed half of the cell cost is due to the base material. In case of multicrystalline silicon (mc-Si) the actual wafer thickness has been thinned from 300 μm of five years ago, to the actual 180 μm. Further improvement can be obtained using thinner saw wire and a reduction to 120 μm is expected. In turn, the thinner mc-Si wafer becomes more fragile since is very large area

156x156 mm^2. Therefore the manufacturing production yield actually is not competitive with the actual production line. Further investments are needed to replace some old technologies and facilities to approach those thinner wafers. On the other hand, it is difficult to image mc-Si wafer thinner than the saw wire. To this aim different approach to wafer cutting are needed. In case of monocrystalline silicon (c-Si) a very promising technique to cut the wafer thinner than 100 μm is now arriving on market as presented by SiGen [152]. The solution presents itself by combining advanced layer transfer cleaving methods with efficient, high-energy ion accelerator technology. The convergence of these two technologies allows a thickness of silicon made from a CZ silicon ingot to be directly detached using a high energy light ion beam with near-zero kerf loss and with low overall process cost. The process is called Direct Film Transfer (DFT) and shown conceptually in Fig. **73**. The thin wafer produced in this way result flexible and then less fragile with respect to thicker one. Moreover it is free from saw damages, therefore can be directly textured saving a costly wet chemical. On this wafer high temperature steps, such as emitter diffusion and high temperature sintering screen printed fired contact should be replaced by different approach using low thermal budget. Thin film technologies are suitable to this aim. Indeed one of the most promising way is the use of a-Si:H/c-Si technology in order to form both the front and the rear side contact of the cell. Then TCO should be used to form large area contact followed by Ag grid shaped metal electrodes. This approach has been successfully demonstrated by Sanyo [139] on silicon wafer thinner as thin as 98 μm, achieving the record efficiency of 22.8% (J_{sc} = 38.96 mA/cm^2; V_{oc} = 743 mV; FF= 79.1% area 100 cm^2).

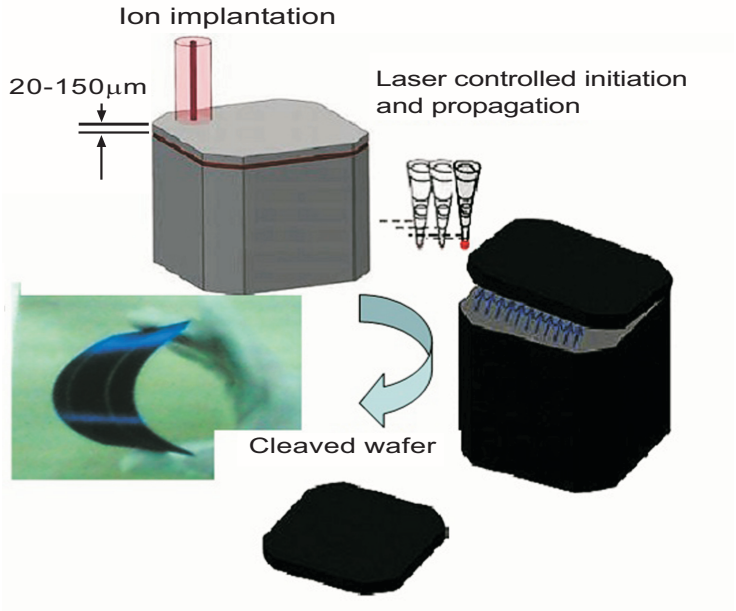


Figure 73: Direct Film Transfer (DFT) process to form a kerf free CZ thin silicon wafer.

Thinning the wafer with the same cell fabrication method, such as heterostructure, several aspects have to be carefully considered to maintain the same efficiency. To this aim we performed numerical simulation, by using PC1D software [149], to evaluate the effect of thinner wafer on the solar cell performances.

The cell under test was a n-type c-Si based heterostructure in which both the front emitter and the back surface field were formed by a-Si:H/c-Si heterojunction. To better evaluate the effect of wafer thickness in the range between 200 μm and 20 μm, we also considered an ITO layer as antireflection coating. The cell structure and parameters used in the simulations are listed in Table **8**. The photovoltaic parameters of the simulated heterostructure cell as a function of silicon wafer thicknesses, normalized to the initial value, are reported in Fig. **74**. The photovoltage (V_{oc}) enhancement is expected due to recombination reduction along the wafer that reflects in higher built-in voltage reducing the wafer thickness. In turn, the thinner the wafer, the lower the photocurrent. From the Fig. **74** it is evident that the photocurrent reduction is stronger than the photovoltage enhancement thus affecting the cell efficiency that reduces as the wafer becomes thinner. These results are in good agreement with SANYO report [139]. This remarks that the use of thinner wafer ensures a cost reduction because of less material, but also produces a cell efficiency reduction. To overcome this undesired condition it is possible to introduce the mirroring effect, such as proposed with the use of DBR concept reported above. To do this in the simulation we use the internal light reflectance parameters as indicated in Table **7**. The evolution of photovoltaic parameters by reducing the wafer thickness is reported in Fig. **75**. Now the cell efficiency remains almost constant from thickness in the range between 200 μm and 60 μm.

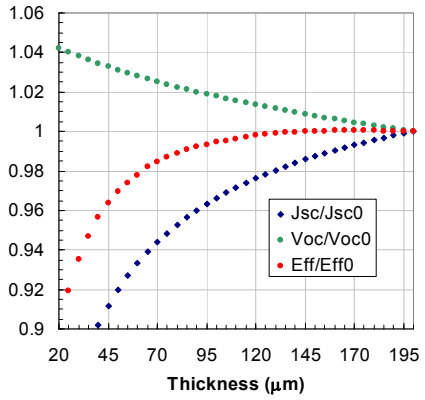


Figure 74: Normalized photovoltaic parameters of the heterojunction cell as a function of the wafer base thickness.

Table 8: Parameters used in PC1D simulations to describe the heterojunction solar cell in which the base wafer thicknes is used as parameter.

Layer	**Parameters**	**Value**
Coating	External Reflectance Thickness (nm)	70
	Reflectance Index	2
a-Si:Hemitter	thickness (nm)	15
	Bandgap (eV)	1.7
	n_i concentration cm^{-3}	1.10^7

Table 8: cont….

	μτ (cm^2/V)	1.10^{-11}
	p-type doping (cm^{-3})	1.10^{16}
c-Sibulk	thickness (μm)	200-20
	Bandgap (eV)	1.124
	mobility μ_n(cm^2/Vs) mobility μ_p (cm^2/Vs)	1417, 470
	n_i concentration cm^{-3}	1.10^{10}
	n-type doping (cm^{-3})	5.10^{15}
	L_d (μm)	1000
a-Si:Hrear	thickness (νm)	20
	Bandgap (eV)	1.7
	μτ (cm^2/V)	1.10^{-11}
	n-type doping (cm^{-3})	1.10^{17}
	Internal Reflect. %	93

Very similar approach to the rear side mirroring has been reported in [153], in which the authors suggest the use of a distributed Bragg reflector made by a stacks of Si/Si_3N_4 having refractive indexes: n_1/n_2 = 3.5/2.0 or Si/SiO_2 n_1/n_2=3.5/1.46 achieving a reflectivity of 99.8% in the wavelength range between 800 and 1100 nm. By the unique combination of grating and DBR, light is tightly trapped within the solar cell, effectively changing the optical path length from the thickness of the cell to its lateral dimension. The schematic cross section of the distributed Bragg reflector is reported in Fig. **76**.

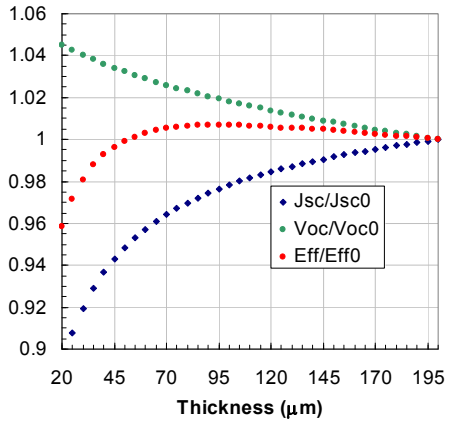


Figure 75: Normalized photovoltaic parameters of the heterojunction cell as a function of the wafer base thickness after the introduction of mirroring effect.

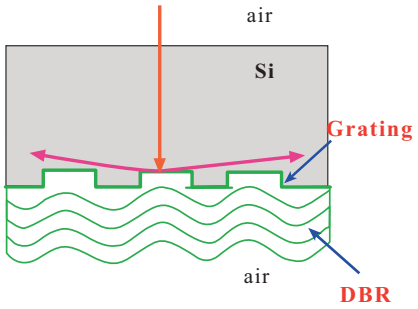


Figure 76: Distributed Bragg reflector for solar cell [153].

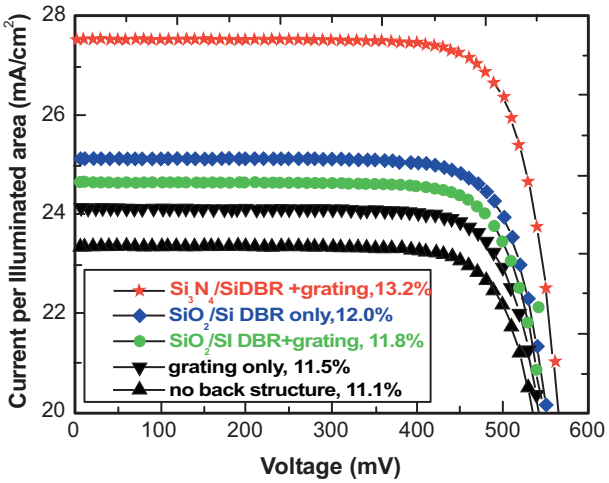


Figure 77: IV characteristics for solar cell with different distributed Bragg reflecting mirror [153].

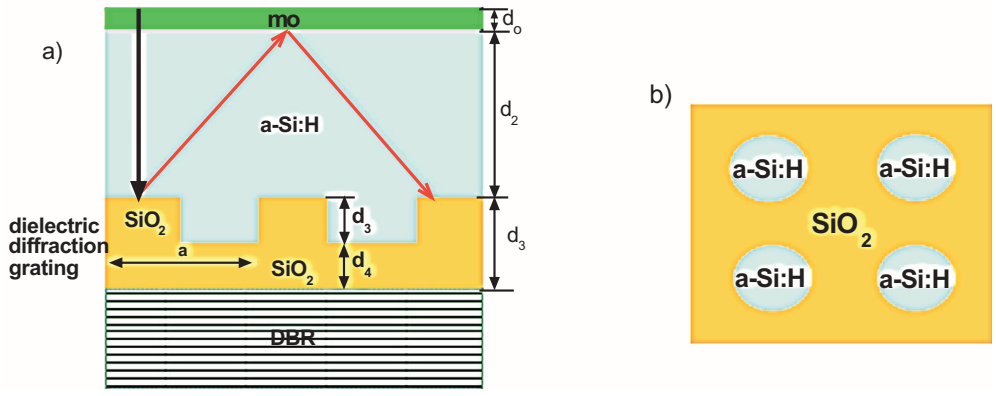


Figure 78: (a) Schematic solar cell cross section with antireflective coating and distributed Bragg reflector and SiO_2 grating layer with amorphous silicon cylinders in background. (b) Top view of the cell [154].

Different materials have been used resulting in different efficacy, as demonstrated by the IV characteristics under AM1.5G sunlight simulator reported in Fig. **77**. This concept can be transferred to amorphous thin film solar cell as reported in ref [153]. The authors have made several simulations using the mirror structure as depicted in Fig. **78** in which both the schematic cross section and the top view of the cell are reported. The mirroring effect has been modelled to enhance the absorption at wavelengths longer than 650 nm. An optimal structure consisted of a = 600 nm, R/a = 0.38, d_1 = 50 nm, d_2 = 500 nm, d_3 = 50 nm and d_5 = 120 nm. The thickness of ITO d_0 is expected to range from 500nm/4n_{ITO}= 64 nm to 775nm/4n_{ITO} = 100 nm.

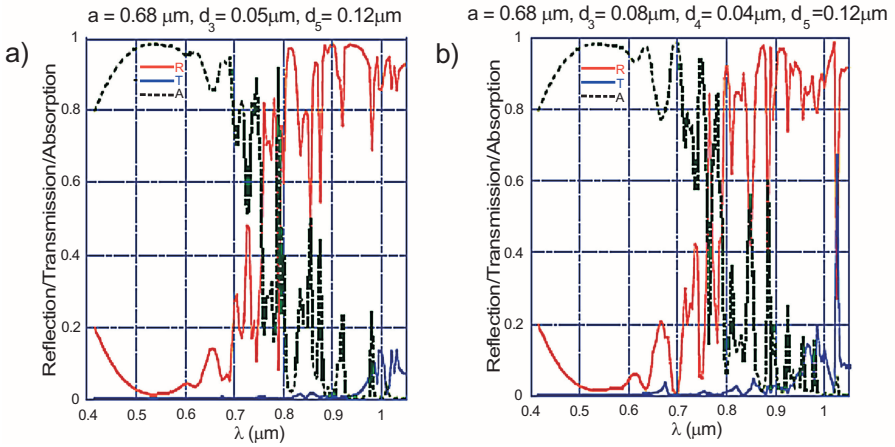


Figure 79: Non specular reflection/transmission/absorption in the absorber layers for the two designs with d0 = 65 nm, d1 = 50 nm, d2 = 500 nm and (a) a-Si layer with SiO2 cylinders (b) SiO2 layer with a-Si cylinders [154].

The optimized solar cell with SiO_2 cylinders inside the a-Si layer (Fig. **79a**) and the complementary structure of a-Si cylinders in the SiO_2 matrix (Fig. **79b**) both demonstrate very high absorption (A > 0.8) through most of the optical wavelengths (0.4-0.7 μm), accompanied by small reflection. The enhanced absorption improves the near-IR solar response. Wavelengths larger than 0.775 μm are largely reflected from the cell in both configurations, but these are above the bandgap and do not contribute to photocurrent. A comparison of the light trapping in the optimized solar cell with a bare a-Si:H film, an a-Si:H film with antireflective coating and an a-Si:H film with DBR and antireflective coating is reported in Fig. **80**.

Even though the efficacy of these last two presented structures, sometimes recalled as "photonic crystals", is out of doubt, nevertheless it is not easy to image how to precisely control the grating sizes over a large area device as required by the PV application.

6. INNOVATIVE CONCEPT

As pointed out in the previous sections, in conventional solar cells where the active absorbing layer is much thicker than the impinging wavelengths, light trapping is usually based on texturing the front solar cell surface in order to randomize the light propagation direction within the cell structure and obtain a total internal reflection between the active material with high refractive

index and the external surrounding material with low refractive index. In this way the fraction of the light lying within the escape cone for refraction out from the substrate toward the external material is reduced and a much longer propagation distance inside the active material of the solar cell is achieved.

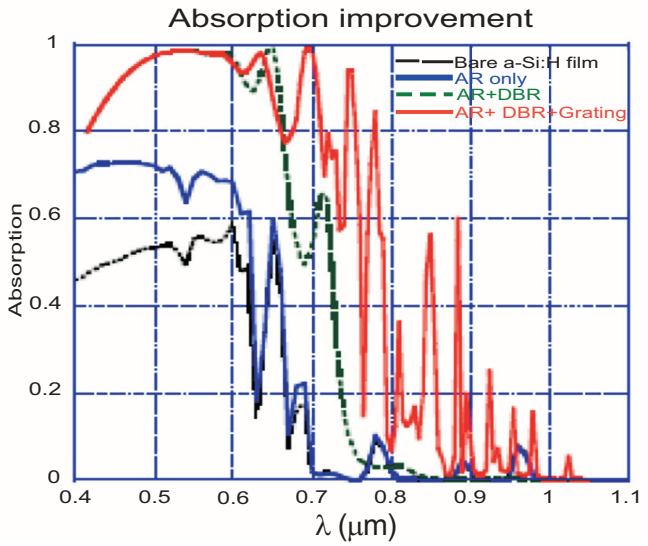


Figure 80: Comparison of absorption of a bare a-Si:H film, a-Si:H film with AR coating only, a-Si:H film with AR coating, and DBR, a-Si:H film with AR coating and DBR and optimized grating [153].

For these textured structures, it has been demonstrated [3, 4] that the light absorption can increase, with respect to a non-textured surface, up to a factor $4n^2/\sin 2\Phi$ where n is the refractive index of the active material and Φ is the angle of the emission cone in the external medium. This limit [3] cannot be exceeded in standard solar where the thickness of the active layer is much larger than the wavelength range. However, in the nanophotonic regime when the thickness is comparable or even smaller than the impinging wavelengths, the absorption enhancement can overcome this limit if a proper design of the solar cell structure is considered. The basic concepts for this enhancement are:

a. the coupling of the incident plane waves with guided optical modes, introduced inside the active material by a grating with specified periodicity or by random Lambertian texturing;

b. the confinement of the guided mode in an active layer with thickness in the deep-subwavelength scale;

c. the achievement of a group index larger than the refractive index of the active material.

The absorption spectrum of film satisfying the first requirement is constituted by a sequence of sharp peaks, one for each guided resonance as reported in Fig. **81**. Since the incident radiation useful in photovoltaic applications has a bandwidth much larger of the bandwidth associated with each resonance, the total absorption is given by the sum of the absorption peak of each resonance,

and can be demonstrated that it is linearly dependent on the number of resonances and inversely proportional to the number of the plane waves that couple to the resonance.

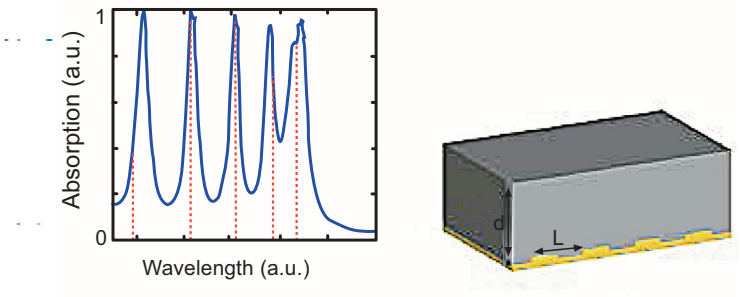


Figure 81: Light-trapping with the use of aperiodic grating on a back-reflector (yellow). d = 2μm. L = 250 nm.

When the solar cell structure has a thickness and periodicity of the grating much larger than the incident radiation, the absorption enhancement factor does not overcome the $4n^2$ limit and nanophotonic effects are absent. They can occur only if the active layer thickness is much smaller than the impinging wavelength and/or the design structure determines a group index much larger than the refractive index of the active material.

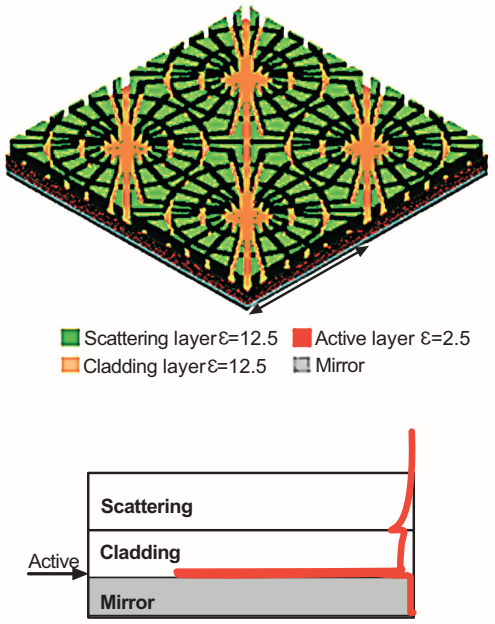


Figure 82: Uper Part: The scattering layer consists of a square lattice of air groove patterns with periodicity L = 1200nm. The thicknesses of the scattering, cladding, and active layers are 80nm, 60nm, and 5nm respectively. The mirror layer is a perfect electric conductor. Lower Part: The profile of electric-field intensity for the fundamental waveguide mode. Fields are strongly confined in the active layer. To obtain the waveguide mode profile, the scattering layer is modelled by a uniform slab with an averaged dielectric constant [154].

The structure proposed by the authors in [154] is reported in Fig. **82** and consists of four layers. Starting from the bottom, the first is a perfect conductor layer and acts as a mirror for the guided wavelength that propagates into the 5nm thick active material which has a refractive index equal to $(2.5)^{1/2}$. This layer therefore has a thickness lying in the deep-subwavelength range and satisfies the second requirement. The cladding layer, with thickness equal to 60nm, has a refractive index equal to $(12.5)^{1/2}$. These characteristics ensure:

1. a fundamental mode traveling along the structure with structure group index very close to the cladding one (third requirement);

2. a field confinement in the low-index material (second requirement). Indeed, following Almeida *et al.* [155], the presented structure behaves as a slot-waveguide, where the radiation energy is confined and concentrated in the low index material thanks to the high-index-contrast interface between the cladding and active layer.

The 80 nm thick scattering layer designed with a periodicity larger than the investigated wavelengths ensures the coupling of the incident radiation into the nanoscale guided modes. Simulations of the entire structure show that the absorption enhancement factor reaches 119 which is well above the $4n^2$ limit for both the active and cladding material demonstrating that nanophotonic light trapping effect can greatly enhance the light absorption, increase the solar cells performance and decrease their costs due to the reduced amount of utilized material.

ACKNOWLEDGEMENT

Declared none.

CONFLICT OF INTEREST

The author(s) confirm that this chapter content has no conflict of interest.

REFERENCES

[1] Neuroth G, Muller A, Seidel J. On the way to a more efficient production of mc-Silicon wafers for PV: increase of mc-si ingot mass and reduction of crystallization process time. Proceedings of 21st European Photovoltaic Solar Energy Conference; 2006; Dresden; Wip Munich; pp. 978-781.

[2] Taretto K, Rau U. Modeling extremely thin absorber solar cells for optimized design. Prog. Photovoltaics Res. Appl.2004; 12: 573-591.

[3] Yablonovitch E. Statistical ray optics. J. Opt. Soc. Am. A 1982; 72: 899-907.

[4] Green MA. High Efficiency Silicon Solar Cells. Trans Tech Publications 1987.

[5] Agrawal M, Peumans P. Broadband optical absorption enhancement through coherent light trapping in thin-film photovoltaic cells. Opt. Express 2008; 16: 5385-5396.

[6] Pala RA, White J, Barnard E, Liu J, Brongersma ML. Design of Plasmonic Thin-Film Solar Cells with Broadband Absorption Enhancements. Adv Mater 2009; 21: 3504-3509.

[7] Zeng L, Yi Y, Hong C, *et al.* Efficiency enhancement in Si solar cells by textured photonic crystal back reflector. Appl Phys Lett 2006; 89: 111111-111113.

[8] Chutinan A, John S. Light trapping and absorption optimization in certain thin-film photonic crystal architectures. Phys Rev A 2008; 78: 023825-023815.

[9] Hu L, Chen G. Analysis of Optical Absorption in Silicon Nanowire Arrays for Photovoltaic Applications. Nano Letters 2007; 7: 3249-3252.

[10] Bermel P, Luo C, Zeng L, Kimerling LC, Joannopoulos JD. Improving thin film crystalline silicon solar cell efficiencies with photonic crystals. Opt Express 2007; 15:16986-17000.

[11] Tian B, Zheng X, Kempa TJ,*et al.* Coaxial silicon nanowires as solar cells and nanoelectronic power sources. Nature 2007; 449: 885-889.

[12] Müller J, Rech B, Springer J, Vanecek M. TCO and light trapping in silicon thin film solar cells. Solar Energy 2004; 77: 917-930.

[13] Zhu J, Yu Z, Burkhard GF, *et al.* Optical Absorption Enhancement in Amorphous Silicon Nanowire and Nanocone Arrays. Nano Letters 2008; 9: 279-282.

[14] Tsakalakos L, Balch J, Fronheiser J, *et al.* Silicon nanowire solar cells. Appl Phys Lett 2007; 91: 233117-233119.

[15] Rockstuhl C, Lederer F, Bittkau K, Carius R. Light localization at randomly textured surfaces for solar-cell applications. Appl Phys Lett 2007; 91: 171104-171106.

[16] Tucci M, Serenelli L, Salza E, *et al.* Bragg reflector and laser fired back contact in a-Si:H/c-Si heterostructure solar cell, Material Science and Eng B 2009; 159-160: 48-52.

[17] Serenelli L, Talgorn E, Salza E, *et.al*. Bragg Reflector in Laser Fired Back Contact Silicon Solar Cells Proceedings of 22nd European Photovoltaic Solar Energy Conference;2007; Milan; Wip Munich; pp. 1470-1473.

[18] Green MA. Solar Cells, operating principles, technology and system applications. University of New South Wales 1996.

[19] Wang EY, Yu FTS, Simms VL, *et al.* Optimum Design of Antireflection Coating for Silicon Solar Cells. Proceedings of the 10th IEEE Photovoltaic Specialistic Conference; 1973; Palo Alto; pp. 168-170.

[20] Cox JT, Hass G., Rowntree RF. Two-layer antireflection coatings for glass in the near infra-red. Vacuum 1951; 4(4): 445-455.

[21] Zhao J, Green MA. Optimized Antireflection Coatings for High-Efficiency Silicon Solar Cells, IEEE Transaction on Electron Devices 1991; 38(8): 1925-1934.

[22] Aberle AG. Overview on SiN surface passivation of crystalline silicon solar cells. Sol En Mat Sol Cells 2001; 65: 239-248.

[23] NKDGEN software [computer program]. Barcelona (E): Optical Characterization Group Universitat de Barcelona: available from: http://www.ub.edu/optmat/prod0.html

[24] Stanbery BJ, Chen WS, Mickelsen RA, *et al.* Silicon nitride anti-reflection coatings for CdS/CuInSe2 thin film solar cells by electron beam assisted chemical vapor deposition. Solar Cells 1985; 14: 289-291.

[25] Aberle AG, Hezel R. Progress in low-temperature surface passivation of silicon solar cells using remote-plasma silicon nitride. Prog. Photovoltaics Res. Appl. 1997; 5: 29-50.

[26] Aberle AG. Crystalline Silicon Solar Cells, Advanced Surface Passivation and Analysis. University of New South Wales: Centre for Photovoltaic Engineering 2004.

[27] Hequan W, Dechun B, Hui S, *et al.* Fabrication and Characterization of TiO_2 Antireflection Thin Film Deposited on the Solar Cell. Proceedings of ISES World Congress 2009; 4:1000-1005.

[28] Chen Z, Rohatgi A, Ruby D. Silicon Surface and Bulk Defect Passivation by Low Temperature PECVD Oxides and Nitrides. Proceedings of 1st WCPVEC; 2001; Hawaii; pp. 49-56.

[29] Tucci M, Serenelli L, De Iuliis S *et al.* Characterization of SiNx/a-Si:H crystalline silicon surface passivation under UV light exposure, Thin Solid Films, 2007; 515: 7625-7628.

[30] Tucci M, Serenelli L, Salza E, *et al.* Innovative design of Amorphous/Cristalline silicon Heterojunction solar cell. Thin Solid Films 2008; 516: 6771-6774.

[31] Nagel H, Aberle AG, Hezel R. Optimised Antireflection Coatings for Planar Silicon Solar Cells using Remote PECVD Silicon Nitride and Porous Silicon Dioxide. Prog Phot Res App 1999; 7: 245-255.

[32] Serenelli L, De Iuliis S, Izzi M, *et al.* Electrical and optical characterization of passivation layers under UV light soaking for concentrated photovoltaic applications. Proceedings of the 20th European Photovoltaics Solar Energy Conference; 2005; Barcelona; pp. 1232-1235.

[33] Hezel R, Jaeger K. Low-temperature surface passivation of silicon for solar cells. J Electrochem Soc 1989; 136 (2): 518-523.
[34] Belyi VI. Silicon nitride in electronic. Elsevier 1988; chap 1.
[35] Hess DW, Graves DB. Plasma-Enhanced Etching and Deposition. Microelectronics Processing: A chemical engineering aspects; Edited by Hess DW, Jensen KF, American Chemical Society 1989; p. 382
[36] Masaki Y, Roderick AG, Le Comber PG. Structural and electrical properties of SiNx:H films. J Appl Phys 1993; 73 (10): 5088-5094.
[37] Holt JK, Goodwin DG, Gabor AM, *et al.* Hot-Wire Chemical Vapor Deposition of High Hydrogen Content Silicon Nitride for Silicon Solar Cell Passivation and Anti-Reflection Coating Applications. NCPV and Solar Program Review Meeting, 2003.
[38] Dekkers HFW, De Wolf S, Agostinelli G, *et al.* Very high frequency PECVD SiNx :H for fast deposition of Anti-Reflection Coating and passivation of mc-Si solar cells. Proceedings of the 19th EUPVSEC; 2004; Paris, France; pp. 982-986.
[39] Roth K, Chen F, Fritzche M, *et al.* Improvements on inline plasma technology for the deposition of silicon nitride films for passivation purpose on crystalline silicon solar cells. Proceedings of the 21st EUPVSEC 2006; Dresden; pp. 1137-1140.
[40] Mota F, Justo JF, Fazzio A. Hydrogen role on the properties of amorphous silicon nitride. J Appl Phys 1999; 86 (4): 1843-1847.
[41] Robertson J, Powell MJ. Gap states in silicon Nitride. Appl Phys Lett. 1984; 44 (4): 415-417.
[42] Lucovsky G, Williams MJ, He SS. *et al.* Nitrogen: not a dopant in crystalline Si (c-Si), but an n-type dopant in a-Si:H, why?. Proceedings of the Mat Res Soc Symp 1994 San Francisco, CA, USA; 336: pp. 637-641.
[43] Lelievre JF, Kaminski A, Lysenko V, *et al.* Comparative Study of structural and optical properties of silicon nitride SiNx:H deposited by PECVD. Proceedings of the 20th EUPVSEC; 2005; Barcelona, Spain; pp. 1442-1445.
[44] Warren WL, Rong FC, Poindexter EL, *et al.* Structural identification of the silicon and nitrogen dangling-bond centers in amorphous silicon nitride. J Appl Phys 1991; 70: 346-354.
[45] Aya Y, Katayama H, Murata K, *et al.* SANYO's R&D on Thin-Film Si Photovoltaic Technologies. Proceedings of the 25th EUPVSEC; 2010; Valencia, Spain; pp. 2394-2397.
[46] Street RA. Hydrogenated amorphous silicon. Solid State Science Series (Cambridge University Press) 1991, Cambridge.
[47] Hartnagel HL, Dawar AL, Jain AK, Jagadish C. Semiconducting Transparent Thin Films. Institute of Physics Publishing 1995, Bristol, UK.
[48] Agashe C, Kluth O, Hupkes J, *et al.* Efforts to improve carrier mobility in radio frequency sputtered aluminum doped zinc oxide films. J. Appl. Phys. 2004; 95: 1911–1917.
[49] Beyer W, Hüpkes J, Stiebig H. Transparent conducting oxide films for thin film silicon photovoltaics. Thin Solid Films 2007; 516: 147–154.
[50] Minami T, Sato H, Nanto H, Takata S. Group III Impurity Doped Zinc Oxide Thin Films Prepared by RF Magnetron Sputtering. Jpn J Appl Phys 1985; 24: L781-L784.
[51] Van de Walle GC. Hydrogen as a Cause of Doping in Zinc Oxide. Phys Rev Lett 2000; 85: 1012-1014.
[52] Kubokawa Y, Toyama O. The Electrical Conductivity Change Caused by the Chemisorption of Hydrogen on ZnO, ZnO. Cr2O3 and ZnO.MoO3. J Phys Chem 1956; 60: 833-836.
[53] Faÿ S, Feitknecht L, Schlüchter R, Kroll U, *et al.* Rough ZnO layers by LP-CVD process and their effect in improving performances of amorphous and microcrystalline silicon solar cells. Sol Energy Mater Sol Cells 2006; 90: 2960-2967.
[54] Kroll U, Meier J, Benagli S, *et al.* Proceedings of the 21th EUPBSEC, 2006 Sep 4-8; Dresden, Germany; pp. 1546-1549.
[55] Available from: http://www.oerlikon.com

[56] Van den Berg R, Calwer H, Marklstorfer, *et al.* 7% stable efficiency large area a-Si:H solar modules by module design improvement. Sol Energy Mater. Sol Cells 1993; 31: 253–261.
[57] Fay S, Dubail S, Kroll U, Meier J, Ziegler Y, Shah A. Light trapping enhancement for thin-film silicon solar cells by roughness improvement of the ZnO front TCO. Proceedings of the 16th EUPVSEC; 2000 May 1-5; Glasgow, UK; pp. 361–364.
[58] Groenen, R, Loffler J, Sommeling J, *et al.* Surface textured ZnO films for thin film solar cell applications by expanding thermal plasma CVD. Thin Solid Films 2001; 392: 226–230.
[59] Ellmer K. Resistivity of polycrystalline zinc oxide films: current status and physical limit. J Phys, D, Appl Phys 2001; 34: 3097-30108.
[60] Look DC. Electrical and optical properties of p-type ZnO. Semicond Sci Technol 2005; 20: S55.
[61] Lee JH, Lee JS, Lee SH, *et al.* Hybrid p-type ZnO film and n-type ZnO nanorod p–n homo-junction for efficient photovoltaic applications. Thin Solid films 2010; 518 (22): 6587-6589
[62] Lee YJ, Ruby DS, Peters DW, *et al.* ZnO nanostructures as efficient antireflection layers in solar cells. Nano Letters 2008; 8 (5): 1501-1505.
[63] Sakai H, Ichikawa Y. Process technology for a-Si/a-Si double stacked tandem solar cells with stabilized 10% efficiency. J Non-Cryst Solids 1991; 137–138: 1155-60.
[64] Palit N, Chatterjee P. Computer analysis of a-Si:H p-i-n solar cells with a hydrogenated microcrystalline silicon p layer. J Appl Phys 1999; 86: 6879-89.
[65] Sato R, Goto Y, Wakayama Y, *et al.* Highly textured SnO_2:F TCO films for a-Si solar cells. Report Res Lab Asahi Glass Co. Ltd. 1992; 42: 129–137.
[66] Paulson PD, Hegedus SS. Accurate determination of optical constants of textured SnO2 using low incidence angle spectroscopic ellipsometry. J Appl Phys 2004; 96 (10): 5469-5476
[67] Rakhshani AE, Makdisi Y, Ramazaniyan HA. Electronic and optical properties of fluorine-doped tin oxide films. J Appl Phys 1998; 83: 1049-57.
[68] De Rosa R, Grillo P, Sinno G, *et al.* Photovoltaic applications for high quality ITO obtained by a low temperature e-gun deposition. Proc. of 2nd WCPVSEC; 1998,Vien, Austria; pp. 1583-1586.
[69] Caputo D, de Cesare G, Tucci M. Built-in enhancement in a-Si:H solar cell by chromium silicide layer. IEEE Electron Device Letters, 2010; 31-7: 689-691.
[70] Hultaker A. Transparent conductive tin doped indium oxide PhD thesis in Solid State Physics Uppsala University Edited by Elander Gotab Stockholm Sweden 2002; ISSN 1104-2516.
[71] Dao VA, Choi H, Heo J. Rf-Magnetron sputtered ITO thin films for improved heterojunction solar cell applications. Current Applied Physics 2010; 10: S506–S509.
[72] Zhao L, Zhou Z, Peng H, Cui R. Indium tin oxide thin films by bias magnetron rf sputtering for heterojunction solar cells application Applied Surface Science 2005; 252: 385–392
[73] Available from: http://www.uni-solar.com/uni-solar-difference/technology/
[74] Available from: http://www.firstsolar.com/en/CdTe.php
[75] Available from: http://global.mitsubishielectric.com/bu/solar
[76] Krc J, Zeman M, Smole F, Topic M. Optical modeling of a-Si:H solar cells deposited on textured glass/SnO_2 substrates. J Appl Phys 2002; 92 2: 749-755.
[77] Zeman M, van Swaaij RA, Metselaar JW, Schropp REI. Optical modeling of a-Si:H solar cells with rough interfaces: Effect of back contact and interface roughness. J Appl Phys 2000; 88 1: 6436-6443.
[78] Jager K, Zeman MA. Scattering model for surface-textured thin films. Appl Phys Lett 2009; 95 171108.
[79] Born M, Wolf E. Principles of Optics, 7th ed. Cambridge University Press, Cambridge, England, 1999.
[80] Carniglia CK. Scalar scattering theory for multilayer optical coatings. Opt Eng 1979; 18, 104.
[81] Beckmann P, Spizzichino A. The Scattering of Electromagnetic Waves from Rough Surfaces. Pergamon, New York, 1963.
[82] Stiebig H, *et al.* Modeling of light scattering from micro-and nanotextured surfaces Proceedings of the 16th EUPVSEC; 2000 May 1-5; Glasgow, UK; pp. 549-552.
[83] Hishikawa Y, *et al.* Proc 11th PVSEC Sapporo Japan 1999; 219-220.

[84] Domine D, Buehlmann P, Bailat J, *et al.* Optical management in high-efficiency thin-film silicon micromorph solar cells with a silicon oxide based intermediate reflector. Phys Status Solidi 2008; 2:163-165.

[85] Jäger K, Isabella O, Zhao L, Zeman M. Light scattering properties of surfacetextured substrates. Phys Status Solidi C 2010; 7, 3–4: 945-948

[86] van Nijnatten P. A. An automated directional reflectance/transmittance analyser for coating analysis. Thin Solid Films 2003; 442, 74-77.

[87] Berginski M, Hüpkes J, Schulte *et al.* The effect of front ZnO:Al surface texture and optical transparency on efficient light trapping in silicon thin-film solar cells. J Appl Phys 2007; 101: 074903

[88] Kluth O, Loffl A, Wieder S, *et al.* Texture Etched Al Doped ZnO: A New Material for Enhanced Light Trapping in Thin Film Solar Cells. Proceedings of the 26th IEEE Photovoltaic Specialists Conference; 1997Anaheim, CA; pp. 715-718.

[89] Hack M, Shaw JG. Amorphous Silicon Technology, edited by A Madan, Y Hamakawa, MJ Thompson, PC Taylor and P G LeComber, Materials Research Society, Pittsburgh, PA, 1991; 315-319.

[90] Bennett MS, Newton JL, Rajan K. Proceedings of the 7th EUPVSEC, Oct. 1987 Sevilla, Spain; pp. 544–548.

[91] Fischer D, Dubail S, Selvan AJA, *et al.* Proceedings of the 25th IEEE Photovoltaic Specialists Conference Washington D. C., USA,IEEE, New York, 1996; pp.1053–1056.

[92] Myong SY, Sriprapha K, Miyajima S, Konagai M. High efficiency protocrystalline silicon/microcrystalline silicon tandem cell with zinc oxide intermediate layer. Appl Phys Lett 2007; 90: 263509.

[93] Dominé D, Bailat J, Steinhauser J, *et al.* Proceedings of the Fourth World Conference on Photovoltaic Energy Conversion, Hawaii, USA IEEE, New York, 2006; 1465–1468.

[94] Buehlmann P, Bailat J, Dominé D, *et al. In situ* silicon oxide based intermediate reflector for thin-film silicon micromorph solar cells. Appl Phys Lett. 2007; 143505

[95] Sai H, Fujiwara H, Kondo M, Kanamori Y. Enhancement of light trapping in thin-film hydrogenatedì microcrystalline Si solar cells using back reflectors with self-ordered dimple pattern. Appl Phys Lett. 2008; 93: 143501.

[96] Heine C, Morf RH. Submicrometer gratings for solar energy applications. Appl Optics 1995; 34: 2476.

[97] Campa A, Isabella O, van Erven R *et al.* Optimal design of periodic surface texture for thin-film a-Si:H solar cells. Prog Photovolt: Res Appl 2010; 18:160–167

[98] Campa A, Krcˇ J, Topicˇ M. Two-dimensional optical model for simulating periodic optical structures in thin-film solar cells. Informacije MIDEM 2008; 38: 5.

[99] Isabella O, Moll F, Krcˇ J *et al.* Modulated surface textures using zinc-oxide films for solar cells applications. Phys Status Solidi A 207, 2010; 3: 642–646.

[100] Available from: http://www.pveducation.org/pvcdrom

[101] Green M A. Silicon Solar Cells: Advanced Principles and Practice. Sydney, Australia: Bridge Printery, 1995.

[102] Green MA, Zhao J, Wang A, *et al.* Very high efficiency silicon solar cells-science and technology. IEEE Trans Electron Dev 1999; 46(10) 1940–1947.

[103] Campbell P, Green MA. Light trapping properties of pyramidally textured surfaces. J Appl Phys 1987; 62: 243–249.

[104] Haase C, Stiebig H. Thin-film silicon solar cells with efficient periodic light trapping texture. Appl Phys Lett 2007; 91: 061116.

[105] Vazsonyi E, De Clercq K, Einhaus R, *et al.* Improved anisotropic etching process for industrial texturing of silicon solar cells. Sol Energy Mater Sol Cells 1999; 57: 179–188.

[106] Bailey WL, Coleman MG, Harris CB, *et al.* U.S. Patent 4137123, 1979.

[107] Iencinella D, Centurioni E, Rizzoli R, *et al.* An optimized texturing process for silicon solar cell substrates using TMAH. Sol Energy Mater Sol Cells 2005; 87: 725–732.

[108] De Wolf S, Schade K, Dekkers HFW, *et al.* In-line plasma surface etching and PECVD SiNx:H deposition for crystalline Si cell processing. Proceedings of 20th European Phtovoltaic Solar Energy Conference, 2005 Jun 6-10; Barcellona, Spain; pp. 729–732.

[109] Jansen H, de Boer M, Wensink H *et al.* The black silicon method. VIII. A study of the performance of etching silicon using SF6/O2-based chemistry with cryogenical wafer cooling and a high density ICP source. J Microelectron 2001; 32 769–777.

[110] Dekkers HFW, Duerinckx F, Carnel L *et al.* Plasma texturing processes for the next generations of crystalline Si solar cells. Proceedings of 21th European Phtovoltaic Solar Energy Conference, 2006 Sep 4-8; Dresden, Germany; pp. 754–757.

[111] Carnel L, Gordon I, Dekkers H, *et al.* Improvement of the short circuit current of thin film polysilicon solar cells using plasma texturing. Proceedings of 21th European Phtovoltaic Solar Energy Conference, 2006 Sep 4-8; Dresden, Germany; pp. 830–833.

[112] Dekkers HF, Agostinelli G, Dechertoghe D, *et al.* Improved performance of mc-Si solar cells by isotropic plasma texturing. Proceedings of the 19th European Photovoltaic Solar Energy Conference; 2004 Jun 7-11; Paris, France: pp. 412–415.

[113] Yoo J, Kim K, Thamilselvan M *et al.* RIE texturing optimization for thin c-Si solar cells in SF_6/O_2 plasma. J Phys D: Appl Phys 2008; 41: 125205.

[114] Moreno M, Daineka D, Roca i Cabarrocas P. Plasma texturing for silicon solar cells: From pyramids to inverted pyramids-like structures. Sol Energy Mater Sol Cells 2010; 94(5): 733-737.

[115] ARC Photovoltaics Centre of Excellence, 2009 Annual Report. Available from: http://www.pv.unsw.edu.au/research/annualreports.asp

[116] Inomata Y, Fukui K, Shirasawa K. Surface texturing of large area multicrystalline silicon solar cells using reactive ion etchin method. Sol Energy Mater Sol Cells 1997; 48: 237-242.

[117] Einhaus R, Vazsonyi E, Szlufcik J *et al.* Isotropic texturing of multi-crystalline silicon wafers with acidic texturing. Proceedings of the 26th IEEE Photovoltaic Specialists Conference; 1997 Sep; Anaheim, California; pp. 167-170.

[118] De Wolf S, Choulat P, Vazsonyi E *et al.* Towards industrial application of isotropic texturing for multi-crystalline silicon solar cells. Proceedings of the 16th European Photovoltaic Solar Energy Conference; 2000 May 1-5; Glasgow, UK; pp. 1521-1523.

[119] Winderbaum S, Reinhold O, Yun F. Reactive ion etching (RIE) as a method for texturing polycrystalline silicon solar cells. Sol Energy Mater Sol Cells 1997; 46, 239-248.

[120] Ruby DS, Zaidi SH, Narayanan S. Plasma texturization for multicrystalline silicon solar cells. Proceedings of the 28th IEEE Photovoltaic Specialists Conference; 2000 Sep 15-22; Anchorage, Alaska (Usa); 75-78.

[121] Damiani BM, Ludemann R, Ruby DS, *et al.* Development of RIE textured silicon solar cells. Proceedings of the 28th IEEE Photovoltaic Specialists Conference; 2000 Sep 15-22; Anchorage, Alaska (Usa); 371-374.

[122] Macdonald DH, Cuevas A, Kerr MJ *et al,* Texturing industrial multicrystalline silicon solar cells. Solar Energy 2004; 76, 277-283.

[123] Zolper JC, Narayanan S, Wenham SR, *et al.* 16.7% efficient, laser textured, buried contact polycrystalline silicon solar cell. Appl Phys Lett 1989; 55(22): 2363–2365.

[124] Abbott M, Cotter J. Optical and Electrical Properties of Laser Texturing for High-efficiency Solar Cells. Prog. Photovolt: Res. Appl. 2006; 14: 225–235.

[125] Stephens RB, Cody GD. Optical reflectance and transmission of a textured surface. Thin Solid Films 1977; 45: 19-29.

[126] Gittleman J, Sichel EK, Lehmann HW, *et al.* Textured silicon: A selective absorber for solar thermal conversion. Appl Phys Lett 1979; 35: 742.

[127] Ruby D S, Schubert WK, Gee JM, *et al.* US Patent No. 6091021, 2000.

[128] Ruby DS, Zaidi SH. US Patent No. 6329296, 2001.

[129] Koynov S, Brandt MS, Stutzmann M. Black non-reflecting silicon surfaces for solar cells. Appl. Phys. Lett. 2006; 88: 203107.

[130] Yablonovitch E, Cody GD. Intensity enhancement in textured optical sheets for solar cells. IEEE Transactions Electron Devices, 1982; ED-29: 300-302.
[131] Green MA. High Efficiency Silicon Solar Cells. Trans Tech Aedermannsdorf, Switzerland/Brookfield, VT, 1987; 70.
[132] Nelson J. The Physics of Solar Cells. Imperial College Edition; London, 2003; 279-282.
[133] Available from: XOP: http://www.esrf.eu/computing/scientific/xop/index.ht-ml
[134] Hermle M, Schneiderlöchner E, Grupp G *et al.* Comprehensive comparison of different rear side contacting methods for high efficiency solar cells. Proceedings of 20th European Phtovoltaic Solar Energy Conference, 2005 Jun 6-10; Barcellona, Spain; pp 810-813.
[135] Tucci M, Talgorn E, Serenelli L, *et al.* Laser fired back contact for silicon solar cells. Thin Solid Films 2008; 516: 6767–6770
[136] Schultz O, Glunz SW, Willeke GP. Multicrystalline silicon solar cells exceeding 20% efficiency Prog in Photovolt: Research and Applications 2004; 12: 553-558
[137] Rostan PJ, Rau U, Nguyen VX, *et al.* Low-temperature a-Si:H/ZnO/Al back contacts for high-efficiency silicon solar cells.Solar Energy Materials & Solar Cells 2006; 90: 1345–1352
[138] Sheppard CJR. Approximate calculation of the reflection coefficient from a stratified medium. Pure Appl Opt 1995; 4: 665-669.
[139] Taira S, Yoshimine Y, Baba T, Taguchi M. Proceedings of 22th European Phtovoltaic Solar Energy Conference, 2007 Sep 3-7; Milan, Italy; pp. 932-935.
[140] Caputo D, Forghieri U, Palma F. Low-temperature admittance measurement in thin film amorphous silicon structures. Journal Appl Phys 1997; 82: 733-741
[141] Tucci M, de Cesare G, 17% efficiency heterostructure solar cell based on p-type crystalline silicon. Journal of Non-Cryst Solids 2004; 338: 663-667.
[142] Tucci M, Serenelli L, De Iuliis S, *et al.* Amorphous/crystalline silicon heterostructure solar cell based on multi-crystalline silicon. Proceedings of 21th European Phtovoltaic Solar Energy Conference, 2006 Sep 4-8; Dresden, Germany; pp 902-905.
[143] Kreinin L, Bordin N, Broder G *et al.* Comparison of two BSF technologies suitable for high efficiency multi-crystalline solar cells. Proceedings of 21th European Phtovoltaic Solar Energy Conference, 2006 Sep 4-8; Dresden, Germany; pp. 855-858.
[144] Tucci M, Serenelli L, Salza E, *et al.* Dielectric Bragg back reflecting mirror in a-Si:H/c-Si heterostructure solar cell. Proceedings of IEEE Conference on Optoelectronic and Microelectronic Materials and Devices COMMAD; 2008 Aug 28-31 Sydney, Australia; pp. 273-276.
[145] Kray D, Hermle M, Glunz S. Theory and experiments on the back side reflectance of silicon wafer solar cells. Prog Photovolt: Res Appl 2008; 16: 1-15.
[146] Takahashi Y, Hirata K, Ogane A, *et al.* Rear side passivated monocrystalline silicon thin film solar cells with laser fired contact process. Appl Phys Express 2008; 1: 085002
[147] Grohe A, Fleischhauer B, Preu R, *et al.* Boundary conditions for the industrial production of LFC cells. Proceedings of Conference record of IEEE 4th World Conference on Photovoltaic Energy Conversion, 2006 May 7-12; Hawaii, USA: pp. 1032-1035.
[148] Hoex B, Peeters FJJ, Erven AJM *et al.* High-rate deposition of silicon nitride and silicon oxide films for surface passivation and (anti)reflection coating applications. Proceedings of the 15th International Photovoltaic Science and Engineering Conference, October 10-15 2005, Shanghai, China, pp. 1106-1110.
[149] Basore PA. PC1D version 5-3. University of New South Wales, Clugston DA. 1998.
[150] Nubile P, Ferreira da Silva. Bandgap narrowing in silicon solar cells considering the p-type doping material. Solid-State Electronics, 1997; 41: 121-124.
[151] Sinton R, Cuevas A. Contactless determination of current-voltage characteristics and minority-carrier lifetimes in semiconductors from quasi-steady-state photoconductance data. Appl Phys Lett 1996; 69: 2510.
[152] Henley F, Lamm A, Kang S *et al.* Direct film transfer (DFT) technology for ker-free silicon eafring. Proceedingsof 23th European Photovoltaic Conference; 2008 Sep 1-5; Valencia, Spain; pp.1090-1093.

[153] Biswas R, Zhou D. Enhancing Light-trapping and Efficiency of Solar Cells with Photonic Crystals. Proceedings of the Mater Res Soc Symp Materials Research Society 2007; 989: 0989-A03-02.

[154] Yu ZF, Raman A, Fan SH. Fundamental limit of nanophotonic light trapping in solar cells. National Accademy of science of the USA 2010; 107(41): 17491-17496.

[155] Almeida VR, Xu Q, Barrios CA, Lipson M. Guiding and confining light in void nanostructure. Opt Lett 2004; 29: 1209-1211.

INDEX

A

a-Si 15-21, 37-42, 44-7, 164-6, 277-83, 286-99, 310-18, 320-4, 326-33, 337-9, 344-6, 359-66, 372-7, 386-9, 446-61
  bare 463-4
  c-Si/i 330
  c-Si/i a-SiH/p 454
  c-Si/n 321
  deposition of 36, 38, 47-8
  device quality 37, 128
  edge of 280, 346
  function of 288, 450
  homogeneous deposition 49
  investigated 198, 234, 236-7
  mobility gap of 230, 237
  n-type c-Si/n-type 318
  obtained depositing 291, 454
  oxidation of 203-4
  p-type c-Si/p-type 318
  protocrystalline 18, 21
  single 455, 457
  single couple of 451, 454, 457
  stable 38, 387
  thick 38, 288-9, 324, 429
  thin 289, 291, 293
a-Si/c-Si interfaces, excellent 299
a -Si cell 12, 164
a -Si cylinders 463
a -Si emitter layer 339
a -Si film 202-3, 288
a -Si layer 345, 362, 463
  doped 344
a -Si network 16, 281
a -Si solar cell 165
a -Si structures 117
a -Si1-xCx 108, 110, 117, 127, 130, 133, 136, 138
a -SiC 16, 40, 169-71, 361, 410, 416
a -SiGe 16, 361
a -SiH 328, 330, 453
Absorbance 130, 178-9, 423, 429
Absorber materials 10, 406
Absorbing layers 171, 382
Absorption 21, 41, 104, 109, 177, 180-2, 198, 317, 335, 368, 374, 416-17, 426-7, 429-32, 463-4

Roberto Murri (Ed)
All rights reserved-© 2013 **Bentham Science Publishers**

Absorption coefficients 16-17, 41, 117-18, 134, 177-82, 184-6, 195, 198-9, 202, 208, 212-13, 220, 225, 359
  low 10, 41-2, 46, 382
  total 181-2, 184
Absorption processes 183
Acid, hydrofluoric 439, 443, 446
Acidic texturing, wet 438-9, 443
Activation energy 41, 43, 257, 318, 325, 346
Active layer 41, 137, 164, 360, 382, 416, 464-6
Active material 395, 463-5
ADIRR 201-4
AFM scan image 418-19, 424
Alloy triple-junction solar cell processor 52
AM1.5G spectrum 271-3
Amorphous 3-4, 10, 15, 19-21, 42-3, 125-7, 131-2, 140, 159, 167-9, 279-80, 290-1, 359-61, 402, 446-7
Amorphous films 161, 169, 324
Amorphous layers 19, 158, 325, 453, 455
  doped 337, 346
Amorphous materials 17-18, 118, 140, 150, 159, 182, 293, 363, 369, 455
Amorphous matrix 91, 150, 159-60
Amorphous phase 11, 33, 43, 131, 134, 158, 160-1, 167, 290-1, 309, 370, 372
Amorphous semiconductors 182, 184, 216, 226, 229
Amorphous silicon 4, 9, 11, 15-16, 20, 29, 39, 117, 164, 166, 169, 360, 362-4, 368-9, 401
  hydrogenated 108, 117, 158, 360, 372, 374
Amorphous silicon films 9, 360, 388
Amorphous silicon layer 21, 387
Amorphous silicon material 373, 377
Amorphous silicon modules 360
Amorphous silicon solar cells 157, 164, 379, 419
Amorphous silicon structure 167, 360
Amorphous solar cells 18, 376, 388
Amorphous superconductors 359
Amorphous thin films 169
Amorphous tissue 40, 369, 375, 380
Amorphous top cell 389
Amount 5, 9, 43, 45, 75-6, 281, 287, 300, 334, 365, 380, 396, 426, 439, 446
Analysis of thin films 157
Angle 85, 87, 99-100, 154-5, 201, 203, 206, 212-13, 215, 221, 231-3, 411-12, 431-2, 444-5, 447
Angle of incidence of radiation 187, 206, 212-13, 221
Angle of light incidence 189-90
Angular dependence 204, 213-14, 231, 233-4
Angular dependencies 204, 214, 235, 237
Angular reflectance transmittance Analyzer (ARTA) 422, 424
Annealing 18, 127, 132, 136, 169, 288-90
Annealing temperature 97, 132, 136-7

Anode 60, 62-3, 65-6, 70-1
Anti Reflection Coating (ARC) 5, 337, 339, 344, 397, 399-401, 441
Arrival rate 92-3, 95
Ashai U-type 417, 419-20
ASi, c-Si/n 322-3
ATLAS software 342-3, 346
Atmosphere 127, 129, 132, 309
Atmospheric Pressure Chemical Vapour Deposition (APCVD) 402-3
Atomic 94, 104, 146-7, 153, 169, 411, 417, 419
Atomic defects 308
Atomic force microscopy (AFM) 104, 146-7, 153, 157, 161, 165, 169-70, 198, 369, 417, 419
Atoms 14, 29, 35, 43, 58-62, 69, 79, 92-5, 99-101, 116, 245-6, 250-1, 281, 369, 402-3
  anion 102-3
  average number of 58, 60
  element 102
  single 94-5, 152-3
  sputtered 59-60, 70, 74
  surface binding energy of 58, 60
Average crystallite size 158, 160, 173
Average grain dimension 108

B

Back amorphous-crystalline silicon heterojunction (BACH) 338
Back surface field (BSF) 318-22, 324, 329, 342, 442, 452, 455-6, 460
Band gap 10-11, 15-17, 109, 245, 247, 257, 445
  graduated 3
Band structure 182, 243-4, 262
Barrier 310, 319-20, 322, 338, 346, 348, 454
Base contact 278, 318, 328, 335-9, 344-6
Basis 31, 152-5, 336
Beam splitter (BS) 114-16, 124
Beams
  diffracted 88, 152, 155
  reflected 201, 205
Beams incident 217, 221, 235
Bending simulations 319, 328, 333, 453
Bias voltage 76, 314
BK-7 substrate, thick 196, 199, 202-4
Bonding 4, 37, 281, 294, 403
Bonds 37, 43, 77, 91, 116-17, 127, 131-3, 281, 292, 308-9, 373, 403-5
Boron 17, 34, 40, 164, 293, 334, 407-8
Boron depod ZnO (BZO) 425
Bottom cells 46, 158, 387
Boundary conditions 223, 230
Boundary layer 32, 445

Bragg reflector 395, 449
Breakdown 22, 62-3, 290
Breakdown voltage 365
Buffer layer thickness 288, 331-2
Buffer layers 32, 35, 133-4, 157, 164, 295, 299, 320, 322, 326, 338, 344, 346
  i-a-Si 337
  intrinsic 293, 295, 326, 341, 453
Built-in 286, 319-20, 332-3, 380
Bulk a-Si 198, 289, 297
Bulk materials 14, 125, 147, 155, 258-9, 263, 280, 297, 310, 445
Bulk plasma 39, 366

C

C-Si 40-1, 43-6, 127-30, 134, 280, 286-7, 289-94, 298, 317-18, 320-4, 330-3, 362-6, 368-78, 380-1, 385-9
  inward 448, 450
C-Si/a-Si 280, 293, 348
C-Si absorber 280, 317, 452
C-Si absorber material 280
C-Si base 311, 317, 320, 455
C-Si BSF 320-1
C-Si bulk 318, 448-50
C-Si cells 41
C-Si films 44-5, 368, 370
C-Si grains 364, 376
C-Si layers 41, 43-4, 46
C-Si photovoltaic layers 44
C-Si solar cells 42, 44, 46, 133, 310, 432, 434
C-Si solar cells series 133
C-Si substrate 159, 169, 287, 295, 297, 310, 451
  doped 295, 320
C-Si surface 280, 286-7, 289, 291-3, 295, 297, 321, 324, 432, 435
  doped 286-7
C-Si surface passivation 287, 291, 295, 342
C-Si surface passivation quality 290, 293
C-Si wafer 279, 288, 291, 293, 296, 311, 317-18, 322, 435, 447, 451
  doped 296, 328
  passivated 288, 311
C-Si wafer thinner 277-8
Cadmium telluride 3
Calculations 31, 193, 197, 201, 207, 214-15, 231, 236, 283
  numerical 191-2, 201, 219, 230-1
Capacitance 269, 314, 316, 327
Capacitance transients 267-9
Capacitance values 268, 314-15, 320, 326

Capacitor 66-7, 326
Carbon content 117, 135-9, 169
Carceri 3, 81, 243
Carrier collection 346, 348, 389, 453-4
Carrier concentration 250, 262, 383, 409-10, 426
Carrier diffusion length 177-8, 217, 219, 231
Carrier photogeneration 182, 215-16
Carriers 8, 51, 109, 173, 183-5, 216, 221-2, 233-4, 244, 252, 264-5, 286-7, 297, 317, 379-80
  extrinsic photogeneration of 181, 183-4
Cathode 58-9, 62-7, 70-1, 79
Cathode sheath 64-5, 69
Cell
  based 277, 279, 322, 343, 395, 401, 416
  best 323, 335, 388
  heterojunction 277-8, 335, 460-1
  new 338, 366
  real 20, 441
  single-crystal 376, 437
Cell absorption 416, 447
Cell area 22, 335, 455
Cell characteristics 365, 380
Cell cost 382, 396, 458
Cell designs 171, 397
Cell efficiency 45, 164, 277, 291, 298, 338, 343, 348, 378, 396, 429, 460
  higher 277, 318
Cell efficiency values, good 146
Cell front side 333, 406
Cell manufacturing 278-9, 416
Cell parameters, main solar 243
Cell performances 133, 169, 320, 334, 386, 443
  c-Si Solar 133
Cell structures 24, 298-9, 317, 331, 340-1, 379, 429, 460, 463
Cell thickness 431-2
Cell window layer 416
Chain curve 193-5, 210-13, 215
Chamber 36, 38, 40, 66, 75, 78, 83-4, 149, 345
Characteristics, spectral 104, 192-5, 197, 213-14, 226
Charge 51, 67, 69, 261, 265-6, 281, 287, 289, 402, 404-5
Charge carriers 40, 82, 243-4, 249-52, 261, 265-7
Chemical vapor deposition (CVD) 3, 14, 29-36, 45, 53, 82, 133, 140, 158, 287, 359-60, 367, 374, 382, 401-2
Chemical solution deposition (CSD) 410
Chemical vapour deposition, enhanced 108
CIS and CIGS-based solar cells 361
Clusters 13, 40, 92, 94-5, 103
Coating layers 186, 191, 208, 213

Coatings 29-30, 32-3, 35, 68, 115, 399, 456, 460
Coefficients 177, 180-1, 183, 187, 217, 227-8, 262
  extinction 130-1, 178, 187, 411-12
  relevant electronic transport 244, 262
  thermal accommodation 93
Collisions 34, 37, 58, 61-2, 71, 77, 83, 403
  inelastic 61-2, 365
Component system 93
Components 10, 77-9, 83-4, 93, 179, 182, 191, 195, 197, 200, 203, 205, 216-17, 219, 247-9
Components of absorption of light 177-8
Composition 29, 31, 68, 77, 81, 147, 150, 152, 169, 301-2, 439, 446
Compound semiconductors 81, 84, 92, 247, 251
Concentration 37, 40, 42, 182, 216-17, 222-3, 226-7, 243, 253, 261, 263, 265, 268, 283, 300-2
  bond 116-18, 133
Conduction 17, 228-9, 245-7, 251, 254, 265, 404
Conduction band (CB) 6, 16, 103, 215, 230, 244-6, 265-7, 280-3, 296, 312, 318, 322, 373
Conduction process 17, 244-5, 247, 249
Conductivity 154, 217, 243-6, 249, 254, 262, 278, 324-5, 329, 332, 337, 345, 375-6, 408, 429
  lighted 325
Conductivity tensor 243, 247-9
Configuration 47-51, 67, 90, 147, 155, 164, 182, 329, 377-9, 382-3, 386-7, 403, 416, 463
  cluster 29, 51-2
  cluster PECVD 52
  in-line 29, 51
  plasma box 47
  superstrate 378-9, 382-3, 386
  thin film cell 416
Constant 53, 62-3, 67-8, 93, 127, 153, 180-1, 185, 231, 254-5, 258, 268-9, 272-3, 295-6, 311-12
Constant photocurrent method (CPM) 184
Construction of solar cells 177
Contact layers 17, 382, 386
Contacts 17, 19, 157, 164, 172, 253-8, 263-4, 292, 333-4, 339-40, 342, 344-6, 382-3, 385-6, 448-9
  doped 346-8
  rear 8, 422, 447, 452
Contaminants 38, 51, 101-2, 300, 388
Contaminations 41, 43, 50, 53, 77, 83, 300, 302-3, 306-7, 317, 434
Convergent beam electron diffraction (CBED) 151
Conversion efficiency 3, 5, 8, 18-19, 23, 129-30, 272, 278-9, 326, 360, 362, 368, 389, 401
  higher 3, 9, 377, 379
Copper indium diselenide 3
Copyright 117, 126, 128-32, 134-8, 149, 152-4, 159-63, 165-8, 170, 172-3, 426-7
Corning glass 138-9, 324, 425
Correlation energy 281, 283
Couples 154, 255, 430, 450-1, 454-5, 465
Cracks 42-3, 166, 254, 303-4, 441
Craters 135, 424, 426

Critical thickness hcrit 97
Crystal nucleation 3
Crystalline 10-11, 22, 33, 100, 109, 125-6, 130, 150, 156, 249, 366, 388
Crystalline silicon 17, 167, 281, 360, 369, 373-4, 405, 432
Crystalline silicon solar cells 5, 431
Crystalline volume fraction 42-3, 108, 126, 133, 135, 137-8, 364-5, 375, 381
Crystallinity 4, 11, 21, 44, 133-6, 173, 362, 372, 381
Crystallites 42, 44, 79, 100, 126-7, 139, 155, 159-60, 169, 446
Crystals 19, 81, 97, 99-102, 121, 160, 182, 251
Current density 63, 73, 172, 222-3, 247-8, 261, 311, 313-15, 320, 323, 330, 338, 341, 377, 389
Current voltage measurements 311, 315
Curves, broken 190, 193-5, 204, 210-15, 226
CVD coatings 32-3
CVD processes 30-3, 408
CVD reaction 29-30, 32-3
CVD techniques 30, 33, 35

D

Damage 153, 303-6, 315, 365, 439, 459
Dangling bonds (DB) 37, 45, 90, 109, 127, 229-30, 280-2, 286-7, 289, 294-5, 307, 309, 313, 369, 373
Dark 6-7, 133, 257, 273, 310, 316-17, 319, 324-5, 328, 452-3
Dark condition 7, 313-15, 330, 453
DBR/Al 451, 456-8
DBR structure 451, 454-6
DC Diode 75
DC glow discharges 63, 66
DC sputtering 69, 78
Debye temperature 252-3
Deep level transient spectroscopy (DLTS) 16, 243, 266, 268
Deep states 16, 243, 265-6, 270, 373
Deep states properties 265-6
Defect concentration 283
Defect density 20, 40, 44, 133, 280, 283, 286, 292, 296-7, 310, 315, 318-20, 323, 326, 329
Defect distribution 280, 283-4, 316
Defect formation 283
Defect pool 281, 283, 285
Defects 16, 18, 20, 32, 41, 45, 83, 97, 100-1, 280-1, 283-5, 293-5, 320-1, 368-9, 373
  interstitial 101, 281
  neutral 284-5
  self-interstitial 101
Deformation, acoustic 251-2
Degradation, light-induced 46, 108, 361, 364, 374, 389
Density 11, 14, 16, 18, 23, 45, 61, 65, 76, 165, 184, 230, 244, 284-5, 435

Density of states (DoS) 3, 11, 16-18, 20, 154, 184, 227-9, 232-6, 280-1, 284, 286-7, 295-8, 312, 316, 323, 453
Dependence 119-20, 136, 203, 213-14, 216, 222, 231, 233-4, 294, 309, 313-14, 332, 337, 381, 398
Depletion region 17, 263, 270, 313, 317, 320, 326
Deposit 16, 23, 42, 53, 60, 68, 77, 164, 295, 305, 332, 344, 346, 368, 428
Deposited layers 19, 39, 340
Deposition 10-11, 23, 34-5, 38-40, 44-5, 83-4, 98-9, 278, 344-6, 359-60, 363, 365, 375, 388, 401-3
  epitaxial 102-3
  high quality 47
  ion-assisted 77
  large area 15, 46, 49-50, 162
  low temperature 29, 387-8
  n-a-Si 344
  sputter 59, 66, 68, 78-9, 408
  uniform 37-8, 47, 49
Deposition chambers 31, 33, 47, 51, 82, 102
Deposition conditions 11, 14, 16, 36, 43, 158, 163, 290, 295, 332, 359, 363, 369, 388, 401
Deposition kinetics 31
Deposition parameters 3, 10, 15-16, 19-20, 33, 50-1, 166, 366, 373, 382, 385, 403-4
Deposition process 15, 29, 45, 50-1, 59, 77, 79, 81, 84-5, 170, 186, 250, 362-3, 367, 435
Deposition process parameters 334, 415
Deposition rates 29, 35-6, 38-9, 44-5, 48, 69, 71-2, 89, 92-3, 365, 368, 402
  higher 38-9, 46, 75, 366
  low 36, 38, 75, 166, 381, 402
  very high 39-40
Deposition sequence 382-3
Deposition system, in-line 51
Deposition techniques 3, 22, 29-30, 35, 38, 47, 133, 363-4, 366, 382, 388, 408
Deposition temperature 22, 35, 162, 287, 290-1, 296-7, 334, 403, 408-9, 415, 426
Depth 104, 135, 158, 169, 186-7, 212, 228, 426, 445
Design 3-4, 16, 19, 22, 31, 47, 52, 121, 163-4, 171, 243, 377-80, 429, 433, 463-4
Development 3, 10-11, 22, 29-30, 34-5, 46, 51, 53, 119, 177, 257, 270, 333, 360, 432-3
Device thickness 395-6
Devices 3, 7, 9, 23, 35, 129-30, 177, 272-3, 311, 326, 344-6, 368, 379-80, 395-6, 416
  electronic 4, 10, 243, 246
  optoelectronic 247, 373
  photovoltaic 5-6, 9, 21, 35, 360
DHF 300-1, 305-7
DHF-dip 306-7, 309
Dielectric bragg reflector (DBR) 449-52, 454-8, 461, 463-4
Dielectric films 178, 185, 397-8, 454
Diffraction patterns 19, 89, 151-2, 155, 159-60, 167
Diffusion coefficient 93-4, 101, 222, 293
Diffusion energy 94, 294
Dilution 20, 31, 36, 38, 42-3, 45, 180, 324, 329, 367, 371-2
Dilution ratio 3, 19-20

Dimensions 14, 103, 113, 221, 243, 255, 257, 259, 437
Direct film transfer (DFT) 459
Direction 91, 97, 120-1, 182, 188, 201, 205, 216-17, 220-1, 248, 261, 263, 396, 426, 447
Discharge 63, 65-7, 69, 71, 73
Distance, increasing 210, 212, 220
Distribution 17, 48, 173, 177, 184-5, 193, 223, 229, 232, 237, 281, 283, 296-7, 309, 314-15
  energy band 280-1
  spatial 177, 199, 201, 205, 212-13, 220-1, 238
Dit values 305
DIW 300-1, 305-6
DIW rinsing 305
DLTS signal 269-70
DLTS technique 243, 267-8, 270
Donor-like states 227-9, 233-4, 237
Donors 17, 246-7, 294, 404
Doped a-Si 40-1, 229, 278, 284-6, 293, 295-6, 317-19, 324, 326, 333, 335, 342-5, 453
Doped c-Si 296, 317, 319-20, 322, 324
Doped layers 38, 287, 293, 295, 299, 324, 336-7, 345, 380, 419
Doping 15-17, 40-1, 81, 102-3, 146, 277, 293-4, 320, 322, 329, 360, 446-7
Doping concentrations 318, 324, 326
Doping level 280, 411-13
Doping of a-Si 294-5
Doping ratio 135-6, 324, 326
DOS parameters 231-2, 236
Drying 302-3, 334
Dual Beam Photoconductivity (DBP) 20

E

E-beam 339-40, 345, 455
Effect, mirroring 460-1, 463
Effective lifetime 288-9, 292, 305
Efficacy 454-5, 463
Efficiency of photogeneration of free carriers 177
Effusion cells 82, 84-5
Electric field 11, 61-6, 70-2, 76-7, 119-20, 147, 187-9, 192, 205, 209, 218, 261, 263-4, 379-80, 403
Electric vector 185-9, 191-2, 205-6, 209-10, 213-15, 218
Electrical conductivity 40, 46, 216, 222, 243, 248, 253, 359
Electrical properties of semiconductors 243, 245, 247, 249, 251, 253, 255, 257, 259, 261, 263, 265, 267, 269, 271
Electrode gap 365
  small 366-7
Electrode spacing 37-8
Electrodes 29, 34, 36, 39, 45, 47-9, 60, 62-5, 67, 69-70, 216-18, 220, 361, 365, 378
  ladder-shaped 47-8
  transparent 378-9

Electron beam 86-7, 89, 147-8, 152
  high-energy 147, 150
Electron beam evaporation 77, 363
Electron concentration 185, 86-7, 266
Electron density 61, 65, 365
  high 38, 44
Electron Energy Loss Spectroscopy (EELS) 152
Electron gun 87
Electron holes 245, 247
Electron mobility 170, 245, 247, 251
Electron sources 78, 147
Electron states 177-8, 244
Electron transport 373, 376
Electron trap 266
Electronic properties 16, 165, 389
Electronic states 121, 230-1, 236-7
  density of 237
Electronic states parameters 177, 226
Electrons 4-6, 60-7, 70-1, 75, 77, 147-52, 222-3, 227-8, 244-7, 249-51, 280-4, 294-5, 373, 380, 403-6
  backscattered 147, 149
  donor 246
  drift mobilities of 183, 222
  equilibrium concentrations of 223, 229
  hot 14, 365
  photogenerated 40, 183
  photogeneration of 183
  recombination rates of 222
  valence 245-6
Emitter contacts 339, 348
Emitter layer 293, 317, 320, 324, 326, 344
Encapsulation 441-3
Energy
  adsorption 93-4
  binding 58, 60, 246
  free 31, 96, 281
  potential 62
  unit 227, 229
Energy gap 3, 6, 41, 43, 178, 181-3, 215-16, 231, 233, 245, 250-1, 280, 282, 298, 318
Energy gap values 233, 245
Energy input 10, 63
Energy pay-back time (EPBT) 10
Energy position 265, 267, 295, 298
Entropy 103, 282-3
Envelopes 190, 193-4, 196-8
Epi-layer 291

Epi-Si 290-2
Epilayer 96-9, 291, 320
Epitaxial films 81, 96, 99, 257, 263, 289
Epitaxial layer 4, 32, 82, 89, 97
Equilibrium 14, 66, 136, 229, 281-2, 288, 403, 405
Equivalent circuit 6, 8-9
Estimate sample thickness 190
Etched surface 303, 305, 424, 442
Etching 45, 58, 159, 301, 341, 344, 367, 431, 441, 443, 446
Evaporation 10, 68, 86-7, 278, 339
Excitation frequency 23, 36, 38, 44-5, 47-8
Excitations 61, 118-19, 121, 135, 402
Experimental conditions 32-3, 35, 214, 219, 231
Experimental data 103, 197, 204, 237, 252, 288, 293, 316, 450-1, 456
External reflectance thickness 456, 460

F

Fabrication of semiconductor devices 102, 300
Fermi energy 244, 380
Fermi level 17, 46, 229, 280-1, 283, 293, 295-7, 312, 314, 322, 326, 329, 406
  quasi 286, 320-1
Field 29, 47, 61, 66, 70-1, 73, 87, 146, 158, 173, 248, 259, 262, 303, 367
Fill Factor 8, 337-8, 342, 458
Film growth 21, 37, 76, 81, 87, 95, 159, 297, 363, 365-6
Film structure 3-4, 16, 19, 189, 376
Film thickness 19, 47, 166, 168, 177, 186, 190, 193, 197-8, 214, 257, 296, 324, 326, 408-10
Films
  air-semiconductor 186
  based 108-9, 133
  deposited 18-19, 68, 76, 79, 401
  doped 40, 295
  evaporated 68, 78
  growing 37, 69, 79, 81, 93
  hydrogenated amorphous silicon carbon 117, 129
  intrinsic 40-1, 128, 296
  investigated 209, 260
  multilayer 132, 137
  obtained 402-3
  polycrystalline 4, 169
  protocrystalline 3, 19
  relatively thick 190, 196
  resulting 74, 363
  rich 403
  semiconducting 157-8
  silicon-based 158, 160-1

single 188, 196, 216
thick 225-6, 403
thicker 96
uniform 13, 37
Films for solar cells 128
Films growth 295-6
Filter 121-2, 124
Flow rates 29
Fluorescence 121, 123-5
Fluxes 77, 79, 85-6, 92, 329
Focused ion beam (FIB) 104
Formation 10, 34, 38, 43, 45, 60-2, 73, 82, 91, 94, 100, 104, 127, 131-3, 136
Forward bias 267, 311, 313-14
Fourier spectroscopy 111
Fourier transform 108-10, 113-15
Fourier transform spectroscopy 110, 112-13
Free carriers 6, 16-17, 110, 177, 183-4, 216-17, 221, 230, 286
Free electrons 73, 103, 177, 183, 228, 365, 368, 373, 403
Frequencies 21, 29, 39, 44, 47, 66, 109-11, 113, 115-16, 119, 123, 271, 314, 326, 373
plasma excitation 366
radio 21, 34-5, 61, 63, 254, 260
Front cell thickness 395
Front contact layer 162, 164
Front surface 5, 24, 188, 206-9, 212, 214, 218, 220, 271, 337, 397, 431-2, 434, 437, 443
Front surface reflection coefficient 207
Front ZnO layers 420, 428
FTIR 108-10, 127
FTIR and Raman spectroscopy 108-10
FTIR spectroscopy 109-15, 117, 127, 129, 133
FTIR technique 110-11
Function of doping dilution 326
Function of film thickness 326, 409
Function of oxygen flux 415
FWHM 118, 129-32, 156-7, 167
FZ c-Si 288-9

G

Gap region 338, 342-3, 348
Gas 3, 15, 36, 38, 58-63, 68, 104, 162, 164, 185, 247, 360, 363, 367, 402
reactive 60, 68, 74-5
Gas atoms 60-1
Gas flow sputtering 78
Gas mixture 34, 39, 325, 329, 365, 367, 402-3
Gas precursors 31, 33, 162
Gaussian distribution 132, 191-3, 195, 208, 211-12, 218, 230, 232, 283-4

Geometries 36, 72-3, 90-1, 155, 254, 257, 263, 342, 380, 432-3
Glass 4, 9, 11, 20, 23, 35, 50, 68, 160, 166-7, 279, 371, 378, 411-12, 416
Glass substrate 4, 11, 49, 157, 360, 379, 382, 411-12, 430, 447
Glow discharge 34-5, 58, 60-3, 173
Glow region, negative 63-5
Graded energy gap semiconductors 177, 216
Grain boundaries 23, 41, 100, 109, 125, 128, 152, 158, 368-9, 375-6, 381, 441
Grain dimensions 167, 381
Grains 43, 100, 167-9, 369, 437, 440-1
Growing 36, 44, 77, 97, 359-60
Growth
  heteroepitaxial 92
  layer-by-layer 69, 95
Growth chamber 83, 89
Growth conditions 14, 16, 81, 103, 368
Growth mechanisms 3, 21, 30-2, 82, 89, 166
Growth modes 96
Growth of high-quality a-Si 37-8
Growth parameters 104
Growth processes 10, 15, 18, 87, 93-5, 146, 157, 166, 250
Growth rate 38, 44-5, 82, 86, 365, 367, 369, 451
Growth techniques 81-2
Growth temperatures 98, 104
GZO films 164

H

H/a-Si 311, 315, 366, 368-9, 374
H-based solar cell 379
H/c-Si 159, 164, 277, 298, 310, 406
H/c-Si/a-Si 406, 451, 458
H/c-Si cells 165
H/c-Si heterojunction 345, 454, 460
H/c-Si heterojunction cell 333
H/c-Si heterojunction cell fabrication processes 278
H/c-Si heterojunction solar cell 452, 457
H/c-Si heterostructure 335, 452
H/c-Si heterostructure solar cells 414, 452
H/c-Si HJ 327-8
H/c-Si HJ sample 297
H/c-Si interface 165, 287, 290, 295, 297-9, 309, 326, 346, 457
H/c-Si interface defects 346, 348
H/c-Si p-type HJ sample 311, 315
H/c-Si Solar Cell 317, 452
H/i-a-Si 319
H/p-a-Si 330, 452

H/p-cSi HJ solar cell 327
H/SiC multilayers 108, 133
H/SiNx 344, 346, 450-1, 454-8
H/SiNx/Al 450-1, 456-8
H/SiNx structures 454
H-terminated Si surfaces 301, 308-9
H/μc-Si 362, 368
Hall coefficient 243, 254, 256-7, 261-4
Hall coefficient measurement 264
Hall coefficient value 263, 265
Hall effect 243, 260-1, 263-4
Hall mobility 243, 256, 260, 262, 264, 407-8
Haze 395, 417-18, 420, 426
Heterojunction 3-4, 10, 164, 277, 280, 326, 329-30, 339, 344, 395, 401, 454
Heterostructure 320, 328-9, 339, 452-5, 459
Heterostructure cell 333, 406
  double 319
HF-dip 307-8
High deposition rates 21, 23, 39, 44-5, 47-8, 367-8, 403
High frequency 29
High-quality a-Si 37-8
High resolution (HR) 112, 122, 124, 159
High-resolution transmission electron microscopy (HRTEM) 173, 291
High stretching mode (HSM) 128
High substrate temperatures 43, 166
High temperature deposition 22-3
High temperatures 127, 247, 268-9, 314, 335, 342, 401-2
HJ cell efficiencies 288, 327-8
HJ cell efficiencies and IPL 326
HJ cells 277, 318, 320, 324, 332, 334-5
  similar 322, 329
HJ n-cSi 320
HJ samples 288, 291
HJ solar cell 288, 293, 310, 317, 322-3, 332
HJ solar cell efficiency 288
HJ solar cell technology 334
HJ solar cells performances 309
HJ structure 318-19, 321
Hole collection 320-1, 329, 377, 380
Holes 5-6, 104, 177-8, 182-3, 222-3, 227-9, 245-7, 266, 286-7, 321, 346, 373, 377, 380, 443
Homojunction c-Si 278
Hot plate (HP) 291-2
Hot wire (HW) 30, 33-4, 133, 367, 374, 402
Hot wire chemical vapor deposition (HWCVD) 34-5, 133-4, 402
HWCVD solar cells 133, 375
HWCVD solar cells series 134

Hydrogen 15-16, 18, 20, 90, 109, 129, 135, 281-2, 287, 292-3, 360, 373, 388, 401-2, 405
Hydrogen content 288-9, 375, 401, 403
Hydrogen dilution 15, 20-1, 126, 136, 140, 161, 383, 388
Hydrogen effusion 293, 295
Hydrogenated microcrystalline silicon films 117
Hydrogenated silicon films 158, 160

I
I-a-Si 346, 455
I-layer 38, 134-5, 364, 380, 386, 389
IBC cells 335, 338, 343
IBC-HJ solar cells 336
IBC-SHJ cell 337-8, 340
IBC solar cell 335
Ideal solar cell 6-7
IL 7, 271, 273
Illumination 6-7, 18, 151, 185, 188-9, 192, 198, 201, 208-9, 216, 218, 226, 235, 272-3, 374
Illumination conditions 273
Illumination intensity 185, 215, 223, 225-7, 232-3, 235, 238, 271
Imperfections 249-50
Impinging wavelengths 463-5
Impurities 9, 47, 69, 81, 84, 101, 109-10, 117, 223, 246-7, 249-50, 265, 300, 359, 407
Impurity and defect levels 265, 359
Incidence 87, 89, 187, 206, 212-13, 221
  angle of 24, 87, 155, 190, 203, 205, 213-14, 217, 220
  plane of 185-9, 191-2, 202, 205-6, 209-10, 213-15, 218
Incident 76, 88, 119, 121, 218, 417-18
Incident light 119, 205, 207, 397-8, 416-17, 423, 428, 447
Incident photons 118, 212, 214-16
Incident radiation 110, 179, 464-6
Indium tin oxide (ITO) 162-3, 291-2, 333-4, 337, 341, 382-3, 407, 412-14, 416, 463
Industrial multi-crystalline silicon solar cells 439
Influence, evident 231-4
Influence of Optimised Wet-Chemical Treatment on Test HJ Solar Cells 309
Influence of Sample Parameters and Experimental Conditions 208
Information 110, 140, 146-7, 152-5, 158, 185, 236, 250, 265, 271, 313, 371-2, 443
Inset 117, 130-1, 160-1, 289, 292, 410-11
Insulators 75, 81, 244-5, 339, 359
Interact 81, 249, 251, 265-6
Interaction 13, 18, 61, 116, 120, 147, 152-3, 245, 249, 251
Interdigitated Back Contact (IBC) 335-6, 344
Interdigitated contact solar cell 344
Interface 21, 146, 164, 186-7, 223, 280, 285-92, 297-9, 319-20, 322-4, 326, 333, 420-3, 428, 453
  first 397
  rough 188, 407, 416-17, 420, 422
Interface plane 97

Interface state densities 165, 305
Interference 87, 192, 200, 207, 209, 214, 218-19, 221, 238, 429-30
Interference effects 207, 213-16, 397
Interference fringes 190, 193-6, 198, 212-13, 216, 224, 447
Interferogram 110, 114-15
Interferometer 110-11, 113-16, 121
Interlayers 21
Intermediate layer, transparent 387-8
Intermediate reflecting layer (IRL) 428-9
Intrinsic a-Si 40, 281, 285, 287, 289, 293, 295-6, 320, 322, 337, 344-6, 373, 429
Intrinsic layer 11, 18, 21, 38, 41-2, 50, 129, 140, 164, 288, 295, 299, 368, 380, 422-3
Intrinsic semiconductors 246
Ion-assisted deposition (IAD) 77
Ion-beam sputtering (IBS) 77
Ion bombardment 45, 79, 365-6
Ionization 58-9, 61, 65, 71, 155, 250
Ions 34-5, 58-61, 63-6, 69, 77-9, 301, 367, 403
  positive 59-60, 366
IPL of a-Si 327-8
IQE 337, 345, 347, 455-7
IR radiation 116
IR spectra of hydrogenated microcrystalline silicon films 117
ITO films 163, 332-3, 412, 414
IV characteristics, lighted 319-20

J

J_{sc} 134, 164, 309, 323-4, 329, 335, 337-8, 342-5, 400, 422, 426, 428, 430-1, 458-9
Junction 3, 5-6, 10, 40-1, 263, 267, 273, 286, 291, 303, 314, 318, 432

K

Kaufman source 77-8
Kinetic energy 62, 87, 302, 403

L

Large areas 29, 43, 46-8, 50, 52, 164, 365, 419
Large scale thin films deposition 47
Laser treatment 169-71, 395, 455
Lasers 23, 30, 116, 119, 121, 123-5, 233, 247, 401, 431, 443, 454, 456, 458
  visible 121, 123-4
Lattice 40, 92, 100-1, 119, 373
Lattice atoms 251
Lattice parameters 94, 97-8
Lattice structure 250

Lattice vibrations 250
Layer-by-layer 96
Layer depositions 22, 50, 315-16, 329, 454
  subsequent 307, 309
Layer growth 41, 295
  subsequent thin film 300
Layer Parameters 456, 460
Layer structure, double 191-2, 196, 199, 208-10, 217, 223
Layer thickness 98, 133, 189, 259, 329, 346, 426
  intrinsic 46, 346, 422
Layer transfer processes 22-3
Layers
  a-SiNx 455
  dielectric 399-400
  extra 99-100
  first 96, 162, 289, 295, 297, 379
  textured 445
  thicker 96, 289, 295, 297
  topmost 91
  type 40
Lenses 122, 148-9, 151
  electromagnetic 147, 150-1
  objective 124, 148-9, 151-2
Lifetime 17, 182-3, 185, 265, 277, 288, 292, 305-6, 376, 380, 389, 395, 405-6
Light 3-5, 7, 10-11, 23-4, 118-19, 171, 177-8, 182, 194-5, 325, 382-3, 396-7, 416-17, 431-3, 447
  inelastic scattering of 118-19
  reflected 5, 421, 423, 432, 447
  scattered 109, 119-22, 124, 418, 422
  scattered sun 406-7
  second component of 195
  wave nature of 177
Light absorption 3-4, 24, 162, 171, 177-9, 182, 220, 380, 395-6, 416, 447, 464, 466
Light confinement 395-6
Light incidence 189-90
Light intensity 185, 238
Light scattering 162, 217, 385, 397, 408, 416-17, 426
Light soaking 3
Light trapping 23-4, 164, 207, 376, 382, 385-6, 389, 395-6, 406-8, 410, 416, 432, 463
Light-trapping 432, 442, 465
Light trapping mechanisms 23-4, 34
Limitations 66, 122-4, 295, 360-1, 388
Longitudinal 125, 251-2
Losses 9, 108, 122, 124, 188, 271-2, 291, 293
Low temperature process, using 277-8
Low temperatures 15, 34, 40, 244, 252, 288, 290, 293, 332, 336, 341, 363-4, 370, 386
LPCVD (Low Pressure Chemical Vapor Deposition) 33-4, 383, 402-3, 408, 428

LSM (low stretching mode) 128

M

Magnetic field 70-1, 74, 77, 182, 215, 223, 247-9, 254, 256-7, 263-4
Magnetrons 70-2, 76-7
Market 3, 9-10, 46, 121, 359-61, 417, 431, 459
Material properties 14-15, 158, 265, 359, 365
Material SiH_4 455
Materials 3-6, 10, 16, 67-8, 108-9, 146-7, 154-5, 243-7, 283, 300, 317-18, 359-60, 364, 372-4, 396-8
  a-Si alloys 15
  crystalline structure of 154
  device grade 128-9
  investigated 173, 177-8, 185, 198, 218, 234, 249, 253
  nanocrystalline 81
  new 140, 360-1
  sputtered 68, 77
  undoped 283, 285
Matrix 101, 109, 129, 132, 136, 138, 179, 443
Matter 116, 118, 152, 154, 303, 365
Maximum intensities 88, 129, 156, 200-1, 203, 205
Mc-Si 329, 374-6, 452, 458
Mean free path (MFP) 14, 62, 69, 71, 78-9, 83, 367
Measurements, c-Si layer 46
Medium range order (MRO) 108, 133, 140
Metal contacts 271, 277, 321-3, 332, 341, 401, 437
Metal electrode 406, 453-4, 459
Metal-Organic Chemical Vapor Deposition (MOCVD) 35, 82
Methods, contactless 186, 253-4, 260
Michelson interferometer 110, 113-16
Micro-wave (MW) 36, 39, 45, 260, 291-2, 360, 435, 455
Microcrystalline 3, 16, 19-20, 41-4, 109, 126-7, 129, 131, 146, 366, 377, 386, 389, 406
Microcrystalline films 15, 45, 375
Microcrystalline phases 19, 21, 131, 369-70
Microcrystalline silicon 29, 36, 39, 46, 108, 117, 127, 140, 166, 290, 320, 359-62, 364, 374-5, 388-9
Microcrystalline silicon cell 165, 381, 386-7
Microcrystalline silicon films preparations 37
Microcrystalline silicon layers 46, 127, 387
Microcrystalline silicon solar cells 108, 140, 376
Microcrystalline silicon thin film solar cells 11
Microcrystallinity 19-21
Microelectronic 29, 34-5, 317, 454
Micromorph cells, tandem 428-9
Micromorph tandem cell 12, 386, 428
Micromorph tandem cell concept 361, 377
Micromorph tandem silicon solar cells 386

Microscope 124-5, 147, 150-2, 154
Microscopy 146, 153, 169-70, 419
Microstructure 18, 29, 42, 46, 60, 79, 150, 163, 359, 369, 376, 388
Microstructure evolution 15, 45
Microstructure factor 108, 128
Midgap 17, 229, 265, 267, 281, 294-5, 297, 326, 404, 406
Minimization 121, 196-8, 236
Mirror 114-16, 122, 288, 395, 442, 452, 454-5, 458, 462, 466
  moving 114-16
Misfit dislocations 96-8
Mobility 69, 185, 234, 243-4, 249-53, 377, 409-10, 426, 455-6, 461
  drift 221-2, 244, 262
Model 85, 103-4, 168, 189, 204, 216, 221-2, 250, 281, 286, 289, 314-16, 340, 445, 458
  defect pool 281, 283
Modes 96, 126-31, 136, 140, 296, 455
  vibrational 108
Modules 3, 44-5, 360-1, 366, 379, 400, 406, 442
Molecules 29, 34-5, 60-2, 81, 84-6, 93-4, 365, 403-4
Molecular beam epitaxy (MBE) 81-3, 85-7, 89, 91, 93, 95, 97, 99, 101-3
Mono- layer (ML) 83, 89, 96, 104
Morphological and Structural Properties 146-7, 149, 151, 153, 155, 157, 159, 161, 163, 165, 167, 169, 171, 173
Morphology 32-3, 78-9, 87, 146, 162-4, 169, 419, 424
Multilayer structure 81, 177-8, 189, 191, 205, 207-8
Multilayers 68, 132, 136, 147, 157, 189, 451
  a-Si1-xCx/SiC 127, 129
MW plasmas 39, 45

N

N-a-Si 319, 322, 324, 340, 344-5, 455
N-type 17, 41-3, 186, 279, 283-8, 295-6, 298, 317, 319-20, 324, 326, 333, 335, 338-40, 428
N-type a-Si 11, 41, 291, 296, 315, 318, 321, 324, 329, 336, 343-4, 346, 404, 420-1, 452
  dark condition of 311
N-type c-Si 318, 320, 322, 324, 333, 344, 452, 460
N-type c-Si base 318, 324
N-type c-Si wafer 279, 322, 343
N-type doping 102-3, 294, 447, 456, 461
N-type layers 18, 378, 380
N-type semiconductor 266, 407
N-type Si 269-70
N-type wafers 338, 342, 344
Nano-crystalline silicon films 140, 159
Nanocrystalline silicon films 125-7, 133, 140
Nanocrystalline silicon solar cells 140
Nanocrystals 104, 109, 125, 136, 157, 369, 371

Nanostructured films 109, 136
Nanostructured silicon carbon films 108, 127, 133, 136
Nanostructures 14, 146-7, 157, 171
Native oxide films, layer-by-layer growth of 309
Nc-Si 4, 158, 364
Negative glow 63-6
NH_4F solutions 301, 306-7
Nitrogen 36, 38, 403-4, 412
Normalized photovoltaic parameters 460-1
Nowak, Marian 177-8, 180, 182, 184, 186, 188, 190, 192, 194, 196, 198, 200, 202, 204, 206
Nucleation 15, 19, 43, 81, 92-5
Numerical model 277, 315, 395

O

Ohmic contacts 253-7, 264, 322
  good 254, 324
Open circuit voltage 24, 39, 164, 271-2, 277, 311, 380-1
Optical absorption 10, 21, 180, 182, 361, 383, 385
Optical inhomogeneity 177, 186, 204
Optical parameters 178, 185-6, 201, 206, 208, 219, 231, 238
  values of 179, 186, 192, 212, 221
Optical properties 76, 109, 163, 177-8, 182, 234, 332, 337, 359, 363, 372-3, 382-3, 385, 389, 446-7
Optical Properties of Semiconductor 179, 181, 183, 185, 187, 189, 191, 193, 195, 197, 199, 201, 203, 205, 207
Optical properties of semiconductors 177, 238
Optical transmittance 180-1, 184, 188-9, 193-5, 197-8, 225, 234
  spectral characteristics of 193-6
Optoelectronic applications 34-5
Oscillations 63, 89, 153, 213-14
Oxidation, initial phase of 308-9
Oxide removal 90, 305-8
Oxides, p-layer/tin 138-9
Oxygen 38, 43, 46, 68, 109, 117, 127, 132, 198, 308-9, 388, 401, 415, 435
Oxygen impurities 108-9, 127

P

P-layer 40, 137, 377, 380, 382-3
P-type 11, 17, 41, 136, 280, 284-6, 289, 291-2, 295-6, 317-18, 324, 333, 339-40, 342-6, 380
P-type a-Si 11, 41, 283, 317-18, 324, 329, 336-7, 340, 343, 345-6
P-type a-SiC 17, 429
P-type c-Si 279, 318, 320, 329, 343
P-type-c-Si/i-a-Si 328, 453
P-type c-Si wafer 329, 448
P-type doping 102-3, 247, 294, 456, 461

P-type layer 376-7
P-type semiconductor 183, 266
P-type substrates 309, 342
Pairs, electron-hole 3, 6, 149-50, 368, 380, 397
Parallel plate plasma deposition 366-8
Parameter Initial Values 236-7
Parameters
  fitted 198, 203-4, 234-7
  geometrical 202, 205, 214, 219-20
  measured 260
  values of 21, 204, 219, 221, 233-5
Parameters of electron states 177-8
Parasitic resistances 3
Particles 13, 32, 62-3, 65, 180, 299-300, 302
Passivated Emitter solar cell (PESC) 436
Passivation 41, 286, 288-9, 292-3, 295, 305, 336-7, 400
Path 62, 171, 180, 280, 312, 339
Path difference 114-16
Path length, optical 396, 447, 461
Pauw geometry 243, 254-7, 264
PC 16, 182, 223-6, 234, 257, 457
PC responses 225-6
PD 455
Peak intensity 371, 405
Peak position 125, 129-32
Peaks 16, 115-18, 125-7, 137, 155, 157, 160-1, 167, 267-9, 283, 291-2, 312, 371-2, 404-5
PECVD solar cells 134
PECVD system 29, 36-7, 138, 140, 288, 403
PECVD technique 18, 23, 41, 364, 366
PEM effect 182-4, 222-3
PEM responses, ratio of 185
Performance 20, 103-4, 123, 157, 164, 166, 172, 177, 310, 324, 329, 332, 335, 436, 454
Permission 117, 126, 128-32, 134-9, 148-9, 152-4, 159-63, 165-8, 170, 172-3, 363, 374, 376, 381, 426-7
Phases 19-21, 109, 115, 125, 128-9, 187-92, 195-6, 201, 207-12, 214, 218, 290, 361, 397
  mixed 19, 21, 291
Phonons 118-19, 125, 180-1, 245, 250-1
  optical 118, 251-2
Photoconductivity 16, 18, 41, 43, 177, 182, 185, 216-17, 220, 224-6, 231, 235
Photothermal deflection spectroscopy (PDS) 20
Photogeneration 41, 177, 183, 216, 222
Photolithographic 436-7
Photolithography 339-40, 344, 432, 437-8, 454
Photolithography steps 336-7, 339, 342, 434-5
Photon energies 3, 16, 179, 183-5, 215-16, 225-7, 291, 295, 298, 374, 445
Photons 5-6, 10, 16, 61, 118, 147-8, 171, 177, 182-3, 185, 206, 209-10, 212, 218, 421

low-energy 104
scattered 118
Photovoltaic parameters 22, 322-3, 332, 335, 343-4, 460
Photovoltaics 24, 29, 34, 46, 81, 108, 140, 341, 359, 400-1
Physical properties 4, 9-10, 14, 19, 41, 43, 118, 244
Physical sputtering 58, 60, 79
Physical vapor deposition (PVD) 59, 79
Pitch 71, 104, 172, 341, 458
Plane 101, 160, 185-9, 191-2, 202, 209-10, 213-15, 217-19, 261, 403
Plasma 29-30, 32-5, 37-40, 42-4, 47, 49, 58, 60-2, 65-7, 70-1, 73, 315-17, 365-7, 382-3, 401-2
Plasma deposition 10, 29, 329
conventional 44, 366
Plasma enhanced chemical vapour deposition (PECVD) 3-4, 15-16, 18-19, 21, 23, 34-6, 40, 82, 133-4, 158-9, 166, 287, 317, 360, 398, 401-3, 454
Plasma etching 164-5
Plasma process 395
Plasma texturing 435, 441
Plasma treatment 277, 315
Plasmonic thin-film solar cells 466
Point defects 101, 250
Polarization 201, 204, 206, 213-15, 219-21, 235
Polarized radiation 185-9, 191-2, 203-4, 209-10, 213-15, 218-19
Powder, silicon polyhydride 38
Pressure 14, 18, 31, 33, 37, 69, 71, 73, 78, 83, 85, 257, 365-7, 373, 402
total 74-5, 82
working 315, 408-9
PRF 455
Probability 61-2, 71, 77, 228, 280, 421
Probes 147, 152-3, 257-9
Process temperatures, low 401-2
Processes
collision 61-2, 249-52
wet 435
Processing, based 436-7
Production system 29, 47, 50, 396
Properties, optoelectronic 39-40, 425
Protocrystalline 3, 18, 20
PV cells 271-3, 396
Pyramid structures, inverted 433
Pyramids 103, 304-6, 441
distributed 166, 303, 307-8
inverted 432-5, 438

Q

Quality

best microcrystalline solar cells 43
high 46, 48, 299, 408
Quantum dots 14, 81-2, 109, 173
Quantum Efficiencies 457
Quantum efficiency 177, 311, 313, 327, 395, 421
Quantum efficiency coefficients (QECs) 177, 183-4, 225

R

Radiation 109-12, 114, 116, 119, 177-8, 180, 185, 187, 189-93, 199-201, 204-18, 220-3, 225, 234-5, 237
absorbed 179, 184-5, 214
absorption of 207, 213, 216
interference of 210, 216, 218-19
perfect coherence of 190-1, 208
plane-polarized 205-6, 214, 217
reflected 192, 200-1, 205, 207, 209, 218
transmitted 177, 199
Radiation incidence 186, 192, 200, 203-4, 214-15, 221
Radiation incident 5, 206, 209-10, 218, 235, 238
Radiation intensity 185, 188, 200-1, 204-8, 210-14, 216-18, 220-1, 225, 234-5
spatial distribution of 177, 206-7, 211-13, 216, 219-21
Radiation of a-Si 181, 183-4
Radiation traversing, phase of 218
Radiation wavelength bandwidth 193-4
Radicals 37-8, 40-1, 79, 403
Radio frequency (RF) 21, 34-5, 38, 61-3, 66, 69, 76, 254, 260, 288, 363
Raman scattering 108, 118-21, 123, 133-4, 178
Raman signal 120-2
Raman spectra 125-6, 136-8, 140, 173
Raman spectra of samples 139
Raman spectroscopy 108-10, 119, 121-5, 127, 133, 135-6, 140, 169, 173
Raman spectroscopy apparatus 121-2
Raman spectrum 118, 372
Rate
electron emission 266
high 44-5, 47, 49, 69, 368
Rate window 268-70
Ratio 11, 14, 22, 24, 29, 66, 93, 112-14, 178-80, 185, 187, 212-15, 231-2, 235-6, 413-14
angular dependence of 232-3
Reaction 29-30, 32, 35, 281, 283, 306, 402-3, 439
Reactive sputtering 69, 74-5
Reactor 18, 32, 35-7, 44, 50, 402-3, 435
Rear side 218, 320, 322, 329, 333-4, 338, 341, 345-6, 348, 395-6, 416, 449, 451-2, 454-5
Rear side c-Si/a-Si 322
Rear side of HJ solar cell 322-3

Recombination 61, 66, 177, 222-3, 229, 234, 280, 285-7, 310, 324, 326, 330, 346-7, 404, 453-4
Reduction 22-3, 30, 39, 41, 44-5, 71, 109, 124, 137, 257, 283, 302, 307, 326, 442-3
Reevaporation 93-5
Reflectance 177, 188-90, 195-9, 208, 234, 345, 347, 385, 398-400, 410, 420-1, 437, 441-3, 448-52, 457
  average 435
  diffuse 180
Reflectance measurements 441-2
Reflectance profiles 398, 451, 455, 457
Reflectance values 432, 434, 455
Reflection coefficients 191-2, 195, 207-8
  value of front surface 207
Reflectivity 177, 204, 383, 434, 445-6, 461
Reflector 395
Refractive index 24, 177, 179, 186-7, 190-1, 194, 197-8, 201-2, 218-21, 397-9, 403-6, 411-12, 428-9, 449-51, 464-6
Refractive indices 177, 185-6, 190-2, 195, 198-9, 205, 418
Regime 95, 311, 363, 366
Regions 63-6, 73, 100, 115, 128, 134, 150, 216, 269, 294, 316, 322, 329, 345-6, 454-5
  infrared 116-17, 332, 450-2
  inhomogeneous 96
  visible 123-4
Remote Plasma Enhanced Chemical Vapour Deposition (RPECVD) 402
Resistance 8-9, 67, 108, 253-4, 257, 259, 271, 273
  shunt 8-9, 271-2, 310, 335
Resistivity 76, 243, 248-9, 253-4, 256-60, 262, 264, 271, 333-4, 338-9, 373, 383, 409-10, 413-15, 447
  values of 255, 333, 414
Resistivity measurements 255-6
Resolution 111-12, 115, 152-3, 155, 268
Resonance 121, 123, 464-5
RF-PECVD 36, 38, 43-4, 134
RF plasma power 435
RF power 36, 39, 48, 338, 365, 403, 415, 435-7, 454
RF power density 37-8
RF sputtering 69-70, 363
RHEED patterns 88-9
RIE (reactive ion etching) 79, 395, 435, 438, 441-2, 445-6
RIE processes 442-3
Rinsing 302, 305-6
Roll-to-roll 29
Room temperature 61, 84, 104, 109, 202, 233, 245-6, 300, 302, 306, 309, 315, 317, 345, 347
Roughness 146, 169, 408, 417, 419, 422, 426
Rs value 273

S

Sample
back-illuminated 201-2
investigated 203-4, 223, 234
nanostructured 171
parallel-sided 189, 223
Sample area 216, 327
illuminated 191, 218
Sample atom 58, 60
Sample border 255-6, 259, 264
Sample chamber 77
Sample dimensions 258-9
Sample geometries 254, 258-9
Sample parameters 184, 201, 208, 253
Sample resistivity 255-6, 258, 260, 264
Sample surface 153, 155, 169, 185, 192, 205, 214, 216-17, 253-4, 256-7, 264
rear semiconductor 212
Sample temperature 252, 298
Sample thickness 179, 213, 255, 264
effective 263
Saturation value 232, 289, 324
SC-1 301-2
SC-1 solution 301-2
SC-2 301-2
SC-2 solution 301-2
SC-values 374
Scanning electron microscopy (SEM) 146-9, 157-8, 163, 165-6, 408, 433-4, 438, 441
Scanning probe microscopy (SPM) 152, 301
Scattering 109, 118, 180, 188, 198, 250, 376, 395, 416, 422, 425, 428, 465
Scattering layer 465
Scattering mechanisms 244, 249-50, 252-3
Scattering process 118, 120, 250, 252
Screen 87-9, 148, 151, 334, 346, 458
Screen printing 277
Se2-based solar cells 379
Secondary electrons (SE) 63, 66, 147-9
Secondary electrons, generation of 64-5
Selected area electron diffraction (SAED) 159-60, 173
SEM images of hydrogenated silicon films 158
SEM images of textured c-Si surfaces 436
SEM pictures 419-20
Semiconductor devices 102, 238, 300, 434
Semiconductor film 81, 186, 191-3, 196, 205-10, 212-13, 216-21, 223-4, 231, 259
parallel-sided 205, 216
thin 186, 191-2, 215, 218-20
Semiconductor industry 32, 34, 68, 127

Semiconductor lattice 243
Semiconductor material conductivity 255
Semiconductor materials 5-6, 17, 177, 243-6, 249, 251-2, 257, 260, 265-6, 396, 454
Semiconductor parameters 234, 236
Semiconductor properties 243, 318
Semiconductor sample 223
Semiconductor-substrate 186, 217
Semiconductor surfaces 190, 207, 212-13, 220, 223, 257, 396-7
Semiconductor thickness 220, 359
Semiconductors 5-6, 34-5, 177-83, 185, 195, 205-23, 225-9, 231, 233-5, 237-8, 243-5, 247-9, 251-3, 261-3, 265-7
  polar 252
Series resistance 8, 271, 273, 311, 334-5, 383
Shadow 218, 220-1
Sheaths 39, 63-6
Sheet resistance 257-8, 383, 385, 406-7, 409
Short range order (SRO) 140, 373
Si atoms 281, 309
Si-based solar cells 104
Si films 11, 18
Si layers 10, 22-3, 103
Si-rich a-Si1-xCx 132, 136
Si-Si bonds, weak 281-2
Si solar cell fabrication 303
Si solar cells 12, 133, 307, 466
Si substrates 9, 171, 303, 308, 446, 449
Si surfaces 300-2, 306-9, 445
Side mirror 452, 454, 456
Signal-to-noise ratio 111-12, 121, 123-4
Silane 20-1, 23, 35, 135, 360, 363-4, 366, 388, 402
Silane concentration 134, 363, 366, 373-4
Silicon (hydrogenated) thin films 108
Silicon, etching of 439, 441
Silicon carbon (hydrogenated) thin films 108
Silicon films 16, 21, 23, 365
  annealed hydrogenated amorphous 170
  nanostructured 126
  thin 23, 173
Silicon layers 23, 45
Silicon nanocrystallites 108, 136
Silicon nitride 5, 300, 339, 398, 400-3, 405
Silicon oxide 173, 309, 401
Silicon oxide intermediate reflector (SOIR) 428-9
Silicon photovoltaics 277, 279, 281, 283, 285, 287, 289, 291, 293, 295, 297, 299, 301, 303, 305
Silicon samples 446
Silicon solar cell production 335

Silicon solar cells 381, 399, 401
Silicon substrates 159, 166, 307, 339
Silicon surface 164, 277, 287, 299, 317, 399, 410, 432, 438, 443, 446, 457
  textured 433-4, 445
Silicon thin films 15
Silicon wafers, multi-crystalline 432, 441, 443, 445
Simulation results 455, 457
Simulations 298, 315-16, 318, 320, 322-3, 329-30, 337-8, 343-4, 346-7, 398, 419, 422, 449, 451-3, 460
Single junction 45, 360-1, 377, 389, 429
Single junction solar cells efficiencies 44
SiO_2 films 301, 379, 401
Sites 101-2, 216, 251, 282
  potential defect 283-4
SnO_2 films 411-12
SOIR layers 428
SOIR thicknesses 429
Solar cell applications 146, 291, 368, 382, 406, 410
  amorphous crystalline heterojunction solar cell 412
Solar cell architecture 342
Solar cell characteristics 165
Solar cell conversion efficiency 163
Solar cell cost 278
Solar cell design 8
Solar cell development 29, 360
Solar cell devices 369
Solar cell efficiency 34, 164, 178, 272, 345, 395
Solar cell efficiency tables 23
Solar cell industry 431
Solar cell junction 9
Solar cell manufacturing 303
Solar cell manufacturing companies 278
Solar cell optimization 110
Solar cell parameters 272, 331
Solar cell performances 38, 45, 313, 364, 400, 410, 459
Solar cell process, reliable 435
Solar cell processing 401
Solar cell production 3, 33, 364, 382
  large scale 446
Solar cell production scale 46
Solar cell research 4, 140
Solar cell results, best 44
Solar cell simulation 20
Solar cell structure 21, 171, 177, 452, 464-5
Solar cell substrates 303
  p-type CZ Si 304

Solar cells 3-12, 16-18, 40-3, 45-6, 127-8, 133-5, 270-2, 359-61, 363-6, 373-4, 376-9, 381-3, 389, 395-7, 416-17
actual 272
all Si tandem 109, 129
amorphous/crystalline heterojunction 309
amorphous/crystalline silicon heterojunction 277
amorphous/microcrystalline silicon 362
based 277-8, 396, 406, 416
based multi-junction 158
based thin film 34-5
based thin films 147
best 388
building-integrated 379
complete 375
conventional 463
developing thin-film 10
effective HJ 291
efficient 16, 109
efficient photovoltaic 68
efficient terrestrial 10
fabricated 10, 129, 344
fabrication of 35, 108, 437, 455
finished 442
first thin-film silicon 361
flexible 164
forward biased 272
generation 127
hetero-junction 164
hetero-junction microcrystalline silicon 163
hetero-structure 454
heterojunction 277-9, 335, 452, 460
heterostructure 333, 455, 458
high efficiency 305
high efficiency mono-crystalline silicon 432
high efficiency pin 368
highest efficiency 454
hphP 135
hybrid 377
identical hetero-structure 454
illuminated 272
industrial silicon 396
intermediate band 104
junction 3-5, 271
large area 46
low-cost 382
low-cost stable 169

lplP 135
manufacture 41
micromorph 19
micromorph tandem 428
modern 171
most commercial 399
most efficient 366
multijunction 108, 137
nanocrystalline 374
new generation 136
obtained stable 374
optimized 463
prepared 364
producing 342
producing low cost 280
real 8
silicon-based 146, 171
silicon-based pin 377
silicon-based thin film 36
silicon-based thin-film 35
silicon-based thin films 146
single junction 361, 389
single-junction 381
stacked 39, 361
stacked quantum dot 83
state-of-the-art 368
tandem 9, 46-7, 359, 362, 386-7
test 309
texture multicrystalline silicon 438, 443
texture silicon 443
textured 172
thick 135
thin-film 10, 41, 361, 368, 380, 382, 410
thin-film amorphous silicon 377
thin film silicon 46, 172, 406
thin-film silicon 41, 140, 361, 380, 382, 385, 388
thin wafer 454
triple junction 109
triple junction amorphous Si 12
type 40, 43
type amorphous silicon 364
typical amorphous silicon 158
ultrathin amorohous silicon 172
very high efficiency 399
Solar cells parameters 108, 133
Solar cells performance 40, 270, 466

better 38
Solar cells processing 401
Solar cells structures 19
Solar energy mater & solar cells 140
Solid curves 186, 190, 193-5, 197-9, 203, 211-15, 225-6, 235-6
Source
field effect 147
ion 58, 60, 77
Source material 14, 59, 68, 82
Source spectrum 114
Spatial distribution of radiation intensity 211, 213
Specimen 147, 150, 152-3, 159
Spectra 111-13, 117-18, 125, 136, 154, 195, 224, 369, 372, 404, 447
Spectral range 111, 115, 124, 182, 197, 422, 445, 455-6
Spectrometer, dispersive 113, 121
Spectroscopy
dispersive 111-13
infrared 108-10
Spectrum 8, 109-12, 114-17, 125, 129, 136-7, 155, 179-80, 182, 195, 267, 272-3, 372, 398, 446
Sphere 61, 417, 423
Spherical 61, 157, 168-9
Sputtered ITO resistivity 334, 415
Sputtering 3, 10, 14, 58-9, 61, 67-9, 73-5, 77-9, 382-3, 402, 408
Sputtering process 58, 60, 69, 73, 76-7, 408, 415
Sputtering systems 70, 73, 75, 412, 454
Sputtering techniques 58, 72, 75-6, 79
SPV measurements 298, 304-5
SSPG measurements 217, 221, 225, 233-4, 236-8
SSPG method 219-21, 226
SSPG results 232-4
Stability 38, 108, 308-9, 335, 374
Stacked cell 3
Stacked layers 4, 293, 454
Stacked structure 21, 293, 315, 318, 454, 457
Stacking faults 99-100, 250, 370
Stacks 287, 293, 344, 359, 387-9, 451, 461
Stainless steel 35-6, 157, 364, 379, 383, 416
Standard effusion cells 84
STAR solar cell 381
States 16-17, 30, 63, 78-9, 184, 227-30, 237, 245, 252, 280-2, 285-6, 304, 307, 314, 403-4
charged 17, 285-6
density of 3, 16-18, 20, 227, 281, 286-7, 296, 307, 312, 346, 376, 453
effective density of 228, 267, 381
empty 245, 247
trap 265, 267, 288
Steady state photocarrier grating (SSPG) 177, 216-17

Sticking coefficient 93
Strain 96-7, 104, 157
Stress 32, 34, 75-6, 157, 454
Stretching modes 117, 127-9, 404
Structural changes 110, 129
Structural characterisations 146
Structural properties 19, 108-9, 146-7, 149, 151, 153, 155, 157, 159, 161, 163, 165-7, 169, 171, 173
Structures
  basic 157, 395
  diode 266-8
  electronic 162, 359, 403
  fragmented island 13
  interdigitated 336, 346
  layered 23, 386
  periodic 429
Substrate 13-15, 18-19, 22-4, 34-6, 38-40, 47-8, 50-1, 59-60, 76-7, 81-2, 84-5, 92-9, 136-8, 365-7, 378-9
  etched 305
  flat 430
  flexible 53, 164, 364, 379, 416
  insulating 65-6, 259, 378
  opaque 377, 379
  polycarbonate 429-30
  semi-insulating 257-9, 263
  textured 164-5, 305, 308, 310, 361, 424
  thick 192, 200-2, 204, 209, 214, 218
Substrate configurations 305, 383
Substrate designs 379
Substrate material 162, 359, 388-9
Substrate resistivity 259, 330, 343
Substrate surface 13, 22, 32, 39, 79, 83, 94, 96, 165, 299, 309, 370, 402
Substrate temperature 14, 29, 37-8, 89, 92-3, 160-1, 163, 167, 291, 315, 324, 365, 382, 384, 413-14
  given 92
  low 38, 43, 45, 68
Sunlight 4, 279, 119, 323, 362, 365, 378, 395
Sunlight exposure 313, 317, 320-1, 332, 335
Surface, rough 179, 191, 304, 307-8, 416-17, 419, 422
Surface atoms 58, 60, 90-1
Surface conditioning 300, 305-7
  wet-chemical 305
Surface morphology 163-5, 169, 299, 305, 308-9, 424, 426
Surface passivation 307-8, 338, 348, 442, 452, 454, 456
Surface photovoltage 165, 297-8
Surface reconstruction 81, 84, 89-90
Surface temperature 93-5

T

Ta, annealing temperature 130-2
TAC 408-9, 425-7
Tails 16, 182, 230, 281-2
  exponential 181, 229, 231
Tandem cell layers 428
Tandem cells 4, 157, 164, 386-7, 389, 428-9
Target atoms 58, 60
Target surface 58, 60, 70, 73, 75, 77
TCO films 162, 332, 382-3, 385-6, 407
TCO layer 378, 382, 385, 422
TCO material 332, 382-3
TCO/p-a-Si 333
TCO work function 333
Techniques
  experimental 14, 119, 243
  isotexturing 441
TEM images 152, 158-9, 167
Temperature
  higher 251, 290, 293, 334
  lower 290, 293, 295
Temperature coefficient 332
Temperature dependence 250-1, 332
Texture 79, 146, 154, 303, 425, 432, 435, 437, 443, 446
Textured c-Si surfaces 436-7
Textured surfaces 171, 299, 305-6, 308, 338, 382, 408, 417, 419, 435, 437, 441-3, 445
Texturing 24, 164, 277, 299, 303, 317, 395-7, 416, 429, 431, 435, 441, 443, 463
Texturing process 303, 305, 435, 442, 446
Texturing technique 416, 437
Theory 108, 110, 113, 119, 283, 396
Thermal annealing 108, 127, 129-30, 133, 136, 287-8, 290-1, 337
Thermal annealing time 288-9, 334
Thermal budget 278, 364, 366
Thermodynamics 13, 30
Thickness 19, 167-9, 185-6, 211-13, 220-1, 318-19, 321-4, 359-60, 387-9, 396-9, 408-10, 412-13, 449-54, 459-61, 464-6
  actual 24
  effective 22, 24
  epilayer 97
  equal optical 399
  evaluated 451-2
  finite 88-9
  largest 168-9
  parallel-sided substrate of 191, 208, 223
  silicon wafer 277, 460

wafer base 460-1
Thin film cells 277, 279, 395-6, 400, 407, 410, 416
Thin film geometry 155-6
Thin film hydrogenation 3
Thin film layer growth 305
Thin film silicon 3, 166
Thin film solar cells 3-5, 7, 9, 11, 13, 15, 17, 19, 21-3, 35, 39, 50-1, 140, 417, 425-6
Thin film solar cells technology 46
Thin film structures 3, 166
Thin film technologies 10, 396, 459
Thin-film technologies 359-60, 362
Thin-film thickness 193
Thin films 3-4, 10, 12-16, 37-9, 45-9, 58-61, 67-9, 81, 108-9, 146-7, 159-61, 193-5, 199-204, 209-11, 257-9
based 36, 108
deposited 76
doped 21
producing 46
un-doped 447
Thin films a-Si 48
Thin films epitaxial growth 87
Thin films solar cells 3
Thin layer 5, 81, 259, 300, 323, 329, 397
Thin Silicon Solar Cells 4, 23, 207, 395, 397, 399, 401, 403, 405, 407, 409, 411, 413, 415, 417
Thin solid films 238
Thinner 96-7, 288, 297, 379, 387, 460
Thinner silicon wafer 277, 396, 416, 431, 458
Thinner wafers 10, 396, 431, 459-60
Throughput, silicon solar cell processing 401
Top cell 39, 46, 361, 387-9, 428
Total energetic spectrum of electronic states 237
Transfer, local energy 61
Transfer function 62
Transparent conductive oxide (TCO) 395
Transient 265, 267-9
Transition 15, 19, 21, 43, 131-3, 252, 368-9, 374, 381, 426
Transmission electron microscopy (TEM) 109, 146-7, 150-2, 157, 166, 369-70, 455
Transmission, energetic 191-2
Transmittance 177, 180, 190, 195-6, 199, 208, 224, 334, 385, 406, 410, 414-15, 418, 420, 425
effective 333-4, 414-15
theoretical 197-8
Transparent substrate 204, 211, 213, 217-18, 378-9
thick 211-12
Traversing 188-9, 191-2, 196, 208, 210
Treatment temperature 302
TTC 162-3

Type a-Si 318

U

U-shaped electrode 49, 51
Ultra-violet (UV) 121, 123, 125, 404
Ultra high vacuum (UHV) 46, 82
Uncertainties 16, 82, 190-1
Undoped a-Si 283, 296

V

Vacuum system 33, 36, 82, 84
Valence band 6, 17, 102, 215, 228-30, 245, 251, 265, 280-1, 295, 297, 312, 318, 321, 329
Valence band edge 295-6, 304, 307, 403-4
Valence band offset 320-1, 346, 453
Values
  curve 202, 208
  evaluated 183, 185
  fitted 204, 236
  higher 19, 44, 252, 259, 305
  ideal 271
  low 134, 203-4
  measured 255-6
Vapor deposition 29
  chemical 29, 31, 359
  plasma-enhanced chemical 140, 287
Variable angle spectroscopic ellipsometry (VASE) 189
VBM 294-5
Very high frequency (VHF) 23, 36, 38, 48, 166, 366, 377, 403
VHF-PECVD 38-9, 44, 47, 361
VHF plasmas 44, 47, 366
Voc of silicon solar cells 381
Voc values 291, 322, 329
Voids 164, 166, 254, 297, 363-4
Voltage 4, 8-9, 35, 63, 69, 73, 77, 154, 222, 249, 254-5, 257-8, 263, 271-3, 323
Voltage distribution, non-uniform 47
Voltage sweep 272-3
Voltage values 264, 273
Voltmeter 255, 257-8

W

Wafer surface 293, 300, 302-3, 432, 439
Wafer thickness 460
Wafers 3, 10, 90, 300-3, 305-6, 317, 329, 340-1, 344, 346, 396, 434, 441-2, 454-5, 459-60

as-cut 303-4, 439, 441
textured 304, 441-2
thin 395, 452, 454, 459
Wavelength range 191, 217-18, 385, 408, 421-2, 425, 461, 464
Wavelengths 109-11, 115-16, 122, 130, 151, 189-91, 196-8, 210-11, 214, 234-6, 362, 385, 397-400, 445-8, 450-1
function of 421-2, 455
Wavenumber 109-11, 114, 117, 130
higher 117, 131-2
Waves 115, 178, 188, 206, 397
steady light 210, 212, 220-1
Wet-chemical smoothing 299, 306, 308
Window layer 40, 317, 361, 377-8, 382, 416, 429
Work function 147, 321-2, 335

X

X-rays 151, 154-5
X-ray diffraction (XRD) 109, 132-3, 146-7, 154, 157-8, 160, 166-7, 169, 173, 369

Z

ZnO films 382, 407-9, 425-7
ZnO layers 409, 420, 428-9